S.S.R Kumar Challa (Ed.)

Chemistry of Nanomaterials

Also of interest

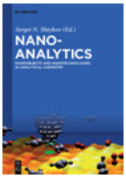

Nanoanalytics
Nanoobjects and Nanotechnologies in Analytical Chemistry
Shtykov (Eds), 2018
ISBN 978-3-11-054006-2, e-ISBN 978-3-11-054024-6

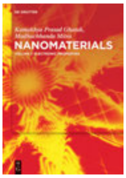

Nanomaterials
Volume 1: Electronic Properties
Ghatak, Mitra, 2018
ISBN 978-3-11-060922-6, e-ISBN 978-3-11-061081-9

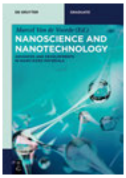

Nanoscience and Nanotechnology
Advances and Developments in Nano-sized Materials
Van de Voorde (Ed.), 2018
ISBN 978-3-11-054720-7, e-ISBN 978-3-11-054722-1

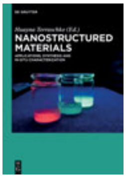

Nanostructured Materials
Applications, Synthesis and In-Situ Characterization.
Terraschke (Ed.), 2019
ISBN 978-3-11-045829-9, e-ISBN 978-3-11-045909-8

Physical Sciences Reviews.
e-ISSN 2365-659X

Chemistry of Nanomaterials

Volume 1: Metallic Nanomaterials (Part A)

Edited by
S.S.R Kumar Challa

DE GRUYTER

Editor
Dr. S.S.R Kumar Challa
Harvard University
Integrated Mesoscale Architectures for Sustainable Catalysis (IMASC)
Rowland Institute of Science
100 Edwin H. Land Blvd
Cambridge MA 02142
USA
challa@fas.harvard.edu
challakumar@gmail.com

ISBN 978-3-11-034003-7
e-ISBN (PDF) 978-3-11-034510-0
e-ISBN (EPUB) 978-3-11-038382-9

Library of Congress Control Number: 2018958583

Bibliographic information published by the Deutsche Nationalbibliothek
The Deutsche Nationalbibliothek lists this publication in the Deutsche Nationalbibliografie; detailed bibliographic data are available on the Internet at http://dnb.dnb.de.

Typesetting: Integra Software Services Pvt. Ltd.
Printing and binding: CPI books GmbH, Leck
Cover image: Science Photo Library / Ella Maru Studio

www.degruyter.com

Contents

He Huang, Hendrik du Toit, Luca Panariello, Luca Mazzei
and Asterios Gavriilidis

Jiangwei Zhang, Zhimin Li, Kai Zheng and Gao Li

List of contributing authors

Samuel E. Lohse
Physical and Environmental Sciences
Program, Chemistry
Colorado Mesa University
Grand Junction
CO 81501, USA,
slohse@coloradomesa.edu
Chapter 1

Volker Hessel
EC&MS Research
University of Adelaide
Engineering North Building
Adelaide SA 5005 Australia
volker.hessel@adelaide.edu.au
Chapter 2

Sergey A. Starostin
Tilburg Research Labs
FUJIFILM Manufacturing Europe
B.V, P.O.Box 90156
Tilburg, The Netherlands
Chapter 2

Liangliang Lin
Micro Flow Chemistry
and Process Technology
Chemical Engineering and Chemistry
Department
Eindhoven University of Technology
P.O. Box 513
5600 MB Eindhoven, The Netherlands
Chapter 2

Sirui Li
Micro Flow Chemistry
and Process Technology
Chemical Engineering and Chemistry
Department
Eindhoven University of Technology
P.O. Box 513
5600 MB Eindhoven, The Netherlands
Chapter 2

José Solla-Gullón
Institute of Electrochemistry
University of Alicante,
Apdo. 99
Alicante E-03080, Spain,
jose.solla@ua.es
Chapter 3

Leticia García-Cruz
Institute of Electrochemistry
University of Alicante,
Apdo. 99
Alicante E-03080, Spain,
Chapter 3

Vicente Montie
Institute of Electrochemistry
University of Alicante,
Apdo. 99
Alicante E-03080, Spain,
Chapter 3

Asterios Gavriilidis
Department of Chemical Engineering
University College London
Torrington Place
London WC1E 7JE, UK,
a.gavriilidis@ucl.ac.uk
Chapter 4

He Huang
Department of Chemical Engineering
University College London
Torrington Place
London WC1E 7JE, UK,
Chapter 4

Hendrik du Toit
Department of Chemical Engineering
University College London
Torrington Place
London WC1E 7JE, UK,
Chapter 4

https://doi.org/10.1515/9783110345100-201

Luca Panariello
Department of Chemical Engineering
University College London
Torrington Place
London WC1E 7JE, UK,
Chapter 4

Luca Mazzei
Department of Chemical Engineering
University College London
Torrington Place
London WC1E 7JE, UK,
Chapter 4

Gao Li
State Key Laboratory of Catalysis, Dalian
Institute of Chemical Physics
Chinese Academy of Sciences (CAS)
Dalian 116023, China
gaoli@dicp.ac.cn
Chapter 5

Jiangwei Zhang
State Key Laboratory of Catalysis, Dalian
Institute of Chemical Physics
Chinese Academy of Sciences (CAS)
Dalian 116023, China
Chapter 5

Zhimin Li
State Key Laboratory of Catalysis, Dalian
Institute of Chemical Physics
Chinese Academy of Sciences (CAS)
Dalian 116023, China
Chapter 5

Kai Zheng
State Key Laboratory of Catalysis, Dalian
Institute of Chemical Physics
Chinese Academy of Sciences (CAS)
Dalian 116023, China
Chapter 5

Samuel E. Lohse

1 Size and shape control of metal nanoparticles in millifluidic reactors

Abstract: Engineered metal nanoparticles (metal NPs) possess unique size-dependent optical and electronic properties that could enable new applications in biomedicine, energy generation, microelectronics, micro-optics, and catalysis. For metal NPs to make a mark in these fields, however, new synthetic strategies must be developed that permit NP synthesis on the kilogram scale, while maintaining precise control over NP physiochemical properties (size, shape, composition, and surface chemistry). Currently, NP batch syntheses produce product on the milligram scale and rely on synthetic strategies that are not readily amenable to scale-up. Flow reactor systems (including lab-on-a-chip devices) provide a synthesis platform that can circumvent many of the traditional limitations of batch-scale NP syntheses. These reactors provide more uniform reagent mixing, more uniform heat transfer, opportunities to interface *in situ* monitoring technology, and allow product yield to be scaled up simply by running multiple reactors in parallel. While many NP syntheses have been successfully transferred to *microfluidic* reactor systems, microfluidic reactor fabrication is time intensive and typically requires sophisticated lithography facilities. Consequently, *millifluidic* flow reactors (reactors with channel dimensions of 0.5–10.0 mm) are gaining popularity in NP synthesis. These millifluidic reactors provide many of the same synthetic advantages as microfluidic devices, but are simpler to construct, easier to reconfigure, and more straightforward to interface with *in situ* monitoring techniques. In this chapter, we will discuss the progress that has been made in developing millifluidic reactors for functionalized metal NP synthesis. First, we will review the basic wet-chemical strategies used to control metal NP size and shape in batch reactors. We will then survey some of the basic principles of millifluidic device design, construction, and operation. We will also discuss the potential for incorporating *in situ* monitoring for quality control during synthesis. We will conclude by highlighting some particularly relevant examples of millifluidic metal NP synthesis that have set new standards for metal NP size, shape, and surface chemistry control.

This article has previously been published in the journal *Physical Sciences Reviews*. Please cite as: Lohse, S. E. Size and shape control of metal nanoparticles in millifluidic reactors. *Physical Sciences Reviews* [Online] **2018**, 3. DOI: 10.1515/psr-2017-0120

https://doi.org/10.1515/9783110345100-001

Graphical Abstract:

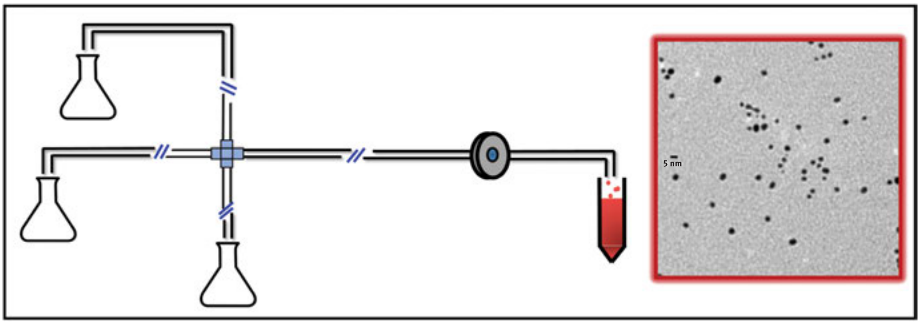

Keywords: nanomaterials, millifluidic synthesis, flow synthesis, nanoparticle, microreactor

1.1 Introduction

The past few decades have brought sustained interest in the size-dependent electronic, optical, catalytic, and biomedical applications of engineered metal nanoparticles (NPs with crystalline cores composed of one or more metallic elements) [1–8]. Engineered metal NPs are now components of thousands of consumer products that exploit their unique properties. Demand for nanotechnology-enhanced consumer products (e. g. Li-Ni-Co battery materials for electric cars) is only expected to grow in the coming years [9–13]. Nevertheless, controlled and reproducible metal NP synthesis, particularly at or above the gram scale, remains a challenge [2–4, 12–15]. Despite several decades of extensive research into the synthesis of metal NPs, most functionalized metal NPs are still prepared using low-yield (milligram-scale) synthetic methods, which are not readily amenable to scale-up [15]. For nanotechnology to truly achieve industrial relevance, kilogram-scale quantities of metal NPs with precisely controlled physiochemical properties (size, shape, composition, and surface chemistry) will be required (Figure 1.1) [2–4, 12, 13] [14, 15].

While scaling up many chemical reactions seems conceptually simple, increasing the scale of a typical metal NP synthesis represents a chemical engineering challenge [12–16]. The size and shape of a metal NP produced during synthesis is generally controlled though a carefully selected (and often synergistic) combination of reagent concentrations, pH, reaction temperature, and reaction time. Therefore, increasing reactant concentration in the reaction mixture (or even the total volume of the reaction) may significantly alter the rates of reagent diffusion and thermal transport, leading to loss of control over product properties [12–16]. Because increasing reagent concentration or reactor size typically leads to reduced product quality,

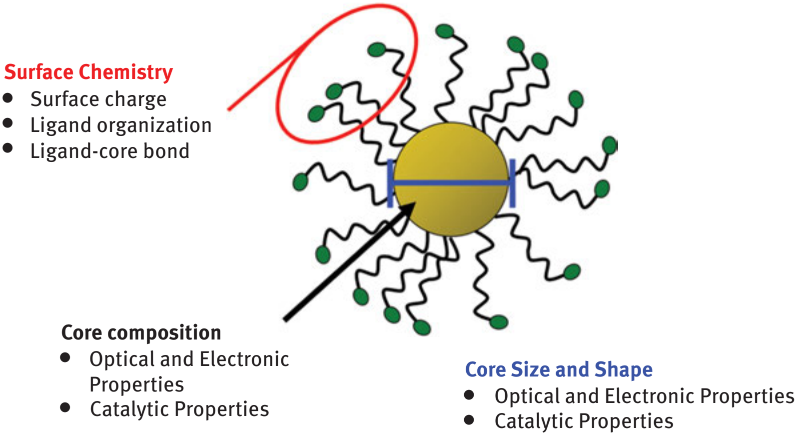

Figure 1.1: Schematic diagram of a “typical” engineered metal NP. The size and shape-dependent optical and electronic properties of the metal NPs result from the size, shape, and composition of the metal core. Organic capping agents (ligands) are bound to the surface of the metal core, providing the interface through which the NP interacts with its environment.

many researchers have instead taken the opposite approach, miniaturizing NP syntheses by transferring them to flow reactors [14–16]. In a flow reactor, reagent streams are mixed on extremely small (sub-millilitre) scales, but through continuous reactor operation, or running multiple reactors in parallel, engineered NPs can actually be prepared on above the gram scale, without losing control over NP physiochemical properties [12–20].

In addition to a viable route to scale-up, nanomaterial synthesis in flow reactors has recently shown the potential to provide superior control of NP size and shape and improved reproducibility compared to batch synthesis methods [12–16, 20–28]. As a result, NP synthesis using flow reactors has piqued the interest of many nanotechnology researchers. A general movement towards flow synthesis, however, particularly in academic research settings, has been relatively slow. Chemists have a certain bias towards batch reactor synthesis. From their earliest chemistry laboratory experiences, most chemists become used to running chemical reactions in flasks. Despite the comforting familiarity of batch synthesis techniques, chemical synthesis in flow reactors (e. g. microfluidic synthesis devices, lab-on-a-chip (LOC) devices) or capillary flow reactors) has already become the industry standard for all kinds of reagent-grade chemicals, both organic and inorganic [12, 13] [14–19]. Flow reactors are typically equipped with much smaller reaction channels (micron scale) than batch reactors (a typical 250 mL round-bottom flask has a mixing diameter of ~70 mm). Reduced channel dimensions allow for much more rapid reagent mixing during synthesis, more efficient heat transport, as well as the opportunity to interface in-line monitoring for quality control purposes [12–20, 29–33]. Therefore, flow synthesis provides a platform that facilitates high-throughput synthesis with less wasted material and a facile engineering strategy for reaction scale-up. LOC systems have been particularly widely investigated in this regard; over the past decade, microfluidic reactors have been employed in the synthesis of quantum dots, metal NPs, and polymeric NPs with a wide variety of sizes and shapes [20,–28].

One of the best-known automated high-throughput microfluidic NP synthesis reactor systems is Workstation for Automated Nanomaterials Discovery and Analysis (WANDA), available at Berkeley National Laboratories, which was developed and made available to users early this past decade[20]. WANDA is a fully automated synthesis reactor, with *in situ* absorption and photoluminescence *in situ* monitoring capabilities for real-time NP characterization. WANDA employs a microfluidic mixing system, which ultimately deposits completed NP solutions into a 96-well plate reader for high-throughput characterization. WANDA has been used for the synthesis of various inorganic nanocrystals, including cadmium selenide quantum dots and upconverting luminescent sodium yttrium fluoride ($NaYF_4$) NPs [20]. The extensive automation of the WANDA system has been shown to provide exceptionally high reproducibility in the synthesized core diameters of the NPs (0.2 % coefficient of variation in d_{core} from batch to batch). This system also shows great promise as a tool for NP synthetic method development, as the effect of simple reaction parameters (such as reagent concentration, reaction time, and temperature) on NP core diameter can be quickly quantified. By combining high-throughput synthesis with high-throughput characterization, WANDA provides a platform to quickly and easily optimize synthetic NP methods, including the development of quantitative models and working curves to guide precisely controlled NP synthesis methods. This reactor system has led to the development of high-quality, photobleaching-resistant $NaYF_4$ NPs (available in a variety of core shapes) that have recently been used in single-molecule biotracking studies [20, 34, 35].

While the benefits of automated synthesis reactors like WANDA are obvious, the development of such finely engineered NP synthesis reactors requires extensive initial investment (both in money and in time) to achieve the level of automation necessary for such precisely controlled NP synthesis [11, 16, 29]. Even the design and fabrication of relatively simple microfluidic reactor systems (for our purposes, we will define microfluidic devices as reactors with channel dimensions smaller than 500 μm) for NP synthesis is expensive, and may be beyond the means or expertise of many smaller NP research laboratories. Buying pre-fabricated microfluidic chips is always an option, but even relatively simple pre-fabricated microfluidic devices are expensive [29]. Even a very rudimentary microfluidic device composed of a common polymer and generic mixer geometry may cost upwards of $100 per chip [29, 36]. Furthermore, microfluidic NP reactor systems remain relatively low throughput (on a per-device basis), and the materials comprising the reactor must be carefully selected to avoid NP aggregation and subsequent reactor fouling during synthesis [11, 16, 29]. If a pre-fabricated microfluidic device fouls, the entire reactor chip must be discarded, and a brand-new chip must be fabricated or purchased. Consequently, a *new* option for NP flow synthesis, millifluidic (also called “capillary flow” or “mesofluidic”) reactors, possessing channel dimensions of 0.50–10.0 mm, are increasing in popularity because they provide many of the advantages of a microfluidic reactor system while reducing fabrication time and cost [11, 15, 16, 29, 31, 37, 38].

Millifluidic reactors encompass a variety of synthetic reactor designs, with the primary point of commonality being that the width of the fluid channels is on the millimetre, rather than the micron scale [11, 15, 16]. While this means that mixing rates and heat transfer in millifluidic reactors are typically measurably slower than they would be in microfluidic reactors, millifluidic reactors offer improved convenience in other key areas. First, millifluidic reactors can often be assembled from commercially available tubing or capillary components, and thus, the reactors are highly modular. They can be re-designed on the fly to support the synthesis of a variety of different NPs, since they do not need to be pre-fabricated. Similarly, if reactor fouling occurs, often only a single commercially available piece of the reactor (such as a polytetrafluoroethylene (PTFE) t-mixer) needs to be replaced, rather than discarding a whole reactor chip. Some millifluidic devices do contain pre-fabricated chips, but since the reaction channels are larger than a microfluidic device, fabrication of a millifluidic chip is typically more straightforward [11, 15, 16, 29]. The basic design of a millifluidic reactor is easy to envisage, as they consist of only four fundamental parts: reagent stock lines, a mixer, connecting tubing, and a collection vessel. The millifluidic reactor can also easily be interfaced with a wide variety of *in situ* characterization methods, including absorbance spectroscopy, fluorescence spectroscopy, X-ray absorbance spectroscopy (XAS) and small-angle X-ray scattering (SAXS) [11, 15, 16, 29, 39]. Often, the *in situ* characterization interface is even simpler to achieve in a millifluidic reactor than a microfluidic device, due to the millifluidic channel’s larger diameters [11, 39]. While a millifluidic reactor may be driven by something as simple as a peristaltic pump, most millifluidic systems are typically driven by syringe pumps and may feature mixing geometries that enable segmented-flow operation. A “typical” millifluidic reactor is diagrammed in Figure 1.2.

Table 1.1 provides a quantitative comparison of the physical dimensions and performance specifications of a typical millifluidic reactor (0.760 mm channel diameter, 4.5 m in length), compared to a batch reactor (250 mL round-bottomed flask, RBF), and a microfluidic reactor (0.250 mm channel diameter, 532 mm length). The millifluidic reactor and microfluidic device, in this case, have mixing diameters that are on the same order of magnitude. While the surface area: volume ratio of the microfluidic device is larger than the millifluidic device (by about 3-fold), both have greater than 100× the surface area:volume ratios of a batch reactor. This leads to faster mixing and faster heat dissipation in flow reactors. Perhaps most powerfully, all flow reactors provide an opportunity to interface *in situ* monitoring with the reactor, at specific residence times, providing a means to monitor NP product quality

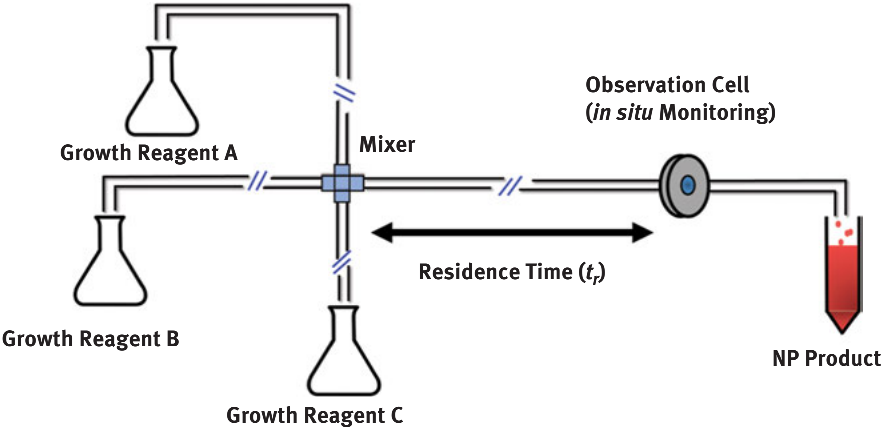

Figure 1.2: Diagram of a characteristic millifluidic NP synthesis reactor.

Table 1.1: Comparing the mixing properties of batch, millifluidic, and microfluidic reactors.

	Batch reactor	Millifluidic reactor	Microfluidic reactor
Mixing dimensions (mm)	76	0.760	0.250
Surface area/volume (mm^{-1})	0.0792	5.30	16.0
Reactor material	Pyrex glass	PTFE tubing, capillary tubing	PDMS, polycarbonate, glass
Mixing type	Vortex stirring	Laminar flow, segmented flow	Laminar flow, segmented flow, turbulent mixing
Fluid throughput (mL/min)	–	60.0	0.150
In situ monitoring	none	Absorbance spectroscopy, fluorescence spectroscopy, SAXS, XAS	Absorbance spectroscopy, fluorescence spectroscopy

Surface area:volume ratio based on a 250 mL RBF (76 mm diameter), millifluidic reactor with interior diameter (ID): 0.760 mm, channel length: 4,500 mm; microfluidic reactor with ID: 0.250 mm, channel length: 532 mm. PTFE, polytetrafluoroethylene; PDMS, polydimethylsiloxane.

in real time, resulting in less wasted solutions, and a viable strategy for high-throughput synthesis optimization [11–16, 29, 37].

Examples of NP flow synthesis can be identified at least as far back as 2002, and the use of small-channel reactors for more efficient chemical synthesis has been reported since the early 1990s; however, millifluidic reactors have only recently beenwidely embraced as an alternative to batch synthesis in the NP synthesis community (Figure 1.3). Within the NP synthesis community, a formal distinction

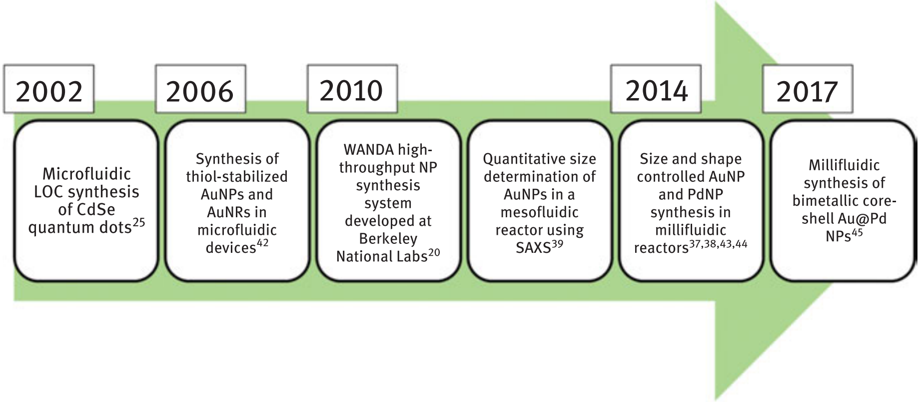

Figure 1.3: Timeline of selected accomplishments in NP flow synthesis.

between microfluidic and millifluidic reactors has not truly been drawn, although arguments can be made that significant changes in fluid mixing behaviour occur between channel dimensions of <500 µm and >500 µm [11, 16, 37]. For the purposes of this chapter, we will consider any reactor with reaction channel diameters between 0.500 mm and 10.00 mm to be “millifluidic” reactors, but we do note that among the reactors highlighted in this chapter, some are classified by their developers as “mesofluidic ” or “capillary flow ” reactors [11, 16, 37]. Partially due to the lack of a hard-and-fast technical distinction between microfluidic and millifluidic systems, while many reviews on microfluidic NP or general reviews of NP flow synthesis can be found, no comprehensive treatment of millifluidic synthesis yet exists (to our knowledge) [11, 15, 16]. Indeed, a 2018 database search for “Nanoparticle Millifluidic Synthesis” returns only 18 total results [40]. Despite this, millifluidic NP synthesis, as a field, has generated significant research interest, as evidenced by the fact that many of the most prominent metal NP synthesis researchers have experimented with millifluidic synthesis in the past few years. This research has already led to several notable examples of millifluidic reactors providing access to precise and reproducible NP size and surface chemistry control that have yet to be realized in either batch synthesis or microfluidic NP synthesis (Figure 1.3) [37, 41]. Because effective millifluidic reactors can be assembled from low-cost, modular components, NP synthesis in millifluidic environments is now open to an unprecedented number of researchers, and the millifluidic synthesis field is poised to expand significantly in the coming years. We hope that this review will provide a compelling and comprehensive entry point into the millifluidic synthesis field for researchers looking to design their own reactors for NP synthesis.

In this chapter, we will provide a detailed review of the key strategies used to achieve size and shape control in the millifluidic syntheses of metal NPs. For the purposes of this chapter, we will focus primarily on noble metal NPs (Ag, Au, Pt, and PdNPs), as the flow synthesis of these metal NPs has generally received the most research attention [11, 37–39, 41, 43, 44]. We will make references to the synthesis of other transition metal NPs where appropriate, but we would recommend that interested readers consult the reviews listed here for a deeper perspective on the synthesis of other functionalized metal NPs [45–49]. We will start with the basic strategies for NP size, shape, and surface chemistry control used in batch synthesis, followed by a review of the general approaches to millifluidic reactor design and construction. We will next highlight some recent advancements in basic reactor design, specifically the design of continuous versus segmented-flow reactors. We will also survey the various types of engineered NPs that have been successfully synthesized in millifluidic reactor systems, paying special attention to cases in which significant advances in NP size, shape, composition, or surface chemistry control have been achieved versus batch synthesis. We will also delineate the types of instrumental techniques that have been incorporated into millifluidic reactors for *in situ* product monitoring. We will conclude by drawing attention to some of the most pressing challenges that millifluidic NP synthesis faces as a field.

1.2 Batch metal nanoparticle synthesis in solution

1.2.1 General strategies in size control for functionalized metal NP synthesis

Metal NPs can be synthesized in batch using a diverse array of synthetic procedures; however, wet-chemical synthesis based on metal ion reduction reactions is now the most common synthetic approach [45–49][50] [51] [52] [53–56]. Traditional metal NP syntheses (dating back several decades) include synthesis by vapour deposition, templated electroplating, reduction by hydrogen gas, and physical milling methods [45, 55, 56] [57–59]. For most metal NPs, wet-chemical syntheses offer improved convenience, faster reactions, and improved physiochemical property control. Today, wet-chemical synthesis methods are available for a wide array of metal NPs, including Cu, Ag, Au, Pt, Pd, Ir, Co, and FeNPs (among others) [45–50] [51–64]. Anisotropic (non-spherical), bimetallic, and core-shell metal NPs can also be prepared for most metals by relatively straightforward solution chemistry [52–60, 64, 65]. Most of these wet-chemical syntheses involve the same basic chemical process; an ionic compound of the desired metal (such as $HAuCl_4$, H_2PdCl_4, or $Fe(CO)_x$) is dissolved in an appropriate solvent, and then reduced in the presence of a capping agent (a passivating organic molecule, polymer, or ligand) to give the metal NPs [45, 51, 60, 64]. The general form of these synthetic schemes is shown in Figure 1.4. These wet-chemical batch procedures are typically adapted with minimal modification for synthesis in flow reactors [11, 22, 37].

The exact chemical strategy used in a wet-chemical metal NP synthesis primarily depends on two factors: which metal element forms the NP core and the desired

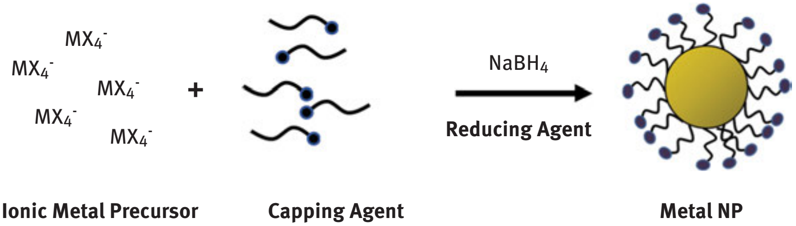

Figure 1.4: Basic reaction scheme for the synthesis of metal NPs.

size or shape of the metal NP (although the surface chemistry of the NP is also an important point of consideration in synthetic design) [45, 51, 55, 64]. The reduction of the metal ion precursor is accomplished by the addition of a reducing agent (such as sodium borohydride or ascorbic acid), thermal decomposition of reactants, or irradiation with UV light [45, 49, 55, 64, 65]. Following the reduction of the metal ion to metal atoms, the formation of the NP is then thought to occur through an analogous process to LaMer 's colloidal sulfur growth model: nucleation (formation of a small metal NP crystal from metal atoms), monomer growth (addition of metal atoms to the crystalline nuclei), and finally, passivation (cessation of crystal growth either due to exhausting the growth monomer or formation of a small molecule organic layer on the crystal's surface) [45, 59, 60, 66–69]. While many wet-chemical metal NP synthesis strategies were ultimately developed through extensive empirical testing, the synthetic strategies used for shape control are generally rationalized by analogy to the LaMer mechanism. In truth, metal NP growth probably occurs by a mixture of multiple possible growth pathways in a single synthesis (e. g. the aggregation of nuclei may provide an alternate growth pathway to NP growth by monomer addition) [68, 70]. Spherical and anisotropic (non-spherical) metal NP syntheses can be achieved through relatively similar procedures, but anisotropic NPs are synthesized via spatial/temporal separation of nucleation and monomer growth ("seeded growth "), the use of milder reducing agents, or the use of specific capping agents [45, 54, 55, 59].

The choices of the ionic compound and the reducing agent to begin the NP synthesis are primarily governed by the relative reduction potentials of the metal NP and the reducing agent [45, 54, 55, 59]. For noble metal NPs, the ionic precursor (e. g. $HAuCl_4$, $AgNO_3$, or $Pt(acac)_2$) is reduced to the native metal using heat, light, or a mild reducing agent (such as sodium borohydride). Stronger reducing agents (for the purposes of nanomaterials synthesis, $NaBH_4$ is typically considered a "strong" reducing agent) tend to give rise to smaller spherical NPs, while milder reducing agents (such as ascorbic acid or hydroquinone) are used in the synthesis of larger spheres or anisotropic NPs [45, [54], 59, [71]. The growth of the metal core is then terminated by the formation of the capping agent layer (sometimes called the ligand shell) on the particle surface [45]. Capping agents are organic molecules that either chemically bind or electrostatically adsorb to the metal core, forming a layer of organic molecules that prevent further monomer addition to the metal core. A surprisingly small number of organic molecules have been shown to be effective capping agents for a wide variety of metal core materials. For instance, citrate, cetyltrimethyl ammonium bromide (CTAB), polyvinlypyrrolidone (PVP), tetraoctyl ammonium bromide, oleic acid, oleyl amine, functionalized thiols, and sodium dodecyl sulfate can be used as capping agents for many metal NPs, including Au, Pd, Pt, and Ag [45, 51, 55]. However, a judicious choice of capping agent can significantly improve NP stability, i. e. by matching the characteristic binding of the capping agent to the metal surface [41, 45, 49, 73, 74]. For instance, functionalized thiols (R-SH) form semi-covalent bonds to the surface of gold NPs and organize into a self-assembled monolayer on the AuNP surface. [41, 45, 72–74] The presence of this monolayer renders the thiol-stabilized AuNPs more stable than AuNPs stabilized with labile, electrostatically adsorbed capping agents, such as citrate or CTAB. Thiol-stabilized AuNPs also provide a useful platform for post-synthetic modification of the ligand shell through typical organic chemistry reactions (e. g. amide coupling or click chemistry) [41, 73, 74].

Size control in metal NP synthesis is generally achieved using the following synthetic parameters: capping agent: metal ratio, reductant:metal ratio, reaction temperature, and pH [37, 45, 53, 75–78]. Increasing the concentration of the reducing agent compared to the metal precursor concentration is thought to favour NP nucleation over monomer growth, leading to the formation of smaller NPs [45, 53, 55, 79, 80]. Increasing the concentration of the capping agent relative to the metal precursor increases the rate of passivation relative to monomer growth, again leading to smaller particles [45, 53, 55, 79, 80]. Increasing the temperature at which the synthesis is performed favours larger particles. This can be rationalized in a number of ways (particle ripening, rapid aggregation of the nuclei, or desorption of the capping agent from the particle surface), depending on the synthesis [66, 69, 70, 75, 76, 78]. pH is a synthetic parameter whose importance has only become fully appreciated relatively recently [37, 45, 78]. The pH of the reaction mixture may affect several mechanistic factors, including metal precursor speciation, reduction potentials, and the protonation state of the capping agent. Because the solution pH interacts synergistically with so many other reaction parameters, the pH effect on NP core diameter (d_{core}) is highly reaction-specific. The effects of these reaction parameters on NP core diameter are summarized in Figure 1.5.

Among metal NPs, the synthesis of spherical gold NPs is possibly the most widely studied synthetic method, and a tremendous variety of syntheses have been established that provide very tight control over both the size of the NP core and the AuNP surface chemistry. AuNPs with specific core diameters between 0.8 and 200 nm can be synthesized with sub-nanometre resolution in the d_{core} for AuNPs with sizes <10.0 nm and 5–10 nm resolution in core diameter for AuNPs >50 nm in diameter [3, 45, 79, 80]. AuNPs are typically synthesized through one of two classes

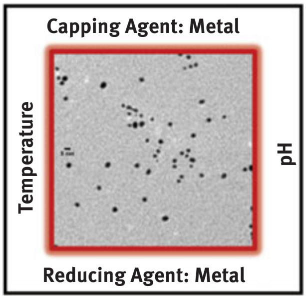

Effect of Synthetic Reaction Paremeters on Metal NP d_{core}

Synthetic Parameter	Typical Effect on NP Core Size
↑ Capping Agent: Metal	Decreased
↑ Reducing Agent: Metal	Decreased
↑ Temperature	Increased
↑ pH	Synthesis Dependent

Figure 1.5: Spherical metal NP core diameter is controlled primarily through four basic reaction parameters during synthesis: capping agent:metal, reducing agent:metal, temperature, and pH.

of synthetic methods: direct synthesis (such as the Brust–Schiffrin method) or a ligand-exchange method [73, 74, 79, 80][81]. In direct synthesis, the AuNPs are synthesized by the reduction of an ionic gold precursor (such as $HAuCl_4$) by sodium borohydride in the presence of the chosen ω-functionalized thiol [79–81]. The NP core size in this case is controlled by the reductant:Au molar ratio, the thiol: Au molar ratio, and the pH of the reaction mixture. Using direct syntheses, spherical gold NPs with core diameters between 2.0 and 8.0 nm possessing a well-defined surface chemistry can easily be prepared. To synthesize AuNPs smaller than 2.0 nm, or larger than 8.0 nm in diameter, a ligand-exchange synthesis is typically employed [73, 74]. The synthesis of AuNPs using ligand-exchange techniques is a multi-step synthetic process. In the first step, a AuNP of the desired core diameter (but stabilized with a labile ligand such as citrate, CTAB, or functionalized phosphines) is synthesized. After the initial AuNPs are purified, the labile ligand is exchanged for a covalently bound functionalized thiol [73, 74, 82, 83]. While a complete and detailed description of all the experimental procedures used to synthesize spherical metal NPs is beyond the scope of this chapter, we do highlight below synthetic procedures for the synthesis of thiol-stabilized AuNPs (d_{core} 2.0–8.0 nm) and ultra-small Cu nanoclusters that will be highly relevant to the later discussion of size control in millifluidic synthesis.

1.2.2 Synthesis of thiol-stabilized spherical AuNPs using Bunte salts (alkylthiosulfates) as thiol precursors [37, 41]

Materials. All materials were obtained from their respective suppliers and were used as received: hydrogen tetrachloroaurate hydrate (Strem, Massachusettes, USA), 2-[2-(2-chloroethoxy)-ethoxy]ethanol 99 % (Aldrich), sodium thiosulfate (Sigma Aldrich, USA), and sodium borohydride (Aldrich, 98 %). Nanopure deionized water was used for the preparation of stock solutions and as a solvent for NP synthesis. Absolute ethanol was prepared by distillation. The Bunte salt of 2-[2-(2-mercaptoethoxy)-ethoxy]ethanol was synthesized by combining 2-[2-(2-chloroethoxy)-ethoxy]ethanol (2.0 g) with sodium thiosulfate (0.80 molar equivalents) in a 50:50 mixture of absolute ethanol and water, then heating at reflux for 3 h. The crude Bunte salt was purified by trituration in ethanol.

Direct synthesis of thiol-stabilized gold nanoparticles. Gold NP synthesis reactions were carried out in *aqua regia*-cleaned 250 mL round-bottomed flasks. In the flask, $HAuCl_4$ (0.1 mmol) was combined with the mercaptoethoxy-ethoxy-ethanol (MEEE) Bunte salt ligand precursor in 125 mL of water, turning the solution from pale yellow to colourless or brown, depending on the ligand:gold ratio. The reaction mixture was stirred for 10 min before an aqueous solution of 0.01 M of ice-cold sodium borohydride was added to the reaction mixture. The precise MEEE BS:Au:$NaBH_4$ ratio varied, depending on the desired size of the product AuNP. This sodium borohydride addition immediately induced a colour change to deep red or deep brown, depending on the final AuNP core diameter. The crude particle solutions were then left to stir for an additional 3 h. Each crude NP solution was purified by diafiltering the crude AuNP solution with 20 volume equivalents of nanopure deionized water to remove the excess free ligand precursor (10 kDa membrane pore size).

1.2.3 Synthesis of sub-1.0 nm Cu nanoclusters [84]

Aqueous solutions of copper (II) nitrate and *O*-[2-(3-mercaptopropionylamino)ethyl]-*O’*-methylpolyethylene glycol (5,000 M_w) were combined in the reaction vessel. To this solution, an aqueous solution of sodium borohydride (pH = 13) was added. The NP growth reaction was quenched by the addition of excess ethanol.

1.2.4 General strategies for anisotropicmetal NP shape control

Unlike the synthesis of spherical metal NPs, the formation of anisotropic metal NPs (rod-shaped, polyhedral, cubic, prismatic, or star-shaped metal NPs) typically requires slower growth kinetics, lower metal monomer concentrations, and milder reducing agents. Wet-chemical synthetic methods for producing anisotropic metal NPs have become relatively ubiquitous in the past decade, and examples of well-defined synthetic strategies for metal NPs with cores of Ag, Au, Pt, Pd, Rh, Ir, Fe, and others can all be found [[47, 50, 53–56, 60, 62, 63, 75–77][78, 85–87]]. The synthesis of anisotropic metal NPs can again be accomplished through a variety of methods (including solvothermal methods, templated electrochemical deposition, and UV light irradiation). In recent years, however, seeded growth approaches have become the most common synthetic route to anisotropic metal NPs [47, 50, 53–56, 60, 62, 63, 75–78, 85–88]. In a seeded growth approach, a small “seed” NP (often a metal NP with a core diameter of 2 nm or less) is synthesized first, and then a small aliquot of these seed NPs is added to a new growth solution containing a specially chosen capping agent (surfactants, such as CTAB, are often chosen for this role), a low concentration of the metal growth monomer, and a mild reducing agent (such as ascorbic acid) [55, 56, 64, 75, 76, 88]. The anisotropic metal NPs are then grown from the seeds, and over a growth period ranging from several hours to a day, anisotropic metal NPs form in the growth solution (Figure 1.6). The exact shape of the product NP is the result of synergistic interactions of surfactant concentration, monomer concentration, reducing agent concentration, and the solution pH[53, 78]. Probably the most extensively studied seeded growth syntheses are the methods that produce low-aspect ratio gold nanorods (AuNRs), discovered independently (but nearly simultaneously) between 2002 and 2004 by Murphy, Mulvaney, El-Sayed, and others [53, 88–90].

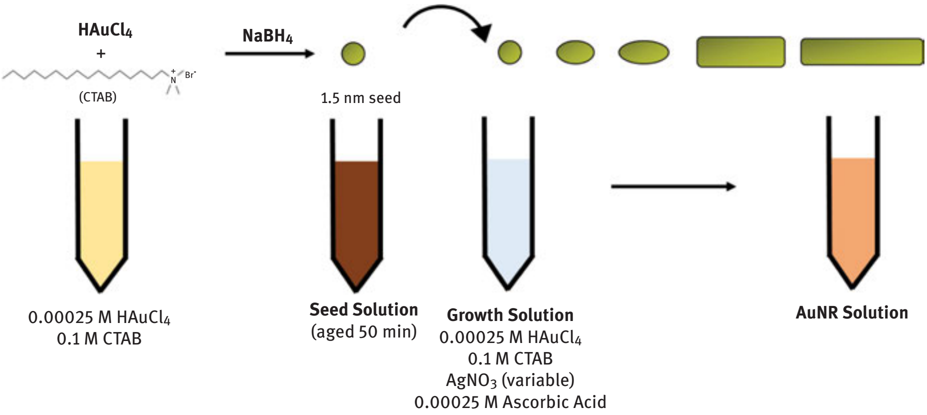

Figure 1.6: Silver-assisted seeded growth synthesis of low-aspect ratio AuNRs. A typical example of achieving metal NP shape control through seeded growth.

The silver-assisted seeded growth synthesis of AuNRs provides an accessible and well-studied example of both the advantages and limitations of a “typical” metal NP batch synthesis [55, 78, 88]. This synthesis begins with the preparation of a “seed” gold NP solution (~1.5 nm in diameter), which is accomplished via the reduction of $HAuCl_4$ in the presence of CTAB by the addition of aqueous sodium borohydride. After the NP seeds form, the seed solution is aged for nearly 50 min, and a small aliquot of the seed solution is then added to a growth solution, where the AuNRs grow from the seed particles. The growth solution contains CTAB, hydrogen tetrachloroaurate, silver nitrate, and ascorbic acid. The ascorbic acid reduces the Au(III) ion to Au(I), which is a suitable monomer for slow AuNP formation (although monomer addition will only occur in the presence of the seed particle under these synthesis conditions). This synthesis provides exceptional control over AuNR length, readily yielding AuNRs with precisely controlled aspect ratios (rod length/rod width) between 1.5 and 4.5 [53, 78]. The aspect ratio of the rods is controlled by changing the concentration of $AgNO_3$ in the growth solution (Figure 1.6). This synthesis is quite versatile and can also be modified to produce other anisotropic AuNP shapes, including prisms, plates, and cubes [53]. Despite the utility of this method for AuNP shape control, this seeded growth approach also illustrates many of the typical drawbacks of metal NP batch syntheses [87]. In this method, only 15 % of the initial Au(III) is converted to AuNRs, which leads to an average yield of ~ 7 mg AuNR/100.0 mL reaction solution [78, 88]. This means that the batch reaction would have to be performed nearly 150 times (on the 100 mL scale) to produce 1.0 g of AuNRs, and the potential for scale-up is quite limited, if precise control of the AuNR aspect ratio is required.

Although recent modifications have provided a means to extend the range of available AuNR aspect ratios that this seeded growth approach provides, attempts to translate this general approach to a gram-scale batch synthesis for AuNRs have met with limited success [71, 78, 91]. Jana demonstrated a gram-scale synthesis for AuNRs in 2005, but increasing the concentration of the reagents used in the nanorod growth solution quickly encouraged the formation of an insoluble $Au{-}Br{-}CTA^+$ complex. This reduced the homogeneity of the reaction mixture, making concentration gradients less uniform within the reaction mixture, and therefore increasing polydispersity in the products at the gram scale [91]. Zubarev also recently developed a modified seeded growth synthesis that requires the slow, mediated addition of an excess of ascorbic acid to increase the synthetic yield and produce a very monodisperse AuNR product (aspect ratio polydispersity ~3 %) at the gram scale [71]. However, the increased ascorbic acid required in the synthesis favours the formation of AuNRs with large transverse diameters (~ 25.0 nm). This limits the overall synthetic control over AuNR dimensions. Representative TEM images of both spherical and anisotropic metal NPs are shown in Figure 1.7.

Anisotropic platinum and palladium NPs can also be prepared by analogous seeded growth techniques [60, 62, 76]. Unlike the synthesis of anisotropic AuNPs,

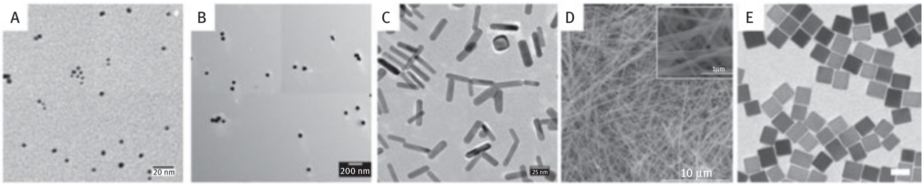

Figure 1.7: Representative TEM images of metal NPs with various core compositions, sizes, and shapes. (A) 5 nm AuNPs [scale bar 20 nm], (B) 40 nm AuNPs [scale bar 200 nm], (C) gold nanorods [scale bar 20 nm], (D) silver nanowires [scale bar 10 μm], and (E) palladium nanocubes [scale bar 20 nm] (B, D, and E, reproduced 2018 with permission from references **43, 112**, and **38**, respectively. Copyright 2014, 2012, and 2014, respectively).Credits: Sam Lohse, References 43, 38, and 112

which are primarily performed in aqueous solutions, anisotropic Pt or PdNPs are often grown in solutions of an appropriate surfactant (such as PVP, TWEEN, or CTAB) dissolved in alcohol. For instance, Wang et al. demonstrated that palladium tetrahedra and cuboctahedra could be synthesized using cuboctahedral Pd seeds dispersed in polyol solutions of PVP, where the final morphology of the product is then controlled by the choice of the palladium growth monomer (Figure 1.8) [76], 92]. The use of $Pd(acac)_2$ as the growth monomer leads to the formation of Pd nano-tetrahedra, while the use of Na_2PdCl_4 leads to the formation of Pd nano-octahedra. The difference in the final NP shape is attributed to the difference in reduction kinetics between the two palladium precursors. Multi-metal NPs, such as gold nano-octopods or concave AuNPs coated with Pd patches, can also be prepared by these types of seeded growth methods (Figure 1.9) [74].

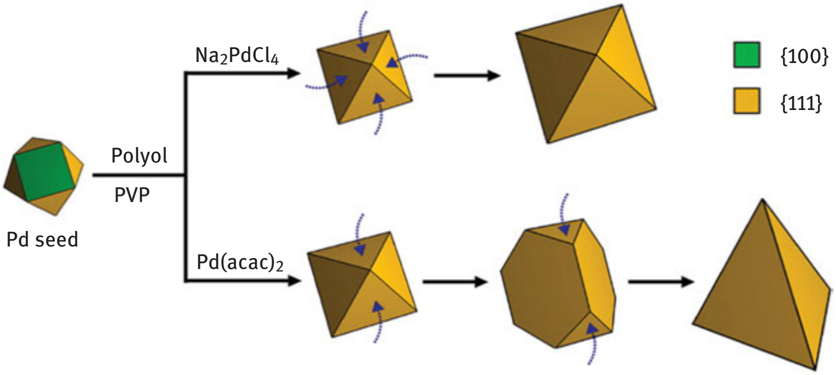

Figure 1.8: Seeded growth synthesis of palladium octahedra and tetrahedra (Reproduced 2018 with permission from reference **92**. Copyright 2015, American Chemical Society).

As with the gold octopods above, metal NPs can be then overcoated with a variety of inorganic shells, including silica shells, gold or silver, or even metal patches, using metal overgrowth steps or galvanic replacement reactions [55, 75, 93, 94]. In principle, any of these wet-chemical methods can be transferred to a millifluidic platform with sufficient care. As we shall see, the primary limitations in converting these batch synthesis methods to flow synthesis methods are material compatibility issues (e. g. reactor materials that limit synthesis temperature), controlled solution feeds, and the ability to provide sufficient residence time in the reactor for anisotropic growth to be completed. Nevertheless, even extremely sophisticated seeded growth (and overgrowth) methods can be successfully adapted for flow synthesis reactors. The basic procedures for several seeded growth syntheses are described below. Again, due to the varied nature of anisotropic metal NP synthesis by seeded growth, we will provide a detailed description of only a few common anisotropic

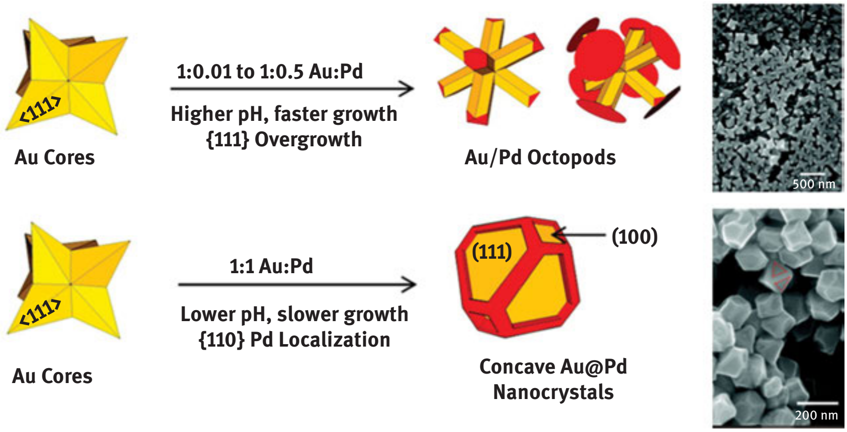

Figure 1.9: Synthesis of bimetallic octapods and concave bimetallic NPs can also be accomplished using seeded growth syntheses (Reproduced 2018 with permission from reference **75**. Copyright 2011 American Chemical Society).

metal NP synthesis below: the seeded growth of AuNRs and Au@Pd core-shell NPs. These synthetic procedures will be relevant to the later discussion of shape control in millifluidic reactors.

1.2.5 Silver-assisted seeded growth synthesis of gold nanorods with aspect ratios (1.5–4.0) [78]

Materials. All reagents and solvents were obtained from their respective suppliers and used as received: hydrogen tetrachloroaurate trihydrate (Sigma-Aldrich, USA), cetyl trimethyl ammonium bromide (CTAB, Sigma), silver nitrate (Sigma-Aldrich), sodium borohydride (Sigma-Aldrich), and *l*-ascorbic acid (Sigma). Nanopure deionized water was prepared using a Barnstead Nanopure filtration system and was used for the preparation of all stock solutions. CTAB stock solutions were briefly immersed in a lukewarm water bath (~ 35 °C) to ensure complete CTAB dissolution, and then returned to room temperature.

1.5 nm AuNP seed synthesis. 500µL of a 0.01 M $HAuCl_4$ aqueous solution was added to 9.5 mL of 0.1M CTAB (aqueous). The solution was stirred vigorously with an *aqua regia*-cleaned stir bar. 600µL of ice-cold aqueous sodium borohydride (0.01 M) was then added to solution, which turned pale brown, indicating the formation of gold NPs smaller than 2.0 nm. The seed solution was aged for 50 min prior to initiating the synthesis of AuNRs.

Gold nanorod synthesis. A growth solution was prepared by combining 9.5 mL of aqueous 0.1 M CTAB with 250 µL of 0.01 M aqueous $HAuCl_4$ and variable volumes of 0.01 M aqueous $AgNO_3$ between (between 20–100 µL) in a 15 mL centrifuge tube. This produced a pale orange solution. 55 µL of 0.1 M aqueous ascorbic acid was added to the growth solution. After the addition of the ascorbic acid, the centrifuge tube was capped and inverted several times, at which point the solution turned clear and colourless. Next, 12 µL of the seed solution was added to the growth solution and the tube was inverted gently to mix. After ~2 h, the growth solution turned pale green or brown, depending on the aspect ratio of the AuNRs. The growth solution was then left to stand for 24 h. At this time, the AuNRs were purified by centrifugation and washing with deionized water (2×, 11,000 rcf).

1.2.6 Au@Pd nanocube seeded growth [45]

Materials. Gold(III) chloride trihydrate ($HAuCl_4 \bullet 3H_2O$), sodium borohydride ($NaBH_4$), sodium citrate, cetyltrimethyl ammonium chloride, palladium (II) chloride, and methanol were obtained from Sigma. BioUltra CTAB was obtained from Sigma Aldrich (USA). Bio Xtra *L*-ascorbic acid was obtained from Sigma Aldrich (USA). Hydrochloric acid and chloroform were purchased from Macron (Pennsylvania, USA). Milli-Q deionized nanopure water was used in all synthesis steps that required aqueous solutions. Silicone oil was purchased from Sigma (USA).

Synthesis of Au nanocubes. AuNP seeds were synthesized by combining 0.25 mL of 10 mM of gold(III) chloride with 7.5 mL of 0.100 M CTAB in a 30 mL conical vial. 0.600 mL of freshly prepared 10 mM $NaBH_4$ was added to this solution to form the AuNP seeds. The seed solution was mixed by inversion for 2 min before being placed in a 25 °C oil bath for 1 h. The AuNP seed solution was then diluted 10-fold. A growth solution was prepared in a separate conical vial, by combining 0.20 mL of 10 mM gold chloride solution with 8 mL of water, and 1.6 mL of 100 mM CTAB, followed by 0.95 mL of 100 mM ascorbic acid, and mixing by inversion. 5 µL of the diluted Au seed solution was then added to the growth solution, which was mixed by inversion, and also placed in the 25 °C oil bath. The Au nanocubes were purified by centrifugation after 15 min of growth time. The purified nanocubes were then mixed with an aqueous solution of 10 mM H_2PdCl_4 for palladium overgrowth.

Synthesis of Au octahedra. In a conical reaction vial, 1.5 mL of 100 mM CTAB, 8.2 mL of water, 0.25 mL of 10 mM of gold (III) chloride, and 0.05 mL of 100 mM sodium citrate were combined and mixed by inversion. The vial was placed in a 110 °C oil bath and left to stand for 24 h. Au octahedra were then collected by centrifugation and washing. The purified nanocubes were then mixed with an aqueous solution of 10 mM H_2PdCl_4 for palladium overgrowth.

1.3 Reactor construction

1.3.1 Basic design elements of millifluidic reactors

Millifluidic synthesis systems are generally more accessible to NP synthesis researchers than microfluidic devices, because millifluidic reactors can be designed and assembled modularly from existing components [11, 16, 37, 38]. This is a more appealing option to many researchers than microfluidic devices, which must be pre-fabricated in chips using lithography facilities, due to their micron-scale dimensions. Indeed, millifluidic reactors have assembled a diverse array of materials, including pre-fabricated polydimethylsiloxane chips (with millimetre-scale reaction channels), commercially available TYGON or poly Teflon (PTFE) tubing, glass capillaries, and polycarbonate mixers, all components that can be purchased from many laboratory supply catalogues [37, 38, 84, 95, 96]. Several commercial suppliers now offer millifluidic chips or entire millifluidic reactors that are suitable for metal NP synthesis [97]. Of course, any reactor design also leaves room for customization to improve reactor performance; many millifluidic systems incorporate custom-made mixers or observation cells. As a result, the cost and preparation time needed to assemble a millifluidic reactor is typically greatly reduced compared to a microfluidic (or particularly a nanofluidic) device, which are generally fabricated as integrated devices, with the mixing zones and main reactor channels built into the device itself. Where a microfluidic device typically requires a clean room and dedicated fabrication facility, a millifluidic device can be assembled right on the laboratory bench top [11, 16]. Furthermore, because millifluidic reactors are generally modular devices, they can be re-designed or re-assembled as needed, in the event of reactor fouling or when the reactor needs to be re-purposed. In contrast, an LOC device needs to be entirely replaced in case of reactor fouling [11, 16]. In the millifluidic channel size range (>500 μm), fluid mixing is typically quite rapid (1–1,000 ms, depending on channel dimensions and flow rate). In principle, millifluidic devices provide comparable control of NP physiochemical properties to microfluidic devices, but provide greater versatility in point-of-use reactor design [97]. As a result of this freedom to create and design modular reactors to suit specific needs, many millifluidic reactors look almost nothing alike, even if they are designed for the same type of NP synthesis (Figure 1.10).

Millifluidic reactors designed for metal NP synthesis come in all shapes and sizes, depending on their chosen purposes, and the resources available to their designer [37, 38, 43, 84, 95–100]. These reactors spanned a wide range of complexity in their design and construction. We have previously assembled a very “bare bones” model millifluidic reactor for the synthesis of functionalized gold NPs, which was constructed entirely from materials that would be available in most undergraduate chemistry laboratories (Tygon tubing, polycarbonate y-mixers, driven by a peristaltic pump) [42]. Despite its relatively humble components (Figure 1.10C), this reactor was capable

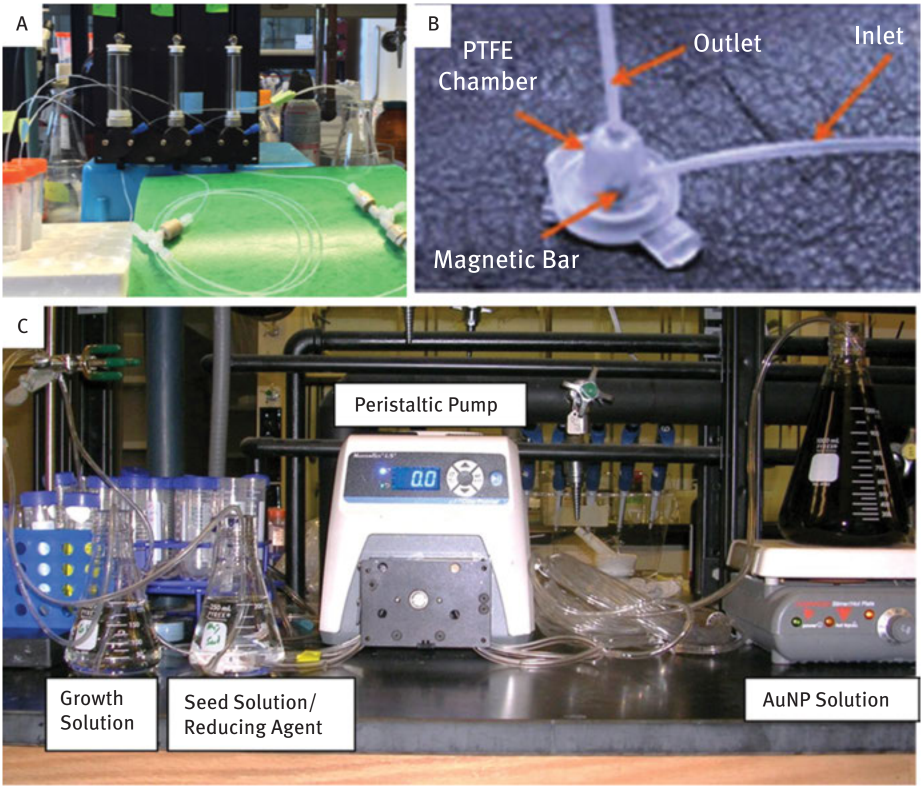

Figure 1.10: Some representative millifluidic reactor designs. (A) Capillary flow in FEP tubing driven by syringe pumps. (B) Custom-fabricated PTFE mixer. (C) TYGON tubing driven by a peristaltic pump. (A, B, and C reproduced 2018 with permission from references **37, 99**, and **43** respectively. Copyright 2015, 2011, and 2014 American Chemical Society).

of producing both spherical and anisotropic gold NPs on the gram scale. The use of a peristaltic pump is not appropriate for the large-scale synthesis of many NPs; however, due to variations in mixing rates within a given run, so the applications of this style of reactor are limited. McKenzie et al. designed a significantly more sophisticated millifluidic reactor using a programmable syringe pump, fluorinated ethylene (FEP) tubing, and PTFE mixers, which has been successfully used in the high-throughput synthesis of many functionalized spherical gold NPs (Figure 1.10A) [37, 39, 41]. Zhang et al. developed a segmented-flow reactor for the synthesis of anisotropic Pd, Au, AgNPs, and core-shell NPs, constructed using PTFE tubing and silica capillary t-mixers (i.d. = 1.58 mm) [38]. Segmented-flow tubular reactors have also been used for the synthesis of a variety of catalytic metal NPs [101–104]. Still other millifluidic reactors have been prepared as pre-fabricated chips or with custom-fabricated mixing components [11, 16]. A summary of some significant reactor designs is given in Table 1.2.

Table 1.2: Some representative millifluidic reactor design elements.

Authors	NP synthesized	Reactor construction	Mixer style	*In Situ* monitoring
Elliott et al. [37]	Spherical AuNPs	FEP tubing and PTFE mixer, syringe pump	Continuous-flow t-mixer	Simultaneous UV-vis/SAXS
Lohse et al. [43]	Spherical and rod-shaped AuNPs	Polycarbonate mixer, TYGON tubing, peristaltic pump	Continuous-flow Y-mixer	UV-vis
Krishna et al. [111]	Spherical and anisotropic AuNPs	Pre-purchased millifluidic chip, syringe pump	Continuous-flow Y-mixer	XAS
Gottesman et al. [112]	AgNWs	PTFE tubing, furnace, syringe pump	Continuous flow	None
Biswas et al. [84]	Spherical CuNPs	PMMA millifluidic chip	Continuous-flow snake mixer	XAS
Zhang et al. [38]	Anisotropic Au and PdNPs	Silica capillary mixers, PTFE tubing	Segmented-flow, successive t-mixers	None
Knauer et al. [105]	Ag nanoprisms	PTFE tubing, syringe pumps	Segmented-flow, T-junction PEEK	None

Despite the diversity of fabrication options when constructing a millifluidic reactor, most millifluidic reactors share the same fundamental design features. Millifluidic reactors consist of reagent reservoirs, a mixer, various lengths of reactor channel tubing (to control the residence time, t_r, the amount of time the NPs grow within the reactor), and often an observation cell (to facilitate real-time monitoring of product quality). The basic components of a millifluidic reactor are shown in Figure 1.2 (*vide supra*). The mixers of millifluidic reactors range from the simple (commercially available continuous-flow T- or Y-mixers) to the complex (segmented-flow mixers, which are designed to mix immiscible solvents or inert gases with the reagent stream) [37, 38, 44]. As with the mixer, the observation cell choice ranges from commercially available options (a simple flow-through quartz cuvette) to custom-made Teflon cells with multiple observation ports (designed to allow users to monitor the reaction using multiple instrumental techniques simultaneously) [37, 38]. Other ancillary components are generally required to ensure that the reactor functions effectively. Check valves are particularly common to ensure uniform fluid flow across all the available reactor channels and prevent the build-up of back pressure within the device [11, 37]. Last, it should be noted that effective control of reagent stream mixing is vital to achieve adequate NP physiochemical property control in a millifluidic synthesis environment. The mixing dynamics of millifluidic reactors may be significantly different than microfluidic devices, and careful thought should be given to selecting a mixer system and geometry. A detailed discussion of fluid mixing is beyond the scope of this chapter, but we would recommend that readers consult the following reviews on reactor construction and fluid mixing [14, 15][16][17, 18, 104].

1.3.2 Continuous-flow reactor systems

The default running state for most millifluidic devices is a continuous-flow mode, in which multiple reagent streams mix by diffusion. Depending on the flow rate of the reagent streams, most reactors that run in a continuous-flow mode mix by diffusion under laminar flow (Reynolds number <2,000) [11, 16, 37, 43]. Continuous-flow devices are the still the most common type of millifluidic reactor, because they are extremely simple to design and operate. Single-phase fluid flow through a standard t-mixer or Y-mixer produces effective laminar mixing. This is typically sufficient to achieve reasonably complete mixing on a 1–1,000 ms time scale, and this rapid mixing can lead to improved product quality (particularly more reproducible control of NP physiochemical properties) compared to batch synthesis. Elliott et al. showed that in the synthesis of gold NPs, laminar mixing in a T-junction leads to a reduction of AuNP core diameter dispersity from ~12 % when synthesized in a round-bottomed flask to 2 % core diameter dispersity in AuNP synthesis on a sample-to-sample basis in a continuous-flow reactor (Figure 1.10A, Figure 1.11A,C) [37]. In this reactor, the reagent mixing time was determined to be ~ 1 ms (at 60 mL/min flow rate), with AuNPs having clearly formed after only 150 ms [37]. Despite this substantial improvement in mixing time compared to the corresponding batch synthesis, mixing by diffusion across the reactor channel is still not instantaneous, and fluid contact with the walls of the channel can lead to a minor (but still significant) spread of residence times among NPs grown in continuous-flow reactors [11, 16, 33]. In order to minimize the residence time spreads, and improve mixing so that it is as rapid and uniform as possible, more sophisticated mixers are being experimented with that could potentially achieve turbulent flow mixing in millifluidic devices [11, 16]. Alternatively, segmented-flow reactors can be used to minimize the residence time spread that growing particles experience while travelling through the reactor channels [11, 33].

The primary disadvantage to metal NP synthesis in a continuous-flow reactor is that synthesis under these conditions will ultimately lead to reactor fouling (a build-up of adsorbed metal on the channel walls, which can clog the reactor). Continuous-flow reactors allow for significant contact between the reaction solvent and the channel walls, leading to the deposition of partially formed NPs along the reactor channels during synthesis [11, 14–16, 37, 43, 104]. Ultimately, these deposits build up (particularly at the reactor's mixer), creating a solid plug which clogs the reactor. This type of reactor fouling can be mitigated by judicious choices in reactor and tubing material, as well as operating parameters. In addition, there have been several

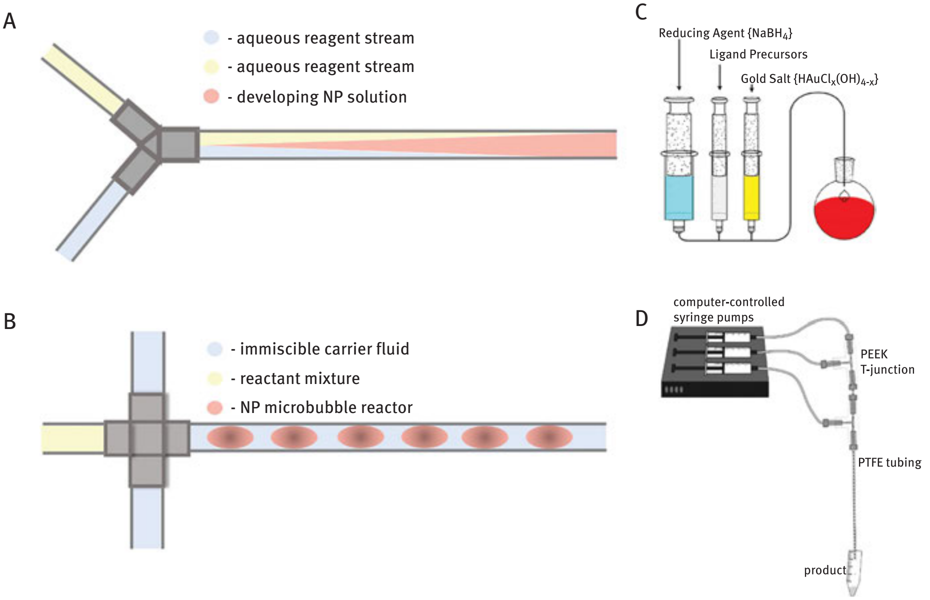

Figure 1.11: Basic reactor geometries for millifluidic devices. (A) Continuous flow. (B) Segmented flow. (C) Example geometry of a continuous-flow millifluidic reactor for AuNP synthesis. (D) Segmented-flow reactor design for AgNP synthesis (C, D reproduced 2018 with permission from references **37** and **105**, respectively. Copyright 2015, 2012 American Chemical Society).

instances reported where continuous-flow reactors have been operated for extended time periods with no channel fouling. Nevertheless, reactor fouling will eventually occur in any continuous-flow reactor that is operated for extended periods, provided the reaction mixture is making contact with the channel walls. [11, 14–16, 37, 43, 104] In order to minimize reactor fouling, an alternative fluid flow setup (segmented flow) can be used to minimize the contact between the reaction mixture and the reactor channel walls.

1.3.3 Construction of a continuous-flow millifluidic reactor [37]

A continuous-flow reactor for the synthesis of aqueous solutions of gold NPs was constructed from the following components: FEP tubing (i.d. = 0.030 in), PTFE t-mixers (i.d. = 0.020 in), fittings, ferrules, and 15 psig check valves (IDEX Health and Science). Three syringe pumps (three-way distribution valves, Versa 6, 48k model, Kloehn) were used to drive reactor flow. Two PTFE t-mixers were used for reagent mixing, and the 15 psig check valves were utilized between the syringe outlets and the t-mixer inlets. The overall flow rate was set to 60 mL/min for AuNP synthesis. 4.5 total meters of FEP tubing was placed after the second t-mixer to give the system an overall residence time of ~2 s at 60 mL/min. A custom-machined Teflon observation cell with orthogonal ports for absorbance spectroscopy fibre optics and mica windows (for SAXS analysis) was placed at various distances from the downstream t-mixer junction to observe the AuNP solution at various residence times. Used t-mixers were cleaned with dilute *aqua regia* following AuNP synthesis. After exiting the reactor, AuNP solution was collected in clean, dry centrifuge tubes.

1.3.4 Segmented-flow reactor systems

Segmented-flow reactor systems involve mixing systems that generate microliter bubbles to serve as individual microscale reactors within the reactor channels [33, 38, 44]. Segmented flow is typically achieved by mixing the reagent streams necessary for NP synthesis with immiscible liquids or carrier gases that ideally separate the reaction mixture into microscale bubbles in which the reaction can occur (Figure 1.11B,C). Running reactions in segmented flow reduces the residence time spread of particles within the microbubbles by minimizing their interactions with the reactor channel walls, leading to more monodisperse core size and shapes in the NP product. Superior mixing rates are also sometimes observed in segmented flow, due to convective mixing within the microreactor bubbles [33]. The trade-off is that while the microbubbles more or less form spontaneously when the immiscible fluids are mixed, segmented-flow reactors require more sophisticated mixer design and construction to ensure that the microbubbles possess as uniform a size and shape as possible; if the microbubbles show significant polydispersity in size, the resulting particles may still show meaningful core size dispersity [11, 33].

Segmented-flow mixers in millifluidic systems typically generate microbubbles using two related mixing strategies, in which reagent streams are either flown together with an immiscible carrier liquid, or flown together with an inert carrier gas [11, 16, 33]. The result of this mixing process is that individual reactor bubbles are separated from each other and from the reactor channel walls by a barrier of immiscible fluid. In principle, this type of segmented flow can be achieved simply by flowing two separate reagent streams together in the presence of an additional stream containing the immiscible carrier fluid. In some cases, segmented flow can be achieved simply by using a three-way mixer with three input streams. Ideally, the dimensions of the resulting microreactor bubbles are on the microliter scale, but reactor bubbles this small can be difficult to achieve in millifluidic systems [11, 38]. One barrier to segmented millifluidic flow systems has been that reactor slugs in a millifluidic system may form on the millilitre volume scale. If the reactor slugs are on this volume scale, the spread of residence times that NPs experience between the leading edge of the slug and the trailing edge can still be considerable, and mixing is less effective [11, 16]. As a result, recent research in this area has focused on designing more sophisticated mixers which will provide microliter-scale bubbles in segmented-flow millifluidic systems. Recent research into segmented-flow millifluidic mixing has already yielded promising results. Knauer et al., among others, recently demonstrated that slug volumes with microliter-scale dimensions could be produced using simple t-mixers, but microreactor volume remains a crucial parameter for NP synthesis in segmented-flow reactors, and this is an area that will require further study to maximize millifluidic segmented-flow reactor performance [101–105].

A particular class of segmented-flow reactor, the segmented-flow tubular reactor (SFTR) has shown promise for synthesizing functionalized metal NPs above the gram scale [101–104]. These reactors allow for non-aqueous, segmented-flow mixing with minimized fluid contact with the container walls and have been successfully used to synthesize catalytic nickel, silver, ultrafine semiconductor NPs, and anisotropic metal NPs. Unlike many millifluidic reactors which are driven by syringe pumps with a finite volume, a typical SFTR allows for hours or continuous operation with closely regulated segmented flow driven by HPLC pumps. Metal NP production up to 10 g NP/h can easily be realized within these systems.

1.3.5 Construction of a segmented-flow reactor for Au@Pd core-shell NP synthesis [44]

Four syringes (KD Scientific Inc., Massachusetts, USA), driven by four different syringe pumps were connected to PTFE tubing (i.d. = 1.58 mm) through silica capillaries, which were attached to the tubing by epoxy resin. The four silica capillaries met at the injector site within a 5 ft length of 5.8 mm i.d. PTFE tubing, which was placed in an oil bath held at 110 °C. The total flow rate through the system was 0.7 mL/h, which ensured that the growth solution passing through the tubing experienced 2 h of residence time in the oil bath.

1.3.6 Controlling NP size and shape through reactor operation parameters

Adapting metal NP synthesis for use in flow reactors provides additional avenues to influence the size and shape of the product NPs compared to batch synthesis. In addition to analogous batch synthesis parameters (e. g. reductant:metal ratio, capping agent: metal ratio, pH, and temperature), NP size and shape can be controlled in flow using flow rate and residence time [11, 16, 84, 95, 100]. Flow rate influences the size of the NPs produced in the reactor because the flow rate influences the Reynolds number, and therefore the rate at which the multiple reagent streams diffuse into one another during laminar flow mixing. Generally, the higher the flow rate, the higher the Reynolds number (given a constant channel diameter), and the faster the two reagent streams will diffuse into one another [16, 37, 84, 95, 100]. A number of researchers have briefly explored the influence of flow rate on particle size and core diameter dispersity, but only a handful of researchers have undertaken detailed studies to determine exactly how flow rates influence NP size in millifluidic reactors [37, 84, 95, 100].

Jun et al. explored the effect of millifluidic flow rate on AuNP core diameter in a millifluidic reactor. In this synthesis, ascorbic acid was used as both the reductant and the capping agent, and the NP d_{core} was determined by *in situ* SAXS [99]. They found that flow rate and residence time acted in concert to determine the final NP size. At extremely low flow rates (< 6 mL/min), they found that reagent mixing occurred too slowly, leading to large core diameter polydispersities (up to 40 % of d_{core}), whereas if the flow rate was 20 mL/min or greater, the reagent streams mixed effectively, and provided that the NPs experienced sufficient residence time in the reactor to fully grow, particle polydispersity was much reduced (to below 19 % of the mean core diameter) [100].

In general, while flow rate and residence time can be used to control particle size, both these parameters are optimized before a millifluidic NP synthesis is begun in earnest, and the established synthetic chemistry of the reaction (discussed in Section 1.2) is then used to control size and shape of the particles [16, 37]. Generally, the flow rate of the reactor is set as high as the reactor system can handle without causing valve/fitting ruptures or back-flow, and since the reagent streams mix by diffusion in most continuous-flow reactors, faster flow rates lead to more uniform reaction initiation. The faster flow rate will also mean that the residence time (i. e. the total tubing length) of the reactor must be extended to ensure that the particles experience sufficient residence time in the reactor to completely form.

1.3.7 Interfacing Real-Time Monitoring

Because NP synthesis in fluidic reactors linearizes synthetic reactions (linear distance from the mixer becomes a direct reflection of reaction time), one of the most powerful advantages of metal NP synthesis in flow reactors is the opportunity to interface continuous reaction monitoring strategies to verify product quality [11, 16, 37, 39, 100, 104]. *In situ* monitoring reduces both solvent and reagent waste, particularly since flow synthesis approaches can be terminated at any time during the reaction, via quenching. A host of optical spectroscopy techniques, including absorbance spectroscopy, luminescence spectroscopy, and X-ray techniques, have all been successfully interfaced with flow reactor systems, in order to determine the core size, concentration, and composition of engineered NPs [11, 16, 39, 84, 95]. Noble metal NPs are particularly well-suited for detailed characterization by optical techniques, as these NPs are strong absorbers and efficient scatterers [1, 56, 106, 107]. For instance, it has been shown on several occasions that the exact size and shape of many AuNPs (both spherical and anisotropic) can be determined with good certainty using their absorbance spectra alone, due to the characteristic absorbance values and wavelengths of their surface plasmon resonance (SPR) absorbance features [88, 106]. Haiss et al. showed that spherical AuNPs with core diameters between 5 and 80 nm could be accurately sized simply by comparing the absorbance of the AuNP solution at 450 nm to the absorbance of the AuNP solution at the wavelength of maximum absorbance (λ_{max}) [106]. Once the size of the particle has been determined, the molar AuNP concentration can readily be calculated using Beer's law. Orendorff et al. have shown that the size and concentration of rod-shaped AuNPs (up to aspect ratio 4.5) could also be determined using the absorbance of the AuNR solution at the λ_{max} [87]. XAS provides both compositional information about the oxidation states of the metal in the NP core, and with extrapolation, information about NP core size [84, 108, 109]. SAXS can be used to quantitatively determine NP size (including polydispersity) and NP concentration for a variety of NP core materials [38, 108, 110].

Optical spectroscopy techniques are particularly well-suited for incorporation into millifluidic systems as quality control instrumentation. The larger channel diameters of millifluidic reactors increase the effective path length available for an absorbance or luminescence measurement (compared to microfluidic devices), which increases the effective S:N ratio in accordance with Beer's law [11, 16, 36, 37]. A reaction channel diameter of even 0.760 mm provides a sufficient path length to easily determine the core size of AuNPs in real time using absorbance spectroscopy or SAXS, and increases the absorbance of a AuNP solution by nearly 8× versus a microfluidic device channel diameter of ~100 µL [37, 38]. Importantly, if the observation cell is set at a fixed distance from the mixer, data from the sample can be collected continuously at a single residence time (t_{r}), and the acquisition time that can be achieved is effectively unlimited.

The larger channel dimensions of a millifluidic reactor system provides an opportunity to interface a wide variety of commercially available and custom observation cells for the purpose of real-time monitoring. Monitoring cells for microfluidic reactors tend to be entirely custom made, and somewhat limited in their ability to incorporate monitoring by multiple instrumental methods [11, 16]. As with mixing devices, observation cells for millifluidic reactors range from the very simple to the extremely complex: a commercially available flow-through cuvette can be used to monitor the growth of gold NPs with $d_{\mathrm{core}} > 5$ nm, or a custom Teflon observation cell can be machined using relatively common metal shop techniques to provide a custom observation cell that will facilitate AuNP characterization by two orthogonal instrumental techniques simultaneously [37, 38].

1.3.8 In situ monitoring using absorbance spectroscopy

UV-vis-NIR absorbance spectroscopy provides a straightforward, but powerful instrumental method to monitor metal NP growth during synthesis [88, 104]. Noble metal NPs display size-and shape-dependent SPR features, which are intense absorbance features that typically occur between 400 and 1,800 nm. Depending on the composition of the metal NP, the peak wavelength of the absorbance feature and the intensity of the plasmon absorbance can be precisely correlated with the size, shape, and concentration of the NP sample. This relationship has been most thoroughly established for AuNPs. Haiss et al.

showed that for spherical AuNPs with $d_{\text{core}} > 4.0$ nm, the core size of the AuNP can be determined using the following equation [104]:

$$d_{\text{core}} = \exp\left(B_1 \frac{A_{\text{spr}}}{A_{450}} - B_2\right) \tag{1.1}$$

In this equation, $B_1 = 3.00$ and $B_2 = 2.20$ are parameters experimentally determined from the relationship between A_{spr}/A_{450} and the $\ln(d_{\text{core}})$ [103]. This analysis method has been shown to provide an accurate core size for AuNPs between 4.00 and 100.0 nm in diameter. The relative error in core diameter size using this method is ~6 % [104]. Once the core diameter has been determined, the molar extinction coefficient for the AuNP sample can also be determined from the absorbance spectrum, allowing for a real-time determination of the AuNP concentration. Orendorff et al. demonstrated through a similar set of experiments, the relationship between AuNR aspect ratio and the $\lambda_{\max}$ of the longitudinal SPR, as well as the average molar absorptivity coefficient as a function of AuNR aspect ratio [87]. Currently, quantitative relationships between plasmon absorbance intensity, excitation energy, and core size/shape have only been explicitly determined for gold NPs, but qualitative monitoring can still be employed for Ag, Pt, and Pd synthesis (or AuNPs < 4.0 nm in diameter).

1.3.9 In situ monitoring using X-ray absorption spectroscopy (XAS)

Absorbance spectroscopy is somewhat limited as a monitoring technique, in that the technique only currently provides quantitative size and concentration data for AuNP solutions. X-ray analysis techniques can provide quantitative size and composition analysis for metal NPs of all core compositions. Various X-ray absorbance techniques have been employed for the analysis of metal NPs in flow, including both extended X-ray absorbance fine structure (EXAFS) and X-ray absorption near-edge structure analysis (XANES) [84, 111]. *In situ* XAFS provides data on the short-range order of chemical systems and permits the *in situ* study of nucleation at short residence times. Typically, the application of XAFS to NP growth during flow synthesis requires high-energy X-rays from a synchrotron source [84, 111]. XAFS studies provide a variety of pertinent data regarding NP size, oxidation state, coordination number, and bond length for many metal and semiconductor NPs. The photon energy in XANES spectra can be related to oxidation state of the metal core. EXAFS spectra can be used to determine the bond lengths (interatom distances) between atoms in the metal core [84, 111].

1.3.10 In situ monitoring using small-angle X-ray scattering (SAXS)

X-ray scattering techniques can also be employed to provide a quantitative determination of metal NP size and concentration for a variety of metal core materials. Metal NPs are excellent X-ray scatterers, and even metal NPs with core diameters less than 1.0 nm provide sufficient scattering intensity to quantitatively determine the metal NP size. SAXS analysis of metal NPs has been successfully achieved using both synchrotron X-ray sources and benchtop instruments [39, 107]. Typically, in SAXS analysis, the raw scattering data are fitted to a scattering distribution using a spheroidal form factor, F. A monomodal spheroidal form factor is shown below [39]:

$$F^2 = \frac{3}{qR^3}\left(\sin(qR) - (qR\cos(qR)\right) \tag{1.2}$$

where q is the scattering vector (nm^{-1}) and R is the spheroid radius. The intensity of the scattering is then fitted to the scattering vector. For example [39]:

$$I_{fit}(q) = |\Delta\rho|^2 \sum_{r_{min}}^{r_{max}} |F(q,r)|^2 V^2(r) NP(r) \Delta\rho \tag{1.3}$$

Here, $\Delta\rho$ refers to contrast, $F(q,r)$ is the structure form factor, $V(r)$ is the particle volume, N is the total number of scatterers, and $P(r)$ is the likelihood that a particle in the Gaussian or log normal particle distribution has a radius (r). From the form factor and scattering distribution, both the NP radius and concentration can be determined. The dispersity in core diameter can be determined from the log normal or Gaussian distribution of the fit [39].

1.3.11 In situ monitoring of metal NP growth

A particularly elegant demonstration of a millifluidic system that could accurately monitor AuNP size and concentration using simultaneous absorbance spectroscopy and SAXS analysis was provided by McKenzie et al. in 2010 [39]. Their millifluidic reactor was assembled from FEP tubing and PTFE Teflon mixers, driven by a programmable syringe pump, and incorporated a custom-made Teflon observation cell with orthogonal observation ports that allowed for simultaneous AuNP characterization using absorbance spectroscopy and SAXS (Figure 1.12A). The inner diameter of the tubing and mixers was ~0.760 mm. The observation cell interfaced with the UV-vis absorbance spectrophotometer using flexible fibre optic cables and contained mica windows set perpendicular to the fibre optics, with the observation cell geometry allowing for simultaneous absorbance spectroscopy and SAXS monitoring of the AuNP sample. In their study, McKenzie et al. did not monitor the growth of particles during synthesis (although the same basic reactor setup would be used for real-time quality control during synthesis in subsequent studies [*vide infra*]) [37, 41]. In this study, they compared the efficacy of characterizing previously synthesized gold NPs using transmission electron microscopy versus SAXS (the SAXS spectra were also

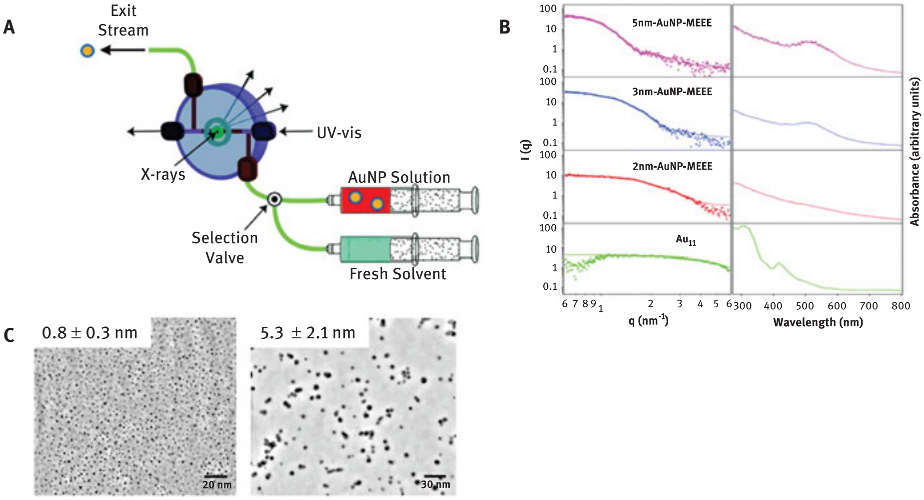

Figure 1.12: *In situ* millifluidic flow reactor monitoring system using small-angle X-ray scattering (SAXS). (A) Millifluidic reactor design. (B) Representative AuNP X-ray scattering spectra and UV-vis absorbance spectra. (C) TEM images of 0.8 nm AuNPs and 5.0 nm AuNPs (Reproduced 2018 with permission from reference **39**. Copyright 2010 American Chemical Society).

correlated with qualitative NP size analysis by UV-vis absorbance spectroscopy, Figure 1.12B). They analysed three cores sizes of AuNPs (monodisperse 0.8 nm Au-11 clusters, and MEEE-stabilized AuNPs with core diameters of both 3.0 nm and 5.0 nm). The 0.8 nm AuNPs used in this study were prepared by ligand exchange on triphenyl phosphine-stabilized Au-11 clusters. The 3.0 nm and 5.0 nm AuNPs were synthesized using direct synthesis methods and purified by diafiltration. The mean core diameters of the particles (according to TEM) were as follows: 0.8 ± 0.3 nm, 3.4 ± 1.7 nm, and 5.3 ± 2.1 nm, respectively (*n* ~ 500, Figure 1.12C) [39]. The AuNP diameters determined by SAXS were as follows: 0.8 nm (statistically negligible polydispersity), 3.6 ± 0.6 nm, and 5.3 ± 0.8 nm, respectively. The reduced polydispersity in the AuNP diameter by SAXS measurement was attributed to a lack of sample preparation artefacts which would be present in microscopy sample preparation, and the far greater population of AuNPs than can be surveyed using TEM (100 trillion-fold increase in the sample population). Time resolution provided by the setup was as low as 2 ms, making it suitable for *in situ* quality control during synthesis or most kinetic analyses of NP growth [37, 39].

Metal NP characterization and monitoring in flow displays a number of advantages versus *ex situ* instrumental analysis. Since the samples are in flow, data acquisition times are unlimited, because the observation cell can be set at a specific distance from the mixer, and collection can be continued at that point as long as sample remains in the reactor reservoir. The use of AuNP size determination in real time by SAXS has therefore subsequently been incorporated as a real-time quantitative monitoring tool in a number of AuNP flow syntheses [37, 39, 95, 107]. While McKenzie et al.'s original study used synchrotron-based X-ray sources for the SAXS analysis, the proliferation of high-quality benchtop SAXS instrumentation has made this instrumental monitoring far more feasible in most laboratories [37, 39].

Effective millifluidic reactor designs for NP synthesis are already relatively varied, considering the youth of this field. Reactors can be prepared from a host of components ranging from the simple (and commercially available) to the complex (and custom-made). In addition, a versatile library of *in situ* monitoring techniques have already been interfaced with millifluidic reactors to provide effective real-time size determinations as NPs are synthesized. While the efficacy of absorbance and luminescence spectroscopy techniques depend heavily on the core material of the NP being synthesized, X-ray absorption and scattering techniques can also be directly interfaced with the reactor, providing accurate size determinations, regardless of the NP core material. Going forward, there are still at least four key challenges to address in reactor design: (1) the development of millifluidic reactors that provide extended, reproducible mixing of large-scale reagent stocks must be developed, (2) more effective segmented-flow reactors, reactors with more robust material compatibility (so that NP syntheses that require high temperatures or corrosive conditions can be effectively run in flow reactors), (3) additional strategies for running long residence time NP synthesis reactions, and (4) post-synthetic modification steps must be integrated into reactor design [11, 16]. Currently, most synthetic reactor systems are designed for noble metal NPs that are synthesized under mild aqueous conditions; however, the synthesis of more reactive metals, such as iron, require harsh or corrosive reaction conditions, so reactor materials must move beyond simple commercially available plastics. The addition of late reaction reagent stream interfaces would enable post-synthetic modification of the ligand shell in flow, and/or the more facile synthesis of bi-metallic or core-shell NPs. The recent development of SFTR reactors, powered by HPLC pumps and capable of producing up to 10 g NP/h, may provide a path towards true large-scale synthesis of engineered NPs.

1.4 Metal NP size control in millifluidic reactors

During millifluidic synthesis, NP size is typically controlled using similar synthetic parameters to those used in the corresponding batch synthesis [37, 43–45, 100]. Based on the essential chemistry of the metal element in question, there are several specific strategies that can be used to control the diameter of the NP core. In general, the core size of the particle is controlled through two synthetic parameters acting in concert: the reductant:metal molar ratio and the capping agent: metal molar ratio [3, 45]. The larger the reductant concentration relative to the metal precursor, the more nucleation is favoured over monomer growth, and a greater number of smaller NPs results [37, 45]. Similarly, the use of stronger reducing agents typically favours the formation of smaller particles [3, 37, 45, 55]. Increasing the capping agent concentration also favours smaller core diameters because the passivating layer forms more rapidly on the NP surface. This reduces the rate of core growth by monomer addition, yielding smaller NPs. Several other parameters can also be used to control NP core diameter, depending on the nature of the synthesis, including reaction temperature, intensity of light irradiation (if light is the reducing agent), and pH.

In the context of a flow reactor, NP core diameter can also be controlled through careful control of residence time [11, 14, 84, 95, 96, 98, 100, 111]. By linearizing the NP synthesis reaction, individual NPs can be grown for specific reaction times, and the reaction can be continuously quenched at that point, leading to NPs of a specific size. For instance, Biswas et al. demonstrated the synthesis of ultra-small spherical Cu nanoclusters (stabilized with thiol polymers) [83]. The copper clusters experienced a residence time of at least 9 s in the millifluidic reactor, and the growth reaction was then quenched by depositing the Cu nanocluster solution into ethanol, as the NP solution exited the reactor [84]. When CuNP growth was quenched by dispersion in ethanol, the average d_{core} (as determined by TEM) was determined to be 1.2 ± 0.3 nm (n = 40) and if the growth reaction was not quenched by ethanol, the CuNPs ultimately grew significantly larger (d_{core} = 2.0 ± 0.5 nm, n = 55). Flow rate can also be used, in principle, to determine the core diameter, but since high flow rates are usually necessary for adequate mixing, flow rate is typically optimized to ensure the most rapid mixing possible, rather than to control NP size [11, 14, 16, 37].

Recent research has shown that there are at least three primary advantages to synthesizing metal NPs inside a millifluidic reactor compared to batch synthesis, when it comes to core size control [37, 84, 95, 96, 98, 100, 110, 111 112]. The first is that millifluidic synthesis provides faster and more controlled mixing than a batch reactor, which leads to more precise control over NP core diameters, with proper reactor design and engineering [37]. The extent to which millifluidic synthesis provides superior mixing compared to the batch synthesis depends strongly on the relative rates of reagent stream mixing within the reactor, compared to the particle growth kinetics, however. The second advantage is that the increased automation provided by the millifluidic device renders NP synthesis more reproducible than reagent addition by hand during batch synthesis. Finally, the high-throughput nature of NP synthesis reactors provides a platform that can be used to optimize a synthetic method in a high-throughput fashion [11, 14, 16, 20, 37].

A number of research groups have successfully used millifluidic synthesis environments to synthesize spherical metal NPs with specific core diameters [37, 43, 84, 95, 96, 98, 100, 110, 111][112]. The extent of size control is typically measured in two ways (ideally, millifluidic synthesis will provide improved size control in both contexts): (1) An enhanced ability to target a specific average core size (e. g. 3.5 nm, not 3.7 nm) and (2) Reduced polydispersity (a reduced sample standard deviation in d_{core}). Even relatively crudely assembled millifluidic reactors provide core diameter distributions that are at least comparable to the same NP synthesis performed in batch. We have previously developed a millifluidic reactor assembled from TYGON tubing and driven by a syringe pump, which provided AuNPs with average core diameters ranging from 2.0 nm to 40.0 nm, and showed slightly reduced polydispersity compared to the same synthesis in batch. McKenzie has also demonstrated the synthesis of monodisperse Au-11 nanoclusters ($d_{\text{core}} = 0.8$ nm) in a millifluidic reactor [107]. Unfortunately, many reports of NP millifluidic syntheses still do not compare the size control provided by the millifluidic synthesis directly to the size control provided by the batch synthesis. On balance, it seems generally safe to assume (unless there are significant material compatibility issues with the reactor which lead to NP adsorption to the reactor walls or NP aggregation) that size control is at least modestly improved by adapting the synthesis for a millifluidic environment.

The utility of a millifluidic NP synthesis displaying multiple size control advantages compared to the corresponding batch synthesis was recently demonstrated by Elliott et al [37]. Using a millifluidic reactor composed of Teflon mixers and FEP tubing (0.762 mm i.d.), Elliott et al. optimized an existing direct AuNP synthesis to provide more precise control over NP core diameter. They studied the direct synthesis of thiol-stabilized spherical AuNPs using alkylthiosulfates (Bunte salts) as capping agents, a synthesis method very much analogous to the Brust–Schiffrin synthesis, but which provides access to larger AuNP core diameters (up to 10 nm) [37, 41, 79]. NP size during this study was determined *in situ* using SAXS (both benchtop and synchrotron X-ray sources) and UV-vis absorbance spectroscopy. The *in situ* size analysis data were then compared to *ex situ* characterization by TEM (Figure 1.13A,B). The Bunte salt capping agents used were analogues of mercapto hexanoic acid and MEEE. The AuNPs were synthesized at a molar reagent ratio of 1:5:2 Bunte salt:Au:sodium borohydride. In this study, they demonstrated that the pH of the reaction mixture could be used to effectively pre-determine the average core diameter of the AuNPs. Both in batch and in flow, they showed that increasing the pH of the reaction mixture (up to pH = 7) led to the formation of larger AuNPs (up to ~8 nm in diameter). The pH of the solution impacts the final particle size by changing the reduction potential of the gold precursor; at higher pH, the speciation of the gold precursor changes from $AuCl_4^-$ (at low pH) to a gold chloro hydroxide species $[AuCl_n(OH)_{4-n}^-]$. The gold hydroxo complex has a smaller reduction potential than the tetrachloroaurate species, decreasing the rate of gold reduction, and increasing the size of the final particle. The relationship between NP core diameter and reaction mixture pH was non-linear; however, the relationship could be fit to a power function (Figure 1.13C) [37].

The advantage of performing this study in flow was obvious from the increased throughput. By determining the core diameter of the particles using *in situ* instrumental methods, the process of optimizing the synthesis (as well as the throughput of the product AuNPs) was greatly enhanced [37]. This allowed the researchers to

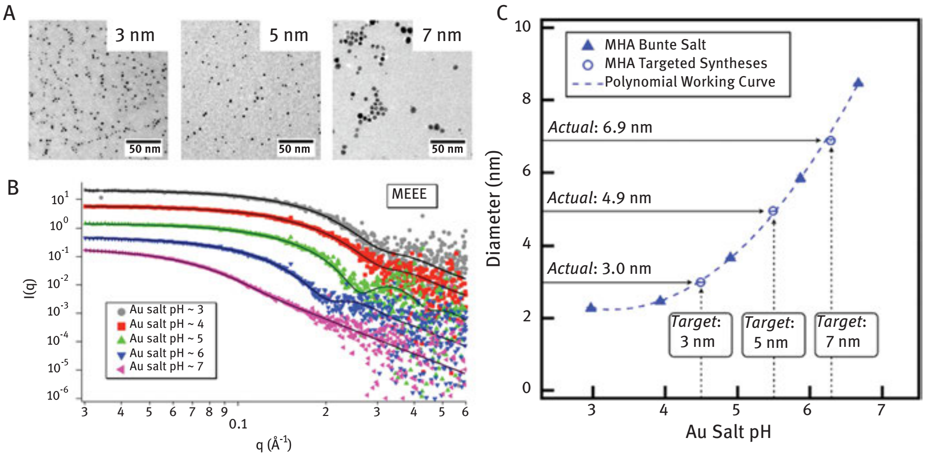

Figure 1.13: Data showing the effect of solution pH on AuNP core diameter in direct synthesis using Bunte salts. (A) Representative TEM images of 3, 5, and 7 nm AuNPs. (B) In situ SAXS data for final AuNP sizes at different solution pH values. (C) Working curve used to predict the pH necessary to synthesize AuNPs of a specific core diameter (Reproduced 2018 with permission from reference **37**, Copyright 2015, American Chemical Society).

determine the precise effect of pH on NP core diameter much more rapidly than batch synthesis with *ex situ* characterization techniques. Furthermore, the reproducibility of the synthesis from trial to trial significantly improved when the syntheses were performed in flow (polydispersity in d_{core} decreased from 18 % in a multiuser batch synthesis to 2 % in a multiuser flow synthesis) [37]. The relationship between NP core diameter and solution pH was fit with a smooth curve, enabling the researchers to develop predictive working curves, which could be used to target a pH which would give a specific AuNP core diameter at a preset gold:ligand:sodium borohydride concentration ratio. The working curves were effective in predicting the average AuNP core diameters to within 0.1 nm, based on SAXS analysis [37]. In addition to their synthetic optimization, by means of the pH–core diameter working curves, the authors credited the improved size control provided by the reactor to significantly improved reagent mixing within the millifluidic environment. They showed that within the millifluidic reactor, the reagent streams mixed in ~1 ms, whereas in the batch reaction, NP nucleation actually occurred before reagent mixing (the sodium borohydride addition) was complete.

Their pH–d_{core} working curves allowed Elliott et al. to address a pressing (though often little discussed) need in NP synthesis [4, 11, 12, 14]. While it is often taken for granted that spherical metal NPs of almost any size can be synthesized with almost arbitrary core diameter resolution, it can be very challenging to synthesize a metal NP that is “exactly” 3.5 nm in diameter. These synthesis challenges are enhanced when a research group is attempting a synthesis that they have little prior experience with, and many NP syntheses still suffer from poor reproducibility when synthesis methods are transferred from group to group. The ability to develop effective working curves on the spot (which is much easier to do in a millifluidic reactor environment) could prove to be a huge boon in the controlled synthesis of spherical metal NPs.

Over the past few years, early results in controlling metal NP core diameter in millifluidic systems appear to be promising; however, a number of key challenges now need to be addressed in order to achieve meaningful size control in all systems. To date, most millifluidic synthesis studies have focused on the synthesis of noble metal NPs; in the immediate future, synthetic studies need to focus on other industrially relevant core materials including Fe, Co, Ir, and Ni. Furthermore, most of the syntheses that have been performed in millifluidic devices thus far were performed in aqueous or ethanol solvent systems; new reactor designs need to be developed that can withstand more corrosive reaction mixtures or a variety of non-polar organic solvents. Last, since mixing rate appears to be a key determinant in producing monodisperse metal NPs in flow reactors, more sophisticated mixer designs must be investigated that can either extend mixing into the turbulent regime or continue to explore the synthesis of metal NPs using segmented-flow reactors.

1.5 Millifluidic shape control in metal NP synthesis

Despite the relative youth of millifluidic NP synthesis as a field, a wide variety of syntheses for anisotropic metal NPs with many different metal cores have successfully been adapted for flow synthesis [38, 43, 44, 112]. Anisotropic metal NPs synthesized in millifluidic flow reactors include Ag nanowires, AuNRs, gold nanocubes, and bimetallic NPs [38, 43, 44, 112]. These NPs have been generated in both continuous and segmented-flow reactors. Many of these NPs were, in fact, generated in the same study using a single reactor, driven by syringe pumps, and composed of PTFE tubing and Teflon mixers, with interior diameters up to 5.8 mm [38]. The synthesis of anisotropic metal NPs in flow reactors raises a number of different challenges compared to the synthesis of spherical metal NPs. Primarily, since most anisotropic metal NPs are synthesized by seeded growth approaches (which generally involve careful kinetic control with respect to both reduction and monomer addition), the residence time in the reactor required for anisotropic NP growth may be extensive (20 min–24 h) [38, 43, 44, 112]. Building extensive residence time into a millifluidic reactor while maintaining sufficiently rapid mixing rates can be a significant challenge in reactor design. We have successfully adapted the silver-assisted seeded growth of AuNRs for synthesis in a simple millifluidic reactor [43]. This millifluidic reactor was quite rudimentary in its design, as it was powered by a peristaltic pump, and assembled from TYGON tubing (i.d. 1.79 mm) and commercially available polycarbonate Y-mixers, with *in situ* monitoring provided by UV-vis absorbance spectroscopy via a flow-through quartz cuvette [42]. The aim here was to design a millifluidic reactor that would be accessible to as wide a variety of researchers as possible, since only inexpensive, commercially available reactor components were required. Using this reactor, we flowed together aqueous solutions of 1.5 nm CTAB-stabilized AuNP seeds, and a growth solution containing $HAuCl_4$, CTAB, $AgNO_3$, and ascorbic acid. We were able to show that AuNRs with different aspect ratios (ranging from 1.5 to 4.0) could be produced by varying the $[AgNO_3]$ in the growth solution (Figure 1.14) [42]. AuNR growth could also be initiated by the addition of aqueous sodium borohydride directly to the growth solution. With extended running time (~120 min of reactor operation), AuNRs with various aspect ratios were produced on the gram scale using this reactor, and UV-vis absorbance spectroscopy could be effectively used to monitor the growth of the AuNRs in the reactor, for either kinetic monitoring or quality control purposes.

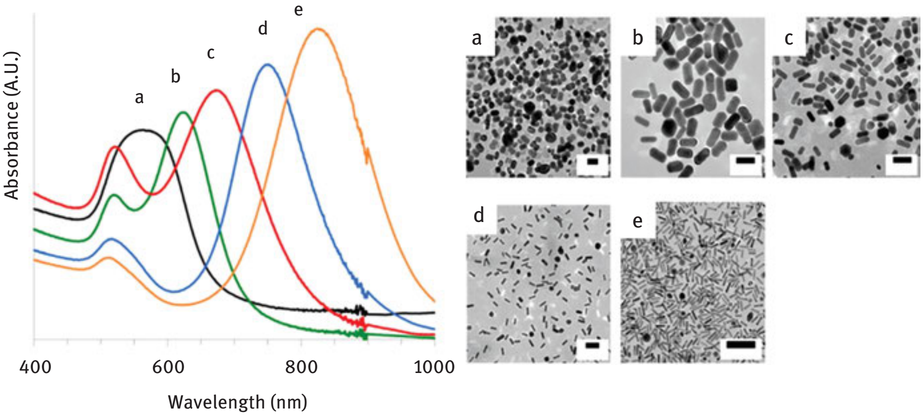

Figure 1.14: Absorbance spectroscopy analysis and TEM images of AuNRs with various aspect ratios prepared in a millifluidic reactor, using increasing concentrations of silver nitrate (a-e) (Reproduced 2018 with permission from reference **43**, copyright 2014, American Chemical Society).

Millifluidic reactors have also been adapted for the synthesis of core:shell bimetallic NPs. Santana et al. recently demonstrated the millifluidic synthesis of Au@Pd nanostructures with various Pd shell thicknesses (Figure 1.15) [43]. This segmented-flow reactor was driven by syringe pumps and composed of PTFE tubing (i.d. = 1.58 mm) and silica capillaries, with the tubing beyond the mixer immersed in a 110 °C oil bath. These anisotropic core:shell NPs were synthesized using a segmented-flow reactor containing silicone oil as a carrier fluid to generate aqueous microreactor bubbles for the synthesis of the anisotropic NPs. In this synthesis, Au nanocubes or octahedra served as seeds for the synthesis of the core:shell NPs. Santana et al. observed that increased flow rate of the palladium precursor (H_2PdCl_4) leads to increasing

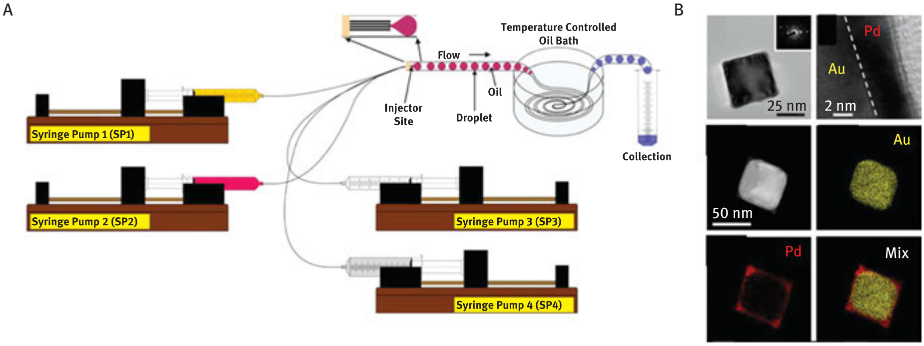

Figure 1.15: Diagram of a millifluidic flow reactor used by Santana et al. for the synthesis of bimetallic Au-Pd nano-octahedra. (A) Millifluidic reactor design, using a segmented-flow reaction. (B) Hi-res TEM images and elemental mapping images of Au-Pd bimetallic NPs (Reproduced 2018 with permission from reference **44**, Copyright 2017, American Chemical Society).

thickness of the conformal Pd shell on the surface of the seed AuNP, although the Pd shell showed a tendency to grow dendritically when octahedral AuNPs were used as seeds in this synthesis [44]. The researchers observed that the quality of the anisotropic core:shell NPs prepared by this method were comparable to the size, shape, and core-shell thickness of the same particles grown under analogous batch synthesis conditions. However, the ability to modify the synthesis conditions in line during millifluidic synthesis represents a potential advantage over the synthesis of these types of anisotropic shapes in batch [43]. Their results show that it is possible to manipulate metal NP shell thickness, and even NP shell growth geometry, by manipulating reagent stream flow rates.

While the synthesis of anisotropic metal NPs in flow reactors has now been demonstrated on a number of occasions, millifluidic synthesis has not yet shown significant improvements in product quality compared to batch synthesis. In our millifluidic synthesis of AuNRs with various aspect ratios, we found that the polydispersity of the AuNR aspect ratio was essentially identical to the polydispersity of the AuNR aspect ratio performed under identical batch conditions. Millifluidic growth of silver nanowires using the polyol synthesis and Santana et al.'s millifluidic synthesis showed similar results; the aspect ratio of the nanowires and the thickness of the Pd shell on the surface of the Au seed crystals were exactly as expected based on the batch synthesis run under identical conditions [43, 44, 96, 112]. Because the growth kinetics of anisotropic metal NPs are typically less rapid than the growth kinetics of spherical metal NPs, the reduced mixing dimensions of the millifluidic reactors are probably less of an advantage in the synthesis on anisotropic metal NPs compared to the synthesis of spherical metal NPs, where metal reduction and particle growth are typically much more rapid. Millifluidic reactors may still provide a means to improve anisotropic metal NP yield and shape dispersity by providing a high-throughput platform for optimizing seeded growth syntheses. Seeded growth syntheses typically require the synergistic interaction of up to six or seven reagents to achieve effective shape control, and the high-throughput synthesis environment may provide an effective platform to develop working curves (*ala* Eliott et al.) to minimize shape polydispersity and maximize NP yield [37, 78].

One of the primary challenges in the millifluidic synthesis of anisotropic metal NPs going forward is ensuring that metal NPs grown in a flow reactor experience their full growth time within the reactor, while ensuring that the reagent streams flow together fast enough to fully mix. The growth time required to achieve anisotropic metal NPs and the temperatures required for anisotropic growth are highly variable from synthesis to synthesis. For instance, the synthesis of the Au@Pd core:shell NPs required 2h of heating (at 110 °C) to produce the palladium-coated gold cubes. To achieve the necessary residence time, 5 feet of PTFE tubing was required, along with a very low flow rate (0.3 mL/min to 0.6 mL/min) [44]. While this low flow rate was adequate for the synthesis of the bimetallic NPs, reducing flow rates reduces mixing efficiency and the rate of reagent diffusion across the interface. Other syntheses may require even longer residence times with more rapid mixing, which will push the potential limits of reactor length. Additionally, to date, anisotropic metal NPs have only been synthesized in millifluidic reactors by synthesizing the seed NP solution first in batch, and then adding the seed solution to a reagent line to begin the millifluidic synthesis. In order to make a truly effective millifluidic synthesis of anisotropic metal NPs, the seed solution should be synthesized within the reactor and then the seeds should be combined in line with the growth solution. Generation of higher-quality seed particles in the millifluidic reactor may be an important key to improving millifluidic shape control versus batch synthesis.

1.6 Surface chemistry control in millifluidic reactors

Because the size and shape of the NP core determines the electronic and optical properties of metal NPs, the ability to control NP core size and shape in millifluidic reactors has easily received the bulk of early research attention [3, 46]. By comparison, few research studies have examined the ability to control NP surface chemistry using millifluidics [41, 113]. NP surface chemistry encompasses almost all aspects of NP structure and composition beyond the core, including inorganic shells grown over the core, as well as the organization and charge of organic molecules and ions adsorbed to the NP surface [114–116]. The importance of controlling NP surface chemistry is difficult to overstate, because the NP surface is the primary interface through which the NP interacts with its immediate environment [114–116]. NP surface chemistry modifications, such as controlling ligand shell composition, overgrowth of additional inorganic shells, or post-synthetic modifications (*e.g.* bio-functionalization), strongly influence NP interactions with their environment and even modify the size-dependent properties of the core. For instance, ligand shells composed of multiple ωfunctionalities are necessary to ensure effective NP performance in many biomedical applications. [114, 115][116] Because millifluidic reactors linearize NP synthesis reactions and provide more rapid mixing than a typical batch synthesis, these reactors provide an opportunity to manipulate NP surface chemistry at specific time points during or after NP synthesis in ways that are not accessible during batch syntheses.

While only a handful of studies have investigated the ability to manipulate NP surface chemistry in millifluidic reactors, several significant gains in surface chemistry control have already be achieved, particularly relating to the ability to manipulate the composition of the NP ligand shell. Metal NPs possessing mixed-ligand shells (capping agent layers composed of two or more ω-functionalized ligands) offer improved performance in a variety of applications, because multiple ligands can impart multifunctional properties to the NPs [114–116]. This is particularly evident in biomedical applications, where theranostic NPs must demonstrate several different properties simultaneously to successfully bind cell membrane receptors – these NPs must show good water solubility, resist non-specific protein adsorption, and display a targeting ligand that will specifically bind the NP to cell membrane receptors [114, 115 116]. While the synthesis of metal NPs with mixed-ligand shells has been demonstrated in batch, these syntheses are often time-consuming (requiring multiple ligand exchange and purification steps) and suffer from questionable reproducibility. Recent studies of the synthesis of multifunctional AuNPs in millifluidic reactors, however, have shown that the reproducible synthesis of mixed-ligand shell NPs in millifluidic reactors can be achieved in a single synthetic step.

Elliot, Kennedy, et al. have shown on several occasions during the past 3 years that the improved reagent mixing provided by millifluidic reactors also provides a facile platform to achieve sophisticated NP ligand shell compositions that are difficult to achieve in batch synthesis [41, 117]. In 2015, Kennedy et al. demonstrated that direct AuNP synthesis in a millifluidic reactor could be used to synthesize thiol-stabilized AuNPs with mixed-ligand shells consisting of various ratios of ethylene glycol (EG) and malonamide ω-functional groups [116]. In this study, the mixed malonamide–EG ligand shell AuNPs were synthesized using a direct synthesis method (analogous to a single-phase Brust-Schiffrin synthesis) where Bunte salts (alkylthiosulfates) acted as ligand precursors. Kennedy et al. were able to take advantage of the superior mixing provided by the millifluidic reactor to precisely control the ratio of both ligands on the NP surface, producing 3.5 nm AuNPs with ligand shell EG:malonamide ratios ranging from 0 % to 90 % EG:malonamide [117]. Increasing malonamide representation in the ligand shell, however, did tend to lead to larger AuNP core diameters at the same ligand:Au ratio. This millifluidic synthesis provides a reliable single-step synthetic route to metal NPs with mixed-ligand shells, without the need for multiple post-synthetic modification ligand exchange and purification steps. It should also be noted that the EG:malonamide ratio that formed

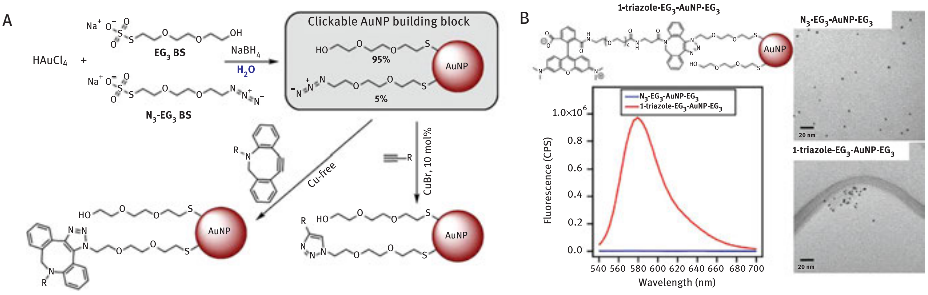

Figure 1.16: 3.5 nm AuNP synthesized with a mixed-ligand shell in a millifluidic flow environment (95:5 MEEE:azide thiol). (A) These mixed-ligand shell AuNPs can then be post-synthetically modified with fluorescent functional groups. (B) 1-triazole-EG3-AuNP fluorescent spectra and TEM images of the AuNPs before and after post-synthetic modification (Reproduced 2018 with permission from reference **41**. Copyright 2017 American Chemical Society).

in the ligand shell was not necessarily identical to the feed ratio of the two ligands entering the synthesis.

Elliott et al. built on this design strategy to synthesize 3.5 nm diameter AuNPs functionalized with mixed thiol ligand shells, containing a mixture of ω-functionalized EG and click-ready azide functional groups (Figure 1.16) [41]. These clickable AuNPs were subsequently functionalized with fluorescent triazole groups, to produce fluorescent NPs via post-synthetic modifications (Figure 1.16B). The use of the millifluidic reactor here not only provided extremely precise control over the composition of the ligand shell, but Eliott et al. also showed how the feed composition of the ligand precursors led to the exact ratio of the two ω-functionalized thiols on the AuNP surface. The use of a 1:19 ratio (azide:EG Bunte salts) during the flow synthesis gave rise to mixed-ligand shell AuNPs with a ~7 % ratio azide:EG in the ligand shell, as determined by nuclear magnetic resonance (^{1}H-NMR) spectroscopy [41]. DBCO-PEG$_4$-Fluor 545 dye then could be clicked to the azide groups displayed on the particle surface to provide fluorescent AuNPs. A host of other relevant functional groups could also be clicked to the particle surface, making the initial azide:EG AuNPs a facile synthetic building block for a vast library of mixed-ligand shell AuNPs [41]. These multifunctional AuNPs provide water-soluble and highly stable clickable metal NPs (a useful combination!). While the click reactions were performed outside the millifluidic reactor environment in this study, the ability to synthesize mixed ligand, water-soluble AuNPs in a single synthetic step using a millifluidic reactor provides a powerful tool to simplify the synthesis of mixed-ligand shell AuNPs with minimal core diameter dispersity.

After only several early studies, millifluidic reactors have already shown significant advantages in their ability to control NP surface chemistry compared to batch synthesis, particularly with respect to ligand shell composition. Therefore, NP surface chemistry control represents a particularly promising area of research for millifluidic reactors. Because NP synthesis is linearized in a millifluidic reactor, ligand-exchange reactions, silica coating, or coating reactions with additional metal shells could be initiated at specific times following the initial NP synthesis in the reactor, and the rapid mixing within the reactor could lead to greater control over shell thickness, or the opportunity for asymmetric functionalization on anisotropic NPs. Furthermore, the ability to monitor chemical reactions *in situ* could lead to useful opportunities to monitor the progress of additional functionalization reactions within the confines of the reactor. The ability to manipulate surface chemistry within a flow reactor could lead to entirely new strategies for surface chemistry control, and thus, to an unprecedented ability to manipulate NP physiochemical properties.

1.7 Essential safety considerations

By the standards on many typical synthetic chemistry reactions, the synthesis of metal NPs can often be achieved by mild and relatively benign means. When synthesizing metal NPs in millifluidic reactor systems, there are several key points where care should be taken to prevent personal injury or damage to the reactor components. First, it should be emphasized that the hazards of metal NPs themselves are not fully understood, and the best safety practices for handling metal NPs continue to evolve. Typically, noble metal NPs (Au, Ag, Pt, and PdNPs) that are dispersed in an aqueous or alcohol solution are considered to be minimally hazardous. Nevertheless, gloves, goggles, and standard laboratory personal protective equipment should be worn when handling any NP solution with an unknown hazard level. If metal NPs are dried to a powder, however, they should be treated as potential inhalation hazard, and should be carefully controlled and only handled in a fume hood until they are redispersed in solution. When handling powdered metal NPs, it may also be necessary to wear a respirator or other personal protective equipment to prevent the inhalation of ultrafine particles.

Particularly in the synthesis of noble metal NPs, any glass ware used in the reactor or the synthesis overall will need to be cleaned with *aqua regia* prior to use. Concentrated *aqua regia* solutions contain both strong acids (HCl and HNO_3) and a strong oxidizer (HNO_3). Therefore, *aqua regia* should be handled and disposed of with due caution. Lastly, the synthesis of noble metal NPs often requires aqueous solutions of sodium borohydride ($NaBH_4$). In water solution, sodium borohydride rapidly decomposes, and can evolve relatively high pressures of gas. Therefore, aqueous sodium borohydride solutions should be disposed of as soon as they are used to prevent the rupture (or in rare cases, the explosion) of the $NaBH_4$ container vessel.

1.8 Conclusions

Millifluidic reactors have begun to gain prominence as synthesis platforms for functionalized NPs of all kinds. Millifluidic systems now provide comparable control over metal NP physicochemical properties (size, shape, composition, and surface chemistry) compared to microfluidic devices, yet millifluidic reactors offer reduced construction time, modular replacement components, and easier interfaces with *in situ* instrumental monitoring. Effective millifluidic reactors can be assembled from a wide variety of commercially available components, but most early reactor designs for metal NP have been constructed from PTFE tubing, connected by t-mixers, and driven by syringe pumps. These millifluidic reactor designs offer mixers that can achieve complete reagent stream mixing on the millisecond time scale, segmented-flow operation, and real-time NP size determinations with 1.0 Angstrom resolution using X-ray analysis techniques.

A wide variety of metal NPs have been synthesized in millifluidic devices, but, to date, noble metal NPs (Ag, Au, Pt, and PdNPs) have received the most extensive investigation. For both spherical and anisotropic metal NPs, millifluidic NP synthesis provides high-throughput product characterization by *in situ* analysis, reduced batch-to-batch variability in core diameter (less than 0.2 %), and sufficient throughput to extend NP synthesis to the gram scale (even when using only a single device). High-throughput synthesis optimization in a millifluidic environment has even produced synthetic NP methods that can control core diameters to within 0.1 nm. New precision in ligand shell composition control has also been demonstrated in millifluidic reactors, where high-quality mixed thiol monolayers on AuNPs can now be synthesized routinely. These mixed-monolayer AuNPs have opened up new opportunities for colorimetric sensing, nanoscale device construction, and studying the aggregation kinetics of gold NPs with improved precision.

Despite the significant achievements made so far in the millifluidic synthesis of engineered NPs, a number of key challenges remain that make it difficult to extend the millifluidic synthesis of metal NPs to all NP shapes and metal core materials. One of the more underappreciated challenges involves interfacing millifluidic reactors with large enough reagent reservoirs that a single continuous synthetic run will yield grams of functionalized NPs, without the need to replenish the reagent reservoirs. Driving millifluidic reactors with HPLC pumps provides a potential solution to this problem, and this approach can be adapted for either continuous or segmented-flow synthesis. Still more research into reactor design is needed to accommodate NP synthesis reactions that require extremely long residence times, extremely high temperatures, or harsh reaction environments. As yet, millifluidic synthesis does not offer improved shape control in anisotropic NP synthesis compared to batch synthesis methods. There is also a pressing demand to develop a broader array of millifluidic post-synthetic modification techniques (including ligand exchange and silica shell coating), millifluidic bio-functionalization methods, and more convenient point-of-use NP synthesis reactors. If these challenges can be overcome, the convenience afforded by modular millifluidic reactors may yet create a research environment in which many NP synthesis researchers, even those with little prior flow chemistry training, can lend their expertise to develop new, more convenient reactor designs and syntheses.

Acknowledgements: The author would like to acknowledge Colorado Mesa University and its Chemistry Faculty for their support. The author would also like to thank Drs. Lallie McKenzie and Pat Haben, as well as Prof. Jim Hutchison, all of whom shaped the author's early conception of metal nanoparticle synthesis in fluid reactors.

References

[1] Daniel M-C, Astruc D. Gold nanoparticles : assembly, supramolecular chemistry, quantum size -related properties, and applications toward biology, catalysis, and nanotechnology. Chem Rev. 2004;104:293–346.

[2] Dreaden EC, Alkilany AM, Huang X, Murphy CJ, El-Sayed MA. The golden age: gold nanoparticles for biomedicine. Chem Soc Rev. 2012;41:2740–79.

[3] Sardar R, Funston AM, Mulvaney P, Murray RW. Gold nanoparticles: past, present, and future. Langmuir. 2009;25:13840–51.

[4] Petros RA, DeSimone JM. Strategies in the design of nanoparticles for therapeutic applications. Nat Rev Drug Discov. 2010;9:615–27.

[5] Cheong S, Watt JD, Tilley RD. Shape control of platinum and palladium nanoparticles for catalysis. Nanoscale. 2010;2:2045–53.

[6] Green MA, Ho-Baillie A, Snaith HJ. The emergence of perovskite solar cells. Nat Photonics. 2014;8:506–14.

[7] Sherman D, Yodh JS, Albrecht SM, Nygard J, Krogstrup P, Marcus CM. Normal, superconducting and topological regimes of hybrid double quantum dots. Nat Nanotechnol. 2017;12:212–7.

[8] Li X, Yang Z, Fu Y, Qiao L, Li D, Yue H, et al. Germanium anode with excellent lithium storage performance in a germanium/lithium-cobalt oxide lithium-ion battery. ACS Nano. 2015;9:1858–67.

[9] Tesla spurs demand for lithium chemicals. Chem Eng News. 2018;94:10.

[10] Green nanotechnology challenges and opportunities. ACS Green Chemistry Institute White Paper, 2011.

[11] Krishna KS, Li Y, Li S, Kumar CS. Lab-on-a-chip synthesis of inorganic nanomaterials and quantum dots for biomedical applications. Adv Drug Deliv Rev. 2013;65:1470–95.

[12] Hutchison JE. Greener nanoscience: a proactive approach to advancing applications and reducing implications of nanotechnology. ACS Nano. 2008;2:395–402.

[13] Gilbertson LM, Zimmerman JB, Plata DL, Hutchison JE, Anastas PT. Designing nanomaterials to maximize performance and minimize undesirable implications guided by the Principles of Green Chemistry. Chem Soc Rev. 2015;44:5758–77.

[14] Marre S, Jensen KF. Synthesis of micro and nanostructures in microfluidic systems. Chem Soc Rev. 2010;39:1183–202.

[15] Valencia PM, Farokhzad OC, Karnik R, Langer R. Microfluidic technologies for accelerating the clinical translation of nanoparticles. Nat Nanotechnol. 2012;7:623–9.
[16] Elvira KS, Solvas CI, Wootton RC, deMello AJ. The past, present and potential for microfluidic reactor technology in chemical synthesis. Nat Chem. 2013;5:905–15.
[17] Wiles C, Watts P. Continuous reactors flow reactor: a perspective. Green Chem. 2012;14:38–54.
[18] Hartman RL, McMullen JP, Jensen KF. Deciding whether to go with the flow: evaluating the merits of flow reactors for synthesis. Angewandte Chemie Int Ed. 2011;50:7502–19.
[19] Wegner J, Ceylan S, Kirschning A. Ten key issues in modern flow chemistry. Chem Commun. 2011;47:4583–92.
[20] Chan EM, Xu C, Mao AW, Han G, Owen JS, Cohen BE, et al. Reproducible, high-throughput synthesis of colloidal nanocrystals for optimization in multidimensional parameter space. Nano Lett. 2010;10:1874–85.
[21] Tsukahara T, Mawatari K, Kitamori T. Integrated extended-nano chemical systems on a chip. Chem Soc Rev. 2010;39:1000–13.
[22] Song Y, Hormes J, Kumar CS. Microfluidic synthesis of nanomaterials. Small. 2008;4:698–711.
[23] Song H, Chen DL, Ismagilov RF. Reactions in droplets in microfluidic channels. Angewandte Chemie Int Ed. 2006;45:7336–56.
[24] Cabeza VS, Kuhn S, Kulkarni AA, Jensen KF. Size-controlled flow synthesis of gold nanoparticles using a segmented flow microfluidic platform. Langmuir. 2012;28:7007–13.
[25] Chan EM, Mathies RA, Alivasatos AP. Size-controlled growth of CdSe nanocrystals in microfluidic reactors. Nano Lett. 2003;3:199–201.
[26] Duraiswamy S, Khan SA. Droplet-based microfluidic synthesis of anisotropic metal nanocrystals. Small. 2009;5:2828–34.
[27] Watt J, Hance BG, Anderson RS, Huber DL. Effect of seed age on gold nanorod formation: a microfluidic, real-time investigation. Chem Mater. 2015;27:6442–9.
[28] Sebastian V, Basak S, Jensen KF. Continuous synthesis of palladium nanorods in oxidative segmented flow. Aiche J. 2015;62:373–80.
[29] Feng VZ, Edelman KR, Swanson BP. Student-fabricated microfluidic devices as flow reactors for organic and inorganic synthesis. J Chem Educ. 2015;92:723–7.
[30] Edel JB, Fortt R, deMello JC, deMello AJ. Microfluidic routes to the controlled production of nanoparticles. Chem Commun. 2002;0:1136–7.
[31] Dong B, Hadinoto K. Direct comparison between millifluidic and bulk-mixing platform in the synthesis of amorphous drug-polysaccharide nanoparticle complex. Int J Pharm. 2017;523:42–51.
[32] Kitson PJ, Rosnes MH, Sans V, Dragone V, Cronin L. Configurable 3D-printed millifluidic and microfluidic ‘lab on a chip’ reactionware devices. Lab on Chip. 2012;12:3267–71.
[33] Kohler JM, Li S, Knauer A. Why is micro segmented flow particularly promising for the synthesis of nanomaterials? Chem Eng Technol. 2013;36:887–99.
[34] Ostrowski AD, Chan EM, Gargas DJ, Katz EM, Han G, Schuck PJ, et al. Controlled synthesis and single-particle imaging of bright, sub 10-nm lanthanide-doped upconverting nanocrystals. ACS Nano. 2012;6:2686–92.
[35] Levy ES, Tajon CA, Bischoff TS, Iafrati J, Fernandez-Bravo A, Garfield DJ, et al. Energy-looping nanoparticles: harnessing excited-state absorption for deep-tissue imaging. ACS Nano. 2016;10:8423–33.
[36] Dolomite microfluidic reactor chips. www.dolomitemicrofluidics.com. Accessed: 19 Jan 2018.
[37] Elliott EW, Haben PM, Hutchison JE. Subnanometer control of mean core size during mesofluidic synthesis of small (D_{core} < 10 nm) water-soluble, ligand-stabilized gold nanoparticles. Langmuir. 2015;31:11886–94.

[38] Zhang L, Niu G, Lu N, Wang J, Tong L, Wang L, et al. Continuous and scalable production of well-controlled noble-metal nanocrystals in milliliter-sized droplet reactors. Nano Lett. 2014;14:6626–31.

[39] McKenzie LC, Haben PM, Kevan SD, Hutchison JE. Determining nanoparticle size in real time by small-angle X-ray scattering in a microscale flow system. J Phys Chem C. 2010;114:22055–63.

[40] SciFinder Search. Nanoparticle Millifluidic Synthesis. 20 Jan 2018.

[41] Elliott EW, Ginsburg AL, Kennedy ZC, Feng Z, Hutchison JE. Single-step synthesis of small azide-functionalized gold nanoparticles: versatile, water-dispersible reagents for click chemistry. Langmuir. 2017;33:5796–802.

[42] Shalom D, Wootlon R, Winkle RF, Cottam BF, Vilar R, deMello AJ. Synthesis of thiol functionalized gold nanoparticles using a continuous microfluidic reactor. Materials Letters. 2007;61:1146–50.10.1016/j.matlet.2006.06.072.

[43] Lohse SE, Eller JR, Sivapalan ST, Plews MR, Murphy CJ. A simple millifluidic benchtop reactor system for the high-throughput synthesis and functionalization of gold nanoparticles with different sizes and shapes. ACS Nano. 2013;7:4135–50.

[44] Santana JS, Koczkur KM, Skrabalak SE. Synthesis of Core@Shell nanostructures in a continuous flow droplet reactor: controlling structure through relative flow rates. Langmuir. 2017;33:6054–61.

[45] Dahl JA, Maddux BLS, Hutchison JE. Toward greener nanosynthesis. Chem Rev. 2007;107:2228–69.

[46] Tavakkoli M, Kallio T, Reynaud O, Nasibulin AG, Johans C, Sainio J, et al. Single-shell carbon-encapsulated iron nanoparticles: synthesis and electrocatalytic activity for hydrogen evolution reaction. Angewandte Chemie Int Ed. 2015;127:4618–21.

[47] Xia X, Figueroa-Cosme L, Tao J, Hsin-Chieh P, Niu G, Zhu Y, et al. Facile synthesis of iridium nanocrystals with well-controlled facets using seed-mediated growth. J Am Chem Soc. 2014;136:10878–81.

[48] Grass RN, Athanassiou EK, Stark WJ. Covalently functionalized cobalt nanoparticles as a platform for magnetic separations in organic synthesis. Angewandte Chemie Int Ed. 2007;46:4909–12.

[49] Huber DL. Synthesis, properties, and applications of iron nanoparticles. Small. 2005;1:482–501.

[50] Sun Y, Xia Y. Shape-controlled synthesis of gold and silver nanoparticles. Science. 2002;298:2176–9.

[51] Ortiz A, Skrabalak SE. On the dual roles of ligands in the synthesis of colloidal metal nanostructures. Langmuir. 2014;30:6649–59.

[52] Gole A, Murphy CJ. Seed-mediated synthesis of gold nanorods: role of the size and nature of the seed. Chem Mater. 2004;16:3633–40.

[53] Sau TK, Murphy CJ. Room temperature, high-yield synthesis of multiple shapes of gold nanoparticles in aqueous solution. J Am Chem Soc. 2004;126:8648–9.

[54] Personick ML, Mirkin CA. Making sense of the mayhem behind shape control in the synthesis of gold nanoparticles. J Am Chem Soc. 2013;135:18238–47.

[55] Lohse SE, Murphy CJ. The quest for shape control: a history of gold nanorod synthesis. Chem Mater. 2013;25:1250–61.

[56] Eustis S, El-Sayed MA. Why gold nanoparticles are more precious than pretty gold: noble metal surface plasmon resonance and its enhancement of the radiative and nonradiative properties of nanocrystals with different shapes. 2006;35:209–17.

[57] Hulteen JC, Martin CR. A general template-based method for the preparation of nanomaterials. J Material Chem. 1997;7:1075–87.

[58] Wagner RS, Ellis WC. Vapor-liquid-solid mechanism of single crystal growth. Appl Phys Lett. 1964;4:89–90.

[59] Grzelczak M, Perez-Juste J, Mulvaney P, Liz-Marzan LM. Shape control in gold nanoparticle synthesis. Chem Soc Rev. 2008;37:1783–91.

[60] Xiong Y, Xia Y. Shape-controlled synthesis of metal nanostructures: the case palladium. Adv Mat. 2007;19:3385–91.

[61] DeSantis CJ, Skrabalak SE. Core values: elucidating the role of seed structure in the synthesis of symmetrically branched nanocrystals. J Am Chem Soc. 2013;135:10–3.

[62] Chen J, Herricks T, Geissler M, Xia Y. Single-crystal nanowires of platinum can be synthesized by controlling the reaction rate of a polyol process. J Am Chem Soc. 2004;126:10584–855.

[63] Wiley B, Sun Y, Xia Y. Polyol synthesis of silver nanostructures: control of product morphology with Fe(II) or Fe(III) species. Langmuir. 2005;21:8077–80.

[64] Xia Y, Xiong Y, Lim B, Skrabalak SE. Shape-controlled synthesis of metal nanocrystals: simple chemistry meets complex physics? Angewandte Chemie Int Ed. 2009;48:60–103.

[65] Kim F, Song JH, Yang P. Photochemical synthesis of gold nanorods. J Am Chem Soc. 2002;124:14316–7.

[66] LaMer VK, Dinegar RH. Theory, production and mechanism of formation of monodispersed hydrosols. J Am Chem Soc. 1950;72:4847–54.

[67] LaMer VK. Nucleation in phase transitions. Ind Eng Chem. 1952;44:1270–7.

[68] Polte J. Fundamental growth principles of colloidal metal nanoparticles-a new perspective. Crystal Eng Commun. 2015;17:6809–30.

[69] Turkevich J, Stevenson PC, Hilier J. A study of the nucleation and growth processes in the synthesis of colloidal gold. Discuss Farraday Soc. 1951;11:55–75.

[70] Kimling J, Maier M, Okenve B, Kotaidis V, Ballot H, Plech A. Turkevich method for gold nanoparticle synthesis revisited. J Phys Chem B. 2006;110:15700–7.

[71] Vigderman L, Zubarev ER. High-yield synthesis of gold nanorods with a longitudinal SPR peak greater than 1200 nm using hydroquinone as a reducing agent. Chem Mater. 2013;25:1450–7.

[72] Parker JF, Fields-Zinna CA, Murray RW. The story of a monodisperse gold nanoparticle: au25-L18. Acc Chem Res. 2010;43:1289–96.

[73] Hostetler MJ, Templeton AC, Murray RW. Dynamics of place-exchange reactions on monolayer-protected gold cluster molecules. Langmuir. 1999;15:3782–9.

[74] Woehrle GH, Brown LO, Hutchison JE. Thiol-functionalized, 1.5 nm gold nanoparticles through ligand exchange reactions: scope and mechanism of ligand exchange. J Am Chem Soc. 2005;127:2172–83.

[75] DeSantis CJ, Peverly AA, Peters DG, Skrabalak SE. Octopods versus concave nanocrystals: control of morphology by manipulating the kinetics of seeded growth via co-reduction. Nano Lett. 2011;11:2164–8.

[76] Xia Y, Xia X, Peng H-C. Shape-controlled synthesis of colloidal metal nanocrystals: thermodynamic versus kinetic products. J Am Chem Soc. 2015;137:7947–66.

[77] O'Brien MN, Jones MR, Brown KA, Mirkin CA. Universal noble metal nanoparticle seeds realized through the iterative reductive growth and oxidative dissolution reactions. J Am Chem Soc. 2014;136:7603–6.

[78] Burrows ND, Harvey S, Idesis FA, Murphy CJ. Understanding the seed-mediated growth of gold nanorods through a fractional factorial design of experiments. Langmuir. 2016;33:1891–907.

[79] Lohse SE, Dahl JA, Hutchison JE. Direct synthesis of large water-soluble functionalized gold nanoparticles using Bunte slats as ligand precursors. Langmuir. 2010;26:7504–11.

[80] Hostetler MJ, Wingate JE, Zhong C-J, Harris JE, Vachet RW, Clark MR, et al. Alkanethiolate gold cluster molecules with core diameters from 1.5 to 5.2 nm: core and monolayer properties as a function of core size. Langmuir. 1998;14:17–30.

[81] Brust M, Walker M, Bethell D, Schiffrin DJ, Whyman R. Synthesis of thiol-derivatised gold nanoparticles in a two-phase liquid-liquid system. J Chem Soc Chem Commun. 1994;0:801–2.

[82] Park J-W, Shumaker-Parry JS. Strong resistance of citrate anions on metal nanoparticles to desorption under thiol functionalization. ACS Nano. 2015;9:1665–82.

[83] Park J-W, Shumaker-Parry JS. Structural study of citrate layers on gold nanoparticles: role of intermolecular interactions in stabilizing nanoparticles. J Am Chem Soc. 2014;136:1907–21.

[84] Biswas S, Miller JT, Li Y, Nandakumar K, Kumar CS. Developing a millifluidic platform for the synthesis of ultrasmall nanoclusters: ultrasmall copper nanoclusters as a case study. Small. 2012;8:688–98.

[85] Hoefelmeyer JD, Niesz K, Somorjai GA, Tilley D. Radial anisotropic growth of rhodium nanoparticles. Nano Lett. 2005;5:435–8.

[86] Xie S, Zhang H, Lu N, Jin M, Wang J, Kim MJ, et al. Synthesis of rhodium concave tetrahedrons by collectively manipulating the reduction kinetics, facet-selective capping, and surface diffusion. Nano Lett. 2013;13:6262–8.

[87] Park S-J, Kim S, Lee S, Khim ZG, Char K, Hyeon T. Synthesis and magnetic studies of uniform iron nanorods and nanospheres. J Am Chem Soc. 2000;122:8581–2.

[88] Orendorff CJ, Murphy CJ. Quantitation of metal content in the silver-assisted growth of gold nanorods. J Phys Chem B. 2006;110:3990–4.

[89] Perez-Juste J, Pastoriza-Santos I, Liz-Marzan LM, Mulvaney P. Gold nanorods: synthesis, characterization and applications. Coord Chem Rev. 2005;249:1870–901.

[90] Nikoobakht B, El-Sayed MA. Preparation and growth mechanism of gold nanorods (NRs) using seed-mediated growth method. Chem Mater. 2003;15:1957–62.

[91] Jana NR. Gram-scale synthesis of soluble, near-monodisperse gold nanorods and other anisotropic nanoparticles. Small. 2005;1:875–82.

[92] Wang Y, Xie S, Liu J, Park J, Huang CZ, Xia Y. Shape-controlled synthesis of palladium nanocrystals: a mechanistic understanding of the evolution from octahedrons to tetrahedrons. Nano Lett. 2013;13:2276–81.

[93] Abadeer NS, Brennan MR, Wilson WL, Murphy CJ. Distance and plasmon wavelength dependent fluorescence of molecules bound to silica coated gold nanorods. ACS Nano. 2014;8:8392–406.

[94] DeSantis CJ, Sue AC, Bower MM, Skrabalak SE. Seed-mediated co-reduction: a versatile route to architecturally controlled bimetallic nanostructures. ACS Nano. 2012;6:2617–28.

[95] Li Y, Sanampudi A, Reddy VR, Biswas S, Nandkumar K, Yemane D, et al. Size evolution of gold nanoparticles in a millifluidic reactor. Chem Phys Phys Chem. 2012;13:177–82.

[96] Lin XZ, Terepka AD, Yang H. Synthesis of silver nanoparticles in a continuous flow tubular microreactor. Nano Lett. 2004;4:2227–32.

[97] UNIQSIS: Accessible flow chemistry. www.uniqsyis.com. Accessed: 19 Jan 2018.

[98] Maguire P, Rutherford D, Macias-Montero M, Mahony C, Kelsey C, Tweedie M, et al. Continuous in-flight synthesis for on-demand delivery of ligand-free colloidal gold nanoparticles. Nano Lett. 2017;17:1336–43.

[99] Wan Zhen, Luan Weiling, Tu Shan-Tung, et al. Size controlled synthesis of blue-emmitting core/shell nanocrystals via microreaction. J Phys Chem C. 2011;115:1569–75. DOI: 10.1021/jp108901z.

[100] Jun H, Fabienne T, Florent T, Coulon P-E, Nicolas M, Olivier S. Understanding of the size control of biocompatible gold nanoparticles in millifluidic channels. Langmuir. 2012;28:15966–74.

[101] Jongen N, Donnet M, Bowen P, Lemaitre J, Hofman H, Schenk R, et al. Development of a continuous segmented flow tubular reactor and the Scale-out concept- In search of perfect powders. Chem Eng Technol. 2003;26:303–5.

[102] Lucchini MA, Testino A, Ludwig C, Kambolis A, El-Kazzi E, Cervellino A, et al. Continuous synthesis of nickel nanopowders: characterization, process optimization, and catalytic properties. Appl Catalysis B: Environ. 2014;156:404–15.

[103] Quinsat JE, Testino A, Pin S, Huthwelker T, Nuesch FA, Bowen P, et al. Continuous production of tailored silver nanoparticles by polyol synthesis and reaction yield measured by X-ray absorption spectroscopy: toward a growth mechanism. J Phys Chem C. 2014;118:11093–103.

[104] Testino A, Pilger F, Lucchini MA, Quinsat JE, Stahli C, Bowen P. Continuous polyol synthesis of metal and metal oxide nanoparticles using a segmented flow tubular reactor (SFTR). Molecules. 2015;20:10566–81.

[105] Knauer A, Csaki A, Moller F, Huhn C, Fritzsche W, Kohler TM. Microsegmented flow-through synthesis of silver nanoprisms with exact tunable optical properties. J Phys Chem C. 2012;116:9251–8.

[106] Haiss W, Thanh NT, Aveyard J, Fernig DG. Determination of size and concentration of gold nanoparticles from UV-vis spectra. Anal Chem. 2007;79:4215–21.

[107] Li T, Sensei AJ, Lee B. Small angle X-ray scattering for nanoparticle research. Chem Rev. 2016;116:11128–80.

[108] Jug K, Zimmerman B. Structure and stability of small copper clusters. J Chem Phys. 2002;116:4497.

[109] Nikam AV, Kulkarni AA, Prasad BL. Microwave-assisted batch and continuous flow synthesis of palladium supported on magnetic nickel nanocrystals and their evaluation as reusable catalyst. Crystal Growth Design. 2017;17:5163–9.

[110] McKenzie L. Mechanistic insights on nanoparticle formation: investigation of reaction pathways and development of controlled synthesis for triphenylphosphine-stabilized undecagold. Dissertation, University of Oregon, Mar 2009.

[111] Krisha KS, Biswas S, Navin C, Yamane DG, Miller JT, Kumar CS. Millifluidics for chemical synthesis and time-resolved mechanistic studies. J Visualized Exp. 2013;81:50711.

[112] Gottesman R, Tangy A, Oussadon I, Zitoun D. Silver nanowires and nanoparticles from a millifluidic reactor: application to metal assisted silicon etching. New J Chem. 2012;36:2456–9.

[113] Shen Y, Abolhasani M, Chen Y, Yang L, Coley CW, Bawendi MG, et al. In-situ microfluidic study of biphasic nanocrystal ligand-exchange reactions using an oscillatory flow reactor. Angewandte Chemie Int Ed. 2017;56:16333–7.

[114] Verma A, Stellacci F. Effect of surface properties on nanoparticle-cell interactions. Small. 2010;6:12–21.

[115] Hauck TS, Ghazani AA, Chan WC. Assessing the effect of surface chemistry on gold nanorod uptake, toxicity, and gene expression in mammalian cells. Small. 2008;4:153–9.

[116] Walkey CD, Olsen JB, Song F, Liu R, Guo H, Olsen DW, et al. Protein corona fingerprinting predicts the cellular interaction of gold and silver nanoparticles. ACS Nano. 2014;8:2439–55.

[117] Kennedy ZC, Lisowski CE, Mitaru-Berceanu DS, Hutchison JE. Influence of ligand shell composition upon interparticle interactions in multifunctional nanoparticles. Langmuir. 2015;31:12742–52.

Bionote

Sam Lohse was born in Salt Lake City, Utah, in 1981. He received his Bachelors of Science degrees in Biochemistry and Chemistry from Idaho State University in 2003 and 2005, respectively. He also received his Masters of Science in Chemistry working under the direction of Dr Jeff Rosentreter in 2005. During his PhD studies, he worked under the direction of Dr Jim Hutchison at the University of Oregon, studying the direct synthesis of spherical gold nanoparticles using alkylthiosulfates (both in batch and millifluidic systems). He received his PhD in Chemistry from the University of Oregon in June of 2011. Sam worked as a postdoctoral researcher in Dr Catherine Murphy's research group at the University of Illinois at Urbana-Champaign from 2011 to 2014, where he studied the connection between nanoparticle surface chemistry and their bio-interactions as a member of the Center for Sustainable Nanotechnology. Following his postdoctoral work, he joined Colorado Mesa University in the Fall of 2014, where his research group studies the physiochemical transformations of metal nanoparticles in environmentally relevant media.

Liangliang Lin, Sergey A. Starostin, Sirui Li and Volker Hessel

2 Synthesis of metallic nanoparticles by microplasma

Abstract: The synthesis of metallic nanoparticles has been of long standing interest, primarily induced by their novel and unique properties that differ considerably from bulk materials. Despite various methods have been developed, it is still a challenge to produce high-quality metallic nanoparticles with controllable properties in a simple, cost-effective and environmentally benign manner. However, the development of the microplasma-assisted technology can bring an answer to this formidable challenge. In the present work, four main microplasma configurations used for metallic synthesis of metallic nanoparticles are reviewed. These are hollow-electrode microdischarges, microplasma jets with external electrodes, microplasma jets with consumable electrodes and plasma–liquid systems. The state of the art characterization methodologies and diagnostic techniques for *in situ* microplasma-assisted precursor dissociation as well as *ex situ* metallic nanoparticles analysis is also summarized. Further, a broad category of representative examples of microplasma-induced metallic nanoparticle fabrication is presented, together with the discussion of possible synthesis mechanisms. This is followed by a brief introduction to related safety considerations. Finally, the future perspectives, associated challenges and feasible solutions for scale-up of this technique are pointed out.

This article has previously been published in the journal *Physical Sciences Reviews*. Please cite as: Hessel, V. Synthesis of Metallic Nanoparticles by Microplasma. *Physical Sciences Reviews* [Online] **2018**, 3. DOI: 10.1515/psr-2017-0121

https://doi.org/10.1515/9783110345100-002

Graphical Abstract:

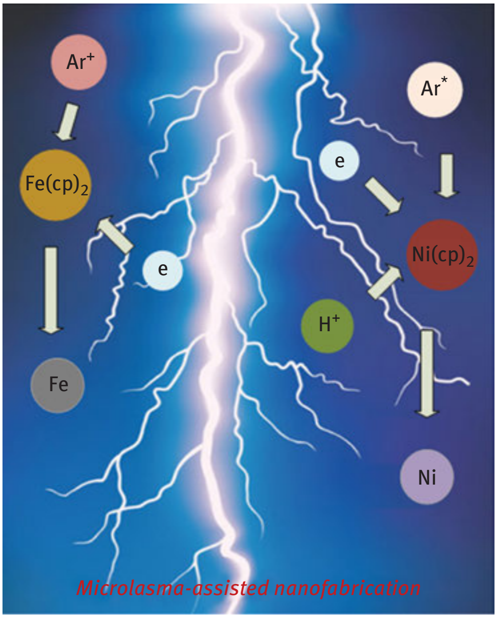

Keywords: microplasma, metallic nanoparticles, plasma–liquid interaction, PECVD, plasma synthesis, plasma technology, nanomaterial, nanoparticle, nanomaterial characterization, nanotechnology, plasma array, nanomaterial synthesis

2.1 Introduction

Due to their low dimensionality and large surface areas, nanoparticles often exhibit novel and unique properties that differ considerably from bulk materials [1]. Among them metallic nanoparticles are one of the most extensively studied systems in terms of preparation, characterization and applications [2, 3]. It is well known that product properties are closely related to their microstructures. One most well-known example is the significant difference of the properties between the diamond and graphite, which can be attributed to the difference of their atomic structures. Metallic nanoparticles also exhibit unique properties compared to bulk metals. Their size, shape and ordered assembly-dependent nature make them versatile and attractive for applications including catalysis [4], sensing [5], drug delivery [6], imaging [7], data storage [8] and bio-medicine [9]. For example, gold nanoparticles are ideal materials for bio-imaging applications owing to their biocompatibility, low short-term toxicity as well as high absorption coefficient for electromagnetic radiation and physical density [10]. But their fluorescence intensity and light absorption are size dependent, with the surface plasmon resonance being red shifted from 517 nm to 532 nm when particle size increases from 10 nm to 50 nm [11]. Another example is Ni nanoparticles utilized as catalysts for the nucleation and growth of carbon nanotubes (CNTs). It is reported that the formation rate of CNTs depends inversely on the Ni nanoparticles size, and no CNTs are formed by particles with diameters larger than 7 nm [12, 13]. In addition to particle size, crystalline facets also proved to affect the photoexcitation performance of Ag nanoparticles, in which oxygen is shown to exist in molecular form on the (111) crystalline surface but is dissociated into atomic form on both (100) and (110) surfaces [14].

In the past few decades, many efforts have been devoted to fabricate metallic nanoparticles with controllable size, shape and structures, aiming to understand how those parameters affect the properties of nanoparticles, and ultimately, to tailor them for specific applications. On the other hand, such extensive studies also result in a variety of novel or already well-established methods for metallic nanoparticles synthesis. Generally they can be subdivided into two categories: The first one consists of physical approaches such as evaporation/condensation [15], sputtering [16], milling [17] and laser ablation [18]. The second one includes chemical methods such as colloidal route [19], sol-gel [20], microemulsion [21] and solvothermal route [22], in which metal ions are reduced in solutions to form small metal clusters or aggregates. However, physical approaches always implement time/energy consuming procedures and take place in in an inert atmosphere, requiring substantial equipment and operation costs. By contrast, chemical methods are relatively simple, low-temperature operation and easily to be controlled. Fine quality products can be produced when the starting materials are properly chosen and processes are well controlled. One inevitable problem is the introduction or generation of byproducts (e. g. surfactants, catalysts, reductants and stabilizers) which requires subsequent purification steps after the synthesis. Meanwhile, the majority of present chemical techniques are lab scale batch processes, while the upscale toward industrial manufacturing with retaining product quality represents very challenging task [23].

Plasma is considered as the forth state of matter which is generated when gases are partially or fully ionized, being characterized by complex collective behavior in the external or self-induced electromagnetic field [24, 25]. It contains charged particles such as electrons, positive and negative ions as well as neutral atoms, which can be chemically radicalized by the dissociation processes and exist in various excited electronic and rovibrational states. Plasma is electrically conductive as well as plasma bulk tends to be electrically quasi-neutral; however, at certain conditions a volumetric charge is formed [26]. Generally plasma is categorized into two main groups: the high-temperature plasma (HTP, e. g. fusion plasmas) and the low-temperature plasma (LTP, e. g. gas discharges) [24]. In HTP gas is fully ionized with the characteristic temperature in the order of ~10^7 K while in LTP the temperatures are considerably lower and the typical degree of ionization is below 1 %. The LTP can be furtherly subdivided into thermal plasmas (the temperature of all species is the same, ~10^4 K) and non-thermal plasmas (the temperatures of different species are different, in which electrons have sufficiently high temperature to maintain ionization balance while heavy particles such as ions and neutral species are at the temperature of few hundreds K or lower), as shown in Table 2.1. Compared to HTP and thermal plasmas, non-thermal (or non-equilibrium) plasmas exhibit higher selectivity and are the most widely used plasmas for different applications. This is because high energy electrons give rise to inelastic collisions, leading to a "chemically-rich" environment, while the bulk temperature remains relatively low, making it attractive for various practical applications [24].

Table 2.1: Plasma classification in terms of radical temperatures [27].

Low temperature plasma (LTP)		**High temperature plasma (HTP)**
Thermal plasma	Non-thermal plasma	
e. g. arc plasma at normal pressure	e. g. low-pressure glow discharge, corona, DBD plasma, plasma jets	e. g. fusion plasmas
$Te \approx Ti \approx T \leq \sim 10^4$ K	$Ti \approx T \leq \sim 300$ K $Ti \ll Te \leq 10^5$ K	$Te \approx Ti \geq \sim 10^7$ K

Starting from the traditional applications such as ozone generation, light sources, thin film deposition and etching [28–30], with the development of plasma technology, it has been expanded to a wide range fields such as methane reforming [31, 32], VOC decomposition [33–35], CO_2 conversion [36–39], surface functionalization [40], medical treatment [41, 42]. There are also a large number of researches focusing on the plasma-assisted nanomaterial synthesis, primarily driven by their fascinating properties. Plasma-enhanced chemistries, in which charged particles, excited states and radicals are expected to play a role in the nanofabrication process, differ essentially from traditional solution based media. In the non-thermal plasma the electrons gain energies in the range of ~ eV from the electric field, which are sufficient to initiate chemical reactions by collision with precursor compounds [43]. Therefore, these processes are inherently solvent and ligand-free, enabling the synthesis of high purity metallic nanoparticles [44]. Meanwhile, the energetic electrons also make it possible to produce composition-adjustable metal alloys with "chosen" properties such as the crystallinity and morphology [45], in some cases plasma-enhanced chemistries enable reactions which are hardly realizable in mild ways [46]. The non-thermal plasmas offer certain benefits for metal nanoparticle synthesis. On the one hand, they provide a highly reactive condition for metal atoms nucleation, in which precursors are dissociated rapidly via impact with electrons, excited heavy particles, radicals and UV radiation generated in plasma. At the same time gas (and substrate) temperature is still low, allowing the use of temperature sensitive precursors and limiting the aggregation of metallic nanoparticles [46, 47]. It should be noted here that plasmas which are closer to thermal equilibrium such as arc or microwave discharges can offer certain advantages for bulk production of nanoparticles at the cost of somewhat less precise process control. In such systems thermal decomposition of precursor will likely to take place. Moreover the high concentration of low energy electrons can contribute to the enhancement of plasma chemistry stimulated by vibrational excitation, this, in turn, can reduce production energy cost [48].

Although in past years significant progress has been achieved in plasma-assisted metallic nanoparticles fabrication, several challenges still need to be solved. Currently most of the reported processes operate at low pressures, requiring expensive vacuum equipment and are not ready for industrialization. Safety concerns are also involved due to the high voltages as well as the high reactivity ofutilized precursors, plasma species and metallic nanoparticles. Additionally, process-relevant microscopic and macroscopic parameters in plasma such as electron density, electron energy, temperature, current density and reduced electric field often have non-uniform spatial distribution, leading to the difficulty to provide homogenous conditions for particle nucleation and growth. As a result, the obtained metallic nanoparticles are commonly characterized by wide size distribution and partial agglomeration [49, 50].

New experimental findings, reported recently, provide increasing evidence that the confining of plasmas to small dimensions will lead to new physical behaviors [51–53]. Due to the increased surface-to-volume ratio and the decreased electrode spacing of plasmas at small dimensions, the electric field distributions are changed. As a consequence, the plasma physical structures and the energy distribution of the species (e. g. electrons, ions, neutrals, and radicals) are also affected. According to the Paschen's law, the breakdown voltage of a certain gas discharge is a function of the pressure and the characteristic length of the discharge [54, 55]. Thus it becomes possible to ignite and sustain the confined microplasma at high pressures even at the atmospheric pressure by applying a relatively low voltage. As indicated by Mariotti et al., with the decreasing spatial size, plasmas operated at a constant pressure undergo a transition from thermal equilibrium to region characterized by thermal instabilities, and ultimately, to a non-thermal equilibrium state [56]. Therefore, by controlling the operation parameters such as pressure, gas composition, input power and electrodes distance, plasma can be maintained at non-equilibrium state even at ambient pressure [56].

As a special category of plasma being confined within submillimeter scale in at least one dimension, microplasma has attracted tremendous interests for nanofabrication due to their unique characteristics [49]. In general, it employs beneficial properties of the atmospheric pressure gas discharge in microscale geometry for various plasma-enabled processes, resulting in a new and facile branch of applied plasma science. Several key advantages of microplasma-assited nanofabrication were summarized by Mariotti D and RM Sankaran: high pressure chemistry, continuous-flow, microreactor geometry and self-assembly/organization [56]. From a cost-efficiency standpoint, the atmospheric pressure operation of microplasmas allows saving of the significant costs associated with maintaining vacuum and using complex transfer chambers [57]. From the process efficiency perspective, microplasmas are characterized by higher densities of radicals, resulting in higher rates of plasma-chemical reactions and, in case of nanomaterials synthesis, leading to improved efficiency in particle nucleation and growth. Meanwhile, since the microscale geometry ensures a short residence time with a narrow residence time distribution (RTD) for precursors, the obtained nanoparticles are relatively smaller and have narrower size distributions compared with bulk plasma processes. In addition, the safety risks are much reduced when operating in microscale, especially when handling toxic materials. Based on these reasons, microplasma is becoming an emerging technique for nanofabrication, and a growing number of researches have been carried out in recent years focusing on its application in metallic nanoparticles synthesis. For a general overview, the advantages and drawbacks of different approaches for metallic nanoparticles synthesis are summed up in Table 2.2.

Table 2.2: Main methods for metallic nanoparticles synthesis and their advantages and drawbacks [46, 58–60].

Methods	**Advantages**	**Drawbacks**
Physical methods	Easy to execute	High energy consumption
	Large quantity production	Huge costs for equipment and operation
	Well-controlled particle interspacing	
Chemical methods	Controllable particle size, shape and morphology	Long reaction time
	Narrow size distribution	Difficult to control the process
	High purity, simple, reproducible	Toxic chemicals involved
Conventional plasmas	Simple, clean, efficient and flexible	Requires low pressure or high temperature
	Products with chosen constituents	Expensive reactors, safety concerns Particle with broad size distribution
Microplasmas	Atmospheric pressure operation	Low throughput, small deposition area, but can be solved by plasma arrays
	Simple, efficient, safe, economical	
	High uniformity of the products	

Despite a series of researches were carried out to fabricate nanomaterials by the microplasma technique, with some review articles being reported [46, 52, 56, 61], to our best knowledge, there is still no publication on reviewing the microplasma-assisted metallic nanoparticles synthesis. The present work, for the first time, focuses on the state of art of metallic nanoparticles synthesis by microplasmas. In the first, it reviews the existing microplasma systems as well as the characterization techniques for the microplasma dissociation process and the obtained metallic nanoparticles. Afterwards, a broad category of common metal nanoparticles is presented, with the possible mechanisms being discussed. Then this is followed by a brief introduction of critical safety considerations. Finally, we also point out the related challenges that need to be overcome and suggest feasible solutions and future perspectives for the industrial-level production of metallic nanoparticles by microplasma. The motivation of this work is to provide readers all the necessary information of this facile technique, including the detailed reactor configurations, characterization methods, representative examples and recipes, mechanism discussions, challenges and possible solutions, which may help to guide them in the process design for metallic nanoparticles production with desired properties using this novel approach.

2.2 Microplasma systems for metallic nanoparticles synthesis

So far a broad range of microplasma systems have been developed and applied for nanofabrication. To give a better overview of the existing microplasma systems, Table 2.3 provides a summary of reported configurations that have been used for

Table 2.3: A summary of microplasma systems used for nanomaterial synthesis.

Microplasma configuration	Power sources*	Generated products**	Ref.
Hollow-electrode microdischarges	CCP./15–35 kHz	CNTs	[62]
	DC/1–20 mA, 500–700 V	CuO/PdO/NiO NSs	[63]
	DC/0–10 kV	Si NCs, Ni/Fe/Cu/Pt NPs, TiN NPs Ni_xFe_{1-x} NPs, $Ni_xFe_yCu_{1-x-y}$ NPs	[64–67, 88, 125, 126, 132, 134, 157]
Microplasma jets with external electrodes	DC/38 kW (700 A/55 V)	Al_2O_3 NPs	[68]
	ICP./CCP.450 MHz, 20 ~ 30	Fe/Ni NPs	[69, 90]
	kHz	Si NPs	[70]
	ICP./CCP.144 MHz	CNTs, C NSs	[71, 92]
	CCP./13.56 MHz, 450MHz	TiO_2 NPs, TiC/TiN NSFs	[72–74]
	CCP./13.56 MHz, 430 MHz		
Microplasma jets with consumable electrodes	ICP./CCP.450 MHz	C-NPs, CNTs	[75]
	CCP./450 MHz	Fe/Cu/Au/Mo/ MoO_3/ WO_x NPs	[76, 77, 78, 79,
	CCP./14 MHz	Ni NPs, CNTs	97, 98]
			[80]
Plasma–liquid systems	ICP./0–10 kV	Ag/Au/Ni/Ti/Ir/ CuO_x/Fe_3O_4 NPs,	[105], 106,
	CCP./2.45 GHz	Si NCs, CNTs	136,
	CCP./15 kHz, 30 kHz	Zn/ZnO NPs	157, 158, 159, 160, 161, 162, 163, 164, 165]
	CCP./13.56 MHz	Ag/Au NPs, Tin, Fe	[81]
		C NS	[82–85]
			[86]

*CCP. = capacitive coupling plasma; ICP. = inductive coupling plasma; DC = DC plasma
**NP = nanoparticles; NS = nanostructures; CNTs = carbon nanotubes; NSF = nanostructured films.

nanofabrication, together with the relevant power sources and target products. These systems not only illustrate the versatility of microplasma sources but also reflect the high degree of flexibility in processing parameters. The classification of microplasma systems is diverse, based on the aspects such as the plasma power source (excitation frequency), electrode geometry, power coupling method, precursor injection way, target products and so on.

In this work, according to their general configurations, we divide the microplasma systems for metallic nanoparticles synthesis into four main categories: hollow-electrode microdischarges, microplasma jets with external electrodes, microplasma jets with consumable electrodes and plasma–liquid systems. Generally for the first three plasma systems, nanoparticles are generated in the gas phase, while in the fourth plasma system nanoparticles are obtained in the liquid phase. It should be noted that the classification is not rigid, since mixed cases can be used.

2.2.1 Microplasma-assisted process for metallic nanoparticles synthesis in the gas phase

2.2.1.1 Hollow-electrode microdischarges

Among microplasma systems hollow-electrode microdischarges are relatively simple and easily to operate. They use DC powers coupling to sustain the plasmas, which is considerably less expensive and easier to implement compared to pulsed plasmas. Generally a hollow capillary functions as one electrode as well as the gas guiding tube, in which metallic precursor vapors are diluted and transported by a flow of inert gas such as argon or helium. Meanwhile, another capillary or mesh is used as the counter electrode, with an interelectrode distance of 1 ~ 2 mm. Both electrodes are connected to a DC power supply, and the plasma is formed in the gaseous gap between the electrodes. An electrostatic precipitator or a filter is installed downstream of the aerosol to collect the obtained products.

A typical configuration of hollow-electrode microdischarges is shown in Figure 2.1, where nickelocene vapors were used as the precursor to produce Ni nanoparticles in a continuous and solvent-free manner [87]. In this study the plasma was formed between a stainless steel (SS) capillary tube (O.D. = 1.6 mm, I.D. = 500 µm) and a SS mesh (Warp Weft opening: 500 × 500 µm), with a gaseous gap of 2 mm. A commercial DC power supply was used to generate and sustain the plasma. The plasma voltage had a constant value of 210 V, while the current varied from 6.0 ~ 16.2 mA. Therefore, the influence of plasma power on the obtained products could be investigated. Meanwhile, the nickelocene vapor concentrations could be controlled by adjusting the dilution ratio in Ar, while the total gas flow through plasma volume was kept constant. Thus the influence of the precursor concentration could also be studied.

Another representative configuration demonstrated by PA Lin et al. is shown in Figure 2.2 [88], in which various organometallic compounds (nickelocene, ferrocene,

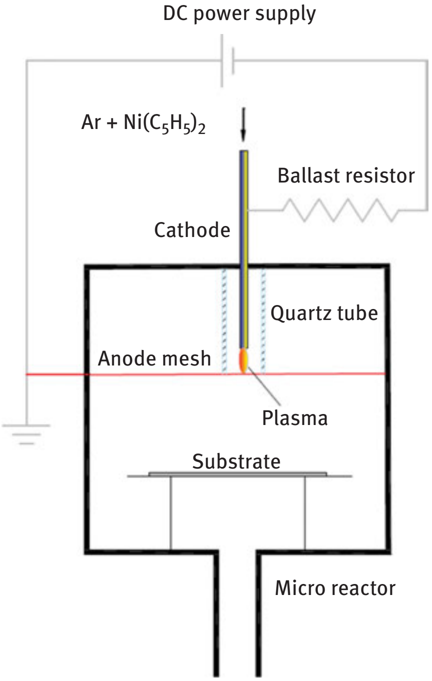

Figure 2.1: Schematic diagram of the hollow-electrode microplasma reactor for the continuous synthesis of Ni nanoparticles. Reprinted with permission from [87], copyright 2017 Wiley-VCH.

copper acetylacetonate and platinum acetylacetonate) were employed to produce metallic or multi-metallic nanoparticles. In this research two SS capillary tubes (O.D. = 1.6 mm, I.D. = 180 µm) were used as the cathode and the anode. After subliming the corresponding metallic precursors, they were carried into the plasma zone by the separate gas lines in continuous argon flows. In all experiments the total gas flow was kept constant at 100 sccm, and the gas flow rates in different precursors lines were individually controlled by mass flow controllers. In this manner metallic nanoalloys of tunable composition were produced by varying the relative gas flow rate in precursor and dilution gas lines. The size and size distributions of the generated nanoparticles were measured *in situ* by a scanning mobility particle sizing system.

The described hollow-electrode microdischarges are operating at atmospheric pressure, with the characteristic interelectrode distance of few mm. For this experimental arrangement the typical plasma voltage and current for a model case of metallic nanofabrication process is kept at the level of hundred V and several mA. Therefore, metallic nanoparticles can be obtained at very low power consumption. In addition, due to the extremely small reaction zone, the residence time of precursor vapors in the plasma is very short. It is calculated to be in the order of ~10^{-4} s for two configurations shown above, derived from the total gas flow rate, tube size as well as electrode distance. As a consequence, the generated nanoparticles are ultra-fine and

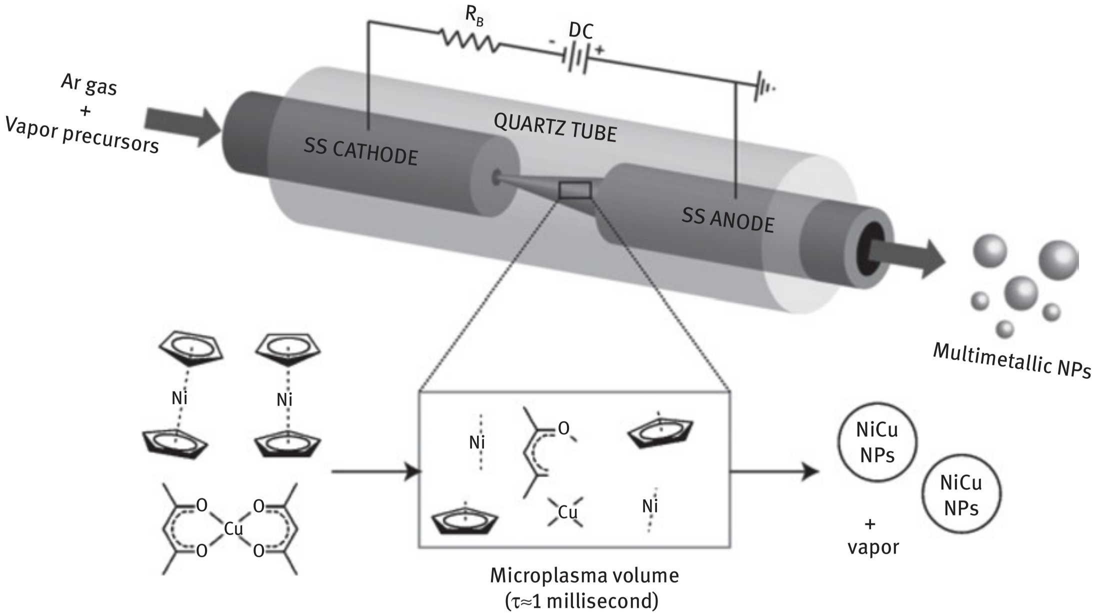

Figure 2.2: Schematic diagram of the atmospheric pressure microplasma reactor used to continuously synthesize compositionally tunable multimetallic nanoparticles (NPs). A hypothesized mechanism for formation of Ni_xCu_{1-x} bimetallic NPs is also shown. Reprinted with permission from [88], copyright 2011 Wiley-VCH.

have relatively narrow size distributions compared to other types of microplasmas. Chiang and Sankaran have shown that in certain cases Fe/Ni nanoparticles with a mean particle diameter of 2.87/3.11 nm and a standard deviation of 1.12/1.16 were synthesized by the hollow-electrode microdischarges [89]. Despite the ability to produce ultra-fine metallic/multimetallic nanoparticles with extremely narrow size distributions by the hollow-electrode microdischarges, several issues still need to be solved: (1) In such configuration, the generated nanoparticles are easily accumulated on the electrodes. Once operated for a relatively long time, the current and voltage may experience an increasing fluctuation trend, resulting in unstable conditions and unreproducible products. (2) Due to the electrode material erosion and sputtering, metal contaminations may exist in the products. (3) Owing to the small inner diameter of the capillaries, it is only allowed to use the gaseous precursors to avoid the blocking problem. Thus the carried precursor quantities are rather limited, leading to quite low throughput of each processing.

2.2.1.2 Microplasma jets with external electrodes

To solve the problems encountered in the hollow-electrode microcharge systems, microplasma jets with external electrodes are proposed and applied for metallic nanoparticles synthesis. In this configuration the plasmas are totally or partially confined in dielectric (e. g., quartz) capillaries or tubes, and are mostly sustained by radio frequency (RF) powers inductively or capacitively coupled by external electrodes outside the capillaries or tubes. The external electrode configuration implies AC or pulsed power coupling, while the frequency and shape of applied voltage in principle may vary in a very broad range, from tens of Hz to GHz region. Precursors are directly injected or carried by gas flows into the plasmas, either inside or outside the capillaries (tubes). The obtained nanoparticles can be collected by depositing onto substrates downstream the gas flows or by flowing through proper solvents.

Figure 2.3 shows several emblematical examples of microplasma jets with external electrodes for metallic nanoparticles synthesis [61]. In general, the capillary/tube is made of quartz for diagnostic purposes. However, sometimes alumina or other

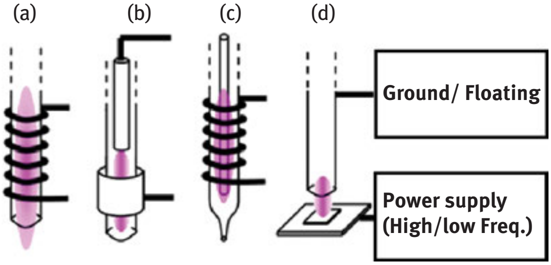

Figure 2.3: Schematic diagram of the microplasma jets with external electrodes. Reprinted with permission from [61], copyright 2009 IEEE.

metals are also adopted. To confine the plasma into a submillimeter spatial scale, a typical internal diameter of the capillary/tube is in the range of 0.3 to 0.7 mm. The microplasma can be generated and sustained by purely inductive (Figure 2.3(a)), purely capacitive (Figure 2.3(b) and (d)), or hybrid (Figure 2.3(c)) power-coupling mode, with the frequency varies from low (e. g. ~ 20 kHz) to high (e. g., 450 MHz) range. Plasma gases (Ar, N_2, He, H_2 or several mixtures thereof) are flown through the capillary/tube vessel, with characteristic flow rate of 50–100 sccm. Due to the flexibility of the configuration, the metallic precursors can either be transported through the tube or be placed outside the tube in direct contact with the microplasma jet, allowing for a wide range of nanoarchitectures/nanostructures to be produced.

Another example of microplasma jets with external electrodes is illustrated in Figure 2.4, where a plasma jet was totally confined inside a DBD reactor to produce Ni nanoparticles from nickelocene vapors [90]. In this study, two types of DBD reactor, with or without a gas injection capillary, were applied in order to control and study the particle nucleation and growth. Both reactors consisted of a quartz tube (O.D. = 6 mm, I.D. = 2 mm) with powered electrodes outside the quartz tube. The plasmas were ignited and operated at steady state by an AC power supply. Copper tapes with the width of 3–4 mm were wrapped around the exterior of the quartz tubes and operated as the powered electrodes. The discharge was sustained at the frequency of 20–30 kHz with peak-to-peak voltage of ~8 kV, being measured by a high voltage probe.

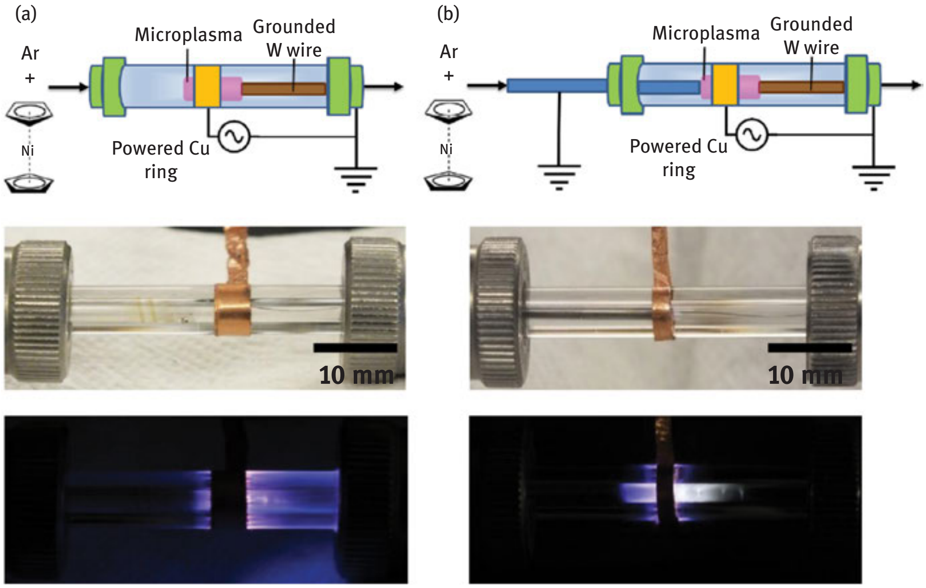

Figure 2.4: Schematic illustration and photos of a totally confined microplasma jet (DBD) with external electrodes: (a) without and (b) with a capillary gas injection for Ni nanofabrication. Reprinted with permission from [90], copyright 2015 IOP Publishing.

Nickelocene vapors of different concentrations (0.21–0.94 ppm) were carried into the plasma zone by an argon flow of 100 sccm flow rate. The generated nanoparticles were collected by a 40 µm pore size Teflon filter placed at the gas effluent of the reactor.

For microplasma jets with external electrodes, there is no direct interaction between plasma and electrode materials, thus eliminating possible contaminations. Meanwhile, the process has larger operational space, since a wider range of processing parameters can be set and tuned, such as precursor's ratio, the power coupling mode, the applied voltage frequency, precursor residence time and so on. In terms of precursors, this type of plasma has more flexibility. Due to the possibility to confine the plasma jet either partially or totally within the tube, in principle, metallic precursors can be gases, liquids or even solids, as long as the jet is appropriately positioned. There is even a study using supercritical CO_2 as the precursor in a DBD microplasma jet to show that supercritical fluids can also serve as alternative precursors [91]. Another distinct advantage is the possibility to apply microplasma jet, installed on the positioning stage, in the fields where local/on-site "dry-process" production of well-defined nanostructures is required i. e. printing-like technologies [51, 92–96]. However, disadvantages also exist for this plasma system. In comparison to the hollow-electrode microplasmas, for jet configuration with external electrodes, the plasma typically occupies larger volume, therefore, the nanoparticles tend to grow larger and have broader size distributions. Moreover, the RF electronics, used in the majority of configurations with external electrodes, are relatively expensive, complex and need matching networks, leading to increased overall costs.

2.2.1.3 Microplasma jets with consumable electrodes

There is also a type of microplasma jet using consumable metal wires as an electrode to produce metallic nanoparticles. In this configuration generally ultra-thin metal wires with a characteristic diameter size of 50–100 µm are inserted into the tubes and act as sacrificial metallic precursors. Plasmas are formed at the end of the electrode and are partially or entirely confined in quartz or alumina tubes. High-frequency powers are coupled outside the tubes to sustain the plasmas. Inert gases such as argon or helium flow into the tube as the plasma gas and at the same time preventing the oxidization of the obtained products. The generated products can be collected by placing a substrate under the consumed wires.

The model case example which demonstrates such a plasma configuration is shown in Figure 2.5, proposed by Shimizu et al. to synthesize Au nanoparticles [97]. In this system a consumed Au wire of 100 µm diameter, inserted into a quartz capillary (O.D. = 1.2 mm, I.D. = 800 µm), was used as the metal source. A flow of H_2/Ar gas mixture was fed into the capillary at a 200 sccm flow rate. A UHF (450 MHz) generator was applied to a 20-turn brass coil outside the tube to generate the microplasma jet. The pulse frequency was varied from 50 to 100 Hz, while the time-averaged power was kept at 0.8 W. After the ignition of the plasma, the Au wire was heated and melted due to

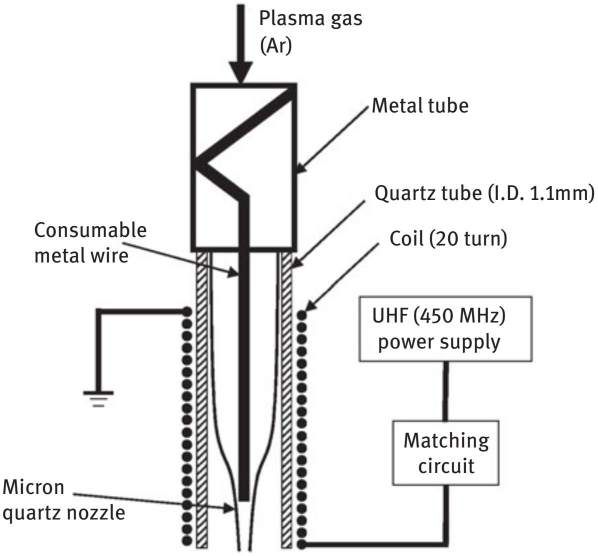

Figure 2.5: Schematic diagram of the microplasma jet with a consumable Au wire to produce gold nanoparticles. Reprinted with permission from [77], copyright 2006 Elsevier.

thermal conduction from the plasma jet as well as the inductive heating. Then the Au droplets produced by atomization of the consumed wire were carried away by the gas flow and deposited on a glass epoxy plate 5 mm downstream to form Au nanoparticles.

Another example of the microplasma jet with a consumable wire electrode is shown in Figure 2.6 [98]. In this structure an argon flow of 20 sccm flow rate was

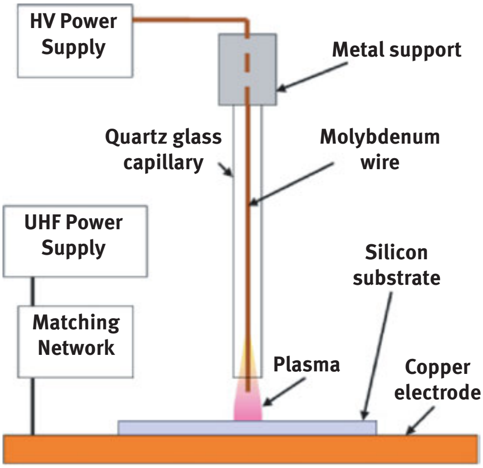

Figure 2.6: Schematic diagram of the microplasma jet with a consumable molybdenum wire to synthesize Mo metallic nanoparticles. Reprinted with permission from [98], copyright 2007 American Vacuum Society.

injected into a quartz capillary (O.D. = 1 mm, I.D. = 700 µm) at the top of the system. A high-frequency power supply was coupled to a copper electrode (2 cm × 2 cm) through a matching network to sustain the plasma. Meanwhile, a silicon substrate of a 0.625 mm thickness was placed on the top of the copper electrode for the deposition of metallic nanoparticles. A molybdenum wire of 0.1 mm diameter was inserted into the capillary and functioned as the sacrificial metal source. The plasma power was set to 31 W, and ignited by a high voltage pulse (~5 kV) applied to the Mo wire. Under the impact of the plasma, the molybdenum wire was consumed to form Mo metallic nanostructures.

Microplasma jet with consumable wire electrodes is a special category of microplasma systems. With such a configuration it is possible to produce a broad range of metal nanoparticles and even nanoalloys, only by changing the relevant metal wires. Another attractive feature is that by feeding oxygen, nitrogen or organic compounds, this microreactor design can be applied to fabricate metal oxides, nitrides or metallic nanoparticles embedded in polymer coatings. Moreover, the product properties can be controlled and tuned "in-flight" by controlling processing parameters, such as the gas composition, plasma power, gas feeding rate and so on. To ensure the continuity of the nanoparticles production, a feeding mechanism for consumable thin wire should be provided. Possible limitation in the process control can be caused by the temperature gradient and the consequent non-uniform volatilization rate of the metal wire, resulting in larger sizes as well as in broader size distributions of the obtained nanoparticles.

2.2.2 Microplasma-assisted process for metallic nanoparticles synthesis in the liquid phase

Plasma–liquid interaction is a multidisciplinary topic including physics, chemistry, electrical and materials science being fundamentally different from classical systems with solid electrodes and liquid electrolytes [99]. A series of complex physical and chemical reactions as well as transfer processes involve in the plasma–liquid systems, which are schematically illustrated in Figure 2.7. In past decades, with the development of nanoscience and the emergence of various reactors based on plasma–liquid interactions, an important question was naturally raised: Can charged radicals be transferred between plasmas and electrolytes to enable chemical or electrochemical reactions and to produce nanoparticles of controlled properties in the plasma–liquid systems [55]? The pursuit of the answer to this question attracted significant academic research from different fields, and many studies were carried to investigate this fascinating concept.

Nowadays various plasma–liquid systems have been designed and explored to synthesize metallic nanoparticles in the liquid phase. According to the plasma configurations or generation methods, they are divided by Bruggeman et al. into the four types, with characteristic plasma properties provided in Table 2.4 [100]. In this section, we simplify the classification and based on whether the plasma contacts the liquid or

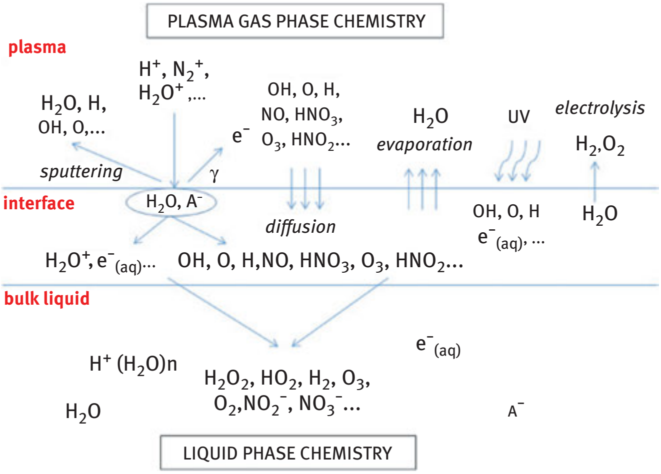

Figure 2.7: Schematic overview of the important transfer processes in the plasma–liquid systems. Reprinted with permission from [115], copyright 2012 IOP Publishing.

Table 2.4: Main plasma–liquid systems for nanoparticles synthesis in the liquid phase and their typical plasma properties. Reprinted with permission from [100], copyright 2016 IOP Publishing.

	Direct liquid discharges	**DC air glow discharges**	**Pulsed jet (non-touching)**	**Filamentary DBD (single filament)**
Medium/gas	Water	Humid air	He-Ar	Air
Plasma generation time	1–10s μs	Continuous	10–100 ns	1–10 ns
Electron density (m^{-3})	10^{24}–10^{26}	10^{18}–10^{19}	10^{19}–10^{20}	10^{19}–10^{21}
Pressure (bar)	10^4 (peak)	1	1	1
Gas temperature (K)	1000–7000	2000–3000	300–400	300–400
Ionization degree	1–10^{-3}	10^{-5}–10^{-7}	10^{-5}–10^{-6}	10^{-5}–10^{-6}
Energy/power	1 J per pulse	5–100 W	<10 μJ per pulse	<10 μJ per pulse
Power density	≤10^{15} W m^{-3}	~10^6 W m^{-3}	<10^{12} W m^{-3}	<10^{12} W m^{-3}
Current	~1 A	5–100 mA	2–10 mA peak	<100 mA
Electron temperature (eV)	1 (close to LTE)	1–2	1–2	2–3
Electric field (kV cm^{-1})	~10^3	1 (in positive column)	1-10	10–100
Ion density at interface (m^{-3})	10^{24}	10^{18}–10^{19}	≤10^{16}	10^{20}–10^{21}
UV ($m^{-2}s^{-1}$)	Broadband UV emission	Strong UV (NO(*A*-*X*), OH(*A*-*X*), N_2(*C*-*B*))	5 × 10^{22}	5 × 10^{23}
Radical density ($m^{-3}s$)	~10^{24}	10^{21}–10^{23}	10^{19}–10^{21}	10^{20}–10^{21}
Reactive species flux (m^{-2} s^{-1})	Extremely large gradients	10^{23}–10^{25}	~10^{21}–10^{23}	~10^{22}–10^{23}
Flow effects	Shockwaves	Thermal convection	Forced flow	Convective

Notes: These values are estimates as a guide to typical plasma conditions.

not, we subdivide the plasma–liquid systems into two categories: indirect contact plasma–liquid systems and direct contact plasma–liquid systems. Representative examples will be provided in each category to illustrate their configurations and how they are applied for metallic nanoparticles synthesis.

2.2.2.1 Indirect contact plasma–liquid systems

Indirect contact plasma–liquid systems refer to the configurations where plasmas are formed in the gas phase above the solution surface. Usually one electrode is in the form of “pin” or with a sharp “edge” and positioned in the gas phase within a distance of few mm above the liquid electrolyte, while the other electrode is immersed inside the electrolyte and can be in various shapes. Power supplies of different frequencies ranging from dc, kHz, MHz and even up to GHz range are coupled to the electrodes to excite and sustain the plasma [101]. In this configuration the discharge is generated between the upper electrode and the electrolyte surface, and the metallic precursors dissolved in the electrolyte will be reduced to form metallic nanoparticles by interaction with plasma-formed charged particles and radicals. With few exceptions including ionic liquids, such plasma systems are operated at atmospheric or higher pressures [102–104].

A typical example of the indirect contact plasma–liquid system is shown in Figure 2.8, where the $HAuCl_4$ solution (0.2 mM) was used as the electrolyte to produce gold nanoparticles [105]. In this research a SS capillary tube (I.D. = 175 µm, Length = 5 cm) was used as the cathode and positioned 2 mm above the electrolyte surface. A Pt foil (Area = $1 \times 1\ cm^2$, thickness = 0.001 inch) functioned as the anode and was placed 3 cm away from the cathode. Both electrodes were connected to a DC high voltage power supply, and plasma was formed between the capillary tube and the electrolyte surface. For each operation a helium flow at 25 sccm gas flow rate was coupled to the capillary

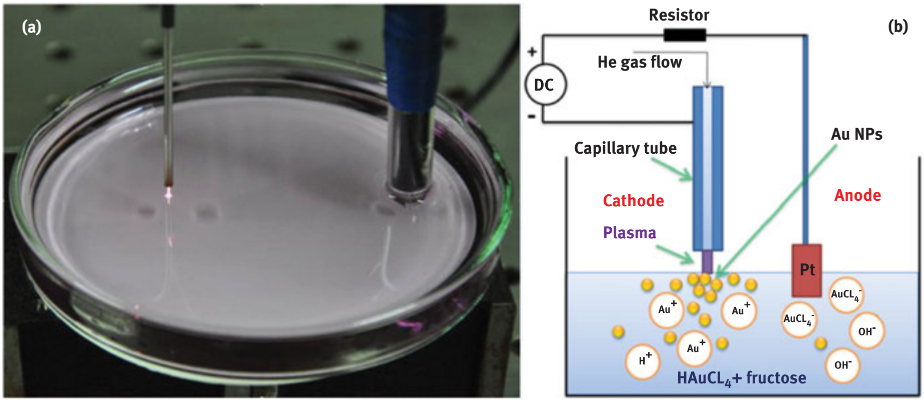

Figure 2.8: The experiment setup of the indirect contact plasma–liquid system (a) and its schematic (b) for preparing Au nanoparticles. Reprinted with permission from [105], copyright 2014 Springer.

acting as the plasma gas. 10 ml of $HAuCl_4$ solution was placed in a petri dish for the plasma processing. A 0.01 M fructose was added to prevent uncontrolled particle growth and agglomeration. Meanwhile, processing parameters such as solution temperature, current, and rate of stirring were adjusted to synthesize Au nanoparticles of controllable size and morphology. In addition to Au nanoparticles, this microplasma configuration has also been employed for the synthesis of other metallic nanoparticles such as Ag [93, 106], Pt [107, 108] and even alloys such as Au_xAg_{1-x} [109], Au_xPt_{1-x} [110].

An alternative promising approach is to use ionic liquids as electrolytes in the indirect contact plasma–liquid systems. Given the unique physicochemical properties of ionic liquids, such as high thermal stability, excellent ionic conductivity, low viscosity and extremely low vapor pressures, they can be beneficial in comparison to aqueous solutions [111–113]. Another distinctive advantage of this electrolyte type is its wide electrochemical window (up to 7 Volt), enabling electrodeposition of the elements such as Ge, Si, Se, Al and many others that cannot be obtained in aqueous solutions [103].

In the study of Meiss et al. [103], a solution of $AgCF_3SO_3$ and 1-butyl-3-methylimidazolium trifluoromethylsulfonate ionic liquid ([BMIm][TfO]) was used as the electrolyte for the liquid phase synthesis of Ag nanoparticles in a glass tube (I.D. = 2.5 cm). The solution typically contained 0.3 g of $AgCF_3SO_3$ in 10 mL ([BMIm][TfO]). The anode was a platinum sheet (1 cm×1 cm), immersed inside the ionic liquid, while the cathode was a platinum hollow cylinder (Diameter = 0.75 cm, Length = 1.5 cm), placed in the gas phase above the ionic liquid (Figure 2.9). Before each operation the reactor was evacuated, while the processing was carried out in the argon atmosphere at 1 mbar gas pressure. During the experiment the current was set at 10 mA, and the voltage stabilized at 470 V. Within several minutes of operation a formation of black reaction products was visually observed at the interface between plasma and ionic liquid,

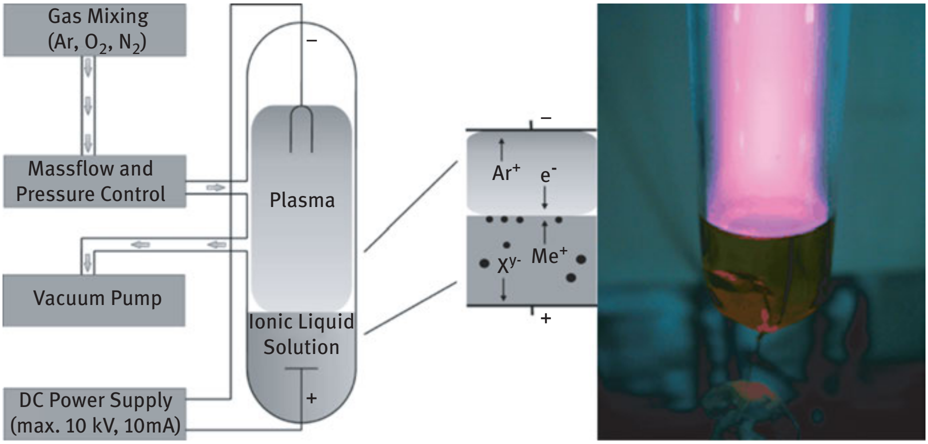

Figure 2.9: The indirect contact plasma–liquid system using ionic liquid as the electrolyte to prepare silver nanoparticles. Reprinted with permission from [103], copyright 2007 Wiley-VCH.

which were gradually dispersed and deposited at the bottom of reactor. Further analysis indicated that the products consisted of crystalline Ag nanoparticles with a characteristic size distribution in the range of 8–30 nm.

2.2.2.2 Direct contact plasma–liquid systems

Direct contact plasma–liquid systems refer to the configurations where plasmas are generated within the liquid volume. In general, the addition of plasma gas (i. e. via bubbling) is not necessary although can facilitate the discharge ignition. This type of plasma is characterized by a large quantity of heat and a high yield of solvent-split radicals generated in the solution. The precursor can be either metallic salts which are dissolved in the water or other solvents to form the electrolyte, or metal wires functioning as the consumable electrodes. The electrical discharge typically develops inside self-generated or introduced gas bubbles with the operating pressure above the atmospheric pressure. The most common electrodes configurations are in the form of pin-to-pin or pin-to-plate geometries, with a characteristic interelectrode distance of few mm. The discharges are usually produced by high voltage pulses and referred as streamers or corona type. A common excitation method is by means of discharging a capacitor where a short-rise-time switch (e. g. a spark gap) produces microsecond pulsed discharges. Recently, more excitation methods such as high voltage nanosecond pulses, radio frequency or microwave excitations were applied to generate plasmas in the liquid phase.

One representative example is demonstrated in Figure 2.10, where Sn nanoparticles were successfully synthesized by a direct contact plasma–liquid system. In this study the tin chloride dehydrate ($SnCl_2 \bullet 2H_2O$) was used as the precursor for the Sn nanoparticles, and the cetyltrimethylammonium bromide (CTAB, $CH_3(CH_2)_{15}N(CH_3)_3Br$) was used as the surfactant. Both were dissolved in pure water to prepare the electrolyte. During each

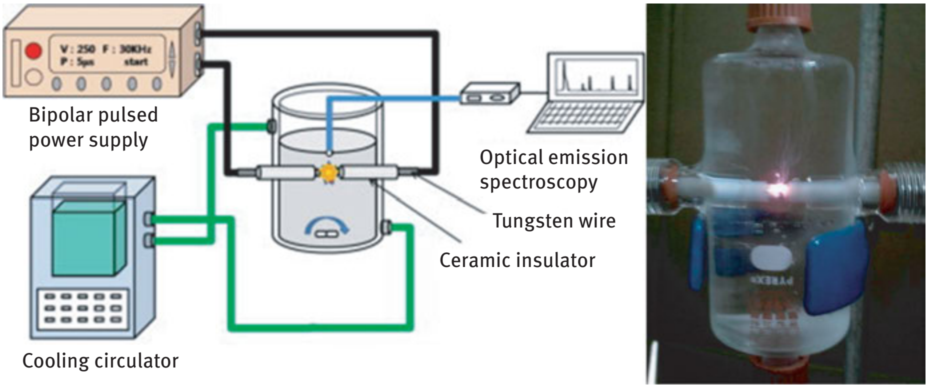

Figure 2.10: The schematic setup and the photograph of the direct contact plasma–liquid system for the synthesis of Sn nanoparticles. Reprinted with permission from [85, 114], copyright 2014 Elsevier, 2013 Materials Research Society.

operation a 300 ml electrolyte with tin chloride concentration of 2–4 mM was added in the reactor. Tungsten capillaries (Diameter = 2 mm) coated by ceramic insulator were chosen as the electrodes and fixed in the "needle-to-needle" configuration, with an interelectrode gap of 0.2 mm. A high-frequency bipolar pulse power supply was used to generate the plasmas directly in the liquid phase in a double annular tube type reactor (I. D. = 50 mm, O.D. = 80 mm, Height = 150 mm). The applied voltage amplitude, pulse width and repetition frequency were set at 250 V, 5 µs and 30 kHz, respectively. Under the plasma treatment the Sn^{2+} was reduced to form the Sn nanoparticles.

Compared to other plasma-assisted metallic nanofabrication techniques, the plasma–liquid systems are rather new and attractive. In these configurations the discharges are spatially located either above the electrolyte surface or inside the electrolyte, thus the bulk liquid still remains undisturbed. The generation of plasmas in the liquid will have additional confinements due to higher density of liquid, which may offer potential routes to prepare metallic nanoparticles [101]. Furthermore, in liquids the plasma-induced heat flux can be rapidly dissipated, ensuring a rather low temperature in the system. Therefore, the particles nucleation and growth rate are limited, resulting smaller sizes as well as narrower size distributions. Regarding precursor selection, numerous metal-containing chemical compounds can be chosen for the plasma–liquid systems, as long as they have good solubility in solvents such as water, ethanol or ionic liquids. Moreover, consumable metal electrodes can be also used as the precursors. Therefore, a variety of metallic nanoparticles can be synthesized by this plasma type. On the other hand, limitations also exist for the plasma–liquid system. Since reactions take place in the liquid phase, and in some cases surfactants are involved in the process, it is unavoidable to use post-treatment like washing, filtering or centrifuging to purify the products. Additionally, the kinetics of physicochemical processes in plasma–liquid system is very complex, due to the existence of various species such as gaseous/solution ions, electrons or neutral radicals. Nowadays, despite significant progress has been achieved in characterizing the plasmas and understanding the mechanisms of charge transfer process, it is still unclear how charged species, neutrals and metastable radicals are transferred from the plasma to the liquid and vice versa [115]. Extensive studies are required to fully understand the plasma–liquid transfer processes and reaction kinetics.

In summary, we have demonstrated representative examples of common microplasma configurations for metallic nanoparticle synthesis both in the gas phase and in the liquid phase. It is shown that a wide range of metallic nanoparticles with tunable properties can be synthesized by the microplasma-assisted technique using various reactor arrangements. In order to provide a guideline for the process design and for the selection of an appropriate microplasma system for metallic nanoparticles synthesis, a brief summary of the advantages and drawbacks of each configuration is provided in Table 2.5.

Table 2.5: A summary of advantages and drawbacks of the microplasma systems for metallic nanoparticles synthesis.

Plasma configurations	Advantages	Drawbacks
Hollow-electrode microdischarges	Simple, safe, easy operation	Low throughput
	Low-power consumption	Metal contaminations
	Ultra-fine particle size, narrow size distribution	Unstable conditions after long time operation
Microplasma jets with external electrodes	Efficient, flexible, high purity products	Large particle size, broad size distribution
	Wide operational windows	Expensive and complex power supply
	Flexible precursor choice (gas, liquid and solid)	
	In situ deposition, i. e. printing, coating	
Microplasma jets with consumable electrodes	Simple, efficient, flexible, in-flight tuning	Large particle size, broad size distribution
	Various high purity metals	
	Feasible for oxides, alloys, nitrides	
Plasma–liquid systems	Flexible, efficient, simple and highly confined	Post-treatment required
	High radical density, low temperature	Unclear mechanisms
	Ultra-fine particle size, narrow size distribution	
	Flexible precursors (salts, consumable wires)	

2.3 Characterization methodologies and analytic techniques

In the past few decades, the development of new techniques leads to significant progress in both the synthesis and characterization of metallic nanoparticles. Intensive studies were carried out to optimize and control the processing parameters for assembling and tailoring properties of metal nanostructures to meet specific application requirements, with the ultimate goal to understand how metallic nanoparticle composition, size, shape, and ordered assembly affect the key product properties. With the development of the nanotechnology and instrumentation techniques, nowadays various complementary approaches to *in situ* characterize the operating microplasma as well as to *ex situ* analyze produced nanoparticles are utilized. As a consequence, a better understanding of the complex kinetics and the underlying mechanisms of the process was achieved in recent years. Here the *in situ* characterization of the plasma-assisted dissociation process will be firstly reviewed, followed by the introduction of the complementary analytical methods for *ex situ* characterizing the synthesized metallic nanoparticles.

2.3.1 *In situ* characterization of the microplasma-assisted precursors dissociation process

The simplest and most convenient way to characterize the microplasma-assisted precursor dissociation process is via the visual observation of the operating plasmas. The atomic and molecular electronically excited states formed in the discharges will emit light during radiative relaxation process. Meanwhile, since different species have their specific excited states and emit lights of different colors (wavelengths), the visual appearance of plasma can already provide direct and useful information about the radical states existing in the plasma.

One example is shown in the Figure 2.11, in which $Ni(Cp)_2$ and $Cu(acac)_2$ vapors were added into an argon microplasma to produce Ni and Cu nanoparticles [116]. For $Ni(Cp)_2$ no significant change in the plasma color was observed. By contrast, the introduction of $Cu(acac)_2$ into the plasma at the same condition resulted in a considerably different plasma appearance with a greenish-blue color, suggesting that the Cu containing precursor dissociated deeper than the Ni precursor. This conclusion,

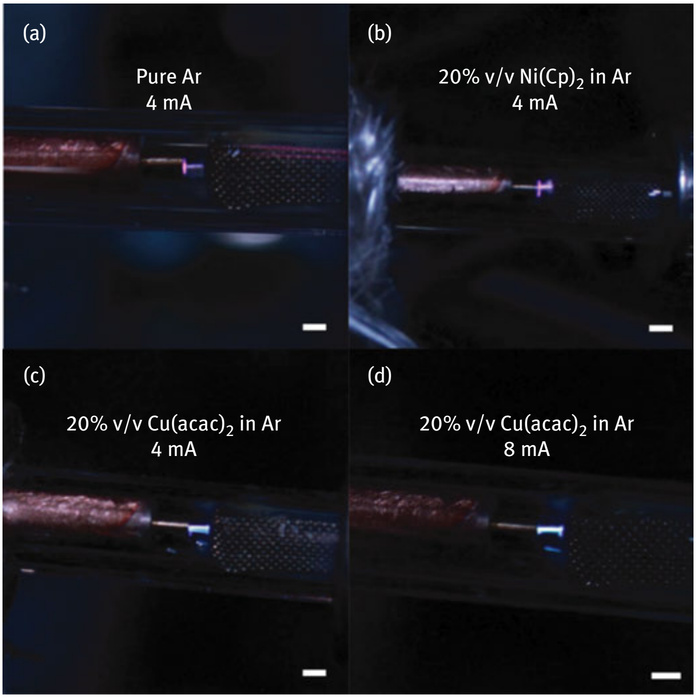

Figure 2.11: Photos of microplasmas operated at the experimental conditions: (a) pure Ar with a discharge current of 4 mA, (b) 20 % v/v $Ni(Cp)_2$/Ar with a discharge current of 4 mA, (c) 20 % v/v $Cu(acac)_2$/Ar with a discharge current of 4 mA, and (d) 20 % v/v $Cu(acac)_2$/Ar with a discharge current of 8 mA. Reprinted with permission from [116], copyright 2012.

based on direct visual observation, was further supported by the detailed analysis of optical emission spectra.

Optical emission spectroscopy (OES) is a non-intrusive technique for plasma diagnostics. It allows an identification of excited states and gives valuable information of reactive species (e. g., excited ions, molecules, etc.) that exist in plasma [116]. In general, by recording the emitted spectrum and correlating the spectral features with emission peaks of the precursor originated radicals, we can not only examine the chemical components in the plasma but also have the detailed radiative transition information of the precursor fragments. Based on the intermediate radicals, it is also possible to gain an insight into the complex precursor dissociation process in the microplasma. The relative intensity distribution in the molecular emission bands can be used as a convenient tool for the contactless gas temperature measurement. Since the rotational temperature of the atmospheric pressure plasma can be regarded as an approximation of the gas temperature, by fitting the experimental spectra profile of certain rovibrational bands with the simulated ones (by i. e. SPECAIR model), the plasma gas temperature can be estimated [117–120]. The second positive system (SPS) of emission bands of nitrogen or the swan bands of C_2 molecules has long been utilized to extract information from plasma spectra [121–124].

Optical emission spectroscopy is widely applied for characterizing the plasma-assisted nanofabrication processes [125–128]. One typical example is in the research of Lin et al., where they used an atmospheric pressure argon microplasma to produce iron nanoparticles with the ferrocene as the precursor [125]. The impact of discharge parameters (ferrocene concentration, discharge power) on plasma characteristics were *in situ* monitored by a spectrometer (HR4000, Ocean Optics, Inc.; spectral resolution: 0.91 nm). The emitted light was collected by an optical fiber fixed at 20 mm distance from the microdischarge. Apart from the atomic Ar lines, the spectra indicated the presence of different excited species originated by ferrocene dissociation (Fe, CH, C_2, C_3 and H), suggesting the decomposition of ferrocene vapors in the argon discharge. Meanwhile, these line intensities and their ratios relative to the argon lines were found to increase with the precursor concentration or the discharge power, indicating the density growth of the corresponding excited species and a higher precursor dissociation rate of the ferrocene vapors (Figure 2.12(a)). Moreover, by fitting the C_2 swan band in the range of 504–520 nm, the gas temperature was estimated to be approximately 900 K at 1.05 W of the plasma power and 1100 K at 2.27 W of the plasma power.

Another is example refers to the study of Sankaran et al., where a hollow-electrode microcharge system was applied to dissociate organometallic vapors for the synthesis of metallic nanoparticles such as Ni, Fe, Cu and Pt [127]. In this study acetylacetonate components (copper acetylacetonate and platinum acetylacetonate) as well as metallocene components (ferrocene and nickelocene) were chosen as the precursors and dissociated at different conditions, which were *in situ* monitored by an optical emission spectroscopy. Results showed that for the metallocene components

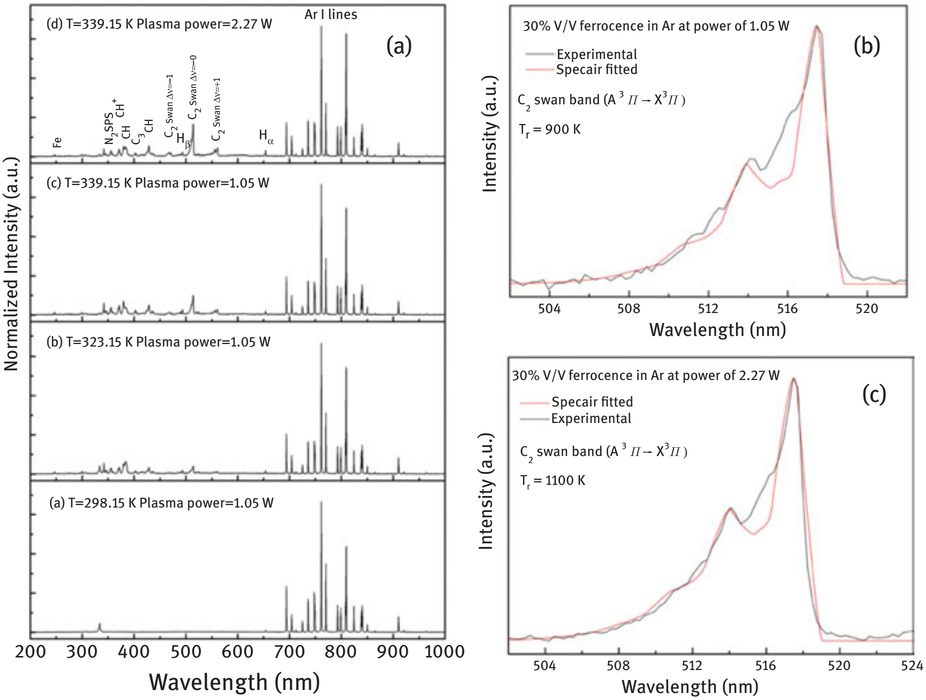

Figure 2.12: (a) OES spectra recorded from discharges operated with different concentrations of ferrocene vapors and plasma powers. (b–c) Experimental spectra and the corresponding SPECAIR simulation of microplasma operated at plasma power of 1.05 W and 2.27 W. Reprinted with permission from [125], copyright 2017 Elsevier.

no emission lines of the metal or carbon species were detected. By contrast, for the acetylacetonate precursors dissociated at the same conditions, emission lines corresponding to carbonaceous species have been clearly observed. It proved that metallocene precursors were more difficult to be dissociated than acetylacetonate precursors, which may be attributed to their mesomeric nature.

In addition to direct imaging and OES, another important technique for *in situ* characterization of the particle formation process is the aerosol measurement for determining the as-grown particle size and size distributions. It usually consists of a differential mobility analyzer (DMA) and an ultrafine condensation particle counter (CPC). The aerosol measurement is based on particle electrical mobility in the carrying gas and corresponds to the projected area. Briefly, particles firstly flow into a bipolar charger and are exposed to ionizing radiation from a sealed ^{85}Kr β-source, being positively or negatively charged. The particle electrical mobility is a function of its projected area. Once they are directed into the DMA, particles of different sizes have distinct trajectories. Therefore, by adjusting the applied voltage, nanoparticles of a specific electrical mobility are transmitted and introduced into a CPC, where the concentration of classified nanoparticles is measured and counted [129–131]. The combined operation of the DMA and CPC allows *in situ* monitoring the particle size and size distributions with high speed and sensitivity, enabling the direct acquisition of information during the microplasma-assisted particle growth process.

In the research of Chiang et al., ferrocene and nickelocene were used as the precursors to prepare metallic nanoparticles and alloys such as Fe, Ni and Fe_xNi_{1-x} [132]. A DMA-CPC system was used for the real-time measurement of particle size and size distributions, as shown in Figure 2.13(a). Meanwhile, in order to prevent Brownian coagulation of the nanoparticles, the aerosol exiting the microplasma zone was immediately diluted by a N_2 flow. Firstly Fe and Ni nanoparticles were obtained at the same metallocene vapor concentrations of 2.6 ppm. It is found that Fe nanoparticles have a larger mean diameter (4.40 nm) than Ni nanoparticles (3.11nm). The reducing of ferrocene concentration to 2.0 ppm led to Fe nanoparticles with

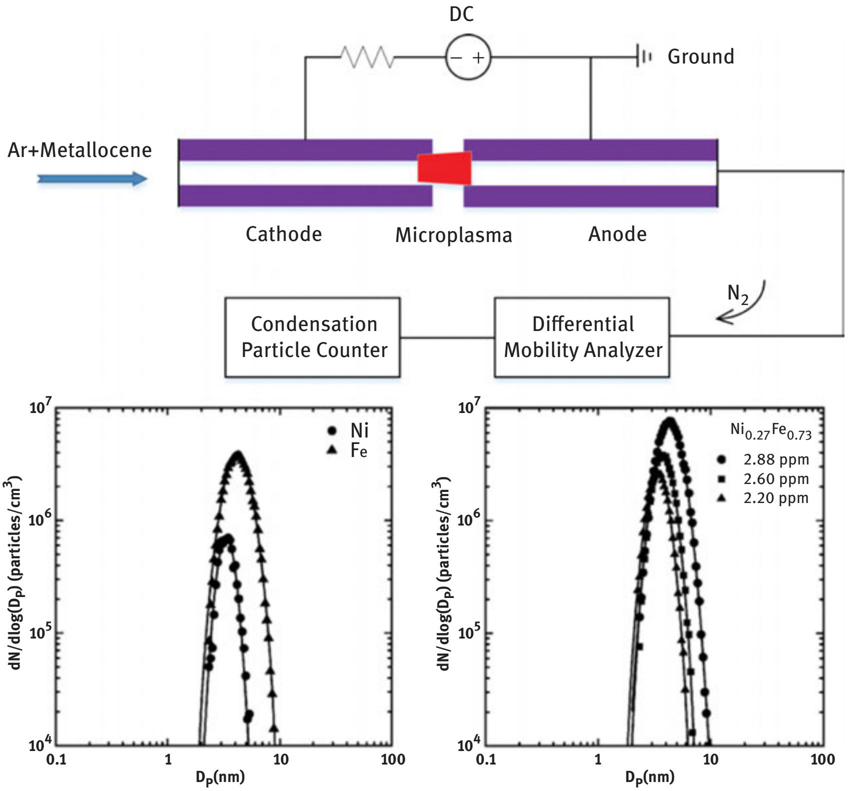

Figure 2.13: (a) Schematic of the DMA and CPC system for the real-time characterization of the generated nanoparticles; (b) Aerosol measurement results of the Ni and Fe nanoparticles with precursor concentrations of 2.60 ppm in Ar and (c) $Ni_{0.27}Fe_{0.73}$ alloys as a function of total metallocene concentration in Ar. Reprinted with permission from [132], copyright 2008 Wiley-VCH.

similar mean diameter of 3.11nm. Afterwards, both ferrocene and nickelocene vapors of various concentrations were introduced simultaneously into the plasma to prepare Fe_xNi_{1-x} nanoalloy. The results showed that their size and size distributions could be tuned by adjusting the total metallocene concentration. Therefore, the aerosol measurement allows us to monitor the real-time particle size and size distributions during the microplasma operation, which in turn, rendering it possible to tune the product properties “in-flight”.

2.3.2 *Ex situ* characterization of the generated nanoparticles

As motioned above, the product properties depend critically on the microstructure, i. e. the arrangement of the atoms (the atomic structure), the chemical composition, the size and the shape [133]. In this section the *ex situ* characterization of the generated nanoparticles is discussed regarding three general aspects which have essential influences on their properties, including particle size, size distributions and morphology; composition; crystalline structure. It is also important to know which analytical instrument can provide specific information on certain aspects. For example, transmission electron microscope (TEM) equipped with certain detectors can be utilized to characterize the particle size, morphology, crystalline structures and even chemical compositions.

2.3.2.1 Particle size, size distributions and morphology

In addition to the aerosol measurement for *in situ* monitoring the as-grown metallic nanoparticle size and size distributions, TEM is the most commonly used instrument for determining the particle size and size distributions. For TEM characterization an electron beam is transmitted through an ultrathin specimen and interacts with it as it passes through. An image is formed from the electrons transmitted through the specimen. By magnifying and focusing the image using optical lens and transmitting to imaging devices (e. g. fluorescent screen) or a CCD camera, the particles sizes and shapes are directly observed, and the particle size distribution can be derived by randomly sorting sufficiently large particle numbers. Short de-Broglie wavelength for electrons enables the instrument to capture ultra-fine details at high magnifications, even as small as a single column of atoms. In this manner the lattice fringes and lattice space of metallic nanoparticle can be observed and calculated, which in turn, helps to confirm their crystalline structure.

There are various methods to prepare metallic nanoparticles samples for TEM analysis. The simplest way is to put a TEM grid downstream the aerosol, thus the metallic particles will directly deposit on the grid [127, 134]. Another common method is by dispersing a small quantity of the metallic nanoparticles into appropriate solvents (distilled water, methanol, ethanol, etc.) and sonicating for a while. Then one or two drops of the solution are casted on the TEM grid [135]. For the plasma–liquid system, since the metallic nanoparticles are generated in the liquid, the samples are prepared by drop-cast the electrolyte directly on to the TEM grids [136].

In the study of Tran et al., Pt nanoparticles prepared by a plasma–liquid system were studied in detail by the transmission electron microscopy [108]. Typical images of the Pt nanoparticles at different magnifications are shown in Figure 2.14. It was observed that the obtained Pt nanoparticles were not only small and uniform, but also well distributed without any aggregation. Moreover, the HRTEM image shows clear lattice fringes, and the lattice spacing was estimated to be of 1.96 Å, corresponding to the (200) plane of the Pt nanoparticles. A size distribution histogram was derived by randomly measuring 500 particles using the TEM images. The result showed particles had a size range of 2–4 nm with a mean value of 3 nm.

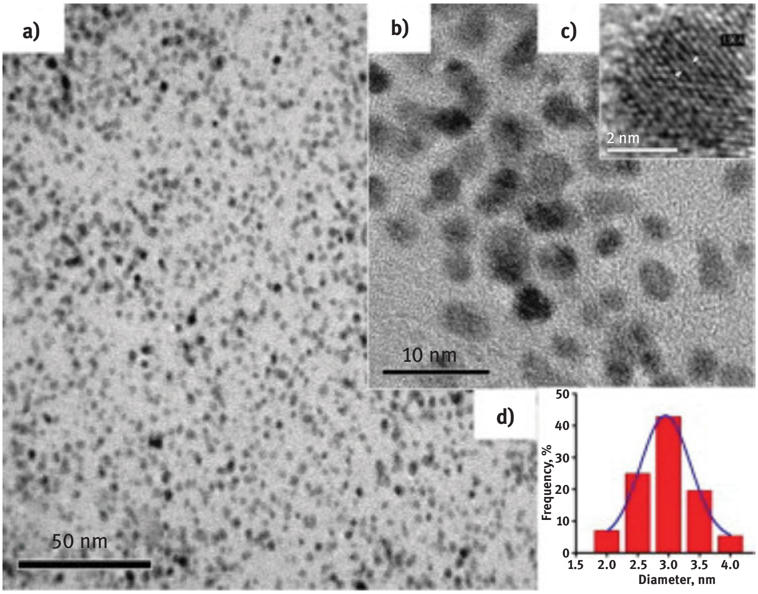

Figure 2.14: (a–b) TEM images of the prepared Pt nanoparticles; (c) HRTEM image of a typical Pt particle; (d) particle size distribution obtained from 500 randomly selected particles in (a). Reprinted with permission from [108], copyright 2014 Elsevier.

In some cases, the size and size distributions of metallic nanoparticles are determined by the dynamic light scattering (DLS) technique [137–139]. It is a non-invasive, well-established method for measuring particles typically in the submicron region, and the latest technology allows the measurement of nanoparticles smaller than 1nm. The basic principle is simple: nanoparticles are dispersed or dissolved in a liquid and illuminated by a laser beam. The Brownian motion of nanoparticles in the liquid causes laser light to be scattered at different intensities, which is then detected at a known scattering angle by a fast photon detector. Analysis of these intensity fluctuations yields the Brownian motion velocity, and hence by using the Stokes–Einstein relationship, the particle size is derived. Compared to the TEM, DLS technique is more efficient while the machine itself is significantly less expensive. However, it is sensitive for mechanical disturbance, has relatively low resolution, and requires optically transparent specimens for the analysis [140].

For the particle morphology characterization, scanning electron microscope (SEM) is the most widely used instrument. It produces images by scanning the sample surface with a focused beam of electrons. In contrast to TEM the electrons transmitting through the sample, the narrow beam of SEM is “scanned” across to create an image of the sample surface, with exceptional depth of field. When the electrons of the primary beam interact with the sample, secondary electrons are emitted from the sample surface, bring main information related to surface topology. In addition, transmitted and backscattered electrons can be analyzed to complement morphological and structural analysis, also giving a certain depth profiling. The electron beam is scanned in a raster pattern, and a variety of detectors are used to analyze scattered electrons to produce an image. Therefore, in addition to morphological, topographical and compositional information (see also EDX method described below), SEM also can detect and analyze surface fractures, examine surface contaminations, reveal spatial element variations, identify crystalline structures and provide qualitative chemical analyses [141, 142]. For metallic nanoparticle, due to their inherent electrical conductivity, the sample preparation is relatively simple. It is commonly prepared by distributing the solid particles on a carbon tape and mounting on a metal stub.

Atomic force microscopy (AFM) is another popular technique for morphology characterization, with demonstrated resolution on the order of ~0.1 nm. It uses a cantilever with an extremely sharp tip to scan over the sample surface. As the tip approaches the surface, the attractive force causes the cantilever to deflect towards the surface. With the closer distance to the surface, increasing repulsive force takes over and causes the cantilever to deflect away. Meanwhile, the deflections towards or away from the surface is detected by a laser beam and tracked by a position-sensitive photo diode. In this way the surface feature is reflected by moving the AFM tip over sample surface. Compared to the SEM, AFM has a higher resolution and produces images in three-dimensional topography instead of two-dimensional projection. More importantly, AFM directly provides quantitative topographic mapping. It also can show contrast between regions with different mechanical characteristics and can map local conductive or dielectric properties as well as electric potential distribution. Moreover, the samples do not require any special treatments (such as metal/carbon coatings) which may damage the sample, and does not suffer from charging artifacts in the final image. However, usually, the scan area is smaller than by SEM (increase in analyzed area leads to considerable processing time), and cannot be applied for chemical identification and mapping.

2.3.2.2 Chemical composition

Chemical composition is one of the most important parameters that determine the properties of metallic nanoparticles. For example, Au nanoparticles demonstrate unique optical properties that cannot be achieved by Fe, Cu, Zn, Al and Ni nanoparticles [143]. On the other hand, tuning of the composition, such as the incorporation of Fe into Ni nanoparticles, can enhance its catalytic activity for CNTs growth to a large extent [132]. There are also reports using metallic alloys for the biomedical applications, in which two or more metallic nanoparticles are combined together for specific performance [144, 145].

Two most widely used techniques for characterizing the chemical composition of metallic nanoparticles are energy dispersive X-ray spectroscopy (EDX) and X-ray photoelectron spectroscopy (XPS). The EDX measurement is conducted by focusing a high-energy beam of electrons on the sample, which may excite the electrons of the sample and eject them from the inner shells of atoms. Meanwhile, electron hole was generated where the electrons were. Then electrons from an outer, higher-energy shell automatically fill the hole and release energy in the form of X-rays. Since each element has a unique atomic structure, the energies of the X-rays are relevant to the energy levels of atoms and can be used to identify the elemental composition [146]. Moreover, the energy densities are related to the element concentration, by scanning the beam over a specific area, this technique can also estimate the relative abundance of elements and their spatial distributions [147]. Due to the apparent synergy with the described above SEM analysis, both topological (SEM) and compositional (EDX) mapping are often combined in one instrument. By contrast, for XPS analysis, a beam of X-ray photons is irradiated to the sample and transfers the energy to core-level electrons. The electrons can be ejected from initial states, with kinetic energies dependent on the incident X-ray, the binding energy of the atomic orbits and the chemical environment of the originated atoms. A photoelectron spectrum is recorded by counting the ejected electrons over a range of electron kinetic energies. The analysis of the energies and intensities of the photoelectron peaks enable identification and quantification of all the present elements.

Compared to the EDX characterization, a distinctive advantage of XPS is the ability to get information of chemical state of atoms (e. g. the oxidation state of element), which has practical importance in many areas. However, due to the limited escape depth of electrons, XPS can only detect signals from sample depth of <10 nm. Therefore, it is considered as a surface characterization technique instead of bulk material analysis. For the compositional depth profiling, as well as to exclude surface contamination effects, XPS is often combined with the sputtering techniques which become a standard feature in modern instruments. On the other hand, angle resolved XPS allows to analyze the uppermost (1–2 nm) surface layers. It should be noted that XPS cannot directly derive information on hydrogen content, which in some situations can be considered as a limitation. Additionally, in order to achieve adequate chemical specificity and spatial resolution, XPS requires ultra-high vacuum ($P < 10^{-9}$ millibar) during measurements.

Ghosh et al. used a microplasma-induced technique for *in situ* formation of electrically conductive metal patterns. In this study Ag cations are contained in PAA solutions and deposited on Si substrates to form Ag-PAA films. The microplasma reduction process was carried out on the as-deposited films to reduce the incorporated Ag cations to metallic Ag patterns. SEM and EDX characterization were carried out to examine the microplasma-reduced lines and to understand the nature of Ag nanoparticle formation. Typical images of the Ag patterns are showed in Figure 2.15. It was revealed that the metallization occurs in a layer of ~5 µm near the film surface, where Ag^+ was reduced to form Ag particles by electron impacts. The cross-sectional analysis and EDX result furtherly confirmed the reduction and formation of Ag particles, which were extensively localized near the film surface.

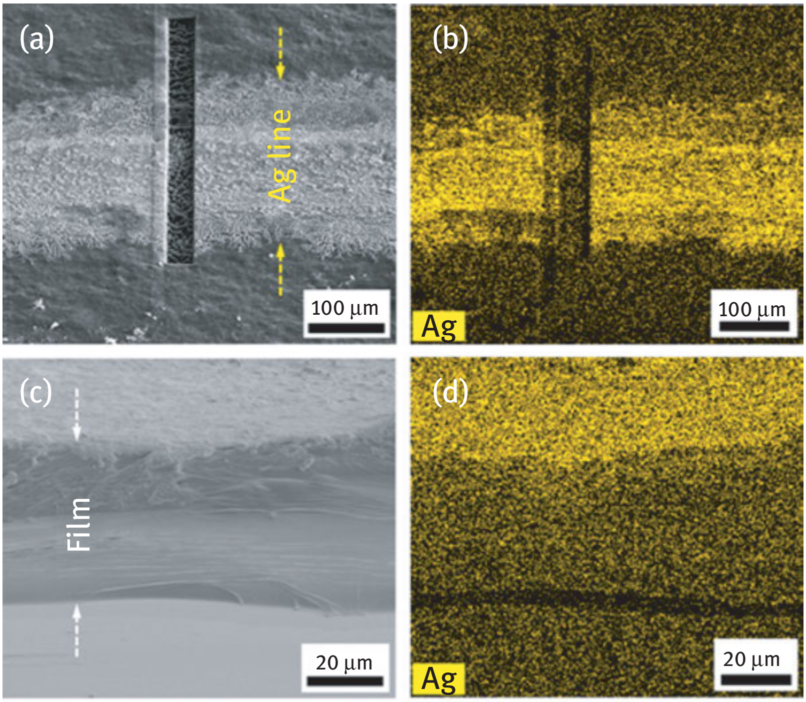

Figure 2.15: (a-b) Surface and (c-d) cross-sectional SEM and EDX images of the Ag metal patterns fabricated by a microplasma-reduced approach. Reprinted with permission from [148], copyright 2014 American Chemical Society.

In addition to the EDX and XPS, there are also various techniques for the characterization of chemical composition, such as X-ray fluorescence (XRF), inductively coupled plasma mass spectrometry (ICP-MS), inductively coupled plasma optical emission spectroscopy (ICP-OES) or atomic absorption spectroscopy (AAS). Also Rutherford back scattering spectroscopy (RBS) and surface sensitive Time-of-Flight Secondary Ion Mass Spectrometry (TOF-SIMS) should be mentioned. However, they are not so frequently used compared to the EDX and XPS for the characterization of metallic nanoparticles, thus is beyond the scope of the present study.

2.3.2.3 Crystalline structure

For specific nanoparticles under a given condition, a particular structure (amorphous, body-centered cubic (bcc), face centered cubic (fcc) or hexagonal close packed (hcp)) is determined by the chemical composition, the number of atoms and the chemical interaction between atoms, which correspond to the optimum stable configurations [149]. It is well-known that the majority of metals adopt a crystalline arrangement, since a stable state is achieved in this way by anchoring interactions between neighboring atoms to minimize the total internal energy [150].

The determination or confirmation of a structure can be performed by a series of analytical techniques, among them X-ray diffractometer (XRD) is one of the most frequently used methods for metallic nanoparticles analysis. In XRD electrons are emitted from a heated filament in a cathode ray tube, being accelerated toward a target material (Cu, Fe, Mo, Cr) in the applied electric field. When electrons have sufficient energy to dislodge inner shell electrons of the target material, characteristic X-ray spectra are generated. During the measurement the X-rays are directed to the sample. Meanwhile, the sample and the detector are rotated at a certain rate, with the intensity of the reflected X-rays being recorded as a function of the position. Once the geometry of the incident X-rays impinging the sample satisfies the Bragg equation, constructive interference occurs and intensive signal peak is generated.

The crystalline structure of the metallic nanoparticles can be also studied by the selected area electron diffraction (SAED) technique, which is often combined in one instrument with a transmission electron microscope. During the measurement the crystalline specimen is subjected to a high-energy electron beam (100–400 keV). Electrons in this case exhibit a wave-like behavior, rather than particle-like. Due to the short wavelength of the high-energy electrons ($\sim 10^{-3}$ nm) as well as the relatively larger atom spacing, the atoms act as a diffraction grating to the electrons. When the electrons pass through atoms, some will be scattered to particular angles to form a spot on the screen, determined by the crystal structure of the sample, while others continue to pass through without deflection. As a result, a diffraction pattern is formed by a series of spots, and each spot corresponds to a satisfied diffraction condition of the sample's crystal structure [151]. Compared to XRD, SAED has higher intensity of diffracted patterns, making them particularly suitable for low atomic number materials. It also has the ability to examine areas as small as several hundred nanometers in size instead of several centimeters. However, the operation of SAED is more complicated and expensive.

Sometimes both the transmitted and the scattered beams are used in the transmission electron microscopy to create a high-resolution image (HRTEM). In this case the phase of electrons wave is modulated by the interaction with crystallographic structure at very low angles and self-interference phenomena take place during propagation through the objective lens. All electrons are combined at a point in the image plane to form an interference pattern, which can be used for the identification of the crystal structures and lattice imperfections of nanoparticles.

A typical example for the crystal structure analysis of metallic nanoparticles is shown in Figure 2.16, where an interaction of plasma with liquid is applied for fabrication of Sn nanoparticles. As indicated by the TEM and SAED images, single-crystalline Sn nanoparticles of tetragonal shape are formed, with the plate faces on the (001) plane. The high-resolution TEM image also shows clear lattice fringes of the Sn particles, confirming their crystalline structures. Meanwhile, SnO_2 particles are observed in the products, suggesting partial oxidation of the Sn particles. Furthermore, XRD measurements are also carried out to examine the products. The result shows the existence of prominent Sn peaks as well as much less intensive SnO_2 peaks, revealing that the crystalline Sn nanoparticles production is dominant in the studied process.

In order to engineer optimal metallic nanoparticles for specific applications, it is essential to have a comprehensive understanding of their physicochemical

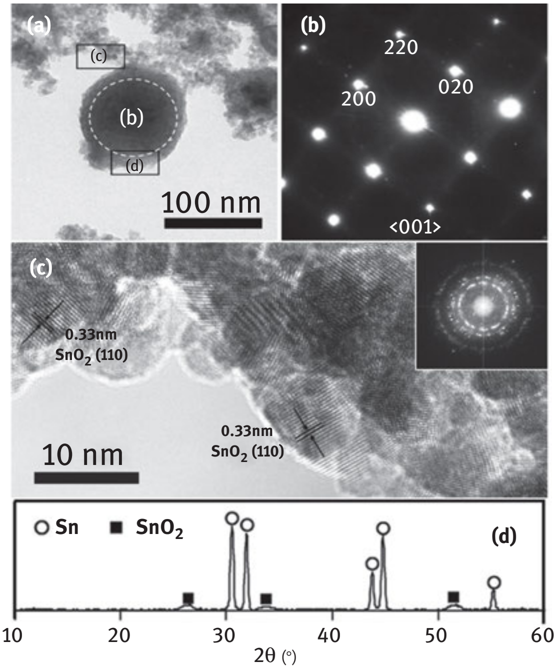

Figure 2.16: (a) TEM, (b–c) SAED and HRTEM, (d) XRD images of the metallic nanoparticles produced by the microplasma method. Reprinted with permission from [152], copyright 2014 Elsevier.

properties. The rapid development of the characterization methodologies and analysis techniques allows us to assess metallic nanoparticles from different aspects. In the present review we attempt to show the most representative and frequently used techniques for the *ex-situ* characterization of the metallic nanoparticles in terms of size, morphology, composition and crystalline structure, summarized in Table 2.6.

Table 2.6: Typical characterization techniques for metallic nanoparticle analysis. reprinted with permission from [153, 154], copyright 2013 American Vacuum Society, copyright 2009 American Chemical Society.

Method	Type of information	Comments
SEM	Particle morphology	Element identification and mapping via EDX
AFM	Surface topography and particle shape	Gas and liquid environment
TEM	Particle shape, size and size distribution	Can be done in gas and liquid environment
HRTEM	Crystalline structure down to the atomic level	Can measure lattice space and identify crystal plane
SAED	Crystal information and planes	
DLS	Common method for sizing particles in solution	Often done together with zeta potential analysis
XRD	Structures present and grain size	Allow liquid and gas environment analysis
XPS	Surface composition chemical state	Can be done for gaseous measurements
XRF	Elemental analysis and chemical analysis	Difficult to quantify elements lighter than sodium
ICP-MS	Elemental analysis and quantification	Elements with atomic mass ranges 7 to 250 (Li to U)
ICP-OES	Elemental analysis and quantification	
AAS	Elemental analysis and quantification	Sample needs to be atomized
UV-Vis	Size of metal nanoparticles	Commonly used for particles in solution
BET	Surface area	Solid samples

2.4 Representative examples and possible mechanisms

As it was demonstrated in the above sections, various microplasma configurations have been developed for the metallic nanoparticles synthesis, with a broad category of nanoparticles being fabricated both in the gas phase and in the liquid phase. Table 2.7 gives a summary of the reported metallic nanoparticles fabricated by microplasma as well as the detailed synthesis recipes (microplasma configuration, precursors and plasma gases). Moreover, it is shown that the size, morphology, composition and microstructure of metallic nanoparticles can be controlled and tuned through processing parameters adjustment. However, due to the complexity of the plasma-activated chemistry, the detailed mechanisms are not fully understood

Table 2.7: Summary of metallic nanoparticles fabricated by microplasma technology.

Metallic nanoparticle	Precursors	Plasma gas	Plasma configuration	Ref.
Ag	$AgNO_3$ solution	Ar	Plasma–liquid systems	[158]
	$AgNO_3$ solution	He	Plasma–liquid systems	[136]
	Ag wire	Ar	Plasma–liquid systems	[93]
	$AgCF_3SO_3$ solution	Ar	Plasma–liquid systems	[103]
	$HAuCl_4$ solution	Ar	Plasma–liquid systems	[105,
Au	Au wire	Ar, H_2	Microplasma jets with consumable electrodes	157,
	Au wire	Ar	Plasma–liquid systems	158]
				[97]
				[93]
Pt	$Pt(C_5H_7O_2)_2$	Ar	Hollow-electrode microdischarges	[88]
	$H_2PtCl_6.xH_2O$ solution	Ar, H_2	Plasma–liquid systems	[108]
Ni	$Ni(C_5H_5)_2$	Ar	Hollow-electrode microdischarges	[87,
	$Ni(C_5H_5)_2$	Ar	Microplasma jets with external electrodes	157]
	Ni wire		Plasma–liquid systems	[90]
				[165]
Fe	$Fe(C_5H_5)_2$	Ar	Hollow-electrode microdischarges	[125,
	Fe wire		Plasma–liquid systems	157]
				[84]
Cu	Cu wire	Ar, H_2	Microplasma jets with consumable electrodes	[77]
	$Cu(C_5H_7O_2)_2$	Ar	Hollow-electrode microdischarges	[88]
	CuCl and $CuCl_2$ solution	Ar	Plasma–liquid systems	[160]
Mo	Mo wire	Ar, H_2	Microplasma jets with consumable electrodes	[76]
Zn	Zinc wire		Plasma–liquid systems	[81]
Ir	$IrCl_3 \cdot xH_2O$ solution	Ar	Plasma–liquid systems	[162]
Sn	$SnCl_2 \cdot 2H_2O$ solution		Plasma–liquid systems	[85]
$Ni_xFe_yCu_{1-x-y}$	$Ni(C_5H_5)_2$, $Fe(C_5H_5)_2$ $Cu(C_5H_7O_2)_2$, Pt $(C_5H_7O_2)_2$	Ar	Hollow-electrode microdischarges	[65, 88, [132]
Ag_xAu_{1-x}	$HAuCl_4$ and $AgNO_3$ solution	Ar	Plasma–liquid systems	[109]
Ag_xPt_{1-x}	$HAuCl_4$ and H_2PtCl_6 solution	Ar	Plasma–liquid systems	[110]

yet. In order to gain more insight into the underlying process, in this section representative examples of metallic nanoparticles production are provided, followed by the discussions of the possible mechanisms.

2.4.1 Gas phase synthesis of metallic nanoparticles and involved mechanisms

2.4.1.1 Representative examples

Lin et al. used a hollow-electrode microdischarge to produce Ni nanoparticles by employing the nickelocene as the precursor and the argon as the plasma gas. This study was aimed to establish the relationship between processing conditions and product magnetic properties, and ultimately, to generate Ni nanoparticles of desired magnetic performance by the microplasma-assisted process. Systematic experiments were carried out to investigate the influence of the plasma power as well as the nickelocene concentration. It was shown that crystalline Ni nanoparticles with controllable magnetic properties were obtained by this technique in a continuous, one step and solvent-free manner. At certain conditions both Ni nanoparticles and carbon nanotubes (CNTs) were simultaneously generated from the nickelocene. However, flexible adjustment of particle size, composition, morphology and structure was governed by tuning processing conditions. For the optimized conditions only Ni nanoparticles of face centered cubic (fcc) phase were formed, with a saturation magnetization value as high as ~44.4 mAm^2/g.

The hollow-electrode microdischarge was also successfully applied for the fabrication of Fe nanoparticles, as was demonstrated in the study of Wei-Hung Chiang [155]. In this research ferrocene was used as the precursor, and C_2H_2 was used as the carbon source for CNTs. Firstly Fe nanoparticles were generated in a microplasma reactor, and then introduced with a gas flow to a tubular furnace as the floating-catalyst to catalyze the C_2H_2 for CNTs formation. The size and size distributions of Fe nanoparticles were controlled by tuning the ferrocene concentration to study their catalytic performance. Results indicated crystalline Fe nanoparticles with controllable size were produced by the process. Moreover, Fe particles were found to catalyze CNT growth at 500°C and 600°C , but lost catalytic activity above 700°C , which was attributed to the increased particle size.

In addition to the hollow-electrode microdischarge, Ghosh et al. demonstrated the feasibility for the Ni nanoparticles synthesis using an atmospheric-pressure DBD reactor [90]. In their research nickelocene vapors were chosen as the precursor and were introduced into the plasma by an argon flow at different dilution ratios (0.21–0.94 ppm). In order to study the influence of the precursor residence time in the plasma, capillary gas injectors of different sizes (180 µm, 510 µm) were applied. Results showed that Ni nanoparticles were successfully synthesized by the atmospheric-pressure DBD plasma systems, and the incorporation of a capillary gas injector to alter the velocity profile could significantly reduce particle size and agglomeration.

The high flexibility in design of microplasma-assisted processes and configurations also renders it possible to directly produce complex composite multimetallicna nanoalloys. PA Lin et al. demonstrated an atmospheric pressure microplasma system for synthesis of compositionally tunable multimetallic nanoparticles or alloyed nanoparticles in the gas phase [88]. Organometallic compounds such as nickelocene, ferrocene, copper acetylacetonate and platinum acetylacetonate were selected as the metal sources and were combined at different mass flow ratios. Afterwards, they were introduced into the microplasma for dissociation and particle growth. Results showed that a series of ultra-fine multimetallic NPs (Ni_xCu_{1-x} NPs, $Ni_xFe_yCu_{1-x-y}$ NPs) with narrow size distributions had been fabricated by the studied gas-phase approach, and their compositions could be tuned by varying the relevant flow rates (i. e. vapor concentrations) of the precursors (Figure 2.17).

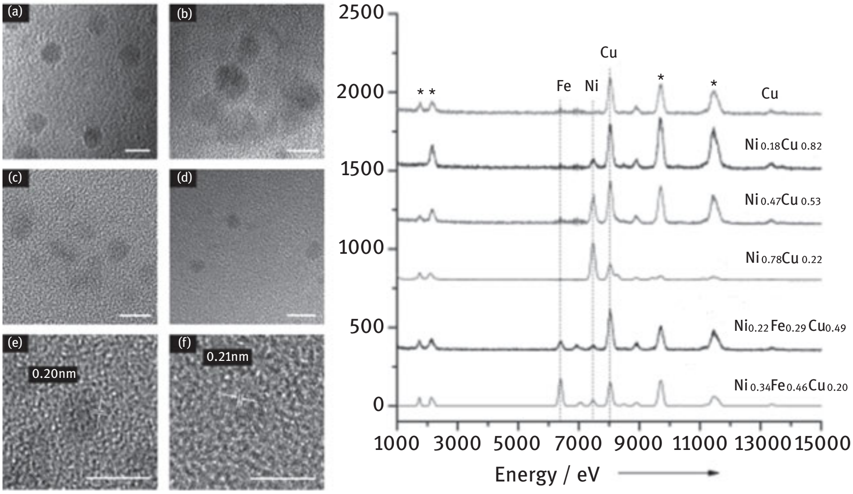

Figure 2.17: TEM images and the relevant EDX spectra of various compositions of Ni_xCu_{1-x} and $Ni_xFe_yCu_{1-x-y}$ NPs. Reprinted with permission from [88], copyright 2011 Wiley-VCH.

2.4.1.2 Possible mechanisms

Almost all the microplasma-assisted processes for the gas phase synthesis of nanoparticles use organometallic compounds as precursors. The decomposition of organometallic precursors are notoriously complex processes consisting of a series of consecutive, parallel as well as catalytic reactions in homogeneous or heterogeneous phase. Due to the relatively small spatial zone as well as multiple reactions involving charged particles, electrons, various atomic or molecular excited states and neutral radicals, the situation becomes even more complicated when it comes to the microplasma. Currently all studies on microplasma-assisted nanofabrication mainly focus on the process optimization and nanomaterials characterization, instead of the mechanism study. Furthermore, owing to the lack of direct experimental studies and complexity of the techniques to *in situ* characterize the pathways of precursor decomposition and particle growth, identifying all involved species, the detailed mechanisms are not clear yet.

In plasma the chemical bonds in the precursor will be broken by the impact with energetic electrons (~eV) or other radicals (e. g. Ar^+, Ar^*). Since different dissociation processes have specific threshold energies as well as energy-dependent cross-sections, while plasma operation conditions determine a certain electron energy distribution function (EEDF), thus, in general, one can have estimation on the preferential dissociation pathway of precursor molecules.

The mechanisms of plasma-assisted dissociation processes of organometallic compounds was discussed by Lin et al., where they use ferrocene as the precursor to produce Fe metallic nanoparticles [125]. First the characteristics of the microplasma were estimated. Depending on the dissipated power, the gas temperature in the range of 900–1100 K for the microplasma in the studied process was derived by the fitting of measured spectra, corresponding to the emission from C_2 swan system, with the spectra simulated using SPECAIR software [117]. While the electron temperature in the range of 2.6–3.1 eV was estimated using BOLSIG+ electron kinetics solver for EEDF, with characteristic EEDF shown in Figure 2.18(a). Although, the electron impact dissociation cross-sections were not reported for ferrocene, by considering the energy diagram of the possible ferrocene dissociation routes (Figure 2.18(b)) and taking into

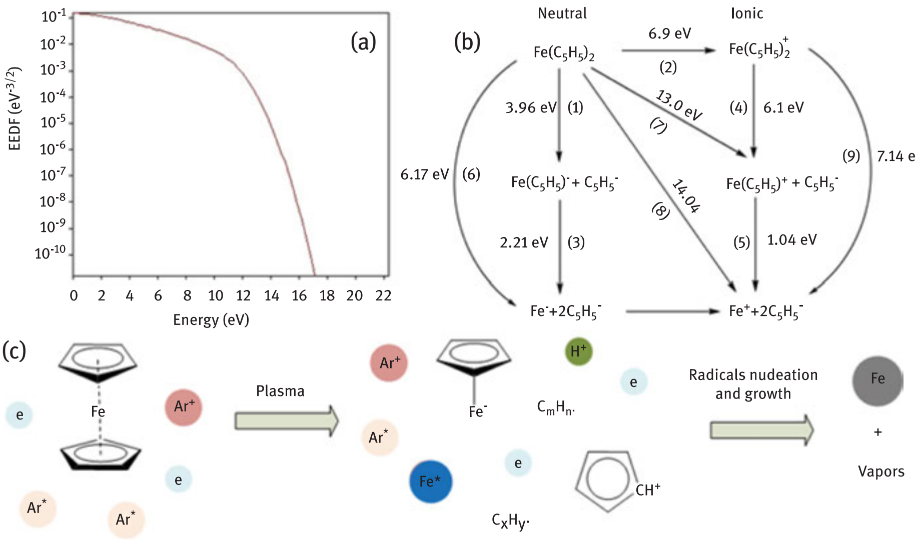

Figure 2.18: (a) Energy distribution functions (EEDFs) of the argon microplasma; (b) Reactions and the relevant energy data of the ferrocene dissociation process; (c) Schematic mechanisms. Reprinted with permission from [125], copyright 2017 Elsevier.

account the steepness of the EEDF tail region, it was expected that the difference in threshold energy would result in significant difference for process rates. Therefore it was concluded that the preferential pathway should be via the neutral dissociation processes by direct electron impact, where ferrocene molecules were supposed to go through the reaction 1 to yield $Fe(C_5H_5)$ and C_5H_5 free radicals by breaking the first ligand. Then the formed $Fe(C_5H_5)$ were furtherly dissociated to generate Fe atoms by the scission of second ligand. The continuous generation of Fe atoms in the aerosol phase eventually led to a supersaturated Fe concentration, which was energetically unstable and tended to form atom-atom bonds via exothermic reaction. As a result, Fe atoms began to assemble together to form clusters. Once the nucleation seed formed, it would act as a convergence point for the growth of Fe nanoparticles.

2.4.2 Liquid phase synthesis of metallic nanoparticles and mechanisms

2.4.2.1 Representative examples

Wang et al. reported an indirect contact plasma–liquid system for the fabrication of gold nanoparticles from the $HAuCl_4$ electrolyte solution [156]. In this study reactions were performed in a U-shaped electrochemical cell. A platinum (Pt) anode was immersed in the electrolyte as the anode, while a copper capillary tube with an inner diameter of 0.355 mm was used as the cathode and placed 1 mm above the electrolyte surface. The microplasma was ignited by a DC high-voltage power supply, and formed between the tip of the copper capillary and the electrolyte surface. It was shown that gold nanoparticles were successfully prepared by the microplasma-electrolyte treatment, in which Au^+ was reduced to Au NPs under the plasma effects. Additionally, the size distribution of gold nanoparticles could be tailored by tuning process parameters such as the stirring mode, plasma power, and precursor concentrations. This method was also successfully expanded to the synthesis of a series of nanoparticles like Ag, Ti, Pt, Ir, CuO_x, Fe_3O_4, Si, etc. [105, 106, 136, 157–165].

A direct contact plasma–liquid system was demonstrated by Lal et al. for the synthesis of nanoparticles such as Au, Cu, Pt or Pt+Au [166]. In this study a Teflon cell (~1 ml volume) was used as the electrochemical cell. A Pt wire of 300 μm diameter acted as the cathode and immersed with a depth of 0.5 mm in the electrolyte, while a large Pt ring was used as the counter electrode. For the preparation of Cu nanoparticles, $CuSO_4+H_2SO_4$ were used as the electrolyte solution. Similarly they also used $H_2PtCl_6+HClO_4$ electrolyte for preparing Pt nanoparticles, $NaAuCl_4+HClO_4$ electrolyte for Au nanoparticles and $H_2PtCl_6+NaAuCl_4+HClO_4$ electrolyte for Pt+Au nanoparticles. In experiments large current density (~1 A/mm^2 at ~20 V) was applied in the aqueous electrolyte, leading to the formation of a “gas film” around the electrode, from which discharges occurred. Results showed metal ions (Cu^{2+}, Pt^+, Au^+) in the electrolyte were reduced to metallic nanoparticles under the plasma treatment. The gas film could prevent them from depositing on the electrode.

In addition to the metal salts, consumable metal electrodes are also used as the precursor for the liquid phase synthesis of metallic nanoparticles. In this case by choosing different metal electrodes, corresponding metallic nanoparticles can be produced in the liquid. A representative example was demonstrated by Kang et al., where Ni, Co, and Fe magnetic nanoparticles were produced by a direct contact plasma–liquid system, without any additional reductants, agents, or treatment (Figure 2.19) [167]. In this study a pair Ni, Co or Fe rods with diameters of 1 mm was used as electrodes and immersed in a benzene solution. The distance between the electrode tips was set to 0.5 mm. Plasma was generated by a bipolar DC-pulsed power supply, with the pulse width and frequency fixed at 2.0 μs and 15 kHz, respectively. Results showed highly pure crystalline Ni, Co, and Fe nanoparticles with average diameters of 5 nm were successfully synthesized. Moreover, magnetic measurements of the obtained products were also carried out, indicating they had superparamagnetic properties at room temperature.

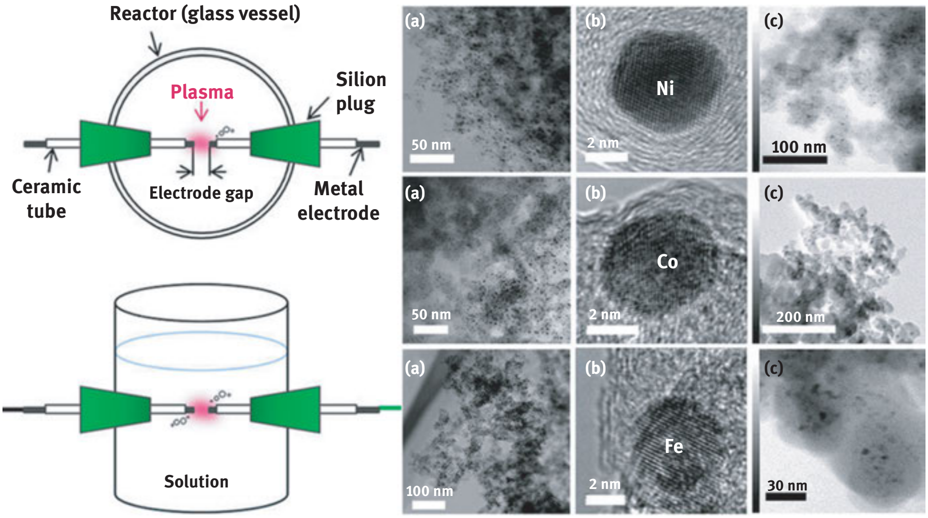

Figure 2.19: A schematic illustration of the direct contact plasma–liquid system for the fabrication of metallic nanoparticles as well as the generated Ni, Co and Fe nanoparticles. Reprinted with permission from [167], copyright 2016 Nature Publishing Group.

There are also reports on the liquid phase synthesis of metallic nanoalloys using the microplasma-assisted technique. A typical example is demonstrated by Ostrikov et al., in which bimetallic Au_xAg_{1-x} alloyed nanoparticles were prepared by an indirect contact plasma–liquid system (as shown in Figure 2.9) [105, 109]. In their research both $HAuCl_4$ and $AgNO_3$ salts were used as the metal sources and dissolved in distilled water to form the electrolyte solution. Helium was used as the plasma gas. A DC-sustained microplasma jet was formed above the electrolyte surface to co-reduce the metallic ions. Results showed bimetallic Au_xAg_{1-x} alloyed nanoparticles were produced by this technique, and a much faster formation rate was achieved compared with conventional colloidal chemistry methods. Moreover, the particle size and composition can be controlled and tuned by variation of the reaction time and the precursor concentration.

2.4.2.2 Possible mechanisms

In general, the plasma–liquid interactions are complex physicochemical processes involving reactions among electrons, ions, molecules and neutral radicals. It is widely accepted that discharges inside or in contact with aqueous solutions efficiently produce radicals, such as H, OH, O, H_2O_2, as well as being a source of UV radiation [168]. Moreover, strong shock waves are also produced in the high-intensity pulsed liquid plasmas. Therefore, the plasma–liquid interactions are affected by a number of factors such as the electron penetration in the interface, diffusion speed of ions, concentrations of radical species, pH and the solution temperature, etc., making it challenging to analyze the kinetics and mechanisms of the metallic nanoparticles formation process.

As mentioned above, both metal salts and metal wires can be used as the precursor for the microplasma-assisted synthesis of metallic nanoparticles in the liquid phase. For metal wires they firstly form metal ions (M^+) by the impact of the plasma-based electrochemistry. Thus the present work deals with the metal ions for the mechanism discussions.

The hypothesized mechanism of microplasma-assisted metallic nanoparticles fabrication was illustrated by Akolkar et al., as shown in Figure 2.20 [55]. A considerable concentration of metal ions (M^+) existing in the electrolyte is transported from the bulk solution to the microplasma–liquid interface under the impacts of convection, diffusion or electric field induced-drift transport. Meanwhile, the plasma electrons were also driven toward the solution surface due to the electrical force. Once the electrons penetrated into the electrolyte interface, they underwent electron transfer process with the M^+ to produce metallic atoms (M^0). However, owing to the complexity of the

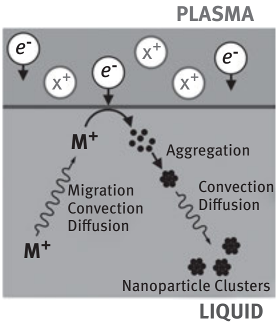

Figure 2.20: Schematic mechanisms of the microplasma-assisted liquid phase synthesis of metallic nanoparticles. Reprinted with permission from [55], copyright 2013 American Vacuum Society.

interface and phase transition processes as well as a number of possible intermediate species involved (i. e. formation of various negative and positive ions), the detailed mechanism of electron and thermal energy transfer process at the interface still remains unclear. Once the metallic atoms M^0 were formed at the interface, they could act as sites for nanoparticle nucleation and growth. With the continuous plasma treatment, these metallic atoms aggregated together to form large nanoparticle clusters or networks, which would be transported to the bulk electrolyte by convection or diffusion processes.

2.5 Critical safety considerations

Most of the existing processes for the microplasma-assisted synthesis of metallic nanoparticles use organometallic compounds as the precursors. In general, they are rather toxic and should be stored and operated by strictly following the safety regulations. The following personal protective equipment is recommended when handling of these chemicals:

i. Eye/face protection: Safety glasses.
ii. Skin protection: Handle with gloves.
iii. Body Protection: Laboratory coat.
iv. Chemicals should be handled in the fume hood for safety reason. For some chemicals with Chemwatch code of 3 or 4 in flammability, toxicity, body contact or chronic (can be referred to material safety data sheet (MSDS)), the usage of glove box is highly suggested. It also needs to be pointed out, there may be certain documents/regulations applied for different countries/regions. For example, “REACH” program was conducted by European commission to collect information for a database over potentially dangerous chemicals.

In addition to toxic chemicals, it is also needed to take the explosion hazards into consideration, since explosive gas (e. g. H_2) is introduced or generated when fabricating metallic nanoparticles. To prevent possible explosions, gas sensors are suggested to detect and monitor the gas concentrations. Once detecting the leakage, the setup should be immediately stopped. Meanwhile, the relevant pipelines should be diluted and washed by other gases to evacuate possible residues of the explosive gas.

Besides, owing to the structural complexities, surface properties and high reactivity of the generated nanomaterials, the potential exposure to nanoparticles may lead to undesired organism-specific responses. Nanomaterials can cause nanotoxicity by penetrating the airway, travelling through the circulatory systems, depositing in various organs and interact with cells at the cellular level [169]. It was estimated that in the US alone more than 2 million people work on nanomaterial-related fields [170]. Unfortunately, till now rather insufficient and controversial data on the toxicity of nanomaterials exist, and only a few regulations or standards are available for the assessment of their toxicological effects. Therefore, special attentions must be paid to avoid the direct contact/exposure to nanomaterials. Moreover, extensive research is required to fully understand the nanotoxicity, including absorption, metabolism, distribution, excretion and biological effects of nanomaterials on biological systems.

Another safety issue of microplasma-assisted nanofabrication is related to electric shock and absorbed radiation hazards. Since high voltages are commonly involved in these processes, special electrical safety measures are required, and insulation protections should be considered. In some cases high frequency discharge powers are utilized, which may cause damage to some parts of the human body that are sensitive to irradiation-induced heating or soft x-ray, such as brain, eyes and the reproductive organs. Therefore, proper shielding has to be undertaken to avoid any permanent body damage, including using highly insulating ceramics and lead-contained materials [169].

2.6 Conclusions and future perspective

The present study is a review of the recent developments in the microplasma-assisted fabrication of metallic nanoparticles. Firstly, four commonly used microplasma systems for metallic nanoparticles synthesis, with representative examples, were described and the pros and cons were demonstrated and discussed. Secondly, the main characterization methodologies and instrumentation techniques were summarized in light of the *in situ* characterization of the plasma-assisted dissociation process as well as the *ex situ* characterization of the obtained metallic nanoparticles. Finally, a broad category of examples on gas/liquid phase metallic nanoparticles synthesis were presented, and the possible mechanisms were also illustrated.

This technique utilizes the synergistic advantages of microreactors and the non-thermal plasma chemistry, resulting in a facile and innovative route for the synthesis of metallic nanoparticles both in gaseous or aqueous phase. Compared to the common wet chemistry methods, the usage of reducing agents, solvents and stabilizers is not needed anymore, and reactions take place in an inert atmosphere. As a result, potential side reactions and by-products have been significantly reduced, obviating the use of complex procedures such as separation, centrifugation and washing to get high purity products. Additionally, the confinement of the plasma in micro spatial scale not only leads to very high energy density, but also ensures a relatively short residence time and uniform RTD for the metallic precursors. Therefore, metallic nanoparticles with smaller average size and narrower size distributions can be fabricated at the dissipated plasma power as low as ~1.0 W, which cannot be realized by the existing approaches. Another distinctive advantage is the demonstrated ability to tune the properties of metallic nanoparticles “in-flight” by simply adjusting the processing conditions. It is expected that this technique can be applied as “dry-process” for local production of well-defined nanostructures (printing-like technologies). Moreover, due to the versatility of microplasma sources and the high degree of flexibility in processing parameters, this technique still has many promising applications. In recent years, Sankaran et al. has successfully fabricated conductive metal patterns at the polymer film surface by the microplasma-assisted method [96, 148, 171]. This in conjunction with the ability to deposit various nanostructures of desired properties may bring critical breakthrough in the fields such as electrical conductors, polymer coatings and surface modifications.

Despite the above advantages, some challenges remain. The involved plasma physics and reaction kinetics are still not fully understood, the rates of many relevant elementary processes remain unknown complicating the analysis of mechanisms. Multi-disciplinary collaborations from physics, chemistry as well as novel diagnostics approaches are required. In terms of application, it should be pointed out that the current throughput of this technique is not high, since most reported lab-scale processes use only a single microplasma unit to fabricate metallic nanoparticles as a prove of principle, and reactions were confined in microreactors. However, the process can be scaled up by using the microplasma array design [172–174]. One possible solution is to arrange microplasma jets in an array structure. As estimated in the study of Lin et al., the production rate of Ni nanoparticles at 35 ppm Ni(cp)$_2$ vapors by a single plasma jet is calculated as 4.65×10^{-3} g/h. If a two-dimensional microplasma array (Figure 2.21(a)) with 100 jets in each dimension (100 × 100) was applied, the throughput could be improved by four orders of magnitude (1116 g/day) [87], much higher than a claimed high-throughput synthesis of Ni nanoparticles by a continuous flow method (27 g/day) [175]. Meanwhile, due to the high flexibility of microplasma configurations, such an array structure could also be applied for the liquid-phase synthesis processes to increase the surface area for plasma-liquid interactions (Figure 2.21(b)). An alternative design of microplasma array is to

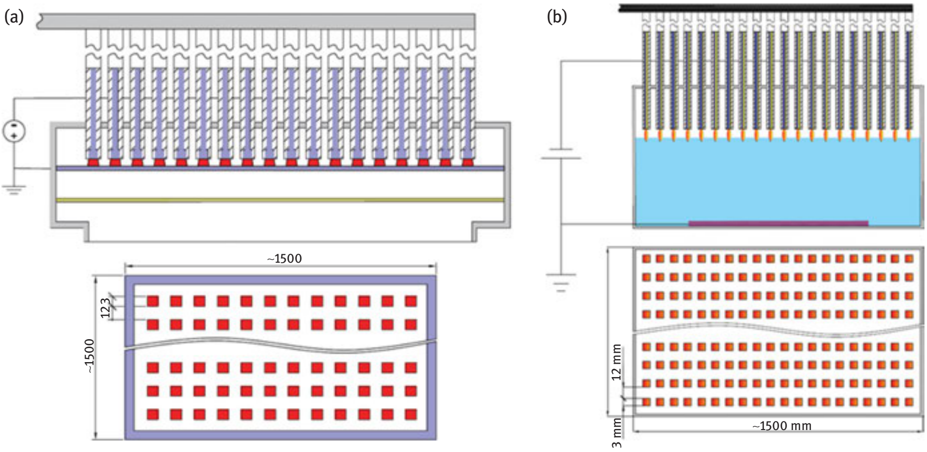

Figure 2.21: Microplasma array design for scaling up the metallic nanoparticles synthesis in (a) gas-phase and (b) liquid phase. Reprinted with permission from [126], copyright 2017 Elsevier.

perforate a matrix of micro holes in two separated planar metallic sheets. By connecting the two metal layers to a power supply, each hole functions as an independent microplasma source [176]. In this manner metallic nanoparticles can be fabricated by delivering the precursors into the holes to be dissociated. On the other hand, owing to the extremely small dimension of the microplasma jet or the micro hole, the array structure is very compact, making them favored by industrial or portable applications. It is reported that a 2D microplasma array with 100 jets in each dimension occupying a spatial space of ~1.5 × 1.5 m^2, while metallic sheets with 200 holes covering ~50 × 50 mm^2. Regarding the scale-up behavior, according to the Yasuda's concept, the product properties are expected to be similar if (1) the plasma power to total gas flow ratio remains constant, while (2) the precursor concentration is kept the same [177]. Therefore, to increase throughput while maintain nanoparticle characteristics, the precursor mass flow should be increased, accompanied by the proportional rise in plasma power and carrying gas flow [87]. As to the continuity of the process, feeding mechanisms for automatically supplying consumable wires or electrolytes can be designed and applied, rendering it possible to fabricate metallic nanoparticles in a continuous manner. With the development of auto-control technology and microplasma arrays reactors, it is expected that the industrial-scale high throughput fabrication of metallic nanoparticles is within reach.

Funding: The authors greatly appreciate the support from Chinese Scholarship Council (CSC) and European LIFE12 ENV_NL_000718 "Green plasma process technology for manufacturing of flexible electronics" project.

References

[1] Zhou G, Liu J, Wang Z, Song L, Hu Y, Fan W, et al. From muticomponent precursor to nanoparticle nanoribbons of ZnO. J Phys Chem B. 2005;109:1113–17.

[2] Sau TK, Rogach AL, Jäckel F, Klar TA, Feldmann J. Properties and applications of colloidal nonspherical noble metal nanoparticles. Adv Mater. 2010;22:1805–25.

[3] Edmundson MC, Capeness M, Horsfall L. Exploring the potential of metallic nanoparticles within synthetic biology. N Biotechnol. 2014;31:572–77.

[4] Pengo P, Baltzer L, Pasquato L, Scrimin P. Substrate modulation of the activity of an artificial nanoesterase made of peptide-functionalized gold nanoparticles. Angew Chemie-Int Ed. 2007;46:400–04.

[5] Chen S, Yuan R, Chai Y, Hu F. Electrochemical sensing of hydrogen peroxide using metal nanoparticles: A review. Microchim Acta. 2013;180:15–32.

[6] Chen XJ, Sanchez-Gaytan BL, Qian Z, Park SJ. Noble metal nanoparticles in DNA detection and delivery. Wiley Interdiscip Rev Nanomed Nanobiotechnol. 2012;4:273–90.

[7] Cao X, Feng J, Pan Q, Xiong B, He Y, Yeung ES. Direct imaging of single plasmonic metal nanoparticles in capillary with laser light-sheet scattering imaging. Anal Chem. 2017;89:2692–97.

[8] Reiss G, Hütten A. Magnetic nanoparticles: applications beyond data storage. Nat Mater. 2005;4:725–26.

[9] Salata O. Applications of nanoparticles in biology and medicine. J Nanobiotechnol. 2004;2:3.

[10] Same S, Aghanejad A, Nakhjavani SA, Barar J, Omidi Y. Radiolabeled theranostics: magnetic and gold nanoparticles. BioImpacts. 2016;6:169–81.

[11] Abdelhalim MA, Mady M. Physical properties of different gold nanoparticles: ultraviolet-visible and fluorescence measurements. J Nanomed Nanotechnol. 2012;3:3.

[12] Chiang WH, Sankaran RM. Relating carbon nanotube growth parameters to the size and composition of nanocatalysts. Diam Relat Mater. 2009;18:946–52.

[13] Li Y, Kim W, Zhang Y, Rolandi M, Wang D, Dai H. Growth of single-walled carbon nanotubes from discrete catalytic nanoparticles of various sizes. J Phys Chem B. 2001;105:11424–31.

[14] Vankayala R, Kuo CL, Sagadevan A, Chen PH, Chiang CS, Hwang KC. Morphology dependent photosensitization and formation of singlet oxygen ($^1\Delta_g$) by gold and silver nanoparticles and its application in cancer treatment. J Mater Chem B. 2013;1:4379.

[15] Förster H, Wolfrum C, Peukert W. Experimental study of metal nanoparticle synthesis by an arc evaporation/condensation process. J Nanoparticle Res. 2012;14:1–16.

[16] Nie M, Sun K, Meng DD. Formation of metal nanoparticles by short-distance sputter deposition in a reactive ion etching chamber. J Appl Phys. 2009;106:1–5.

[17] Prasad Yadav T, Manohar Yadav R, Pratap Singh D. Mechanical milling: a top down approach for the synthesis of nanomaterials and nanocomposites. Nanosci Nanotechnol. 2012;2:22–48.

[18] Povarnitsyn ME, Itina TE, Levashov PR, Khishchenko KV. Mechanisms of nanoparticle formation by ultra-short laser ablation of metals in liquid environment. Phys Chem Chem Phys. 2013;15:3108–14.

[19] Liu K, Lukach A, Sugikawa K, Chung S, Vickery J, Therien AH, et al. Copolymerization of metal nanoparticles: A route to colloidal plasmonic copolymers. Angew Chemie-Int Ed. 2014;53:2648–53.

[20] Nahar L, Arachchige I. Sol-Gel methods for the assembly of metal and semiconductor nanoparticles. JSM Nanotechnol Nanomedicne. 2013;1:1104.

[21] Stubenrauch C, Wielpütz T, Sottmann T, Roychowdhury C, DiSalvo FJ. Microemulsions as templates for the synthesis of metallic nanoparticles. Colloids Surfaces A Physicochem Eng Asp. 2008;317:328–38.

[22] Tang KB, Qian YT, Zeng JH, Yang XG. Solvothermal route to semiconductor nanowires. Adv Mater. 2003;15:448–50.

[23] Shahbazali E, Hessel V, Noël T, Wang Q. Metallic nanoparticles made in flow and their catalytic applications in organic synthesis. Nanotechnol Rev. 2013;1:1–23.

[24] Bogaerts A, Neyts E, Gijbels R, Van der Mullen J. Gas discharge plasmas and their applications. Spectrochim Acta Part B At Spectrosc. 2002;57:609–58.

[25] Ito T, Terashima K. Thermoelectron-enhanced micrometer-scale plasma generation. Appl Phys Lett. 2002;80:2648–50.

[26] Kareem TA, Kaliani AA. Glow discharge plasma electrolysis for nanoparticles synthesis. Ionics. 2012;18:315–27.

[27] Patil BS, Wang Q, Hessel V, Lang J. Plasma N_2-fixation: 1900-2014. Catal Today. 2015;256:49–66.

[28] Eliasson B, Hirth M, Kogelschatz U. Ozone synthesis from oxygen in dielectric barrier discharges. J Phys D Appl Phys. 1987;20:1421–37.

[29] Shimizu T, Sakiyama Y, Graves DB, Zimmermann JL, Morfill GE. The dynamics of ozone generation and mode transition in air surface micro-discharge plasma at atmospheric pressure. New J Phys. 2012;14:103028.

[30] Lim H, Lee Y, Han S, Cho J, Kim KJ. Surface treatment and characterization of PMMA, PHEMA, and PHPMA. J Vac Sci Technol Vacuum Surfaces Film. 2001;19:1490–96.

[31] Wang Q, Cheng Y, Jin Y. Dry reforming of methane in an atmospheric pressure plasma fluidized bed with $Ni/\gamma\text{-}Al_2O_3$ catalyst. Catal Today. 2009;148:275–82.

[32] Shirazi M, Neyts EC, Bogaerts A. DFT study of Ni-catalyzed plasma dry reforming of methane. Appl Catal B Environ. 2017;205:605–14.

[33] Kim HH, Ogata A, Futamura S. Complete oxidation of volatile organic compounds (VOCs) using plasma-driven catalytic and oxygen plasma. Plasma Environ Sci Technol. 2007;1:46–51.

[34] Huang Y, Dai S, Feng F, Zhang X, Liu Z, Yan K. A comparison study of toluene removal by two-stage DBD – catalyst systems loading with MnO_x, $CeMnO_x$, and $CoMnO_x$. Environ Sci Pollut Res. 2015;22:19240–50.

[35] Ye L, Feng F, Liu J, Tang X, Zhang XM, Huang YF, et al. Toluene decomposition by a two-stage hybrid plasma catalyst system in dry air. IEEE Trans Plasma Sci. 2014;42:3529–38.

[36] Ihara T, Kiboku M, Iriyama Y. Plasma reduction of CO_2 with H_2O for the formation of organic compounds. Bull Chem Soc Jpn. 1994;67:312–14.

[37] Paulussen S, Verheyde B, Tu X, Bie CD, Martens T, Petrovic D, et al. Conversion of carbon dioxide to value-added chemicals in atmospheric pressure dielectric barrier discharges. Plasma Sources Sci Technol. 2010;19:34015.

[38] Michielsen I, Uytdenhouwen Y, Pype J, Michielsen B, Mertens J, Reniers F, et al. CO_2 dissociation in a packed bed DBD reactor: first steps towards a better understanding of plasma catalysis. Chem Eng J. 2017;326:477–88.

[39] Snoeckx R, Ozkan A, Reniers F, Bogaerts A. The quest for value-added products from carbon dioxide and water in a dielectric barrier discharge: A Chemical Kinetics Study. ChemSusChem. 2017;10:409–24.

[40] Boeuf JP. Plasma display panels: physics, recent developments and key issues. J Phys D Appl Phys. 2003;36:R53–R79.

[41] Ishaq M, Evans M, Ostrikov K. Effect of atmospheric gas plasmas on cancer cell signaling. Int J Cancer. 2014;134:1517–28.

[42] Fridman G, Friedman G, Gutsol A, Shekhter AB, Vasilets VN, Fridman A. Applied plasma medicine. Plasma Process Polym. 2008;5:503–33.

[43] Vons V, Creyghton Y, Schmidt-Ott A. Nanoparticle production using atmospheric pressure cold plasma. J Nanoparticle Res. 2006;8:721–28.

[44] Kortshagen UR, Sankaran RM, Pereira RN, Girshick SL, Wu JJ, Aydil ES. Nonthermal plasma synthesis of nanocrystals: fundamental principles, materials, and applications. Chem Rev. 2016;116:11061–127.

[45] Ostrikov K. Reactive plasmas as a versatile nanofabrication tool. Rev Mod Phys. 2005;77:489–511.

[46] Lin L, Wang Q. Microplasma: a new generation of technology for functional nanomaterial synthesis. Plasma Chem Plasma Process. 2015;35:925–62.

[47] Fridman A, Chirokov AG. Non-thermal atmospheric pressure discharges. J Phys D Appl Phys. 2005;38:R1–R24.

[48] Fridman AA. Plasma chemistry. Cambridge: Cambridge University Press, 2008.

[49] Belmonte T, Arnoult G, Henrion G, Gries T. Nanoscience with non-equilibrium plasmas at atmospheric pressure. J Phys D Appl Phys. 2011;44:363001.

[50] Mariotti D, Ostrikov K. Tailoring microplasma nanofabrication: from nanostructures to nanoarchitectures. J Phys D Appl Phys. 2009;42:92002.

[51] Eden JG, Park SJ. Microcavity plasma devices and arrays: a new realm of plasma physics and photonic applications. Plasma Phys Control Fusion. 2005;47:B83–B92.

[52] Foest R, Schmidt M, Becker K. Microplasmas, an emerging field of low-temperature plasma science and technology. Int J Mass Spectrom. 2006;248:87–102.

[53] Iza F, Kim GJ, Lee SM, Lee JK, Walsh JL, Zhang YT, et al. Microplasmas: sources, particle kinetics, and biomedical applications. Plasma Process Polym. 2008;5:322–44.

[54] Tachibana K. Current status of microplasma research. IEEJ Trans Electr Electron Eng. 2006;1:145–55.

[55] Akolkar R, Sankaran RM. Charge transfer processes at the interface between plasmas and liquids. J Vac Sci Technol Vacuum Surfaces Film. 2013;31:50811.

[56] Mariotti D, Sankaran RM. Microplasmas for nanomaterials synthesis. J Phys D Appl Phys. 2010;43:323001.

[57] Mariotti D, Sankaran RM. Perspectives on atmospheric-pressure plasmas for nanofabrication. J Phys D Appl Phys. 2011;44:174023.

[58] Parveen K, Banse V, Ledwani L. Green synthesis of nanoparticles: their advantages and disadvantages. AIP Conf Proc. 2016;1724:020048.

[59] Martin CR. Membrane-based synthesis of nanomaterials. Chem Mater. 1996;8:1739–46.

[60] Bang JH, Suslick KS. Applications of ultrasound to the synthesis of nanostructured materials. Adv Mater. 2010;22:1039–59.

[61] Mariotti D, Bose AC, Ostrikov K. Atmospheric-microplasma-assisted nanofabrication: metal and metal-oxide nanostructures and nanoarchitectures. IEEE Trans PLASMA Sci. 2009;37:1027–33.

[62] Kona S, Kim JH, Harnett CK, Sunkara MK. Carbon nanotube growth studies using an atmospheric, microplasma reactor. IEEE Trans Nanotechnol. 2009;8:286–90.

[63] Koh TL, O’Hara EC, Gordon MJ. Microplasma-based synthesis of vertically aligned metal oxide nanostructures. Nanotechnology. 2012;23:425603.

[64] Chiang WH, Richmonds C, Sankaran RM. Continuous-flow, atmospheric-pressure microplasmas: a versatile source for metal nanoparticle synthesis in the gas or liquid phase. Plasma Sources Sci Technol. 2010;19:34011.

[65] Lin L, Starostin SA, Hessel V, Wang Q. Synthesis of iron oxide nanoparticles in microplasma under atmospheric pressure. Chem Eng Sci. 2017;168:360–71.

[66] Chiang WH, Sankaran RM. In-flight dimensional tuning of metal nanoparticles by microplasma synthesis for selective production of diameter-controlled carbon nanotubes. J Phys Chem C. 2008;112:17920–25.

[67] Dao VD, Tran CQ, Ko SH, Choi HS. Dry plasma reduction to synthesize supported platinum nanoparticles for flexible dye-sensitized solar cells. J Mater Chem A. 2013;1:4436.

[68] Li CJ, Sun B. Microstructure and property of Al_2O_3 coating microplasma -sprayed using a novel hollow cathode torch. Mater Lett. 2004;58:179–83.

[69] Shimizu Y, Sasaki T, Liang C, Bose AC, Ito T, Terashima K, et al. Cylindrical metal wire surface coating with multiwalled carbon nanotubes by an atmospheric-pressure microplasma CVD technique. Chem Vap Depos. 2005;11:244–49.

[70] Nozaki T, Sasaki K, Ogino T, Asahi D, Okazaki K. Microplasma synthesis of tunable photoluminescent silicon nanocrystals. Nanotechnology. 2007;18:235603.

[71] Yang Z, Kikuchi T, Hatou Y, Kobayashi T, Shirai H. Carbon microstructures synthesized utilizing the RF microplasma jet at atmospheric pressure. Japanese J Appl Physics. 2005;44:4122–27.

[72] Yoshiki H, Mitsui T. TiO_2 thin film coating on a capillary inner surface using atmospheric-pressure microplasma. Surf Coatings Technol. 2008;202:5266–70.

[73] Suzuki T, Kato M, Shimizu Y. Fabrication of titanium-based hard coatings by atmospheric microplasma-metal organic chemical vapor deposition using titanium tetraisopropoxide. Int J Autom Technol. 2013;7:720–25.

[74] Yoshiki H, Saito T. Preparation of TiO_2 thin films on the inner surface of a quartz tube using atmospheric-pressure microplasma. J Vac Sci Technol Vacuum Surfaces Film. 2008;26:338–43.

[75] Shimizu Y, Sasaki T, Ito T, Terashima K, Koshizaki N. Fabrication of spherical carbon via UHF inductively coupled microplasma CVD. J Phys D Appl Phys. 2003;36:2940–44.

[76] Shimizu Y, Koga K, Sasaki T, Mariotti D, Terashima K, Koshizaki N, Localized deposition of metallic molybdenum particles in ambient air using atmospheric-pressure microplasma,

Microprocess Nanotechnol 2007 In: 20th Int Microprocess Nanotechnol Conf MNC, 2007;4256:174–75.

[77] Shimizu Y, Sasaki T, Chandra Bose A, Terashima K, Koshizaki N. Development of wire spraying for direct micro-patterning via an atmospheric-pressure UHF inductively coupled microplasma jet. Surf Coatings Technol. 2006;200:4251–56.

[78] Bose AC, Shimizu Y, Mariotti D, Sasaki T, Terashima K, Koshizaki N. Flow rate effect on the structure and morphology of molybdenum oxide nanoparticles deposited by atmospheric-pressure microplasma processing. Nanotechnology. 2006;17:5976.

[79] Mariotti D, Lindstrom H, Bose AC, Ostrikov K. Monoclinic β-phase nanosheets produced by atmospheric microplasma: application to lithium-ion batteries. Nanotechnology. 2008;19:495302.

[80] Yoshiki H, Orada T, Hirai K, Hatakeyama R. Growth of vertically aligned carbon nanotube bundles using atmospheric-pressure microplasma. Japanese J Appl Physics. 2006;45: 9276–79.

[81] Hattori Y, Mukasa S, Toyota H, Inoue T, Nomura S. Synthesis of zinc and zinc oxide nanoparticles from zinc electrode using plasma in liquid. Mater Lett. 2011;65:188–90.

[82] Lee CM, Choi SI, Choi SS, Hong SH. Synthesis of boron nitride nanotubes by arc-jet plasma. Curr Appl Phys. 2006;6:166–70.

[83] Hieda J, Saito N, Takai O. Exotic shapes of gold nanoparticles synthesized using plasma in aqueous solution. J Vac Sci Technol Vacuum Surfaces Film. 2008;26:854–56.

[84] Kelgenbaeva Z, Omurzak E, Takebe S, Sulaimankulova S, Abdullaeva Z, Iwamoto C, et al. Synthesis of pure iron nanoparticles at liquid-liquid interface using pulsed plasma. J Nanoparticle Res. 2014;16:2603.

[85] Lee H, Park SH, Kim SJ, Park YK, Kim BH, Jung SC. Synthesis of tin and tin oxide nanoparticles using liquid phase plasma in an aqueous solution. Microelectron Eng. 2014;126:153–57.

[86] Chen Q, Kitamura T, Saito K, Haruta K, Yamano Y, Ishikawa T, et al. Microplasma discharge in ethanol solution: characterization and its application to the synthesis of carbon microstructures. Thin Solid Films. 2008;516:4435–40.

[87] Lin L, Li S, Hessel V, Starostin SA, Lavrijsen R, Zhang W. Synthesis of Ni nanoparticles with controllable magnetic properties by atmospheric pressure microplasma assisted process. AIChE J. 2017. DOI: 10.1002/aic.16054

[88] Schaefer M, Kumar A, Mohan Sankaran R, Schlaf R. Synthesis and in vacuo deposition of iron oxide nanoparticles by microplasma-assisted decomposition of ferrocene. J Appl Phys. 2014;116:133703.

[89] Chiang WH, Sankaran RM. Microplasma synthesis of metal nanoparticles for gas-phase studies of catalyzed carbon nanotube growth. Appl Phys Lett. 2007;91:2005–08.

[90] Ghosh S, Liu T, Bilici M, Cole J, Huang IM. Staack, Atmospheric-pressure dielectric barrier discharge with capillary injection for gas-phase nanoparticle synthesis. J Phys D Appl Phys. 2015;48:314003.

[91] Tomai T, Katahira K, Kubo H, Shimizu Y, Sasaki T, Koshizaki N, et al. Carbon materials syntheses using dielectric barrier discharge microplasma in supercritical carbon dioxide environments. J Supercrit Fluids. 2007;41:404–11.

[92] Cao Z, Walsh JL, Kong MG. Atmospheric plasma jet array in parallel electric and gas flow fields for three-dimensional surface treatment. Appl Phys Lett. 2009;94:021501.

[93] Richmonds C, Sankaran RM. Plasma-liquid electrochemistry: rapid synthesis of colloidal metal nanoparticles by microplasma reduction of aqueous cations. Appl Phys Lett. 2008;93:91–94.

[94] Lee SW, Kumpfer JR, Lin PA, Li GD, Gao XP, Rowan SJ, et al. In situ formation of metal nanoparticle composites via “soft” plasma electrochemical reduction of metallosupramolecular polymer films. Macromolecules. 2012;45:8201–10.

[95] Lee SW, Sankaran RM. Direct writing via electron-driven reactions. Mater Today. 2013;16:117–22.

[96] Ghosh S, Ostrowski E, Yang R, Debnath D, Feng PX, Zorman CA, et al. Atmospheric-pressure plasma reduction of metal cation-containing polymer films to produce electrically conductive nanocomposites by an electrodiffusion mechanism. Plasma Chem Plasma Process. 2016;36:295–307.

[97] Shimizu Y, Kawaguchi K, Sasaki T, Koshizaki N. Generation of room-temperature atmospheric H_2/Ar microplasma jet driven with pulse-modulated ultrahigh frequency and its application to gold nanoparticle preparation. Appl Phys Lett. 2009;94:2007–10.

[98] Mariotti D, Švrček V, Kim DG. Self-organized nanostructures on atmospheric microplasma exposed surfaces. Appl Phys Lett. 2007;91:2005–08.

[99] Rumbach P, Bartels DM, Sankaran RM, Go DB. The solvation of electrons by an atmospheric-pressure plasma. Nat Commun. 2015;6:7248.

[100] Bruggeman PJ, Kushner MJ, Locke BR, Gardeniers JGE, Graham WG, Graves DB, Hofman-Caris RCHM, Maric D, Reid JP, Ceriani E, Rivas Fernandez D, Foster JE, Garrick SC, Gorbanev Y, Hamaguchi S, Iza F, Jablonowski H, Klimova E, Kolb J, Krcma F, Lukes P, Machala Z, Marinov I, Mariotti D, Mededovic Thagard S, Minakata D, Neyts EC, Pawlat J, Petrovic ZL, Pfliege R, Reuter S, Schram DC, Schröter S, Shiraiwa M, Tarabová B, Tsai PA, Verlet JRR, Verlet T von, Wilson KR, Yasui K, Zvereva G. Plasma–liquid interactions: a review and roadmap. Plasma Sources Sci Technol. 2016;25:53002.

[101] Lu Y, Xu SF, Zhong XX, Ostrikov K, Cvelbar U, Mariotti D. Characterization of a DC-driven microplasma between a capillary tube and water surface. Europhysics Lett. 2013;102:15002.

[102] Baba K, Kaneko T, Hatakeyama R. Ion irradiation effects on ionic liquids interfaced with rf discharge plasmas. Appl Phys Lett. 2007;90:1–4.

[103] Meiss SA, Rohnke M, Kienle L, Zein El Abedin S, Endres F, Janek J. Employing plasmas as gaseous electrodes at the free surface of ionic liquids: deposition of nanocrystalline silver particles. ChemPhysChem. 2007;8:50–53.

[104] Lin L, Starostin SA, Li S, Khan SA, Hessel V. Synthesis of yttrium oxide nanoparticles via a facile microplasma-assisted process. Chem Eng Sci. 2017;178:157–66.

[105] Huang X, Li Y, Zhong X. Effect of experimental conditions on size control of Au nanoparticles synthesized by atmospheric microplasma electrochemistry. Nanoscale Res Lett. 2014;9:572.

[106] Ghosh S, Bishop B, Morrison I, Akolkar R, Scherson D, Sankaran RM. Generation of a direct-current, atmospheric-pressure microplasma at the surface of a liquid water microjet for continuous plasma–liquid processing. J Vac Sci Technol Vacuum Surfaces Film. 2015;33:21312.

[107] Koo IG, Lee MS, Shim JH, Ahn JH, Lee WM. Platinum nanoparticles prepared by a plasma-chemical reduction method. J Mater Chem. 2005;15:4125.

[108] Tran QC, Dao VD, Jung KD, Choi HS. Plasma-ionic liquid reduction for synthesizing platinum nanoparticles with size dependent crystallinity. Electrochim Acta. 2014;143:357–65.

[109] Yan T, Zhong X, Rider A E, Lu Y, Furman SA, Kk O. Microplasma-chemical synthesis and tunable real-time plasmonic responses of alloyed Au_xAg_{1-x} nanoparticles. Chem Commun. 2014;50:3144–47.

[110] Kim JS, Dao VD, Larina LL, Choi HS. Optimum alloying of bimetallic PtAu nanoparticles used as an efficient and robust counter electrode material of dye-sensitized solar cells. J Alloys Compd. 2016;682:706–12.

[111] Buzzeo MC, Evans RG, Compton RG. Non-haloaluminate room-temperature ionic liquids in electrochemistry-A review. Chem Phys Chem. 2004;5:1106–20.

[112] Zhang J, Bond AM. Practical considerations associated with voltammetric studies in room temperature ionic liquids. Analyst. 2005;130:1132.

[113] Vennekamp M, Janek J. Control of the surface morphology of solid electrolyte films during field-driven growth in a reactive plasma. Phys Chem Chem Phys. 2005;7:666.

[114] Lee H, Park SH, Jung SC, Yun JJ, Kim SJ, Kim DH. Preparation of nonaggregated silver nanoparticles by the liquid phase plasma reduction method. J Mater Res. 2013;28:1105–10.

[115] Samukawa S, Hori M, Rauf S, Tachibana K, Bruggeman P, Kroesen G, et al. The 2012 Plasma Roadmap. J Phys D Appl Phys. 2012;45:253001.

[116] Lin PA. Design and fabrication of compositionally and shape controlled metal nanoparticles for semiconductor nanowire growth. Cleveland, USA: Case Western Reserve University, 2012.

[117] Laux CO, Gessman RJ, Kruger CH, Roux F, Michaud F, Davis SP. Rotational temperature measurements in air and nitrogen plasmas using the first negative system of N_2\n$^+$. J Quant Spectrosc Radiat Transf. 2001;68:473–82.

[118] Laux CO, Spence TG, Kruger CHJ, Zare RN. Optical diagnostics of atmospheric pressure air plasmas. Plasma Sources Sci Technol. 2003;12:125.

[119] Song MA, Lee YW, Chung TH. Characterization of an inductively coupled nitrogen-argon plasma by Langmuir probe combined with optical emission spectroscopy. Phys Plasmas. 2011;18:23504.

[120] Staack D, Farouk B, Gutsol A, Fridman A. Spectroscopic studies and rotational and vibrational temperature measurements of atmospheric pressure normal glow plasma discharges in air. Plasma Sources Sci Technol. 2006;15:818–27.

[121] Phillips DM. Determination of gas temperature from unresolved bands in the spectrum from a nitrogen discharge. J Phys D Appl Phys. 2001;9:507–21.

[122] Huang XJ, Xin Y, Yang L, Yuan QH, Ning ZY. Spectroscopic study on rotational and vibrational temperature of N_2 and N^{2+} in dual-frequency capacitively coupled plasma. Phys Plasmas. 2008;15:113504.

[123] Jain DC. Transition probability parameters of the swan and the fox-herzberg band systems of the C_2 molecule. J Quant Spectrosc Radiat Transf. 1964;4:427–40.

[124] Lombardi G, Benedic B, Mohasseb F, Hassouni K, Gicquel A. Determination of gas temperature and C_2 absolute density in $Ar/H_2/CH_4$ microwave discharges used for nanocrystalline diamond deposition from the C_2 Mulliken system. Plasma Sources Sci Technol. 2004;13:375–86.

[125] Lin PA, Sankaran RM. Plasma-assisted dissociation of organometallic vapors for continuous, gas-phase preparation of multimetallic nanoparticles. Angew Chemie-Int Ed. 2011;50:10953–56.

[126] Lin L, Starostin SA, Wang Q, Hessel V. An atmospheric pressure microplasma process for continuous synthesis of titanium nitride nanoparticles. Chem Eng J. 2017;321:447–57.

[127] Lin PA, Kumar A, Mohan Sankaran R. New insights into plasma-assisted dissociation of organometallic vapors for gas-phase synthesis of metal nanoparticles. Plasma Process Polym. 2012;9:1184–93.

[128] Kumar A, Ann Lin P, Xue A, Hao B, Khin Yap Y, Sankaran RM. Formation of nanodiamonds at near-ambient conditions via microplasma dissociation of ethanol vapour. Nat Commun. 2013;4:1–8.

[129] Kuga Y, Okauchi K, Takeda D, Ohira Y, Ando K. Classification performance of a low pressure differential mobility analyzer for nanometer-sized particles. J Nanoparticle Res. 2001;3:175–83.

[130] Camata RP, Atwater HA, Vahala KJ, Flagan RC. Size classification of silicon nanocrystals. Appl Phys Lett. 1996;68:3162–64.

[131] Knutson EO, Whitby KT. Aerosol classification by electric mobility: apparatus, theory, and applications. J Aerosol Sci. 1975;6:443–51.

[132] Chiang WH, Sankaran RM. Synergistic effects in bimetallic nanoparticles for low temperature carbon nanotube growth. Adv Mater. 2008;20:4857–61.

[133] Gleiter H. Nanostructured materials: basic concepts and microstructure. Acta Mater. 2000;48:1–29.

[134] Sankaran RM, Holunga D, Flagan RC, Giapis KP. Synthesis of blue luminescent Si nanoparticles using atmospheric-pressure microdischarges. Nano Lett. 2005;5:537–41.

[135] Askari S, Levchenko I, Ostrikov K, Maguire P, Mariotti D. Crystalline Si nanoparticles below crystallization threshold: effects of collisional heating in non-thermal atmospheric-pressure microplasmas. Appl Phys Lett. 2014;104:163103.

[136] Huang XZ, Zhong XX, Lu Y, Li YS, Rider AE, Furman SA, et al. Plasmonic Ag nanoparticles via environment-benign atmospheric microplasma electrochemistry. Nanotechnology. 2013;24:095604.

[137] Ghomi H, Yousefi M, Shahabi N, Khoramabadi M. Ultrasonic-assisted spark plasma discharge for gold nanoparticles synthesis. Radiat Eff Defects Solids. 2013;168:881–91.

[138] Kakati M, Bora B, Sarma S, Saikiaa BJ, Shripathic T, Deshpandec U, et al. Synthesis of titanium oxide and titanium nitride nano-particles with narrow size distribution by supersonic thermal plasma expansion. Vacuum. 2008;82:833–41.

[139] Lin H, Huang CP, Li W, Ni C, Shah SI, Tseng YH. Size dependency of nanocrystalline TiO_2 on its optical property and photocatalytic reactivity exemplified by 2-chlorophenol. Appl Catal B Environ. 2006;68:1–11.

[140] Bootz A, Vogel V, Schubert D. Comparison of scanning electron microscopy, dynamic light scattering and analytical ultracentrifugation for the sizing of poly (butyl cyanoacrylate) nanoparticles. Eur J Pharm Biopharm. 2004;57:369–75.

[141] Mcmullan D. Scanning electron microscopy 1928–1965. Scanning. 1995;17:175–85.

[142] Buhr E, Senftleben N, Klein T, Bergmann D, Gnieser D, Frase CG, et al. Characterization of nanoparticles by scanning electron microscopy in transmission mode. Meas Sci Technol. 2009;20:084025.

[143] Tanabe K. Optical radiation efficiencies of metal nanoparticles for optoelectronic applications. Mater Lett. 2007;61:4573–75.

[144] Ylonen M, Tauno V, Kattelus H. Amorphous metal alloy based MEMS for RF applications. Sensors Actuators A. 2006;132:283–88.

[145] Mao L, Chen J, Zhang X, Kwak M, Wu Y, Fan R. A promising biodegradable magnesium alloy suitable for clinical vascular stent application. Sci Rep. 2017;7:46343.

[146] Herzing AA, Watanabe M, Edwards JK, Conte M, Tang ZR, Hutchings GJ, et al. Energy dispersive X-ray spectroscopy of bimetallic nanoparticles in an aberration corrected scanning transmission electron microscope. Faraday Discuss. 2008;138:337–51.

[147] Oxley MP, Lupini AR, Pennycook SJ. Elemental mapping in scanning transmission electron microscopy. J Phys Conf Ser. 2010;241:12061.

[148] Ghosh S, Yang R, Kaumeyer M, Zorman CA, Rowan SJ, Feng PXL, et al. Fabrication of electrically conductive metal patterns at the surface of polymer films by microplasma-based direct writing. ACS Appl Mater Interfaces. 2014;6:3099–104.

[149] Shevchenko VY, Madison AE. Structure of nanoparticles: I. Generalized crystallography of nanoparticles and magic numbers. Glas Phys Chem. 2002;28:40–43.

[150] Delavari HH, Hosseini HR, Simchi A. Effects of particle size, shape and crystal structure on the formation energy of Schottky vacancies in free-standing metal nanoparticles: A model study. Phys B Condens Matter. 2011;406:3777–80.

[151] Srivastava N, Mukhopadhyay M. Green synthesis and structural characterization of selenium nanoparticles and assessment of their antimicrobial property. Bioprocess Biosyst Eng. 2015;38:1723–30.

[152] Saito G, Zhu C, Akiyama T. Surfactant-assisted synthesis of Sn nanoparticles via solution plasma technique. Adv Powder Technol. 2014;25:728–32.

[153] Baer DR, Engelhard MH, Johnson GE, Laskin J, Lai JF, Mueller K, Munusamy P, Thevuthasan S, Wang HF, Washton N. Surface characterization of nanomaterials and nanoparticles: important needs and challenging opportunities. J Vac Sci Technol Vacuum Surfaces Film. 2013;31:050820.

[154] Richman EK, Hutchison JE. The nanomaterial characterization bottleneck. ACS Nano. 2009;3:2441–46.

[155] Chiang WH. Engineering nanocatalysts for selective growth of carbon nanotubes. Cleveland, USA: Case Western Reserve University, 2009

[156] Wang R, Zuo S, Wu D, Zhang J, Zhu WD, Becker KH, et al. Microplasma-assisted synthesis of colloidal gold nanoparticles and their use in the detection of cardiac Troponin I (cTn-I). Plasma Process Polym. 2015;12:380–91.

[157] Chiang WH, Sakr M, Gao XP, Sankaran RM. Nanoengineering NixFe1-x catalysts for gas-phase, selective synthesis of semiconducting single-walled carbon nanotubes. ACS Nano. 2009;3:4023–32.

[158] Shirai N, Uchida S, Tochikubo F. Synthesis of metal nanoparticles by dual plasma electrolysis using atmospheric dc glow discharge in contact with liquid. Jpn J Appl Phys. 2014;53:1–5.

[159] Mitra S, Cook S, Švrček V, Ross AB, Zhou WZ, Kovač J, et al. Improved optoelectronic properties of silicon nanocrystals/polymer nanocomposites by microplasma-induced liquid chemistry. J Phys Chem C. 2013;117:23198–207.

[160] Kulbe N, Höfft O, Ulbrich A, Abedin SZ, Krischok S, Janek J, et al. “Plasma” electrochemistry in 1-Butyl-3-methylimidazolium dicyanamide: copper nanoparticles from CuCl and $CuCl_2$. Plasma Process Polym. 2011;8:32–37.

[161] Lee SW, Zamani H, Feng PX, Sankaran RM. Extraction of a low-current discharge from a microplasma for nanoscale patterning applications at atmospheric pressure. J Vac Sci Technol B Microelectron Nanom Struct. 2012;30:10603.

[162] Lee SW, Janyasupab M, Liu CC, Sankaran RM. Fabrication of Ir nanoparticle-based biosensors by plasma electrochemical reduction for enzyme-free detection of hydrogen peroxide. Catal Today. 2013;211:137–42.

[163] Wang R, Zuo S, Zhu W, Zhang J, Fang J. Rapid synthesis of aqueous-phase magnetite nanoparticles by atmospheric pressure non-thermal microplasma and their application in magnetic resonance imaging. Plasma Process Polym. 2014;11:448–54.

[164] Imasaka K, Kato Y, Suehiro J. Enhancement of microplasma -based water-solubilization of single-walled carbon nanotubes using gas bubbling in water. Nanotechnology. 2007;18:335602.

[165] Saito G, Hosokai S, Tsubota M, Akiyama T. Nickel nanoparticles formation from solution plasma using edge-shielded electrode. Plasma Chem Plasma Process. 2011;31:719–28.

[166] Lal A, Bleuler H, Wüthrich R. Fabrication of metallic nanoparticles by electrochemical discharges. Electrochem Commun. 2008;10:488–91.

[167] Kang J, Kim Y, Kim H, Hu XL, Saito N, Choi JH, et al. In-situ one-step synthesis of carbon-encapsulated naked magnetic metal nanoparticles conducted without additional reductants and agents. Sci Rep. 2016;6:38652.

[168] Sato M, Ohgiyama T, Clements JS. Formation of chemical species and their effects on microorganisms using a pulsed high-voltage discharge in water. IEEE Trans Ind Appl. 1996;32:106–12.

[169] Han ZJ, Levchenko I, Kumar S, Yajadda MM, Yick S, Seo DH, et al. “Plasma” nanofabrication and nanomaterials safety. J Phys D Appl Phys. 2011;44:174019.

[170] Ray PC, Yu H, Fu PP. Toxicity and environmental risks of nanomaterials: challenges and future needs. J Environ Sci Health Part C. 2009;27:1–35.

[171] Ghosh S, Klek E, Zorman CA, Mohan Sankaran R. Microplasma-induced in situ formation of patterned, stretchable electrical conductors. ACS Macro Lett. 2017;6:194–99.

[172] Sankaran RM, Giapis KP. Hollow cathode sustained plasma microjets: characterization and application to diamond deposition. J Appl Phys. 2002;92:2406–11.

[173] Meng LG, Liu CL, Liang HF, Liang ZH. Microplasma array devices with coplanar electrodes operating in neon. Phys Lett A. 2008;372:6504–08.

[174] Eden JG, Park SJ, Ostrom NP, Chen KF. Recent advances in microcavity plasma devices and arrays: a versatile photonic platform. J Phys D-Applied Phys. 2005;38:1644–48.
[175] Roberts EJ, Habas SE, Wang L, Ruddy DA, White EA, Baddour FG, et al. High-throughput continuous flow synthesis of nickel nanoparticles for the catalytic hydrodeoxygenation of guaiacol. ACS Sustain Chem Eng. 2017;5:632–39.
[176] Penache C, Cga BD, Scheffler P, Spielberger L, Hohn O, Schössler S, et al. Micro-structured electrode arrays: a source of high-pressure non-thermal plasma. Selected research papers on spectroscopy of nonequilibrium plasma at elevated pressures. Moscow: Russian Federation; 2002.
[177] Yasuda H. Plasma Polymerization. Orlando, Florida: Academic Press, INC; 1985.

Bionotes

Liangliang Lin received his B.S. degree from Chemical Engineering and Processing Department, Hefei University of Technology in 2010. Then he joined Chemical Engineering Department, Zhejiang University in 2010 under the supervision of Prof. Chaohong He and got his master degree in 2013. Since 2014, he continued pursuing his PhD degree in the Chemical Engineering and Chemistry Department, Eindhoven University of Technology under the supervision of Prof. Volker Hessel. His current research focuses on the plasma-assisted synthesis of functional nanomaterials and their applications.

Sergey A. Starostin graduated as engineer physicist (MS degree equivalent) from Moscow State Engineering Physics Institute (MEPhI), Chair of Plasma Physics in 1992. He started his work as researcher in Low Temperature Plasma Optics Department of Lebedev Physical Institute, Russian Academy of Science. In 2002 he received his PhD degree in Laser and Non-Linear Optics group in University of Twente (The Netherlands) on the topic of gas discharge lasers under the supervision of Professor Klaus Boller. Then gaining research experience consecutively working in Leibniz Institute for Plasma Science and Technology (INP Greifswald, Germany), Eindhoven University of Technology (The Netherlands) and Dutch Institute for Fundamental Energy Research (DIFFER). Presently he is employed as Sr Research Engineer in FUJIFILM Manufacturing Europe, focusing on industrial applications of atmospheric pressure plasma.

Sirui Li was born in Yunnan, China, in 1988. He received the B.Eng. (with honours), M.Sc. degrees in Electronic and Electrical Engineering from the University of Strathclyde, Glasgow, U.K., in 2010 and 2011. After finishing his study in the non-thermal plasma discharge in 2016, he was awarded the Ph. D degree from the University of Strathclyde. Now, he works in the Chemical Engineering and Chemistry Department, Eindhoven University of Technology, majoring non-thermal plasma for chemical conversion.

Volker Hessel studied chemistry at Mainz University (PhD in organic chemistry, 1993). In 1994 he entered the Institut für Mikrotechnik Mainz GmbH and became group leader in Microreaction Technology. In 2002, Prof. Hessel was appointed vice director R&D at IMM and in 2007 as director R&D. In 2005 and 2011, Prof. Hessel was appointed as part-time and full professor at Eindhoven University of Technology, respectively, for the chair of “Micro Flow Chemistry and Process Technology”. He is honorary professor at TU Darmstadt, Germany, and guest professor at Kunming University of Science and Technology, China.

Leticia García-Cruz, Vicente Montiel and José Solla-Gullón

3 Shape-controlled metal nanoparticles for electrocatalytic applications

Abstract: The application of shape-controlled metal nanoparticles is profoundly impacting the field of electrocatalysis. On the one hand, their use has remarkably enhanced the electrocatalytic activity of many different reactions of interest. On the other hand, their usage is deeply contributing to a correct understanding of the correlations between shape/surface structure and electrochemical reactivity at the nanoscale. However, from the point of view of an electrochemist, there are a number of questions that must be fully satisfied before the evaluation of the shaped metal nanoparticles as electrocatalysts including (i) surface cleaning, (ii) surface structure characterization, and (iii) correlations between particle shape and surface structure. In this chapter, we will cover all these aspects. Initially, we will collect and discuss about the different practical protocols and procedures for obtaining *clean* shaped metal nanoparticles. This is an indispensable requirement for the establishment of correct correlations between shape/surface structure and electrochemical reactivity. Next, we will also report how some *easy-to-do* electrochemical experiments including their subsequent analyses can enormously contribute to a detailed characterization of the surface structure of the shaped metal nanoparticles. At this point, we will remark that the key point determining the resulting electrocatalytic activity is the surface structure of the nanoparticles (obviously, the atomic composition is also extremely relevant) but not the particle shape. Finally, we will summarize some of the most significant advances/results on the use of these shaped metal nanoparticles in electrocatalysis covering a wide range of electrocatalytic reactions including fuel cell-related reactions (electrooxidation of formic acid, methanol and ethanol and oxygen reduction) and also CO_2 electroreduction.

This article has previously been published in the journal *Physical Sciences Reviews*. Please cite as: García-Cruz, L., Montiel, V., Solla-Gullón, J. Shape-controlled metal nanoparticles for electrocatalytic applications. *Physical Sciences Reviews* [Online] **2018**, 3. DOI: 10.1515/psr-2017-0124

https://doi.org/10.1515/9783110345100-003

Graphical Abstract:

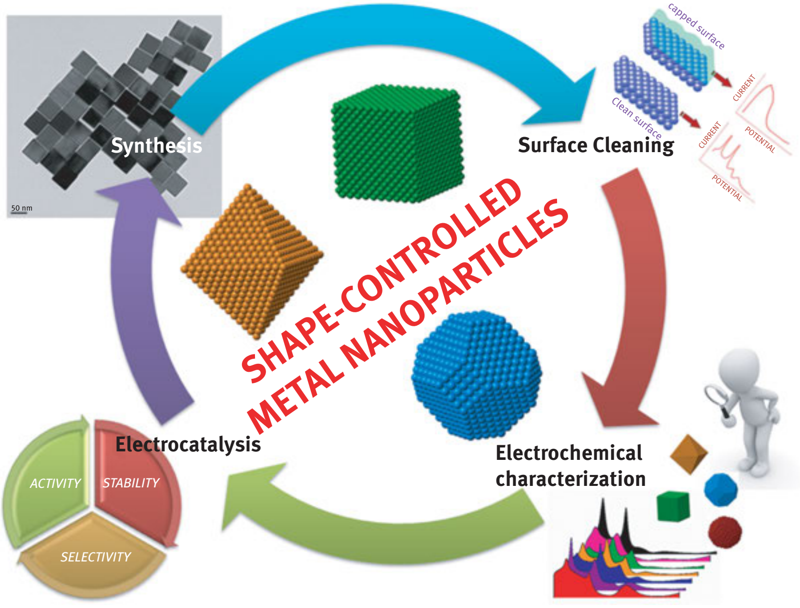

Keywords: silver, nanoparticle, biofouling

3.1 Introduction

Based on the extensive and intensive knowledge gained with the use of metal single-crystal electrodes in electrocatalysis, it is now widely accepted that the surface structure, that is, the arrangement of the atoms at the surface, is one of the most relevant parameter determining the electrocatalytic properties of the material under study [1–3]. Consequently, all this knowledge must serve as a guide for the understanding and evaluation of the effect of the surface structure on the electrocatalytic properties of metal nanoparticles [4–7]. Particularly, this previous knowledge must be used to learn the methods, protocols, precautions, and requirements to be fulfilled to properly study the surface structure–reactivity correlations on the nanoscale materials.

With the aim of understanding the effect of the surface structure on metal nanoparticles, the availability of shape-controlled metal nanoparticles is extremely useful because by controlling the shape of a nanoparticle, it is possible to provide metal nanoparticles with a well-defined surface atomic arrangement and coordination, that is, nanoparticles having a well-defined surface structure. In this regard, Sun and co-workers [8, 9], based on a previous contribution [10], illustrated the correlation between surface structure and particle shape by using the stereographic triangle of a face-centred cubic (fcc) metal (Figure 3.1). In this way, by simple analogy with the unit stereographic triangle, the low index or basal planes, located at the three vertices of the triangle, would be represented by polyhedral nanocrystals/nanoparticles bounded by the corresponding basal facets, i. e. a cube, an octahedron, and a rhombic dodecahedron corresponding with the {100}, {111}, and {110} basal planes, respectively. On the other hand, the polyhedra lying on the three sidelines (crystallographic zones) and inside of the triangle are polyhedra-containing stepped surfaces, that is, surfaces having a terrace-step structure. These polyhedra are also called high-index faceted nanoparticles, that is, nanoparticles containing surfaces having a set of Miller indices {hkl} with at least one index being larger than 1 ({hk0}, {hkk}, {hhl}, and {hkl} ($h > k > l \geq 1$)) and with a surface coordination number being generally equal to or smaller than 7 (the low-index planes have a coordination number of 9, 8, and 7 corresponding with the {111), {100), and {110) surfaces, respectively). These high-index-faceted nanoparticles are also known as nanoparticles with high-energy surfaces since the surface energy (γ) associated with the different crystallographic planes increases in the order $\gamma\{111\} < \gamma\{100\} < \gamma\{110\} < \gamma\{hkl\}$. Finally, the nanoparticles inside the triangle are characterized by surfaces having kink sites, which induces intrinsic chirality properties.

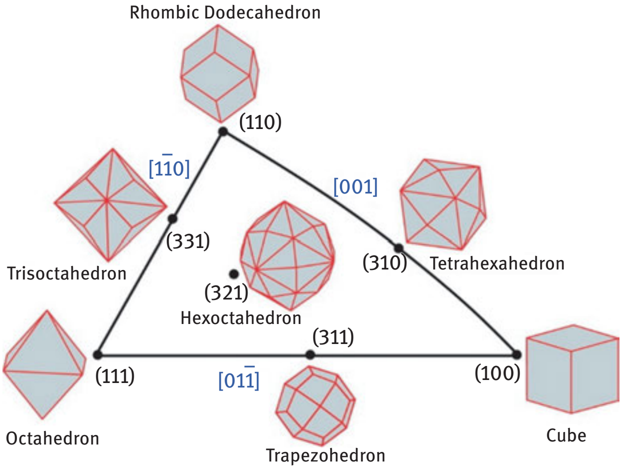

Figure 3.1: Unit stereographic triangle containing polyhedral nanocrystals with different surface planes. Reproduced from Ref. [9] with permission from The Royal Society of Chemistry.

It is worth noting that all these polyhedra are convex ones. In contrast, concave polyhedra are also possible by “pushing in” the centres of the corresponding facets/surfaces. However, it should be mention that the surfaces of these polyhedra are exclusively composed of similar high-index facets regardless of the curvature of polyhedra (convex or concave). To complete this collection of morphologies, it is important to include the so-called excavated and also twinned polyhedral structures.

Obviously, the stereographic triangle of polyhedral shapes shown in Figure 3.1 is exclusively based on geometric aspects. By incorporating *thermodynamic* arguments, and considering the γ of the different crystallographic planes, a metal nanoparticle would tend to have a shape in which the total surface energy is minimized. From this energetic point of view, a shape exclusively composed by {111} facet, that is, an octahedron, would be the most favourable one. However, this shape has a larger surface area than a cube of the same volume. Consequently, the Wulff analysis predicts a shape enclosed by a mixture of {111} and {100} facets. In fact, the most energetically stable shape would be a truncated octahedron with an optimal truncation fulfilling the condition of $\gamma(100)/\gamma(111) = d(100)/d(111)$, where d represents the distance of the facets from the centre of the particle [11]. In addition, *kinetic* factors also play a key role and, in general, the resulting shape will determine by the relative growth rates along the ⟨100⟩ and ⟨111⟩ directions. The ratio of these two growth rates is generally defined as R and changes from 0.58 to 0.87 and eventually to 1.73 for a cube, cuboctahedron, and octahedron, respectively. Fortunately, this energetic (thermodynamic) and/or dynamic (kinetic) control can be overcome by controlling a number of experimental parameters such as (i) the use of capping agents (to conveniently modify the surface energies and inducing the growth in a specific direction), (ii) reaction temperature, (iii) nature and concentration of reducing agents, (iv) presence of additives, and (v) metal salt precursors, among many others, to prepare nanoparticles with tuned morphologies/shapes.

On the other hand, it is worth noting that these correlations between surface structure and particle shape are based on *ideal* polyhedral crystals, that is, polyhedra containing *perfect* surface facets which is, indeed, a non-realistic situation. In fact, the *real* surface of a metal nanoparticle, even a very well-defined one (in terms of size and shape), is extremely complex and its surface structure will not only be constituted by well-ordered surface facets of different dimensions but also by a determined amount of surface imperfections (defect, corner, edge, step, and kink sites), all of them contributing in a different extension (depending on the reaction under study) to the electrocatalytic activity. This aspect points out the outstanding important of having tools to characterize in detail the surface structure of a nanoparticle to then establish the correlations between its surface structure and its electrocatalytic activity. At this respect, a forthcoming section of this chapter will be devoted to the application of easy electrochemical experiments to gain both qualitative and quantitative information about the surface structure of the different metal nanoparticles and particularly shaped ones. At this point, it is again relevant to recall that, from an electrocatalytic point of view, the shape of a nanoparticle is not the key point but its surface structure.

With all these previous questions in mind, this chapter will be focused on the application of shape-controlled metal nanoparticles in electrocatalysis but exclusively from a purely electrochemical point of view. From this electrochemical perspective, a first section will be dedicated to one of the most critical requirements to perform any electrochemical analysis, the surface cleaning. As previously stated, the use of capping or additive agents is a standard way of preparing shape-controlled metal nanoparticles. However, the presence of these surface-regulating agents at the surface of the nanoparticles hinders its direct application in electrocatalysis. Therefore, once the nanoparticles are synthetized, it is mandatory to apply specific decontamination protocols to completely remove (without altering the initial surface structure of the nanoparticles) the presence, even in residual amounts, of these agents at the surface of the nanoparticles. This is not a trivial step, and, from our point of view, this aspect has been underestimated in the extensive literature related to the electrocatalytic properties of shape-controlled metal nanoparticles. Clearly, this is an innovative section in comparison with other contributions made by different groups and dealing with the electrocatalysis on shaped metal nanoparticles. Furthermore, an important section will cover the use of different electrochemical approaches to characterize the surface structure of distinct types of nanoparticles. Interestingly, this *in situ* surface structure characterization is not only statistically representative (thousands of nanoparticles are simultaneously measured) but also performed under similar conditions than those that will be used in the electrochemical reaction. It is worth noting that the existing literature reviewing the catalytic or electrocatalytic properties of different shaped metal nanoparticle consider the particle shape as the key point determining the resulting activity. However, from an electrochemical point of view, it is well-recognized that it is the surface structure the crucial parameter controlling the electrochemical reactivity. Consequently, the description of available electrochemical tools to characterize in detail the surface structure of these shaped metal nanoparticles is an innovative approach in comparison with previous contributions. To conclude this chapter, a last section containing some of the most significant advances/results on the use of these shaped metal nanoparticles in electrocatalysis will be included. This section will not only cover relevant reactions for low-temperature fuel cells such as formic acid, methanol, and ethanol electrooxidation or oxygen reduction but also other interesting reactions such as CO_2 electroreduction.

3.2 Preparation methods

3.2.1 Synthesis of shape-controlled metal nanoparticles

To the best of our knowledge, the first examples of preparation of shape-controlled nanoparticles were achieved by using gas chemisorption. In 1985, Wang et al. observed that the shape of Pt nanocrystals (supported on an amorphous SiO_2 substrate) was modified in the presence of different gas molecules at 600° C for 24 h [12].

Under these conditions, Pt nanocrystals with a truncated cuboctahedral and cubic shape were obtained when samples were annealed in N_2 and H_2, respectively. Similarly, Harris in 1986 observed that cubic Pt nanocrystals (supported on Al_2O_3) were obtained when a H_2 atmosphere containing a trace amount of H_2S at 500 °C for 16 h was used [13]. These two examples clearly showed that by using some gaseous species able to be adsorbed in a specific type of facet, the shape of a metal nanocrystal supported on a solid substrate can be effectively modified.

Going from this gas-phase method to a solution-phase one, El-Sayed and co-workers in 1996 reported the first example of shape-controlled synthesis of metal nanocrystals in water solution by preparing cubic and tetrahedral Pt nanoparticles through a chemical reduction of K_2PtCl_4 by H_2 in the presence of sodium polyacrylate (NaPa) [14]. Obviously, the employ of solution-phase methods for the synthesis of shape-controlled metal nanoparticles seems more convenient than the gas-phase ones where limited option of gases, as well as the use of elevated temperatures, is required. In contrast, in solution phase, there is not only a great availability of capping agents that can be used for each type of facet, but also the experimental conditions are mild.

From these pioneer contributions and due to the enormous efforts coming from many research groups, the existing literature contains now an incredible number of methodologies for the preparation of shape-controlled metal nanoparticles. In this chapter, we are not going to review the innumerable methodologies for the preparation of shape-controlled metal nanoparticles and the readers interested in this topic are referred to some of the relevant and excellent reviews exclusively focused on synthetic aspects [15–28].

Among all these different methods, the use of colloidal routes is one of the most employed. This method is essentially based on the chemical reduction of a metallic precursor in the presence of a capping agent. The role of this capping agent is extremely important in the process because during the growth step, it can selectively bind to a specific facet on the nanoparticles, thus altering their surface energies and promoting the formation of the nanoparticles with a preferential shape that maximizes the expression of that type of facet. Additionally, the effect of the capping can be also explained from a kinetic perspective, that is, taking into consideration the relative growth rates of different crystallographic structures. When the capping is adsorbed in a facet, the subsequent deposition of new atoms onto this facet will be importantly reduced and, therefore, that facet will have a slower growth rate. Consequently, the resulting nanoparticles will have a preferential shape in which that facet will be preferentially expressed. Xia et al. [23] schematically illustrated the role of two complementary capping agents, one for {100} facets and the other for {111} facets during the growth of a truncated octahedral seed, Figure 3.2.

As shown in Figure 3.2, the resulting shape is determined by the capping agent used. Thus, a cubic crystal is obtained when a capping agent with a preference for the {100} facets is employed. Contrarily, when a capping agent with a preference for the {111} facets is introduced, a crystal with an octahedral shape is achieved. Under this

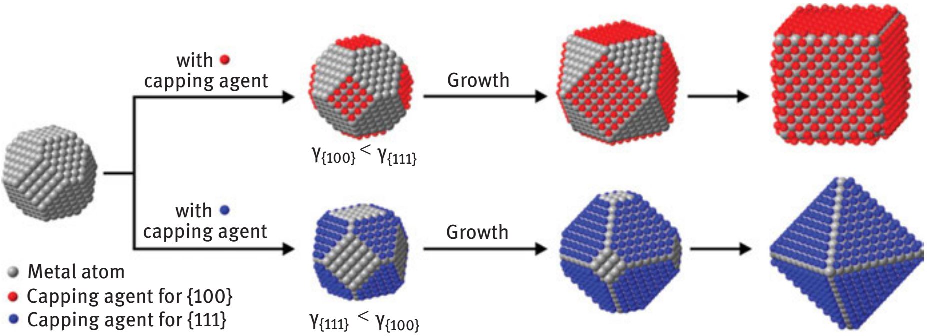

Figure 3.2: Schematic illustration explaining the role of capping agents during the growth of a single-crystal truncated octahedral seed of an fcc metal. Reprinted with permission from Ref [23]. Copyright (2015) American Chemical Society.

thermodynamic control, different nanoparticles with well-controlled shapes can be obtained. However, under realistic condition, the capping agent is not the only parameter determining the resulting shape but also other experimental parameters including temperature, electrolyte, reducing time, nature of the reducing agent, and some others will play a significant role in defining the final shape obtained which will be ultimately determined by both thermodynamic and kinetic control [23].

Interestingly, it is also worth noting that some shape-controlled metal nanoparticles can also be prepared using capping-free methodologies. In this regard, the electrochemical approach initially developed by Sun and co-workers is particularly interesting [8, 9, 29–31]. Other interesting approaches are capping-free solvothermal synthesis [32–35], cathodic corrosion [36], or solid-state chemistry methods [37, 38].

3.2.2 Surface cleanness: a key point in electrocatalysis

It is well-documented that the electrocatalysis on metal single crystals is profoundly marked by the publication in 1980 of the flame annealing treatment by Clavilier et al. [39] This work represents the starting point from which it was possible to correctly understand the relationships between surface structure and electrocatalytic surface reactivity. Very briefly, this simple and elegant cleaning treatment allows obtaining clean and well-ordered Pt single-crystal surfaces to be used in electrochemical measurements in a reproducible way [40]. For instance, this worldwide adapted treatment allowed correlating the voltammetric profile in the so-called hydrogen adsorption/desorption region of any Pt single-crystal electrode including basal, stepped, and kinked surfaces with their intrinsic surface structure (surface orientation, ordered domains, and population of step and terrace sites). Consequently, to correctly understand the correlations between particles shape, surface structure, and electrocatalytic properties with the shaped metal nanoparticles, this cleaning requirement must be fully satisfied.

This *cleaning* requirement is obviously faced with the employ of capping or surface-stabilizing agents which are fundamental to obtain shaped nanoparticles. Therefore, once shaped metal nanoparticles are synthesized, these surface-regulating agents must be completely removed from the surface of the shaped nanoparticles [41]. Consequently, the development of effective surface cleaning methodologies capable of removing such capping or surface-regulating agents from the surface of the corresponding nanoparticles becomes an extremely important prerequisite to subsequently evaluate their electrocatalytic properties for any reaction of interest. If the cleaning is not properly performed, the electrocatalytic activity of the nanoparticles will be affected in a non-controlled way, and non-reproducible and non-comparable results will be obtained. Figure 3.3 schematically represents the effect of an incomplete removal of the capping or surface-regulating agents from the surface of the shaped nanoparticles on their electrocatalytic properties. In addition, there are some important aspects to mention. The first one deals with the wide variety of capping and/or surface-regulating agents that have been used for the synthesis of shaped nanoparticles. This fact implies that a "common" cleaning methodology is not available, and a specific decontamination must be developed, optimized, and tested for each capping agent. In this way, each specific cleaning will basically depend on two main parameters such as (i) the chemical nature of the capping agent and (ii) its interaction with the surface of the shaped nanoparticles, the latter being also affected by the nature of the metal as well as by their surface structure. On the other hand, it is worth noting that this decontamination method must be able to remove the capping agents but without affecting the intrinsic surface structure of the nanoparticles. This point will be exemplified and discussed in a forthcoming section.

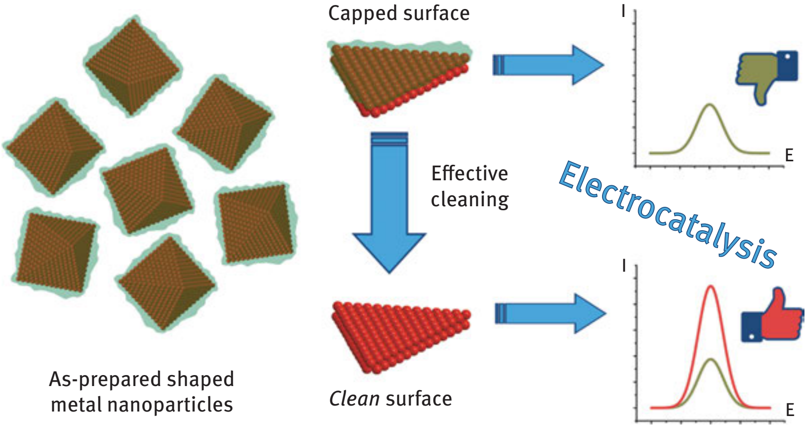

Figure 3.3: Schematically representation of the importance of having clean shaped metal nanoparticles. Reprinted from Ref. [41], Copyright (2017) with permission from Elsevier.

3.2.2.1 Electrochemical probes for surface cleanness evaluation on shaped metal nanoparticles

Once discussed about the mandatory requirement of having shaped nanoparticles with *clean* surfaces to properly study their electrochemical properties, the question now is how to evaluate this surface cleanness. Fortunately, and again from previous knowledge of surface electrochemistry on metal single crystals, it is possible to perform some electrochemical analysis to evaluate this surface cleanness. For Pt and Pd surfaces, it is widely accepted that the so-called hydrogen region (involving the hydrogen and anion adsorption–desorption states) obtained in 0.5 M H_2SO_4 solution is a very sensitive process for the evaluation of the level of cleanness of the surface [2, 3, 40, 42–45]. Very briefly, if the voltammetric profile displays well-defined contributions, in terms of sharpness and reversibility (between desorption vs. adsorption states), that is an indisputable proof of the adequate cleanness of the surface. To illustrate that, Figure 3.4 shows the voltammetric profiles in the so-called hydrogen region obtained with (a) clean and [46] (b) contaminated [47] cubic and octahedral/tetrahedral Pt nanoparticles both obtained in 0.5 M H_2SO_4. The sharpness and reversibility of the adsorption desorption states showed with clean samples clearly contrast with the poor definition of the voltammetric features obtained with contaminated samples are evaluated.

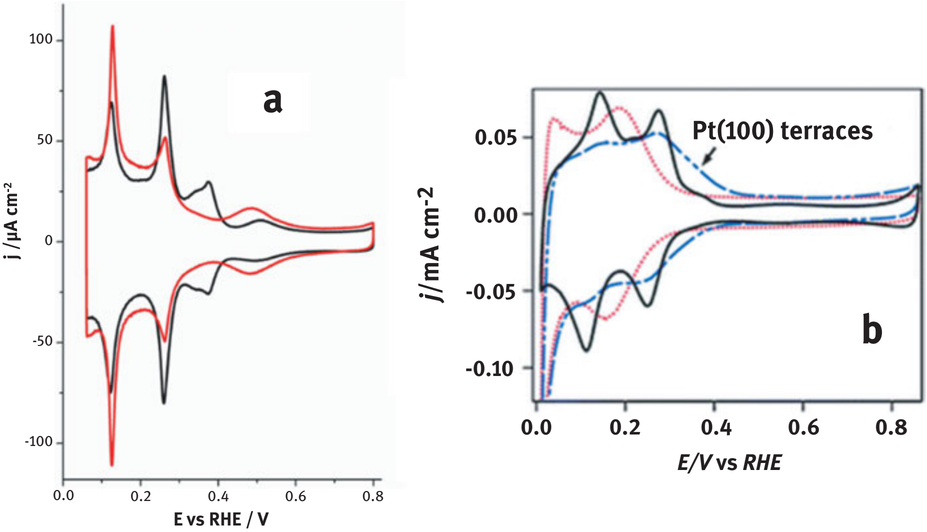

Figure 3.4: Cyclic voltammograms corresponding with (a) *clean* cubic (black line) and octahedral (red line) Pt nanoparticles (data taken from Ref. [46]) and with (b) *contaminated* cubic (blue dashed line) and octahedral (red dotted line) Pt nanoparticles (a commercial Pt black (black solid line) is also included) obtained in 0.5 M H_2SO_4 at 50 mV s^{-1}. Reproduced from Ref. [47] with permission from The Royal Society of Chemistry.

Obviously, for shape-controlled Pt and Pd-based alloy and/or core-shell nanoparticles (this is one of the hot topics in electrocatalysis), the evaluation of the surface cleanness through the so-called hydrogen region is much more complex due to the intrinsic complexity of the surfaces [48–50]. However, at least, one should verify that monometallic samples, prepared in similar conditions than those used for the synthesis of the shaped alloy and/or core-shell nanoparticles, display the voltammetric features corresponding to clean surfaces.

For Au surfaces, the situation is little bit more difficult due to the inexistence of hydrogen adsorption–desorption features on this metal. An interesting alternative is the analysis of the voltammetric profile of the oxide region based on previous contributions by Hamelin et al. [51, 52] with Au single-crystal electrodes. This analysis has been already used with different shape-controlled Au nanoparticles containing both low- and high-index surfaces [53–55]. However, it is important to mention that for all these Au surfaces, the voltammetric profile in the oxide region as well as the charge involved in both the surface oxide process and its subsequent surface reduction should remain stable during the first cycles (about five cycles). In this sense, it is worth recalling that, at these high potential values, the organic impurities can be electrochemical oxidized, thus *in situ* cleaning the surface. However, this *electrochemical* surface oxidation/reduction cleaning also perturbs the surface structure and, as shown with gold single-crystal electrodes [56, 57], the well-defined surface structure of the Au single-crystal electrodes is clearly modified with the electrochemical oxidation/reduction cycles. In this way, despite the structural changes induced by a single-oxidation cycle with gold surfaces are remarkably smaller than those observed for Pt electrodes [58], this surface oxidation/reduction cleaning treatment should not be performed.

Also, by using different underpotential deposition (UPD) processes, some information about the surface cleanness can be also deduced. Among others, lead (Pb) UPD on Au [59–65] and copper (Cu) UPD on Pd [66–68] and Pt [69, 70] are particularly interesting. Figure 3.5 displays the corresponding Pb UPD features obtained with *clean* and *contaminated* Au nanoparticles [63]. As previously discussed, through the analysis of the definition of the different voltammetric features, relevant information about the cleanness of the surface can be extracted.

With all these previous aspects in mind, in the following section, we will summarize some of the most representative decontamination protocols that have been verified, particularly using electrochemical probes, and applied to different shape-controlled metal nanoparticles.

3.2.2.2 Surface cleaning methodologies for shape-controlled metal nanoparticles

The first examples of clean shaped metal nanoparticles were reported by our group in 2004 [71, 72]. In brief, cubic Pt nanoparticles prepared in the presence of NaPA were cleaned by direct addition of some NaOH pellets to the colloidal suspension. The

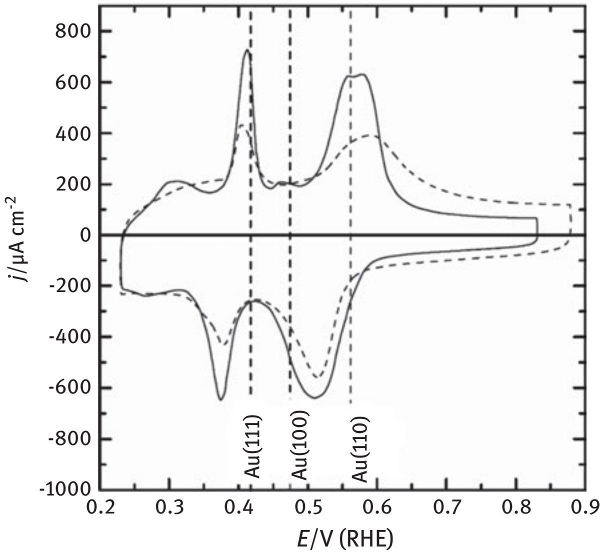

Figure 3.5: Voltammetric profiles corresponding with *clean* (solid line) and *contaminated* (dashed line) Au nanoparticles obtained in 0.1 M NaOH + 10^{-3} M $Pb(NO_3)_2$ at 50 mV s^{-1}. Reprinted from Ref. [63], Copyright (2014) with permission from Elsevier.

addition of the NaOH induces the destabilization of the colloid and the nanoparticles precipitate. The samples are then collected and washed a couple of times with ultrapure water. The clean cubic Pt nanoparticles were finally stored in ultrapure water. The same cleaning protocol was applied later to cuboctahedral and tetrahedral–octahedral Pt nanoparticles prepared using a similar methodology (using NaPA as capping agent). The effectiveness of the cleaning was evidenced by the definition and reversibility of the cyclic voltammograms in the so-called hydrogen region obtained in 0.5 M H_2SO_4.

This cleaning protocol was found to be also effective with cubic Pd nanoparticles prepared in the presence of cetyltrimethylammonium bromide (CTAB) [73–75]. Interestingly, Coutanceau and co-workers also verified that this alkaline cleaning protocol was again effective, in this case, with cubic Pt nanoparticles prepared using tetradecyltrimethylammonium bromide (TTAB) as capping agent [76, 77]. The electrochemical response of these TTAB-prepared cubic Pt nanoparticles in 0.5 M H_2SO_4 was essentially similar to that observed with the NaPA-prepared cubic Pt nanoparticles [46, 78–80], thus pointing out that, independent of the synthetic methodology used, and particularly the chemical nature of the capping agent employed, similar nanoparticles must display similar voltammetric features if they are properly cleaned.

Unfortunately, this cleaning protocol did not provide satisfactory results with shaped Pt nanoparticles prepared with polyvinylpyrrolidone (PVP) [76, 81–83]. In these contributions, the absence of well-defined voltammetric features denoted the important presence of residual PVP blocking the surface sites. The PVP is one of the most usual capping agents for the preparation of shape-controlled metal nanoparticles [84] and, to the best of our knowledge, the first evidence of clean shape-controlled Pt nanoparticles prepared with PVP was published by Koper and co-workers [85] by employing a H_2O_2/H_2SO_4 solution to remove the PVP. They claimed that the PVP removal was physically removed from the surface of the nanoparticles by the oxygen bubbling produced during the decomposition of the H_2O_2. Subsequently, Levendorf et al. proposed a new protocol to obtain PVP-free cubic and octahedral/tetrahedral Pt nanoparticles using an adapted liquid phase UV photo-oxidation technique [86]. In this case, after different washing steps with different solvents – acetone, ethanol–hexane mixtures, and ethanol – the ethanolic suspension containing the nanoparticles was initially alkalinized. This basic solution containing the nanoparticles was UV irradiated (254 nm) for 1 h, while about 1 mL of O_2-saturated H_2O_2 solution was added to the solution every 10 min. After that, the solution containing the nanoparticles was finally purified by repetitive centrifugation and precipitation with ethanol. The voltammetric profiles of these shaped Pt nanoparticles recorded in 0.5 M H_2SO_4 as well as TGA analyses evidenced the effectiveness of the cleaning protocol proposed.

Later, Yang et al. proposed an alternative electrochemical cleaning procedure to obtained clean shape-controlled Pt nanoparticles prepared with PVP and also with oleylamine/oleic acid [87]. The removal of the different capping agents was achieved by cycling the samples (initially washed with a NaOH saturated ethanolic solution (PVP samples) or with a hexane/ethanol mixture (oleylamine/oleic acid samples), and finally redispersed in ethanol and hexane, respectively) between 0 and 1.0 V (vs. RHE) in 0.5 M NaOH at a scan rate of 0.5 V $s^{-}1$ for at least 100 cycles. The sample was then transferred to an electrochemical cell containing 0.5 M H_2SO_4 where, by regarding the so-called hydrogen region, the cleanness of the surface was evaluated. The results obtained indicated that both PVP and oleylamine/oleic acid could be effectively removed from the surface of the nanoparticles.

Very interestingly, Coutanceau and co-workers [88, 89] reported a much easier method to clean shaped controlled Pd nanoparticles prepared with PVP. This protocol is essentially similar to the alkaline cleaning one but using a significantly higher NaOH concentration. Briefly, the PVP-colloidal suspension containing the shaped Pd nanoparticles was diluted with H_2O after which NaOH was added until getting a 1 M NaOH solution. Under these conditions, the nanoparticles were collected by precipitation and washed with water. The voltammetric profiles obtained in 0.5 M H_2SO_4 displayed characteristics features of clean samples.

Neergat and co-workers reported two new cleaning protocol s for the removal of PVP and others surface-regulating additives such as Br^-, Cl^-, and citrate ions employed during the preparation of shape-controlled Pd nanoparticles [90, 91]. After some preliminary cleaning steps for the removal of the excess of chemicals, the samples were subsequently treated with tert-butylamine (TBA) [91] or $NaBH_4$ [90] and finally collected by centrifugation and washed with different solvents (ethanol or water). However, and despite some improvement in terms of cleaning (about a 90 % cleaning was estimated) and consequently on their electrocatalytic properties (enhanced ORR activities), the samples were not completely clean as deduced from CHN analyses.

Luo et al. employed a combined TBA/$NaBH_4$ cleaning to produce clean Pt-Pd nanocubes obtained in the presence of PVP [92]. The removal of the PVP was carried out by dispersing the nanoparticles in a TBA/$NaBH_4$ aqueous solution ($NaBH_4$/TBA/water, 1.9 mg/20 mL/5 mL) for 30 min under continuous stirring and at room temperature. The sample was then collected by centrifugation and washed with an ethanol/acetone mixture. In this case, the surface cleaning was confirmed by Raman and FTIR studies, and the electrocatalytic activity of the clean Pt–Pd nanocubes towards methanol oxidation in 0.1 M $HClO_4$ displayed an evident enhancement.

Arán-Ais et al. presented a new methodology to clean various shape-controlled Pt nanoparticles prepared in oleylamine/oleic acid [93]. The different shaped Pt nanoparticles were initially washed with a hexane/ethanol mixture and then with a methanolic solution containing NaOH. After complete precipitation of the nanoparticles, the sample was washed with acetone. This treatment was repeated at least three times, after which the sample was washed and stored in ultrapure water. Subsequently, the samples were electrochemically characterized in 0.5 M H_2SO_4 displaying well-defined voltammetric features. Interestingly, as shown in Figure 3.6, if the shaped Pt nanoparticles were not conveniently cleaned, they showed a voltammetric profile with a poor definition as a consequence of their insufficient surface cleanness.

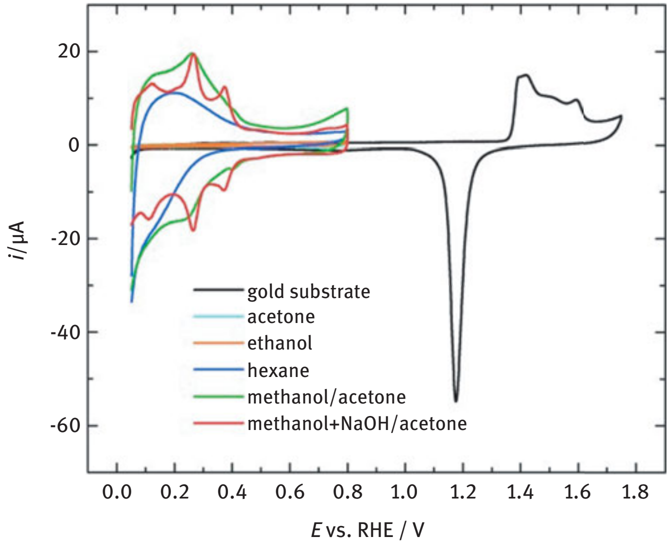

Figure 3.6: Voltammetric profiles obtained with cubic Pt nanoparticles after being treated with different cleaning protocols. Test solution: 0.5 M H_2SO_4. Sweep rate: 50 mV s^{-1}. Reprinted from Ref. [93] with permission from John Wiley and Sons.

More recently, Oezaslan et al. reported two novel approaches to clean Pt nanocubes obtained in the presence of PVP [94, 95]. In the first case [94], they proposed an electrochemical cleaning for the removal of the capping agent. Thus, after testing different supporting electrolytes (pH~ 1, 0.1 M $HClO_4$ and pH~ 13, 0.1 M NaOH) as well as different upper potential limits (0.8, 1.0, 1.2 and 1.4 V/RHE), they stated that the electrochemical cycling (200 cycles at a scan rate of 200 mV s^{-1}) up to 0.8 V in 0.1 M $HClO_4$ was the most convenient one in terms of cleaning and particle shape stability. In a subsequent contribution, they incorporated an optimized washing step before electrochemical cleaning [95]. Based on FTIR results, they suggested that a washing process in methanol/ethanol (3:1) significantly removed the physisorbed PVP. After this washing step, the samples were electrochemically treated by cycling between 0.06 and 1.0 V vs. RHE for 200 cycles in an Ar-saturated 0.1 M $HClO_4$ solution.

For shape-controlled Au nanoparticles, the electrochemical deposition of a PbO_2 film in alkaline solution [63–65, 96] has been shown to be a very effective cleaning protocol. In brief, the cleaning consists in cycling the gold nanoparticles in the Pb^{2+} containing alkaline solution from 0.25 to 1.70 V (vs. RHE) to form the PbO_2 film. The electrocatalytic properties of the PbO_2 film for the oxidation of organic species contribute to the removal of the capping agents used. Interestingly, and despite the high potential values, this process preserves the surface structure of the nanoparticles as it was demonstrated with both single-crystal and polyoriented Au electrodes [65]. This cleaning protocol has been successfully used for different shaped Au nanoparticles prepared using very different capping agents including polyethylene glycol dodecyl ether (Brij®30) [63], CTAB [55, 64], and PVP [97], among others. For instance, Hassel et al. applied this cleaning methodology to different Au nanoplates prepared with PVP [97]. As illustrated in Figure 3.7, the good definition of the voltammetric profile for the Pb UPD process obtained with the clean samples in comparison with the contaminated ones clearly point out the effectiveness of this cleaning process.

Lee and co-workers used an O_2 plasma treatment to obtain clean gold nanocrystals prepared with PVP [54, 98]. After the cleaning, the cubic and octahedral gold nanocrystals displayed well-defined voltammetric features in the surface oxide region which were completely missing before the oxygen plasma treatment.

3.3 Characterization methodologies

3.3.1 Electrochemical probes for the characterization of the surface structure of the shaped metal nanoparticles: qualitative and quantitative approaches

As discussed in the previous section, by using some electrochemical probes, the surface cleanness of different shaped metal nanoparticles can be easily visualized. However, these electrochemical probes can be also employed to gain relevant and very detailed information about the surface structure of the different nanoparticles. Thus, in this section, we will describe some of the most interesting electrochemical

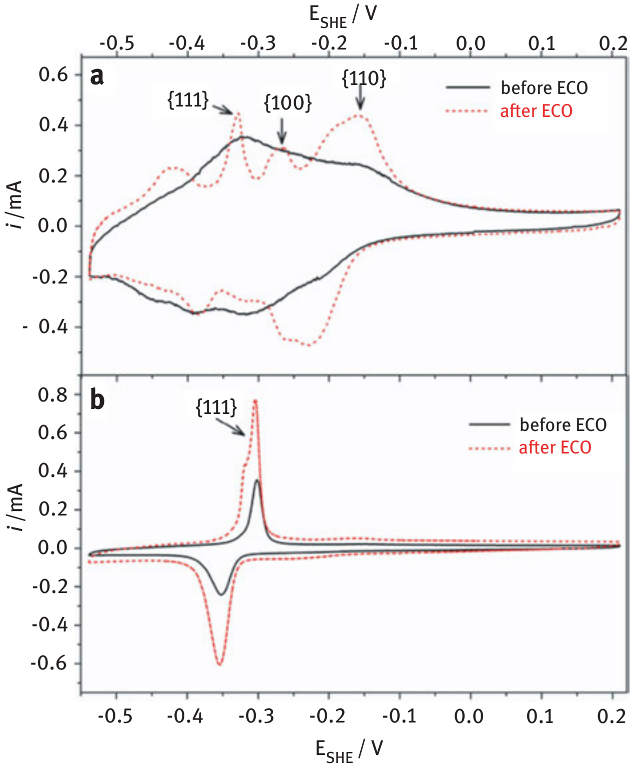

Figure 3.7: CV profiles of (a) {110} and (b) {111} Au nanoplates in 0.1 M NaOH+ 10^{-3} M $Pb(NO_3)_2$ before and after ECO. Scan rate: 20 mV s^{-1}. Reprinted from Ref. [97] with permission from John Wiley and Sons.

analysis to characterize the surface structure of the shaped metal nanoparticles. For Pt and Pd surfaces, it is well-recognized that the voltammetric profile in the so-called hydrogen region obtained in 0.5 M H_2SO_4 solution can be taken as fingerprint of their crystalline surface structure [99]. In this way, by simple inspection of the relative intensity of the different voltammetric features present in this hydrogen region, one can directly obtain qualitative information about the surface structure of the sample, that is, about the different active sites present on the surface. To illustrate the case, and focusing exclusively on Pt, Figure 3.8 shows the voltammograms obtained in 0.5 M H_2SO_4 with quasi-spherical, cubic, octahedral/tetrahedral, and truncated octahedral Pt nanoparticles [46]. First, as mentioned in the previous section, the well-resolved hydrogen peaks point out the correct surface cleanness of the shaped Pt nanoparticles. Then, it is obvious that the voltammetric responses of the samples are clearly different. As extensively described in previous contributions, and based on Pt single-crystal surfaces, the main voltammetric features are (i) the peak at 0.12 V, which is related to {110}-type sites; (ii) the peak at 0.27 V, which contains two

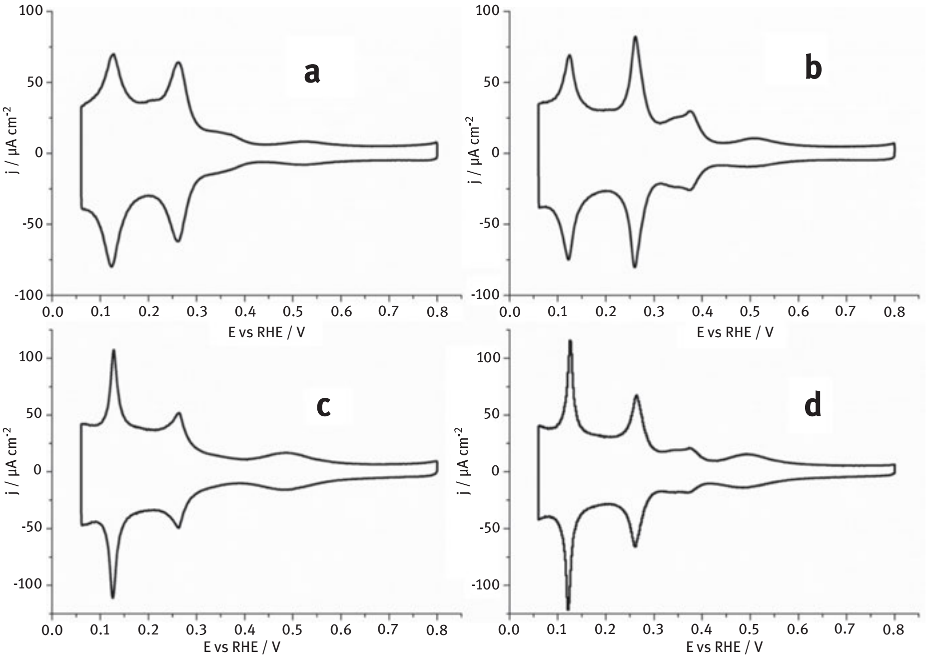

Figure 3.8: Representative voltammetric profiles of (a) quasi-spherical, (b) cubic, (c) octahedral/tetrahedral, and (d) truncated octahedral Pt nanoparticles obtained in different supporting electrolytes at 50 mV s^{-1}. Data taken from [46].

contributions from (100) step sites on {111} terraces and the sites close to the steps on the {100} terraces; (iii) the signals at 0.35–0.37 V attributed to ordered {100} terraces; and (iv) the signal at 0.5 V, related to the ordered {111} terraces. As expected, all these voltammetric profiles can be perfectly correlated with those reported with Pt single-crystal electrodes [99].

In this way, and from the relative distribution of charge among the voltammetric peaks, it is possible to get a qualitative analysis of the relative distribution of electrochemically available Pt sites present at the whole surface of each type of sample [99, 100]. Figure 3.9 schematically illustrates the correspondence between the voltammetric features and the different types of active sites present at the surface of a Pt nanocube. By performing a similar analysis, but using the voltammetric profiles displayed in Figure 3.8, it is now consistent to correlate the particle shape with the corresponding surface structure and the quasi-spherical, cubic, octahedral/tetrahedral and truncated octahedral Pt nanoparticles present a polyoriented, (100), (111), and (100)-(111) preferentially oriented surface structure, respectively. These results are in good agreement with what it would be expected from the correlation between surface structure and particle shape by using the stereographic triangle of a fcc metal (Figure 3.1). However, it is also evident that the surface of all these Pt nanoparticles

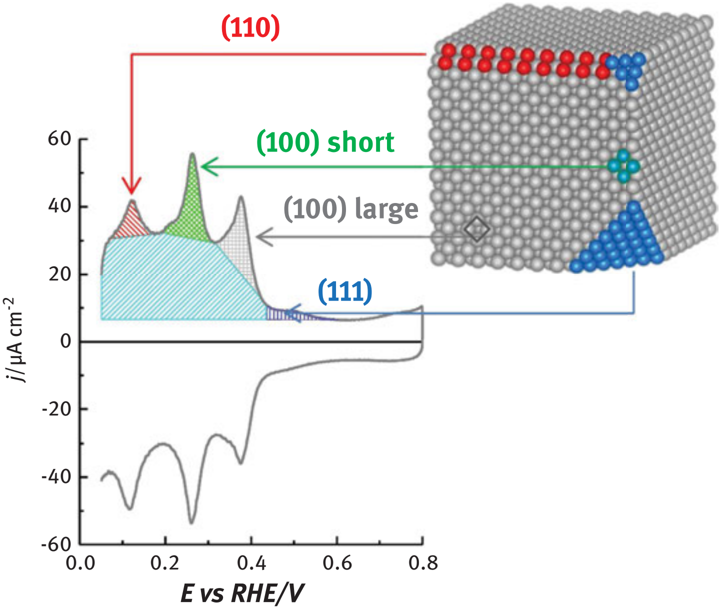

Figure 3.9: Characteristic voltammetric profile and atomic model of (100)-preferentially oriented Pt nanoparticles in 0.5 H_2SO_4, showing bevelled and truncated edges and its correspondence with the different voltammetric features. Reprinted from Ref. [101], Copyright (2018) with permission from Elsevier.

is very complex and it does not contain only a single type of surface sites, but all the adsorption–desorption states are observed but presenting a different contribution as a function of their particular surface structure [101]. In addition, it is worth noting that these surfaces always present a determined number of surface defects (corner, edge, step, and kink sites) also contributing to the resulting voltammetric profile.

Analogue studies can be also performed in other supporting electrolytes (0.1 M NaOH and 0.1 M $HClO_4$), although these media are less convenient for the analysis of the surface structure of the shaped Pt nanoparticles due to the overlapping of some voltammetric features [46]. Finally, it is worth mentioning that the overall charge involved in the so-called hydrogen region is also known to be proportional to the total amount of surface Pt atoms and, therefore, the integrated charge obtained from the CV can be used to properly calculate the electroactive surface area of the Pt nanoparticles. A similar analysis between the voltammetric profile in the hydrogen region obtained in different supporting electrolytes and the surfaces structure of the electrodes is also possible for Pd surfaces. Readers interested in this topic are referred to [49].

As previously stated, the surface cleaning must be performed without perturbing the surface structure of the nanoparticles. In this way and considering the high sensitivity of the hydrogen region to the surface structure, this reaction can help to verify if the cleaning protocol alters or not the surface structure of the sample. To exemplify this question, Vidal et al. [102] electrochemically showed that the UV/ozone cleaning protocol strongly perturbed the surface structure of different shaped Pt nanoparticles. However, in agreement with Somorjai and co-workers [103–105] for shaped Pt nanoparticles and with Kiwi-Minsker [106] with PVP-stabilized Pd nanocubes, neither the shape nor the size of nanoparticles was affected by the treatment. This contribution clearly evidenced that the key parameter determining the resulting catalytic or electrocatalytic activity is the surface structure but not the shape of the nanoparticles, Figure 3.10.

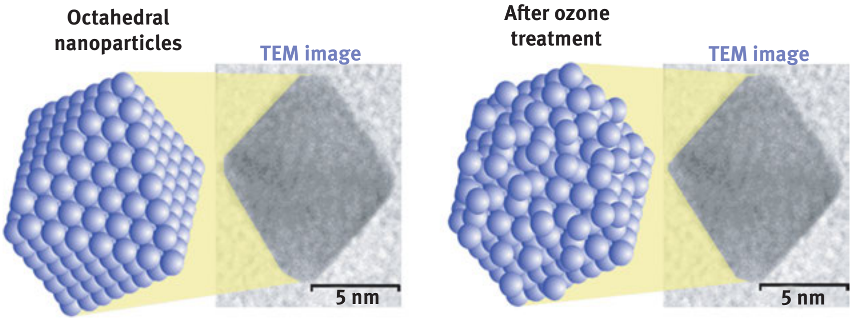

Figure 3.10: Schematic representation showing two Pt nanoparticles with a similar particle shape (octahedron) but distinct surface structure. Reprinted from Ref. [102], Copyright (2011) with permission from Elsevier.

On the other hand, from the analysis of the oxide formation region, some information about the surface structure can be extracted particularly for Au and Pd surfaces. For Au surfaces, the voltammetric profile of the surface oxide region displayed characteristics features that can be assigned to specific surface structures. This analysis is again based on Au single-crystal electrodes [51, 52] and it has been already employed for the characterization of the surface structure of different shape-controlled Au nanoparticles [53–55]. For instance, Figure 3.11 shows the cyclic voltammogram of octahedral, truncated octahedral, and truncated tetrahexahedra (THH) Au nanocrystals obtained in 0.5 M H_2SO_4 solution [53]. From the different voltammetric features appearing in the surface oxide region and based on the previous information gained with Au single-crystal electrodes, the correlations between particle shape and surface structure of the gold nanocrystals can be properly established. Monzó et al. performed a similar analysis of the oxide formation region in alkaline solution [55]. Cubic and octahedral Au nanoparticles displayed distinct voltammetric features in this region which were compared with those previously reported with Au single-crystal electrodes.

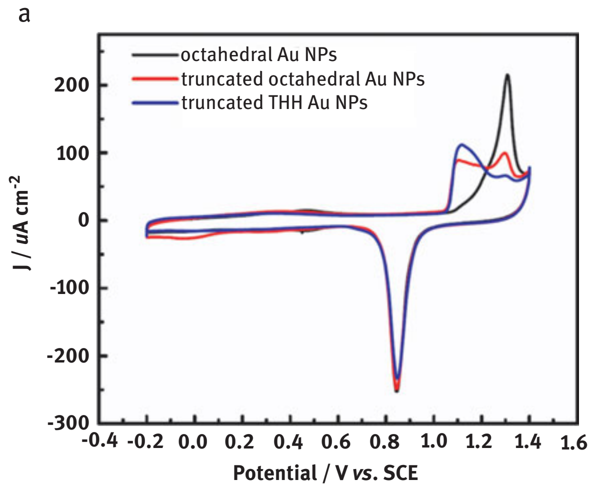

Figure 3.11: Cyclic voltammogram of octahedral, truncated octahedral and truncated tetrahexahedra (THH) Au nanocrystals obtained in 0.5 M H_2SO^4 solution. Sweep rate 50 mV s^{-1}. Reprinted from Ref. [53], Copyright (2014) with permission from Elsevier.

The employ of some UPD processes to characterize the surface structure of different shaped metal nanoparticles is also a very interesting approach because these processes are very sensitive to the surface structure of the electrodes [107, 108]. For instance, Pb UPD has been extensively used on different shaped Au nanoparticles [55, 64, 65, 97, 109–111]. As shown in Figure 3.12, the Pb UPD displays distinctive features as a function of the surface structure of the shaped Au nanoparticles. The figure clearly shows a preferential {100} and {111} surface structure for the (C) cubic and (D) octahedral Au samples, respectively. However, for the spherical samples, and independently of their particle size, the Pb UPD profile shows the characteristic response of a polyoriented surface structure.

Also, Cu UPD has been used for shaped Pd nanoparticles, particularly for Pd nanocubes [112–114]. In addition, these UPD processes can be also used to calculate the real area of the electrode from the charge involved in the UPD reaction and subsequently normalized with a specific charge density normalization (generally obtained from a polyoriented surface).

Up to now, the different surface structure electrochemical probes discussed are essentially qualitative, that is, from the relative intensity of the characteristic features, it is possible to visualize which surface structure is preferentially present at the surface of the shaped metal nanoparticles. However, it would be much more desirable to have some electrochemical surface probes to quantitatively analyse the surface structure of the nanoparticles. Thus, in the following, we will summarize some of the different approaches proposed for the quantitative characterization of the surface structure of the shaped metal nanoparticles. For Pt surfaces, different alternatives

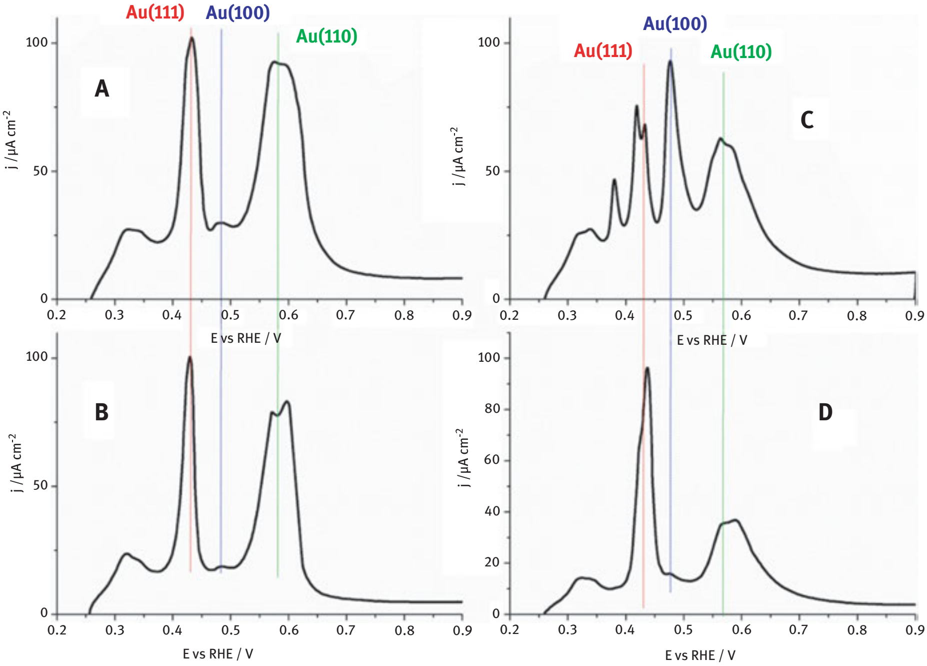

Figure 3.12: Pb UPD voltammetric profiles of the unsupported gold nanoparticles in Ar-saturated 0.1 M NaOH containing 10^{-3} M $Pb(NO_3)_2$: (A) spherical 5 nm, (B) spherical 30–40 nm, (C) cubic, and (D) octahedral nanoparticles. Scan rate: 50 mV s^{-1}.

have been reported. Feliu and co-workers proposed a methodology based on the redox behaviour of some adatoms, (Bi, Te, and Ge) spontaneously adsorbed at the surface of different Pt single crystals [99]. They found that Bi [115, 116] and Te [117] were sensitive to the presence of {111} terrace domains, while Ge [118] was sensitive to the {100} ordered domains. Interestingly, by using basal planes and stepped surfaces, they observed a linear correlation between the specific response of the adatom and the terrace density of the different Pt electrodes (Figure 3.13). In this way, for any Pt surface, after performing the Bi and Ge experiments, and using these calibration plots, the quantification of the {111} and {100} oriented domains present at the surface is possible.

This methodology has been satisfactorily applied to quantify the {111} and {100} oriented domains at the surface of different shape-controlled Pt nanoparticles [99, 116] and it is now worldwide adapted [119–124]. Using a similar concept, other surface structure-sensitive reactions have been proposed including the desorption–adsorption of hydroquinone-derived adlayers (Figure 3.14) [125] and the reduction of acetaldehyde [126] for {111} domains, and the ammonia electrooxidation [127] for {100} domains.

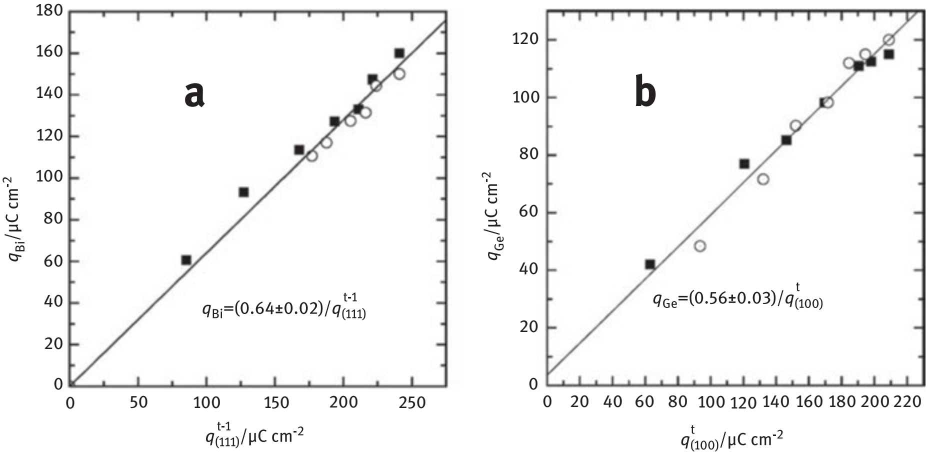

Figure 3.13: (a) Charge density values of the bismuth redox peak vs. the charge associated with the (111) sites on the terrace. (■) Pt(*n*, *n*, *n*−2) electrodes; (○) Pt(*n* + 1, *n*−1, *n*−1) electrodes. (b) Charge density values of the germanium redox peak vs. the charge associated with the (100) sites on the terrace: (■) Pt(2*n*−1, 1, 1) electrodes; (○) Pt(*n*, 1, 0) electrodes. Reproduced from Ref. [99] with permission from The Royal Society of Chemistry.

For Au surfaces, El-Deab et al. [128–131] showed that the reductive desorption of different thiol compounds such as cysteine, mercaptoacetic acid, or cystamine can be used to obtain the fraction of the surface sites in various gold nanostructures. In this regard, it is worth noting that although the Pb UPD has been widely used for different shaped Au nanoparticles, to the best of our knowledge, a quantitative analysis of this Pb UPD voltammetric profile is still missing.

Similarly, but for Pd surfaces, Cu UPD can be used to quantify the {100}, {110}, and {111} surface domains. To illustrate this analysis, Figure 3.15 shows the Cu UPD obtained with Pd nanocubes also including the corresponding fitting using five Lorentzians located at the characteristic contributions of the {100}, {110}, and {111} surface domains (based on similar experiments on Pd single crystals [132, 133]). The percentage of sites of a given surface is calculated by normalizing the area under its corresponding signal also taking into consideration the calculated charges for a complete Cu monolayer on Pd(111), Pd(100), and Pd(110) single crystals (486, 421, and 297 $\mu C\ cm^{-2}$, respectively). In this particular case, the percentage of {100} surface sites on the Pd nanocubes was found to be 57 ± 3 % [113].

Obviously, it is worth noting that all these previous methodologies are particularly interesting for pure metal nanoparticles (Pt, Pd, and Au). However, it is also evident that the increasing use of more complex systems including alloys, core-shell, nanoframes, high-index-faceted (convex or concave) and excavated metal nanoparticles, among others, makes this electrochemical surface structure characterization including a correct determination of the electroactive surface area [48–50, 134] much more difficult. These are remaining challenges to be overcome in the forthcoming years.

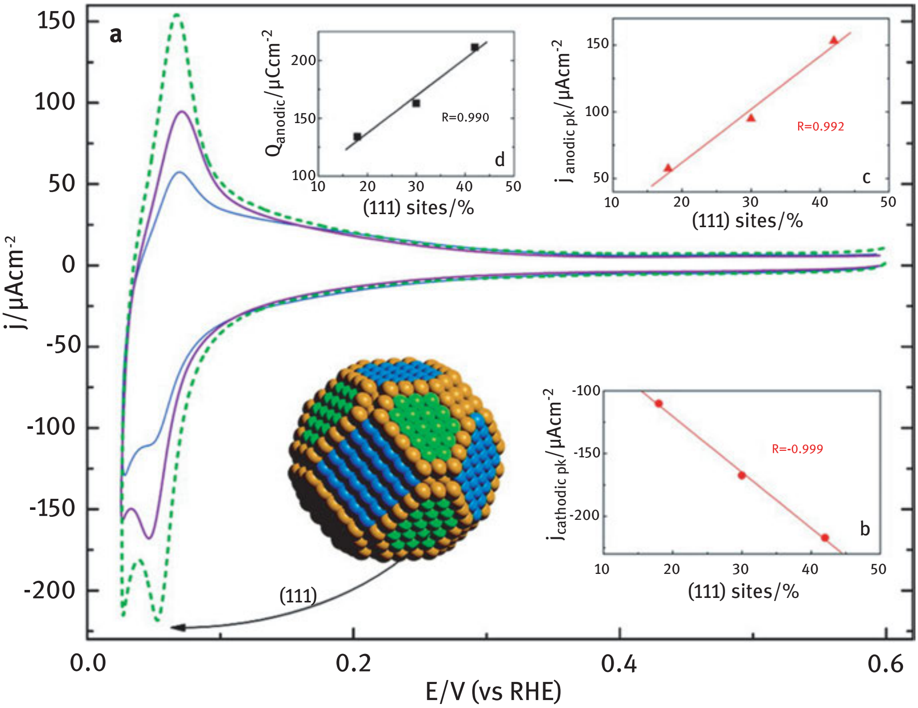

Figure 3.14: (a) Cyclic voltammograms of different shaped Pt nanoparticle in 2 mM H_2Q + 0.5 M H_2SO_4 solution: (i) thick dashed line (green) for nano-Pt(111)-(110), (ii) medium-thickness solid line (purple) for nano-Pt(111)-(100), and (iii) thin solid line (blue) for nano-Pt(100). Scan rate 50 mV s^{-1}. Insets show (b) the cathodic peak current densities, (c) the anodic peak current densities, and (d) the total anodic charge densities as a function of the density of {111} surface sites, expressed as a percent of the electrochemically available surface in each sample. Reprinted with permission from Ref [125]. Copyright (2010) American Chemical Society.

3.3.2 Electrocatalysis on shape-controlled metal nanoparticles: representative cases for relevant electrochemical reactions

In this next section, we will review some of the most relevant advances on the use of shape-controlled metal nanoparticles in electrocatalysis. This section will cover reactions of interest for low-temperature fuel cells such as formic acid, methanol and ethanol electrooxidations and oxygen reduction, and also other relevant electrochemical reactions such as CO_2 electroreduction. However, it is worth mentioning that this section will only include contributions that fulfil with the requirement of surface cleanness and that contribute to a better understanding of the correlations between surface structure/shape and electrochemical reactivity.

To the best of our knowledge, the first examples of shape-controlled metal nanoparticles in electrocatalysis were reported by our group in 2004 [71, 72]. In these

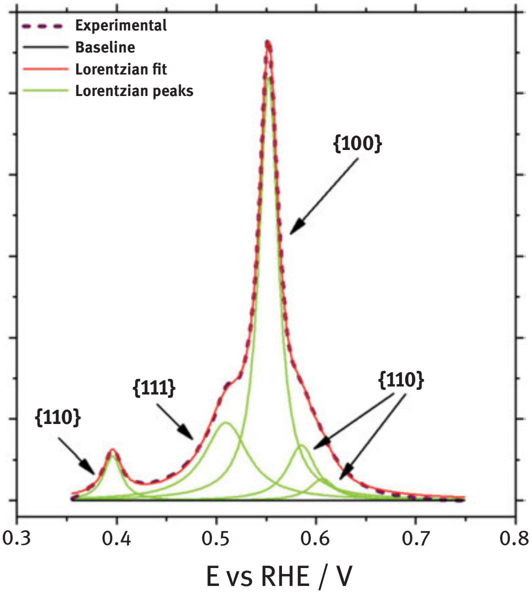

Figure 3.15: Cu UPD fitting on the Pd nanocubes. Test solution 0.1 M H_2SO_4 + 1 mM $CuSO_4$ + 1 mM NaCl, scan rate 50 mV s^{-1}. Reproduced from [113] with permission of the International Union of Crystallography.

contributions, we synthetized cubic Pt nanoparticles using a similar methodology to that described in 1996 by El-Sayed and co-workers [14] and based in a chemical reduction of K_2PtCl_4 by H_2 in the presence of NaPA. As expected from Figure 3.1, the cubic Pt nanoparticles displayed a preferential {100} surface structure as deduced from the voltammetric profile of the nanoparticles obtained in 0.5 M H_2SO_4. The cubic Pt nanoparticles were tested towards ammonia electrooxidation in alkaline solution and showed an enhanced activity due to extreme sensitivity of this reaction to the presence of {100} sites as illustrated from Pt single-crystal studies [135, 136]. These results clearly evidenced that by tuning the surface structure of the nanoparticles by means of controlling their particle shape, improved electrocatalytic activity were achieved. From these first examples, many other contributions have been and are being currently published reporting a clear correlation between particle shape and or surface structure and enhanced electrocatalytic activities. In fact, there already exist several and excellent reviews related to the application of shaped metal nanoparticles for different electrocatalytic reactions [6, 7, 20, 137–150].

3.4 Formic acid electrooxidation

Formic acid electrooxidation is a very valuable reaction, not only because it is a model reaction for a two-electron-transfer reaction, but also for its possible use as fuel in the so-called direct formic acid fuel cells (DFAFCs) [5, 151–153]. On metal surfaces, this process is accepted to proceed through a dual path mechanism [154–156]: a direct pathway via an adsorbed active intermediate (the nature and role of this active intermediate are still under strong discussion at fundamental level) that readily yield to CO_2, and a second pathway involving the formation of adsorbed CO, which is considered to be a poisoning intermediate, that is subsequently oxidized to CO_2 at high overpotentials. On Pt surfaces, both reaction paths are structure sensitive, and the Pt(100) surface is the most active but also the most sensitive to the CO poisoning [152]. This surface structure sensitivity was first observed with shape-controlled Pt nanoparticles by Tian and co-workers [29] who reported that tetrahexahedral (THH) Pt nanocrystals displayed, in comparison with polycrystalline Pt nanospheres and commercial Pt/C catalyst (E-TEK Co., Ltd), a clear enhanced activity (about 4 and 3 times higher than for the nanospheres and the commercial catalyst, respectively).

The effect of the presence of {100} Pt domains at the surface of the nanoparticles was subsequently explored by our group by using cubic Pt nanoparticles [78, 157]. In brief, spherical, cubic, cubo-octahedral, and tetrahedral-octahedral Pt nanoparticles were prepared in the presence of NaPA and employed towards formic acid electrooxidation. As expected, we observed clear similarities between the response of the nanoparticles and those obtained with the model Pt surfaces. In particular, the cubic Pt nanoparticles, that is, those nanoparticles having a preferential (100) orientation showed the highest activity as well as the fastest CO poisoning in good agreement with previous single-crystal experiments [152].

Since these initial works, some other contributions have reported enhanced activities towards formic acid electrooxidation by using shaped Pt nanoparticles including concave Pt nanocrystals having {411} high-index facets [158], trapezohedral (TPH) Pt nanocrystals enclosed by {522} high-index facets [159], highly concave Pt nanoframes [160], truncated octahedral, cuboctahedral, and cubic shape-controlled (< 10 nm) Pt nanoparticles [34], and concave Pt nanocubes [161], among others.

Shape-controlled Pd nanoparticles have been also extensively used for formic acid electrooxidation due to their unique properties. On Pd surfaces, the dehydration step is strongly hindered (CO is not spontaneously formed) and, therefore, the reaction directly proceeds through the direct path. In addition, the onset oxidation potential is about 200 mV lower than that observed for Pt [153, 162]. Also, the reaction is structure sensitive and the Pd(100) was found to be the most active surface among the basal planes, both in sulphuric and in perchloric acid solutions [163, 164]. In this regard, Jin et al. [112] and Zhang et al. [165] reported the first examples of shaped Pd nanoparticles towards formic acid electrooxidation. Jin et al. evaluated a collection of shaped Pd nanoparticles including cubes, truncated cubes, cuboctahedra, truncated octahedra, and octahedral [112]. As expected from single crystals, the activity was found to be dependent on the fraction of {100} domains, and the cubic nanoparticles displayed the highest activity, Figure 3.16. Similarly, Zhang et al. employed rhombic

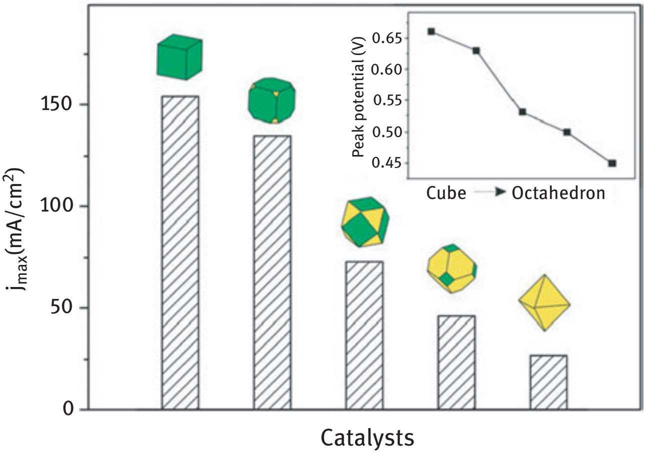

Figure 3.16: Maximum current densities for formic acid electrooxidation (normalized to the electrochemical surface area) for different shaped Pd nanoparticles in 0.1 M $HClO_4$ + 2 M HCOOH at 10 mV s^{-1}. The inset shows their corresponding peak potentials. Reproduced from Ref. [112]with permission from The Royal Society of Chemistry.

dodecahedra and cubic Pd nanoparticles and again the cubic ones displayed the highest electrocatalytic activity towards formic acid electrooxidation [165].

Different contributions were subsequently reported using very different shaped Pd samples including, among others, cubic and spherical Pd nanoparticles [75]; different concave Pd nanocrystals (nanocubes, fivefold twinned nanorods and right bipyramids) [166]; twinned icosahedra, cubic and octahedral Pd nanoparticles [167]; cubic, octahedra, icosahedra, and right bipyramids [168–170]; monodispersed (50 nm) palladium nanocrystals, including cubes, octahedral, and rhombic dodecahedra [171]; length tuneable penta-twinned Pd nanorods [172]; tetrahedral Pd nanocrystals [173]; cubes [174]; penta-twinned Pd nanowires [175]; and branched Pd nanoparticles [176].

The incorporation of a second element both on Pt and on Pd surfaces is a classical approach to enhance their electrocatalytic properties towards formic acid electrooxidation [153, 177, 178]. The resulting enhancements can be justified by third-body, electronic, and/or bifunctional effects. Third-body effects take place when the second element acts as a mere spectator, blocking certain surface sites, thus effectively inhibiting some undesired reactions. On the other hand, electronic effects happen when the second element changes the electronic properties of the bare surface. In this aspect, the so-called d-band centre model [179] is widely accepted and explains the possible modifications of the electronic properties and binding energies of a transition metal surface, after the incorporation of a second metal, and their correlations with the resulting catalytic activity. Finally, bifunctional effects take place if the second metal facilitates the reaction mechanism by providing some functional groups at low potentials. Obviously, this strategy has been also employed with shape-controlled metal nanoparticles by exploring two different approaches: (a) shape-controlled Pt or Pd alloy-based nanoparticles and (b) decoration of the surface of the shaped Pt and Pd nanoparticles with different adatoms.

Several and outstanding contributions have been reported on the use of shape-controlled Pt and Pd alloy nanoparticles towards formic acid electrooxidation [21, 139, 143, 144, 180]. These contributions include PdPt alloy nanocubes with tunable compositions [181], Pt_3Fe nanocubes [182], PtCu nanocubes of different atomic composition (Pt_xCu_{100-x} (x = 54–80 atomic %)) [183, 184], Pt-Cu nanooctahedra [185, 186], PtMn nanocubes [187], different polyhedral AuPd core-shell structures (60–80 nm) having high-index facets (concave trisoctahedral (TOH) and hexoctahedral (HOH) crystals both with {hkl} facets and THH crystals with {hk0} facets)) [188], HOH AuPd alloy nanoparticles [189], THH PdPt alloy nanocrystals [190], excavated rhombic dodecahedral (ERD) $PtCu_3$ alloy nanoparticles[191], cubic Pd–Ni–Pt core-sandwich-shell nanoparticles [192], and PdCu bimetallic tripods [193], among many others. Obviously, the optimal atomic composition and particle shape depends on each specific system.

On the other hand, the use of certain adatoms to selectively decorate the surface of different shape-controlled metal nanoparticles towards formic acid electrooxidation has been also explored in different contributions. Feliu and co-workers employed different adatoms including Bi [194, 195], Pd [196, 197], Sb [198], and more recently Tl [199] and Pb [200] as surface modifiers on different shaped Pt nanoparticles. Sun and co-workers also used Bi [194] and Au [201] with THH Pt nanocrystals. Improved electrocatalytic activities were obtained in all these cases, although the enhancement factor is determined by the surface structure of the substrate and the nature and coverage of each adatom.

Using a similar concept, Yang and Lee reported a very interesting approach by which the surface of gold octahedral nanocrystals was decorated with the epitaxially deposited Pt atoms [54]. In this case, the shaped gold nanoparticles acted as substrate to control the Pt deposition which varied from fully covered multiple overlayers (about 5 monolayers) to atomically dispersed sub-monolayer (0.05 monolayer). The electrocatalytic activity of the Pt modified gold nanoparticles was found to be strongly dependent of the Pt coverage and, for a Pt coverage of about 0.05 monolayer, a huge enhancement was observed.

3.5 Methanol electrooxidation

Methanol electrooxidation is also of great interest for fuel cell applications [5, 202]. On metal surfaces, this reaction is also known to be sensitive to the surface structure [203–205] and therefore, many different shaped controlled metal nanoparticles have been evaluated. For Pt nanoparticles, we clearly showed the effect of the shape/surface structure of the nanoparticles by using cubic, octahedral/tetrahedral, and truncated octahedral Pt nanoparticles (about 8–10 nm) prepared with NaPA [78]. The results obtained indicated that the octahedral Pt nanoparticles displayed the highest activity towards methanol electrooxidation in 0.5 M H_2SO_4 solution.

Chen et al. studied very small (about 3.5 nm) cubic Pt nanoparticles prepared in the absence of surfactant [206]. The activity of the cubic nanoparticles towards methanol oxidation in KOH solution was found to be significantly higher than that obtained with a commercial Pt/C catalyst.

Interesting contributions have been reported for Pd nanoparticles due to their intrinsic CO tolerance. Arjona et al. prepared 10 nm cubic Pd nanoparticles and reported an enhanced activity towards methanol oxidation in alkaline solution in comparison with a commercial Pd catalyst [207]. Cubic Pd nanoparticles were also evaluated toward methanol electrooxidation by Kannan et al. who reported a clear enhancement (about 11 times) in comparison with a commercial Pd/C catalyst in $HClO_4$ solution [208]. Qin et al. employed star-like and concave Pd nanoparticles which also showed an enhanced activity (more than three times) in comparison with commercial Pd/C in alkaline medium [209].

As previously discussed for formic acid electrooxidation, the use of shaped controlled Pt and Pd alloy nanoparticles and the adatom surface decoration of different shaped metal nanoparticles are widely accepted strategies for obtaining better electrocatalysts for methanol electrooxidation. Two contributions will be briefly discussed to exemplify these two different approaches, both dealing with the Pt-Ru system which has been widely considered for this reaction and where the incorporation of Ru promotes the formation of oxygen species at low potential, thus facilitating the reaction through a bifunctional mechanism [210, 211] On the one hand, Sun and co-workers reported that Ru-decorated THH Pt nanoparticles displayed a high tolerance to CO poisoning and an onset oxidation potential shift of about 100 mV towards more negative potentials [212]. In comparison with Ru-decorated Pt/C and with commercial PtRu alloy nanoparticle catalyst, these Ru-decorated THH Pt NPs showed a higher activity in the low potential range.

On the other hand, very recently, Huang et al. reported the preparation of shaped controlled PtRu alloy nanoparticles and their use for methanol electrooxidation in $HClO_4$ solution [213]. In more detail, PtRu nanowires, nanocubes, and nanorods were synthetized through a one-step solvothermal method. The results indicated that the {111}-terminated PtRu nanowires displayed higher activity and stability than those obtained with the {100}-terminate PtRu nanocubes.

Obviously, many other systems have been evaluated for methanol electrooxidation including PtPd nanocubes [214]; PtPd nanotetrahedra [215]; octahedral PtPd alloy nanoparticles [216]; multiply twinned PtPd nanoicosahedra [217]; concave PtPd nanocubes [218]; cubic, rod-like, quasi spherical, concave cubic, and TOH Au nanoparticles [219]; plate-like and truncated octahedral Cu nanocrystals [220]; concave PtCu [221] and PtPdCu [222] nanocubes; Pt3Co nanoflowers and nanocubes [223]; PtZn nanocubes [224]; platinum–copper nanowires [225]; deeply excavated Pt3Co nanocubes [226]; excavated octahedral Pt-Co alloy nanocrystals [227];

platinum–copper rhombic dodecahedral (RD) nanoframes [228]; platinum–silver alloyed octahedral nanocrystals [229]; screw-like PdPt nanowires [230]; and Cu-rich PtCu octahedral alloy nanocrystals [231], among others.

3.6 Ethanol electrooxidation

Ethanol electrooxidation has been also the subject of innumerable studies. Due to difficulties in C–C bond cleavage, the ethanol oxidation, however, is often incomplete, resulting in a number of by-products other than CO_2 such as acetaldehyde and acetic acid. As previously stated for methanol, on metal surfaces, this reaction is also surface structure sensitive [232–234] and, consequently, susceptible of being studied on shaped controlled metal nanoparticles. Tian and co-workers [29] reported that THH Pt nanocrystals displayed an enhanced activity towards ethanol electrooxidation in comparison with polycrystalline Pt nanospheres and commercial Pt/C catalyst (E-TEK Co.). Wei et al. also reported that concave THH Pt nanocrystals (bounded by {910} faces) prepared in deep eutectic solvents were more active (about 2 times) than a Pt black catalyst in $HClO_4$ solution [235]. Also, Huang et al. showed that concave polyhedral Pt nanoparticles having {411} high-index faces exhibited an enhanced electrocatalytic activity over commercial Pt catalysts towards ethanol oxidation reaction in $HClO_4$ [158]. Similarly, Zhang et al. also reported a higher ethanol oxidation activity (in $HClO_4$) with multipod and concave Pt nanocrystals, mainly exposing {211} and {411} high-index facets, respectively, than that observed with Pt/C and Pt nanocubes [236]. Interestingly, Zhou et al. showed that THH Pt nanoparticles, prepared from an electrochemical perturbation of Pt nanocubes (10 nm) in H_2SO_4, displayed a remarkable increase in activity towards ethanol oxidation, in comparison with the original Pt nanocubes and commercial Pt nanoparticles [237]. All these previous contributions clearly point out the benefits of having nanoparticles containing high-index surfaces for ethanol electrooxidation. However, “low-index” metal nanoparticles have been also evaluated and, for instance, Busó-Rogero et al. systematically evaluated the ethanol oxidation on different shaped Pt nanoparticles including spherical, cubic, and octahedral Pt nanoparticles both in acidic and in alkaline solution [238–240]. The results obtained clearly agreed with those previously found with Pt single-crystal electrodes [232–234].

Apart from Pt, shaped controlled Pd and Rh nanoparticles have also been employed for ethanol electrooxidation including cubic Pd nanoparticles [207], concave Pd nanocubes [241], and THH Rh nanocrystals [242]. Obviously, several shaped metal alloy nanoparticles have been considered for this reaction. Among others, Chen et al. used different shaped PtPd alloys supported in graphene for ethanol electrooxidation [243]. Higher electrocatalytic activities and better tolerance to poisoning were observed for all shapes in comparison with Pt nanoflowers, Pd nanoparticles, and unshaped PtPd nanoparticles supported on carbon black. Rao et al. employed different PtRh alloy nanocubes supported on graphene [244]. In this case, a Pt:Rh atomic ratio = 9:1 was found to be the most convenient for ethanol oxidation. High-index PtRh nanocrystals including {830}-bounded THH and {311}-bounded trapezohedron (TPH) have been also tested [30]. Hong et al. evaluated AuPd octapodal nanoparticles in comparison with flower-like AuPd alloy nanoparticles and a commercial Pd/C catalyst [245]. Also, Zhang et al. reported the preparation of monodisperse Au–Pd alloy nanoparticles with systematic shape evolution from RD to TOH, and HOH structures by varying the concentration of surfactant in the surfactant-mediated synthesis [246]. The catalytic activities toward ethanol electrooxidation were in the order of HOH > RD > TOH, following the same order of their corresponding surface energies. More recently, Rizo et al. studied the ethanol electrooxidation on PtSn nanocubes [247]. They observed that the electrochemical activity of the cubic Pt–Sn nanoparticles was found to be about three times higher than that obtained with unshaped Pt–Sn nanoparticles and six times higher than that of Pt nanocubes. Very interestingly, Erini et al. have recently explored the use of octahedral PtNiRh nanoparticles, having a fixed Pt:Ni ratio and different Rh contents (between 1 and 6 atomic %), towards ethanol electrooxidation [248]. These multimetallic samples displayed a good electrochemical activity and stability towards ethanol oxidation in alkaline solution.

On the other hand, ethanol electrooxidation is also suitable of being optimized by using adatom-decorated shaped metal nanoparticles. For instance, Wang et al. studied Bi-decorated THH Pd nanoparticles towards ethanol oxidation in alkaline medium [249]. The activity of the Bi-decorated samples was found to be about 3 and 12 times higher than that of bare THH Pd nanoparticles and a Pd/C catalyst, respectively, at the optimum Bi coverage. Similarly, Busó-Rogero et al. employed different adatoms (Sn, Rh, Ru, and Pb) to systematically decorate the surface of different shaped Pt nanoparticles and studied their electrocatalytic properties for ethanol electrooxidation both in acidic and in alkaline solutions [250]. However, in all cases, the enhancement was very limited.

3.7 Oxygen reduction reaction

Oxygen reduction reaction (ORR) is, without any doubt, one of the most studied reactions in electrocatalysis [139, 143, 251–255]. Among pure metals, Pt presents the highest electrocatalytic activity for the $4e^-$ pathway to water [256–259]. ORR is also known to be sensitive not only to the surface structure of the electrode but also to the used electrolyte [260]. This surface structure sensitivity has been also demonstrated on different shaped metal nanoparticles. Thus, for instance, Inaba et al. used cubic Pt nanoparticles prepared in the presence of NaPA which displayed a high activity for ORR in H_2SO_4 solution [261]. Similarly, Sánchez-Sánchez et al. also evaluated the ORR activity of different shape-controlled Pt nanoparticles by using the scanning electrochemical microscope (SECM) [262]. The results pointed out the good agreement between the ORR activity of the shaped Pt nanoparticles and the results obtained with Pt single-crystal electrodes. In this regard, Tripkovic et al. [263] reported a density functional theory (DFT) study dealing with the effect of the shape of Pt nanoparticles on the ORR activity in a non-adsorbing electrolyte. The results showed that the tetrahedral Pt nanoparticles provided the highest activities and the cubic Pt nanoparticles the least actives. These findings are in good agreement with previous experimental observations on shape-controlled Pt nanoparticles [262] in a non-adsorbing electrolyte such as $HClO_4$. In addition, taking into account that stepped Pt single-crystal surfaces usually displayed higher ORR catalytic activity than that observed for the basal surfaces [256–259], several high-index Pt nanoparticles have been explored towards ORR. Readers interested in this topic are referred to some relevant reviews [141, 147–149].

Shaped Pd nanoparticles have been also extensively tested for ORR. Xiao et al. used Pd nanorods and observed a specific activity about 10 times higher than that of Pd spherical nanoparticles [264]. Shao et al. [265], Erikson et al. [73, 74], and Lee et al. [266] also reported enhanced ORR activities by using Pd nanocubes containing a preferential {100} surface structure. Relevant reviews about the electrocatalysis of Pd-based nanomaterials for ORR are already available in the literature [267, 268].

Among the vast literature existing dealing with the use of shaped metal alloy nanoparticles towards ORR [32, 33, 37, 139, 143, 146, 150, 180, 253, 255, 262, 269–272], the system Pt-Ni is particularly relevant. Stamenkovic et al. published that the ORR-specific activity at 0.9 V of a single-crystal $Pt_3Ni(111)$ surface was about 90 times higher than that of a commercial Pt/C in 0.1 M $HClO_4$ solution [273]. This finding clearly marked the efforts towards the preparation of octahedral Pt_3Ni nanoparticles and their use for ORR [274]. To the best of our knowledge, the first example of shape-controlled Pt_3Ni nanoparticles was reported by Zhang et al. [275] who prepared Pt_3Ni octahedra and nanocubes and observed that the ORR-specific activity of the Pt_3Ni octahedra was about five times higher than that obtained with Pt_3Ni nanocubes, Figure 3.17. In addition, the specific and mass activities of Pt_3Ni-octahedra/C were about seven and four times higher than that of a commercial Pt/C electrocatalysts.

Since this first contribution, many other approaches have been reported and for the readers' interests in this particular topic, we refer to some recent reviews by Strasser et al. in which the most relevant advances are visually summarized (Figure 3.18) in terms of ORR Pt mass activities [150, 276, 277].

3.8 CO_2 electroreduction

The electrochemical reduction of CO_2 is being the subject of numerous efforts basically with two main objectives: (i) decreasing the CO_2 concentration at the atmosphere (this high concentration strongly contributes to the greenhouse effect and climate change) and (ii) transforming this CO_2 into valuable chemicals and/or fuels. However, this reaction presents a very complicated chemical reaction mechanism, and multiple electron-transfer processes with manifold coupled consecutives intermediates can take place [278–282]. In addition, and due to its particular structure,

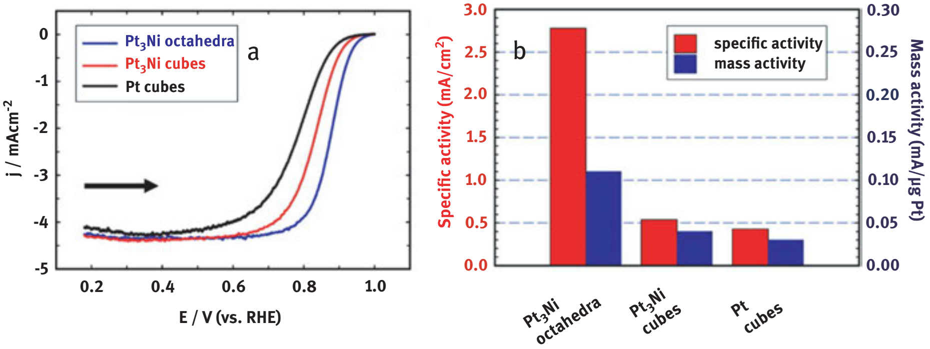

Figure 3.17: (a) ORR behaviour of Pt_3Ni nanoctahedra, Pt_3Ni nanocubes, and Pt nanocubes supported on a rotating GC disk electrode in O_2 saturated 0.1 M $HClO_4$ solution at 20 mV s^{-1} and at 295 K; rotation rate, 900 rpm. (b) Comparison of the ORR activities at 0.9 V vs. RHE at 295 K. Reprinted with permission from Ref [275]. Copyright (2010) American Chemical Society.

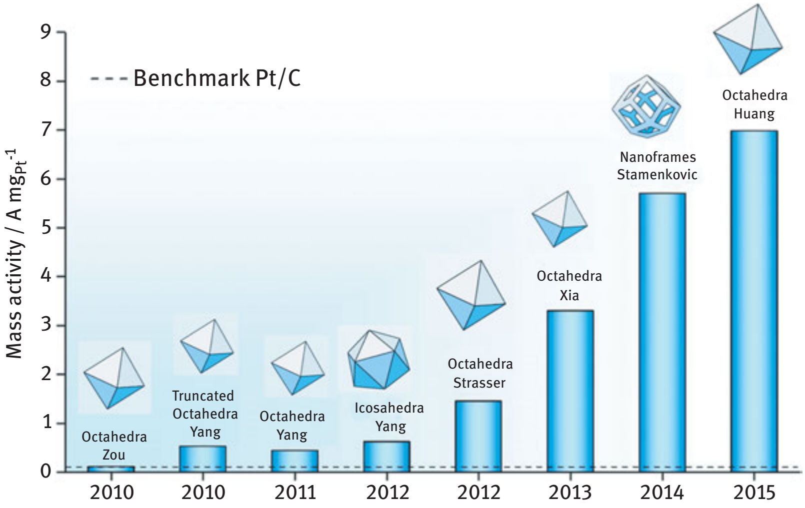

Figure 3.18: Schematic representation of the performance of the most relevant shaped PtNi nanoparticles (given in A mg^{-1}(Pt) at + 0.9 V vsRHE (iR-corrected electrode potential)) towards ORR. Reproduced from Ref. [150] with permission from The Royal Society of Chemistry.

CO_2 is quite thermodynamically and kinetically stable, requiring usually high overpotentials in order to produce C1, C2, and even C3 compounds. Also, the hydrogen evolution reaction (HER) is its serious competitive reaction in aqueous solution which give rises to low faradaic efficiencies. Nevertheless, on the other hand, it is also well-established that the product selectivity during the CO_2 electroreduction is strongly determined by the nature of the metal and also by the surface structure [283–288].

Therefore, and due to this surface structure sensitivity, different shape-controlled metal nanoparticles have been evaluated. Among others, Cu is particularly the most interesting metal due its unique properties to convert CO_2 into different hydrocarbons, mainly methane (CH_4) and ethylene (C_2H_4) [150, 289–292]. For instance, Chen et al. [293] showed that on Cu mesocrystals having {100} oriented facets, the faradaic efficiency towards ethylene formation was about 18 times larger than that of methane. Similarly, Nilsson and co-workers used Cu nanocubes to selectively produce ethylene over methane due to their preferential {100} surface structure [294, 295]. Also, Kwon et al. [296] reported a selective production of ethylene on Cu nanocubes prepared using a halide based electrochemical treatment. On these nanocubes, the faradaic efficiency towards ethylene was found to be 1.5 higher than that for polycrystalline copper (at −1.0 V vs. RHE). Interestingly, the faradaic efficiency for ethanol was also remarkably high (about 8 %). Gao et al. tested the behaviour of Cu nanocubes with tunable {100} facet and oxygen/chlorine ion content by using a low-pressure plasma pre-treatment towards CO_2 electroreduction [297]. The results obtained displayed high selectivity for ethylene, ethanol, and *n*-propanol and a maximum faradaic efficiency of about 73 % for C_2 and C_3 compounds. Additionally, Cu nanocubes with different edge length (24, 44, and 63 nm) were also evaluated by Loiudice et al. [298]. Among the samples, the 44 nm cubic samples displayed the highest faradaic efficiency for ethylene (about 41 %). More recently, Jeon et al. reported that prism-shaped Cu catalysts displayed a high C_2H_4 production (about four times higher) in comparison with that observed with a planar Cu electrode (figure 19) [299].

Other shapes such as Cu nanowires [300–302], hierarchical Cu pillar [303], and Cu nanofoam [304] have been also explored.

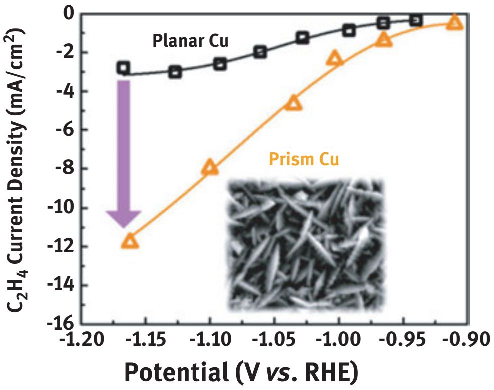

Figure 3.19: Partial current densities vs. applied potential for C_2H_4 of a planar Cu foil and a Prism Cu electrode. Reprinted with permission from Ref [299]. Copyright (2018) American Chemical Society.

Different shaped silver (Ag) nanoparticles were also evaluated for CO_2 electroreduction. For instance, Liu et al. showed that triangular Ag nanoplates having {100} domains exhibited improved electrochemical properties towards CO in comparison with similarly sized Ag nanoparticles (SS-Ag-NPs) and bulk Ag [305].

Lately, Peng et al. employed a simple anodization treatment to prepare preferentially oriented metallic Ag nanoparticles with high activity and high selectivity for the reduction of CO_2 to CO [306]. The {110} and {100} preferentially oriented Ag nanocrystals displayed faradaic efficiency of about 97 % (at −0.69 V vs. RHE), which was significantly higher than that obtained with polycrystalline Ag (60 % at −0.87 V vs. RHE). Other systems such as Ag nanocorals [307] and Ag nanoporous electrodes [308] have also exhibited high selectivity towards CO.

Shape-controlled Pd nanoparticles are particularly interesting to produce formate. Klinkova et al. [309] employed different shaped Pd nanoparticles for the electroreduction of CO_2 to formate. The results obtained suggested that the presence of high-index surfaces enhances the electrocatalytic performance (figure 3.20). Thus, the high-index samples displayed a faradaic efficiency of about 97 % towards formate at a low overpotential (−0.2 V vs. RHE).

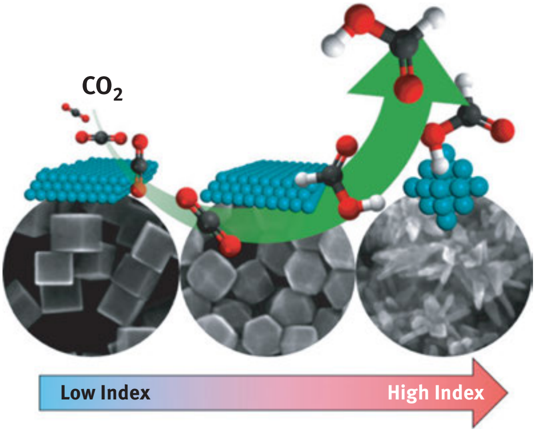

Figure 3.20: Schematic representation displaying the beneficial effect of the abundance of high-index Pd surfaces to maximize the electrocatalytic reduction of CO_2 towards formate. Reprinted with permission from Ref [309]. Copyright (2016) American Chemical Society.

Interestingly, Gao et al. have recently published a perspective summarizing the behaviour of different Pd- and Pd-based nanostructures towards CO_2 electroreduction mainly towards formate [310]. Moreover, the electrochemical reduction of CO_2 towards CO is also possible on Pd surfaces. In this regard, Huang et al. reported the CO production on octahedral and icosahedral Pd nanoparticles. The results obtained showed that the faradaic efficiency for CO production on Pd icosahedra (about 91 % at 0.8 V vs. RHE) was found to be almost two times higher than that observed on Pd octahedra [311].

Some zinc (Zn)-shaped nanostructures have been also studied. In particular, nanodendrites [312] and hexagonal [313] Zn electrodes have demonstrated remarkable activities for the selective production of CO.

Besides, different Bi nanostructures have been also considered for the selective production of formate. Thus, Bi nanodendrites [314, 315] and Bi nanoflakes [316] have displayed very high faradic efficiencies towards formate (96.4 % and about 100 % respectively). On the other hand, in acetonitrile solution, shaped Bi nanoparticles have displayed very high faradaic efficiency (about 96.1 %) towards CO production [317].

Furthermore, some shaped Au nanoparticles have been also explored including nanowires [318, 319], concave RD [320], pore-like or pillar-like structures [321], and nanocubes [322], among others. In all these cases, a selective conversion of CO_2 to CO is observed.

To complete this section, it is worth noting some relevant contributions dealing with the use of metal alloy, core-shell, and adatom-decorated shaped electrocatalysts for CO_2 electroreduction. Very briefly, Zhao et al. employed Cu–Pt alloy nanocube [323] with different Pt:Cu atomic compositions. The reduction potential becomes more positive with increasing Cu content, and $Cu_{85}Pt_{15}$ nanocubes were found to be the most convenient system for CO_2 reduction.

On the other hand, Monzó et al. [322] tested Au–Cu core-shell nanoparticles in which Au nanocubes were systematically covered with increasing Cu layers. As illustrated in Figure 3.21, the product selectivity for the CO_2 reduction was clearly dependent on the thickness of the Cu shells.

Finally, Sun and co-workers evaluated the electrochemical reduction CO_2 on Cu decorated THH and {111}-faceted Pd nanoparticles [324]. In this case, both the Cu

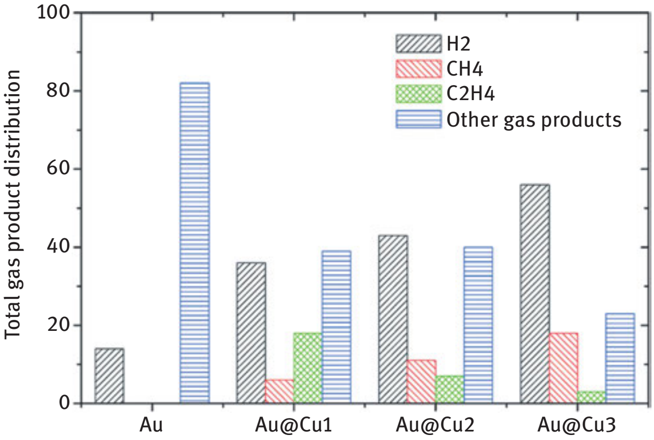

Figure 3.21: Total gas product distribution of H_2, CH_4, and C_2H_4 on Au nanocubes covered with increasing Cu layers during CO_2 electroreduction in PBS (pH = 8) at −0.6 V vs. RHE. Reproduced from Ref. [322] with permission from The Royal Society of Chemistry.

coverage and the surface structure of the substrate strongly determined the resulting selectivity towards methanol and ethanol.

For those readers particularly interested in this reaction, we refer to some of the recent and excellent reviews widely covering this topic [150, 277, 325–327].

3.9 Critical safety considerations

Due to the increasing number of applications using different types of nanomaterials, and in particular metal nanoparticles, a great emphasis is nowadays focused on risk assessment of these nanoscale metal materials. To the best of our knowledge, there is no specific international protocols dealing with the possible risks of nanoparticles and safety aspects to face during the various stages of preparation, manipulation, and use. However, relevant contributions have been already reported on the literature about the potential toxicological effects associated with the employment of nanomaterials in human environments [328–330] and in agriculture and food [331].

Additionally, some safety considerations for the employ of nanomaterials have been also reported [332–336].

Very recently, Jeevanandam et al. have discussed about the types of toxic reactions associated with different types of nanomaterials and the regulations implemented by different countries to reduce the associated risks [337].

It is worth noting that the toxicity degree of these metal nanoparticles is affected by a number of factors including size, shape, agglomeration state, surface functionalization, atomic composition, and dose, among others [338–342 343–345]. Consequently, their interaction with biological environment and living systems will be determined by their physicochemical properties.

In conclusion, and despite some considerations and recommendations being reported, there is no common international legislation dealing with their manipulation and hazard assessment. More work is still required to properly understand the toxic effects and safety aspects for short- and/or long-term exposition.

3.10 Conclusions and future perspective

Understanding the correlations between the shape and the surface structure of metal nanoparticles and their resulting electrocatalytic properties necessarily requires the use of *clean* nanoparticles. In this contribution, we have reviewed and discussed the most significant protocols and procedures for producing clean shaped metal nanoparticles. In addition, a section focused on the employ of *easy-to-do* electrochemical experiments to evaluate the cleanness of the nanoparticles have been also included. Interestingly, the use of electrochemical surface structure-sensitive reaction allows obtaining a detailed characterization of the surface structure of the shaped nanoparticles both from qualitative and quantitative points of view. Finally, a collection of relevant studies on the use of different shaped metal nanoparticles for relevant electrochemical reaction including electrooxidation of formic acid, methanol and ethanol, and electroreduction of oxygen and CO_2 have been also reported.

Despite the significant improvements due to the use of shaped metal nanoparticle in the field of the Electrocatalysis, there are still a number of issues waiting to be explored including, (i) systematic long-term stability measurements, particularly *in-operando* conditions, (ii) selectivity issues still need more systematic studies, and (iii) the incorporation of these shaped metal electrocatalysts on practical electrochemical devices such as fuel cells, electrolysers, or filter press-type reactors is still scarce.

Funding: The authors acknowledge financial support from the Spanish Ministry of Economy and Competitiveness (MINECO) (project CTQ2016-76231-C2-2-R (AEI/FEDER, UE)). J.S-G. also acknowledges financial support from VITC (Vicerrectorado de Investigación y Transferencia de Conocimiento) of the University of Alicante (UATALENTO16-02).

References

[1] Wieckowski A. Interfacial electrochemistry: theory, experiment, and applications. New York: Marcel Dekker, 1999.

[2] Climent V, Feliu JM. Thirty years of platinum single crystal electrochemistry. J Solid State Electrochem. 2011;15:1297–315.

[3] Martínez-Hincapié R, Sebastián-Pascual P, Climent V, Feliu JM. Investigating interfacial parameters with platinum single crystal electrodes. Russ J Electrochem. 2017;53:227–36.

[4] Wieckowski A, Savinova ER, Vayenas CG. Catalysis and electrocatalysis at nanoparticle surfaces. New York: CRC Press, 2003.

[5] Koper MT. Fuel cell catalysis: a surface science approach. electrocatalysis and electrochemistry. Hoboken, New Jersey: John Wiley & Sons, 2009.

[6] Koper MT. Structure sensitivity and nanoscale effects in electrocatalysis. Nanoscale. 2001;3:2054–73.

[7] Solla-Gullón J, Vidal-Iglesias FJ, Feliu JM. Shape dependent electrocatalysis, annual reports on the progress of chemistry. Section C: Phys Chem. 2011;107:263–97.

[8] Tian N, Zhou ZY, Sun SG. Platinum metal catalysts of high-index surfaces: from single-crystal planes to electrochemically shape-controlled nanoparticles. J Phys Chem C. 2008;112:19801–17.

[9] Zhou Z-Y, Tian N, Huang -Z-Z, Chen D-J, Sun S-G. Nanoparticle catalysts with high energy surfaces and enhanced activity synthesized by electrochemical method. Faraday Discuss. 2009;140:81–92.

[10] Proussevitch AA, Sahagian DL. Recognition and separation of discrete objects within complex 3D voxelized structures. Comput Geosci. 2001;27:441–54.

[11] Baletto F, Ferrando R. Structural properties of nanoclusters: energetic, thermodynamic, and kinetic effects. Rev Mod Phys. 2005;77:371–423.

[12] Wang T, Lee C, Schmidt LD. Shape and orientation of supported platinum particles. Surf Sci. 1985;163:181–97.

[13] Harris PJ. Sulphur-induced faceting of platinum catalyst particles. Nature. 1986;323:792–4.

[14] Ahmadi TS, Wang ZL, Green TC, Henglein A, El-Sayed MA. Shape-controlled synthesis of colloidal platinum nanoparticles. Science. 1996;272:1924–6.

[15] Burda C, Chen X, Narayanan R, El-Sayed MA. Chemistry and properties of nanocrystals of different shapes. Chem Rev. 2005;105:1025–102. (Washington, DC, United States).

[16] Tao AR, Habas S, Yang P. Shape control of colloidal metal nanocrystals. Small. 2008;4: 310–25.

[17] Xia Y, Xiong Y, Lim B, Skrabalak SE. Shape-controlled synthesis of metal nanocrystals: simple chemistry meets complex physics? Angew Chem Int Ed. 2009;48:60–103.

[18] Sau K, Rogach AL. Non-spherical noble metal nanoparticles: colloid-chemical synthesis and morphology control. Adv Mater. 2010;22:1781–804. (Weinheim, Germany).

[19] Gu J, Zhang YW, Tao F. Shape control of bimetallic nanocatalysts through well-designed colloidal chemistry approaches. Chem Soc Rev. 2012;41:8050–65.

[20] You H, Yang S, Ding B, Yang H. Synthesis of colloidal metal and metal alloy nanoparticles for electrochemical energy applications. Chem Soc Rev. 2013;42:2880–904.

[21] Quan Z, Wang Y, Fang J. High-index faceted noble metal nanocrystals. Acc Chem Res. 2013;46:191–202.

[22] Leong GJ, Schulze MC, Strand MB, Maloney D, Frisco SL, Dinh HN, et al. Shape-directed platinum nanoparticle synthesis: nanoscale design of novel catalysts. Appl Organomet Chem. 2014;28:1–17.

[23] Xia Y, Xia X, Peng HC. Shape-controlled synthesis of colloidal metal nanocrystals: thermodynamic versus kinetic products. J Am Chem Soc. 2015;137:7947–66.

[24] Gilroy KD, Ruditskiy A, Peng HC, Qin D, Xia Y. Bimetallic nanocrystals: syntheses, properties, and applications. Chem Rev. 2016;116:10414–72.

[25] Chen Q, Jia Y, Xie S, Xie Z. Well-faceted noble-metal nanocrystals with nonconvex polyhedral shapes. Chem Soc Rev. 2016;45:3207–20.

[26] Yang TH, Gilroy KD, Xia Y. Reduction rate as a quantitative knob for achieving deterministic synthesis of colloidal metal nanocrystals. Chem Sci. 2017;8:6730–49.

[27] Xia Y, Gilroy KD, Peng H-C, Xia X. Seed-mediated growth of colloidal metal nanocrystals. Angew Chem Int Ed. 2017;56:60–95.

[28] Gilroy KD, Yang X, Xie S, Zhao M, Qin D, Xia Y. Shape-controlled synthesis of colloidal metal nanocrystals by replicating the surface atomic structure on the seed. Adv Mater. 2018;1706312. DOI: 10.1002/adma.201706312

[29] Tian N, Zhou Z-Y, Sun S-G, Ding Y, Wang ZL. Synthesis of tetrahexahedral platinum nanocrystals with high-index facets and high electro-oxidation activity. Science. 2007;316:732–35.

[30] Tian N, Xiao J, Zhou Z-Y, Liu H-X, Deng Y-J, Huang L, et al. Pt-group bimetallic nanocrystals with high-index facets as high performance electrocatalysts. Faraday Discuss. 2013;162: 77–89.

[31] Wei L, Tian N, Zhou ZY, Sun SG. Electrochemically shape-controlled nanoparticles in advances in electrochemical science and engineering:nanopatterned and nanoparticle-modified electrode. In: Alkire RC, Bartlett PN, Lipkowski J, editors. Wiley-VCH, 2017:59–95.

[32] Carpenter MK, Moylan TE, Kukreja RS, Atwan MH, Tessema MM. Solvothermal synthesis of platinum alloy nanoparticles for oxygen reduction electrocatalysis. J Am Chem Soc. 2012;134:8535–42.

[33] Cui C, Gan L, Li HH, Yu SH, Heggen M, Strasser P. Octahedral PtNi nanoparticle catalysts: exceptional oxygen reduction activity by tuning the alloy particle surface composition. Nano Lett. 2012;12:5885–9.

[34] Gumeci C, Marathe A, Behrens RL, Chaudhuri J, Korzeniewski C. Solvothermal synthesis and electrochemical characterization of shape-controlled Pt nanocrystals. J Phys Chem C. 2014;118:14433–40.

[35] Zhang N, Tsao KC, Pan YT, Yang H. Control of the composition of Pt–ni electrocatalysts in surfactant-free synthesis using neat N-formylpiperidine. Nanoscale. 2016;8:2548–53.

[36] Duca M, Rodriguez P, Yanson AI, Koper MT. Selective electrocatalysis on platinum nanoparticles with preferential (100) orientation prepared by cathodic corrosion. Top Catal. 2014;57:255–64.

[37] Zhang C, Hwang SY, Trout A, Peng Z. Solid-state chemistry-enabled scalable production of octahedral Pt-Ni alloy electrocatalyst for oxygen reduction reaction. J Am Chem Soc. 2014;136:7805–8.

[38] Choi J, Jang JH, Roh CW, Yang S, Kim J, Lim J, et al. Gram-scale synthesis of highly active and durable octahedral PtNi nanoparticle catalysts for proton exchange membrane fuel cell. Appl Catal B: Environ. 2018;225:530–7.

[39] Clavilier J, Faure R, Guinet G, Durand R. Preparation of monocrystalline Pt microelectrodes and electrochemical study of the plane surfaces cut in the direction of the {111} and {110} planes. J Electroanalytical Chem. 1980;107:205–9.

[40] Clavilier J. Flame-annealing and cleaning technique in interfacial electrochemistry. Interfacial Electrochemistry: Theory: Experiment, and Applications. In: Wieckowski A, editor. Marcel Dekker, 1999:231–48.

[41] Montiel MA, Vidal-Iglesias FJ, Montiel V, Solla-Gullón J. Electrocatalysis on shape-controlled metal nanoparticles: progress in surface cleaning methodologies. Curr Opin Electrochem. 2017;1:34–9.

[42] Climent V, Feliu JM. Surface electrochemistry with Pt single-crystal electrodes. In: Alkire RC, Bartlett PN, Lipkowski J, editors. Advances in electrochemical science and engineering: nano-patternedand nanoparticle-modified electrode. Wiley-VCH, 2017:1–57.

[43] Hoshi N, Kagaya K, Hori Y. Voltammograms of the single-crystal electrodes of palladium in aqueous sulfuric acid electrolyte: pd(S)-[n(111)×(111)] and Pd(S)-[n(100)×(111)]. J Electroanalytical Chem. 2000;485:55–60.

[44] Hoshi N, Kuroda M, Hori Y. Voltammograms of stepped and kinked stepped surfaces of palladium: pd(S)-[n(111)×(100)] and Pd(S)-[n(100)×(110)]. J Electroanalytical Chem. 2002;521:155–60.

[45] Hara M, Linke U, Wandlowski T. Preparation and electrochemical characterization of palladium single crystal electrodes in 0.1 M H_2SO_4 and $HClO_4$ part I.Low-index phases. Electrochim Acta. 2007;52:5733–48.

[46] Vidal-Iglesias FJ, Arán-Ais RM, Solla-Gullon J, Herrero E, Feliu JM. Electrochemical characterization of shape-controlled pt nanoparticles in different supporting electrolytes. ACS Catal. 2012;2:901–10.

[47] Susut C, Chapman GB, Samjeské G, Osawa M, Tong Y. An unexpected enhancement in methanol electro-oxidation on an ensemble of Pt(111) nanofacets: A case of nanoscale single crystal ensemble electrocatalysis. Phys Chem Chem Phys. 2008;10:3712–21.

[48] Van Der Vliet DF, Wang C, Li D, Paulikas AP, Greeley J, Rankin RB, et al. Unique electrochemical adsorption properties of Pt-skin surfaces. Angew Chem Int Ed. 2012;51:3139–42.

[49] Shao M, Odell JH, Choi SI, Xia Y. Electrochemical surface area measurements of platinum- and palladium-based nanoparticles. Electrochem commun. 2013;31:46–8.

[50] Rudi S, Cui C, Gan L, Strasser P. Comparative study of the electrocatalytically active surface areas (ECSAs) of Pt alloy nanoparticles evaluated by hupd and CO-stripping voltammetry. Electrocatalysis. 2014;5:408–18.

[51] Hamelin A. Cyclic voltammetry at gold single-crystal surfaces 0.1. Behaviour at low-index faces. J Electroanalytical Chem. 1996;407:1–11.

[52] Hamelin A. Cyclic voltammetry at gold single-crystal surfaces 0.2. Behaviour of high-index faces. J Electroanalytical Chem. 1996;407:13–21.

[53] Ke F-S, Solomon B, Ding Y, Xu G-L, Sun S-G, Wang ZL, et al. Enhanced electrocatalytic activity on gold nanocrystals enclosed by high-index facets for oxygen reduction. Nano Energy. 2014;7:179–88.

[54] Yang S, Lee H. Atomically dispersed platinum on gold nano-octahedra with high catalytic activity on formic acid oxidation. ACS Catal. 2013;3:437–43.

[55] Monzó J, Malewski Y, Vidal-Iglesias FJ, Solla-Gullón J, Rodriguez P. Electrochemical oxidation of small organic molecules on Au nanoparticles with preferential surface orientation. Chem Electro Chem. 2015;2:958–62.

[56] Nichols RJ, Magnussen OM, Hotlos J, Twomey T, Behm RJ, Kolb DM. An in-situ STM study of potential-induced changes in the surface topography of Au(100) electrodes. J Electroanalytical Chem. 1990;290:21–31.

[57] Schneeweiss MA, Kolb DM. Oxide formation on Au(111) - An in situ STM study. Solid State Ionics. 1997;94:171–9.

[58] Itaya K, Sugawara S, Sashikata K, Furuya N. In situ scanning tunneling microscopy of platinum (111) surface with the observation of monatomic steps. J Vac Sci Technol, A-Vacuum Surf Films. 1990;8:515–9.

[59] Hamelin A. Lead adsorption on gold single crystal stepped surfaces. J Electroanalytical Chem. 1979;101:285–90.

[60] Hamelin A, Katayama A. Lead underpotential deposition on gold single-crystal surfaces: the (100) face and its vicinal faces. J Electroanalytical Chem. 1981;117:221–32.

[61] Hamelin A. Underpotential deposition of lead on single crystal faces of gold. Part I. The influence of crystallographic orientation of the substrate. J Electroanalytical Chem. 1984;165:167–80.

[62] Hamelin A, Lipkowski J. Underpotential deposition of lead on gold single crystal faces. Part II. General discussion. J Electroanalytical Chem. 1984;171:317–30.

[63] Hernández J, Solla-Gullón J, Herrero E. Gold nanoparticles synthesized in a water-in-oil micro-emulsion: electrochemical characterization and effect of the surface structure on the oxygen reduction reaction. J Electroanalytical Chem. 2004;574:185–96.

[64] Hernández J, Solla-Gullón J, Herrero E, Aldaz A, Feliu JM. Electrochemistry of shape-controlled catalysts: oxygen reduction reaction on cubic gold nanoparticles. J Phys Chem C. 2007;111:14078–83.

[65] Hernández J, Solla-Gullón J, Herrero E, Feliu JM, Aldaz A. In situ surface characterization and oxygen reduction reaction on shape-controlled gold nanoparticles. J Nanosci Nanotechnol. 2009;9:2256–73.

[66] Chierchie T, Mayer C. Voltammetric study of the underpotential deposition of copper on polycrystalline and single crystal palladium surfaces. Electrochim Acta. 1988;33:341–5.

[67] Cuesta A, Kibler LA, Kolb DM. A method to prepare single crystal electrodes of reactive metals: application to Pd(hkl). J Electroanalytical Chem. 1999;466:165–8.

[68] Fang LL, Tao Q, Li MF, Liao LW, Chen D, Chen YX. Determination of the real surface area of palladium electrode. Chin J Chem Phys. 2010;23:543–8.

[69] Francke R, Climent V, Baltruschat H, Feliu JM. Electrochemical deposition of copper on stepped platinum surfaces in the 01 (1)over-barzone vicinal to the (100) plane. J Electroanalytical Chem. 2008;624:228–40.

[70] Danilov AI, Molodkina EB, Rudnev AV, Polukarov YM, Feliu JM. Kinetics of copper deposition on Pt(111) and Au(111) electrodes in solutions of different acidities. Electrochim Acta. 2005;50:5032–43.

[71] Vidal-Iglesias FJ, Solla-Gullón J, Rodríguez P, Herrero E, Montiel V, Feliu JM, et al. Shape-dependent electrocatalysis: ammonia oxidation on platinum nanoparticles with preferential (100) surfaces. Electrochem commun. 2004;6:1080–4.

[72] Solla-Gullón J, Vidal-Iglesias FJ, Rodríguez P, Herrero E, Feliu JM, Clavilier J, et al. In situ surface characterization of preferentially oriented platinum nanoparticles by using electrochemical structure sensitive adsorption reactions. J Phys Chem B. 2004;108:13573–5.

[73] Erikson H, Sarapuu A, Tammeveski K, Solla-Gullón J, Feliu JM. Enhanced electrocatalytic activity of cubic Pd nanoparticles towards the oxygen reduction reaction in acid media. Electrochem commun. 2011;13:734–7.

[74] Erikson H, Sarapuu A, Alexeyeva N, Tammeveski K, Solla-Gullón J, Feliu JM. Electrochemical reduction of oxygen on palladium nanocubes in acid and alkaline solutions. Electrochim Acta. 2012;59:329–35.

[75] Vidal-Iglesias FJ, Arán-Ais RM, Solla-Gullon J, Garnier E, Herrero E, Aldaz A, et al. Shape-dependent electrocatalysis: formic acid electrooxidation on cubic Pd nanoparticles. Phys Chem Chem Phys. 2012;14:10258–65.

[76] Coutanceau C, Urchaga P, Brimaud S, Baranton S. Colloidal syntheses of shape- and size-controlled Pt nanoparticles for electrocatalysis. Electrocatalysis. 2012;3:75–87.

[77] Urchaga P, Baranton S, Napporn TW, Coutanceau C. Selective syntheses and electrochemical characterization of platinum nanocubes and nanotetrahedrons/octahedrons. Electrocatalysis. 2010;1:3–6.

[78] Solla-Gullón J, Vidal-Iglesias FJ, López-Cudero A, Garnier E, Feliu JM, Aldaz A. Shape-dependent electrocatalysis: methanol and formic acid electrooxidation on preferentially oriented Pt nanoparticles. Phys Chem Chem Phys. 2008;10:3689–98.

[79] Brimaud S, Jusys Z, Behm RJ. Controlled surface structure for in situ ATR-FTIRS studies using preferentially shaped Pt nanocrystals. Electrocatalysis. 2011;2:69–74.

[80] Brimaud S, Jusys Z, Behm RJ. Shape-selected nanocrystals for in situ spectro-electrochemistry studies on structurally well-defined surfaces under controlled electrolyte transport: A combined in situ ATR-FTIR/online DEMS investigation of CO electrooxidation on Pt, Beilstein. J Nanotechnol. 2014;5:735–46.

[81] Susut C, Nguyen TD, Chapman GB, Tong Y. Shape and size stability of Pt nanoparticles for MeOH electro-oxidation. Electrochim Acta. 2008;53:6135–42.

[82] Susut C, Tong Y. Size-dependent methanol electro-oxidation activity of Pt nanoparticles with different shapes. Electrocatalysis. 2011;2:75–81.

[83] Levendorf A, Sun SG, Tong Y. In situ FT-IR investigation of methanol and CO electrooxidation on cubic and octahedral/tetrahedral Pt nanoparticles having residual PVP. Electrocatalysis. 2014;5:248–55.

[84] Koczkur KM, Mourdikoudis S, Polavarapu L, Skrabalak SE. Polyvinylpyrrolidone (PVP) in nanoparticle synthesis. Dalton Trans. 2015;44:17883–905.

[85] Monzó J, Koper MT, Rodriguez P. Removing polyvinylpyrrolidone from catalytic Pt nanoparticles without modification of superficial order. Chem Phys Chem. 2012;13:709–15.

[86] Levendorf AM, Chen D-J, Rom CL, Liu Y, Tong YJ. Electrochemical and in situ ATR-SEIRAS investigations of methanol and CO electro-oxidation on PVP-free cubic and octahedral/tetrahedral Pt nanoparticles. RSC Adv. 2014;4:21284–93.

[87] Yang H, Tang Y, Zou S. Electrochemical removal of surfactants from Pt nanocubes. Electrochem commun. 2014;38:134–7.

[88] Zalineeva A, Baranton S, Coutanceau C. Bi-modified palladium nanocubes for glycerol electrooxidation. Electrochem commun. 2013;34:335–8.

[89] Zalineeva A, Baranton S, Coutanceau C, Jerkiewicz G. Electrochemical behavior of unsupported shaped palladium nanoparticles. Langmuir. 2015;31:1605–9.

[90] Nalajala N, Gooty Saleha WF, Ladewig BP, Neergat M. Sodium borohydride treatment: A simple and effective process for the removal of stabilizer and capping agents from shape-controlled palladium nanoparticles. Chem Commun. 2014;50:9365–8.

[91] Naresh N, Wasim FG, Ladewig BP, Neergat M. Removal of surfactant and capping agent from Pd nanocubes (Pd-NCs) using tert-butylamine: its effect on electrochemical characteristics. J Mater Chem. 2013;1:8553–9.

[92] Luo M, Hong Y, Yao W, Huang C, Xu Q, Wu Q. Facile removal of polyvinylpyrrolidone (PVP) adsorbates from Pt alloy nanoparticles. J Mater Chem. 2015;3:2770–5.

[93] Arán-Ais RM, Vidal-Iglesias FJ, Solla-Gullon J, Herrero E, Feliu JM. Electrochemical characterization of clean shape-controlled Pt nanoparticles prepared in presence of oleylamine/oleic acid. Electroanalysis. 2014;27:945–56.

[94] Safo IA, Oezaslan M. Electrochemical Cleaning of Polyvinylpyrrolidone-capped Pt Nanocubes for the Oxygen Reduction Reaction. Electrochim Acta. 2017;241:544–52.

[95] Safo IA, Dosche C, Oezaslan M. TEM, FTIR and Electrochemistry Study: desorption of PVP from Pt Nanocubes. Zeitschrift für Physikalische Chemie. 2018. DOI: 10.1515/zpch-2018-1147

[96] Hernández J, Solla-Gullón J, Herrero E, Aldaz A, Feliu JM. Characterization of the surface structure of gold nanoparticles and nanorods using structure sensitive reactions. J Phys Chem B. 2005;109:12651–4.

[97] Chen Y, Milenkovic S, Hassel AW. {110}-Terminated square-shaped gold nanoplates and their electrochemical surface reactivity. Chem Electro Chem. 2017;4:557–64.

[98] Yang S, Park N-Y, Han JW, Kim C, Lee S-C, Lee H. A distinct platinum growth mode on shaped gold nanocrystals. Chem Commun. 2012;48:257–9.

[99] Solla-Gullón J, Rodríguez P, Herrero E, Aldaz A, Feliu JM. Surface characterization of platinum electrodes. Phys Chem Chem Phys. 2008;10:1359–73.

[100] Solla-Gullón J, Vidal-Iglesias FJ, Herrero E, Feliu JM, Aldaz A. Electrocatalysis on shape-controlled Pt nanoparticles in polymer electrolyte fuel cells: science, applications and challenges. Polymer Electrolyte Fuel Cells: Science, Applications, and Challenges. In: Franco AA, editor. Pan Stanford, 2013:93–151.

[101] Arán-Ais RM, Solla-Gullón J, Herrero E, Feliu JM. On the quality and stability of preferentially oriented (100) Pt nanoparticles: an electrochemical insight. J Electroanalytical Chem. 2018;808:433–8.

[102] Vidal-Iglesias FJ, Solla-Gullón J, Herrero E, Montiel V, Aldaz A, Feliu JM. Evaluating the ozone cleaning treatment in shape-controlled Pt nanoparticles: evidences of atomic surface disordering. Electrochem commun. 2011;13:502–5.

[103] Park JY, Aliaga C, Renzas JR, Lee H, Somorjai GA. The role of organic capping layers of platinum nanoparticles in catalytic activity of CO oxidation. Catal Lett. 2009;129:1–6.

[104] Aliaga C, Park JY, Yamada Y, Lee HS, Tsung CK, Yang P, et al. Sum frequency generation and catalytic reaction studies of the removal of organic capping agents from Pt nanoparticles by UV-Ozone treatment. J Phys Chem C. 2009;113:6150–5.

[105] Krier JM, Michalak WD, Baker LR, An K, Komvopoulos K, Somorjai GA. Sum frequency generation vibrational spectroscopy of colloidal platinum nanoparticle catalysts: disordering versus removal of organic capping. J Phys Chem C. 2012;116:17540–6.

[106] Crespo-Quesada M, Andanson JM, Yarulin A, Lim B, Xia Y, Kiwi-Minsker L. UV-ozone cleaning of supported poly(vinylpyrrolidone)-stabilized palladium nanocubes: effect of stabilizer removal on morphology and catalytic behaviour. Langmuir. 2011;27:7909–16.

[107] Herrero E, Buller LJ, Abruña HD. Underpotential deposition at single crystal surfaces of Au, Pt, Ag and other materials. Chem Rev. 2001;101:1897–930. (Washington, DC, United States).

[108] Oviedo OA, Vélez P, Macagno VA, Leiva EP. Underpotential deposition: from planar surfaces to nanoparticles. Surf Sci. 2015;631:22–34.

[109] Jiang Q, Jiang Z, Zhang L, Lin H, Yang N, Li H, et al. Synthesis and high electrocatalytic performance of hexagram shaped gold particles having an open surface structure with kinks. Nano Res. 2011;4:612–22.

[110] Hebié S, Kokoh KB, Servat K, Napporn TW. Shape-dependent electrocatalytic activity of free gold nanoparticles toward glucose oxidation. Gold Bulletin. 2013;46:311–8.

[111] Jeyabharathi C, Zander M, Scholz F. Underpotential deposition of lead on quasi-spherical and faceted gold nanoparticles. J Electroanalytical Chem. 2018. DOI: 10.1016/j.jelechem.2017.10.011

[112] Jin M, Zhang H, Xie Z, Xia Y. Palladium nanocrystals enclosed by {100} and {111} facets in controlled proportions and their catalytic activities for formic acid oxidation. Energy Environ Sci. 2012;5:6352–7.

[113] Solla-Gullón J, Garnier E, Feliu JM, Leoni M, Leonardi A, Scardi P. Structure and morphology of shape-controlled Pd nanocrystals. J of. Appl Crystallogr. 2015;48:1534–42.

[114] Higuchi E, Kawai M, Chiku M, Inoue H. Synthesis and electrochemical characterization of palladium crystals enclosed by (100) facets by seed-mediated fabrication. Int J Electrochem. 2018. Article ID 7138638. DOI: 10.1155/2018/7138638.

[115] Rodríguez P, Solla-Gullón J, Vidal-Iglesias FJ, Herrero E, Aldaz A, Feliu JM. Determination of (111) ordered domains on platinum electrodes by irreversible adsorption of bismuth. Anal Chem. 2005;77:5317–23.

[116] Rodríguez P, Herrero E, Solla-Gullón J, Vidal-Iglesias FJ, Aldaz A, Feliu JM. Specific surface reactions for identification of platinum surface domains - Surface characterization and electrocatalytic tests. Electrochim Acta. 2005;50:4308–17.

[117] Rodríguez P, Herrero E, Aldaz A, Feliu JM. Tellurium adatoms as an in-situ surface probe of (111) two-dimensional domains at platinum surfaces. Langmuir. 2006;22:10329–37.

[118] Rodríguez P, Herrero E, Solla-Gullón J, Vidal-Iglesias FJ, Aldaz A, Feliu JM. Electrochemical characterization of irreversibly adsorbed germanium on platinum stepped surfaces vicinal to Pt (100). Electrochim Acta. 2005;50:3111–21.

[119] Brimaud S, Pronier S, Coutanceau C, Léger JM. New findings on CO electrooxidation at platinum nanoparticle surfaces. Electrochem commun. 2008;10:1703–7.

[120] Devivaraprasad R, Ramesh R, Naresh N, Kar T, Singh RK, Neergat M. Oxygen reduction reaction and peroxide generation on shape-controlled and polycrystalline platinum nanoparticles in acidic and alkaline electrolytes. Langmuir. 2014;30:8995–9006.

[121] Bertin E, Garbarino S, Guay D. Formic acid oxidation on Bi covered Pt electrodeposited thin films: influence of the underlying structure. Electrochim Acta. 2014;134:486–95.

[122] Devivaraprasad R, Kar T, Chakraborty A, Singh RK, Neergat M. Reconstruction and dissolution of shape-controlled Pt nanoparticles in acidic electrolytes. Phys Chem Chem Phys. 2016;18:11220–32.

[123] Liu J, Fan X, Liu X, Song Z, Deng Y, Han X, et al. Synthesis of cubic-shaped Pt particles with (100) preferential orientation by a quick, one-step and clean electrochemical method. ACS Appl Mater Interfaces. 2017;9:18856–64.

[124] Liu Z, Ma C, Liu J, Chen X, Song Z, Hu W, et al. Studies on the electrochemical stability of preferentially (100)-oriented Pt prepared through three different methods. Chem Electro Chem. 2017;4:66–74.

[125] Rodriguez-Lopez M, Solla-Gullón J, Herrero E, Tuñon P, Feliu JM, Aldaz A, et al. Electrochemical reactivity of aromatic molecules at nanometer-sized surface domains: from Pt(hkl) single crystal electrodes to preferentially oriented platinum nanoparticles. J Am Chem Soc. 2010;132:2233–42.

[126] Rodríguez P, Herrero E, Solla-Gullón J, Feliu JM, Aldaz A. Selective electrocatalysis of acetaldehyde oxime reduction on (111) sites of platinum single crystal electrodes and nanoparticles surfaces. J Solid State Electrochem. 2008;12:575–81.

[127] Martínez-Rodríguez RA, Vidal-Iglesias FJ, Solla-Gullón J, Cabrera CR, Feliu JM. synthesis and electrocatalytic properties of H_2SO_4-induced (100) Pt nanoparticles prepared in water-in-oil microemulsion. Chem Phys Chem. 2014;15:1997–2001.

[128] El-Deab MS. On the preferential crystallographic orientation of Au nanoparticles: effect of electrodeposition time. Electrochim Acta. 2009;54:3720–5.

[129] El-Deab MS, Sotomura T, Ohsaka T. Size and crystallographic orientation controls of gold nanoparticles electrodeposited on GC electrodes. J Electrochem Soc. 2005;152:C1–C6.

[130] El-Deab MS, Arihara K, Ohsaka T. Fabrication of Au(111)-like polycrystalline gold electrodes and their applications to oxygen reduction. J Electrochem Soc. 2004;151:E213–E218.

[131] Arihara K, Ariga T, Takashima N, Arihara K, Okajima T, Kitamura F, et al. Multiple voltammetric waves for reductive desorption of cysteine and 4-mercaptobenzoic acid monolayers self-assembled on gold substrates. Phys Chem Chem Phys. 2003;5:3758–61.

[132] Cuesta A, Kibler LA, Kolb DM. A method to prepare single crystal electrodes of reactive metals: application to Pd(hkl). J Electroanalytical Chem. 1999;46:165–8.

[133] Vidal-Iglesias FJ, Al-Akl A, Watson DJ, Attard GA. A new method for the preparation of PtPd alloy single crystal surfaces. Electrochem commun. 2006;8:1147–50.

[134] Moniri S, Cleve TV, Linic S. Pitfalls and best practices in measurements of the electrochemical surface area of platinum-based nanostructured electro-catalysts. J Catal. 2017;345:1–10.

[135] Vidal-Iglesias FJ, García-Aráez N, Montiel V, Feliu JM, Aldaz A. Selective electrocatalysis of ammonia oxidation on Pt (1 0 0) sites in alkaline medium. Electrochem Commun. 2003;5:22–6.

[136] Vidal-Iglesias FJ, Solla-Gullón J, Montiel V, Feliu JM, Aldaz A. Ammonia selective oxidation on Pt (100) sites in an alkaline medium. J Phys Chem B. 2005;109:12914–9.

[137] Peng Z, Yang H. Designer platinum nanoparticles: control of shape, composition in alloy, nanostructure and electrocatalytic property. Nano Today. 2009;4:143–64.

[138] Chen J, Lim B, Lee EP, Xia Y. Shape-controlled synthesis of platinum nanocrystals for catalytic and electrocatalytic applications. Nano Today. 2009;4:81–95.

[139] Bing Y, Liu H, Zhang L, Ghosh D, Zhang J. Nanostructured Pt-alloy electrocatalysts for PEM fuel cell oxygen reduction reaction. Chem Soc Rev. 2010;39:2184–202.

[140] Wu B, Zheng N. Surface and interface control of noble metal nanocrystals for catalytic and electrocatalytic applications. Nano Today. 2013;8:168–97.

[141] Sanchez-Sanchez CM, Solla-Gullon J, Montiel V. Electrocatalysis at nanoparticles in Electrochemistry: nanosystems Electrochemistry. Royal Soc Chem. 2013;11:34–70.

[142] Kleijn SE, Lai SC, Koper MT, Unwin PR. Electrochemistry of nanoparticles. Angew Chem Int Ed. 2014;53:3558–86.

[143] Wang YJ, Zhao N, Fang B, Li H, Bi XT, Wang H. Carbon-supported Pt-based alloy electrocatalysts for the oxygen reduction reaction in polymer electrolyte membrane fuel cells: particle size, shape, and composition manipulation and their impact to activity. Chem Rev. 2015;115: 3433–67.

[144] Vidal-Iglesias FJ, Solla-Gullón J, Feliu JM. Recent advances in the use of shape-controlled metal nanoparticles in electrocatalysis. In: Ozoemena IK, Chen S, editors. Nanomaterials for fuel cell catalysis. Springer International Publishing, 2016:31–92.

[145] Cao S, Tao FF, Tang Y, Li Y, Yu J. Size-and shape-dependent catalytic performances of oxidation and reduction reactions on nanocatalysts. Chem Soc Rev. 2016;45:4747–65.

[146] Kang Y, Yang P, Markovic NM, Stamenkovic VR. Shaping electrocatalysis through tailored nanomaterials. Nano Today. 2016;11:587–600.

[147] Hong JW, Kim Y, Kwon Y, Han SW. Noble metal nanocrystals with controlled facets for electrocatalysis. Chem: Asian J. 2016;11:2224–39.

[148] Liu X, Li W, Zou S. Electrocatalysis of Facet-controlled Noble Metal Nanomaterials for Low-temperature Fuel Cells. In: Maiyalagan T, Saji VS, editors. Electrocatalysts for low temperature fuel cells: fundamentals and recent trends. Wiley-VCH, 2017:373–99.

[149] Tian N, Lu B-A, Yang X-D, Huang R, Jiang Y-X, Zhou Z-Y, et al. Rational design and synthesis of low-temperature fuel cell electrocatalysts. Electrochem Energy Rev. 2018;1:54–83.

[150] Strasser P, Gliech M, Kuehl S, Moeller T. Electrochemical processes on solid shaped nanoparticles with defined facets. Chem Soc Rev. 2018;47:715–35.

[151] Shao M. Electrocatalysis in fuel cells: a non- and low- platinum approach. London: Springer, 2013.

[152] Feliu JM, Herrero E. Formic acid oxidation in handbook of fuel cells - Fundamentals, technology and applications, vol. 2. Vielstich W, Gasteiger H, Lamm A editors, John Wiley & Sons, 2003:625–34.

[153] Jiang K, Zhang HX, Zou S, Cai WB. Electrocatalysis of formic acid on palladium and platinum surfaces: from fundamental mechanisms to fuel cell applications. Phys Chem Chem Phys. 2014;16:20360–76.

[154] Capon A, Parsons R. The oxidation of formic acid at noble metal electrodes: I. Review of previous work. J Electroanalytical Chem. 1973;44:1–7.

[155] Capon A, Parsons R. The oxidation of formic acid on noble metal electrodes: II. Comp Behav Pure Electrodes J Electroanal Chem. 1973;44:239–54.

[156] Capon A, Parsons R. The oxidation of formic acid at noble metal electrodes Part III. Intermediates and mechanism on platinum electrodes. J Electroanalytical Chem. 1973;45:205–31.

[157] Grozovski V, Solla-Gullon J, Climent V, Herrero E, Feliu JM. Formic acid oxidation on shape-controlled Pt nanoparticles studied by pulsed voltammetry. J Phys Chem C. 2010;114:13802–12.

[158] Huang X, Zhao Z, Fan J, Tan Y, Zheng N. Amine-assisted synthesis of concave polyhedral platinum nanocrystals having {411} high-index facets. J Am Chem Soc. 2011;133:4718–21.

[159] Li Y, Jiang Y, Chen M, Liao H, Huang R, Zhou Z, et al. Electrochemically shape-controlled synthesis of trapezohedral platinum nanocrystals with high electrocatalytic activity. Chem Commun. 2012;48:9531–3. (Cambridge, United Kingdom).

[160] Xia BY, Wu HB, Wang X, Lou XW. Highly concave platinum nanoframes with high-index facets and enhanced electrocatalytic properties. Angew Chem Int Ed. 2013;52:12337–40.

[161] Lu B-A, Du J-H, Sheng T, Tian N, Xiao J, Liu L, et al. Hydrogen adsorption-mediated synthesis of concave Pt nanocubes and their enhanced electrocatalytic activity. Nanoscale. 2016;8:11559–64.

[162] Rice C, Ha S, Masel RI, Wieckowski A. Catalysts for direct formic acid fuel cells. J Power Sources. 2003;115:229–35.

[163] Hoshi N, Kida K, Nakamura M, Nakada M, Osada K. Structural effects of electrochemical oxidation of formic acid on single crystal electrodes of palladium. J Phys Chem B. 2006;110:12480–4.

[164] Baldauf M, Kolb DM. Formic acid oxidation on ultrathin Pd films on Au(hkl) and Pt(hkl) electrodes. J Phys Chem. 1996;100:11375–81.

[165] Zhang H-X, Wang H, Re Y-S, Cai W-B. Palladium nanocrystals bound by {110} or {100} facets: from one pot synthesis to electrochemistry. Chem Commun. 2012;48:8362–4.

[166] Shao Z, Zhu W, Wang H, Yang Q, Yang S, Liu X, et al. Controllable synthesis of concave nanocubes, right bipyramids, and 5-fold twinned nanorods of palladium and their enhanced electrocatalytic performance. J Phys Chem C. 2013;117:14289–94.

[167] Kuo CH, Lamontagne LK, Brodsky CN, Chou LY, Zhuang J, Sneed BT, et al. The effect of lattice strain on the catalytic properties of Pd nanocrystals. Chem Sus Chem. 2013;6:1993–2000.

[168] Xia X, Choi SI, Herron JA, Lu N, Scaranto J, Peng HC, et al. Facile synthesis of palladium right bipyramids and their use as seeds for overgrowth and as catalysts for formic acid oxidation. J Am Chem Soc. 2013;135:15706–9.

[169] Lv T, Wang Y, Choi SI, Chi M, Tao J, Pan L, et al. Controlled synthesis of nanosized palladium icosahedra and their catalytic activity towards formic-acid oxidation. Chem Sus Chem. 2013;6:1923–30.

[170] Shao M, Odell J, Humbert M, Yu T, Xia Y. Electrocatalysis on shape-controlled palladium nanocrystals: oxygen reduction reaction and formic acid oxidation. J Phys Chem C. 2013;117:4172–80.

[171] Zhang X, Yin H, Wang J, Chang L, Gao Y, Liu W, et al. Shape-dependent electrocatalytic activity of monodispersed palladium nanocrystals toward formic acid oxidation. Nanoscale. 2013;5:8392–7.

[172] Tang Y, Edelmann RE, Zou S. Length tunable penta-twinned palladium nanorods: seedless synthesis and electrooxidation of formic acid. Nanoscale. 2014;6:5630–3.

[173] Chen Q-S, Xu Z-N, Peng S-Y, Chen Y-M, Lv D-M, Wang Z-Q, et al. One-step electrochemical synthesis of preferentially oriented (111) Pd nanocrystals supported on graphene nanoplatelets for formic acid electrooxidation. J Power Sources. 2015;282:471–8.

[174] Zheng W, Qu J, Hong X, Tedsree K, Tsang SC. Probing the size and shape effects of cubic- and spherical-shaped palladium nanoparticles in the electrooxidation of formic acid. Chem Cat Chem. 2015;7:3826–31.

[175] Huang H, Ruditskiy A, Choi S, Zhang L, Liu J, Ye Z, et al. One-pot synthesis of penta-twinned palladium nanowires and their enhanced electrocatalytic properties. ACS Appl Mater Interfaces. 2017;9:31203–12.

[176] Klinkova A, Luna PD, Sargent EH, Kumacheva E, Cherepanov PV. Enhanced electrocatalytic performance of palladium nanoparticles with high energy surfaces in formic acid oxidation. J Mater Chem. 2017;5:11582–5.

[177] Sheng T, Xu Y-F, Jiang Y-X, Huang L, Tian N, Zhou Z-Y, et al. Structure design and performance tuning of nanomaterials for electrochemical energy conversion and storage. Acc Chem Res. 2016;49:2569–77.

[178] Boronat-Gonzalez A, Herrero E, Feliu JM. Fundamental aspects of HCOOH oxidation at platinum single crystal surfaces with basal orientations and modified by irreversibly adsorbed adatoms. J Solid State Electrochem. 2014;18:1181–93.

[179] Nørskov JK, Abild-Pedersen F, Studt F, Bligaard T. Density functional theory in surface chemistry and catalysis. Proc Natl Acad Sci. 2011;108:937–43.

[180] Porter NS, Wu H, Quan Z, Fang J. Shape-control and electrocatalytic activity-enhancement of Pt-based bimetallic nanocrystals. Acc Chem Res. 2013;46:1867–77.

[181] Yuan Q, Zhou Z, Zhuang J, Wang X. Pd-Pt random alloy nanocubes with tunable compositions and their enhanced electrocatalytic activities. Chem Commun. 2010;46:1491–3.

[182] Zhang J, Yang H, Yang K, Fang J, Zou S, Luo Z, et al. Monodisperse Pt_3Fe nanocubes: synthesis, characterization, self-assembly, and electrocatalytic activity. Adv Funct Mater. 2010;20: 3727–33.

[183] Yang H, Dai L, Xu D, Fang J, Zou S. Electrooxidation of methanol and formic acid on PtCu nanoparticles. Electrochim Acta. 2010;55:8000–4.

[184] Xu D, Bliznakov S, Liu Z, Fang J, Dimitrov N. Composition-dependent electrocatalytic activity of Pt-Cu nanocube catalysts for formic acid oxidation. Angew Chem Int Ed. 2010;49:1282–5.

[185] Zhang J, Yang H, Martens B, Luo Z, Xu D, Wang Y, et al. Pt-Cu nanoctahedra: synthesis and comparative study with nanocubes on their electrochemical catalytic performance. Chem Sci. 2012;3:3302–6.

[186] Bromberg L, Fayette M, Martens B, Luo ZP, Wang Y, Xu D, et al. Catalytic performance comparison of shape-dependent nanocrystals and oriented ultrathin films of Pt_4Cu alloy in the formic acid oxidation process. Electrocatalysis. 2013;4:24–36.

[187] Kang Y, Murray CB. Synthesis and electrocatalytic properties of cubic Mn–Pt nanocrystals (nanocubes). J Am Chem Soc. 2010;132:7568–9.

[188] Yu Y, Zhang Q, Liu B, Lee JY. Synthesis of nanocrystals with variable high-index Pd facets through the controlled heteroepitaxial growth of trisoctahedral Au templates. J Am Chem Soc. 2010;132:18258–65.

[189] Zhang L, Zhang J, Kuang Q, Xie S, Jiang Z, Xie Z, et al. Cu^{2+}-assisted synthesis of hexoctahedral Au-Pd alloy nanocrystals with high-index facets. J Am Chem Soc. 2011;133:17114–7.

[190] Deng YJ, Tian N, Zhou ZY, Huang R, Liu ZL, Xiao J, et al. Alloy tetrahexahedral Pd-Pt catalysts: enhancing significantly the catalytic activity by synergy effect of high-index facets and electronic structure. Chem Sci. 2012;3:1157–61.

[191] Jia Y, Jiang Y, Zhang J, Zhang L, Chen Q, Xie Z, et al. Unique excavated rhombic dodecahedral PtCu3 alloy nanocrystals constructed with ultrathin nanosheets of high-energy {110} facets. J Am Chem Soc. 2014;136:3748–51.

[192] Sneed BT, Young AP, Jalalpoor D, Golden MC, Mao S, Jiang Y, et al. Shaped Pd–ni–pt core-sandwich-shell nanoparticles: influence of Ni sandwich layers on catalytic electrooxidations. ACS Nano. 2014;8:7239–50.

[193] Zhang L, Choi S-I, Tao J, Peng H-C, Xie S, Zhu Y, et al. Pd-Cu bimetallic tripods: a mechanistic understanding of the synthesis and their enhanced electrocatalytic activity for formic acid oxidation. Adv Funct Mater. 2014;24:7520–9.

[194] López-Cudero A, Vidal-Iglesias FJ, Solla-Gullón J, Herrero E, Aldaz A, Feliu JM. Formic acid electrooxidation on Bi-modified polyoriented and preferential (111) Pt nanoparticles. Phys Chem Chem Phys. 2009;11:416–24.

[195] Chen QS, Zhou ZY, Vidal-Iglesias FJ, Solla-Gullón J, Feliu JM, Sun SG. Significantly enhancing catalytic activity of tetrahexahedral Pt nanocrystals by Bi adatom decoration. J Am Chem Soc. 2011;133:12930–3.

[196] Vidal-Iglesias FJ, Solla-Gullón J, Herrero E, Aldaz A, Feliu JM. Pd adatom decorated (100) preferentially oriented Pt nanoparticles for formic acid electrooxidation. Angew Chem Int Ed. 2010;49:6998–7001.

[197] Vidal-Iglesias FJ, Lopez-Cudero A, Solla-Gullón J, Aldaz A, Feliu JM. Pd-modified shape-controlled Pt nanoparticles towards formic acid electrooxidation. Electrocatalysis. 2012;3: 313–23.

[198] Vidal-Iglesias FJ, López-Cudero A, Solla-Gullón J, Feliu JM. Towards more active and stable electrocatalysts for formic acid electrooxidation: antimony-decorated octahedral platinum nanoparticles. Angew Chem Int Ed. 2013;52:964–7.

[199] Busó-Rogero C, Perales-Rondón JV, Farias MJ, Vidal-Iglesias FJ, Solla-Gullón J, Herrero E, et al. Formic acid electrooxidation on thallium-decorated shape-controlled platinum nanoparticles: an improvement in electrocatalytic activity. Phys Chem Chem Phys. 2014;16:13616–24.

[200] Perales-Rondón JV, Solla-Gullón J, Herrero E, Sánchez-Sánchez CM. Enhanced catalytic activity and stability for the electrooxidation of formic acid on lead modified shape controlled platinum nanoparticles. Appl Catal B: Environ. 2017;201:48–57.

[201] Liu HX, Tian N, Brandon MP, Pei J, Huangfu ZC, Zhan C, et al. Enhancing the activity and tuning the mechanism of formic acid oxidation at tetrahexahedral Pt nanocrystals by Au decoration. Phys Chem Chem Phys. 2012;14:16415–23.

[202] Li M, Adzic R. Low-platinum-content electrocatalysts for methanol and ethanol electrooxidation. In: Shao M, editor. Electrocatalysis in fuel cells, vol. 9. Lecture Notes in Energy. London: Springer, 2013:1–25.

[203] Lamy C, Leger JM, Clavilier J, Parsons R. Structural effects in electrocatalysis: a comparative study of the oxidation of CO, HCOOH and CH3OH on single crystal Pt electrodes. J Electroanalytical Chem. 1983;150:71–7.

[204] Xia XH, Iwasita T, Ge F, Vielstich W. Structural effects and reactivity in methanol oxidation on polycrystal line and single crystal platinum. Electrochim Acta. 1996;41:711–8.

[205] Housmans TH, Wonders AH, Koper MT. Structure sensitivity of methanol electrooxidation pathways on platinum: an on-line electrochemical mass spectrometry study. J Phys Chem B. 2006;110:10021–31.

[206] Chen J, Mao J, Zhao J, Ren M, Wei M. Surfactant-free platinum nanocubes with greatly enhanced activity towards methanol/ethanol electrooxidation. RSC Adv. 2014;4:28832–5.

[207] Arjona N, Guerra-Balcázar M, Ortiz-Frade L, Osorio-Monreal G, Álvarez-Contreras L, Ledesma-García J, et al. Electrocatalytic activity of well-defined and homogeneous cubic-shaped Pd nanoparticles. J Mater Chem. 2013;1:15524–9.

[208] Kannan P, Maiyalagan T, Opallo M. One-pot synthesis of chain-like palladium nanocubes and their enhanced electrocatalytic activity for fuel-cell applications. Nano Energy. 2013;2:677–87.

[209] Qin Y-L, Zhang X-B, Wang J, Wang L-M. Rapid and shape-controlled synthesis of “clean” star-like and concave Pd nanocrystallites and their high performance toward methanol oxidation. J Mater Chem. 2012;22:14861–3.

[210] Waszczuk P, Solla-Gullon J, Kim H-S, Tong YY, Montiel V, Aldaz A, et al. Methanol electrooxidation on platinum/ruthenium nanoparticle catalysts. J Catal. 2001;203:1–6.

[211] Maillard F, Lu G-Q, Wieckowski A, Stimming U. Ru-decorated Pt surfaces as model fuel cell electrocatalysts for CO electrooxidation. J Phys Chem B. 2005;109:16230–43.

[212] Liu H-X, Tian N, Brandon MP, Zhou Z-Y, Lin J-L, Hardacre C, et al. Tetrahexahedral Pt nanocrystal catalysts decorated with ru adatoms and their enhanced activity in methanol electrooxidation. ACS Catal. 2012;2:708–15.

[213] Huang L, Zhang X, Wang Q, Han Y, Fang Y, Dong S. Shape-control of Pt–ru nanocrystals: tuning surface structure for enhanced electrocatalytic methanol oxidation. J Am Chem Soc. 2018;140:1142–7.

[214] Chen X, Cai Z, Chen X, Oyama M. Synthesis of bimetallic PtPd nanocubes on graphene with N,N-dimethylformamide and their direct use for methanol electrocatalytic oxidation. Carbon. 2014;66:387–94.

[215] Yin AX, Min XQ, Zhang YW, Yan CH. Shape-selective synthesis and facet-dependent enhanced electrocatalytic activity and durability of monodisperse Sub-10 nm Pt-Pd tetrahedrons and cubes. J Am Chem Soc. 2011;133:3816–9.

[216] Lee Y-W, Ko AR, Han S-B, Kim H-S, Park K-W. Synthesis of octahedral Pt-Pd alloy nanoparticles for improved catalytic activity and stability in methanol electrooxidation. Phys Chem Chem Phys. 2011;13:5569–72.

[217] Yin A-X, Min X-Q, Zhu W, Wu H-S, Zhang Y-W, Yan C-H. Multiply twinned Pt-Pd nanoicosahedrons as highly active electrocatalysts for methanol oxidation. Chem Commun. 2012;48:543–5.

[218] Zhan F, Bian T, Zhao W, Zhang H, Jin M, Yang D. Facile synthesis of Pd-Pt alloy concave nanocubes with high-index facets as electrocatalysts for methanol oxidation. Cryst Eng Comm. 2014;16:2411–6.

[219] Zhang J, Xi C, Feng C, Xia H, Wang D, Tao X. High yield seedless synthesis of high-quality gold nanocrystals with various shapes. Langmuir. 2014;30:2480–9.

[220] Venkatasubramanian R, He J, Johnson MW, Stern I, Kim DH, Pesika NS. Additive-mediated electrochemical synthesis of platelike copper crystals for methanol electrooxidation. Langmuir. 2013;29:13135–9.

[221] Qi Y, Bian T, Choi S-I, Jiang Y, Jin C, Fu M, et al. Kinetically controlled synthesis of Pt-Cu alloy concave nanocubes with high-index facets for methanol electro-oxidation. Chem Commun. 2014;50:560–2.

[222] Yin A-X, Min X-Q, Zhu W, Liu W-C, Zhang Y-W, Yan C-H. Pt-Cu and Pt-Pd-Cu concave nanocubes with high-index facets and superior electrocatalytic activity. Chem – Eur J. 2012;18:777–82.

[223] Luo X, Liu Y, Zhang H, Yang B. Shape-selective synthesis and facet-dependent electrocatalytic activity of CoPt3 nanocrystals. Cryst Eng Comm. 2012;14:3359–62.

[224] Kang Y, Pyo JB, Ye X, Gordon TR, Murray CB. Synthesis, shape control, and methanol electro-oxidation properties of Pt-Zn alloy and Pt 3Zn intermetallic nanocrystals. ACS Nano. 2012;6:5642–7.

[225] Zhang N, Bu L, Guo S, Guo J, Huang X. Screw thread-like platinum–copper nanowires bounded with high-index facets for efficient electrocatalysis. Nano Lett. 2016;16:5037–43.

[226] Du H, Luo S, Wang K, Tang M, Sriphathoorat R, Jin Y, et al. High-quality and deeply excavated Pt_3Co nanocubes as efficient catalysts for liquid fuel electrooxidation. Chem Mater. 2017;29:9613–7.

[227] Chen Q, Cao Z, Du G, Kuang Q, Huang J, Xie Z, et al. Excavated octahedral Pt-Co alloy nanocrystals built with ultrathin nanosheets as superior multifunctional electrocatalysts for energy conversion applications. Nano Energy. 2017;39:582–9.

[228] Sun X, Huang B, Cui X, Feng BE, Huang X. Platinum–copper rhombic dodecahedral nanoframes with tunable channels as efficient bifunctional electrocatalysts for fuel-cell reactions. Chem Cat Chem. 2018;10:931–5.

[229] Li J, Rong H, Tong X, Wang P, Chen T, Wang Z. Platinum–silver alloyed octahedral nanocrystals as electrocatalyst for methanol oxidation reaction. J Colloid Interface Sci. 2018;513:251–7.

[230] Tang J-X, Chen Q-S, You L-X, Liao H-G, Sun S-G, Zhou S-G, et al. Screw-like PdPt nanowires as highly efficient electrocatalysts for methanol and ethylene glycol oxidation. J Mater Chem. 2018;6:2327–36.

[231] Li C, Liu T, He T, Ni B, Yuan Q, Wang X. Composition-driven shape evolution to Cu-rich PtCu octahedral alloy nanocrystals as superior bifunctional catalysts for methanol oxidation and oxygen reduction reaction. Nanoscale. 2018;10:4670–4.

[232] Colmati F, Tremiliosi-Filho G, Gonzalez ER, Berná A, Herrero E, Feliu JM. Surface structure effects on the electrochemical oxidation of ethanol on platinum single crystal electrodes. Faraday Discuss. 2009;140:379–97.

[233] Koper MT, Lai SC, Herrero E. Mechanisms of the oxidation of carbon monoxide and small organic molecules at metal electrodes in fuel cell catalysis, a surface science approach. Fuel Cell Catalysis: A Surface Science Approach. In: Koper MT, editor. John Wiley & Sons, 2009:159–208.

[234] Busó-Rogero C, Herrero E, Feliu JM. Ethanol oxidation on pt single-crystal electrodes: surface-structure effects in alkaline medium. Chem Phys Chem. 2014;15:2019–28.

[235] Wei L, Zhou ZY, Chen SP, Xu CD, Su D, Schuster ME, et al. Electrochemically shape-controlled synthesis in deep eutectic solvents: triambic icosahedral platinum nanocrystals with high-index facets and their enhanced catalytic activity. Chem Commun. 2013;49:11152–4.

[236] Zhang L, Chen D, Jiang Z, Zhang J, Xie S, Kuang Q, et al. Facile syntheses and enhanced electrocatalytic activities of Pt nanocrystals with {hkk} high-index surfaces. Nano Res. 2012;5:181–9.

[237] Zhou ZY, Shang SJ, Tian N, Wu BH, Zheng NF, Xu BB, et al. Shape transformation from Pt nanocubes to tetrahexahedra with size near 10 nm. Electrochem commun. 2012;22:61–4.

[238] Buso-Rogero C, Grozovski V, Vidal-Iglesias FJ, Solla-Gullon J, Herrero E, Feliu JM. Surface structure and anion effects in the oxidation of ethanol on platinum nanoparticles. J Mater Chem. 2013;1:7068–76.

[239] Busó-Rogero C, Solla-Gullón J, Vidal-Iglesias FJ, Herrero E, Feliu JM. Oxidation of ethanol on platinum nanoparticles: surface structure and aggregation effects in alkaline medium. J Solid State Electrochem. 2016;20:1095–106.

[240] Busó-Rogero C, Brimaud S, Solla-Gullón J, Vidal-Iglesias FJ, Herrero E, Behm RJ, et al. Ethanol oxidation on shape-controlled platinum nanoparticles at different pHs: A combined in situ IR spectroscopy and online mass spectrometry study. J Electroanalytical Chem. 2016;763:116–24.

[241] Zhang J, Zhang L, Xie S, Kuang Q, Han X, Xie Z, et al. Synthesis of concave palladium nanocubes with high-index surfaces and high electrocatalytic activities. Chem Eur J. 2011;17:9915–9.

[242] Yu N-F, Tian N, Zhou Z-Y, Huang L, Xiao J, Wen Y-H, et al. Electrochemical synthesis of tetrahexahedral rhodium nanocrystals with extraordinarily high surface energy and high electrocatalytic activity. Angew Chem Int Ed. 2014;53:5097–101.

[243] Chen X, Cai Z, Chen X, Oyama M. Green synthesis of graphene-PtPd alloy nanoparticles with high electrocatalytic performance for ethanol oxidation. J Mater Chem. 2014;2:315–20.

[244] Rao L, Jiang Y-X, Zhang B-W, Cai Y-R, Sun S-G. High activity of cubic PtRh alloys supported on graphene towards ethanol electrooxidation. Phys Chem Chem Phys. 2014;16:13662–71.

[245] Hong JW, Lee YW, Kim M, Kang SW, Han SW. One-pot synthesis and electrocatalytic activity of octapodal Au-Pd nanoparticles. Chem Commun. 2011;47:2553–5. (Cambridge, United Kingdom).

[246] Zhang J, Hou C, Huang H, Zhang L, Jiang Z, Chen G, et al. Surfactant-concentration-dependent shape evolution of Au–pd alloy nanocrystals from rhombic dodecahedron to trisoctahedron and hexoctahedron. Small. 2013;9:538–44.

[247] Rizo R, Arán-Ais RM, Padgett E, Muller DA, Lázaro MJ, Solla-Gullón J, et al. Pt-richcore/Sn-richsubsurface/Ptskin nanocubes as highly active and stable electrocatalysts for the ethanol oxidation reaction. J Am Chem Soc. 2018;140:3791–7.

[248] Erini N, Beermann V, Gocyla M, Gliech M, Heggen M, Dunin-Borkowski RE, et al. The effect of surface site ensembles on the activity and selectivity of ethanol electrooxidation by octahedral PtNiRh nanoparticles. Angew Chem Int Ed. 2017;56:6533–8.

[249] Wang P, Lin X, Yang B, Jin JM, Hardacre C, Yu NF, et al. Activity enhancement of tetrahexahedral Pd nanocrystals by Bi decoration towards ethanol electrooxidation in alkaline media. Electrochim Acta. 2015;162:290–9.

[250] Busó-Rogero C, Solla-Gullón J, Vidal-Iglesias FJ, Herrero E, Feliu JM. Adatom modified shape-controlled platinum nanoparticles towards ethanol oxidation. Electrochim Acta. 2016;196:270–9.

[251] Xing W, Yin G, Zhang J. Rotating electrode methods and oxygen reduction electrocatalysts. Elsevier Science, 2014.

[252] Katsounaros I, Cherevko S, Zeradjanin AR, Mayrhofer KJ. Oxygen electrochemistry as a cornerstone for sustainable energy conversion. Angew Chem Int Ed. 2014;53:102–21.

[253] Guo S, Zhang S, Sun S. Tuning nanoparticle catalysis for the oxygen reduction reaction. Angew Chem Int Ed. 2013;52:8526–44.

[254] Lee J, Jeong B, Ocon JD. Oxygen electrocatalysis in chemical energy conversion and storage technologies. Curr Appl Phys. 2013;13:309–21.

[255] Wu J, Yang H. Platinum-based oxygen reduction electrocatalysts. Acc Chem Res. 2013;46:1848–57.

[256] Maciá MD, Campina JM, Herrero E, Feliu JM. On the kinetics of oxygen reduction on platinum stepped surfaces in acidic media. J Electroanalytical Chem. 2004;564:141–50.

[257] Kuzume A, Herrero E, Feliu JM. Oxygen reduction on stepped platinum surfaces in acidic media. J Electroanalytical Chem. 2007;599:333–43.

[258] Gómez-Marín AM, Rizo R, Feliu JM. Oxygen reduction reaction at Pt single crystals: a critical overview. Catalysis Sci Technol. 2014;4:1685–98.

[259] Bandarenka AS, Hansen HA, Rossmeisl J, Stephens IE. Elucidating the activity of stepped Pt single crystals for oxygen reduction. Phys Chem Chem Phys. 2014;16:13625–9.

[260] Briega-Martos V, Herrero E, Feliu JM. Effect of pH and water structure on the oxygen reduction reaction on platinum electrodes. Electrochim Acta. 2017;241:497–509.

[261] Inaba M, Ando M, Hatanaka A, Nomoto A, Matsuzawa K, Tasaka A, et al. Controlled growth and shape formation of platinum nanoparticles and their electrochemical properties. Electrochim Acta. 2006;52:1632–8.

[262] Sanchez-Sanchez CM, Solla-Gullon J, Vidal-Iglesias FJ, Aldaz A, Montiel V, Herrero E. Imaging structure sensitive catalysis on different shape-controlled platinum nanoparticles. J Am Chem Soc. 2010;132:5622–4.

[263] Tripković V, Cerri I, Bligaard T, Rossmeisl J. The influence of particle shape and size on the activity of platinum nanoparticles for oxygen reduction reaction: A density functional theory study. Catal Lett. 2014;144:380–8.

[264] Xiao L, Zhuang L, Liu Y, Lu J, Abruña HD. Activating Pd by morphology tailoring for oxygen reduction. J Am Chem Soc. 2008;131:602–8.

[265] Shao M, Yu T, Odell JH, Jin M, Xia Y. Structural dependence of oxygen reduction reaction on palladium nanocrystals. Chem Commun. 2011;47:6566–8.

[266] Lee C-L, Chiou H-P, Liu C-R. Palladium nanocubes enclosed by (100) planes as electrocatalyst for alkaline oxygen electroreduction. Int J Hydrogen Energy. 2012;37:3993–7.

[267] Zhang H, Jin M, Xiong Y, Lim B, Xia Y. Shape-controlled synthesis of Pd nanocrystals and their catalytic applications. Acc Chem Res. 2012;46:1783–94.

[268] Shao M. Palladium-based electrocatalysts for oxygen reduction reaction in electrocatalysis in fuel cells, vol. 9. Lecture Notes in Energy Shao M. editor. Springer, 2013:513–31.

[269] Lim B, Jiang M, Camargo PH, Cho EC, Tao J, Lu X, et al. Pd-Pt bimetallic nanodendrites with high activity for oxygen reduction. Science. 2009;324:1302–5.

[270] Oezaslan M, Hasché F, Strasser P. Pt-based core-shell catalyst architectures for oxygen fuel cell electrodes. J Phys Chem Lett. 2013;4:3273–91.

[271] Gan L, Cui C, Rudi S, Strasser P. Core-shell and nanoporous particle architectures and their effect on the activity and stability of Pt ORR electrocatalysts. Top Catal. 2014;57:236–44.

[272] Li D, Wang C, Strmcnik DS, Tripkovic DV, Sun X, Kang Y, et al. Functional links between Pt single crystal morphology and nanoparticles with different size and shape: the oxygen reduction reaction case. Energy Environ Sci. 2014.

[273] Stamenkovic VR, Fowler B, Mun BS, Wang GF, Ross PN, Lucas CA, et al. Improved oxygen reduction activity on $Pt_3Ni(111)$ via increased surface site availability. Science. 2007;315:493–7.

[274] Gasteiger HA, Markovic NM. Just a dream or future reality? Science. 2009;324:48–9.

[275] Zhang J, Yang H, Fang J, Zou S. Synthesis and oxygen reduction activity of shape-controlled Pt_3Ni nanopolyhedra. Nano Lett. 2010;10:638–44.

[276] Strasser P. Catalysts by platonic design. Science. 2015;349:379–80.

[277] Mistry H, Varela AS, Kühl S, Strasser P, Cuenya BR. Nanostructured electrocatalysts with tunable activity and selectivity. Nat Rev Mater. 2016;1. Article number: 16009. DOI: 10.1038/natrevmats.2016.9.

[278] Hori Y, Murata A, Takahashi R. Formation of hydrocarbons in the electrochemical reduction of carbon dioxide at a copper electrode in aqueous solution. J Chem Soc, Faraday Trans I: Phys Chem Condens Phases. 1989;85:2309–26.

[279] Kortlever R, Shen J, Schouten KJ, Calle-Vallejo F, Koper MT. Catalysts and reaction pathways for the electrochemical reduction of carbon dioxide. J Phys Chem Lett. 2015;6:4073–82.

[280] Gupta N, Gattrell M, Macdougall B. Calculation for the cathode surface concentrations in the electrochemical reduction of CO_2 in $KHCO_3$ solutions. J Appl Electrochemistry. 2006;36:161–72.

[281] Varela AS, Ju W, Reier T, Strasser P. Tuning the catalytic activity and selectivity of Cu for CO_2 eletroreduction in the presence of halides. ACS Catal. 2016;6:2136–44.

[282] Varela AS, Kroschel M, Reier T, Strasser P. Controlling the selectivity of CO_2 electroreduction on copper: the effect of the electrolyte concentration and the importance of the local pH. Catalysis Today. 2016;260:8–13.

[283] Azuma M, Hashimoto K, Hiramoto M, Watanabeand M, Sakata T. Electrochemical reduction of carbon dioxide on various metal electrodes in low-temperature aqueous $KHCO_3$ media. J Electrochem Soc. 1990;137:1772–8.

[284] Hori Y, Wakebe H, Tsukamoto T, Koga O. Electrocatalytic process of CO selectivity in electrochemical reduction of CO_2 at metal electrodes in aqueous media. Electrochim Acta. 1994;39:1833–9.

[285] Hori Y. Electrochemical CO_2 reduction on metal electrodes. In: Modern aspects of electrochemistry, vol. 42. New York: Springer, 2008:89–189.

[286] Durand WJ, Peterson AA, Studt F, Abild-Pedersen F, Nørskov JK. Structure effects on the energetics of the electrochemical reduction of CO_2 by copper surfaces. Surf Sci. 2011;605(15-16:1354–9.

[287] Kuhl KP, Hatsukade T, Cave ER, Abram DN, Kibsgaard J, Jaramillo TF. Electrocatalytic conversion of carbon dioxide to methane and methanol on transition metal surfaces. J Am Chem Soc. 2014;136:14107–13.

[288] Qiao J, Liu Y, Zhan J. Electrochemical reduction of carbon dioxide: fundamentals and technologies. CRC Press, Taylor and Francis Group, 2016.

[289] Kuhl KP, Cave ER, Abram DN, Jaramillo TF. New insights into the electrochemical reduction of carbon dioxide on metallic copper surfaces. Energy Environ Sci. 2012;5:7050–9.

[290] Reske R, Mistry H, Behafarid F, Cuenya BR, Strasser P. Particle size effects in the catalytic electroreduction of CO_2 on Cu nanoparticles. J Am Chem Soc. 2014;136:6978–86.

[291] Kas R, Kortlever R, Milbrat A, Koper MT, Mul G, Baltrusaitis J. Electrochemical CO_2 reduction on Cu_2O-derived copper nanoparticles: controlling the catalytic selectivity of hydrocarbons. Phys Chem Chem Phys. 2014;16:12194–201.

[292] Huang Y, Handoko AD, Hirunsit P, Yeo BS. Electrochemical reduction of CO_2 using copper single-crystal surfaces: effects of CO* coverage on the selective formation of ethylene. ACS Catal. 2017;7:1749–1756.

[293] Chen CS, Handoko AD, Wan JH, Ma L, Ren D, Yeo BS. Stable and selective electrochemical reduction of carbon dioxide to ethylene on copper mesocrystals. Catal Sci Technol. 2015;5: 161–8.

[294] Roberts FS, Kuhl KP, Nilsson A. High selectivity for ethylene from carbon dioxide reduction over copper nanocube electrocatalysts. Angew Chem Int Ed. 2015;54:5179–82.

[295] Eilert A, Roberts FS, Friebel D, Nilsson A. Formation of copper catalysts for CO_2 reduction with high ethylene/methane product ratio investigated with in situ X ray absorption spectroscopy. J Phys Chem Lett. 2016;7:1466–70.

[296] Kwon Y, Lum Y, Clark EL, Ager JW, Bell AT. CO_2 electroreduction with enhanced ethylene and ethanol selectivity by nanostructuring polycrystalline copper. Chem Electro Chem. 2016;3:1012–9.

[297] Gao D, Zegkinoglou I, Divins NJ, Scholten F, Sinev I, Grosse P, et al. Plasma-activated copper nanocube catalysts for efficient carbon dioxide electroreduction to hydrocarbons and alcohols. ACS Nano. 2017;11:4825–31.

[298] Loiudice A, Lobaccaro P, Kamali EA, Thao T, Huang BH, Ager JW, et al. Tailoring copper nanocrystals towards C2 products in electrochemical CO_2 reduction. Angew Chem Int Ed. 2016;55:5789–92.

[299] Jeon HS, Kunze S, Scholten F, Cuenya BR. Prism-shaped Cu nanocatalysts for electrochemical CO_2 reduction to ethylene. ACS Catal. 2018;8:531–5.

[300] Ma M, Djanashvili K, Smith WA. Selective electrochemical reduction of CO_2 to CO on CuO-derived Cu nanowires. Phys Chem Chem Phys. 2015;17:20861–7.

[301] Raciti D, Livi KJ, Wang C. Highly dense Cu nanowires for low-overpotential CO_2 reduction. NanoLett. 2015;15:6829–35.

[302] Ma M, Djanashvili K, Smith WA. Controllable hydrocarbon formation from the electrochemical reduction of CO_2 over Cu nanowire arrays. 2016;55:6680–4.

[303] Chung J, Won DH, Koh J, Kim E-H, Woo SI. Hierarchical Cu pillar electrodes for electrochemical CO_2 reduction to formic acid with low overpotential. Phys Chem Chem Phys. 2016;18:6252–8.

[304] Sen S, Liu D, Palmore GT. Electrochemical reduction of CO_2 at copper nanofoams. ACS Catal. 2014;4:3091–5.

[305] Liu S, Tao H, Zeng L, Liu Q, Xu Z, Liu Q, et al. Shape-dependent electrocatalytic reduction of CO_2 to CO on triangular silver nanoplates. J Am Chem Soc. 2017;139:2160–3.

[306] Peng X, Karakalos SG, Mustain WE. Preferentially oriented Ag nanocrystals with extremely high activity and faradaic efficiency for CO_2 electrochemical reduction to CO. ACS Appl Mater Interfaces. 2018;10:1734–42.

[307] Hsieh Y-C, Senanayake SD, Zhang Y, Xu W, Polyansky DE. Effect of chloride anions on the synthesis and enhanced catalytic activity of silver nanocoral electrodes for CO_2 electroreduction. ACS Catal. 2015;5:5349–56.

[308] Lu Q, Rosen J, Zhou Y, Hutchings GS, Kimmel YC, Chen JG, et al. A selective and efficient electrocatalyst for carbon dioxide reduction. Nat Commun. 2014;5:3242.

[309] Klinkova A, De Luna P, Dinh C-T, Voznyy O, Larin EM, Kumacheva E, et al. Rational design of efficient palladium catalysts for electroreduction of carbon dioxide to formate. ACS Catal. 2016;6:8115–20.

[310] Gao D, Zhou H, Cai F, Wang J, Wang G, Bao X. Pd-Containing nanostructures for electrochemical CO_2 reduction reaction. ACS Catal. 2018;8:1510–9.

[311] Huang H, Jia H, Liu Z, Gao P, Zhao J, Luo Z, et al. Understanding of strain effects in the electrochemical reduction of CO_2: using Pd Nanostructures as an Ideal Platform. Angew Chem Int Ed. 2017;56:3594–8.

[312] Rosen J, Hutchings GS, Lu Q, Forest RV, Moore A, Jiao F. Electrodeposited Zn dendrites with enhanced CO selectivity for electrocatalytic CO_2 reduction. ACS Catal. 2015;5:4586–91.

[313] Won DH, Shin H, Koh J, Chung J, Lee HS, Kim H, et al. Highly efficient, selective, and stable CO_2 electroreduction on a hexagonal Zn catalyst. Angew Chem Int Ed. 2016;55:9297–300.

[314] Zhong H, Qiu Y, Zhang T, Li X, Zhang H, Chen X. Bismuth nanodendrites as a high performance electrocatalyst for selective conversion of CO_2 to formate. J Mater Chem. 2016;4:13746–53.

[315] Koh JH, Won DH, Eom T, Kim N-K, Jung KD, Kim H, et al. Facile CO_2 electro-reduction to formate via oxygen bidentate intermediate stabilized by high-index planes of Bi dendrite catalyst. ACS Catal. 2017;7:5071–7.

[316] Kim S, Dong WJ, Gim S, Sohn W, Park JY, Yoo CJ, et al. Shape-controlled bismuth nanoflakes as highly selective catalysts for electrochemical carbon dioxide reduction to formate. 2017;39:44–52.

[317] Zhang Z, Chi M, Veith GM, Zhang P, Lutterman DA, Rosenthal J, et al. Rational design of Bi nanoparticles for efficient electrochemical CO_2 reduction: the elucidation of size and surface condition effects. ACS Catal. 2016;6:6255–64.

[318] Zhu W, Zhang Y-J, Zhang H, Lv H, Li Q, Michalsky R, et al. Active and selective conversion of CO_2 to CO on ultrathin Au nanowires. J Am Chem Soc. 2014;136:16132–5.

[319] Back S, Yeom MS, Jung Y. Understanding the effects of Au morphology on CO_2 electrocatalysis. J Phys Chem C. 2018;122:4274–80.

[320] Lee H-E, Yang KD, Yoon SM, Ahn H-Y, Lee YY, Chang H, et al. Concave rhombic dodecahedral Au nanocatalyst with multiple high-index facets for CO_2 reduction. ACS Nano. 2015;9: 8384–93.

[321] Kim J, Song JT, Ryoo H, Kim J-G, Chung S-Y, Oh J. Morphology-controlled Au nanostructures for efficient and selective electrochemical CO_2 reduction. J Mater Chem. 2018;6:5119–28.

[322] Monzó J, Malewski Y, Kortlever R, Vidal-Iglesias FJ, Solla-Gullón J, Koper MT, et al. Enhanced electrocatalytic activity of Au@Cu core@shell nanoparticles towards CO_2 reduction. J Mater Chem. 2015;3:23690–8.

[323] Zhao X, Luo B, Long R, Wang C, Xiong Y. Composition-dependent activity of Cu–pt alloy nanocubes for electrocatalytic CO_2 reduction. J Mater Chem. 2015;3:4134–8.

[324] Zhang F-Y, Sheng T, Tian N, Liu L, Xiao C, Lu B-A, et al. Cu overlayers on tetrahexahedral Pd nanocrystals with high-index facets for CO_2 electroreduction to alcohols. Chem Commun. 2017;53:8085–8.

[325] Zhang L, Zhao Z-J, Gong J. Nanostructured materials for heterogeneous electrocatalytic CO_2 reduction and related reaction mechanisms. Angew Chem Int Ed. 2017;56:11326–53.

[326] Zhang W, Hu Y, Ma L, Zhu G, Wang Y, Xue X, et al. Progress and perspective of electrocatalytic CO_2 reduction for renewable carbonaceous fuels and chemicals. Adv Sci. 2018;5:1700275–99.

[327] Yang W, Dastafkan K, Jia C, Zhao C. Design of electrocatalyst and electrochemical cells for carbon dioxide reduction reactions. Adv Mate Technol. 2018;1700377–97.

[328] Sahu SC, Hayes AW. Toxicity of nanomaterials found in human environment: A literature review. Toxicol Res Appl. 2017;1:1–13.

[329] Handy RD, Shaw BJ. Toxic effects of nanoparticles and nanomaterials: implications for public health, risk assessment and the public perception of nanotechnology. J Health, Risk Soc. 2007;9:125–44.

[330] Buzea C, Pacheco II, Robbie K. Nanomaterials and nanoparticles: sources and toxicity. Biointerphases. 2007;2:MR17–MR71.

[331] Kaphle A, Navya PN, Umapathi A, Daima HK. Nanomaterials for agriculture, food and environment: applications, toxicity and regulation. Environ Chem Lett. 2018;16:43–58.

[332] Lee J, Mahendra S, Alvarez PJ. Nanomaterials in the construction industry: a review of their applications and environmental health and safety considerations. ACS Nano. 2010;4:3580–90.

[333] Benson JM. Safety considerations when handling metal powders. J South Afr Inst Mining Metallurgy. 2012;112:563–75.

[334] Bussy C, Ali-Boucetta H, Kostarelos K. Safety considerations for graphene: lessons learnt from carbon nanotubes. Acc Chem Res. 2013;46:692–701.

[335] Park MV, Bleeker EA, Brand W, Cassee FR, Van Elk M, Gosens I, et al. Considerations for safe innovation: the case of graphene. ACS Nano. 2017;11:9574–93.

[336] Al-Mubaddel FS, Haider S, Al-Masry WA, Al-Zeghayer Y, Imran M, Haider A, et al. Engineered nanostructure: a review of their synthesis, characterization and toxic hazard considerations. Arabian J Chem. 2017;10:S376–S388.

[337] Jeevanandam J, Barhoum A, Chan YS, Dufresne A, Danquah MK. Review on nanoparticles and nanostructured materials: history, sources, toxicity and regulations. Beilstein J Nanotechnol. 2018;9:1050–74.

[338] Lee CC, Mackay JA, Fréchet JM, Szoka FC. Designing dendrimers for biological applications. Nat Biotechnol. 2005;23:1517–26.

[339] Carlson C, Hussain SM, Schrand AM, Braydich-Stolle LK, Hess KL, Jones RL, et al. Unique cellular interaction of silver nanoparticles: size-dependent generation of reactive oxygen species. J Phys Chem B. 2008;112:13608–19.

[340] El Badawy AM, Silva RG, Morris B, Scheckel KG, Suidan MT, Tolaymat TM. Surface charge-dependent toxicity of silver nanoparticles. Environ Sci Technol. 2011;45:283–7.

[341] Albanese A, Tang PS, Chan WC. The effect of nanoparticle size, shape, and surface chemistry on biological systems. Annu Rev Biomed Eng. 2012;14:1–16.

[342] Daima HK, Towards fine-tuning the surface corona of inorganic and organic nanomaterials to control their properties at nano-bio interface, 2013, PhD thesis, School of Applied Sciences RMIT.

[343] Daima HK, Selvakannan PR, Shukla R, Bhargava SK, Bansal V. Fine-tuning the antimicrobial profile of biocompatible gold nanoparticles by sequential surface functionalization using polyoxometalates and lysine. PLoS One. 2013;8:e79676–90.

[344] Chen LQ, Fang L, Ling J, Ding CZ, Kang B, Huang CZ. Nanotoxicity of silver nanoparticles to red blood cells: size-dependent adsorption, uptake, and hemolytic activity. Chem Res Toxicol. 2015;28:501–9.

[345] Navya PN, Daima HK. Rational engineering of physicochemical properties of nanomaterials for biomedical applications with nanotoxicological perspectives. Nano Convergence. 2016;3:1–14.

Bionotes

Leticia García Cruz received her Ph.D. from University of Alicante in 2016. She is currently senior research in Institute of Electrochemistry of University of Alicante. She has over 7 years of experience in the field of development of electrocatalysts, nanoparticle synthesis, and carbon materials, for electrochemical oxidation process. Her research covers manufacture of gas diffusion electrodes, design of electrochemical reactors and optimization of electrochemical process, and ion-exchange membrane synthesis. More recently, her research is focused on the development of electrocatalysts for electrochemical reduction of CO_2.

Vicente Montiel Leguey is full professor of Physical Chemistry at the University of Alicante and current director of the Institute of Electrochemistry. His research is mainly focused on Applied Electrochemistry (electrosynthesis; wastewater treatment by electrochemical methods without and with photovoltaic energy coupling; sensors and biosensors; preparation, characterization, and use of nanoparticulated materials; and design and optimization of redox flow batteries). His experience covers the development of different electrochemical processes, from laboratory scale to pre-industrial pilot plant. Several processes have been transferred to the industry. He was President of the Electrochemistry Group of the Spanish Society of Chemistry (since 2012 to 2016). Currently, he is President of the Division of Chemistry at Alicante territory.

Jose Solla Gullón studied at the Universidad de Santiago de Compostela, and carried out his PhD at the Universidad de Alicante (awarded in 2003). Currently, he is senior researcher in the Institute of Electrochemistry at the University of Alicante. His research is focused on the synthesis, characterization, and electrocatalytic properties of size- and shape-controlled metal nanoparticles.

He Huang, Hendrik du Toit, Luca Panariello, Luca Mazzei
and Asterios Gavriilidis

4 Continuous synthesis of gold nanoparticles in micro- and millifluidic systems

Abstract: Gold nanomaterials have diverse applications ranging from healthcare and nanomedicine to analytical sciences and catalysis. Microfluidic and millifluidic reactors offer multiple advantages for their synthesis and manufacturing, including controlled or fast mixing, accurate reaction time control and excellent heat transfer. These advantages are demonstrated by reviewing gold nanoparticle synthesis strategies in flow devices. However, there are still challenges to be resolved, such as reactor fouling, particularly if robust manufacturing processes are to be developed to achieve the desired targets in terms of nanoparticle size, size distribution, surface properties, process throughput and robustness. Solutions to these challenges are more effective through a coordinated approach from chemists, engineers and physicists, which has at its core a qualitative and quantitative understanding of the synthesis processes and reactor operation. This is important as nanoparticle synthesis is complex, encompassing multiple phenomena interacting with each other, often taking place at short timescales. The proposed methodology for the development of reactors and processes is generic and contains various interconnected considerations. It aims to be a starting point towards rigorous design procedures for the robust and reproducible continuous flow synthesis of gold nanoparticles.

This article has previously been published in the journal *Physical Sciences Reviews*. Please cite as: Huang, H., du Toit, H., Panariello, L., Mazzei, L., Gavriilidis, A. Continuous synthesis of gold nanoparticles in micro- and millifluidic systems. *Physical Sciences Reviews* [Online] **2018**, 3. DOI: 10.1515/psr-2017-0119

https://doi.org/10.1515/9783110345100-004

Graphical Abstract:

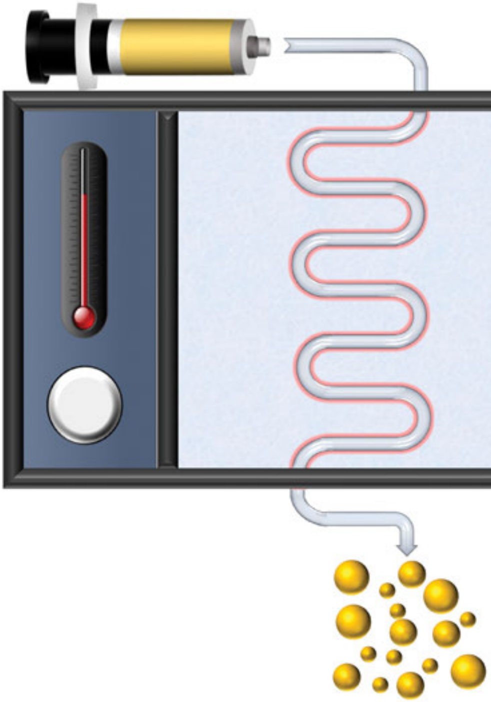

Keywords: gold nanomaterials, flow chemistry, microfluidics, microreactors, millireactors, multiphase flow

4.1 Introduction

4.1.1 Applications of gold nanoparticles

Gold nanomaterials have been a topic of intense investigation in the last few decades owing to their unique optical, chemical, biological and catalytic properties. This is due to some attractive physical characteristics, which are determined by physical parameters such as particle size, morphology, surface, crystallinity and composition. Gold nanomaterials are attracting a lot of interest in healthcare applications, analytical sciences and catalysis [1–7]. In nanomedicine, Au nanomaterials offer the potential to work on the same scale as many biological processes and cellular mechanisms. They are applied as diagnostic, imaging and therapeutic agents or a combination thereof [4, 5].

When Au nanoparticles (NPs) are illuminated, conduction band electrons on their surface are delocalized and undergo collective oscillation at the same frequency as the incident light. This phenomenon, known as localized surface plasmon resonance (LSPR), is responsible for absorption and scattering of light, which can aid their detection by optical microscopy and enhance optical contrast as well as lead to localized heating [8, 9]. The LSPR effect is sensitive to the size, shape and environment of the NPs and this allows tuning their optical properties. If analyte molecules bind to Au NPs either directly or via some linker ligands, the local refractive index changes and the plasmon absorption shifts to longer wavelengths. The former results in colour change, which makes NPs attractive for colorimetric sensors, while the latter can be detected both by LSPR extinction or the angle of reflected light and are exploited in other plasmonic sensors [5, 10]. Electric fields generated on the surface of the NPs enhance Raman signals from molecules in their vicinity. This is termed as surface enhanced Raman scattering [11]. Light absorption by very small NPs (nanoclusters) induces photoluminescence, which is affected if analyte molecules interact with the nanoclusters, either through covalent bonding or physical absorption. Fluorescence quenching is another phenomenon that occurs when fluorophores are appended onto Au NPs, and this is exploited in fluorescence resonance energy transfer assays [6, 12].

In addition to the above optical properties, Au NPs demonstrate catalytic properties, which can be tuned by particle size, surface functionality and intraparticle separation. Such properties are exploited in various electrochemical and electrocatalytic sensors. These optical, optoelectronic, electrochemical and electrocatalytic properties are utilized for detection of biomolecules, such as proteins, DNA, oligonucleotides and pathogens, but also whole cancer cells which are important for healthcare applications [6, 7, 11, 13–15]. In addition, the same properties can be applied for sensing various chemical compounds, such as heavy metal ions, toxic gases and organic compounds, which are important for environmental and safety applications [12, 16]. In Lateral Flow Assays, Au nanomaterials are conjugated with various recognition markers, such as antibodies, and implemented in paper-based devices. They offer low-cost, robust, point of care diagnostics for the detection of viruses, bacteria, biomarkers, proteins, drugs, hormones contaminants, toxins and pathogens [10, 17–21]. By conjugating the NPs to molecules that bind to cells, the above optical properties can be exploited for cellular imaging (e. g. stem cells and cancer cells). The NPs can also be used for enhancing contrast of other imaging modalities. Au NPs can enhance X-ray attenuation increasing contrast in X-ray CT imaging [6]. Au nanostructures can be functionalized by radionucleotides and hence used for PET imaging of tumours [6, 7].

In targeted drug delivery, a drug is delivered locally to the tissue of interest, leaving surrounding tissues unaffected. The drug concentration can be modulated as a function of time. This approach offers various advantages, such as decreased toxic side effects, reduced dose of drugs, increased treating efficacy and development of new therapeutic strategies extending product life cycles [22]. Drug molecules can be loaded onto the surface of Au nanostructures by direct conjugation, grafting the drugs to the capping ligand or adsorbing the drug by electrostatic interactions, van der Waals forces or hydrogen bonding. Targeting agents can be attached to Au NPs for specific uptake by tumours. The release of the drug can be achieved by thermally activated desorption and diffusion employing the selective heating ability of the Au nanostructures. To increase the amount of drug, the drug can by encapsulated in thermally responsive polymers. The stimulus for drug release can also be a change in ionic concentration [6, 7, 23].

Au nanomaterials (mainly Au nanorods, nanoshells and nanocages) have been studied for photothermal cancer therapy, which is based on their LSPR properties. They absorb and convert the photon energy into thermal energy when a laser beam irradiates them at the LSPR wavelength. Photothermal heating only occurs in the area directly surrounding the NPs, damaging cancer cells, particularly those that are more sensitive to heat. By exploiting the enhanced permeability and retention of tumours (passive targeting), or by functionalizing NPs with molecules that selectively bind to cancer cells (active targeting), NPs deliver the heat selectively to tumour sites [6, 7, 23–26]. In photodynamic cancer therapy, Au nanomaterials are used as carriers for photosensitizers, or are photosensitizers themselves. Upon specific wavelength light radiation, they produce reactive oxygen species that induce cell death [6, 7, 25]. Au nanomaterials are also attracting attention as radiosensitizers in X-ray radiotherapy. As a treatment it has the advantage of deeper penetration in tissues than the NIR light typically used for photothermal or photodynamic therapy. Au NPs absorb the X-rays and thus localize the X-ray damage by reactive free radicals and secondary electrons to tumour sites [25, 27, 28].

Even though bulk gold is inert, in the form of NPs it can display high catalytic activity for a variety of reactions. These include oxidations of olefins, alcohols and alkanes, hydrogenations, aminations and C–C coupling reactions. Au NP size as well as the material on which the particles are supported is critical for catalyst reactivity [1, 29, 30]. Supported Au NPs can catalyse important industrial reactions, such as hydrogen peroxide production, oxidative esterification of methacrolein to methyl methacrylate and hydrochlorination of acetylene to vinyl chloride monomer [31].

The performance of NPs for most of the applications presented above is affected by their size, shape and functionalization. For example, the size and shape of nanoparticle influences the LSPR shift [24]. The extinction coefficient of 5 nm Au NPs is much lower than that of larger Au NPs. When the size of Au NPs approaches the Fermi wavelength of electrons (<2 nm), molecule-like optical properties and size-dependent fluorescence appear [6, 15]. Large Au NPs have a longer electromagnetic field decay length and provide higher sensitivity; hence, they are more efficient at enhancing Raman signals [6]. Size, shape and surface chemistry affect nanoparticle circulation in the body and distribution to different organs. In general, NPs smaller than 6 nm are filtered by the kidneys, larger than 200 nm are retained by the spleen, while in the 30–200 nm range typically show better tumour accumulation.

Penetration of Au NPs through biological barriers depends on their size and surface charge [32–34]. Toxicity of NPs to cells is also size dependent, even though results are often contradictory [6, 7, 24, 35, 36]. For Au NPs used in catalysis, size critically influences their performance. Catalytic activity of Au NPs typically increases substantially as size decreases below 5 nm (e. g. carbon monoxide (CO) oxidation). However, selectivity to desired products can increase or decrease with nanoparticle size, depending on the particular reaction [37, 38].

4.1.2 Continuous synthesis of gold NPs

Since the performance of Au NPs depends on their size (and hence size distribution), shape, chemical composition and surface functionalization, controllable and repeatable processes for the synthesis of Au NPs are important to guarantee consistent performance. Most of the synthetic routes are performed in batch systems [39]. Batch processes are solution-phase synthesis techniques where reagents (precursor, reducing agent, capping agent) are mixed at controlled temperature. The precursor is reduced or decomposed generating atoms, the atoms nucleate and the nuclei grow into seeds and subsequently into NPs with desired characteristics. Batch-to-batch variations are problematic and a synthesis approach that gives uniform materials consistently is of paramount importance [40, 41]. However, if the kinetics of the synthesis processes are fast, mass and heat transfer can play an important role in the synthesis. Mass/heat transfer rates change with reactor size, limiting the control of the experimental conditions [42]. In conventional synthetic methods, the immediate addition of the reducing agent (and/or other reactants) leads to localized high concentrations (and in turn to concentration gradients) which can cause variable sizes and broad size distribution of the final particles, since these grow from nuclei produced at different times in places within the solution where the reactant concentrations are different. Such inhomogeneity can lead to coexistence of nucleation and growth, which can result in wide NP size distributions and poor control of shape and aggregation [39, 43]. Batch processes are often not amenable to scale-up, and they may not provide an appropriate balance between control of nanoparticle characteristics and productivity [39]. If promising laboratory results of Au NPs are to translate into commercial applications, larger scale reproducible manufacturing with satisfactory control of the NP desired characteristics needs to be developed [44].

Microreactors, which allow manipulating the fluid dynamics, heat transfer, and mixing at the sub-millimetre scale precisely, offer advantages in these cases. Due to the large surface-to-volume ratio and a decrease in diffusion paths, microreactors exhibit much better mixing, which plays an important role in monodisperse nanoparticle formation. In addition to this, because of the smaller volumes in microreactors, various parameters (temperature, pressure, residence time, etc.) can be controlled easily and safely, which can lead to precise control of the reaction with shorter response time [45].

The diffusive mixing in microreactors can reduce agglomeration as compared to conventional convective turbulent mixing [39]. Continuous microfluidic synthesis can make scaling to large production possible through parallel operation of multiple identical reactor units, reducing labour and time of processes [46–48]. It further allows easier automation, online monitoring of nanoparticle characteristics and use of closed loop control systems to achieve quality control [40, 49, 50]. Microfluidic systems offer the opportunity for easier integration of complex sequential processes, such as those required for the functionalization of Au NPs, which is a key step for biomedical applications [41].

Taylor dispersion in micro or millifluidic reactors can arise from the shear on the fluid caused by no-slip boundaries at the channel walls. This leads to a parabolic velocity profile, which generates a spread in the residence times of the fluid elements, and therefore of the NPs present in them, because the elements flowing near the channel axis move more quickly than those flowing near the channel walls. Taylor dispersion can increase polydispersity in channels where the residence time distribution (RTD) is wide. Fouling of the microreactors due to nanoparticle nucleation/growth/attachment on the wall material can also be an issue [51]. These disadvantages can be addressed by segmented flow microreactors, where the synthesis takes place in isolated droplets (behaving as moving batch reactors) protected by the segmenting fluid from the tubing wall [52–56]. Fouling and higher productivity can also be addressed by millifluidic systems (increasing channel dimension by an order of magnitude). Moreover, these devices are often cheaper and easier to clean, if the requirements for mass and heat transfer are not severe [41].

There have been various reviews on the preparation methods of Au NPs mostly from the viewpoint of chemistry routes [1, 34, 57–60]. Reviews in the use of microreactors for the synthesis of various types of inorganic NPs have been presented [39, 41–43, 50, 52, 53, 61–64] and some focus on Au NP synthesis using microfluidics [45, 65]. In this chapter, we aim at reviewing the current state of the art in flow synthesis of Au NPs from a reactor engineering point of view, highlighting the inherent differences of flow reactors from conventional batch reactors, as well as potential issues that may be encountered during the development of continuous processes for the production of this class of materials. This culminates to a design methodology that highlights key steps for the development of a manufacturing flow system for the synthesis of Au NPs. The proposed design procedure is based on a series of interconnected steps that emphasize the importance of an interdisciplinary effort between chemists, engineers and physicists, and is summarized in 10 main design rules.

4.2 Requirements for quality-by-design synthesis

Currently, the design of nanoparticle reactors strongly relies on a trial-and-error experimental approach, occasionally guided by design-of-experiments methods. Mathematical models for the syntheses based on first principles are rarely used to design and optimize these reactors. This is in stark contrast with the design methodology adopted in the manufacturing of more conventional products, for which the principles, methods and models of reaction engineering (or more advanced approaches) are commonly employed. This *modus operandi* prevents, or at least complicates, the attainment of *quality-by-design*, where one aims to build quality into a product, instead of testing quality from a product. Theoretical models for particle syntheses would allow rationalizing nanoparticle reactor design and developing systems able to deliver products with the desired characteristics in a more robust and cost-effective manner, whilst building valuable process knowledge.

Due to the complexity of nanoparticle syntheses, which involve many physical and chemical concurrent phenomena, developing models for these systems is truly challenging. In addition to an accurate mechanistic description of a specific synthesis method, model development necessitates the knowledge of the kinetics of the reactions and processes (such as particle nucleation, aggregation and growth) involved in the synthesis as well as of the fluid dynamics in the reactor, which affects heat and mass transfer. Obtaining accurate kinetic information is particularly critical, but at the same time particularly difficult.

4.2.1 Characterization and kinetics of nanoparticle synthesis

In this section we introduce experimental techniques that are useful for the characterization of gold NPs. We first comment on the most commonly employed techniques, and then we focus on techniques useful for the quantification of NPs synthesis kinetics. This last point is of relevance for the development of flow reactors, as an optimized reactor design procedure is based on the knowledge of reaction kinetics [66]. In the last paragraphs we discuss the possibilities offered by flow systems for *in situ* synthesis monitoring, appealing features for both kinetics studies and process control.

Key parameters of interest in nanoparticle syntheses are product concentration (as in “conventional” chemical syntheses), as well as particle size and particle size distribution (PSD). Measurement of unconverted precursor or product yield is important too, not only for improved process performance but also because unconsumed precursor can keep reacting during storage if it is not removed. Other important parameters, which require at least qualitative information, include particle shape and surface properties. Hence, more than one experimental technique is generally required to fully describe nanoparticle synthesis processes.

Electron [67, 68] and scanning probe [69] microscopy have been widely employed to characterize particle size and shape. Au NP sizes and size distributions can be measured by dynamic light scattering [70], which however requires relatively monodisperse samples to render accurate measurements, and by differential centrifugation sedimentation, down to 2 nm in size [71]. For sub-2 nm gold NPs, whose structure could be altered by conventional techniques, such as transmission electron microscopy, size can be measured by mass spectroscopy [72]. Average particle size and PSD can be measured via small angle X-ray scattering (SAXS) with a very low detection limit [73]. This technique also allows *in situ* measurements of the particle size evolution during the synthesis with resolution down to 2 nm, but synchrotron radiation is required [74–78]. SAXS also allows evaluating nanoparticle volume fraction in solution. Nanoparticle crystal structure and crystallite size can be determined by means of X-ray diffraction [79].

Gold concentration can be measured by means of several techniques. Very low detection limits can be achieved with inductively coupled plasma mass spectroscopy (ICP-MS) [80], which, with recent advances, can now also be used to determine NP number concentration and number size distribution (Single Particle ICP-MS) [81]. Voltammetric methods have been employed to determine gold concentration as well as NP number concentration [82–84]. After dissolution in strong acids, the elemental gold concentration (and in some cases the packing density of ligands) can be measured by means of atomic absorption spectroscopy [85] or optical emission spectroscopy [86–88]. Gold elemental analysis can also be performed with neutron activation analysis [89]; however, this requires complex instrumentation.

The oxidation states of gold can be obtained via X-ray photoelectron spectroscopy (XPS) [90] and X-ray absorption near-edge spectroscopy (XANES) [76–78, 91, 92]. Extended X-ray absorption spectroscopy fine structure can be used to gather information on crystal lattice properties and how these are affected by ligands [93]. The interactions between ligands and the gold NP surface can be studied by XPS [90, 94] and Fourier transform infrared spectroscopy [94, 95].

A simple yet powerful tool used for gold nanoparticle characterization is UV–vis spectroscopy. This technique offers the major advantage of requiring relatively cheap benchtop instrumentation, and is suitable for both *ex situ* and *in situ* measurements, which makes it very attractive for kinetic and mechanistic studies [74, 96–98]. Studies to link both particle size and Au(0) concentration to the solution UV–vis spectrum have been reported in the literature, where either the position of the LSPR and the extinction at this wavelength [88, 100] or the ratio between the extinctions at the LSPR wavelength and that at 450 nm [100] have been used. Hendel et al. demonstrated that the UV–vis absorbance at 400 nm (Abs_{400}) can be used to determine the Au(0)· concentration in NP solutions, but pointed out that particle size, surface modification, or oxidation state can affect the measurement [101]. The type of ligands and the dielectric properties of the surrounding medium also significantly affect the UV–vis spectra; hence, this technique has to be correctly calibrated considering the ligands and solvent employed in the synthesis [102, 103]. UV–vis spectra can also be used to analyse the speciation of $HAuCl_4$ [97, 104], the most common gold precursor used for Au NP synthesis. Finally, this technique also allows assessing the quality of the gold precursor employed, whose spectra depend on its “age” and purity [73].

From a reaction engineering point of view, experimental techniques that are able to provide time-resolved data during the synthesis are of great interest, since they permit quantifying reaction kinetics, which is an essential element for reactor design. Determining kinetics and rate laws is a major challenge in the field of nanoscience, both from an experimental and a theoretical standpoint, because these syntheses involve many concurrent physical and chemical phenomena belonging to synthetic chemistry, colloidal science and particle technology. Experimentally, a complete description of the kinetics of these processes requires several techniques as well as a wide scientific background for the correct interpretation of the data gathered.

Generally, the theoretical framework used to describe the kinetics of the nucleation process in nanoparticle syntheses is the classic nucleation theory, developed by Becker and Doring [105] and later extended by Lamer and co-workers [107]. However, several studies demonstrated that many nanoparticle syntheses are not well described by this theory [107, 108]. In this sense, Zeng and Oxtoby stated that "nucleation theory is one of the few areas of science in which agreement of predicted and measured rates to within several orders of magnitude is considered as major success" [109]. Xia et al. appropriately described the current state of progress in the study of nanoparticle formation kinetics, stating that "at the current stage of development, it is not an exaggeration to say that the chemical synthesis of metal nanocrystals (as well as for other solid materials) remains an art rather than a science" [110]. Along the same line, Polte recently pointed out that "the main reason for this lack of knowledge was the absence of reliable experimental information about the particle growth process, in particular of the particle size and concentration during the growth process" [111].

Some of the characterization methods presented above have been used *in situ* in batch systems to obtain mechanistic/kinetic information. Polte and co-workers [75, 76, 78, 97], employed SAXS combined with XANES to provide time-resolved average particle size, relative PSD standard deviation and gold oxidation state for the classical Turkevich synthesis in a wide parameter space. Abecassis et al. employed similar techniques to study the evolution of the PSD and of the Au oxidation state during different $NaBH_4$-based synthetic routes [74, 77]. Comparison between the total amount of Au(0) present in the solution (obtained by XANES) and the amount of Au(0) inside the NPs (obtained from SAXS) showed that a measurable amount of Au (0) existed transiently as monomers, suggesting burst nanoparticle nucleation. They further showed that ligands affect reduction kinetics and nucleation rate, and thus indirectly also NP growth. A model including reduction kinetics, nucleation and growth rates enabled the fitting of NP size and concentration time evolution. UV–vis spectroscopy was used by Hendel et al. to track the reduction of Au(III) to Au(0) in real time by measuring the Abs_{400} during the synthesis [101]. The data acquired via UV–vis spectroscopy were consistent with the experimental observations obtained by SAXS. Luty-Blocho et al. and Paclawski et al. used UV–vis spectroscopy and dynamic light scattering [112, 113] to quantitatively study the kinetics of the $HAuCl_4$ to $HAuCl_{4-x}(OH)_x$ reaction, which plays an important role in several Au NP synthetic routes [97]. A rate law for Au NP formation, according to a Finke-Watzky model (slow nucleation, fast autocatalytic surface growth) [108], was formulated and utilized to design a microfluidic reactor system and select suitable operating conditions for the synthesis of Au NPs by glucose reduction. Georgiev et al. [69] studied the kinetics of the gold NP synthesis by the Turkevich method employing time-resolved UV–vis spectroscopy, as well as *ex situ* atomic force microscopy and obtained rate constants for a Finke-Watzky model that were similar for both techniques. However, *ex situ* measurements may give "drying" artefacts during the sample preparation, affecting the precision of the data acquired. As a consequence, the development of time-resolved *in situ* measurement techniques is one of the bottlenecks for the acquisition of reliable kinetic data. In this regard, interesting opportunities are offered by liquid phase transmission electron microscopy [114, 115] and cryo-transmission electron microscopy [116].

Flow systems allow also *in situ* characterization, with the added advantage that, since real time is replaced by space time (i. e. reactor location), information at very short reaction times can be obtained. In addition, in-line monitoring by optical techniques can be easily implemented. This feature is attractive, as it opens up possibilities in reaction kinetic studies, also enabling simple implementation of process control loops. For instance, McKenzie et al. combined SAXS and UV–vis spectroscopy in a microscale flow system (Figure 4.1a) for *in situ* monitoring of PSD and UV–vis absorbance of sub-5 nm gold NPs at different concentrations, with results that correlated well with *ex situ* TEM and UV–vis measurements [117]. Watt studied the effect of seed age on gold nanorods formation by using a microfluidic system with in-line UV–vis–NIR spectroscopy [118], which was combined with *ex situ* SAXS measurements to observe the change of the nanoparticle population during aging. However, UV–vis is not suitable if there is no LSPR band [119]. Polte et al. employed *in situ* SAXS in combination with XANES to monitor the synthesis of Au NPs with size between 0.8 and 2 nm (Figure 4.1b) [76]. A static micromixer was used to provide homogeneous mixing between gold precursor and $NaBH_4$, and then the products were detected by SAXS in a flow cell. As $NaBH_4$ is quite a strong reducing agent, the reaction finished within 100 ms and increasing residence time did not change the size. The work suggested a two-step mechanism of gold nanoparticle formation: a rapid conversion of the ionic gold precursor into metallic gold nuclei, followed by particle growth via coalescence of smaller entities. Similarly, Tofighi et al. used *in situ* XANES assisted by a microfluidic silicon chip to study the early reaction stages of the polyvinyl pyrrolidone (PVP)-stabilized Au NP synthesis by $NaBH_4$ reduction (Figure 4.1c) [120]. The chip allowed the beam focusing on different positions along the microchannel to track the reaction. It was observed all the gold ions were reduced to Au(0) · within the first 10 ms. Yue et al. described how to monitor the synthetic process of Au NPs with in-line UV–vis in segmented flow by a cross-type flow-through cell (Figure 4.1d) [121]. However, the main difficulty to apply in-line UV–vis on a segmented flow system is that the detection limit could be affected by the background from the carrier fluid and reflection/scattering from the

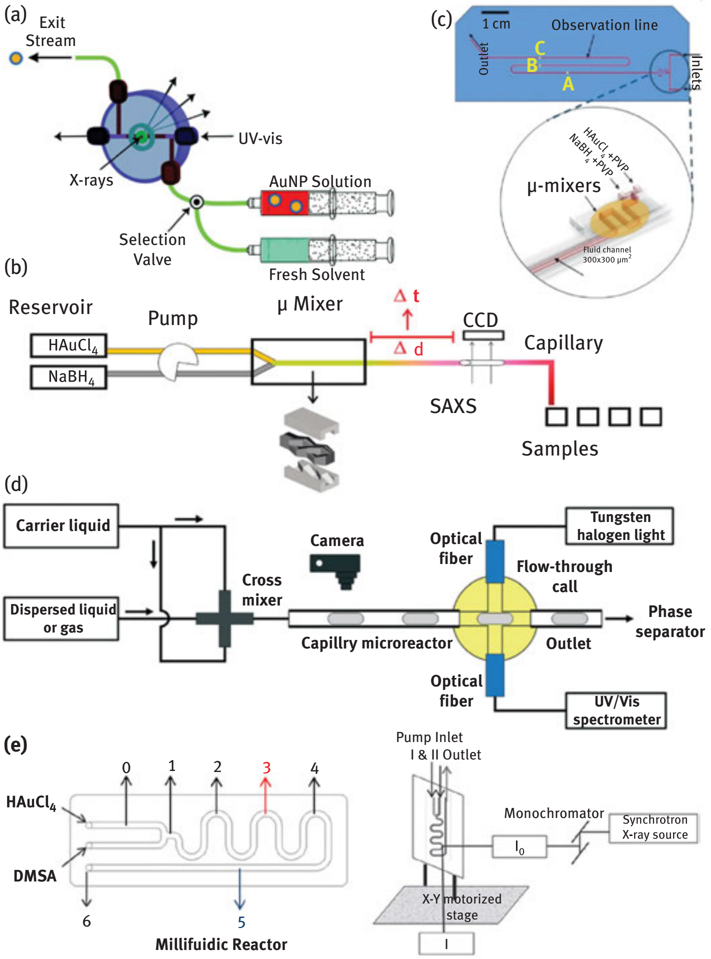

Figure 4.1: (a) Schematic of microscale flow system with a specially designed cell for *in situ* SAXS and UV–vis measurement of nanoparticle size distribution (reprinted with permission from Ref. [117]. Copyright 2010, American Chemical Society). (b) Experimental setup with flow cell for *in situ* SAXS (reprinted with permission from Ref. [76]. Copyright 2010, American Chemical Society). (c) Schematic illustration of microfluidic chip with different measuring points for *in situ* XAS; insert is the schematic of micromixer employed (adapted from Ref. [120]. with permission of The Royal Society of Chemistry, https://doi.org/10.1039/C7RE00114B). (d) Experimental setup for *in situ* UV–vis monitoring of reaction in segmented flow (adapted from Yue et al., Copyright 2013 Royal Society of Chemistry, Microreactors with integrated UV/Vis spectroscopic detection for online process analysis under segmented flow, https://doi.org/10.1039/C3LC50876E, https://creativecommons.org/licenses/by/3.0/legalcode) [121]. (e) Experimental design of millifluidic chip for *in situ* XAS monitoring at different locations along the channel (reprinted with permission from Ref. [122]. Copyright 2013, American Chemical Society).

slug curved surfaces. Krishna et al. used a millifluidic device for time-resolved mapping of the Au NP size evolution in growth (Figure 4.1e) [123]. The work identified the formation of stable gold sulphide NPs when chloroauric acid and meso-2,3-dimercapto succinic acid were mixed in the millifluidic reactor. The gold nanostructures formed deposited at the channel and were subsequently reduced by flowing $NaBH_4$. The reduction was monitored with XAS spatially with a time resolution of 5 ms.

4.2.2 Mathematical modelling of nanoparticle synthesis

We have shown how a wide variety of experimental techniques are required to characterize nanomaterial synthesis kinetics. Similarly, a variety of modelling techniques can be adopted to describe nanoparticle syntheses and extract useful kinetic information. These techniques differ in the level of detail that can be captured, and accordingly in the computational cost of the numerical simulations. Modelling techniques used to describe processes occurring in nanoparticle syntheses range from quantum chemical calculations (e. g. Density Functional Theory) to molecular dynamics, Brownian dynamics and Monte Carlo simulations. A detailed review of the applications of these techniques in describing nanoparticle structures is provided in Barnard [124]. The modelling approaches just mentioned are powerful tools for describing in detail “single” nanoparticle synthesis aspects, like precursor reduction [124], particle growth [125], interaction of nanoparticle surfaces with other molecules [126], crystal structure and stability of nanoclusters [127]. However, they cannot be used to model the entire nanoparticle synthesis, since this would be computationally too demanding. A tool that fits the need of both accuracy and fast computation, and which is thus useful for process development, is population balance modelling (PBM). A population balance equation (PBE) is an equation that allows describing the evolution of the nano-PSD during the synthesis (even though it cannot capture other details, such as crystal structure or particle morphology).

PBM is widely used in reaction engineering [128] for the rational design of polymerization [129–131] and crystallization [132–134] reactors. It has also been used to describe the process of nanoparticle formation [136–138], in particular semiconductor nanoparticle synthesis, both in batch [138] and in flow reactors [139, 140]. The PBM thus seems to be an approach best suited to rationalize the design of nanoparticle synthesis reactors and achieve quality-by-design.

If we consider a batch reactor, in which the solution is assumed to be perfectly mixed, so that all the properties, such as concentration and temperature, are spatially uniform, the PBE describing the NPs evolution during the synthesis can be written as:

$$\frac{\partial n(v,t)}{\partial t} = g\delta(v - v_{\min})$$

$$+\frac{1}{2}\int\limits_{v_{\min}}^{v} \alpha(v-v',v')n(v-v',t)n(v',t)dv' - n(v,t)\int\limits_{v_{\min}}^{+\infty} \alpha(v,v')n(v',t)dv' + G,$$

where $n(v,t)$ is the number density function defined so that $n(v,t)dv$ yields the number of particles with volume in the infinitesimal range dv about the value v at time t. This function is thus closely related to the PSD. The first term on the right-hand side of the equation models nucleation, with g being the nucleation rate and $\delta(v-v_{\min})$ a delta function centred at the nuclei size $v_{\min}$ (here it is assumed that all nuclei share the same size). The second and third are generation and consumption terms, respectively, that model particle agglomeration, with α being the agglomeration kernel. The last term represents particle surface growth. In general, these terms (in particular g and G) depend on the concentration of the various precursors present in the system and on the physicochemical properties of the latter. From this equation we observe how different physical phenomena contribute in making the PSD change. For example, both agglomeration and surface growth cause an increase in the average particle size. Furthermore, one must keep in mind that the evolution of the PSD depends on the concentration of the precursors, so that the PBE is in general coupled with the material balances of all the other species involved in the synthesis (for instance, through g and G). Consequently, the mathematical model can be solved only if the rates of all the reactions are known and kinetic expressions for nucleation (via the term g), aggregation (via the term α) and growth (via the term G) are available. Hence, a significant amount of kinetic information is required, which cannot be obtained merely via the experimental acquisition of data on the PSD evolution.

A PBM for the Brust-Schiffrin method [141] shows how it is possible to improve the nanoparticle quality based on theoretical findings, significantly reducing the effort in reaction optimization. The model was based on a continuous nucleation – growth – capping mechanism, which indicated that, if the reaction conditions were kept constant, the particles born at different times through continued nucleation would grow to the same size before being capped. This is in contrast to the perception that continued nucleation is the main reason for poor PSD control. The authors were in fact able to propose a modified protocol based on their model, which led to an improvement of the Au PSD from 2.0 ± 0.6 nm to 1.7 ± 0.3 nm.

On the other hand, the work from Kumar et al. on the Turkevich synthesis [142] shows how significant effort has to be put in the understanding of the mechanism behind the synthesis. Despite the fact that this model qualitatively describes several aspects of the synthesis observed experimentally (in particular particle size plateauing for high citrate-to-chloroauric acid ratio values), Agunloye et al. showed that it poorly predicts experimental data from the literature [143]. This is most probably due to an inaccurate description of the synthesis mechanism. While Kumar and co-workers employed the Turkevich organizer theory [144], recent work from Polte's group showed experimental findings supporting a different mechanistic route [97].

4.3 Review of research on gold nanoparticle flow synthesis

4.3.1 Gold nanoparticle synthesis in single-phase flow systems

4.3.1.1 Microfluidic reactors

Most microfluidic reactors are made using microfabrication methods and have characteristic dimensions in the order of hundreds of microns. However, the use of capillary tubes is also gaining interest owing to their simplicity and low cost. An important aspect for the application of continuous flow in the manufacturing of nanomaterials is its production capacity. Hence, for the sake of convenience, in this chapter flow systems with characteristic size (such as diameter) smaller than 1 mm are referred to as microfluidic reactors, while those with larger size (up to some mm) are referred to as millifluidic reactors. For Au NP synthesis, the most common microfabricated reactor materials are Si, glass and polydimethylsiloxane (PDMS). Glass and silicon not only involve special working conditions (clean room), but may also require careful sealing procedures, particularly for high temperature/pressure operation. Capillaries and tubes made of silica, polytetrafluoroethylene (PTFE) are common, while polyether ether ketone (PEEK), polyethylene and Tygon have also been used.

Among all the chemistry routes for Au NP synthesis, the Turkevich method has been the most popular [60] for synthesizing citrate-capped Au NPs. It was first proposed by Turkevich [144] in 1951, and produced around 20 nm Au NPs by adding trisodium citrate dehydrate quickly into a boiling $HAuCl_4$ solution under vigorous stirring. The mechanism was described as "seed-mediated growth" by Wuithschick et al. [97] who proposed a fast nucleation and a subsequent slow growth stage, as the gold ions preferentially bind onto the existing solid gold surface with lower surface potential [145]. On the basis of the Turkevich method, various researchers sought to improve this method [96, 146–151] or substitute the reducing agent (e. g. ascorbic acid [152] and tannic acid [153]) or capping agents [154–156] to achieve smaller/different particle size or narrower size distribution. For the synthesis of sub-5 nm Au NPs, sodium borohydride ($NaBH_4$) is the reducing agent most frequently used, having far higher reducing ability than citrate to reduce gold ions to metallic atoms (order of magnitude of milliseconds [76]) To limit the growth of particles, strong capping agents such as thiols in the Brust-Schiffrin method [157] are used during $NaBH_4$ reduction.

In single-phase microfluidic systems, the flow pattern is usually laminar, characterized by low Reynolds number [42]. Thus, mixing only occurs at the interface between miscible streams by molecular diffusion. This characteristic is attractive for some synthetic processes which need precise control. Citrate-capped Au NPs are usually synthesized by the Turkevich method for around 30 min under elevated temperature. Singh et al. produced citrate-capped Au NPs with lower reaction time at room temperature by substituting citrate with the strong reducing agent $NaBH_4$ in the microreactor [156]. The laminar flow forming in the microreactor played an important role to slow down mixing and avoid the uncontrollable reaction owing to the high conversion rate of $NaBH_4$. On the other hand, for slower reducing agents efficient mixing is beneficial. Jun et al. studied the size control of Au NPs produced by ascorbic acid, by comparing different mixers. Similar size and size distribution were obtained with both microfluidic butterfly-shape and millifluidic compressed-tubing mixers (Figure 4.2), as long as the flow rate was sufficient to attain efficient mixing [158]. Sufficiently high flow rates could guarantee fast mixing, but too high flow rates did not allow enough time for the reaction to complete.

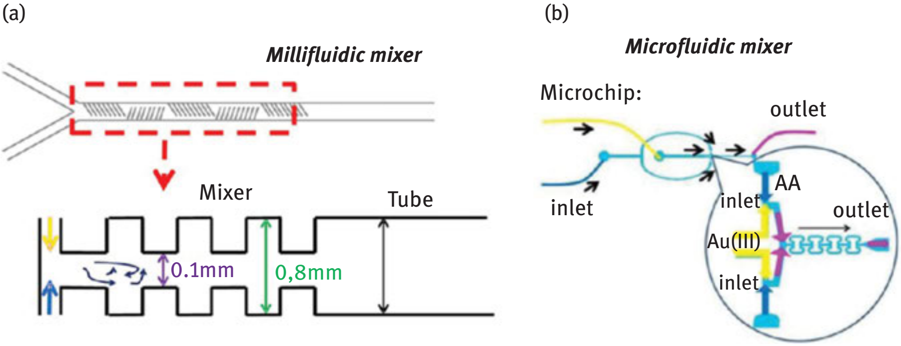

Figure 4.2: Schematic of different mixers used for Au NPs synthesis by ascorbic acid: (a) compressed Teflon millifluidic mixer and (b) butterfly microfluidic mixer (reprinted with permission from Ref. [159]. Copyright 2012, American Chemical Society).

Shalom et al. adapted the Brust-Schifrin method to a flow system by mixing a prepared thiolate polymer and aqueous $NaBH_4$ in a radial interdigitated mixer (Figure 4.3a) [159]. The reagents passed through a circular channel and were then split into eight streams flowing towards the centre of a mixing chamber, while the outlet was in the centre of the chamber. For the same gold-thiol ratio (e. g. 2), the size and standard deviation in the microfluidic reactor were smaller (2.9 ± 0.6 nm) than those in batch systems (4.9 ± 2.1 nm). Tsunoyama et al. used a similar mixing approach with a multi-laminated mixer (from IMM) to improve mixing (Figure 4.3b) [160]. With $NaBH_4$ as reducing agent, they produced PVP-stabilized sub-2 nm Au NPs with high monodispersity, which showed higher catalytic activity in aerobic alcohol oxidation than Au NPs prepared in a batch reactor. Using the same micromixer, Luty-Błocho et al. studied the effect of flow rate on Au nanoparticle synthesis. Increasing the flow rate led to smaller polyvinyl alcohol (PVA)-capped Au NPs in the range of 1.5–3 nm when using ascorbic acid or $NaBH_4$ as reducing agent [161]. Interestingly, batch processing resulted in sediment formation after 1 h for the ascorbic acid system.

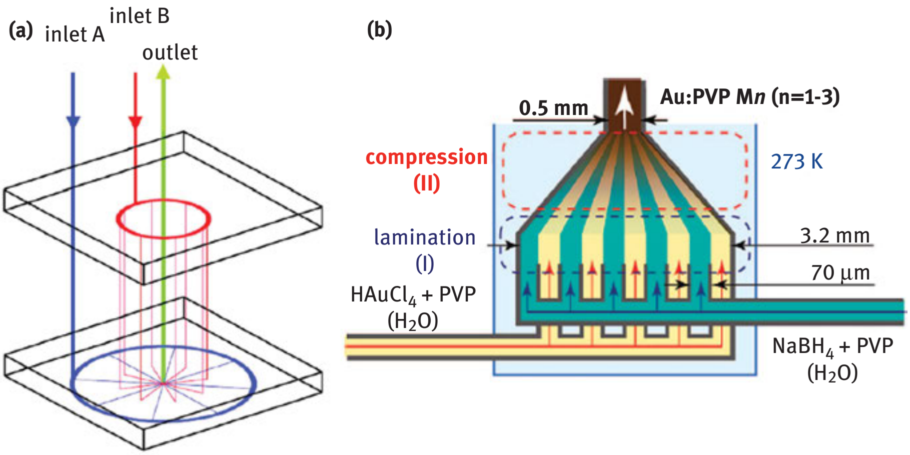

Figure 4.3: (a) Schematic of radial interdigitated mixer used for Au NPs synthesis by $NaBH_4$ (reprinted from Materials Letters, 61(4), Shalom et al., Synthesis of thiol functionalized gold nanoparticles using a continuous flow microfluidic reactor, 1146–1150, Copyright 2018, with permission from Elsevier) [160]. (b) Schematic of the multi-laminated mixer used for Au NPs synthesis by $NaBH_4$ (reprinted with permission from Ref. [161]. Copyright 2008, American Chemical Society).

For the $NaBH_4$ system, particles of similar sizes were obtained (~1.5 nm), but in the batch reactor much larger ones (~2 µm) were also produced.

A glass-silicon microreactor with three mixing zones of split-and-recombine type allowing the consecutive addition of reducing agent solution containing ascorbic acid and Fe(II) and three modifier solutions (citric acid, sodium metasilicate and PVA) was utilized to synthesize Au NPs [162]. Wagner and Köhler improved this glass/silicon reactor with eight split-recombine units (Figure 4.4a) which could provide improved RTD and used it to synthesize PVP-capped Au NPs with sizes between 5 and 50 nm by ascorbic acid reduction [163]. Au NPs with coefficient of variation (CV) two times smaller than that in a conventional batch reactor was achieved and smaller Au NPs were obtained at high flow rates, high concentration of the reducing agent or stabilizer and high pH. In a subsequent design, residence loops were added to allow for multi-step addition of the reagents and reduction of the risk of fouling (Figure 4.4b) [164]. They synthesized 4–7 nm Au NPs using $NaBH_4$ as the reducing agent. The Au NP size could be reduced by decreasing the reactant concentrations.

Sugano et al. developed a microreactor system comprising a Y-mixer and two piezoelectric valveless pumps to achieve pulsed mixing of chloroauric acid and trisodium citrate at room temperature (Figure 4.5) [165]. The switching frequency controlled the thickness of the pulsed layers, the square of which has a proportional relationship with the diffusion time. The mixing time at 100 Hz was short enough as to reduce the CV of the PSD to ~10 % for Au NPs of ~40 nm mean size.

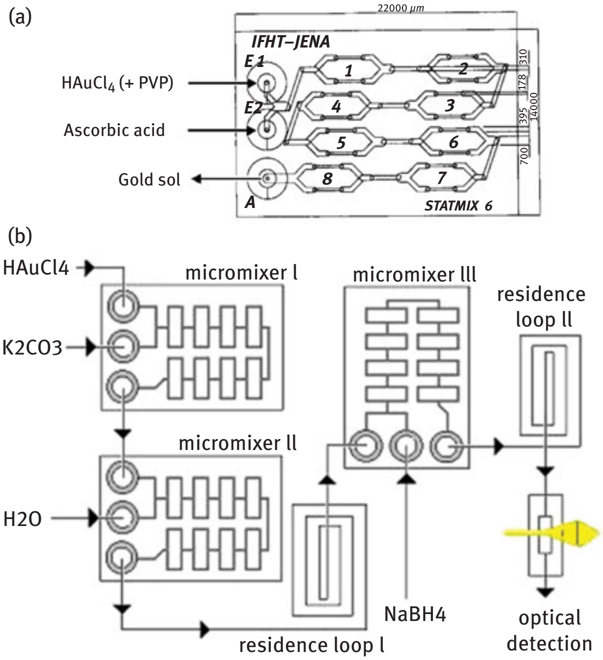

Figure 4.4: (a) Schematic of the reactor with split-and-recombine mixers used for synthesis of Au NPs by ascorbic acid (reprinted with permission from Ref. [164]. Copyright 2005, American Chemical Society). (b) Microreactor system with micromixers and residence loops used for synthesis of Au NPs by NaBH$_4$ (reprinted from *Chemical Engineering Journal*, 135, Wagner et al., Microfluidic generation of metal nanoparticles by borohydride reduction, S104–S109, Copyright 2008, with permission from Elsevier) [165].

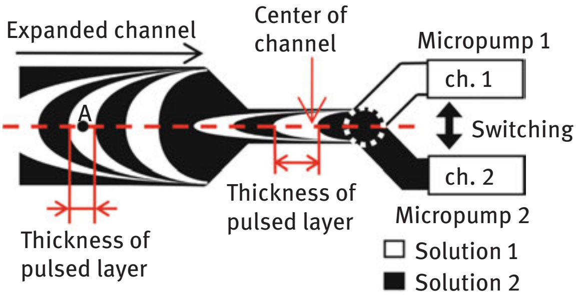

Figure 4.5: Y-shape pulsing mixer used for synthesis of Au NPs by trisodium citrate (reprinted by permission from Springer Customer Service Centre GmbH: Springer, *Microfluidics and nanofluidics*, Ref. [165], Sugano et al., Copyright 2010).

Verma and Kumaran formed co-axial flow in a microchannel ($H \times W$: 100 µm × 1.5 mm) so that the gold precursor (chloroauric acid) was surrounded by the reducing agent (tannic acid). As the Reynolds number increased, the flow regime transitioned from laminar to turbulent. At high Reynolds number (up to ~350) the PSD could be controlled better, while the mean particle size, between 4 and 7 nm (achieved at different molar ratios of tannic acid to chloroauric acid) was not significantly affected by mixing conditions [166]. Bandulasena et al. also used a co-axial flow setup operating at laminar flow with an injection orifice diameter of the inner tube between 100 and 240 μm (Figure 4.6) [167]. The particle size of PVP-capped Au NPs produced by ascorbic reduction decreased from ~135 nm to ~50 nm by decreasing the injection orifice diameter (which increased the mixing efficiency), increasing the flow rate of the ascorbic acid stream and increasing the pH (which enhanced the reducing power of ascorbic acid). However, polydispersity increased with increasing the flow rate and the pH of the ascorbic acid stream.

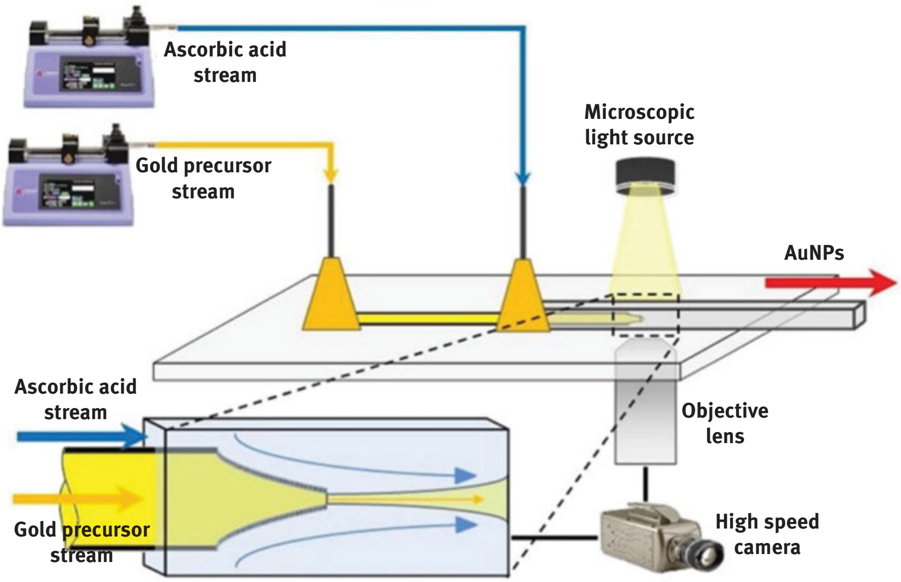

Figure 4.6: Schematic of the co-axial microfluidic setup with round capillary orifice inside a square microchannel used for Au NPs synthesis by ascorbic acid (adapted from Bandulasena et al., Copyright 2017 Elsevier, https://doi.org/10.1016/j.ces.2017.05.035, http://creativecommons.org/licenses/by/4.0) [167].

Baber et al. utilized a co-axial flow reactor comprised of an outer glass tube (2 mm I.D.) and an inner glass tube (0.8 mm I.D.) to bring in contact chloroauric acid and trisodium citrate, while avoiding fouling. This was followed by an ethylene tetrafluoroethylene-coiled flow inverter with 0.75 mm I.D., which helped to improve the RTD. Au NPs with minimum size of 17.9 ± 2.1 nm were synthesized at 80 °C (Figure 4.7) [168].

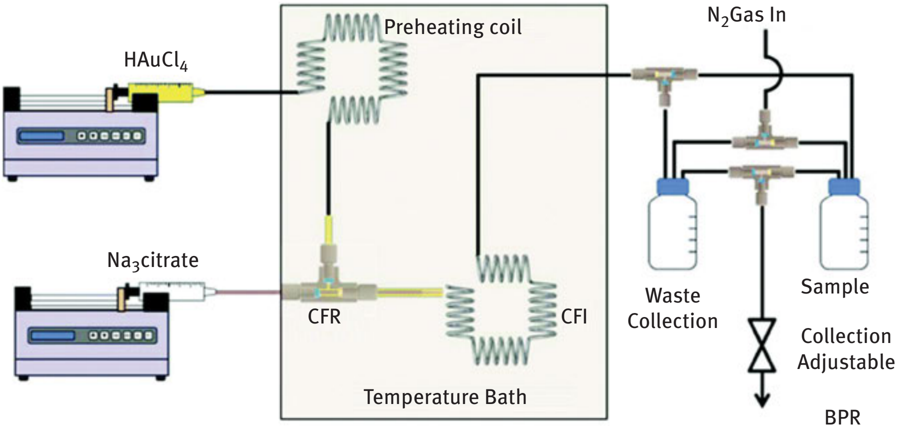

Figure 4.7: Schematic of the experimental setup for Au NP synthesis by the Turkevich method comprising coiled flow inverter (CFI) for preheating, a co-axial flow reactor as a mixer, and another CFI as reactor (adapted from Baber et al., Copyright 2017 Royal Society of Chemistry, An engineering approach to synthesis of gold and silver nanoparticles by controlling hydrodynamics and mixing based on a co-axial flow reactor, https://doi.org/10.1039/C7NR04962E, https://creativecommons.org/licenses/by/3.0/legalcode) [168].

Yang et al. designed a vortex-type mixer in a three-layer microfluidic reaction chip (Figure 4.8) [169]. Using the new chip, almost complete mixing was achieved within 1 s, and 19–58 nm Au NPs were obtained by tuning the volumes of citrate and gold precursor for the Turkevich method.

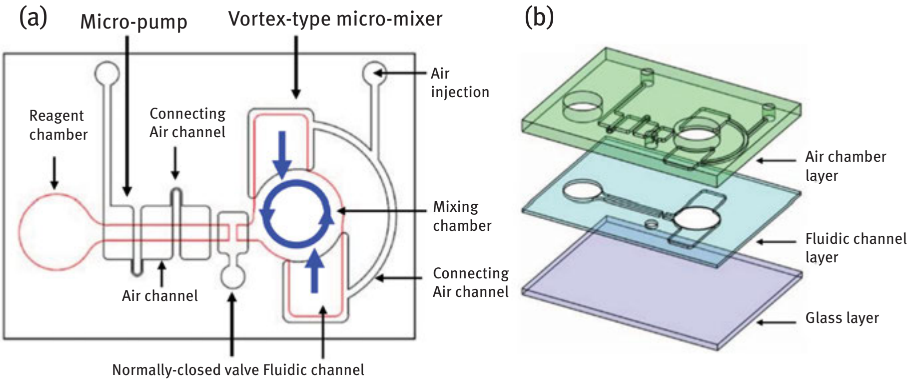

Figure 4.8: Components of three-layer microfluidic reaction chip with vortex-type flow field used for Au NPs synthesis by trisodium citrate (a) top view and (b) exploded view (reprinted by permission from Springer Customer Service Centre GmbH: Springer, *Microfluidics and Nanofluidics*, Ref. [170]., Yang et al., Copyright 2010).

Kitson et al. designed 3D printed serpentine reactors with 0.8 mm channels made of polypropylene (PP) to synthesize Au NPs [170]. Compared to the PDMS which is commonly used, PP is cheaper and the maximum material cost for one reactor was ca. $0.31. Even though fouling was observed on the surface of the reactor, this design is attractive because of the low cost for each reactor, which is disposable after one use.

The batch Turkevich method does not produce Au NPs <5 nm. However, Ftouni et al. produced ultra-small (i. e. <2 nm) Au NPs at residence time <50 s in a citrate-only system by taking advantage of efficient mixing and quick heating and quenching in a fused silica capillary (200 µm I.D.) [171, 172]. As the residence time was quite short and the product was quenched rapidly to terminate the reaction, no further growth after the quenching led to NPs with ultra-small size. Gomez-de Pedro et al. fabricated a ceramic microfluidic device based on low-temperature co-fired ceramics technology [173]. The shape of the three-dimensional serpentine structure caused advective patterns that enhanced the mixing. The reactor was used to synthesize 11-mercaptoundecanoic acid (MUA)-capped Au NPs. Pulsed dosing of $HAuCl_4$ solution to a continuous flow of $NaBH_4$, with a continuous downstream feed of an MUA solution, resulted in 2.7 nm Au NPs. Hydrophobic gold NPs have attracted less attention. Sugie et al. used a Y-mixer/PTFE microreactor assembly maintained at 25–60 °C to reduce $HAuCl_4$ in tetrahydrofuran solvent using organosilane as mild reducing agent and alkyl thiol (RSH) as capping agent [174]. Increasing residence time to over an hour led to the increase of the Au NP size from 4.3 to 8.7 nm.

Microfluidic systems have also been employed to form gold nanomaterials with different shapes. Kumar et al. used Br^- ions from cetyltrimethylammoniumbromide (CTABr) or HBr with citrate reduction to produce triangular gold nanoplates [175]. They implemented a Y-shape micromixer and a tubular PTFE tube with 0.9 mm internal diameter (I.D.) to tune the operational parameters (volumetric flow ratios, temperature and reagent concentrations) and improve the yield of triangular particles from ~25 % to ~51 %. Reducing the amount of citrate yielded a larger amount of polyhedral particles; this was attributed to the particle growth rate dominating the initial nucleation rates. Fu et al. developed a three-inlet micromixer and a subsequent PDMS microchannel (400 mm × 400 mm cross-section and 3 cm in length) for the synthesis of seed-mediated gold nanoplates [177]. The thickness of the nanoplates was tuned from 1 nm to a few nm by varying the flow rate. The nanoplates were rigid and flat when their thickness was >2 nm and had crumpled/rolled shapes when the thickness was ~ 1 nm. Sebastián et al. utilized a coiled PTFE tubing (0.76 mm I.D., Figure 4.9) to synthesize biocompatible gold nanorods (Au NRs) with a residence time of 10 min in continuous flow [178]. In order to circumvent toxicity issues of silver/CTABr that are typically used for Au nanorod synthesis, they employed lysine as capping agent with $NaBH_4$ as reducing agent. The presence of two amino groups in the lysine is critical for the anisotropic growth of the Au particles. By tuning the lysine concentration, Au nanorods with strong absorption in the near infrared (700–900 nm) were prepared.

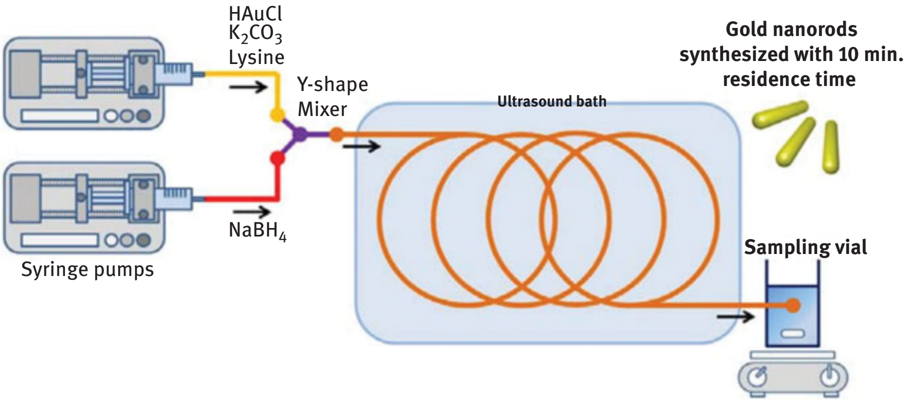

Figure 4.9: Schematic of continuous flow setup Au NRs synthesis via $NaBH_4$ reduction with residence time of 10 min (adapted from Ref. [178], with permission of The Royal Society of Chemistry, https://doi.org/10.1039/C2CC32969G).

Ishizaka et al. made use of continuous flow to tune the pH of the gold precursor by adding the reagents stepwise (Figure 4.10) [178]. Glucose was used as an environmentally benign reducing agent. Star-shape Au NPs were synthesized when the pH was 6.9, which was not observed in batch systems under similar experimental conditions; nevertheless, the particles gradually coalesced into single round shape particles.

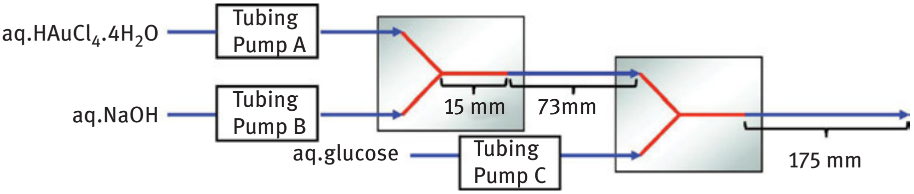

Figure 4.10: Schematic of multi-step addition in a microfluidic system for the synthesis of Au nanostars by glucose (reprinted from *Journal of Colloid and Interface Science*, 367(1), Ishizaka *et al.*, Dynamic control of gold nanoparticle morphology in a microchannel flow reactor by glucose reduction in aqueous sodium hydroxide solution, 135–138, Copyright 2018, with permission from Elsevier) [179].

An important issue during single-phase flow is the appearance of fouling on the microreactor wall. Wagner et al. observed gold precipitation on the wall of a glass microreactor, even though the synthesis was implemented carefully with small volume and short running time [163, 179]. They proposed various solutions to suppress fouling. Operation at high pH (~9.5) leads to negative charge on silicon surface because of the deprotonated Si–OH groups. As the citrate-capped gold NPs are also negatively charged, the electrostatic repulsion between product and tubing wall prevented fouling. Another way is to reduce the wettability of the channel walls by turning the surface from hydrophilic to hydrophobic via silanization. Higher shear forces induced by increasing flow rate seemed also to help reduce fouling.

4.3.1.2 Millifluidic reactors

Because of potential fouling problems and their inherent small volume, it is difficult for microfluidic devices to provide gram-scale production [39, 45, 52, 62, 180]. Millifluidic reactors, which have one order of magnitude larger dimensions compared to microreactors, mitigate the risk of fouling blockages and depend less on expensive fabrication technologies [41]. Compared to batch synthesis, millifluidic devices can still provide satisfactory mixing (although this depends on the synthesis) and are more amenable to scale-up [158].

Lohse et al. proposed a millifluidic reactor system (Figure 4.11) comprised of simple components to improve the operation control compared to batch reactors, as well as to enable high-throughput synthesis at the gram-scale of functionalized gold NPs [181]. The reactants were mixed in a polyethylene (PE) Y-mixer (I.D. 1.79 mm), and the residence time was controlled by adjusting the length of the TYGON polyvinyl tubing reactor (I.D. 2.79 mm). The reactor could be integrated with online UV–vis absorbance spectroscopy analysis for product monitoring during synthesis, as well as flow NP purification techniques. Various functionalized (citrate, mercaptohexanoic acid and CTAB) spherical Au NPs with controlled sizes (4, 2 and 2–40 nm, respectively) were produced by $NaBH_4$ reduction. Furthermore, CTAB-stabilized gold seeds (2.0 nm) were mixed with a growth solution containing chloroauric acid, CTAB, silver nitrate, and ascorbic acid leading to Au nanorods with various aspect ratios and lengths of 15–50 nm.

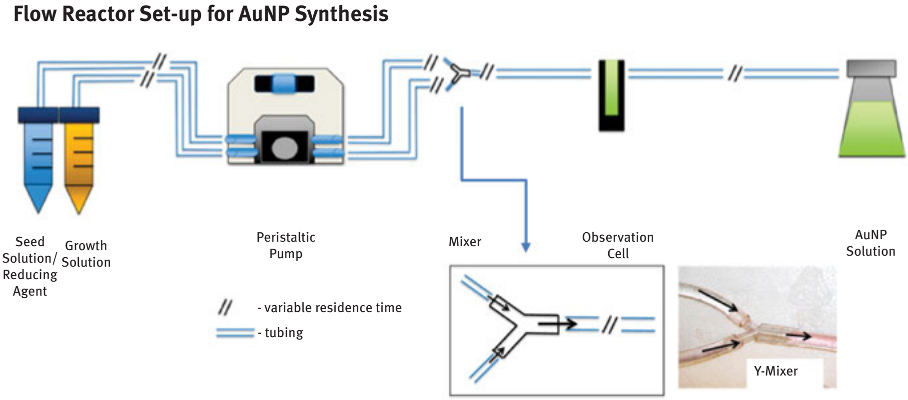

Figure 4.11: Schematic of a millifluidic reactor for Au nanomaterials synthesis by ascorbic acid (reprinted with permission from Ref. [182]. Copyright 2013, American Chemical Society).

Gomez et al. reported that the good quality of hollow Au NPs produced by galvanic replacement of cobalt NPs synthesized by $NaBH_4$ reduction in batch reactors could only be achieved with a volume up to 480 ml, as insufficient mixing limited the scale-up [182]. They achieved higher productivity by scaling up a continuous flow reactor from a PTFE tube with I.D. of 0.8 mm and length of 913 cm to millifluidic scale with 10 times higher throughput (I.D. of 1.6 mm, length of 3088 cm) (Figure 4.12). Moreover, multiple reaction stages, by adding new streams into the coils with T-junctions, and downstream processes (functionalization and

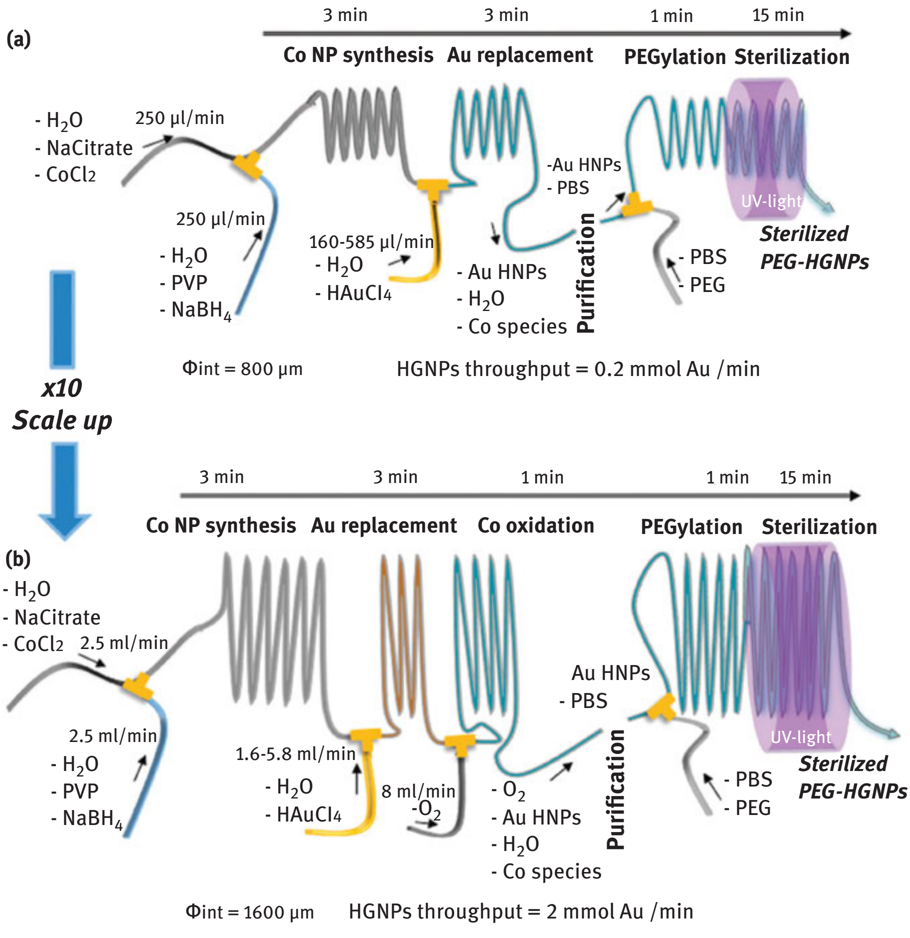

Figure 4.12: (a) Microfluidic setup with coiled capillary (I.D. of 0.8 mm) for the synthesis of sterilized PEG-capped hollow Au NPs by $NaBH_4$ through a galvanic displacement process. (b) Millifluidic setup with 10 times higher throughput (I.D. of 1.6 mm) than (a) (reprinted from *Chemical Engineering Journal*, 285, Uson et al., Continuous microfluidic synthesis and functionalization of gold nanorods, 286–292, Copyright 2016, with permission from Elsevier) [184].

sterilization) could be incorporated. Uson et al. utilized a similar setup based on PTFE tubing (I.D. = 1.016 mm) and PEEK Y-junctions to synthesize and functionalize Au nanorods in one continuous process [183]. The multi-addition of reactants allowed to separate and control – in a single stream – different stages of seed formation, nanorod growth and functionalization with poly(ethylene glycol)-methyl ether thiol (SH-PEG). Appropriate lengths of the tubing ensured the desired residence times (2–10 min) with a total residence time of 32 min. These short residence times eliminated detrimental effects associated with uncontrolled ageing-related processes observed in batch synthesis. The continuous system allowed a 100-fold reduction in the consumption of SH-PEG compared to a conventional batch reactor.

Bullen et al. used a rotating tube processor (RTP) with 6 cm I.D. and 30 cm in length with centrifugal force generating dynamic thin films 0.3 mm thick as the liquid moved along the rotating tube. The mixed reactant was delivered to a narrow channel processor (NCP) through jet feeds for longer residence time (Figure 4.13) [184]. Using this flow system, Au seeds were prepared with $HAuCl_4$/CTAB/acetylacetone and $AgNO_3$/CTAB/carbonate solutions in the RTP and grown to Au nanorods in the NCP. Long-term operation (19 days) was demonstrated with this system. Boleininger et al. [98] grew Au NRs from Au seeds and $HAuCl_4$/CTAB/ascorbic acid in short polyvinyl chloride (PVC) tubing (1 mm I.D.). The aspect ratio of the nanorods became smaller with a higher ratio of seed-to-growth solution or under higher growth temperature. Fouling was reduced by flushing polyethylene glycol before synthesis experiments. Different tubing materials were also tested. PVC, PTFE, PEEK and silicone tubes were filled with a growth solution containing gold precursor, ascorbic acid and CTAB for 3 h. There was no fouling observed in PVC and PEEK tubing, unlike PTFE and silicone.

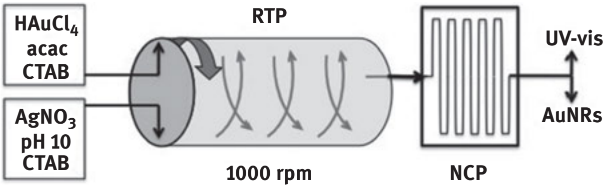

Figure 4.13: Schematic of the experimental setup for synthesizing Au nanorods by acetylacetone with a rotating tube processor (RTP) and a sequential narrow channel processor (NCP) (adapted from Ref. [185]. with permission of The Royal Society of Chemistry, https://doi.org/10.1039/C0CC05175F).

In addition to conventional heating for nanoparticle synthesis, there are other energy vectors that can be utilized. Sans et al. premixed the gold precursor and citrate at room temperature and then injected the solution into a coiled fluorinated ethylene propylene (FEP) tube (1.58 mm I.D.) placed inside a microwave cavity [185]. With this setup, rapid feedback control during the experiments was obtained and hyperbranched gold nanostructures were discovered. Bayazit used a microwave-assisted flow system to synthesize Au NPs [186]. The 3.2 mm O.D. PTFE tube reactor produced Au NPs with average particle width 4–15 nm and aspect ratio ~1.4–2.2 after only 90 s residence time.

4.3.2 Gold nanoparticle synthesis in two-phase flow systems

4.3.2.1 Microfluidic reactors

Segmented (also Taylor or slug) flow induced by an immiscible fluid stream can provide better mixing via transverse convection, enhanced mass transfer and reduced dispersion [47, 53, 54, 56, 61, 187]. Furthermore, when the synthesis is conducted in the dispersed phase, the reactor wall is protected by a thin liquid film which helps to avoid fouling. However, some of the drawbacks are the necessity of downstream separation processes of the immiscible fluid streams, potential adsorption of NPs at the two-phase interface, keeping slugs uniform and avoiding their coalescence, and the difficulty of adding subsequent reactants in a uniform manner.

The slug length and slip velocity between the two phases are quite important parameters which determine the mass transfer between slugs [188]. In Cabeza et al.'s design (Figure 4.14) [189], the aqueous phase of gold precursor and $NaBH_4$ was

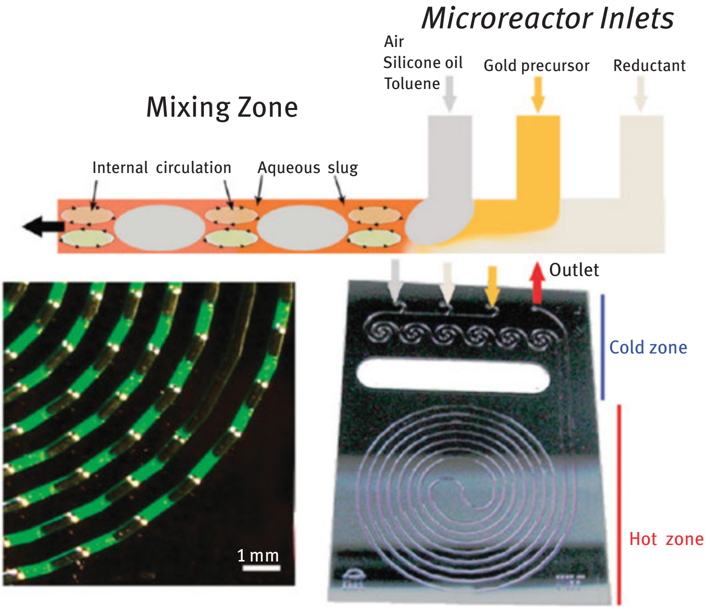

Figure 4.14: Segmented flow generation in a Si-glass microfluidic reactor used for Au NPs synthesis by $NaBH_4$ (reprinted with permission from Ref. [190]. Copyright 2012, American Chemical Society).

segmented by air, toluene or silicone oil inside a silicon microchannel ($H \times W$: 0.4 mm × 0.4 mm). The air-water two-phase flow resulted in the smallest and most monodisperse Au NPs with size 2.8 ± 0.2 nm, even though the reaction was in the continuous phase; this was attributed mainly to improved internal recirculation in the slugs. This system also led to the smallest amount of particle loss by interfacial absorption.

The same silicon microreactor was used as a hydrophilic reactor by Kulkarni and Sebastian Cabeza, and compared with a hydrophobic PTFE reactor (2.5 mm I.D.) for biphasic synthesis of Au NPs at the interface between an aqueous gold precursor and organic reducing agents (triethylamine, butyl amine, etc.) with CTABr as capping agent (Figure 4.15) [190]. The authors made use of the internal convection in segmented flow to renew the reactant at the interface in order to synthesize and grow the gold nanostructures. Nanoparticle preferential self-assembly at the water-oil interface by Pickering stabilization may have played a role in this synthesis [191]. Figure 4.15(d)–Figure 4.15(g) indicate different locations of particle accumulation for different wettability of tubing wall, which ultimately determined the nanoparticle size and shape. In hydrophilic microchannels the particles remained in the continuous aqueous slug and were located at the lower pressure region at the end of the slug [190]. When the particles moved to the end of one slug, they could be transferred to the next one along the film in the continuous phase while the droplet of the reducing agent would provide successive growth for these particles. The particles grew to form hexagonal bypyramidal shapes with a size of 42 nm. On the other hand, in hydrophobic microchannels the particles were trapped in individual droplets. The nuclei preferentially formed at the front-end of the droplet and then moved to the low-pressure end as their size increased. This movement enhanced the internal-mixing which led to higher nucleation rates and smaller final Au NPs (12 nm), whilst retaining the spherical shape.

Khan and Duraiswamy utilized N_2-aqueous segmented flow to synthesize Au NPs in a PDMS reactor with CTAB as a capping agent ($W \times D \times L$: 300 μm × 120 μm × 0.4 m) not only for better mixing, but also to stop the H_2 liberated from the $NaBH_4$ decomposition disrupting the flow (Figure 4.16) [192]. The evolved H_2 transferred to the N_2 bubbles leading to controllable stable flow. The authors showed that ultra-small Au NPs (<5 nm) could be synthesized with satisfactory quality to be used as seeds for CTAB-capped Au nanorod formation by off-chip synthesis.

Although internal recirculation in the slugs helps improve mixing, the mixing time scale may not be sufficient for nanoparticle syntheses which exhibit fast kinetics. In this case, winding microchannels can help break the symmetry of recirculation patterns and enhance mixing [193, 194]. While this is easily implemented in a planar microfabricated device, it is rather more difficult if one uses standard tubing. Thus, Zhang and Xia employed periodically pinched PTFE tubes with I.D. of 0.5 mm during droplet flow to decrease the mixing time from 15 to less than 1 s (Figure 4.17a), which led to more monodisperse Au NPs (Figure 4.17b) compared to the product under the same experimental conditions except without a pinched mixing zone (Figure 4.17c) [195].

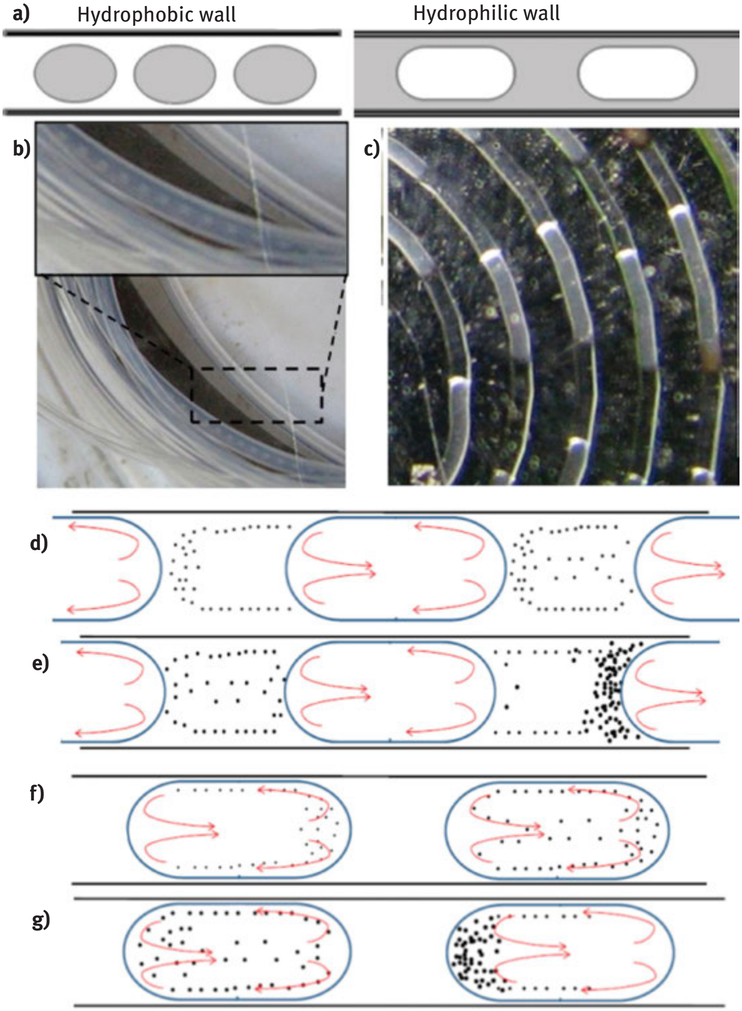

Figure 4.15: Schematic (a) and photograph (b) and (c) of flow patterns inside hydrophobic PTFE (left) and hydrophilic silicon-glass (right) reactors during slug flow (aqueous phase in grey and organic phase in white); (d) and (e) nanomaterial formation in hydrophilic reactor; (f) and (g) nanomaterial formation in hydrophobic reactor (reprinted with permission from Ref. [191]. Copyright 2017, American Chemical Society).

The flow patterns in the droplet-based systems depend on fluid properties [197]. Sometimes, a high concentration of the surfactant in seeded growth methods is necessary to guide the orientated growth or maintain the colloidal stability. These surfactant-rich reagents could increase the viscosity of the aqueous phase and change the interfacial tension to affect the droplet characteristics [197]. Duraiswamy and Khan employed a droplet-based microfluidic method during the surfactant-rich anisotropic

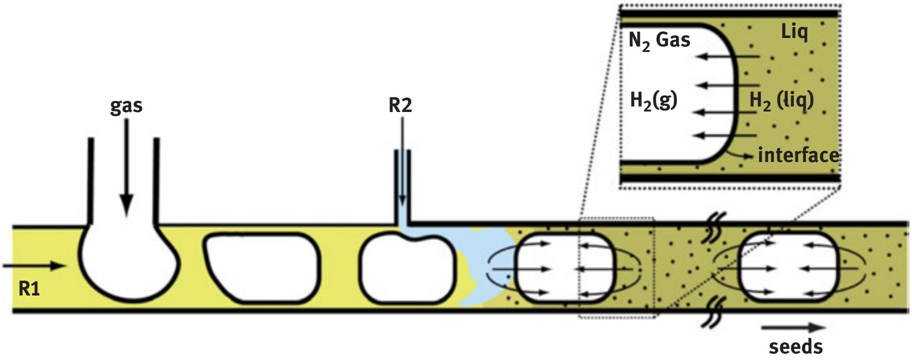

Figure 4.16: Schematic illustration of segmented N_2-liquid two-phase continuous flow for Au NPs synthesis by $NaBH_4$. The inset indicates the transport of H_2 from aqueous phase across to gas phase (adapted from Ref. [193]. with permission of The Royal Society of Chemistry, https://doi.org/10.1039/C2LC21198J).

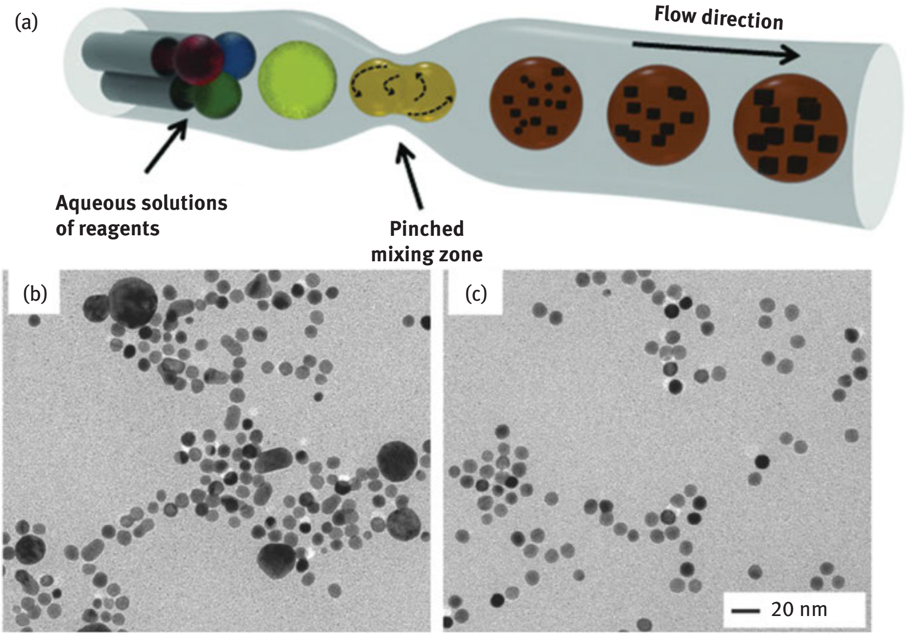

Figure 4.17: (a) Schematic of segmented flow inside 0.5 mm I.D. PTFE tube for Au NPs synthesis (b) with and (c) without pinched mixing zone (reprinted from Zhang and Xia, *Advanced Materials*, Copyright 2014 with permission from John Wiley and Sons) [196].

Au nanorod synthesis (Figure 4.18a) [198]. Three streams of gold seed solution, premixed gold precursor with capping agent (CTAB) and reducing agent (ascorbic acid) passed through one arm of the T-junction in a “flow-focusing” geometry and then

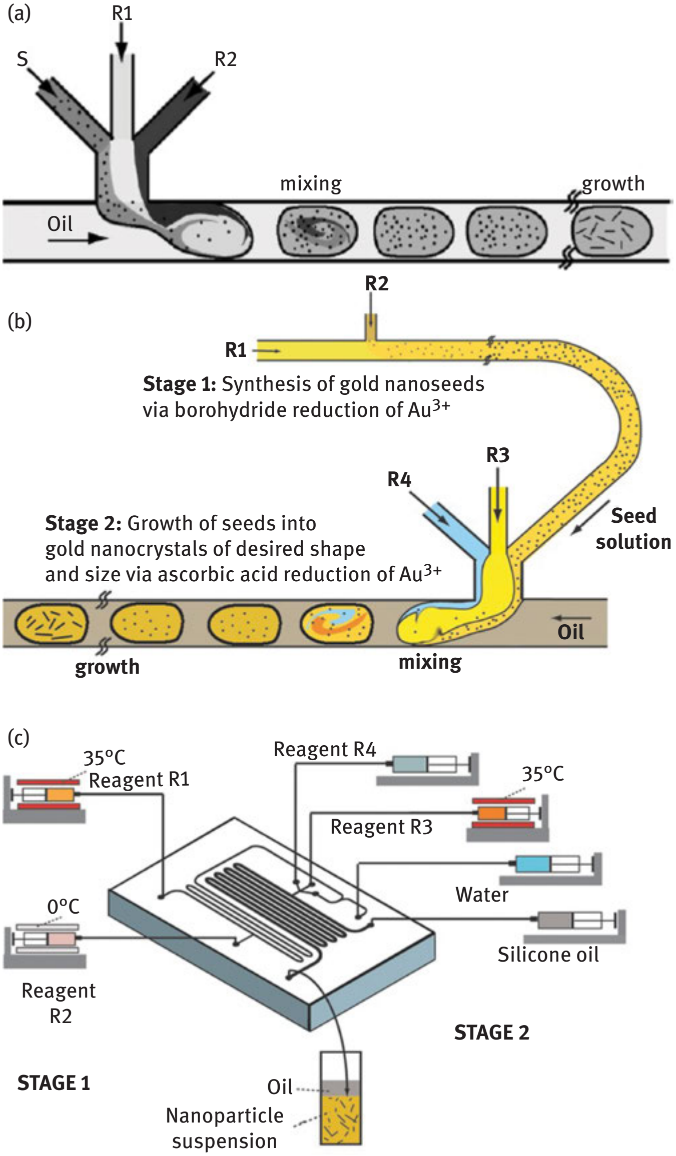

Figure 4.18: (a) Schematic of droplet-based microfluidic with three-arm mixer for aqueous droplet generation used for Au nanorod synthesis with ascorbic acid (reprinted from Duraiswamy and Khan, *Small*, Copyright 2009 with permission from John Wiley and Sons) [199]. (b) Schematic of the two-stage microfluidic method included gold nanoparticle seeds formation in Stage 1 and the growth of gold nanocrystals in Stage 2 and (c) the experimental setup (Reagent R1: aqueous mixture of gold salt and surfactant, Reagent R2: aqueous $NaBH_4$ solution, Reagent R3: aqueous mixture of gold salt, surfactant, and $AgNO_3$ and Reagent R4: ascorbic acid) (reprinted from Duraiswamy and Khan, *Particle & Particle Systems Characterization*, Copyright 2014 with permission from John Wiley and Sons) [200].

mixed with silicone oil to form homogeneous droplets inside a PDMS microreactor. By manipulating reagent concentrations and flowrates, Au nanorods with aspect ratio 2.3–2.7, as well as other shapes (e. g. cube, star, tetrapods), were obtained. Later, Duraiswamy and Khan combined the gold seed formation and the CTAB-capped nanorod growth together in a dual-stage continuous flow system (Figure 4.18b and Figure 4.18c). This time, the seed particles (<5 nm) were formed inside the PDMS microreactor channel ($W \times L$: 100 µm × 0.4 m) by $NaBH_4$ reduction and entered the subsequent growth section, which was a microchannel with $W \times L$: 300 µm × 0.45 m. Au nanorods with mean length ~35 nm and width ~12 nm were obtained [199]. The setup was further improved by adding a gas stream (N_2) to prevent the coalescence between droplets [200]. This microfluidic system was used to synthesize gold nanorods, but primarily gold-coated silicon-core particles by seeded growth.

Lazarus et al. employed a similar PDMS microreactor utilizing ionic liquid as solvent to synthesize Au NPs [201]. Ionic liquids, such as the 1-butyl-3-methylimidazolium tetrafluoroborate ($BMIM\text{-}BF_4$) used, are salts in liquid form which have poor-coordinated ions. The high nucleation rate caused by the high concentration in pure salt, low interfacial tension and chemical stability makes ionic liquids attractive for nanoparticle synthesis. With the aid of the microfluidic device to form homogeneous and stable droplets of ionic liquid, spherical Au NPs were smaller and with lower polydispersity (4.38 ± 0.53 nm) compared to those obtained in single-phase flow (6.25 ± 1.29 nm). Later, Lazarus et al. altered the synthesis by substituting the capping agent $BMIM\text{-}BF_4$ with 1-butyl-3-methylimidazolium bis-(trifluoromethylsulphonyl)imide ($BMIM\text{-}Tf_2N$) for greater stability and substituting the reducing agent $NaBH_4$ with $BMIM\text{-}BH_4$ for better solubility and prevention of sodium-containing by-products using a similar droplet-based microfluidic system and obtained 4.28 ± 0.84 nm Au NPs [202].

Taifur-Rahman et al. [203] utilized CO as a reducing agent in a membrane-based droplet microfluidic system to produce 10 nm Au NPs, as well as grow Au shells on gold nanoparticle seeds pre-attached on silica surfaces (Figure 4.19). The CO flowed

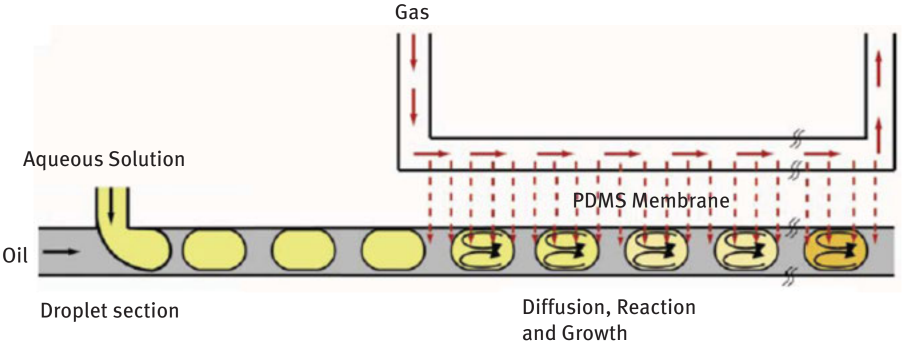

Figure 4.19: Schematic of the droplet microfluidic system with gas reducing agent (carbon monoxide) diffusing through a membrane (adapted from Ref. [204]. with permission of The Royal Society of Chemistry).

through a parallel gas channel ($W \times D \times L$: 100 μm × 124 μm × 21.8 cm) and could diffuse into the liquid channel ($W \times D \times L$: 300 μm × 124 μm × 91.5 cm) containing the water-fluorinated oil droplets flow via a PDMS membrane with thickness of 200 μm. Each droplet behaved as a reaction unit reacting with nearly equal amounts of CO with the same volume and good internal convection. The residence time could be controlled by the gas-liquid contact time. Calculations indicated that the CO mass transfer resistance in the liquid phase was the rate-limiting step. The mixing time (~0.1 s) was smaller by at least one order of magnitude than the residence time, enabling a controlled amount of the CO reducing agent to enter each droplet under shorter times.

Abalde-Cela et al. mixed an aqueous solution with a continuous phase of HFE-7500 fluid containing 2.5 % of Picosurf-1 surfactant for quick addition of ascorbic acid, which is critical for the synthesis of Au nanostars [204]. PDMS reactors with 100 μm × 75 μm or 80 μm × 75 μm T-junctions were utilized (Figure 4.20). The size of Au nanostars obtained was 170 ± 7.8 μm for a surfactant free synthesis and 90 ± 2.0 μm when PVP was utilized.

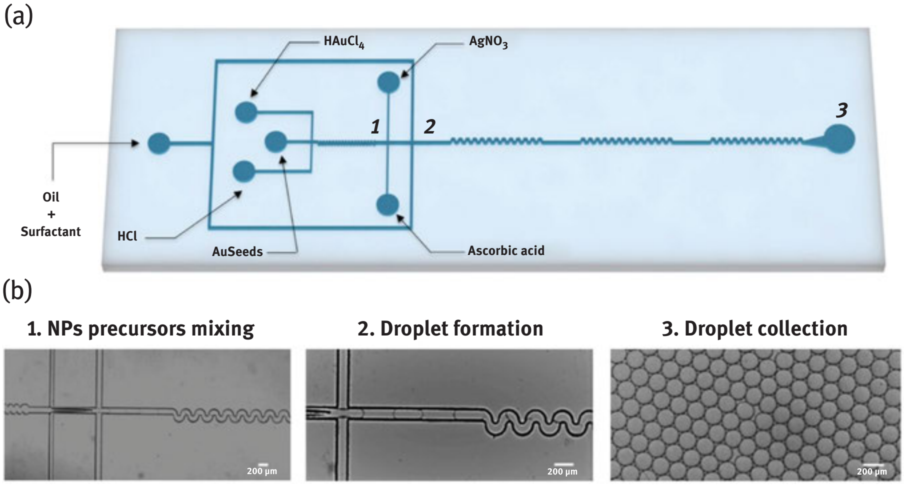

Figure 4.20: (a) Schematic and (b) optical images of a droplet microfluidic device to synthesize Au nanostars by ascorbic acid (adapted from Abalde-Cela et al., Copyright 2018 *Scientific Report*, https://doi.org/10.1038/s41598-018-20754-x, http://creativecommons.org/licenses/by/4.0) [204].

UV irradiation has been utilized to initiate the nucleation of NPs in segmented flow systems. Hafermann and Köhler used a solution of chloroauric acid, a photoinitiator and PVP that was exposed to a UV ray for a short period of time (30–300 ms) to induce nucleation followed by a growth section in the same 0.5 mm I.D. PTFE tube. Perfluoromethyldecalin was used as the segmenting fluid. In this system nucleation and growth could be spatially separated. The particle size was tuned between 2.5 and

4 nm by varying the composition of reactant solutions or the flow rate [204]. du Toit et al. synthesized citrate-capped Au NPs within heptane-water droplet flow using the Turkevich method [71]. UVC lamps were used to enhance the nucleation rate in a 0.8 mm I.D. glass capillary followed by FEP tube (1 mm I.D.) for controllable growth with conventional heating (Figure 4.21). By varying the UV intensity and growth temperature at an exposure time of 10 s, the nanoparticle size was tuned between 6.6 ± 0.8 nm and 36.1 ± 6.9 nm.

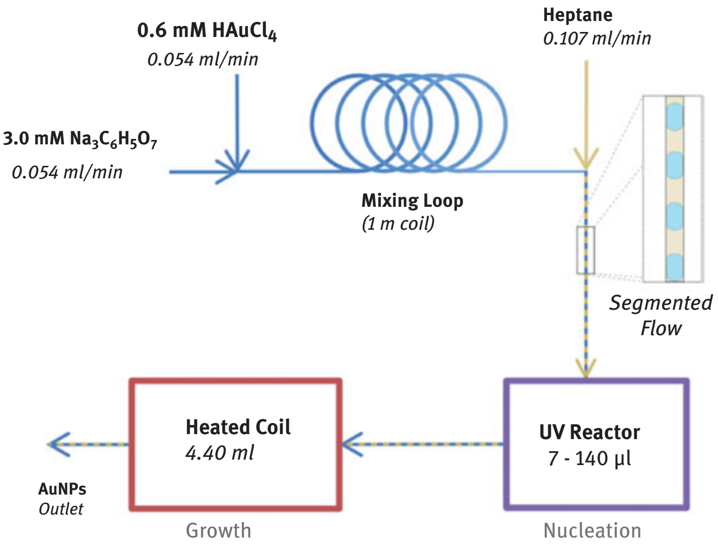

Figure 4.21: Schematic of continuous segmented flow for Au NPs synthesis with UV radiation by citrate (adapted from du Toit et al., Copyright 2017 Royal Society of Chemistry, Continuous flow synthesis of citrate-capped gold nanoparticles using UV induced nucleation, https://doi.org/10.1039/C6RA27173A, https://creativecommons.org/licenses/by/3.0/legalcode) [71].

All the above systems operated under Taylor flow (i. e. the equivalent droplet diameter was larger than the microchannel diameter). Lee et al. employed a flow-focusing microfluidic device (orifice $W \times H$: 50 µm × 110 µm) to generate microdroplets forming an emulsion (Figure 4.22). They used a silicone emulsifier (Abil-Em90) to prevent the coalescence of the microdroplets. The microdroplets contained a *N*-isopropylacrylamide (NIPAM) matrix, and when the NIPAM was polymerized it created a permeable membrane to isolate the inner compounds from the carrier solution. Thus, each droplet could function as an individual artificial cellular bioreactor to synthesize NPs by precursor solutions diffusing into the droplet. Au NPs with size 5–40 nm were obtained when different precursor concentrations (5–50 mM) were used [206].

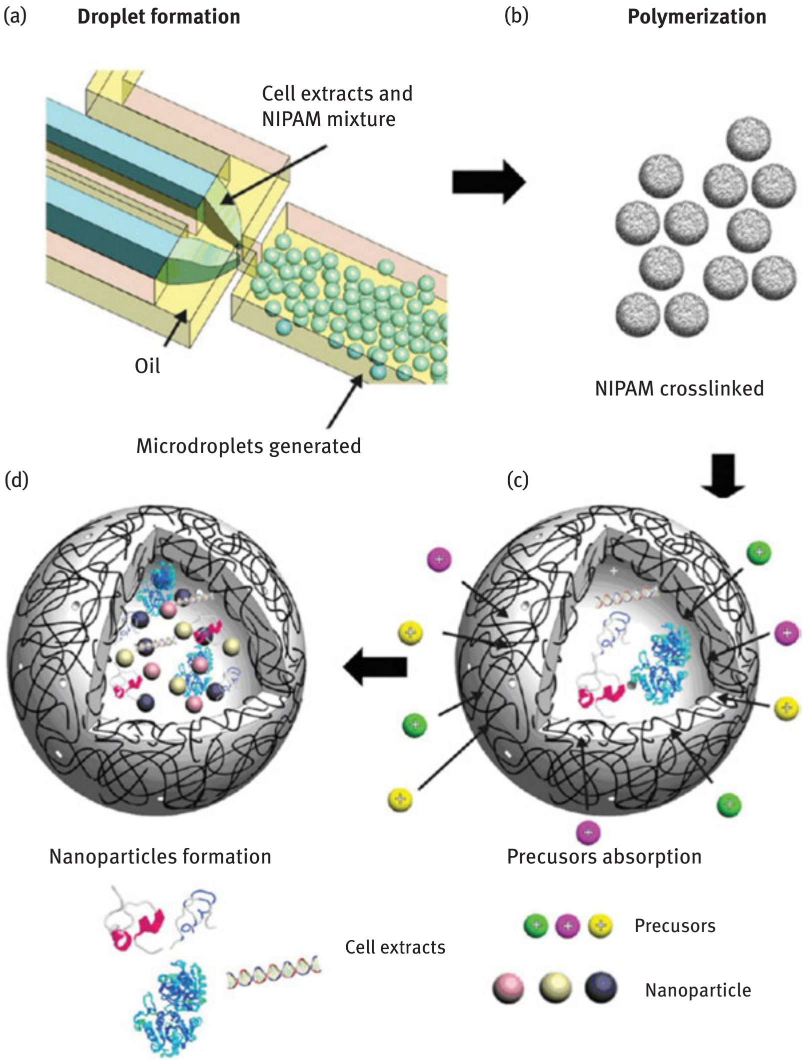

Figure 4.22: Schematic of microdroplet generation with the mixture of cell extracts and NIPAM monomer in a microfluidic device for nanoparticle synthesis (reprinted with permission from Ref. [207]. Copyright 2012, American Chemical Society).

Gu et al. proposed a novel method to dose the reducing agent ascorbic acid in the form of miniemulsion (continuous phase) into microfluidic droplets of gold precursor (dispersed phase). Transport of ascorbic acid from the miniemulsion nanodroplets into the microdroplets was achieved via electrocoalescence, induced by an applied alternating electrical field (Figure 4.23) [207]. The electrical field was applied between two parallel electrodes placed outside the FEP tube reactor (0.76 mm I.D.) without

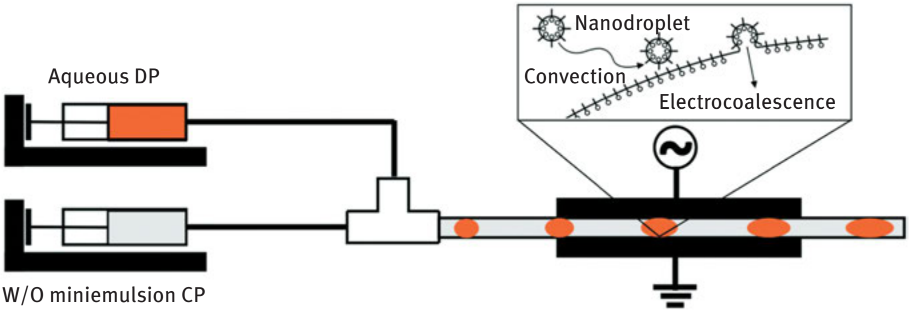

Figure 4.23: Experimental setup for dosing ascorbic acid from nanodroplets by electrocoalescence under high strength electrical field to synthesize Au NPs (adapted from Ref. [208]. with permission of The Royal Society of Chemistry, https://doi.org/10.1039/C8LC00114F).

any physical contact with the reactants and controlled the rate of addition of the reducing agent nanodroplets to the gold precursor microdroplets. PVP-capped Au NPs were produced with size tailored from 44.6 ± 12.6 nm to 81.2 ± 25.5 nm by the strength of the electrical field from 11,400 to 4300 V/cm.

4.3.2.2 Millifluidic reactors

Millifluidic slug flow reactors are less common due to difficulties in attaining stable slug flow in larger channels. Furthermore, as the size of the tube, and hence of the droplet, increases, mixing by internal recirculation within the droplet becomes less efficient. For this reason synthesis of NPs in millifluidic reactors has received less attention. Zhang et al. demonstrated a millidroplet reactor which could produce droplets with a volume of 0.25 ml inside a PTFE tube of I.D. 5.8 mm (Figure 4.24a) [208]. Co-axial flow with reversed flow direction of two streams was used to obtain better mixing in mixer T1 (Figure 4.24b). The well-mixed reagents were subsequently merged with silicon oil and formed a co-axial jet instead of droplets in the channel in mixer T2 and the exiting PTFE tube (I.D. = 1.58 mm). The jet was stabilized due to the high flow rate of the silicone oil stream, but when it entered the PTFE tube (I.D. = 5.8 mm) the flow rate for the silicone oil suddenly dropped, resulting in ml-sized droplets together with small, satellite droplets (Figure 4.24e). The satellite droplets merged quickly with the adjacent large droplets before they entered the reaction zone. With this setup, 10–30 nm spherical cetyltrimethylammonium chloride-capped Au NPs were produced by seeded growth with ascorbic acid, as well as Au cubes with 50 nm in edge length. The productivity of this system was in the 1–10 g/h range. The PTFE tube size of 5.8 mm appeared to be the largest size that could be used when silicone oil was employed as carrier phase. When tubes with larger diameter were used, it became difficult to generate stable droplets [53].

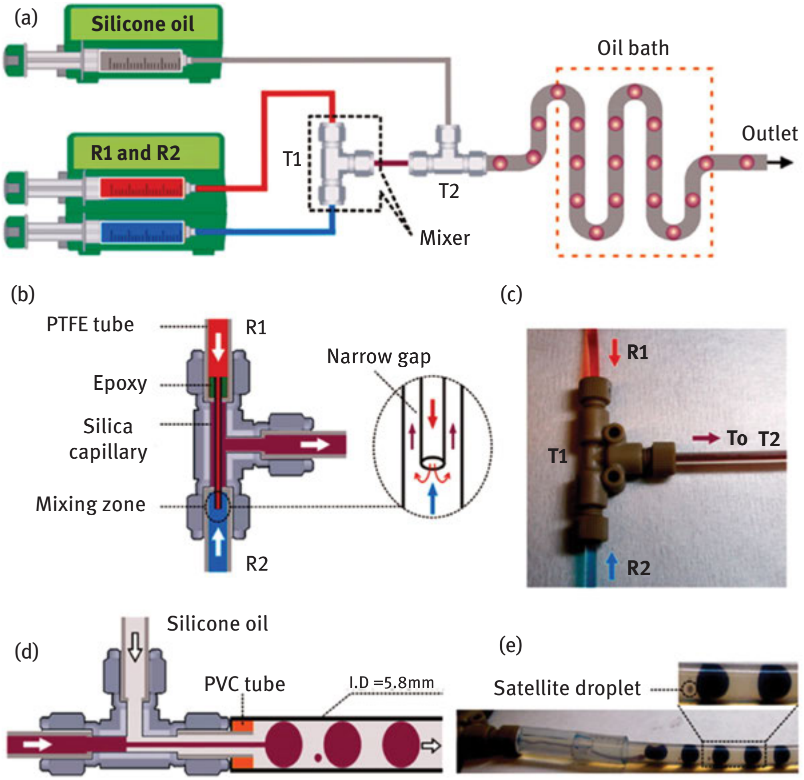

Figure 4.24: (a) Schematic illustration of the millilitre-sized droplet reactor used for the synthesis of Au NPs by ascorbic acid. (b) Schematic illustration of the flow mixer (T1) with three PTFE tubes connected to the T-junction and one silica tube fixed in the centre of the top PTFE tube. (c) Photograph of mixing demo based on the design of (b) with red and blue dye. (d) Schematic illustration of the design for droplet generating (T2). (e) Photograph of 0.25 ml droplets and 0.5 µl satellite droplets in the PTFE tube with an I.D. of 5.8 mm (reprinted with permission from Ref. [208]. Copyright 2014, American Chemical Society).

4.4 Guidelines for the design of continuous nanoparticle processes

4.4.1 A general overview of nanoparticle synthesis process development

The most important consideration for designing any Au NP synthesis process (batch or continuous flow) is the desired end use of the Au NPs. Since the properties of Au NPs vary depending on their size and shape, and also on their conjugated functionality, it is important to establish exactly what properties are required before starting any design process. There is no synthesis process that fits all needs. Many different synthesis processes produce Au NPs which are pre-functionalized with a specific ligand which cannot be easily removed or exchanged and thus are only suitable in cases where the ligand has no impact on the application, or is the exact ligand required for said application. Similarly, some processes utilize toxic reagents which, though they might not be present in the final product, may make them unsuitable for pharmaceutical applications. Thus, the particular application will provide targets for size (or size range), polydispersity, choice of stabilization agents and throughput. The choice of stabilization agents affects hydrophobicity/philicity, subsequent functionalization, as well as long-term stability and storage of the particular nanoparticle formulation. It is important to note that if the conversion of the precursor is not complete during the synthesis, unreacted precursor will lead to nanoparticle growth/aggregation during storage.

Typically, there is more than one way to achieve the desired outcome. For example 7 nm particles functionalized with an amine can be achieved in a variety of ways. The Turkevich method has been shown to produce particles as small as 6 nm [71]. Such particles can be synthesized and consequently functionalized with other capping agents, such as thiol, cysteine or short proteins. Alternatively oleylamine-based synthesis can also achieve 7 nm Au NPs with very tight size control which can also subsequently be functionalized [209]. At the start of the design process it is important to establish as many suitable synthesis routes as possible, since one or more of these could later become discounted due to further complications downstream.

Once a suitable process (or processes) has been chosen there are several key design considerations which should be taken into account when trying to transfer an Au NP synthesis process into flow. Without being exhaustive, Figure 4.25 illustrates some of the considerations and challenges which can be encountered when developing an Au NP synthesis process, along with corresponding tools for addressing them. Some of the tools are chemistry-based, while others are engineering-based. Thus, a multidisciplinary approach will have more chances for developing an optimized process. Due to the relatively low annual production rates required and the sensitivity of most Au NP synthesis techniques, this schematic focuses on the design aspects which would be addressed for developing micro or millifluidic reactor systems.

As illustrated by Figure 4.25, there are relatively few design considerations to be made when developing a batch process, though their complexity should not be underestimated. In a typical batch process the chosen synthesis route is the greatest factor in the design, since this predetermines the size of the particles, their polydispersity and their functionality or ability to be functionalized. These properties can be manipulated by studying the kinetics of the system (as discussed earlier), where a design-of-experiments approach can also provide additional guidance. Varying the temperature, pH or chemical composition of a reaction mixture can be used to fine tune the process, but ultimately does not change the physical design of a batch reactor. Small batch systems, such as lab scale synthesis in a round bottom flask,

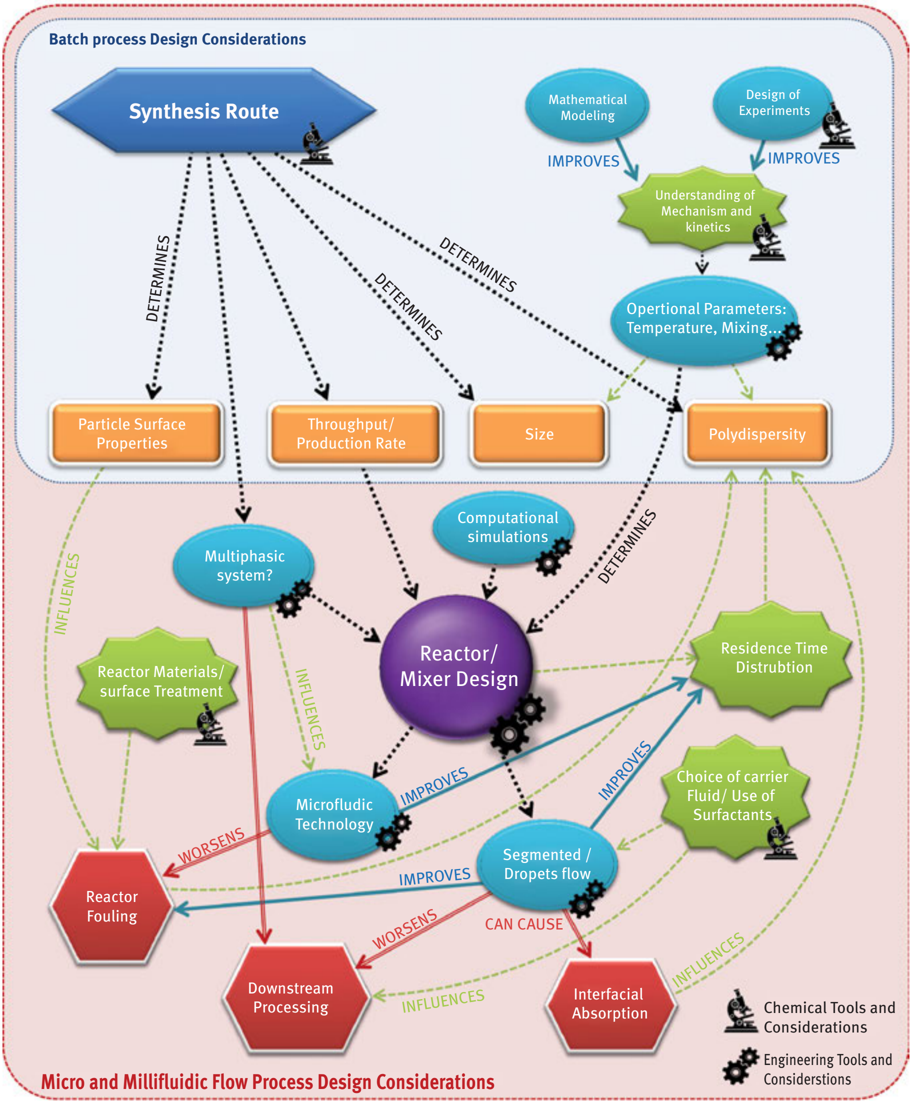

Figure 4.25: Key considerations for the development of a nanoparticle synthesis process in batch and flow systems “Chemical tools” indicate chemistry-based approaches for addressing the corresponding consideration, while “Engineering tools” indicate engineering-based approaches.

offer moderate reactor surface area to volume ratios (SA:Vs); this needs to be considered when synthesizing particles, since any surface or interface can act as a nucleation zone or potentially provide surfaces for fouling. This is less critical in larger vessels used for process scale-up, though other problems can arise, such as inefficient mixing/heating.

When the mixing efficiency of the reaction mixture plays an important role in product quality, batch reactors may be unsuitable. In cases where a reaction is very rapid (in the order of milliseconds), then it becomes crucial that the mixing time is even faster (or very well controlled), lest product quality suffers due to the formation of polydisperse particles. In this case the size of the reactor would be limited, since mixing efficiency decreases as reactor size increases. In addition to improving mixing as extensively demonstrated earlier, another way to control the process is slowing down the kinetics of the synthesis. A deeper understanding of the reaction kinetics can thus aid in identifying conditions for slowing down the synthesis, so that mixing speed is not the rate controlling step. By, for example, manipulating the pH of a system, the initial rate of reaction can be slowed and mixing can be allowed to complete before the reaction starts.

4.4.2 Challenges and solutions of micro/millifluidic processes

In contrast to batch process design, the scope of design considerations for developing a continuous flow process is much broader. In addition to all of the batch process design considerations, such as the fundamental reaction kinetics, understanding the physico-mechanical aspects of the reactors also becomes imperative. Unlike many chemical synthesis processes that only benefit from the improved RTD, mixing efficiency, heat transfer and control afforded by milli- and microfluidic devices, the synthesis of *particles* in flow systems is much more complex due to the potential for reactor surface interactions. This is due to the fact that surface area to volume ratio increases quickly in milli- and microfluidic devices. A batch reactor comprising of a 1 litre round bottom flask, for example, has a SA:V of approximately 0.5 cm^{-1}. This is much lower when compared to a 1 cm I.D. tube of the same volume which has a SA:V of 4 cm^{-1}, or a 0.5 mm I.D. capillary with a SA:V of 80 cm^{-1}. In addition to a vastly different SA:V, the materials employed also typically have drastically different physicochemical properties. Since a 1 litre reactor made from a 1 cm I.D. tube would have to be over 12 m long, the use of glass tubing becomes prohibitive and is thus typically substituted for etched glass chips with much lower volumes, or flexible plastic tubing. This means that the surface roughness and the surface chemistry of the reactors are not directly comparable with typical batch reactor systems and can have very different interactions. Altogether this may lead to fouling on the reactor walls.

4.4.2.1 Reactor design – residence time distribution

Control over the PSD is a key point for gold NPs synthesis, as many applications demand very reproducible and narrow size distributions, as discussed earlier. Recalling Figure 4.25, flow-synthesized particle characteristics are strongly affected by the RTD of the reactor. To explain what this distribution represents and why it affects NPs synthesis in flow rectors, we first need to have a brief introduction to reactor design.

A general approach to tackle reactor design is to solve the mass, momentum and energy balance equations. If all the input data (flow conditions at the inlet, temperature and composition of the feed stream, etc.) and the reaction rate laws are known, this design approach is possible. Because the equations are coupled and complex to solve, they need to be integrated numerically by means of a computational fluid dynamics (CFD) code. CFD offers the advantage to reduce to the minimum the amount of assumptions required by the model. Its major drawback, however, is the relatively high computational cost of the simulations. It should be borne in mind that the reactor design procedure aims to provide an efficient relation between the input and output of the reactor that permits reducing the parameter space in which the designer must operate and determining the optimal conditions at which to operate the reactor. For this analysis – which involves scanning over a broad range of conditions – CFD models are not well suited. The appropriate models should be able to describe the reactor performance, with reasonable accuracy, at much less computational cost. To achieve this, one usually favours simpler models, based on a larger number of simplifying assumptions, that are fast to solve numerically and able to provide the information of interest to the accuracy required.

A modelling approach frequently employed consists of determining the contacting patterns in the reactor first and then use them to evaluate the reactor performance. The contacting patterns can be determined either by solving for the fluid dynamics in *absence of reaction* or by assuming the fluid dynamic behaviour so that the momentum balance equation does not need to be solved, or by experimentally analysing the behaviour of inert tracers in the reactor [210, 211]. Quantitatively, the contacting patterns are expressed by means of the RTD function [66]. Denoted by $E(t)$, this is defined so that $E(t)\mathrm{d}t$ yields the fraction of fluid that spends in the reactor a time in the range $\mathrm{d}t$ around the value t. Therefore, the RTD is a probability density function that describes the amount of time spent in the reactor by each fluid element (infinitesimally small macroscopically, but containing a statistically significant number of molecules).

One can imagine each one of these fluid elements as a batch reactor characterized by a certain reaction time t. The “weight” of the contribution of each fluid element to the overall reactor output is given by the RTD, which indicates how many fluid elements are characterized by any given residence time t. For continuous reactors synthesizing NPs, one is usually interested not only in the reactor conversion (as in “conventional” reactors), but also in the PSD. Denoted by $n(v)$, the PSD is defined so that $n(v)\mathrm{d}v$ yields the number of particles with volume in the range $\mathrm{d}v$ around v. If we know the time evolution of the PSD for a hypothetical batch reactor (even though we have pointed out how complex this is earlier), then the PSD at the outlet of a continuous flow reactor $\bar{n}(v)$ is given by:

$$\bar{n}(v) = \int_0^{+\infty} n(v, t)E(t)\mathrm{d}t.$$

This equation reveals the key role that the RTD plays in determining the characteristics of the NPs synthesized in a flow reactor. The width of the RTD makes the PSD of the continuous flow reactor differ from that of the batch (or of the plug flow) reactor. In particular, the “wider” the RTD, the “wider” the PSD. Hence, effort has to be put in “narrowing” the RTD of these reactors [43, 212–214]. It has been recently shown how the RTD-based approach can be employed to predict the outcome of flow reactors synthesizing NPs, taking into account different contacting patterns as well as the different diffusivities of precursors and NPs [215]. In this work, the PSD was determined for a single-phase (laminar) microreactor and a segmented flow microreactor as these reactors represent the most commonly encountered continuous reactors employed, as discussed earlier. While segmented flow reactors led to narrow PSDs due to their narrow RTD, single-phase laminar reactors characterized by a wider RTD, led to wider PSDs.

The RTD approach is no longer valid when mixing time significantly affects the synthesis product. In this case, PBEs have to be implemented within CFD codes to solve for the evolution of the PSD. This approach has been used by Marchisio and coworkers [216] to model a confined impinging jet reactor synthesizing barium sulphate NPs via a precipitation reaction. In this system, mixing and reaction have the same timescale, and so the RTD approach would not have been suitable.

4.4.2.2 Reactor fouling/interfacial absorption

Fouling (either due to fully formed particles depositing on the reactor walls or from reactants reacting and plating the walls) often creates complications in milli- and microfluidic flow systems used for synthesizing particles. Not only does fouling lead to a loss of material, and therefore a lower product yield, but it can also create secondary heterogeneous nucleation sites and “particle incubation zones”. Since the rate of nucleation on the tubing walls would be inherently different than that in the bulk of the solution, this can lead to increased polydispersity in the product. Similarly, if particles foul or get temporarily entrapped on or in the surface of the material where the concentration of unreacted Au NP precursors is still high, they can continue to grow to much larger sizes, and often take on unusual shapes. The slow build-up of fouling also leads to a gradual change in the reactor’s physical properties during use (from hydrophobic to hydrophilic for example). This can lead to a variable product, since the yield and polydispersity change as fouling increases and can eventually even block the flow through the reactors. This is especially evident when using synthesis techniques where the Au NPs are charge stabilized, such as the classical citrate reduction method. As illustrated in Figure 4.26, a purple-gold

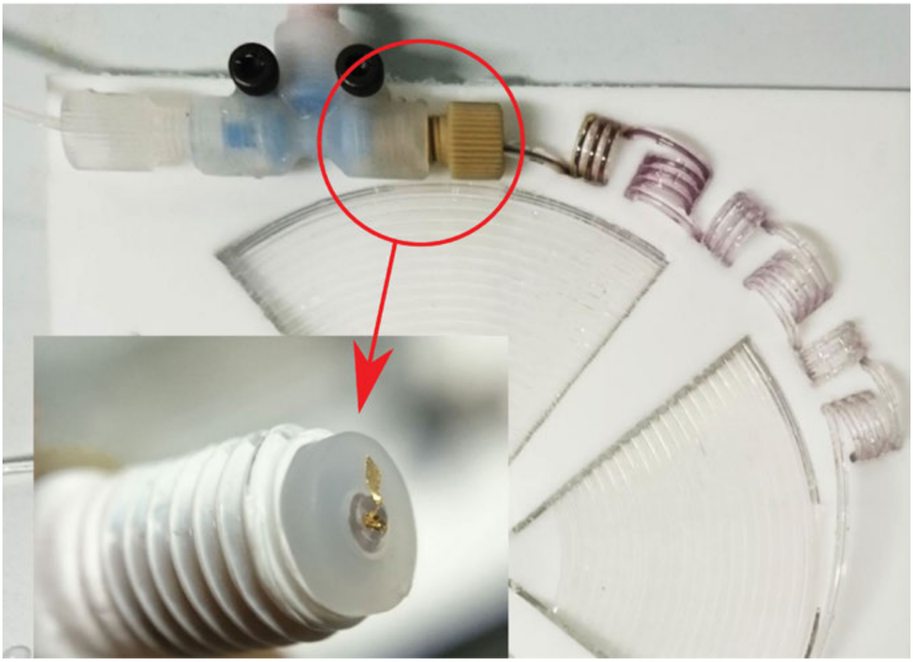

Figure 4.26: Typical level of fouling observed when classical citrate reduction was employed in a microfluidic reactor (0.5 mm I.D. FEP tubing) with flows of 0.2 ml/min each of a 1 mM $HAuCl_4$ solution and a 5 mM trisodium citrate solution mixed with a T-mixer at 90 °C. Blockage (inset) observed after approximately 8 h continuous operation.

fouling was often evident immediately after the reagents ($HAuCl_4$ and $Na_3C_6H_5O_7$) were mixed. During prolonged operation, the level of fouling could be so high as to form sheets of gold leaf inside the tubing which eventually led to the formation of blockages (Figure 4.26 inset).

In order to counteract fouling various techniques can be employed. Since a high SA:V is difficult to overcome without sacrificing on efficient heat and mass transfer, as well as the residence time (or RTD), physicochemical steps are generally taken to discourage fouling, and some of them have been detailed earlier. These include carefully considering the choice of tubing material (the use of high density plastics, or plastics with a lower porosity), chemically treating tubing to change the hydrophobicity [217] and surface charge, or the use of segmented flow to prevent contact between the reaction medium and the tubing wall. However, it is important to note that each step taken to prevent fouling can lead to further complications of their own. A chemical surface treatment can wear off over time, contaminating the product and causing variable conditions inside the reactor. The use of immiscible segmenting fluids can cause interfacial absorption [218] and can also increase the complexity of downstream processing, since the carrier fluid would then have to be separated from the product. Figure 4.27a illustrates how extensive interfacial absorption can be. In this case toluene was compared with dodecane to create segmented flows for a classical citrate reduction Au NP synthesis method. Both fluids prevented fouling within the reactor; however, in the case of toluene nearly all of the synthesized particles were lost due to interfacial absorption.

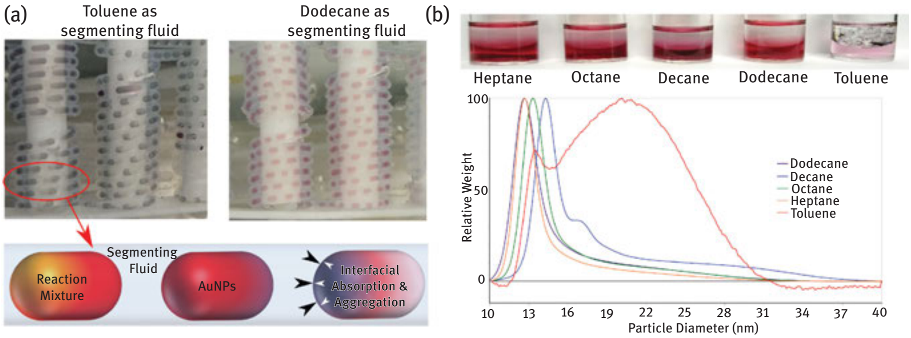

Figure 4.27: The effect of different segmenting fluids on the interfacial absorption of Au NPs during classical citrate reduction synthesis (a reaction mixture consisting of 0.5 mM $HAuCl_4$, 5 mM trisodium citrate and 1 mM citric acid prepared in-line at room temperature) segmented with the chosen segmenting fluid using a T-mixer before entering a hot (90 °C) millifluidic reactor (2.1 mm I.D. FEP tubing); (A) schematic and photos illustrating the occurrence of interfacial absorption, and (B) effect of interfacial absorption on the PSD of the remaining Au NPs depending on the segmenting fluid chosen (measured by differential centrifugal sedimentation).

In addition to leading to a loss of material, the occurrence of interfacial absorption can also affect the size and size distribution of the particles that remain. Figure 4.27b shows the PSDs achieved when the same reaction mixture was segmented with five different segmenting fluids, namely heptane, octane, decane, dodecane and toluene. In addition to the loss of material observed through the appearance of a dark film of aggregates at the interface between solutions (with toluene being by far the worst), the size and size distributions varied in each case. This suggests that similarly to fouling on the reactor wall, the occurrence of interfacial absorption also leads to heterogeneous nucleation sites or “particle incubation zones”. In order to reduce this effect it is clear that a good understanding of the interactions between fluids is required, but also that a certain degree of investigation is needed to determine the best segmenting fluid to use. In Figure 4.27b for example, there does not appear to be a distinct trend between the length of the alkane used (and consequently the density, viscosity, miscibility or interfacial surface tension) and its effect on particle size, but it is evident that both heptane and dodecane performed best.

Ultimately fouling, or the secondary complications arising from attempts to mitigate fouling, might not be overcome to a satisfactory standard (if, for example, the added downstream processing becomes cost prohibitive). In these cases it is worth reconsidering which synthesis routes are available, which will ultimately produce the same product. For example, Au NPs conjugated with thiol-based molecules have a much lower prevalence to foul. A route which employs these ligands during synthesis will not present as much of a fouling problem, so, if what is needed is amine functionalized Au NPs, it might be best to use a process that employs an amine thiol.

4.4.2.3 Multiphasic reaction systems

The use of multiphasic reaction systems must be carefully considered when designing a continuous flow process. This is not only due to the added difficulties involved in in-flow phase separation, but also due to the different interfacial surface areas achieved in batch and flow systems (analogous to the difference in SA:V between batch and flow systems). In multiphase reaction systems (where reactants are separated by a phase boundary), maintaining a constant size of the interface is paramount in order to ensure that the product produced is of good and reproducible quality. This is due to the fact that the interfacial surface area limits the rate at which reactants and products can be transferred between phases.

In batch systems, the interface between two phases is dynamic with both solutions free to circulate throughout the reactor and disperse into each other through the formation of droplets under agitation. Since the phases are not isolated (droplets can subsequently coalesce and re-join the bulk of the solutions) a chaotic and poorly regulated interface is present. The formation of additional phases (such as the evolution of gas) does not interfere, since gas bubbles are rapidly removed from the system. In contrast, when using a milli or microfluidic reactor system, each droplet is spatially isolated from the next. Thus each droplet has its own interface and ensuring that each droplet has the same interfacial surface area is necessary. Thus, systems like this have to be well ordered. In order to achieve the same rate of phase transfer, the size of each droplet has to be identical every time the experiment is run. This can be difficult to achieve, especially in cases where gas evolution also takes place.

A good example to illustrate the potential complications of using multiphasic reaction systems in a continuous flow process is the technique for synthesizing thiol capped Au NPs proposed by Brust et al. [157]. In the classical Brust-Schiffrin method, a prepared Au(*x*) and dodecanethiol in toluene solution (where *x* denotes the mixture of Au(I) and Au(III) resulting from the partial and incomplete reduction of Au(III) to Au(I) by dodecanethiol), is continuously mixed with an aqueous $NaBH_4$ solution to facilitate the reduction of the Au(*x*) to Au(0) forming dodecanethiol capped Au NPs. The reduction of Au(*x*) by $NaBH_4$ results in the rapid evolution of hydrogen gas.

Since the interface between the toluene and the water phases plays an important role during reduction, either as the site of the reaction or as the medium through which phase transfer of $NaBH_4$ occurs, it is important to maximize the size of this interface in flow. The most obvious choice is thus to employ droplet flow with small droplets of an Au(*x*) solution dispersed in an aqueous $NaBH_4$ solution as this ensures the greatest possible interfacial surface area. However, as illustrated by Figure 4.28, complications can arise in this case due to the evolution of hydrogen gas.

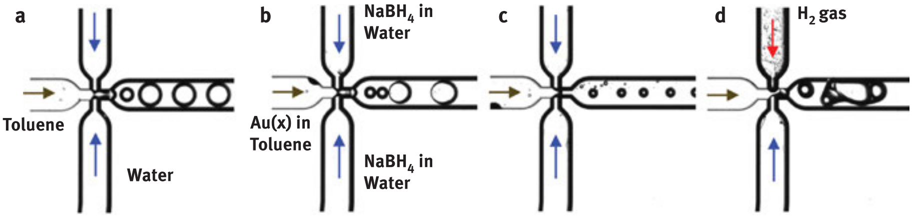

Figure 4.28: Multiphasic reaction system in a microfluidic droplet chip (3200130, Dolomite); (a) toluene (50 µl/min) as dispersed/droplet phase and water (210 µl/min) as continuous phase, (b–d) a 11.25 mM Au(*x*), 10.5 mM dodecanthiol and 50 mM tetraoctylammonium bromide in toluene solution as the dispersed phase (50 µl/min) and 30 mM NaBH$_4$ aqueous solution as continuous phase (210 µl/min).

As can be seen in Figure 4.28a, when pure toluene and water were used, stable droplet flow was achieved with uniform sized toluene droplets which would result in very high interfacial surface areas for the transfer of NaBH$_4$ into toluene. However, when the reactant solutions were used, highly variable and uncontrolled flow was achieved due to the rapid evolution of hydrogen gas in the aqueous NaBH$_4$ stream. This not only resulted in inconsistent droplet sizes (Figure 4.28b and Figure 4.28c), but also in a complex three-phase flow where the toluene and water phases did not make contact (Figure 4.28d). The end result was that the droplet flow was unstable causing the coalescence of the toluene droplets to form segmented or slug flow. These segments were uneven in size, not uniformly distributed, and often separated by H$_2$ gas segments. Figure 4.29 shows the particles produced in the batch and flow processes as analysed by TEM. The particles produced in the batch experiment were very similar to the particles produced in the classical Brust-Schiffrin method with an average particle size of 2.3 ± 0.4 nm. In contrast, the particles produced in segmented flow were more polydispersed, with a significant number of larger Au NPs (approximately 5 nm) produced as well. These results are likely a result of H$_2$ gas formation. As illustrated in Figure 4.29b, the evolution of gas in a segmented flow system results in a reduction of the interfacial surface area between the aqueous solution and toluene, since the gas bubbles form segments of their own which block the interaction between the phases. In addition, the evolution of gas increases the overall flow rate and therefore reduces the actual residence time in the reactor. Conversely, in a batch system (Figure 4.29a), the evolution of gas bubbles enhances mixing and recirculation of material in both phases. Since the gas is free to escape there is also no build-up at the interface between the water and toluene phases, so no “blocking” effect is achieved. This results in smaller and less polydisperse particles.

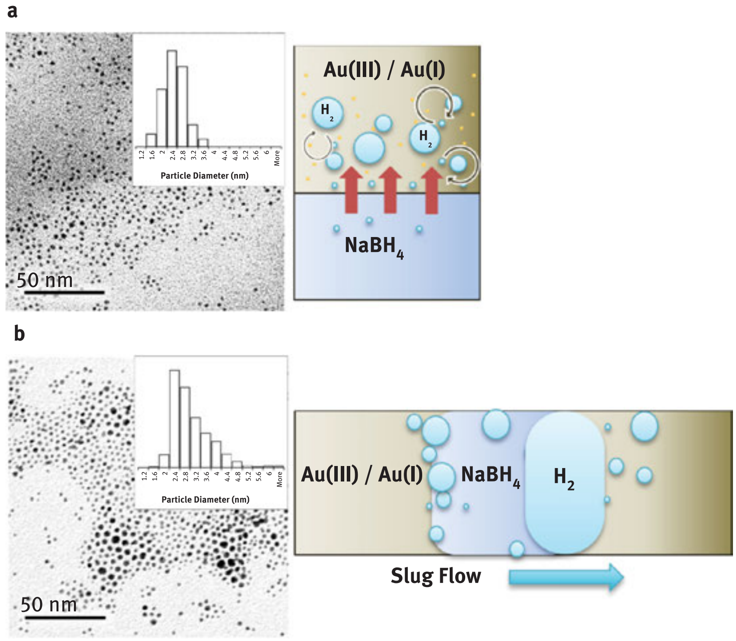

Figure 4.29: Particle size distributions and schematic of flow patterns obtained in; (a) batch and (b) continuous flow "Brust-Schiffrin" synthesis of dodecanethiol capped Au NPs. In both cases, 11.25 mM Au(*x*), 10.5 mM dodecanthiol and 50 mM tetraoctylammonium bromide in toluene solution were employed with a 120 mM $NaBH_4$ and 725 mM NaOH aqueous solution. The batch experiment utilized 2 ml of each solution in flask agitated by magnetic stirrer for 1 h. The continuous flow setup utilized a T-mixer to create segmented flow through a length of FEP tubing (5 m long, 0.5 mm I.D., 1.0 ml volume) with both solutions flowing at approximately 0.5 ml/h resulting in a 1 h residence time. Size distributions were determined by TEM.

A potential solution to this problem is to prevent the evolution of hydrogen gas from the $NaBH_4$ by either using much lower concentrations (so that the H_2 formed remains dissolved in the water), or to use higher pH solution to buffer the release of H^+ from $NaBH_4$ and thus prevent the formation of H_2 altogether. These types of changes could however have knock-on effects on the chemistry of the Au NP synthesis reactions. Changing the concentrations of reactants can change the kinetics and mechanisms involved in particle formation, resulting in Au NPs of different sizes or in the formation of by-products. Altering the pH can also change the species of the reactants present which can in turn alter their reactivity.

4.4.2.4 Downstream processing

Whenever continuous flow reactor systems are used, continuous downstream processing needs to be considered. The benefits attained by continuous manufacturing processes could be lessened if downstream processing is conducted in a batch wise fashion. For example, there is little gain from continuously synthesizing Au NPs, if one then has to wait and collect a litre at a time to purify and wash the products in batches. If synthesis is conducted in flow, then downstream processing (purification, precipitation or further functionalization, etc.) should also be conducted in flow.

One of the principle concerns in continuous flow downstream processing involved in Au NP production is phase separation. Using segmented flow to control RTD, prevent fouling or due to the fact that the reaction system is multiphasic, creates the need to subsequently separate the phases. In a batch manufacturing process this is simple, since different phases will naturally separate in the reactor due to gravity. Gas bubbles will dissipate and oils will self-separate and fractionate based on their density, allowing the Au NP phase to be siphoned off. However, in a flow system phase separation is more complex and typically requires additional equipment such as a membrane separator.

Figure 4.30 shows a continuous flow membrane separator which can perform in-line phase separation of a segmented flow stream [219]. A PTFE membrane is used to separate a hydrophilic phase from a hydrophobic phase which readily wets the PTFE membrane. When a membrane-based continuous flow phase separator is employed, it is important to ensure that the pressure difference across the membrane is tightly

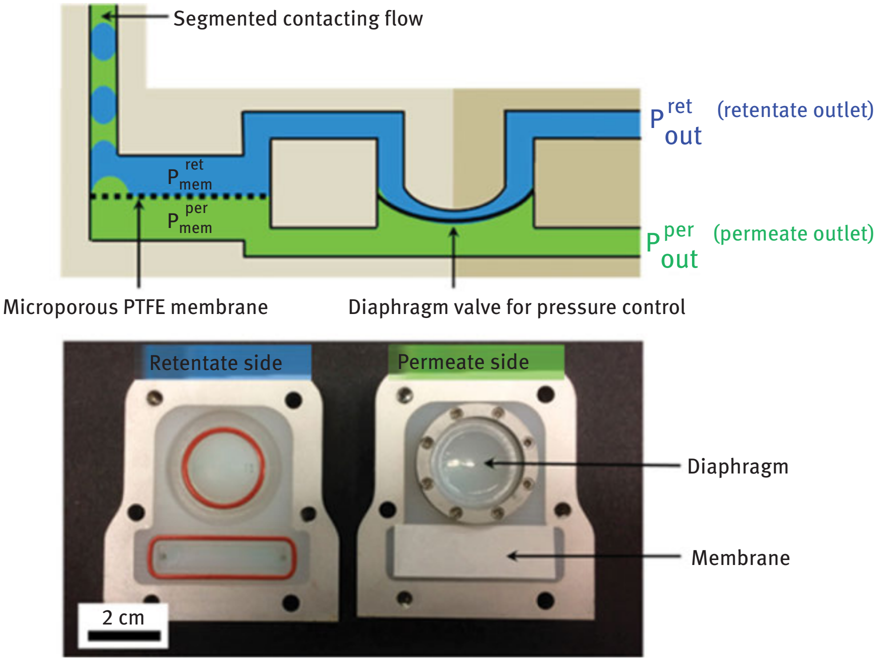

Figure 4.30: Schematic of operation and pictures of a disassembled membrane-based separator integrated with a self-tuning pressure control element (reprinted with permission from Ref. [220]. Copyright 2017, American Chemical Society).

controlled to avoid breakthrough, where both phases cross the membrane and separation is not achieved. This typically requires the use of back pressure regulators to modulate the outlet pressure of the two streams exiting the membrane separator, which not only increase the complexity of the system, but can greatly increase the cost of operation. In the separator shown in Figure 4.30 an integrated diaphragm is used to modulate the pressure between the two outlet streams and ensure that the pressure drop across the membrane is kept stable.

The introduction of such systems can result in the introduction of new problems. Fouling is a key concern whenever additional materials are introduced to a flow system (especially high surface area materials such as a membrane). We must also consider what would happen to any particles that are trapped at the phase interface due to interfacial absorption. Either these particles are forced through the membrane and leave in the permeate, are retained in the retentate, or become lodged in the membrane itself. Each of these scenarios can have significant implications for the continuous production process. In a continuous flow system it might be apt to employ several redundancies (multiple interchangeable membrane separators for example) which can allow for routine maintenance and downtime to mitigate potential problems.

Another major downstream processing operation is the continuous purification of Au NPs in flow. Many synthesis routes use one or more reactants or functionalizing agents in excess. Prior to the use of Au NPs from such synthesis techniques, the Au NP mixture has to be purified to remove these superfluous reagents. This typically involves a complex multistage process to remove the Au NPs from solution and then to repeatedly wash the particles. For example, in the classical Brust-Schiffrin method the synthesized thiolate Au NPs have to be precipitated and washed prior to use. The precipitation process involves the concentration of the Au NP in toluene solution by evaporation of toluene (an energy intensive process), the subsequent addition of a large volume of ethanol to increase the polarity of the solvent, and refrigeration (typically −18 °C for 4 h). Following precipitation the particles are removed from the solution via filtration and redispersed in toluene. The overall process is time consuming and energy intensive. It is also difficult to adapt to flow, since the process of concentrating, diluting with ethanol, cooling for 4 h, and filtration would involve many different unit operations. Thus a new approach is required.

Figure 4.31 illustrates a procedure for the in-line purification of thiolate Au NPs using continuous diafiltration [220]. In this case, slightly different water-soluble thiolate Au NPs were purified. The crude Au NP mixture was mixed with fresh solvent prior to passing through a dialysis membrane. Since the Au NPs were too large to pass through the membrane they exited the membrane in the retentate with a small amount of the solvent. The vast majority of the impurities were removed with the majority of the solvent in the permeate. Though not as effective a purification technique as precipitation and washing (where all impurities are considered

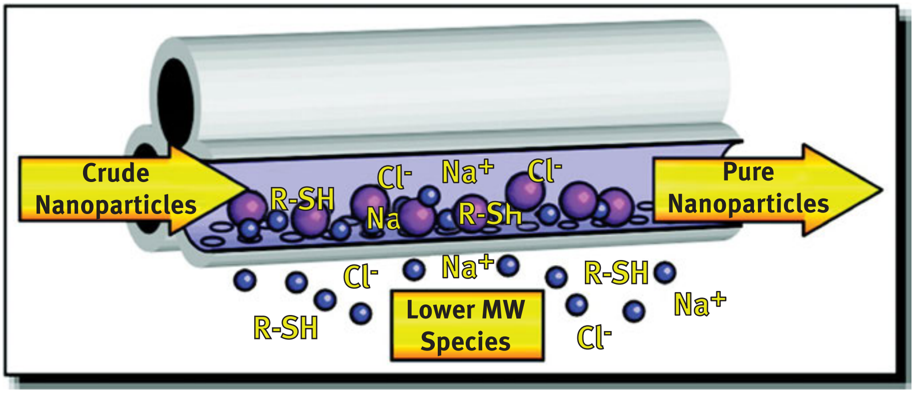

Figure 4.31: Schematic of continuous diafiltration of water-soluble thiol-stabilized 3-nm gold nanoparticles. Small molecule impurities and small gold nanoparticles (blue) are eluted in the permeate, while the larger gold nanoparticles (purple) are retained (reprinted with permission from Ref. [221]. Copyright 2006, American Chemical Society).

removed) this technique is much less energy intensive and less time consuming, since it can be performed in-line with the original reactor system. It thus provides a good compromise to the batch purification process without the costs and complexities associated with adapting the native “Brust-Schiffrin” purification process to flow. Such in-line tangential flow filtration (TFF) integrated with a millifluidic reactor was demonstrated by Lohse et al. for the removal of CTAB and by-products from the crude reaction product of gold nanorods synthesis and thiol exchange on gold nanorods [181]. TFF can potentially reduce product losses due to aggregation, because the Au NPs are not forced into close physical contact as for example during centrifugation. This type of approach relies on well stabilized Au NPs. Such high surface area membranes might be susceptible to fouling from particles which are not well stabilized, such as simple citrate charge stabilized particles. The message behind continuous flow purification, downstream processing, and indeed any flow process relating to the manufacture of Au NPs, is that compromise will be necessary and complications are likely. It is important to have a wide ranging arsenal for dealing with these problems and to be highly flexible in one’s approach. If for example the Au NPs synthesized with one particular synthesis route cannot be effectively purified in flow, then it may be prudent to pursue an alternative synthesis route altogether.

4.4.2.5 Summary of main design rules for continuous flow NP reactor design

The discussion above clearly reveals the complexity of the design of continuous flow reactors for the synthesis of NPs. A large number of aspects, most of which are closely related, need to be considered, while all the necessary information (such as kinetics of synthesis processes) to make fully informed decisions, are not always available.

Here, we present a brief summary of the main design rules that we suggest should be followed when undertaking the design of continuous flow reactors for gold nanoparticle synthesis.

1. Specify the desired end use of the Au NPs, and identify the desired Au NP properties (size, polydispersity, shape, functionality, etc.) and final process targets (throughput, purity).
2. Identify a range of suitable synthesis routes and consider each one individually.
3. Gather kinetic data for the reactions (and any other relevant process) involved, if possible. Estimate their characteristic times and assess how critical are the heat and mass transfer rates.
4. Depending on the desired throughput and on how fast the relevant kinetics are, decide whether to use a milli- or a microreactor. For larger throughputs and syntheses involving slower reactions, millireactors should be more suitable.
5. Assess the implications of mixing and RTD on PSD, which are usually more severe for larger diameter devices and single-phase reactors.
6. If fouling presents a problem, multiphase reactors (in which the flow is segmented) may be more suitable. Consider, however, the implications in terms of downstream processing and select carefully the segmenting fluid to minimize interfacial absorption.
7. If a single-phase reactor is preferable, select a channel material that prevents or reduces fouling, treat the tube or manipulate the synthesis chemistry.
8. Design the reactor and select operating conditions that result to full consumption of precursor.
9. Select the operating conditions carefully. Low concentrations and appropriate pH can be used to reduce or prevent the formation of gas products.
10. Consider separation and purification procedures at the outset, as these may affect process viability.

We also recommend considering the schematic in Figure 4.25, which, in addition presenting the key considerations for the development of nanoparticle synthesis processes in batch and flow systems, highlights as well their multiple connections.

4.5 Critical safety considerations

While many of the materials employed for the syntheses of Au NPs described in this chapter are safe to use (e. g. sodium citrate or ascorbic acid), some of the chemicals are toxic and/or flammable, hence they should be carefully handled and the experimental conditions should be strictly controlled.

1. Read the Material Safety Data Sheet (MSDS) before using any chemicals. The hazardous chemicals (with labels like Explosive, Highly Flammable, Toxic, Harmful, Corrosive, Oxidizing or Irritant) should be strictly controlled and stored

under proper conditions. A spillage kit suitable for the types of chemicals being handled, as well as the correct type of personal protective equipment (PPE) must be used. If special first-aid facilities or equipment (e. g. extinguishing media) are required, then training is essential in their use. For environmental precautions, do not let chemicals enter drains. Store the chemicals in cool place. Keep containers tightly closed in a dry and well-ventilated place.

2. If using special experimental conditions (e. g. elevated temperature, high pressure, microwaves, lasers or radiation), suitable training is required. All the relevant equipment should be checked regularly to ensure their proper operation. Appropriate operating procedures are required for risk management.
3. Gold(III) chloride hydrate needs special attention, since it is corrosive to metals and to skin, and can cause serious eye damage and skin sensitization. For safe storage, note that gold(III) chloride hydrate is light sensitive and strongly hygroscopic.
4. Sodium borohydride, a widely used strong reducing agent, could emit flammable gases which may ignite spontaneously in contact with water. Thus, it should be handled under inert gas and protected from moisture. For cleaning up, do not flush with water. Keep in suitable, closed containers for disposal. For firefighting measures, the suitable extinguishing media is dry powder.
5. For the use of thiols, be aware that special hazards (sulphur oxides) might arise from the substance or mixture.
6. Aqua regia is commonly used to clean up the apparatuses used to synthesize Au NPs. It is acutely toxic if inhaled or ingested, corrosive to skin and eyes and extremely destructive to the tissue of the mucous membranes and upper respiratory tract. It should be kept and stored away from clothing/combustible materials. Appropriate PPE (lab coat, safety glasses, with side shields or splash goggles and gloves compatible with nitric and hydrochloric acid) should always be used. Handling of aqua regia must be done only inside a fume hood and with glassware. Mix the solution in a fume hood with the sash between you and the solution. Never add any organics to aqua regia solution, it could cause an explosion. When preparing aqua regia, always add nitric acid to hydrochloric acid, never vice versa. Never store aqua regia solutions, as it will oxidize over time to form toxic gases. Make only small, fresh batches of aqua regia for each use.
7. Where hazardous or flammable gases (e. g. CO, hydrogen) are intended to be used, gas alarms/monitors are required and cylinders must be stored in vented enclosures. Purge the reactor system with dry inert gas (e. g. helium or nitrogen) before the hazardous gas is introduced and when the system is switched off. Keep away from combustible materials, heat, hot surfaces, sparks, open flames and other ignition sources.

4.6 Conclusions and future perspective

If the predicted markets for Au NPs reach their full potential, their demand will increase significantly. Since their performance is critically affected by their properties (size, size distribution, composition, surface functionality), even small deviations can render them unsuitable for the target application. Obtaining Au NPs with consistent properties with robust manufacturing processes will be required. Currently manufacturing of Au NPs is based on batch processes, which are similar to the ones used for their lab synthesis. Batch-to-batch variability however can be an issue, particularly as the scale increases, due to the inherent limitations of batch processes in terms of mass/heat transfer, hydrodynamics and reaction time control.

Microreactors and millireactors can solve some of the challenges faced to achieve high quality/quantity products. This has been demonstrated by various studies, using for example controlled or fast mixing devices, segmented flow systems, dynamic reactor operation. Such reactors can overcome issues of reproducibility, scalability and size control. They can be complex, but others, mainly millifluidic reactors, are more user-friendly. However, even though flow systems address some limitations of current batch reactor technology, they may introduce other challenges that need to be resolved before they become mainstream synthesis technology. Some of these originate from the fact that even though high surface-to-volume ratios of micro- and millifluidic reactors is advantageous in terms of mass and heat transfer, it may introduce reactor fouling.

In this chapter, we attempted to give an overview of the various challenges that can be encountered in the development of continuous Au NP synthesis and gave guidelines of how they can be addressed. Our suggestions are by no means complete. The area is at an early stage of maturity and will benefit by additional research to better understand the various physicochemical phenomena involved in the synthesis, as well as comprehensively analyse reactor performance by modelling tools. By approaching the process design in a multidisciplinary fashion, new tools and innovative solutions can be devised. This is particularly so, because nanoparticle synthesis is complex, requiring knowledge of synthetic/physical/analytical chemistry, physics, particle technology and chemical engineering. Such multidisciplinary research can expand the range of solutions available. For example, the fouling issue can be tackled from an engineering perspective through segmented flow or from a chemistry perspective by changing the synthesis chemistry reactor wall properties.

It is worth mentioning that most studies on nanoparticle synthesis in microreactors translated batch protocols to a flow process. This approach though overlooks the unique advantages offered by microreactors, such as fast heating/cooling, high pressure operation, short reaction times, staged addition of reactants. Thus, there may be new opportunities, if the advantages offered by flow operation are considered from the beginning.

Contributions from reactor engineering, separation technology, process analytic and control, chemical/systems engineering will be vital for the development of robust, reliable, cost-effective manufacturing processes, with long operating times.

Traditional chemical engineering can play an important role here. Furthermore, a knowledge-based approach, relying on mechanistic and kinetic studies of reaction, nucleation and growth can lead to the development of robust well-designed processes. However, such a rigorous approach can be time consuming, so one must consider an appropriate balance between rigour and practicality. Design of experiments can play a role in this context and can aid in minimizing the effort invested in and maximizing information obtained from experiments.

As the scale of production increases, process yield and product purity become as important as size, shape, monodispersity. Efficient coupling of the synthesis with downstream processing and purification, as well as with analytical systems for in-line/online product characterization and process control will affect process economic viability. Lessons can be learned from the various microfluidic systems that have been used with *in situ* analysis, aiming to better understand the nanoparticle mechanism and kinetics. The emergence of advanced software, machine learning and the industry 4.0 framework will allow high level of process automation. Notwithstanding that, manufacturing routes will need to be carefully selected based not only on the scalability and production cost, but also on the particular properties required for the final application.

Acknowledgements: We would like to acknowledge funding for our research from EPSRC (grant EP/M015157/1) and European Union's Horizon 2020 research and innovation programme under the Marie Skłodowska-Curie grant agreement No. 721290. A special thanks to Prof. Peter Dobson and Prof. Ivan Parkin for their insightful feedback to this chapter and our work in general. He Huang acknowledges support from the program of China Scholarships. This publication reflects only the authors' view, exempting the Community from any liability.

References

[1] Daniel MC, Astruc D. Gold nanoparticles: assembly, supramolecular chemistry, quantum-size related properties and applications toward biology, catalysis and nanotechnology. Chem Rev. 2004;104:293–346.

[2] Barreto JA, O'Malley W, Kubeil M, Graham B, Stephan H, Spiccia L. Nanomaterials: applications in cancer imaging and therapy. Adv Mater. 2011;23:12.

[3] In: Rai M., Shegokar R., editor(s). Metal nanoparticles in pharma. Cham: Springer, 2017

[4] Thota S, Crans DC. Metal nanoparticles: synthesis and applications in pharmaceutical sciences. Weinheim: John Wiley & Sons, 2018

[5] Dykman L, Khlebtsov N. Gold nanoparticles in biomedical applications: recent advances and perspectives. Chem Soc Rev. 2012;41:2256–82.

[6] Yang X, Yang M, Pang B, Vara M, Xia Y. Gold nanomaterials at work in biomedicine. Chem Rev. 2015;115:10410–88.

[7] Dreaden EC, Alkilany AM, Huang X, Murphy CJ, El-Sayed MA. The golden age: gold nanoparticles for biomedicine. Chem Soc Rev. 2012;41:2740–79.

[8] Sardar R, Funston AM, Mulvaney P, Murray RW. Gold nanoparticles: past, present, and future. Langmuir. 2009;25:13840–51.

[9] Willets KA, Van Duyne RP. Localized surface plasmon resonance spectroscopy and sensing. Annu Rev Phys Chem. 2007;58:267–97.

[10] Wilson R. The use of gold nanoparticles in diagnostics and detection. Chem Soc Rev. 2008;37:2028–45.

[11] Lane LA, Qian X, Nie S. SERS nanoparticles in medicine: from label-free detection to spectroscopic tagging. Chem Rev. 2015;115:10489–529.

[12] Saha K, Agasti SS, Kim C, Li X, Rotello VM. Gold nanoparticles in chemical and biological sensing. Chem Rev. 2012;112:2739–79.

[13] Zhang Y, Chu W, Foroushani AD, Wang H, Li D, Liu J, et al. New gold nanostructures for sensor applications: a review. Materials. 2014;7:5169–201.

[14] Matias AS, Carlos FF, Pedrosa P, Fernandes AR, Baptista PV. Gold nanoparticles in molecular diagnostics and molecular therapeutics. In: Rai M., Shegokar R, editor(s). Metal nanoparticles in pharma. Cham: Springer, 2017:365–87.

[15] Zhou W, Gao X, Liu D, Chen X. Gold nanoparticles for in vitro diagnostics. Chem Rev. 2015;115:10575–636.

[16] Vs AP, Joseph P, Scg KD, Lakshmanan S, Kinoshita T, Muthusamy S. Colorimetric sensors for rapid detection of various analytes. Mater Sci Eng: C. 2017;78:1231–45.

[17] Singh J, Sharma S, Nara S. Evaluation of gold nanoparticle based lateral flow assays for diagnosis of enterobacteriaceae members in food and water. Food Chem. 2015;170:470–83.

[18] Bahadır EB, Sezgintürk MK. Lateral flow assays: principles, designs and labels. TrAC Trends Anal Chem. 2016;82:286–306.

[19] Quesada-González D, Merkoçi A. Nanoparticle-based lateral flow biosensors. Biosens Bioelectron. 2015;73:47–63.

[20] Cordeiro M, Ferreira Carlos F, Pedrosa P, Lopez A, Baptista PV. Gold nanoparticles for diagnostics: advances towards points of care. Diagnostics. 2016;6:43.

[21] Huang X, Jain PK, El-Sayed IH, El-Sayed MA. Gold nanoparticles: interesting optical properties and recent applications in cancer diagnostics and therapy. Nanomedicine. 2007;2:681–93.

[22] Kumar A, Zhang X, Liang X-J. Gold nanoparticles: emerging paradigm for targeted drug delivery system. Biotechnol Adv. 2013;31:593–606.

[23] Alkilany AM, Thompson LB, Boulos SP, Sisco PN, Murphy CJ. Gold nanorods: their potential for photothermal therapeutics and drug delivery, tempered by the complexity of their biological interactions. Adv Drug Deliv Rev. 2012;64:190–9.

[24] Abadeer NS, Murphy CJ. Recent progress in cancer thermal therapy using gold nanoparticles. J Phys Chem C. 2016;120:4691–716.

[25] Yao C, Zhang L, Wang J, He Y, Xin J, Wang S, et al. Gold nanoparticle mediated phototherapy for cancer. J Nanomater. 2016;2016:Article ID 5497136

[26] Hwang S, Nam J, Jung S, Song J, Doh H, Kim S. Gold nanoparticle-mediated photothermal therapy: current status and future perspective. Nanomedicine. 2014;9:2003–22.

[27] Haume K, Rosa S, Grellet S, Śmiałek MA, Butterworth KT, Solov'yov AV, et al. Gold nanoparticles for cancer radiotherapy: a review. Cancer Nanotechnol. 2016;7:8.

[28] Her S, Jaffray DA, Allen C. Gold nanoparticles for applications in cancer radiotherapy: mechanisms and recent advancements. Adv Drug Deliv Rev. 2017;109:84–101.

[29] Corma A, Garcia H. Supported gold nanoparticles as catalysts for organic reactions. Chem Soc Rev. 2008;37:2096–126.

[30] Stratakis M, Garcia H. Catalysis by supported gold nanoparticles: beyond aerobic oxidative processes. Chem Rev. 2012;112:4469–506.

[31] Ciriminna R, Falletta E, Della Pina C, Teles JH, Pagliaro M. Industrial applications of gold catalysis. Angew Chem Int Ed. 2016;55:14210–7.

[32] Cebrián V, Martín-Saavedra F, Yagüe C, Arruebo M, Santamaría J, Vilaboa N. Size-dependent transfection efficiency of PEI-coated gold nanoparticles. Acta Biomater. 2011;7:3645–55.

[33] Chithrani BD, Ghazani AA, Chan WC. Determining the size and shape dependence of gold nanoparticle uptake into mammalian cells. Nano Lett. 2006;6:662–8.

[34] Leifert A, Pan-Bartnek Y, Simon U, Jahnen-Dechent W. Molecularly stabilised ultrasmall gold nanoparticles: synthesis, characterization and bioactivity. Nanoscale. 2013;5:6224–42.

[35] Dykman L, Khlebtsov N. Gold nanoparticles in biology and medicine: recent advances and prospects. Acta Nat. 2011;3:34–55

[36] Pan Y, Neuss S, Leifert A, Fischler M, Wen F, Simon U, et al. Size-dependent cytotoxicity of gold nanoparticles. Small. 2007;3:1941–9.

[37] Hvolbæk B, Janssens TV, Clausen BS, Falsig H, Christensen CH, Nørskov JK. Catalytic activity of Au nanoparticles. Nano Today. 2007;2:14–8.

[38] Hashmi ASK, Rudolph M. Gold catalysis in total synthesis. Chem Soc Rev. 2008;37:1766–75.

[39] Sebastian V, Arruebo M, Santamaria J. Reaction engineering strategies for the production of inorganic nanomaterials. Small. 2014;10:835–53.

[40] Valencia PM, Farokhzad OC, Karnik R, Langer R. Microfluidic technologies for accelerating the clinical translation of nanoparticles. Nat Nanotechnol. 2012;7:623.

[41] Krishna KS, Li Y, Li S, Kumar CS. Lab-on-a-chip synthesis of inorganic nanomaterials and quantum dots for biomedical applications. Adv Drug Deliv Rev. 2013;65:1470–95.

[42] Puigmartí-Luis J. Microfluidic platforms: a mainstream technology for the preparation of crystals. Chem Soc Rev. 2014;43:2253–71.

[43] Marre S, Jensen KF. Synthesis of micro and nanostructures in microfluidic systems. Chem Soc Rev. 2010;39:1183–202.

[44] Tsuzuki T. Commercial scale production of inorganic nanoparticles. Int J Nanotechnol. 2009;6:567–78.

[45] Taifur-Rahman M, Rebrov E. Microreactors for gold nanoparticles synthesis: from Faraday to flow. Processes. 2014;2:466.

[46] deMello AJ. Control and detection of chemical reactions in microfluidic systems. Nature. 2006;442:394–402.

[47] Nightingale AM, deMello JC. Segmented flow reactors for nanocrystal synthesis. Adv Mater. 2013;25:1813–21.

[48] Saldanha PL, Lesnyak V, Manna L. Large scale syntheses of colloidal nanomaterials. Nano Today. 2017;12:46–63.

[49] Maceiczyk RM, Lignos IG. Online detection and automation methods in microfluidic nanomaterial synthesis. Curr Opin Chem Eng. 2015;8:29–35.

[50] Park JI, Saffari A, Kumar S, Günther A, Kumacheva E. Microfluidic synthesis of polymer and inorganic particulate materials. Annu Rev Mater Res. 2010;40:415–43.

[51] Shestopalov I, Tice JD, Ismagilov RF. Multi-step synthesis of nanoparticles performed on millisecond time scale in a microfluidic droplet-based system. Lab Chip. 2004;4:316–21.

[52] Zhao C-X, He L, Qiao SZ, Middelberg APJ. Nanoparticle synthesis in microreactors. Chem Eng Sci. 2011;66:1463–79.

[53] Niu G, Ruditskiy A, Vara M, Xia Y. Toward continuous and scalable production of colloidal nanocrystals by switching from batch to droplet reactors. Chem Soc Rev. 2015;44:5806–20.

[54] Shang L, Cheng Y, Zhao Y. Emerging droplet microfluidics. Chem Rev. 2017;117:7964–8040.

[55] Pan LJ, Tu JW, Ma HT, Yang YJ, Tian ZQ, Pang DW, et al. Controllable synthesis of nanocrystals in droplet reactors. Lab Chip. 2018;18:41–56.

[56] Kim JH, Jeon TY, Choi TM, Shim TS, Kim S-H, Yang S-M. Droplet microfluidics for producing functional microparticles. Langmuir. 2013;30:1473–88.

[57] Alexandridis P. Gold nanoparticle synthesis, morphology control, and stabilization facilitated by functional polymers. Chem Eng Technol. 2011;34:15–28.

[58] Grzelczak M, Pérez-Juste J, Mulvaney P, Liz-Marzán LM. Shape control in gold nanoparticle synthesis. Chem Soc Rev. 2008;37:1783–91.

[59] Guo S, Wang E. Synthesis and electrochemical applications of gold nanoparticles. Anal Chim Acta. 2007;598:181–92.

[60] Zhao P, Li N, Astruc D. State of the art in gold nanoparticle synthesis. Coord Chem Rev. 2013;257:638–65.

[61] Günther A, Jensen KF. Multiphase microfluidics: from flow characteristics to chemical and materials synthesis. Lab Chip. 2006;6:1487–503.

[62] Song Y, Hormes J, Kumar CS. Microfluidic synthesis of nanomaterials. Small. 2008;4: 698–711.

[63] Shahbazali E, Hessel V, Noël T, Wang Q. Metallic nanoparticles made in flow and their catalytic applications in organic synthesis. Nanotechnol Rev. 2014;3:65–86.

[64] Sebastian V, Khan SA, Kulkarni AA. Flow synthesis of functional materials. J Flow Chem. 2017;7:96–105.

[65] Navin CV, Krishna KS, Theegala CS, Kumar CS. Lab-on-a-chip devices for gold nanoparticle synthesis and their role as a catalyst support for continuous flow catalysis. Nanotechnol Rev. 2014;3:39–63.

[66] Levenspiel O. Chemical reaction engineering, 3rd ed. Weinheim: John Wiley & Sons, 1999

[67] Wang ZL. Transmission electron microscopy of shape-controlled nanocrystals and their assemblies. J Phys Chem B. 2000;104:1153–75.

[68] Young NP, Van Huis MA, Zandbergen HW, Xu H, Kirkland AI. Transformations of gold nanoparticles investigated using variable temperature high-resolution transmission electron microscopy. Ultramicroscopy. 2010;110:506–16.

[69] Georgiev P, Bojinova A, Kostova B, Momekova D, Bjornholm T, Balashev K. Implementing atomic force microscopy (AFM) for studying kinetics of gold nanoparticle’s growth. Colloids Surf. A. 2013;434:154–63.

[70] Khlebtsov BN, Khlebtsov NG. On the measurement of gold nanoparticle sizes by the dynamic light scattering method. Colloid J. 2011;73:118–27.

[71] Du Toit H, Macdonald T, Huang H, Parkin I, Gavriilidis A. Continuous flow synthesis of citrate capped gold nanoparticles using UV induced nucleation. RSC Adv. 2017;7:9632–38.

[72] Chaki NK, Negishi Y, Tsunoyama H, Shichibu Y. Ubiquitous 8 and 29 kDa gold: alkanethiolate cluster compounds: mass-spectrometric determination of molecular formulas and structural implications. J Am Chem Soc. 2008;130:8608–10.

[73] Kettemann F, Birnbaum A, Witte S, Wuithschick M, Pinna N, Kraehnert R, et al. Missing piece of the mechanism of the Turkevich method: the critical role of citrate protonation. Chem Mater. 2016;28:4072–81.

[74] Abécassis B, Testard F, Spalla O, Barboux P. Probing in situ the nucleation and growth of gold nanoparticles by small-angle X-ray scattering. Nano Lett. 2007;7:1723–27.

[75] Polte J, Erler R, Thünemann AF, Emmerling F, Kraehnert R. SAXS in combination with a free liquid jet for improved time-resolved in situ studies of the nucleation and growth of nanoparticles. Chem Commun. 2010;46:9209–11.

[76] Polte J, Erler R, ThüNemann AF, Sokolov S, Ahner TT, Rademann K, et al. Nucleation and growth of gold nanoparticles studied via in situ small angle X-ray scattering at millisecond time resolution. ACS Nano. 2010;4:1076–82.

[77] Abécassis B, Testard F, Kong Q, Francois B, Spalla O. Influence of monomer feeding on a fast gold nanoparticles synthesis: time-resolved XANES and SAXS experiments. Langmuir. 2010;26:13847–54.

[78] Polte J, Ahner TT, Delissen F, Sokolov S, Emmerling F, Thunemann AF, et al. Mechanism of gold nanoparticle formation in the classical citrate synthesis method derived from coupled in situ XANES and SAXS evaluation. J Am Chem Soc. 2010;132:1296–301.
[79] Kwon K, Lee KY, Lee YW, Kim M, Heo J, Ahn SJ, et al. Controlled synthesis of icosahedral gold nanoparticles and their surface-enhanced Raman scattering property. J Phys Chem C. 2007;111:1161–65.
[80] Allabashi R, Stach W, De La Escosura-Muñiz A, Liste-Calleja L, Merkoçi A. ICP-MS: a powerful technique for quantitative determination of gold nanoparticles without previous dissolving. J Nanopart Res. 2008;11:2003.
[81] Laborda F, Bolea E, Jiménez-Lamana J. Single particle inductively coupled plasma mass spectrometry: a powerful tool for nanoanalysis. Anal Chem. 2014;86:2270–8.
[82] Dequaire M, Degrand C, Limoges B. An electrochemical metalloimmunoassay based on a colloidal gold label. Anal Chem. 2000;72:5521–8.
[83] González García MB, Costa García A. Adsorptive stripping voltammetric behaviour of colloidal gold and immunogold on carbon paste electrode. Bioelectrochem Bioenerg. 1995;38:389–95.
[84] Pumera M, Aldavert M, Mills C, Merkoçi A, Alegret S. Direct voltammetric determination of gold nanoparticles using graphite-epoxy composite electrode. Electrochim Acta. 2005;50:3702–7.
[85] Welz B, Becker-Ross H, Florek S, Heitmann U. High-resolution continuum source AAS: the better way to do atomic absorption spectrometry. Weinheim: John Wiley & Sons, 2006
[86] Elzey S, Tsai DH, Rabb SA, Yu LL, Winchester MR, Hackley VA. Quantification of ligand packing density on gold nanoparticles using ICP-OES. Anal Bioanal Chem. 2012;403:145–9.
[87] Hendel T, Lesnyak V, Kühn L, Herrmann AK, Bigall NC, Borchardt L, et al. Mixed aerogels from Au and CdTe nanoparticles. Adv Funct Mater. 2013;23:1903–11.
[88] Liu X, Atwater M, Wang J, Huo Q. Extinction coefficient of gold nanoparticles with different sizes and different capping ligands. Colloids Surf. B. 2007;58:3–7.
[89] Kattumuri V, Katti K, Bhaskaran S, Boote EJ, Casteel SW, Fent GM, et al. Gum arabic as a phytochemical construct for the stabilization of gold nanoparticles: in vivo pharmacokinetics and X-ray-contrast-imaging studies. Small. 2007;3:333–41.
[90] Park J, Shumaker-Parry JS. Structural study of citrate layers on gold nanoparticles: role of intermolecular interactions in stabilizing nanoparticles. J Am Chem Soc. 2014;136:1907–21.
[91] Koziej D. Revealing complexity of nanoparticle synthesis in solution by in situ hard X-ray spectroscopy – today and beyond. Chem Mater. 2016;28:2478–90.
[92] Ohyama J, Teramura K, Higuchi Y, Shishido T, Hitomi Y, Aoki K, et al. An in situ quick XAFS spectroscopy study on the formation mechanism of small gold nanoparticles supported by porphyrin-cored tetradentate passivants. Phys Chem Chem Phys. 2011;13:11128–35.
[93] Zhang P, Sham T. X-ray studies of the structure and electronic behavior of alkanethiolate-capped gold nanoparticles: the interplay of size and surface effects. Phys Rev Lett. 2003;90:245502.
[94] Park J-W, Shumaker-Parry JS. Strong resistance of citrate anions on metal nanoparticles to desorption under thiol functionalization. ACS Nano. 2015;9:1665–82.
[95] Badia A, Cuccia L, Demers L, Morin F, Lennox RB. Structure and dynamics in alkanethiolate monolayers self-assembled on gold nanoparticles: a DSC, FT-IR, and deuterium NMR study. J Am Chem Soc. 1997;119:2682–92.
[96] Ji X, Song X, Li J, Bai Y, Yang W, Peng X. Size control of gold nanocrystals in citrate reduction: the third role of citrate. J Am Chem Soc. 2007;129:13939–48.
[97] Wuithschick M, Birnbaum A, Witte S, Sztucki M, Vainio U, Pinna N, et al. Turkevich in new robes: key questions answered for the most common gold nanoparticle synthesis. ACS Nano. 2015;9:7052–71.

[98] Boleininger J, Kurz A, Reuss V, Sönnichsen C. Microfluidic continuous flow synthesis of rod-shaped gold and silver nanocrystals. Phys Chem Chem Phys. 2006;8:3824–7.

[99] Pellegrino T, Sperling RA, Alivisatos AP, Parak WJ. Gel electrophoresis of gold-DNA nanoconjugates. Journal of Biomedicine and Biotechnology. 2007;2007:Article ID 26796.

[100] Haiss W, Thanh NTK, Aveyard J, Fernig DG. Determination of size and concentration of gold nanoparticles from UV–Vis spectra. Anal Chem. 2007;79:4215–21.

[101] Hendel T, Wuithschick M, Kettemann F, Birnbaum A, Rademann K, Polte J. In situ determination of colloidal gold concentrations with UV–Vis spectroscopy: limitations and perspectives. Anal Chem. 2014;86:11115–24.

[102] Liz-Marzán LM. Tailoring surface plasmons through the morphology and assembly of metal nanoparticles. Langmuir. 2006;22:32–41.

[103] Schneider G, Decher G. From functional core/shell nanoparticles prepared via layer-by-layer deposition to empty nanospheres. Nano Lett. 2004;1833–9.

[104] Peck JA, Tait CD, Swanson BI, Brown GE. Speciation of aqueous gold (III) chlorides from ultraviolet/visible absorption and Raman/resonance Raman spectroscopies. Geochim Cosmochim Acta. 1991;55:671–6.

[105] Becker R, Doring W. Kinetic treatment of the nucleation in supersaturated vapors. Washington: National Advisory Committee for Aeronautics, 1954

[106] LaMer VK, Dinegar RH. Theory, production and mechanism of formation of monodispersed hydrosols. J Am Chem Soc. 1950;72:4847–54.

[107] Bogush GH, Zukoski CF. IV, Uniform silica particle precipitation: an aggregative growth model. J Colloid Interface Sci. 1991;142:19–34.

[108] Watzky MA, Finke RG. Transition metal nanocluster formation kinetic and mechanistic studies. a new mechanism when hydrogen is the reductant: slow, continuous nucleation and fast autocatalytic surface growth. J Am Chem Soc. 1997;119:10382–400.

[109] Zeng XC, Oxtoby DW. Gas–Liquid nucleation in Lennard–Jones fluids. J Chem Phys. 1991;94:4472–8.

[110] Xia Y, Xiong Y, Lim B, Skrabalak SE. Shape-controlled synthesis of metal nanocrystals: simple chemistry meets complex physics? Angew Chem Int Ed. 2009;48:60–103.

[111] Polte J. Fundamental growth principles of colloidal metal nanoparticles – A new perspective. Cryst Eng Comm. 2015;17:6809–30.

[112] Luty-Blocho M, Pacławski K, Jaworski W, Streszewski B, Fitzner K. Kinetic studies of gold nanoparticles formation in the batch and in the flow microreactor system. Trends in colloid and interface science XXIV, Progr Colloid Polym Sci Vol. 138. Berlin: Springer, 2011:39–44.

[113] Pacławski K, Streszewski B, Jaworski W, Luty-Błocho M, Fitzner K. Gold nanoparticles formation via gold (III) chloride complex ions reduction with glucose in the batch and in the flow microreactor systems. Colloids Surf. A. 2012;413:208–15.

[114] De Jonge N, Ross FM. Electron microscopy of specimens in liquid. Nat Nanotechnol. 2011;6:695–704.

[115] Kim BH, Yang J, Lee D, Choi BK, Hyeon T, Park J. Liquid-phase transmission electron microscopy for studying colloidal inorganic nanoparticles. Adv Mater. 2018;30:1–20.

[116] Baumgartner J, Dey A, Bomans PHH, Le Coadou C, Fratzl P, Sommerdijk NAJM, et al. Nucleation and growth of magnetite from solution. Nat Mater. 2013;12:310–14.

[117] McKenzie LC, Haben PM, Kevan SD, Hutchison JE. Determining nanoparticle size in real time by small-angle X-ray scattering in a microscale flow system. J Phys Chem C. 2010;114:22055–63.

[118] Watt J, Hance BG, Anderson RS, Huber DL. Effect of seed age on gold nanorod formation: a microfluidic, real-time investigation. Chem Mater. 2015;27:6442–9.

[119] Buining PA, Humbel BM, Philipse AP, Verkleij AJ. Preparation of functional silane-stabilized gold colloids in the (sub) nanometer size range. Langmuir. 1997;13:3921–6.

[120] Tofighi G, Lichtenberg H, Pesek J, Sheppard TL, Wang W, Schöttner L, et al. Continuous microfluidic synthesis of colloidal ultrasmall gold nanoparticles: in situ study of the early reaction stages and application for catalysis. React Chem Eng. 2017;2:876–84.

[121] Yue J, Falke FH, Schouten JC, Nijhuis TA. Microreactors with integrated UV/Vis spectroscopic detection for online process analysis under segmented flow. Lab Chip. 2013;13:4855–63.

[122] Sai Krishna K, Navin CV, Biswas S, Singh V, Ham K, Bovenkamp GL, et al. Millifluidics for time-resolved mapping of the growth of gold nanostructures. J Am Chem Soc. 2013;135:5450–6.

[123] Barnard AS. Modelling of nanoparticles: approaches to morphology and evolution. Rep Prog Phys. 2010;73:086502.

[124] Ojea-Jiménez I, Campanera JM. Molecular modeling of the reduction mechanism in the citrate-mediated synthesis of gold nanoparticles. J Phys Chem C. 2012;116:23682–91.

[125] Grochola G, Snook IK, Russo SP. Computational modeling of nanorod growth. J Chem Phys. 2007;127:194707.

[126] Häkkinen H. The gold–Sulfur interface at the nanoscale. Nat Chem. 2012;4:443.

[127] Taylor MG, Mpourmpakis G. Thermodynamic stability of ligand-protected metal nanoclusters. Nat Commun. 2017;8:15988.

[128] Ramkrishna D. Population balances – theory and applications to particulate systems in engineering, 1. Academic Press, 2000:355.

[129] Crowley T. Control of particle size distribution described by a population balance model of semibatch emulsion polymerization. J Process Control. 2000;10:419–32.

[130] Immanuel CD, Doyle FJ, III. Computationally efficient solution of population balance models incorporating nucleation, growth and coagulation: application to emulsion polymerization. Chem Eng Sci. 2003;58:3681–98.

[131] Kotoulas C, Kiparissides C. A generalized population balance model for the prediction of particle size distribution in suspension polymerization reactors. Chem Eng Sci. 2006;61:332–46.

[132] Marchal P, David R, Klein JP, Villermaux J. Crystallization and precipitation engineering-I. An efficient method for solving population balance in crystallization with agglomeration. Chem Eng Sci. 1988;43:59–67.

[133] Puel F, Févotte G, Klein JP. Simulation and analysis of industrial crystallization processes through multidimensional population balance equations. Part 1: a resolution algorithm based on the method of classes. Chem Eng Sci. 2003;58:3715–27.

[134] Puel F, Févotte G, Klein JP. Simulation and analysis of industrial crystallization processes through multidimensional population balance equations. Part 2: a study of semi-batch crystallization. Chem Eng Sci. 2003;58:3729–40.

[135] Bogush GH, Zukoski CF, IV. Studies of the kinetics of the precipitation of uniform silica particles through the hydrolysis and condensation of silicon alkoxides. J Colloid Interface Sci. 1991;142:1–18.

[136] Park J, Joo J, Soon GK, Jang Y, Hyeon T. Synthesis of monodisperse spherical nanocrystals. Angew Chem Int Ed. 2007;46:4630–60.

[137] Stolzenburg P, Garnweitner G. Experimental and numerical insights into the formation of zirconia nanoparticles: a population balance model for the nonaqueous synthesis. React Chem Eng. 2017;2:337–48.

[138] Rempel JY, Bawendi MG, Jensen KF. Insights into the kinetics of semiconductor nanocrystal nucleation and growth. J Am Chem Soc. 2009;131:4479–89.

[139] Maceiczyk RM, Bezinge L, deMello AJ. Kinetics of nanocrystal synthesis in a microfluidic reactor: theory and experiment. React Chem Eng. 2016;1:261–71.

[140] Lazzari S, Abolhasani M, Jensen KF. Modeling of the formation kinetics and size distribution evolution of II–VI quantum dots. React Chem Eng. 2017;2:567–76.

[141] Perala SRK, Kumar S. On the mechanism of metal nanoparticle synthesis in the Brust-Schiffrin method. Langmuir. 2013;29:9863–73.

[142] Kumar S, Gandhi K, Kumar R. Modeling of formation of gold nanoparticles by citrate method. Ind Eng Chem Res. 2007;46:3128–36.

[143] Agunloye E, Gavriilidis A, Mazzei L. A mathematical investigation of the Turkevich organizer theory in the citrate method for the synthesis of gold nanoparticles. Chem Eng Sci. 2017;173:275–86.

[144] Turkevich J, Stevenson PC, Hillier J. A study of the nucleation and growth processes in the synthesis of colloidal gold. Discuss Faraday Soc. 1951;11:55–75.

[145] Biggs S, Chow M, Zukoski CF, Grieser F. The role of colloidal stability in the formation of gold sols. J Colloid Interface Sci. 1993;160:511–13.

[146] Frens G. Controlled nucleation for the regulation of the particle size in monodisperse gold suspensions. Nature. 1973;241:20–2.

[147] Kimling J, Maier M, Okenve B, Kotaidis V, Ballot H, Plech A. Turkevich method for gold nanoparticle synthesis revisited. J Phys Chem B. 2006;110:15700–7.

[148] Sivaraman SK, Kumar S, Santhanam V. Monodisperse sub-10 nm gold nanoparticles by reversing the order of addition in Turkevich method–The role of chloroauric acid. J Colloid Interface Sci. 2011;361:543–47.

[149] Xia H, Bai S, Hartmann JR, Wang D. Synthesis of monodisperse quasi-spherical gold nanoparticles in water via silver (I)-assisted citrate reduction. Langmuir. 2009;26:3585–9.

[150] Schulz F, Homolka T, Bastús NG, Puntes V, Weller H, Vossmeyer T. Little adjustments significantly improve the Turkevich synthesis of gold nanoparticles. Langmuir. 2014;30:10779–84.

[151] Bastús NG, Comenge J, Puntes V. Kinetically controlled seeded growth synthesis of citrate-stabilized gold nanoparticles of up to 200 nm: size focusing versus Ostwald ripening. Langmuir. 2011;27:11098–105.

[152] Ziegler C, EychmüLler A. Seeded growth synthesis of uniform gold nanoparticles with diameters of 15–300 nm. J Phys Chem C. 2011;115:4502–06.

[153] Piella J, Bastús NG, Puntes V. Size-controlled synthesis of sub-10-nanometer citrate-stabilized gold nanoparticles and related optical properties. Chem Mater. 2016;28:1066–75.

[154] Slot JW, Geuze HJ. A new method of preparing gold probes for multiple-labeling cytochemistry. Eur J Cell Biol. 1985;38:87–93.

[155] Brown KR, Fox AP, Natan MJ. Morphology-dependent electrochemistry of cytochrome c at Au colloid-modified SnO_2 electrodes. J Am Chem Soc. 1996;118:1154–7.

[156] Singh A, Shirolkar M, Lalla NP, Malek CK, Kulkarni S. Room temperature, water-based, microreactor synthesis of gold and silver nanoparticles. Int J Nanotechnol. 2009;6:541–51.

[157] Brust M, Walker M, Bethell D, Schiffrin DJ, Whyman R. Synthesis of thiol-derivatised gold nanoparticles in a two-phase liquid–liquid system. J Chem Soc, Chem Commun. 1994;0:801–2

[158] Jun H, Fabienne T, Florent M, Coulon P-E, Nicolas M, Olivier S. Understanding of the size control of biocompatible gold nanoparticles in millifluidic channels. Langmuir. 2012;28:15966–74.

[159] Shalom D, Wootton RC, Winkle RF, Cottam BF, Vilar R, Wilde CP. Synthesis of thiol functionalized gold nanoparticles using a continuous flow microfluidic reactor. Mater Lett. 2007;61:1146–50.

[160] Tsunoyama H, Ichikuni N, Tsukuda T. Microfluidic synthesis and catalytic application of PVP-stabilized, ~1 nm gold clusters. Langmuir. 2008;24:11327–30.

[161] Luty-Błocho M, Fitzner K, Hessel V, Löb P, Maskos M, Metzke D, et al. Synthesis of gold nanoparticles in an interdigital micromixer using ascorbic acid and sodium borohydride as reducers. Chem Eng J. 2011;171:279–90.

[162] Köhler J, Wagner J, Albert J. Formation of isolated and clustered Au nanoparticles in the presence of polyelectrolyte molecules using a flow-through Si chip reactor. J Mater Chem. 2005;15:1924–30.

[163] Wagner J, Köhler JM. Continuous synthesis of gold nanoparticles in a microreactor. Nano Lett. 2005;5:685–91.

[164] Wagner J, Tshikhudo TR, Köhler JM. Microfluidic generation of metal nanoparticles by borohydride reduction. Chem Eng J. 2007;135:104–9.

[165] Sugano K, Uchida Y, Ichihashi O, Yamada H, Tsuchiya T, Tabata O. Mixing speed-controlled gold nanoparticle synthesis with pulsed mixing microfluidic system. Microfluid Nanofluidics. 2010;9:1165–74.

[166] Verma M, Kumaran V. Effect of ultra-fast mixing in a microchannel due to a soft wall on the room temperature synthesis of gold nanoparticles. Sadhana. 2015;40:973–83.

[167] Bandulasena MV, Vladisavljević GT, Odunmbaku OG, Benyahia B. Continuous synthesis of PVP stabilized biocompatible gold nanoparticles with a controlled size using a 3D glass capillary microfluidic device. Chem Eng Sci. 2017;171:233–43.

[168] Baber R, Mazzei L, Thanh NTK, Gavriilidis A. An engineering approach to synthesis of gold and silver nanoparticles by controlling hydrodynamics and mixing based on a coaxial flow reactor. Nanoscale. 2017;9:14149–61.

[169] Yang SY, Cheng FY, Yeh CS, Lee GB. Size-controlled synthesis of gold nanoparticles using a micro-mixing system. Microfluid Nanofluidics. 2009;8:303–11.

[170] Kitson PJ, Rosnes MH, Sans V, Dragone V, Cronin L. Configurable 3D-printed millifluidic and microfluidic ‘lab on a chip’ reactionware devices. Lab Chip. 2012;12:3267–71.

[171] Ftouni J, Penhoat M, Addad A, Payen E, Rolando C, Girardon J-S. Highly controlled synthesis of nanometric gold particles by citrate reduction using the short mixing, heating and quenching times achievable in a microfluidic device. Nanoscale. 2012;4:4450–4.

[172] Jamal F, Jean-Sébastien G, Maël P, Edmond P, Christian R. Gold nanoparticle synthesis in microfluidic systems and immobilisation in microreactors designed for the catalysis of fine organic reactions. MicrosystTechnol. 2012;18:151–58.

[173] Gómez-De Pedro S, Puyol M, Alonso-Chamarro J. Continuous flow synthesis of nanoparticles using ceramic microfluidic devices. Nanotechnology. 2010;21:415603.

[174] Sugie A, Song H, Horie T, Ohmura N, Kanie K, Muramatsu A, et al. Synthesis of thiol-capped gold nanoparticle with a flow system using organosilane as a reducing agent. Tetrahedron Lett. 2012;53:4457–59.

[175] Kumar DR, Kulkarni A, Prasad B. Microfluidic platform for continuous flow synthesis of triangular gold nanoplates. Colloids Surf., A. 2014;443:149–55.

[176] Fu Q, Ran G, Xu W. A microfluidic-based controllable synthesis of rolled or rigid ultrathin gold nanoplates. RSC Adv. 2015;5:37512–6.

[177] Sebastián V, Lee S, Zhou C, Kraus MF, Fujimoto JG, Jensen KF. One-step continuous synthesis of biocompatible gold nanorods for optical coherence tomography. Chem Commun. 2012;48:6654–6.

[178] Ishizaka T, Ishigaki A, Kawanami H, Suzuki A, Suzuki TM. Dynamic control of gold nanoparticle morphology in a microchannel flow reactor by glucose reduction in aqueous sodium hydroxide solution. J Colloid Interface Sci. 2012;367:135–8.

[179] Wagner J, Kirner T, Mayer G, Albert J, Köhler J. Generation of metal nanoparticles in a microchannel reactor. Chem Eng J. 2004;101:251–60.

[180] Sebastian V, Khan SA, Kulkarni AA. Perspective article: flow synthesis of functional materials. J Flow Chem. 2017;7:96–105.

[181] Lohse SE, Eller JR, Sivapalan ST, Plews MR, Murphy CJ. A simple millifluidic benchtop reactor system for the high-throughput synthesis and functionalization of gold nanoparticles with different sizes and shapes. ACS Nano. 2013;7:4135–50.

[182] Gomez L, Sebastian V, Irusta S, Ibarra A, Arruebo M, Santamaria J. Scaled-up production of plasmonic nanoparticles using microfluidics: from metal precursors to functionalized and sterilized nanoparticles. Lab Chip. 2014;14:325–32.

[183] Uson L, Sebastian V, Arruebo M, Santamaria J. Continuous microfluidic synthesis and functionalization of gold nanorods. Chem Eng J. 2016;285:286–92.

[184] Bullen C, Latter MJ, D'Alonzo NJ, Willis GJ, Raston CL. A seedless approach to continuous flow synthesis of gold nanorods. Chem Commun. 2011;47:4123–5.

[185] Sans V, Glatzel S, Douglas FJ, Maclaren DA, Lapkin A, Cronin L. Non-equilibrium dynamic control of gold nanoparticle and hyper-branched nanogold assemblies. Chem Sci. 2014;5:1153–7.

[186] Bayazit MK, Yue J, Cao E, Gavriilidis A, Tang J. Controllable synthesis of gold nanoparticles in aqueous solution by microwave assisted flow chemistry. ACS Sustain Chem Eng. 2016;4:6435–42.

[187] Köhler JM, Li S, Knauer A. Why is micro segmented flow particularly promising for the synthesis of nanomaterials? Chem Eng Technol. 2013;36:887–99.

[188] Liu H, Vandu CO, Krishna R. Hydrodynamics of Taylor flow in vertical capillaries: flow regimes, bubble rise velocity, liquid slug length, and pressure drop. Ind Eng Chem Res. 2005;44:4884–97.

[189] Sebastian Cabeza V, Kuhn S, Kulkarni AA, Jensen KF. Size-controlled flow synthesis of gold nanoparticles using a segmented flow microfluidic platform. Langmuir. 2012;28:7007–13.

[190] Kulkarni AA, Sebastian Cabeza V. Insights in the diffusion controlled interfacial flow synthesis of Au nanostructures in a microfluidic system. Langmuir. 2017;33:14315–24.

[191] In: Ngai T, Bon SAF, editor(s). Particle-stabilized emulsions and colloids. Cambridge: Royal Society of Chemistry, 2014

[192] Khan SA, Duraiswamy S. Controlling bubbles using bubbles – microfluidic synthesis of ultra-small gold nanocrystals with gas-evolving reducing agents. Lab Chip. 2012;12:1807–12.

[193] Song H, Tice JD, Ismagilov RF. A microfluidic system for controlling reaction networks in time. Angew Chem. 2003;115:792–6.

[194] Günther A, Jhunjhunwala M, Thalmann M, Schmidt MA, Jensen KF. Micromixing of miscible liquids in segmented gas–liquid flow. Langmuir. 2005;21:1547–55.

[195] Zhang L, Xia Y. Scaling up the production of colloidal nanocrystals: should we increase or decrease the reaction volume? Adv Mater. 2014;26:2600–6.

[196] Christopher GF, Anna SL. Microfluidic methods for generating continuous droplet streams. J Phys D Appl Phys. 2007;40:R319.

[197] Garstecki P, Fuerstman MJ, Stone HA, Whitesides GM. Formation of droplets and bubbles in a microfluidic T-junction – scaling and mechanism of break-up. Lab Chip. 2006;6:437–46.

[198] Duraiswamy S, Khan SA. Droplet-based microfluidic synthesis of anisotropic metal nanocrystals. Small. 2009;5:2828–34.

[199] Duraiswamy S, Khan SA. Dual-stage continuous-flow seedless microfluidic synthesis of anisotropic gold nanocrystals. Part Part Syst Charact. 2014;31:429–32.

[200] Duraiswamy S, Khan SA. Plasmonic nanoshell synthesis in microfluidic composite foams. Nano Lett. 2010;10:3757–63.

[201] Lazarus LL, Yang AS, Chu S, Brutchey RL, Malmstadt N. Flow-focused synthesis of monodisperse gold nanoparticles using ionic liquids on a microfluidic platform. Lab Chip. 2010;10:3377–9.

[202] Lazarus LL, Riche CT, Marin BC, Gupta M, Malmstadt N, Brutchey RL. Two-phase microfluidic droplet flows of ionic liquids for the synthesis of gold and silver nanoparticles. ACS Appl Mater Interfaces. 2012;4:3077–83.

[203] Taifur-Rahman M, Krishnamurthy PG, Parthiban P, Jain A, Park CP, Kim D-P, et al. Dynamically tunable nanoparticle engineering enabled by short contact-time microfluidic synthesis with a reactive gas. RSC Adv. 2013;3:2897–900.

[204] Abalde-Cela S, Taladriz-Blanco P, De Oliveira MG, Abell C. Droplet microfluidics for the highly controlled synthesis of branched gold nanoparticles. Sci Rep. 2018;8:2440.

[205] Hafermann L, Köhler JM. Small gold nanoparticles formed by rapid photochemical flow-through synthesis using microfluid segment technique. J Nanopart Res. 2015;17:1–8.

[206] Lee KG, Hong J, Wang KW, Heo NS, Kim DH, Lee SY, et al. In vitro biosynthesis of metal nanoparticles in microdroplets. ACS Nano. 2012;6:6998–7008.

[207] Gu T, Zheng C, He F, Zhang Y, Khan SA, Hatton TA. Electrically controlled mass transport into microfluidic droplets from nanodroplet carriers with application in controlled nanoparticle flow synthesis. Lab Chip. 2018;18:1330–40.
[208] Zhang L, Niu G, Lu N, Wang J, Tong L, Wang L, et al. Continuous and scalable production of well-controlled noble-metal nanocrystals in milliliter-sized droplet reactors. Nano Lett. 2014;14:6626–31.
[209] Yang Y, Serrano González LA, Guldin S. A versatile AuNP synthetic platform for decoupled control of size and surface composition. Langmuir. 2018;34:6820–6
[210] Rossi D, Gargiulo L, Valitov G, Gavriilidis A, Mazzei L. Experimental characterization of axial dispersion in coiled flow inverters. Chem Eng Res Des. 2017;120:159–70.
[211] Trachsel F, Günther A, Khan S, Jensen KF. Measurement of residence time distribution in microfluidic systems. Chem Eng Sci. 2005;60:5729–37.
[212] Günther A, Khan SA, Thalmann M, Trachsel F, Jensen KF. Transport and reaction in microscale segmented gas-liquid flow. Lab Chip. 2004;4:278–86.
[213] Khan SA, Günther A, Schmidt MA, Jensen KF. Microfluidic synthesis of colloidal silica. Langmuir. 2004;20:8604–11.
[214] Krishnadasan S, Tovilla J, Vilar R, deMello AJ, deMello JC. On-line analysis of CdSe nanoparticle formation in a continuous flow chip-based microreactor. J Mater Chem. 2004;14:2655.
[215] Panariello L, Mazzei L, Gavriilidis A. Modelling the synthesis of nanoparticles in continuous microreactors: the role of diffusion and residence time distribution on nanoparticle characteristics. Chem Eng J. 2018;350:1144–54
[216] Marchisio DL, Rivautella L, Barresi AA. Design and scale-up of chemical reactors for nanoparticle precipitation. AIChE J. 2006; 1877–87.
[217] Tae G, Lammertink RG, Kornfield JA, Hubbell JA. Facile hydrophilic surface modification of poly (tetrafluoroethylene) using fluoroalkyl-terminated poly(ethylene glycol)s. Adv Mater. 2003;15:66–9.
[218] Zhang L, Wang Y, Tong L, Xia Y. Synthesis of colloidal metal nanocrystals in droplet reactors: the pros and cons of interfacial adsorption. Nano Lett. 2014;14:4189–94.
[219] Weeranoppanant N, Adamo A, Saparbaiuly G, Rose E, Fleury C, Schenkel B, et al. Design of multistage counter-current liquid–Liquid extraction for small-scale applications. Ind Eng Chem Res. 2017;56:4095–103.
[220] Sweeney SF, Woehrle GH, Hutchison JE. Rapid purification and size separation of gold nanoparticles via diafiltration. J Am Chem Soc. 2006;128:3190–97.

Bionotes

He Huang received her BS degree from the department of Chemical Engineering, Dalian University of Technology (Liaoning Province, China) in 2012. She obtained an MSc degree in 2014 and continued her study as a PhD candidate at the department of Chemical Engineering, University College London under the supervision of Prof. Gavriilidis. Her research area is the controlled synthesis of gold nanocrystals in microfluidic systems.

Hendrik du Toit received an MEng in Chemical Engineering from Imperial College London in 2011. He subsequently received his PhD from the University of Bath in 2015 whilst conducting research into the production of biocompatible biosensors and biofuel cells for implantable medical devices. He then joined Prof. Gavriilidis' research group at University College London where his focus has been on developing continuous flow gold nanoparticle synthesis systems. His research interests include fuel cells, biosensing, nanomaterials, fluidic technologies and reactor design.

Luca Panariello received both a BS (2014) and MSc (2016) degree in Chemical Engineering with honours at the University of Naples "Federico II" (Italy). He joined the department of Chemical Engineering at University College London in 2016 in a joint research project with the University of Naples "Federico II". He was then awarded a Marie Skłodowska-Curie PhD scholarship in 2017 to work on process intensification of nanomaterials production under the supervision of Prof. Gavriilidis.

Luca Mazzei graduated in Chemical Engineering from the University of Naples "Federico II" (Italy) in 2001. He spent 3 years working for Technip KTI as a process and start-up engineer on sulphur recovery and refinery tail gas treatment. Subsequently he joined the Department of Chemical Engineering at University College London, first as a student, where he was awarded a PhD in 2008, and then promoted to Lecturer in 2009. His research activities deal with experimental and modelling of polydisperse multiphase systems, with focus on crystallization processes and nanoparticles synthesis, relying on advanced mathematical modelling and CFD.

Asterios Gavriilidis obtained a Diploma from the University of Thessaloniki (Greece) in 1988, and an MSc in 1990 and PhD in 1993 from the University of Notre Dame, USA, all in Chemical Engineering. He joined the Department of Chemical Engineering at University College London (UK) in 1993, where he has been professor of Chemical Reaction Engineering since 2004. His research interests include chemical and catalytic reaction engineering, microreaction and microprocess technology, continuous nanomaterials synthesis.

Jiangwei Zhang, Zhimin Li, Kai Zheng and Gao Li

5 Synthesis and characterization of size-controlled atomically precise gold clusters

Abstract: In this article, synthetic strategies and characterization methodologies of atomically precise gold clusters have been summarized. The typical and effective synthetic strategies including a systematic “size-focusing” methodology has been developed for attaining atomically precise gold clusters with size control. Another universal synthetic methodology is ligand exchange-induced size/structure transformation (LEIST) based on from one stable size to another. These two methodologies have largely expanded the “universe” of atomically precise gold clusters. Elite of typical synthetic case studies of ligand protected gold clusters are presented. Important characterization techniques of these atomically precise gold clusters also are included. The identification and characterization of gold clusters have been achieved in terms of nuclearity (size), molecular formulation, and geometrical structures by the combination of these techniques. The determination of gold cluster structure based on single crystals is of paramount importance in understanding the relationship of structure–property. The criterion and selection of these typical gold clusters are all “strictly” atomically precise that all have been determined ubiquitously by single crystal diffraction. These related crystallographic data are retrieved from Cambridge Crystallographic Data Centre (CCDC) up to 30th November 2017. Meanwhile, the cutting edge and other important characterization methodologies including electron diffraction (ED), extended X-ray absorption fine structure (EXFAS), and synchrotron sources are briefly reviewed. The new techniques hold the promise of pushing the limits of crystallization of gold clusters. This article is not just an exhaustive and up to date review, generally summarized synthetic strategies, but also a practical guide regarding gold cluster synthesis. We called it a “Cookbook” of ligand protected gold clusters, including synthetic recipes and characterization details.

This article has previously been published in the journal *Physical Sciences Reviews*. Please cite as: Zhang, J., Li, Z., Zheng, K., Li, G. Synthesis and characterization of size-controlled atomically precise gold clusters. *Physical Sciences Reviews* [Online] **2018**, 3. DOI: 10.1515/psr-2017-0083

https://doi.org/10.1515/9783110345100-005

Graphical Abstract:

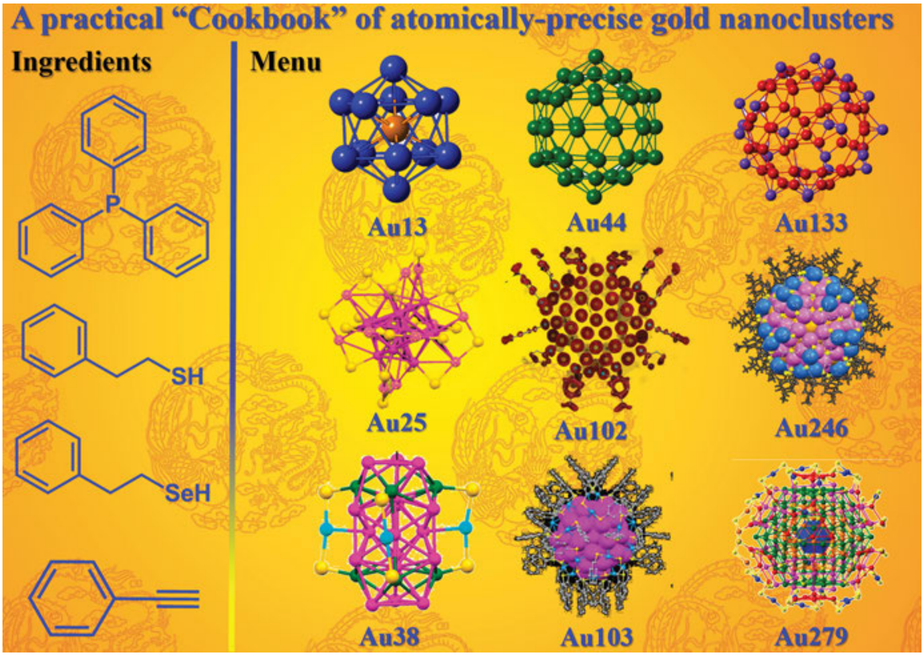

Keywords: alkyne, gold cluster, ligand exchange-induced size/structure transformation, phosphine, size-controlled synthesis, thiolate, "size-focusing" methodology

5.1 Introduction

The polydispersity of nanoparticles has long been a major phenomenon in nanoscience research. To synthesize strictly uniform nanoparticles at the ultimate atomic level, namely, atomically precise clusters, is of a great fundamental and important issue in nanoscience that can be glimpsed at the atomic level [1, 2]. Metal clusters containing 10 to 300 atoms are of great scientific interest as the nanomaterials with their dimensions and novel molecular properties evolving in the cluster regime. They bridge the gap between discrete atoms and bulk metals [3]. They can serve as models for structure and bonding of cluster compounds. In particular, atomically precise gold clusters have gained increasing attention due to their stability as compared with other noble metal clusters and their remarkable relativistic effect leading to the corresponding applications in a wide range of disciplines, including catalysis, biology, and sensors, a few to name [4–9]. In this article, only atomically precise gold clusters, composed with a definite ligand shell forming molecules of definite composition, will be reviewed because structurally defined molecular gold clusters offer nice models to establish the structure–property relationship in the subnanometer regime.

One of the major goals in the cluster research is to investigate their unique properties, which cannot see in both the bulk materials and small molecules. By tailoring the size or shape of clusters, their physical and chemical properties exhibit significant changes compared to bulk materials [1]. The stability of gold clusters in electronic terms has been explained by the superatom model, which is based on the "jellium" model of electrons confined within a spherically symmetric potential well of the metal core. If the number of free electrons falls in the "magic" number series of 2, 8, 18, 20, 34, 58, . . ., the clusters show high stability. The size of the gold clusters is largely affected by the surface ligands, thus, a major task is to find appropriate ligands for stabilizing clusters and more importantly enabling controlled synthesis.

In terms of the controlled synthesis of atomically precise gold clusters, employing phosphine ligands to protect gold clusters can be traced back to 1960s [10]. Further, thiolate (-SR) and alkynyl ligands (-C ≡ CR) also are developed to afford the gold clusters (formulated as $Au_n(PR_3)_m$[11], $Au_n(SR)_m$[12], $Au_n(C \equiv CR)_m$ [13], Figure 5.1]. These gold clusters can be determined via detailed mass spectrum analysis, and their packing structure can be characterized by single crystal X-ray diffraction.

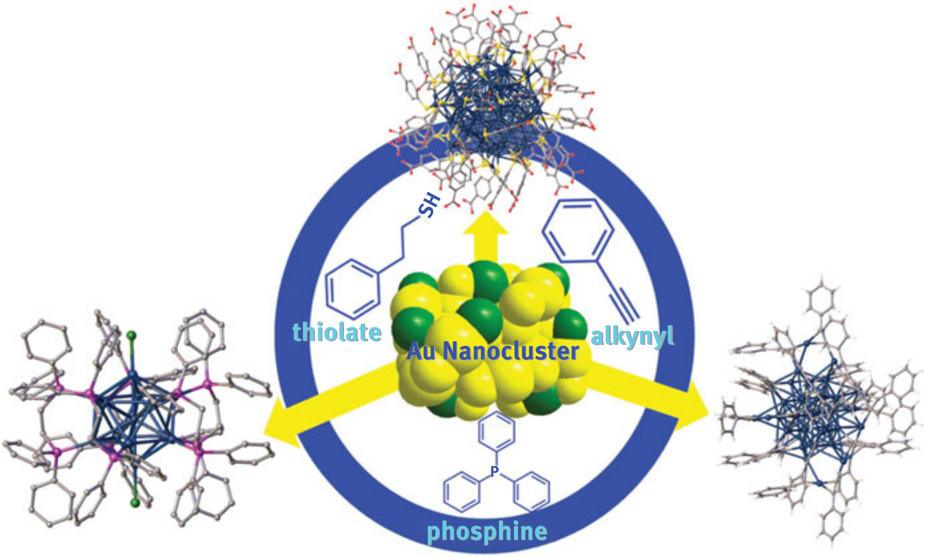

Figure 5.1: Three major ligands protected atomically precise gold clusters.

In this article, we only focused on the synthetic strategies and characterization methodologies of atomically precise gold clusters. We called it a "Cookbook" of ligand protected gold clusters, including synthetic recipes and characterization details. The criterion and selection of the typical gold clusters in this article are all “strictly” atomically precise that all have been characterized ubiquitously by single crystal diffraction. These related crystallographic data are retrieved from Cambridge Crystallographic Data Centre (CCDC) up to 30th November 2017. Meanwhile, the cutting edge and important characterization methodologies including electron diffraction (ED), extended X-ray absorption fine structure (EXFAS), and synchrotron sources are briefly reviewed. The new techniques hold the promise of pushing the limits of crystallization of gold clusters.Of note, all the Terms and Abbreviations appear the first time in this chapter are also summarized and presented in Appendix Table 5.2.

5.2 Preparation methods

5.2.1 Phosphine protected gold clusters

Phosphine-type ligands were firstly applied in 1960s to protect the gold core. The first report of $Au_{11}(SCN)_3(PPh_3)_7$[14] cluster came in 1969. Then the following crystal structure of $Au_{11}I_3[P(C_6H_4Cl)_3]_7$ was reported in 1970 [15]. A conventional direct synthesis of the phosphine-protected Au_{11} can be briefly described as following: $HAuCl_4$ was dissolved in ethanolic solution, and two equivalent phosphines were added to form the monoatomic Au precursor Au^IPPh_3Cl (i. e., $HAuCl_4 + 2\ PPh_3 + H_2O \rightarrow Au^IPPh_3Cl + O = PPh_3 + 3\ HCl$). And then under suitable condition and reductant (e. g., $NaBH_4$), a part of Au^I would be further reduced to Au^0 species and Au_{11} cluster was finally formed through nucleation. The Au_{11} cluster can be best described in terms of an incomplete icosahedron, where the central gold atom Au is surrounded by additional ten Au atoms[14]. Further, many other sized clusters have been reported, such as $[Au_6(PPh_3)_6]^{2+}$ [16, 17], $[Au_9(PR_3)_8]^{3+}$ [18, 19], $Au_{10}Cl_3(PCy_2Ph)_6{}^+$[20], $[Au_{13}(dppmH)_6]^+$[21], $[Au_{14}(PPh_3)_8]^{4+}$[22] and $[Au_{39}(PPh_3)_{14}Cl_6]^{2+}$[23]. The $[Au_9(PR_3)_8]^{3+}$ clusters exist an incomplete icosahedron core. The $Au_{10}Cl_3(PCy_2Ph)_6{}^+$ shows a D_{3h} symmetry. And the Au_{13}[11] has a perfect icosahedral structure.

In 1981, $[Au_{55}(PPh_3)_{12}]^{6+}$ was founded by Schmid[24]. However, single crystal studies and mass spectral characterization of the cluster have not been reported yet, which makes the existence of Au_{55} controversial. Recently, Palmer et al. probed the structure of Au_{55}, using direct atomic imaging techniques [25] based on aberration-corrected scanning transmission electron microscopy (STEM) combined with multi-slice simulation of STEM images. The most interesting aspect of clusters such as Au_{13} or Au_{55} is the unique full shell structures which explain their stability. The expression “full shell cluster” refers to a cluster composed of a central atom that is surrounded by individual shells of atoms, eventually resulting in perfect geometry. The icosahedral geometry is a perfect example of this kind. The general rule for construction of such clusters is the number of atoms in the cluster = $1 + \Sigma(10\ n^2 + 2)$, where the summation runs over all the shell numbers ($n = 1, 2, \ldots$) in the cluster. A schematic is given to understand the formation of such shells: initially a single atom is surrounded by 12 other atoms to form a 13 atom core–shell M_{13} cluster. Then, 42 atoms can be densely packed on the surface of 12 atoms to produce a two-shell Mackay icosahedron M_{55} cluster; in a similar pattern, a shell of 92 atoms can form over the second shell to generate a three-shell M_{147} cluster and this series may continue (Figure 5.2).

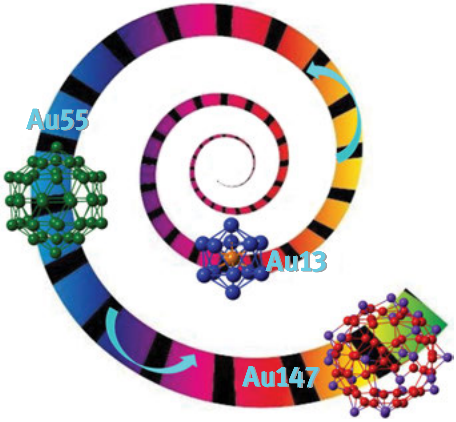

Figure 5.2: Schematic view of the growth of shell structure of clusters through Fibonacci Golden spiral line Law.

As the extension of monodentate phosphine to multidentate phosphine ligands, a chiral $[Au_{20}(PR_3)_4]^{4+}$ structure with tetradentate phosphine was reported. The Au_{20} is consisting of an icosahedral Au_{13} motif (achiral) and a helical Y-shaped Au_7 motif (chiral) [26, 27], Figure 5.3, down panel. Next, Au_{22} cluster was protected by six bidentate diphosphine ligands [1, 8-bis(diphenylphosphino)octane, dppo] was also

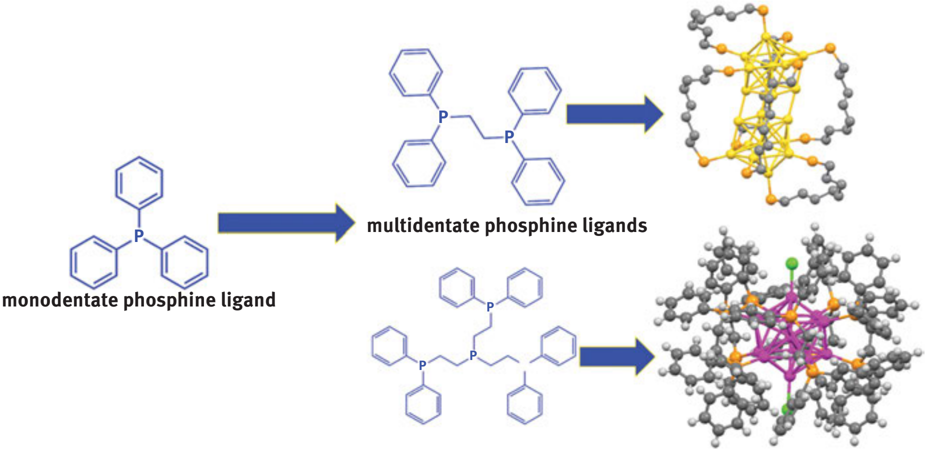

Figure 5.3: Gold cluster synthesis applied the extension of monodentate phosphine to multidentate phosphine ligands.

reported [28]. The Au_{22} cluster consists of two Au_{11} units clipped together by four dppo ligands, with the remaining two ligands coordinating to the two Au_{11} units in a bidentate manner (Figure 5.3, top panel).

The use of particular diphosphines results in the formation of different cluster species due to the steric and chelation effects of diphosphines. Pettibone and coworkers [29–31] revealed the mechanistic insights of size-selective growth of Au_n clusters. For example, in the reduction of $Au(PPh_3)Cl$ with $BuNH_2{\cdot}BH_3$ in chloroform in the presence of C_3-bridged diphosphine 1,3-propanediylbis(diphenylphosphine) (dppp), the predominant formation of $Au_{11}P_{10}$ cluster ($[Au_{11}(dppp)_5]^{3+}$ is detected. The simple $NaBH_4$ reduction of $Au_2(dppp)Cl_2$ in ethanol also gives the same $Au_{11}P_{10}$ cluster as the main cluster product [32]. On the other hand, the reduction system [33] $Au(PPh_3)Cl/BuNH_2{\cdot}BH_3$ coupled with non-phenyl type C_3-bridged diphosphine ligand 1,3-bis (diethylphosphino)propane ($Et_2P(CH_2)_3PEt_2$, depp) shows the preferential formation of $Au_{11}P_8Cl_2$ $[Au_{11}(depp)_4Cl_2]^+$ with two side-products (i. e., $[Au_{12}(depp)_4Cl_3]^+$ and $[Au_{13}(depp)_4Cl_3]^+$). Robinson et al. found that the $(CH_2)_x$ spacer length of diphosphine ligand affects the cluster size. For example, the above $Au(PPh_3)Cl/BuNH_2{\cdot}BH_3$ system coupled with C_5- 1,5-bis(diphenylphosphino)pentane (dpppe, $Ph_2P(CH_2)_5PPh_2$) or C_6-bridged 1,6-bis(diphenylphosphino)hexane (dpph, $Ph_2P(CH_2)_6PPh_2$) diphosphine gives $[Au_8(dpppe)_4]^{2+}$ and $[Au_{10}(dpph)_4]^{2+}$ as the main cluster products. The $NaBH_4$ reduction of chlorogold(I) complex of C_8-bridged diphosphine (dppo) affords a larger cluster $Au_{22}(dppo)_6$[28].

Furthermore, the solvent effect also was observed. The use of C_2-bridged 1,2-bis (diphenylphosphino) ethane (dppp) for the $NaBH_4$ reduction of chlorogold(I) complex in ethanol results in the formation of $[Au_{11}(dppe)_6]^{3+}$. The same reduction system [34] from the C_3-bridged complex ($Au_2(dppp)_2Cl_2$) in $CH_2Cl_2/EtOH$ (50/50, v/v) affords to higher nuclearity clusters $[Au_{38}(dppp)_9Cl_2]^{4+}$. These results strongly imply that the cluster growth processes are not only governed by the intrinsic stability of the gold core but also notably affected by the steric and cheating effects of multidentate ligands and reaction conditions.

5.2.2 Thiolate protected gold clusters

Gold–thiol chemistry started to bloom in the 1980s owing to research on self-assembled monolayers (SAMs) of thiols on bulk gold surfaces [34]. Investigations of thiolate-protected gold clusters synthesis experienced several stages, from polydispersed clusters to monodispersed ones and finally to atomically precise ones [35]. In recent years, the research progress has evolved to large-scale and controlled synthesis strategy [1, 2]. Compared with phosphine ligands, thiolate ligands render highly stable clusters, and thus are of wide interest. The extraordinary stability of thiolate-protected gold clusters originates from the strong covalent bonding of Au-S compared with the corresponding Au-P bond [1].

In 1994, Brust [36] first reported the synthesis of less than 5 nm-sized alkane thiolate-protected gold clusters by using $NaBH_4$ as a reducing agent. Of note, these clusters should exhibit intriguing properties due to quantum confinement effects. The Brust method is a typical example of the "bottom-up" approach to obtain gold clusters. Since then, the synthetic method of Brust has been refined and optimized by numerous researchers. The typical procedure followed a two-phase synthetic protocol in which water and an organic nonpolar solvent (e. g., toluene) were utilized. The gold source $HAuCl_4$ was first dissolved in an aqueous solution and then transferred to the organic solvent using phase transfer reagents (e. g., tetraoctylammonium bromide, TOABr). Finally, organic protecting ligands and reducing agents were added to the organic phase to prepare gold clusters. The mechanism of this method is illustrated as follows. Phase transfer of chloroauric acid to the organic phase in the presence of the phase transfer reagents occurs through the following equation:

$$\mathrm{H^+\,AuCl_4^-(aq) + (R)_4N^+\,Br^-(toluene) \rightarrow (R)_4N^+\,AuX_4^-(toluene) + HX\ (aq)} \tag{5.1}$$

Then the reduction of Au(III) to Au(I) by thiol occurs via the following equation:

$$n\mathrm{(R)_4N^+\,AuX_4^-} + 3n\mathrm{R^1SH} \rightarrow \mathrm{(AuSR)}_n + n\mathrm{R^1S - SR^1} + n\mathrm{(R)_4N^+\,X^-} + 3n\mathrm{HX} \tag{5.2}$$

At this stage, it was believed that the toluene phase contains phase transfer reagents, dialkyl sulfide, and Au(I)SR polymer, either mixed with excess RSH depending on the ratio of the ingredients. In the final step, the reduction of Au^+ to Au^0 happens by borohydride according to the following equation:

$$4\ \mathrm{(AuSR)}_n + \mathrm{(x-y)BH_4^-} \rightarrow 4\ \mathrm{Au_x(SR)_y} + \mathrm{(x-y)B^{3+}} + 4\ \mathrm{(AuSR)_{n-x}} + 4\ \mathrm{(RSH)_{x-y}} \tag{5.3}$$

The structure of gold clusters, depending on the ratio of Au, thiol, and sodium borohydride. Impurities such as other clusters or some thiolates are also present in the final product, which can be removed during the purification step.

In the one-phase Brust–Schiffrin method, a polar solvent (such as methanol and tetrahydrofuran (THF)) was used as the solvent. Several modifications of this method have appeared, mainly by controlling different parameters, such as temperature, solvents, concentration of each reactant, reducing agents, to get highly thiolate protected gold clusters.

Among the synthetic methods for atomically precise gold clusters, the recently established "size-focusing" methodology has been demonstrated to be quite universal [37]. There are two primary steps for a "size-focusing" synthesis (Figure 5.4).

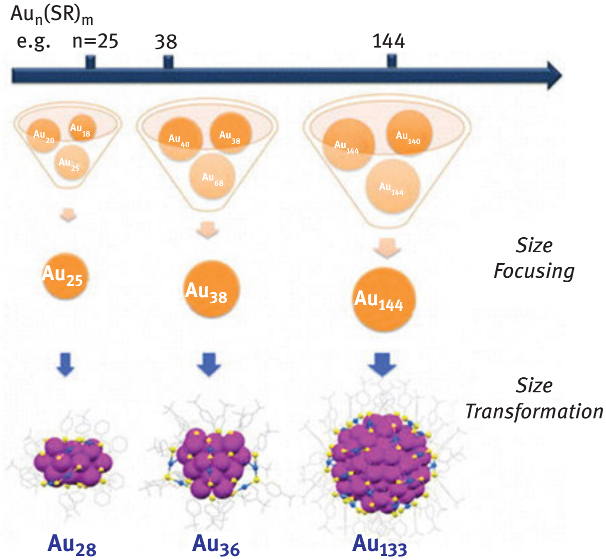

Figure 5.4: Size-focusing and exchange-induced size/structure transformation methdology for the synthesis of thiolate protected gold clusters. (Adapted with permission from ref. 37. Copyright 2010. American Chemical Society).

In step 1, polydispersed gold clusters with a controlled size range are obtained by turning the reaction conditions (e. g. the static and dynamic factors). Of note, the concept of "size-focusing" by controlling the several reaction conditions to afford the effective and high yield of thiolate protected gold nanoclusters was first proposed by Jin and Zhu [1]. In step 2, these initially polydispersed gold clusters are focused into the single-size product by aging/etching under a harsh environment. The foundation of "size focusing" is based on the inherent stability difference of different-sized clusters. When a punitive environment is applied to the mixture of clusters, only the most robust species can survive via the size-focusing process. The other species are either decomposed or converted to the most stable size [38]. The "survival of the most robust" principle somewhat resembles nature's law "survival of the fittest".

With respect to the stability of magic-size clusters, there are generally arguments invoking the geometric and electronic factors. For the geometric factor, certain geometric core arrangements (e. g., icosahedron), as well as the arrangement of surface thiolate ligands, impart particular stability to the overall cluster structure. While for the electronic factor, those gold clusters with the number of Au 6s free electrons satisfying electron-shell closing are regarded to be stable. Some gold clusters may be viewed as superatoms, such as anionic $[Au_{25}(SR)_{18}]^-$ in which the number of Au 6s free electrons are counted as follows: 25 (the number of gold atoms) −18 (the number of thiolate, each consumes 1e) + 1 (the anionic charge state) = 8e.

Ligand-exchange-induced “size-conversion” method has been discovered [39, 40], which become another universal synthetic methodology for gold clusters. The size-conversion method also called ligand exchange-induced size/structure transformation (LEIST) methodology provides an opportunity to expand the size library of gold clusters. It was found that the structure of the thiolate ligands plays an important role in controlling the size and structure of gold clusters. A detail example of the LEIST process of $Au_{38}(PET)_{24}$ (PET: phenylethanethiolate) to $Au_{36}(TBBT)_{24}$ (TBBT: 4-tert-butylbenzenethiolate) was illustrated [39]. Starting with molecularly pure $Au_{38}(PET)_{24}$, ligand-exchange reaction with a large excess of TBBT under thermal conditions (~80 °C) led to the production of $Au_{36}(TBBT)_{24}$ after 12 h under harsh reactions. The $Au_{36}(TBBT)_{24}$ yield was exceptionally high (>90 %), and the product was molecularly pure, as evidenced by the clean mass spectrum and thermogravimetry analysis.

A few key conditions were found to affect the LEIST process: (i) the molar ratio of incoming TBBT to the original PET on the Au_{38} cluster was kept very high (~160:1), much higher than in conventional ligand-exchange processes. (ii) Thermal conditions were used to overcome the energy barrier between stable sizes. The discovery of this elegant yet simple transformation chemistry greatly facilitated the crystallization of the Au_{36} cluster. The $Au_{36}(TBBT)_{24}$ structure was indeed significantly different from that of the starting biicosahedral $Au_{38}(PET)_{24}$ cluster, that is, the structural transformation occurred, even though their sizes differ by only two gold atoms. Next, $Au_{25}(PET)_{18}$ and $Au_{144}(PET)_{60}$ can convert to $Au_{28}(TBBT)_{20}$ and $Au_{133}(TBBT)_{52}$ in the presence of TBBT at 80 °C, respectively [40, 41].

Other methods for gold cluster synthesis including post-synthetic size separation, kinetic control, and size conversion. The $Au_{15}(SR)_{13}$, $Au_{18}(SR)_{14}$, $Au_{40}(SR)_{24}$, $Au_{55}(SR)_{31}$, $Au_{67}(SR)_{35}$, $Au_{130}(SR)_{50}$, and $Au_{187}(SR)_{68}$ were obtained through post-synthetic size separation step from a mixture of clusters [42–47]. The separation methods such as high performance liquid chromatography (HPLC), solvent fractionation, and polyacrylamide gel electrophoresis (PAGE) were successfully applied to the separation of gold clusters. The separation is based primarily on the difference in solubility, size, charge state, and other factors among the clusters.

5.2.3 Alkynyl protected gold clusters

In very recent years, the alkynes were explored as protecting ligands, which was firstly reported by Tsukuda’s group [48]. Synthetic methods for the alkyne-capped gold cluster are similar with the thiolate-ligated clusters. By the developing protocol, several well-defined clusters, such as $Au_{54}(C \equiv CR)_{26}$[49], $Au_{44}(PA)_{28}$ and $Au_{36}(PA)_{24}$ [50] (PA: phenylacetylene), are discovered. Of note, the structures of $Au_{44}(PA)_{28}$ and $Au_{36}(PA)_{24}$ are similar to these of $Au_{44}(SR)_{28}$ and $Au_{36}(SR)_{24}$, but the optical spectra are different. Protecting ligands significantly influence the electronic structures of the clusters. The synthesis of these alkynyl-protected gold clusters indicates that a series of clusters in the general formula $Au_n(RC \equiv C)_m$ as counterparts to $Au_n(SR)_m$ can be expected. Of note, most alkynyl protected gold clusters are not homoleptic, which remains to explore in the future. They are protected by mixed ligands, accompanied with other ligands including phosphine and thiolate.

5.2.4 Selenolate protected gold clusters

Formation Au-Se bonds are similar to Au-S bond, hence the synthetic strategies can be extended to selenolate protected gold clusters synthesis.

The Negishi group reported a method for the direct synthesis of $Au_{25}(SeC_8H_{17})_{18}$[51]. Zhu demonstrated ligand exchange of $Au_{25}(SR)_{18}$ with selenol and obtained $Au_{25}(SePh)_{18}$ and $Au_{18}(SePh)_{14}$ [52]. The X-ray structure of $Au_{25}(SePh)_{18}$ shares the same framework as its thiolate counterpart [53]. The structure of a $Au_{24}(SePh)_{20}$ nanocluster has been reported to consist of a prolate Au_8 kernel [54]. This kernel can be viewed as two Au_4 tetrahedra cross-joined together that are then protected by two trimeric staple-like motifs as well as two pentameric staple motifs. It is interesting to compare the structure of $Au_{24}(SePh)_{20}$ with that of its thiolate counterpart, $Au_{24}(SCH_2Ph\text{-}^tBu)_{20}$. The latter structure contains a different Au_8 kernel and, accordingly, different surface motifs. The difference is caused by ligand anchoring atom (Se versus S). In a theoretical work on $Au_{24}(SePh)_{20}$, Takagi [55] pointed out that the Au_8 kernel coordinates with the selenolate staple motifs more strongly than with the thiolate staples and that the aurophilic interactions between the staples themselves and between the Au_8 core and the staples play an important role in stabilizing the cluster. Negishi [56] reported the isolation selenolate-protected Au_{38} clusters $Au_{38}(SeC_{12}H_{25})_{24}$ through ligand exchange of thiolate protected gold nanoclusters $Au_{38}(SC_2H_4Ph)_{24}$ with didodecyldiselenide $(C_{12}H_{25}Se)_2$.The electronic and geometrical structures, bonding characteristics, of $Au_{38}(SeC_{12}H_{25})_{24}$ clusters were assessed using extended X-ray fine structure and X-ray absorption (EXFAS) near edge structure measurements. Negishi compares [57] the stability of precisely synthesized $[Au_{25}(SC_8H_{17})_{18}]^-$ and $[Au_{25}(SeC_8H_{17})_{18}]^-$against degradation in solution, thermal dissolution, and laser fragmentation. The results demonstrate that changing the ligand from thiolate to selenolate increases cluster stability in reactions involving dissociation of the gold–ligand bond but reduces cluster stability in reactions involving intramolecular dissociation of the ligand. These results reveal that using selenolate ligands makes it possible to produce gold clusters that are more stable against degradation in solution than thiolate-protected gold nanoclusters.

5.2.5 Mixed ligands protected gold clusters

Apart from the homoleptic ligand protected gold nanoclusters discussed above, there also exist many mixed ligands protected gold nanoclusters. While these mixed ligands are the combination of phosphine, thiolate, selenolate, alkynyl, and even single sulfur (sulfide) or single selenium (selenide).

Jin [58] reported the direct synthesis of $[Au_{24}(PPh_3)_{10}(SC_2H_4Ph)_5X_2]^+$ through the $NaBH_4$ reduction of $HAuCl_4$ based on the Brust's two-phase method with the stepwise addition of mixed ligands of phosphine and thiolate. Mixed ligands protected gold nanoclusters can also be obtained through partial ligand exchange employing homoleptic ligand protected gold nanoclusters as precursor. By this strategy, the reaction [59] of $[Au_9(PPh_3)_8]^{3+}$ with 4-pyridinethiol in alkaline methanol results in the formation of mixed phosphine and thiolate protected gold nanoclusters $Au_{11}(PPh_3)_7$ $(4\text{-pyS})_3$. Shichibu [60] reported the synthesis of $[Au_{25}(PPh_3)_{10}(SEt)_5Cl_2]^{2+}$ by the reaction of $[Au_{11}(PPh_3)_8Cl_2]Cl$ and ethanethiol. With phenylethanethiol, Jin [61] also obtained $[Au_{25}(PPh_3)_{10}(SC_2H_4Ph)_5Cl_2]^{2+}$ by a direct route, namely, the reaction of HSC_2H_4Ph with polydisperse PPh_3-capped Au nanoparticles (as opposed to Au_{11} clusters), and the structure was found to the same as that of the ethanethiolate counterpart. Linear growth of three icosahedral units was achieved, giving rise to Au_{37} triicosahedral rod structure. The $[Au_{37}(PPh_3)_{10}(SC_2H_4Ph)_{10}X_2]^+$ (where X = Cl/Br,) nanocluster was achieved by a kinetically controlled approach[62]. The successful synthesis of this new nanocluster allows one to gain insight into the size, structure, and property evolution of gold nanoclusters from the monoicosahedral $[Au_{13}(PPh_3)_{10}X_2]^{3+}$ to the biicosahedral $[Au_{25}(PPh_3)_{10}(SR)_5X_2]^{2+}$ and the triicosahedral $[Au_{37}(PPh_3)_{10}(SC_2H_4Ph)_{10}X_2]^+$. This growth is reminiscent of the “cluster of clusters” reported previously by Teo [63]. Its HOMO (Highest Occupied Molecular Orbital)–LUMO (Lowest Unoccupied Molecular Orbital) gap systematically shrinks with increasing size. The possibility of achieving even longer rod nanoclusters based on the assembly of icosahedral building blocks remains to be seen. For mixed phosphine and selenolate protected gold nanoclusters synthesis. Zhu[64] report a highly stable gold nanocluster co-protected by the selenophenol and 1,5-bis(diphenylphosphino)pentane (L^5 for short) ligands, formulated as $[Au_{11}(L^5)_4$ $(SePh)_2]^+$.They systematically investigated the stability of the $[Au_{11}(L^5)_4(SePh)_2]^+$. The results show that it is significantly more stable than both $Au_{11}(PPh_3)_7{}^{3+}$ and $[Au_{11}(PPh_3)_8Cl_2]^+$. For mixed phosphine and alkynyl protected gold nanoclusters synthesis. Wang crystallized three mixed phosphine and alkynyl protected gold nanoclusters $[Au_{19}L_9(PPR)_3]^{2+}$, $[Au_{23}L_9(PR)_6]^{2+}$, and $[Au_{24}L_{14}(PR)_4]^{2+}$ (where L represents PhC ≡ C-).The Au_{19} structure contains a Au_{13} icosahedral kernel, which is further protected by three V-shaped PhC ≡ C-Au-C ≡ C(Ph)-Au-C ≡ CPh motifs (Au_2L_3) [65]. This motif resembles the RS-Au-SR-Au-SR dimeric staples. Theoretical analysis revealed that the PhC ≡ C-groups participate in the frontier orbitals of the cluster. The Au_{19} is an 8e cluster assuming that each alkynide ligand localizes one electron, as does the thiolate ligand, while the phoshpine ligand does not. But the Au_{23} cluster contains 12e and contains a Au_{17} kernel protected by three Au_2L_3 dimeric staples and six PPh_3 ligands [66]. Regarding the Au_{24} cluster, its Au_{22} rod-like kernel is constructed by the sharing of a common square face of two Au_{13}

cuboctahedra and is then protected by two PhC ≡ C-Au-C ≡ CPh staples and other units [67]. The observation of some common sizes between alkynide and thiolate ligand systems is interesting.

Besides, organic ligands, there also existed a special types of atoms including single sulfur (sulfide) or single selenium (selenide), that can serve as special coordination atom regarding the ligands protected gold nanoclusters synthesis. For mix phosphine sulfide ligands protected gold nanoclusters, Antonio Laguna [68] first reported the treatment of $[Au_2Cl_2(\mu\text{-dppf})]$ (dppf = 1,1-bis(diphenylphosphino)ferrocene) with Li_2S (molar ratio 1:1) in ethanol gives a yellow solid $[S(Au_2dppf)]$ and further determinated its corresponding crystal structure. Thus single sulfur atom can also be incorporated in gold nanoclusters as special ligand. Furthermore, the addition $AuPR_3^+$ fragments stepwise to the dinuclear gold cluster $[S(AuPR_3)_2]$ form the cationic gold nanoclusters [69] $[S(AuPR_3)_3]^+$, $[S(AuPR_3)_4]^{2+}$, $[S(AuPR_3)_5]^{3+}$ and $[S(AuPR_3)_6]^{4+}$. V. W.-W. Yam [70] reported the reaction of H_2S with a suspension of $[Au_2\{Ph_2PN(p\text{-}CH_3C_6H_4)PPh_2\}Cl_2]$ in ethanol/pyridine and recrystallization from acetone/dichloromethane/diethyl ether yielded $[Au_6\{\mu\text{-}Ph_2PN(p\text{-}CH_3C_6H_4)PPh_2\}_3(\mu_3\text{-}S)_2]^{2+}$. They also synthesized macrocyclic μ_3-sulfido gold nanoclusters $[Au_{18}(\mu\text{-dpepp})_6(\mu_3\text{-}S)_6]^{6+}$ [dpepp = bis(2-diphenylphosphinoethyl)phenylphosphine][71] with unprecedented luminescent and $[Au_{10}\{Ph_2PN(C_nH_{2n+1})PPh_2\}_4(\mu_3\text{-}S)_4]$ [72]. Schnepf [73] reported the synthesis of $Au_{108}S_{24}(PPh_3)_{16}$ while the sulfide atoms originated from H-SC $(SiMe_3)$ ligand by the S-C bond break.

For mix thiolate sulfide ligands protected gold nanoclusters, Hakkinen [74] first reported the synthesis of $Au_{30}S(S\text{-}t\text{-}Bu)_{18}$ without extra S^{2-} addition. Such sulfide atoms originated from tert-butanethiol ligand by the S-C bond break. Recently, they [75] reported the reducing $(Ph_3P)AuSC(SiMe_3)_3$ with L-Selectrides gives the medium-sized metalloid gold cluster $Au_{70}S_{20}(PPh_3)_{12}$. Similarly, Zhu [76] also synthesized $[Au_{60}Se_2(PR_3)_{10}(SeR)_{15}]^+$ and solved its structure. Interestingly, this cluster contains five icosahedral Au_{13} building blocks, forming a closed ring with Au-Se-Au linkages. Two bare Se atoms are located in the center and stabilize the cluster through $Se\text{-}(Au)_5$ pentacoordinate bonding. While the selenide atoms originated from PhSeH ligand by the Se-C bond break. It remains to explore further the similarities and differences in gold nanocluster sizes between different ligand systems in future work.

5.3 Characterization methodologies and instrumentation techniques

The development of atomically precise gold cluster synthesis into a predictable and reproducible discipline requires a more detailed understanding and control of the atomic structures of the metallic cores and spectroscopic and analytical techniques, which lead to identification and location of ligands on clusters surface. The characterization of these gold clusters with precise number of atoms has been one of the prime interests of materials chemists. The size, composition, and structure are the three essential aspects of gold clusters. The rapid development of gold clusters in recent years can be partly attributed to the well-developed analytic techniques. It is of the utmost importance for understanding the fundamental science of clusters [1, 2]. For molecularly pure clusters, numerous well established characterization tools for the traditional molecular chemistry can be employed and provide in-depth characterization of these gold clusters. Identification and characterization of gold clusters have been achieved in terms of nuclearity (size), molecular formulae, and geometrical structures by various analytical techniques.

The mass spectrometry (e. g., electrospray ionization (ESI) and matrix-assisted laser desorption ionization (MALDI) mass spectrometry) can unambiguously determine the molecular weight of gold clusters. Single-crystal X-ray crystallography gives the total structure of gold clusters, nuclear magnetic resonance (NMR) spectroscopy probes organic ligand environment, and so forth. These molecular characterization tools lead to a fundamental understanding of the physical and chemical properties of these atomically precise gold clusters.

5.3.1 Mass spectrometry

Emergence of mass spectrometry as a principal tool of characterization of gold clusters is largely due to the versatility of soft ionization tools, e. g. electrospray ionization and matrix-assisted laser desorption ionization. Mass resolution has also changed tremendously in recent years with new instrumentation touching numbers of the order of 50,000 ($m/\Delta m$). This makes it possible to assign mass peaks to unique products in view of the specific isotope patterns of various entities. Mass spectrometry has been used as a key tool to monitor the formation and reactions of gold clusters. Especially, mass spectrometry coupled with soft-ionization techniques (e. g., electrospray ionization, fast atom bombardment ionization) are found to be powerful tools to obtain direct information about the cluster mass of clusters.

Laser irradiation in TOF-MS (LDI) can efficiently cleave the S–C and Au–S bonds, or even cause loss of gold atoms. Hence the observed mass peak, especially before the purification procedure, may be a result of fragmentation/recombination in the gas phase, and the consequences sometimes strongly depend on the measurement conditions(e. g., voltage). It is not a perfect mode to determine the intact gold clusters mass and to further deduce the formula. For example, a fragment corresponding to a loss of $Au_4(PET)_4$ appeared in positive mode using trans-2-[3-(4-tert-butylphenyl) –2-methyl-2-propenylidene]malononitrile (abbreviated as DCTB) as matrix in the case of $Au_{25}(PET)_{18}$ (Figure 5.5) [78, 79]. The crystal structure of $[Au_{25}(PET)_{18}]^-$ did not show $Au_4(PET)_4$ as a prominent feature[79].

Compared with laser desorption ionization(LDI) and MALDI method, ESI mass spectrometry is a much softer ionization technique and does not induce

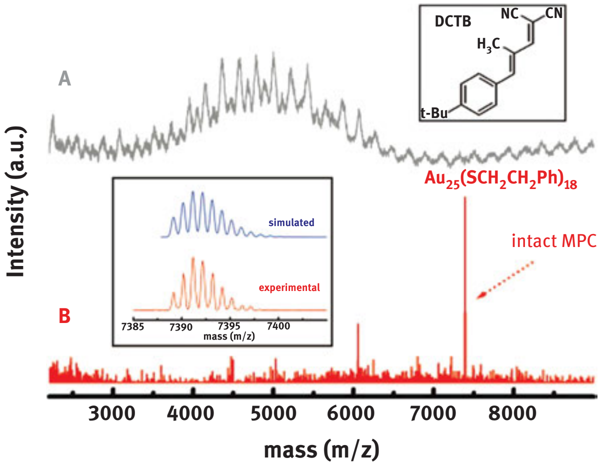

Figure 5.5: Positive MALDI-TOF-MS spectrum of $Au_{25}(PET)_{18}$ with DCTB matrix. (Adapted with permission from ref. 57. Copyright 2008. American Chemical Society).

fragmentation/recombination during the analysis. It allows for the determination of the intact gold clusters mass and the exact cluster composition. Negishi [80] reassigned the $Au_{25}(SG)_{18}$ in 2005; no fragments were found in the ESI-MS analysis. It can be noticed that ESI-MS in the negative mode shows a single peak corresponding to $[Au_{25}(SC_6H_{13})_{18}]^-$, and interestingly, the positive mode also shows the cluster with the counterion, TOA^+.

IM-MS is ideal for studying fragments generated from gold clusters, because of the signal-to-noise enhancement and structural characterization capability. Harkness [81] has reported the application of combined ion mobility–mass spectrometry (IM-MS) to the analysis of Au clusters. In the negative ion mode, these fragments correlate to the capping structural motifs. In the positive ion mode, the fragment ions are nearly identical to the positive ions generated from the gold-thiolate precursor complexes. This suggests that energetic processes during laser desorption/ionization induce a structural rearrangement in the capping gold-thiolate structure of the gold clusters. This result in the generation of positively charged clusters and complexes were similar to the precursors of Au cluster formation by reduction and negatively charged complexes. They are more representative of the cluster surface.

Tandem mass spectrometry or MS/MS is the best analytical technique for understanding the fragmentation pattern of ions. Although this technique has been used for a variety of biological samples, e. g. proteins of similar masses, it has not been explored much in the context of gold clusters. Fields-Zinna et al. [82] performed the tandem mass spectrometric analysis of $Au_{25}(SR)_{18}$ cluster. They conducted the low energy collisioninduced dissociation tandem mass spectrometry (CID MS/MS) study of mixed ligand PET and methoxy penta(ethylene glycol) thiolate (SPEG) protected Au_{25} clusters. The spectrum showed the generation of lower m/z fragment ions derived from $[Na_4Au_{25}(PET)_8(SPEG)_{10}]^{3+}$ (m/z 2929). Several fragments of the type (AuL_2, Au_2L_3, etc.) were observed along with the Au_4L_4 fragment, which confirmed the occurrence of the semi ring rearrangements on the surface of the gold clusters. Analogous fragments have also been observed for bigger clusters, such as $Au_{38}(SR)_{24}$, $Au_{144}(SR)_{60}$, etc., indicative of a similar surface structure[83].

5.3.2 UV-Visible absorption spectrometry

Gold clusters were believed to have discrete energy levels (asopposed to continuous band in the metallic state). Usual characteristic of Au clusters is an exhibition of prominent quantum confinement. Therefore, optical spectroscopy is a useful tool to identify Au clusters, serving as the "fingerprint". The UV-vis property of the clusters appears step-like features; there may not be distinct steps all the time. It is due to a molecule-like HOMO–LUMO transition and the absence of the plasmon resonance. Conversion of the electronic band structure to distinct energy levels leads to well-defined optical bands. Based on the size-sensitive optical characteristics of Au clusters, the spectral features in the sub-nanometer regime are unique to individual clusters and are sensitive to the structures/nucleation as well. Thus it is possible to identify unknown species based on the spectral pattern comparison of structurally identified authentic samples. Further, since the spectral profiles are closely correlated with the electronic structures, they are useful to understand the geometry- or nucleation (size)-dependent profiles of atomically precise.

For example, the Au_{25} clusters [84, 85] show distinct absorption bands at 1.8, 2.75, and 3.1 eV. Multiple molecular-like transitions in the absorption spectrum can be ascribed to the strong quantum size effects of Au_{25} clusters, which are different from the surface plasmon resonance at ca. 2.4 eV for large gold nanoparticles (3–30 nm). The relationship between structure and optical properties of $Au_{25}(SH)_{18}$ clusters was studied by performing time-dependent density functional theory (TD-DFT) calculations [86]. The multiple absorptions can be attributed to the intraband (sp) HOMO→LUMO transmission, interband transition (d→sp), mixed sp→sp intraband, and d→sp interband transitions. Devadas et al. [87] have explored temperature dependent optical measurements of $Au_{38}(SR)_{24}$ clusters. Intriguely, the peak maximum at 1.81 eV is shifted to 1.90 eV when the temperature decreases from 323 to 78 K. A new vibronic feature is also noticeable. The single peak at 1.81 eV (at 323 K), corresponding to the HOMO–LUMO transition for the $Au_{38}(SR)_{24}$ cluster, resolves into two peaks with maxima at ~1.67 and ~1.90 eV at lower temperatures (Figure 5.6). Three main points could be confirmed from this study: (i) the absorption maxima shifted to higher energies, (ii) the absorption feature became sharper and new peaks emerged, and (iii) the oscillator strength increased significantly with a decrease in temperature. Experimental results

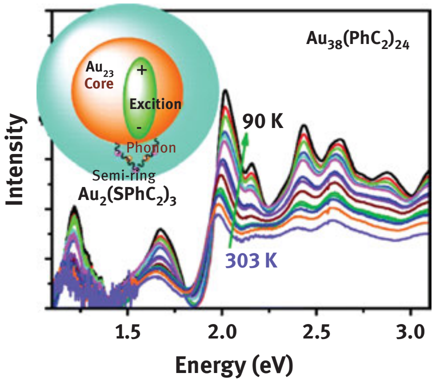

Figure 5.6: Optical absorption spectra of $Au_{38}(PET)_{24}$ clusters at different temperatures. (Adapted with permission from ref. 66. Copyright 2011. American Chemical Society).

fitted with models suggested that the gold clusters had significantly larger phonon energy due to the semi-ring gold, one of the structural units of the cluster.

5.3.3 X-ray single crystal diffraction

There are a number of reports of atomically precise gold clusters confirmed by mass spectrometry and other characterization techniques. Some of them are available with single crystal structure. Single-crystal X-ray crystallography is still the most definitive and reliable technique to elucidate the geometrical structures, but it is restricted to the clusters that give high-quality crystals suitable for the structure determination. Unlike inorganic clusters, obtaining a single crystal structure of Au clusters is somewhat difficult primarily due to stability and sensitivity issues. The crystallization methodology and solvents also play important roles in forming diffractable crystals. For most cases, the vapor diffusion method works well, but concentrated cluster solutions are required for this case and the clusters must be highly pure.

The first total structure determination of thiolate protected Au_{102}(p-MBA)$_{44}$ cluster [12] was achieved by the conventional single-crystal the X-ray crystallography (Figure 5.7). Structure of gold clusters plays a decisive role in determining their unique properties. A precise knowledge of the cluster atomic is important in order to fully understand their physical and chemical properties. Based upon the crystal structures, the relationship between the structure and the electronic, optical, and catalytic properties as well as the size-dependent evolution can be ultimately understood. In general, the single crystal data suggests that most of Au clusters have a core–shell structure. The core is composed of 15, 13, 20, 28, 23, and 79 atoms for Au_{23}, Au_{25}, Au_{28}, Au_{36}, Au_{38}, and Au_{102}, respectively. In each case, the core is surrounded by a shell, which is composed of two types of staple motifs: $Au(SR)_2$ and $Au_2(SR)_3$. In smaller clusters such as $Au_{25}(SR)_{18}$, the latter one is predominant, but in larger clusters, e. g. $Au_{102}(SR)_{44}$, the $Au(SR)_2$ motif dominates. In a few cases (e. g., Au_{23} and Au_{28} clusters)

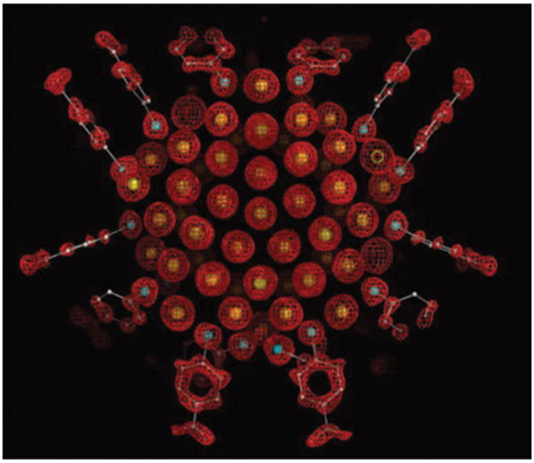

Figure 5.7: X-ray crystal structure determination of the Au_{102}(p-MBA)$_{44}$ cluster. Electron density map (redmesh) and atomic structure. (Adapted with permission from ref. 12. Copyright 2007. Science Publishing Group).

bridging –SR motifs are also present in their structure. Typically, the Au–Au bond distance average varies between 2.95 and 3.0 Å in these clusters. These structural illustrations help us to understand gold clusters in a much deeper way.

Low temperature techniques, narrower beams and synchrotron sources have all contributed to a situation where smaller crystals have become more amenable to X-ray structural techniques, which provide unambiguous structural information on the metal cores and the mode of attachment of the ligands on their surface. This detailed structural information has proved invaluable for providing background knowledge about the structures of gold clusters. The typical crystal structures of several large gold clusters have been crystallographically determined including $[Au_{25}(SR)_{18}]^q$ (q = 1, 0), $Au_{28}(SR)_{20}$, $Au_{36}(SR)_{24}$, $Au_{38}(SR)_{24}$ and $Au_{102}(SR)_{44}$. These clusters have provided excellent models that produced in non-aqueous solvents in the presence of thiolate ligands. These structural determinations have established that the metal core geometries do not necessarily adopt the face-centred cubic (fcc) packing arrangement observed in bulk gold and alternative structures based on polyhedra with fivefold symmetry are also observed. They have indicated that these large cluster species do not necessarily adopt “full-shell magic number” close packed arrangements with 13, 55, 147, 309 and 561 metal atoms. Their cores exhibited unique molecule-like atomic structures. For instance, Au_{25} has a centered icosahedral Au_{13} core capped by an exterior shell composed of the remaining 12 Au atoms in the form of six –RS–Au–RS–Au–RS– motifs. Furthermore, the structures have revealed that the surfaces of thiolate protected gold clusters may not necessarily involve simple metal-ligand bonds but metallo-thiolate fragments. These structures and bonding models have been developed to rationalize the structures. The steric requirements of the ligands are also important in determining the nucleation of the clusters and the geometry of the metal cores. These effects were recognized for phosphine-protected gold clusters, and a “cluster cone angle” was defined which was analogous to the Tolman cone angle for mononuclear co-ordination and organometallic compounds.

5.3.4 Electron diffraction

Besides the single-crystal X-ray crystallography (SXRD), electron diffraction also has been employed in determining the structures of gold clusters. This technique opens up another way to examine the structures of clusters as structure determination through SXRD has not been an easy task so far. Electron microscopy tomography requires a series of images for many different specimen orientations and is most effective for larger gold clusters which are not modified greatly by the electron beam. Aberration-corrected scanning transmission electron microscopy coupled with image simulation has been used to study smaller gold clusters. The rapid development of technologies and physics of aberration-corrected electron microscopy (AC-TEM and AC-STEM) has resulted from improvements in physical toolkits for the conversion of single-shot images into 3D representations by combining them with image simulation techniques (Figure 5.8)[88].

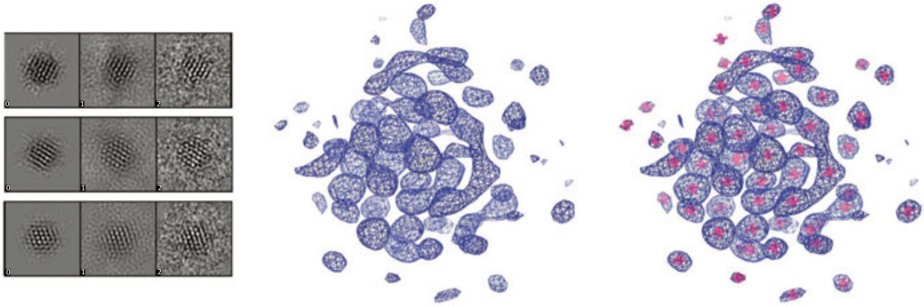

Figure 5.8: Three-dimensional reconstruction of Au_{68} structure from electron micrographs. (Adapted with permission from ref. 67. Copyright 2008. Nature Publishing Group).

5.3.5 Nuclear magnetic resonance

Nuclear magnetic resonance spectroscopy is a powerful analytical tool to examine the environment of protecting ligands on the cluster surface. ^{1}H, ^{13}C, and ^{31}P NMR spectra are useful to investigate the dynamics of the coordinated ligands on the gold clusters but are not suitable to obtain definitive cluster structures. NMR can also be employed for the charge state detection of these Au clusters, and it has also been used to investigate their structural stability. Solution and solid-state NMR were used to study the structures of clusters with 4–13 metal atoms. NMR studies on phosphine-protected clusters are structurally informative since their $^{31}P/^{1}H$ nuclei have the appropriate abundance and sensitivity to provide good high-resolution spectra. However, many of the larger gold nanoclusters have stereochemically non-rigid skeletal geometry in solution (even at low temperatures), and the consequently structural information was not as helpful as originally anticipated. While $^{31}P/^{1}H$ NMR proved to be more helpful for studying clusters in the solid state, where their stereochemical rigidity provides more structural information. Since the majority of stabilizing ligands used in gold cluster synthesis is organically based, ^{1}H NMR is very useful for confirming the presence of these ligands on the surface of clusters. However, the technique does not provide direct information regarding the ratio of ligands to the number of gold atoms in the core and even the size of the cluster.

NMR also can be used as an analytical tool to estimate the size of thiolate-protected gold clusters in solution. For example, by using diffusion-ordered NMR spectroscopy (DOSY), Salorinne et al. [89] successfully estimated the size of Au_{25}, Au_{38} and Au_{144} clusters by determining the diffusion coefficient and hydrodynamic radius from solution samples. The determined cluster sizes agree well with the diameters from the measurements of the corresponding single-crystal or theoretical structures reported previously. Based on the different chemical shifts of free ligands and metal core-bound ligands, NMR can be used to probe the protecting ligands surround the metal core and check the purity of the synthesized clusters. Previous studies showed that substantial spectral broadening occurred when protecting ligands were bound onto the cluster surface. The spectral broadening was attributed to the following several factors. First, the solid-like structure at the ligand–core interface results in rapid spin relaxation from dipolar interactions. Second, different cluster surface sites for ligand binding may also cause a distribution of the chemical shifts. Third, metal core size dispersity will lead to the spin–spin relaxation broadening. For instance, in the ^{13}C NMR spectrum of octanethiolate protected gold clusters, the resonances from C_{α} and C_{β} closest to the gold cores are broadened into the baseline, indicating that the synthesized clusters were highly pure without the presence of free ligands and other organic byproducts [90]. Parker[91] has shown electron self-exchange dynamics of nanoparticle-coupled $[Au_{25}(PET)_{18}]^{0/1-}$ by NMR line broadening.

Further, this technique has also been extended to probe the chirality of gold clusters. Recently, the $Au_{38}(PET)_{24}$ and $Au_{25}(PET)_{18}$ was analyzed by ^{1}H NMR [92]. For $Au_{38}(SR)_{24}$ clusters, distinct NMR signals for each proton in both α and β-CH_2 groups of the ligands were observed. Especially for the α-CH_2, there is 0.8 ppm difference in chemical shift for each germinal proton, which could be ascribed to the chirality of the Au_{38} clusters. However, no chemical shift difference was observed for the two protons in –CH_2 groups in the case of the $Au_{25}(SR)_{18}$, strongly suggesting the Au_{25} clusters were achiral. This typical study demonstrates that NMR spectroscopy is a useful tool for studying the chirality of clusters.

NMR spectroscopy could also be used to identify the reaction precursors of gold clusters. By using ^{1}H NMR spectroscopy, Goulet[93] and Li [94] found that Au(I) thiolate

$[AuSR]_n$ was not a measurable (^{1}H NMR) precursor in the typical Brust–Schiffrin reaction, which was contrary to the assumptions of previous reports. It can be concluded from NMR studies that Au(I)–and Au(III)–tetraalkylammonium complexes are the relevant Au species in the reaction solution prior to reduction with $NaBH_4$. From the crystal structure analysis, it has been observed that $Au_{25}(SR)_{18}$ cluster has $Au@Au_{12}@Au_{12}$ type structure, where the first shell (shell 1) surrounds the central Au atom to form an Au_{13} kernel that is further encapsulated by another shell (shell 2) of Au_{12} atoms. In this cluster, two types of thiolate binding modes were identified: (I) 12-SR ligands which join the Au shells 1 and 2; (II) 6-SR ligands located on the Au_{12} shell 2. To determine which of these thiolate binding modes is more stable, Jin's group [95] performed an NMR study focusing on the oxidation resistance and thermal stability of the Au–S bond. In this experiment, $Au_{25}(SG)_{18}$ was systematically oxidized using $Ce(SO_4)_2$ and a time dependent NMR was measured. Assignments of all the peaks have been mentioned in another report [96]. Protons attached with C7 atom of the ligand split into two parts (because of chirality) to form a doublet at 3.6 and 3.8 ppm corresponding to α-H of thiolate binding mode I and another doublet at 3.3 and 3.4 ppm corresponding to α-of thiolate binding mode II. The ratio of mode I to mode II is 2:1. Upon addition of $Ce(SO_4)_2$, the doublet at 3.3/3.4 ppm was broadened and was almost lost after 6 h, which suggests that binding mode II is comparatively weak and is attacked first by the oxidant. In contrast, the doublet at 3.6/3.8 ppm remained unaffected even after 5 days, from which it can be concluded that the binding mode I is much stronger than binding mode II. Thus, with an NMR study, one can correlate the structural stability in terms of Au–S bond strength under an oxidative atmosphere. The effect of charge state on NMR of $Au_{25}(SR)_{18}$ cluster has been demonstrated by Venzo[97]. ^{31}P NMR is also very useful in structural analysis of phosphine-protected clusters. Clayden [98] has shown the importance of high resolution solid and solution state ^{31}P NMR to understand the dynamics of phosphine-protected gold clusters.

5.3.6 X-Ray photoelectron spectroscopy

From X-Ray photoelectron spectroscopy (XPS) measurements, the surface chemistry of Au clusters can also be studied. For thiolate protected clusters, in $[Au_{25}(PET)_{18}]$ gold nanocluster[64], the binding energy of S $2p_{3/2}$ compares very well with the typical value of chemisorbed S species (162.7 eV), one can infer that the Au–S bonds were formed in the synthesis of thiolate protected gold clusters. Tanaka [99] studied the Au binding energy of dodecanethiolate-passivated Au clusters. They found that Au $4f_{7/2}$ peaks actually consist of two components, originating from the inner Au atoms and the surface Au atoms bonded with dodecanethiolate ligands. It was found that the binding energy of the surface Au components is higher than that of the corresponding inner components and the binding energies increase with the cluster diameter decreasing. These results clearly indicate that XPS measurements can provide valuable information about the band structure of clusters and the surface interaction between the metal core and capping ligands.

5.3.7 Extended X-ray absorption fine structure

Structurally characterized gold clusters have enabled atomic site-specific analysis of local structure and electronic character by X-ray absorption spectroscopy (XAS). EXAFS has been used recently to study the cluster nucleation process when solutions of $HAuCl_4$ are reduced [100]. An example of the power of EXAFS was shown by Yamazoe [101], where hierarchy in the bond stiffness in clusters such as $Au_{25}(PET)_{18}$, $Au_{38}(PET)_{24}$, and $Au_{144}(PET)_{60}$ has been measured successfully. They found that the Au–Au bonds have different stiffnesses depending on their lengths. Structurally characterized clusters have enabled atomic site-specific analysis of local structure and electronic character by XAS. Unlike optical absorption spectroscopy, which probes electronic transitions in valence orbitals, XAS involves electronic transitions from the core level to unoccupied valence states. The core-level energies are highly element-specific, and thus, XAS enables element-specific analysis of electronic properties of the absorbing atom in the near-edge region (i. e., X-ray absorption near-edge structure, XANES). For example, holes in the d state can be determined by monitoring the intensity of the first spectral feature (historically called the “white line”) in XANES spectra. Accurate information on the local structure of the X-ray-absorbing atom (e. g., bond length, coordination number) can be obtained from extended X-ray absorption fine structure (EXAFS) signals by fitting the EXAFS spectrum. Zhang et al. [102] carried out a series of works using the XANES and EXAFS techniques, including studies of the effects of solvation and the temperature dependence of gold clusters.

Tsukuda [101] recently investigated bond stiffness in $Au_{25}(SR)_{18}$, $Au_{38}(SR)_{24}$, and $Au_{144}(SR)_{60}$ by EXAFS spectroscopy and revealed the following hierarchy (Figure 5.9). Long Au-Au bonds (those at the icosahedron-based gold core surface) are more flexible than those in the bulk metal. In contrast, short Au-Au bonds (in the radial direction of the core) are stiffer than those in the bulk metal and form a cyclic structural backbone with rigid Au-SR oligomeric staple motifs. Wei [103] reported an icosahedral-to-cuboctahedral structural transformation of Au clusters driven by a changing chemical environment. Specifically, for the icosahedral Au_{13} clusters protected by binary ligands (dodecanethiolate and triphenylphosphine), a solvent change from ethanol to hexane caused the rapid selective desorption of the thiolates and then the conversion of the to a cuboctahedral structure. Jiang [104] also investigated the critical role of the solvent in the controlled synthesis of gold–thiolate clusters using XAS. They found that increasing the solvent polarity leads to higher thiol coverage on the cluster surface and, accordingly, retards the growth of the particles. XAS techniques are advantageous for probing the structures of gold

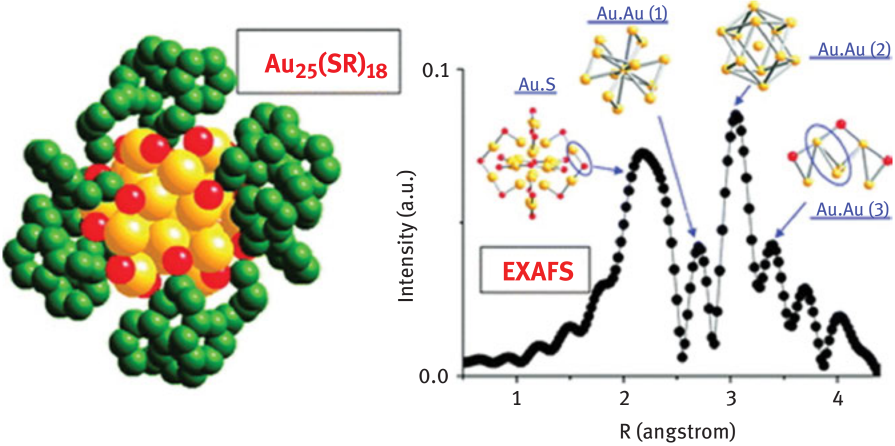

Figure 5.9: FT-EXAFS of Au_{25} cluster. (Adapted with permission from ref. 81. Copyright 2014. American Chemical Society).

clusters, in particular the solution-phase or oxide-supported clusters used in catalysis research, as well as the growth process under physical or chemical influences.

5.3.8 Powder X-ray diffraction spectroscopy

PXRD is usually used to analyze the solid state, crystal structures and evaluate the crystal size of nanomaterials. However the size of nanocrystal is less than 1 nm, the appreciable broadening of diffraction peaks into the baseline always occurs, which makes it not easy to get XRD information for gold nanoclusters. Jin [105] studied crystal structures of gold nanoparticles with different core sizes through XRD measurements. Glutathione (denoted as SG) capped $Au_{25}(SG)_{18}$ (~1.0 nm in diameter), 2.0 and 4.0 nm nanoparticles were compared. For 4.0 nm glutathione protected gold nanoparticles show a well-defined diffraction pattern with four distinct diffraction peaks at 38.51, 44.61, 64.81, and 77.81, corresponding to (111), (200), (220) and (311) of the Au face-centered cubic (fcc) crystal structure, respectively. With the nanoparticle size decreased to 2.0 nm, a broad diffraction peak at 38.51 and three weak peaks at around 44, 65 and 781 can be observed. The weak diffraction peaks indicate that the 2.0 nm glutathione protected gold nanoparticles still adopt the fcc structure, except that the (200) peak is almost merged into the broad (111) peak. However, in the PXRD pattern of $Au_{25}(SG)_{18}$ nanoclusters there are two very broad diffraction peaks centered at around 37.5 and 66.5, indicating the non-fcc crystal structure of the Au_{25} clusters. The result is in accordance with their previous study, in which the $Au_{25}(SG)_{18}$ nanocluster was proposed to be a Au_{13}(icosahedron)/Au_{12} core–shell structure with a D_{2h} symmetry. On the basis of the XRD data and Debye–Scherrer equation, the calculated particle sizes are 0.74, 1.5, and 3.97 nm, which agree well with the sizes of

$Au_{25}(SG)_{18}$ nanoclusters, 2.0 nm and 4.0 nm, respectively, determined by transmission electron microscope (TEM) measurements.

5.4 Typical synthetic case studies

This article is mainly focused on practical aspects of gold clusters synthesis, and the synthetic strategy was well summarized in Section 5.3. In this section, we discuss the synthetic details and recipes of the atomically-precise gold clusters with ubiquitous structures determined by single crystal diffraction. Under such strict criterion, some gold nanoclusters discussed regarding synthetic strategy in Section 5.3 or concerning characterization techniques in Section 5.4 may not appear in this section. This is not lack of links between each section, actully we selected typical but as less as possible ligand protected gold nanoclusters examples to give the readers a comprehensive perspective about this research filed. The crystallographic data were retrieved from Cambridge Crystallographic Data Centre (CCDC) up to 30th November 2017.A summary of typical synthetic protocols of ligand protected atomically-precise gold clusters determined by single crystal diffraction so far are also presented in Appendix Table 5.1.

The synthesis of $Au_4(\mu\text{-}I)_2(PPh_3)_4$ cluster[106]

$Au_4(\mu\text{-}I)_2(PPh_3)_4$ was prepared by reaction of $Au_9(PPh_3)_8(NO_3)_3$ and KI in acetone in a molar ratio of 1: 4. After ca. 30 min, a pale yellow precipitate was obtained. The crystals were recrystallized from $CHCl_3$-acetone.

The synthesis of $[Au_5(dppmH)_3(dppm)](NO_3)_2$ cluster[107]

The evaporation of metallic gold into an ethanolic solution of bis(dipheny1-phosphino) methane (dppmH) and NH_4NO_3. Different mol ratios were used, all of which resulted in the formation of $[Au_5(dppmH)_3(dppm)](NO_3)_2$. The red reaction mixture was evaporated to dryness and subsequently passed over a celite 505 column to remove any metallic gold. Red crystals were isolated by crystallization from methylene chloride-diethyl ether.

The synthesis of $[Au_6(PPh_3)_6]NO_3$ cluster[16]

$K[Ag(CN)_2]$ was added to a methanolic solution of $[Au_8(PPh_3)_8](NO_3)_2$ in a l/l molar ratio, and the solution stirred for approximately 1 h. Adding diethyl ether into the solution, the clusters were precipitated, and its subsequent recrystallization from CH_2Cl_2/toluene resulted in the isolation of red-brown crystals of $[Au_6(PPh_3)_6]NO_3$.

The synthesis of $[Au_7(PPh_3)_7]^+$ cluster[108]

With use of the rotary metal evaporation apparatus, 800 mg of Au was evaporated into 300 mL of toluene containing 1.60 g of L at $-100\ ^{\circ}C$, resulting in a dark red-brown slurry. After warming up to room temperature, the reaction mixture consisted of a brown solution and a brown solid. The latter could be isolated by filtration. The brown solid is washed with 20 mL of acetone. A compound is isolated, containing the

$[Au_7L_7]^+$ cation and as yet an unidentified anion. A dark brown solid remained after filtration and washing with diethyl ether. The yield is 20–30 % (based on Au). Crystals suitable for X-ray analysis could be obtained by slow diffusion of diethyl ether into an acetone solution.

The synthesis of $[Au_8(PPh_3)_6I]PF_6$ cluster[108]

0.50 g $[Au_9(PPh_3)_8]NO_3$ was dissolved in 20 mL of methanol, and the solution was cooled to −60 °C. A solution of excess Bu_4NI (0.45 g) in 10 mL of methanol was slowly added in ca. 5 min. The color of the reaction mixture remained dark red. A brick red solid was precipitated from this solution by adding the cold reaction mixture dropwise to a solution of 0.20 g of NH_4PF_6 in methanol (50 mL). The process of precipitation can be accelerated by the addition of water. The precipitate was isolated by filtration. To remove any traces of Bu_4NI, it was washed with a mixture of methanol/water (7/3, v/v).

The synthesis of $[Au_8(C_2But)_6(PPh_2C_6H_4PPh_2)_2](PF_6)_2$ cluster[13]

$(AuC_2But)_n$ (50 mg) and $[Au_2(PPh_2C_6H_4PPh_2)_2](PF_6)_2$ (48 mg) were suspended in 10 mL CH_2Cl_2. The suspension was stirred for 1.5 h in the absence of light. The resulting transparent pale-yellow solution was filtered, evaporated and recrystallized by slow evaporation of its solution in CH_2Cl_2/acetone/methanol/EtOH mixture at room temperature using minimum amount of CH_2Cl_2. Bright yellow block crystals were washed with diethyl ether and vacuum dried (83 mg, 85 %)

The synthesis of $[Au_9(P(C_6H_4\text{-p-Me})_3)_8][PF_6]_3$ cluster[109]

$[Au_9(P(C_6H_4\text{-p-Me})_3)_8][PF_6]_3$ was obtained by reaction of ethanolic solutions of $LAuNO_3$ (L = tris-para-substituted-phenylphosphin) with $NaBH_4$ (molar ratio 1:0.25). Green crystals separated when the mixture is set aside.

The synthesis of $[Au_{10}Cl_3(PCy_2Ph)_6]NO_3$ cluster[20]

The reaction of $Au(NO_3)(PCy_2Ph)$ with $NaBH_4$ in ethanol yielded a dark brown solid, which on recrystallisation from CH_2C1_2-hexane led to a separation of $[Au_3O_3(PCy_2Ph)_3]NO_3$ (yellow crystals, 25 %) and $[Au_{10}Cl_3(PCy_2Ph)_6](NO_3)$ brown crystals, 10 %).

The synthesis of $Au_{11}(PPh_3)_7Cl_3$ cluster [14, 15]

$Au(PPh_3)Cl$ was reduced by $NaBH_4$ in ethanol. After reduction and precipitation, the dark brown residue was cleaned by copious cycles of fractionated precipitation. Further crystallization from CH_2Cl_2/diethyl ether led to the formation of red needle-shaped crystals.

The synthesis of $[Au_{13}(PMe_2Ph)_{10}Cl_2](PF_6)_3$ cluster[11]

In the case of the $PPhMe_2$ complex, addition of NEt_4Cl to alcoholic solutions of the $[Au_{11}(PMe_2Ph)_{10}]^{3+}$on leads to its conversion into the higher nuclearity cluster ion $[Au_{13}(PMe_2Ph)_{10}Cl_2]^{3+}$ with high yields. Very dark red crystals of $[Au_{13}(PMe_2Ph)_{10}Cl_2](PF_6)_3$ which were suitable for X-ray crystallographic analysis were obtained by adding NH_4PF_6 to these alcoholic solutions.

The Synthesis of $[Au_{13}(Dppm)_6](BPh_4)_3$[110]

120 mg $HAuCl_4 \cdot {}_3H_2O$ is added to the 20 mL methanol under vigorous stirring. Then 100 mg bis-(diphenylphosphino)methane (Dppm) and 100 mg adamantane mercaptan are added to form a colorless solution. After 10 min, a freshly prepared solution of 200 mg $NaBH_3CN$ (in 2 mL of H_2O) is added. The color of the solution gradually changes from colorless to dark over 1 min. After 5 h, the precipitate is collected by centrifugation. Later, the obtained product is dissolved in 2 mL of CH_2Cl_2, and 20 mg $NaBPh_4$ in 2 mL of CH_3OH is added into the solution to replace the anions for crystallization. Orange block crystals are crystallized from CH_2Cl_2/hexane at room temperature after 4 days.

The synthesis of $[Au_{14}(PPh_3)_8(NO_3)_4]$ cluster[22]

$NaBH_4$ (0.034 g) dissolved in ethanol (40 mL) was added dropwise into a stirring suspension of ethanol (60 mL) and $Au(PPh_3)NO_3$ (1.874 g). After 2 h of stirring at r.t., the dark red reaction mixture was filtered once, dried in vacuo, redissolved in methylene dichloride (7 mL) and filtered a second time. After subsequent solvent evaporation under vacuum, the solid was washed with tetrahydrofuran and hexane (20 mL each) and once again solvents were removed thoroughly. Crystals were obtained by a slow diffusion of diethyl ether into a saturated solution of the solid in methanol.

The synthesis of $Au_{18}(SC_6H_{11})_{14}$ cluster[111]

SG-caped Au_{18} clusters were prepared by $NaBH_3CN$ reduction of $HAuCl_4$ in water in the presence of glutathione (H-SG). The as-obtained $Au_{18}(SG)_{14}$ clusters were then used as the precursor for the synthesis of $Au_{18}(SC_6H_{11})_{14}$ by reaction with cyclohexylthiol. $Au_{18}(SG)_{14}$ (200 mg in 5 mL pure water) was added to a CH_2Cl_2 solution (5 mL) of cyclohexylthiol (1 mL) under vigorous stirring at 313 K. After 6 h, the product was transferred from water to CH_2Cl_2 solution, then the organic layer was separated and dried in vacuum, washed several times with ethanol/hexane (1:3, v/v). The pure $Au_{18}(SR)_{14}$ were then dissolved in CH_2Cl_2/MeCN (2:1, v/v), followed by slow vapor (CH_2Cl_2) diffusion into the cluster solution over about 7 days at 18°C.

The synthesis of $[Au_{19}(PhC \equiv C)_9(Hdppa)_3](SbF_6)_2$ cluster[65]

A freshly prepared solution of $NaBH_4$ (0.95 mg in 1 mL of ethanol) was added dropwise to 4 mL CH_2Cl_2 suspension of 0.15 mmol $PhC \equiv CAu$ and 0.025 mmol $HdppaAu_2(SbF_6)_2$ Bis(diphenylphosphino)amine(Hdppa) under vigorous stirring. The color changed from orange to pale brown and finally dark brown. The reaction continued for 18 h at room temperature in the dark. The mixture was then dried by evaporation to give a dark solid, which was dissolved in 2.2 mL CH_2Cl_2. This crude solution was centrifuged for 3 min at 10,000 rpm, and the supernatant was subjected to the diffusion of mixed solvents (ether/n-hexane, v/v = 1). Brown-red crystals formed after 2 weeks in 20.3 % yield.

The synthesis of $Au_{20}(TBBT)_{16}$ cluster[112]

The $[Au_{25}(PET)_{18}]^-$ were then reacted with 0.3 mL TBBT in 1 mL toluene at 40 °C for 8 h. The reaction was quenched by adding ~10 mL methanol, followed by 3000 rpm centrifugation for 5 min. The supernatant was collected and the solvent was removed by rotary evaporation. 2 mL methanol was added to the remaining liquid, followed by 10,000 rpm centrifugation for 5 min. The precipitate was collected and subjected to methanol wash for two times to remove excess of TBBT thiol. Crystallization was performed by diffusion of pentane into a CH_2Cl_2 solution of clusters. After a month needle-like dark orange crystals of $Au_{20}(TBBT)_{16}$ were observed.

The synthesis of $[Au_{20}(PPh_3)_4]Cl_4$ cluster[26]

A CH_2Cl_2 solution (25 mL) of $Au_4Cl_4PPh_3$ (32 mg) was heated to 50 °C in a water bath until all of the $Au_4Cl_4PPh_3$ was dissolved, and then an ethanol solution (1 mL) of $NaBH_4$ (7.5 mg) was quickly added. The mixture was stirred at 50 °C for 4 hours. After removal of the solvent, the dark red residue was washed by a toluene/CH_2Cl_2 (10:3; 10:5, v/v) solution at 50 °C until the color of the wash solution changed from brown to pale. And then the left residues were dissolved in a CH_2Cl_2/toluene (1:1, v/v) solution at 50 °C which became a red solution. Red crystals were grown by evaporation of the CH_2Cl_2/toluene (1:1, v/v) solution at 50 °C. Finally 13 mg red crystals were obtained with a yield of 48 % on the basis of the initial amount of Au in $Au_4Cl_4PPh_3$. The red needle crystals suitable for x-ray analysis were grown in a CH_2Cl_2/toluene (1:1) mixed solvent by natural evaporating at room temperature.

The synthesis of $Au_{21}(S\text{-}Adm)_{15}$ cluster[113]

The as-obtained $Au_{18}(SR)_{14}$ clusters were then used as the precursor for the synthesis of $Au_{21}(S\text{-}Adm)_{16}$ by reaction with adamantanethiolate (HS-Adm). Typically, 30 mg $Au_{18}(SR)_{14}$ and 0.5 g adamantanethiolate were dissolved in 10 mL CH_2Cl_2. The solution was heated to 40 °C and maintained at this temperature with vigorous stirring for 12 h. Then the solvent was removed by rotary evaporation, and methanol (20 mL) was added to the solution and the mixture was centrifuged at 3500 rpm for 5 min. The supernatant was discarded and the precipitate was washed with MeOH for 3 times. Acetone/MeOH (1:2, v/v) was used to extract $Au_{21}(S\text{-}Adm)_{15}$ clusters. The yield is ca. 20 % (Au atom basis). Needle-like single crystals of $Au_{21}(S\text{-}Adm)_{15}$ cluster were obtained by vapor diffusion of acetonitrile into toluene solution of clusters.

The synthesis of $Au_{22}(L)_6$ (L = 1,8-bis(diphenylphosphino)octane) cluster[28]

A CH_2Cl_2 solution (180 mL) of Au_2LCl_2 (142 mg, 0.15 mmol) was cooled to 0 °C in an ice bath over a period of ~30 min under magnetic stirring, and then an ethanol solution (8 mL) of $NaBH_4$ (22.7 mg, 0.6 mmol) was quickly added. The mixture was stirred at 0 °C for 24 hours. After removal of the solvent, the dark brown residue was washed by a CH_2Cl_2:hexane (1:5, v/v) mixed solution (20 mL × 3), and re-dissolved in a minimum amount of CH_2Cl_2, then purified by column chromatography (silica gel). 35 mg brown powder was obtained after solvent evaporation with a yield of 36 % on the basis of the initial amount of Au in Au_2LCl_2. The 35 mg brown powder was then crystallized by ethyl ether diffusion into a CH_2Cl_2/methanol (5:1) solution to give 13 mg branch-like crystals. The branch-like crystals were recrystallized in a CH_2Cl_2/toluene (1:1) mixed solvent to give plate crystals suitable for X-ray analysis.

The synthesis of $[Au_{23}(SC_6H_{11})_{16}]^-$ cluster[114]

$HAuCl_4 \cdot 3H_2O$ (118 mg) and tetraoctylammonium bromide (TOABr, 190 mg) were dissolved in methanol (15 mL) in a 50 mL trineck round-bottom flask. After vigorously stirring for 15 min, the solution color changed from yellow to dark reddish orange. Then, excess cyclohexanethiol (196 μL) was added to the mixture at room temperature. After ~15 min, $NaBH_4$ (114 mg dissolved freshly in 6 mL of cold Nanopure water) was rapidly added to the solution under vigorous stirring. The reaction mixture was further allowed to stir overnight and finally gave rise to pure $[Au_{23}(SC_6H_{11})_{16}]^-$ (yield ~20 %, Au atom basis). Single crystal growth of the clusters was performed by first dissolving ~4 mg $[Au_{23}(SC_6H_{11})_{16}]^-$ clusters in 1 mL CH_2Cl_2.

The synthesis of $[Au_{23}(PhC\equiv C)_9(PPh_3)_6](SbF_6)_2$ cluster[66]

To a solution of Ph_3PAuCl (24.7 mg) in CH_2Cl_2 (2 mL), $AgSbF_6$ (17.2 mg) in methanol (0.1 mL) was added with vigorous stirring. After 15 min stirring at room temperature, the resulting solution was centrifuged for 4 min at 10,000 rpm, and the AgCl precipitate was filtered off. The solvent of the filtrate was removed under vacuum to give a colorless residue, which was dissolved in CH_2Cl_2 (4 mL). To this solution $PhC\equiv CAu$ (29.8 mg) was added, and then a freshly prepared solution of $NaBH_4$ (0.71 mg in 1.0 mL of ethanol) was added dropwise with vigorous stirring. The solution color changed from orange to pale brown and finally to dark brown. Then the reaction continued for 22 h at room temperature in air in the dark. The mixture was evaporated to dryness to give a black solid. The solid was washed with *n*-hexane (2 × 5 mL) and ether (2 × 5 mL), then dissolved in CH_2Cl_2 (2.2 mL), and the resulted solution was centrifuged for 4 min at 10,000 rpm. The brown supernatant was collected and subjected to vapor diffusion with ether:hexane (1:1, v:v) to afford black crystals after two weeks.

The synthesis of $[Au_{24}(PPh_3)_{10}(PET)_5X_2]^+$ cluster[58]

$HAuCl_4 \cdot 3H_2O$ (0.090 g) was first dissolved in 5 mL water, then added to 10 mL toluene solution of TOABr (0.145 g). The two-phase solution was vigorously stirred for 15 min to effect phase transfer of gold salt from aqueous to toluene phase. The aqueous layer was then removed, and PPh_3 (0.180 g) was added under vigorous stirring. The solution turned cloudy white immediately. A freshly prepared ethanolic solution of $NaBH_4$ (0.026 g, 5 mL) was rapidly added to the whitish suspension to reduce $Au^I(PPh_3)X$ (X = Cl or Br) to clusters. After 2–16 h (this reaction time is not critical), toluene was rotavaporated and the reddish brown product was extracted with CH_2Cl_2. Excess phenylethylthiol (200 μL) was added to this solution and then heated to 313 K (note: room temperature also worked but took a longer reaction time (overnight)). The reaction was allowed to proceed at 313 K for 4–6 h, during which the optical spectrum of the crude product exhibited features of $[Au_{25}(PPh_3)_{10}(PET)_5X_2]^{2+}$. Then, to the crude product solution (without any processing), excess PPh_3 (~1.20 g, powders) was added. The reaction was continued for extra 24 h at 313K. Finally, the obtained product was washed with hexane:CH_2Cl_2 (15:1, v/v) and extracted with toluene. The as-obtained clusters were determined to be $[Au_{24}(PPh_3)_{10}(PET)_5X_2]^+$ (counterion = X, where X is Cl/Br). Single crystals were grown by vapor diffusion of hexane into a concentrated solution of the cluster in toluene (5–10 mg in 1 mL toluene).

The synthesis of $Au_{24}(SePh)_{20}$ cluster[54]

$HAuCl_4.3H_2O$ (0.0788 g) was dissolved in 5 mL water, and TOABr (0.125 g) was dissolved in 5 mL CH_2Cl_2. The solution was vigorously stirred (~1,200 rpm) with a magnetic stir bar to facilitate phase transfer of Au salt into the toluene phase. After ~15 min, phase transfer was completed, and the aqueous was then removed. The CH_2Cl_2 solution of Au(III) was cooled to 0°C in an ice bath over ~30 min without stirring. Then, C_6H_5SeH (0.042 mL) was dissolved in 1 mL ice-cold toluene, and $NaBH_4$ (11.34 mg) was dissolved in 1mL ice-cold water. As soon as both of which were added drop-wise to the solution at the same time under vigorous stirring, the solution's color slowly changed from orange to dark brown. After reaction overnight, the aqueous phase was removed. The mixture in the organic phase was rotavaporated, and then washed several times with CH_3OH/hexane to remove excess selenolate. Then, the crude product of $Au_{24}(SeC_6H_5)_{20}$ was extracted with CH_2Cl_2 or toluene, and was used to crystallize directly.

The synthesis of $Au_{24}(SAdm)_{16}$ cluster[115]

Synthesis involved three steps. In step 1, 20 mL of THF containing 100 mg $HAuCl_4 \cdot 3H_2O$ is initially combined with 98.8 mg of adamantanethiol for a 1:3 mole ratio. After stirring at 450 rpm for 15 min, 110 mg of $NaBH_4$ (dissolved in 5 mL of cold, distilled H_2O) was then added instantaneously, turning the light-yellow mixture to the characteristic black color observed in nanoparticle crude mixtures. The reaction mixture is then continued stirring for an additional 1 h, after which the product was collected and rotary-evaporated to dryness in order to remove the THF solvent. After using sequential rounds of MeOH cleansing and centrifugation, the nanoparticles were purified of any excess thiol present from the reaction.

In step 2, ~40 mg of crude product after cleaning/drying is added to 15 – 20 mL of acetone. The 20 mL screw-cap vial is then centrifuged, which separated into a distinct soluble layer, and insoluble precipitate. The soluble layer is transferred to a separate vial and subject to rotary evaporation to remove the acetone solvent. This process is repeated a total of three times in order to obtain purely acetone-soluble material without any insoluble material left over.

In step 3, to further purify the material, vapor diffusion of an insoluble ethanol portion into a soluble portion of the nanoparticles in toluene is conducted for crystallizing the material. After 5 – 7 days,brown plate-like crystals were observed at the bottom of the soluble portion.

The synthesis of $Au_{25}(PET)_{18}$ cluster[86]

About 2 mL of 50 mM $HAuCl_4 \cdot 3H_2O$ in THF was diluted to 7.5 mL using THF. About 65 mg TOABr was added to this solution and stirred at 1,500 rpm for 30 min at room temperature. The initial yellow color of the solution turned deep red during stirring. About 0.5 mmol of pure thiol was added at a stretch while stirring at the same speed. The deep red color slowly turned to yellow and eventually became colorless after about 45 min. After stirring further for 2 h, 2.5 mL of ice-cold aqueous $NaBH_4$ (0.2 M) was added in one shot. The solution turned black immediately, and stirring was continued for 5 – 8 h depending on the ligands. A continuous monitoring of the UV/vis spectra is needed. Once the Au_{25} cluster has formed, all features will be prominent and optical spectra will not change over time. The solution was rotary evaporated and precipitated with methanol (~4 mL), washed repeatedly with the same, and dried (three times, until the smell of thiol was completely gone). This gives the purified and dried Au_{25} cluster which can be stored in a refrigerator (4 °C). With this methodology all alkanethiol and PET protected Au_{25} cluster can be synthesized.

The synthesis of $[Au_{25}(PPh_3)_{10}(SC_nH_{2n+1})_5Cl_2]^{2+}$ cluster[60]

By the reaction of $AuPPh_3Cl$ with n-alkanethiol ($C_nH_{2n+1}SH$; n = 2, 8, 10, 12, 14, 16, and 18). $C_nH_{2n+1}SH$ was added to the chloroform solution (30 mL) of $AuPPh_3Cl$ (20.1 mg) at $[C_nH_{2n+1}SH]/[AuPPh_3Cl] = 60$) under vigorous stirring at 298 K. After 3 h, the products were dried in vacuo, washed several times with hexane, redissolved in a minimum amount of ethanol, and passed through a Sephadex LH-20 column. The brownish yellow fraction that was eluted first was collected and mixed with an excess amount of $NaSbF_6$ for 15 min. Insoluble products were collected on a filter and redissolved in CH_2Cl_2 to obtain cluster. Prism-like crystals for XRD measurement were grown from ethanol/CH_2Cl_2 (1/1, v/v).

The synthesis of $Au_{25}(SePh)_{18}$ cluster[53]

$HAuCl_4 \cdot 3H_2O$ (79.12 mg) was dissolved in 1 mL nanopure water, and then phase transferred to toluene with the aid of tetraoctylammonium bromide. After that, the toluene solution of Au(III) was cooled to 0 °C in an ice bath over ~30 min without stirring. Then, both C_6H_5SeH (63 µL, dissolved in 1 mL ice-cold toluene) and $NaBH_4$ (11.34 mg, dissolved in 1 mL ice-cold nanopure water) were dropwise added simultaneously to convert Au(III) to clusters. After reaction overnight, the aqueous phase was removed. The mixture in the organic phase was rotavaporated, and then washed several times with CH_3OH to remove the redundant PhSeH and byproducts. Finally, pure Au_{25} clusters were obtained through extraction using acetonitrile. The Au_{25} clusters were crystallized in CH_2Cl_2–ethanol at room temperature (2–3 days).

The synthesis of $Au_{28}(TBBT)_{20}$ cluster[40]

The $Au_{28}(TBBT)_{20}$ were synthesized by reacting $Au_{25}(PET)_{18}$ clusters with excess TBBT under 80 °C. 10 mg of $Au_{25}(PET)_{18}$ was dissolved in 0.5 mL toluene, then mixed with 0.5 mL TBBT. The reaction mixture was incubated in a 80 °C oil bath under stirring for 2 h; of note, the 2 h reaction time was an optimized time window for $Au_{25}(PET)_{18}$ to completely transform to $Au_{28}(PET)_{20}$. The reaction was quenched by adding ~10 mL of methanol, followed by centrifugation at 3,000 rmp for 5 min to separate clusters from excess TBBT. The supernatant was discarded and more methanol was added to the pellet. This process was repeated for three times. Finally, the precipitate was extracted with CH_2Cl_2. The yield of $Au_{28}(TBBT)_{20}$ was >90 % (Au atom basis). The as-obtained clusters were crystalized in a mix solvent of 1.5 mL CH_2Cl_2 and 1 mL ethanol. Rhombic brown crystals were observed after one day.

The synthesis of $Au_{30}S(S\text{-}t\text{-}Bu)_{18}$ cluster[74]

0.254 mmol of $HAuCl_4 \cdot 3H_2O$ is dissolved in 15–20 mL of tetrahydrofuran to which 0.762 mmol of tert-butanethiol is added to give a 1:3 metal–ligand molar ratio. After stirring vigorously for 15 min, an aqueous solution of $NaBH_4$ (2.54 mmol) in 10 mL of cold H_2O was added instantaneously. The reaction mixture turned dark in color immediately, and the stirring was continued for 1 h and processed via an initial rotary evaporation of the THF solvent (drying the crude product) followed by sequential rounds of washing with excess methanol and centrifugation to cleanse the product of excess $t\text{-}C_4H_9$. The thermochemical treatment, in a solution of 1:3 (% v/v) toluene/$t\text{-}C_4H_9$ gives rise to >90 % pure $Au_{30}(S\text{-}tC_4H_9)_{18}$ after 5 h of stirring at 75 °C. The samples were further purified using SEC (THF as eluent) on Bio-Rad SX1 beads. Crystals were grown by a vapor-vapor diffusion method, whereby the pure product was dissolved in toluene and placed in an ethanol bath. Rhombic platelike crystals suitable for measurement were obtained within 7–10 days.

The synthesis of $Au_{36}(TBBT)_{24}$ cluster[39]

10 mg $Au_{38}(PET)_{24}$ were dissolved in 0.5 mL toluene containing 0.5 mL TBBT. The mixture was heat to 80 °C under gentle stirring for >12 h. After that, the greenish crude product was treated in the same method as for Au_{38} to obtain pure $Au_{36}(TBBT)_{24}$. In crystallization experiments, ~ 5 mg $Au_{36}(TBBT)_{24}$ was dissolved in 1.5 mL CH_2Cl_2 and 1 mL ethanol. After 1–2 days, rhombus crystals were obtained.

The synthesis of $Au_{36}(SCH_2Ph\text{-}^tBu)_8Cl_{20}$[116]

0.5 mmol $HAuCl_4$ dissolved in 1 mL water, 25 mL CH_2Cl_2 and 156 mg TOAB added to a flask. After 15 min, the system was palced in a static ice bath, and 150 uL $HSCH_2Ph\text{-}^tBu$ thiol was added. 170 mg borane tert-butylamine complex were added simultaneously. After one h, the aqueous phase was removed. The mixture in the organic phase was rotavaporated, and then washed with methanol. The salmon pink crystals were crystallized from CH_2Cl_2/ethanol over 2 – 3 days.

The synthesis of $Au_{36}(PhC\equiv C)_{24}$ cluster[50]

To 3 mL CH_3OH suspension containing $PhC\equiv CAu$ (0.1 mmol, 29.8 mg), a freshly prepared solution of $NaBH_4$ (0.02 mmol in 1 mL of ethanol) was added dropwise under vigorous stirring. The solution color changed from yellow to pale brown to dark brown. Then 3 mL $CHCl_3$ solution containing H_4TCA (9.8 mg) was added to the mixture and followed by addition of Et_3N (20 uL). The reaction continued for 4 h at room temperature in air in the dark. The mixture was evaporated to dryness to give a dark solid. This solid was suspended in 8 mL *n*-pentane, and collected by centrifuge (10,000 rpm, 2 min). This crude solid was dissolved in CH_2Cl_2 (2 mL), and centrifuged (10,000 rpm, 2 min). The resulting solution was subject to diffusion of *n*-pentane to afford dark sheet-like crystals after ca. two weeks (yield 5.0 %).

The synthesis of $Au_{38}(PET)_{24}$ cluster[117]

0.5 mmol $HAuCl_4\cdot 3H_2O$ and 2.0 mmol glutathione (GS-H) were mixed in 20 mL acetone at room temperature under vigorous stirring (~20 min). The mixture (yellowish cloudy suspension) was then cooled to ~0 °C in an ice bath. After ~20 min, a fresh solution of $NaBH_4$ (5 mmol, dissolved in 6 mL cold Nanopure water) was rapidly added to the suspension under vigorous stirring. After ~20 min, black $Au_n(SG)_m$ nanoparticles precipitated out of solution and stuck to the inner wall of the flask. The clear acetone solution was decanted and 6 mL water was added to dissolve the $Au_n(SG)_m$ nanoparticles. The aqueous solution of $Au_n(SG)_m$ was mixed with 0.3 mL ethanol, 2 mL toluene and 2 mL PET. The diphase solution was heated to 80 °C and maintained at this temperature (under air atmosphere). The $Au_n(SG)_m$ nanoparticles were found to transfer from the water phase to the organic phase in less than 10 min. The thermal process was allowed to continue for ~40 h at 80 °C. Over the prolonged etching process, the initial polydisperse Au_n nanoparticles were converted to monodisperse $Au_{38}(PET)_{24}$ nanoparticles finally. The organic phase was thoroughly washed with ethanol (or methanol) to remove excess thiol. Then, the $Au_{38}(PET)_{24}$ nanoparticles were separated from Au(I)SR side-product by extraction with CH_2Cl_2 or toluene. $Au_{38}(SR)_{24}$ nanoparticles were crystallized in toluene/ethanol under ambient conditions (3–5 days). Black crystals were collected and subject to X-ray diffraction analysis.

The synthesis of $[Au_{38}S_2(S\text{-}Adm)_{20}]$ cluster[118]

78.8 mg $HAuCl_4\cdot 3H_2O$ and 109.4 mg TOABr were mixed in 15 mL THF at room temperature, and stirred for 30 min. After that, adamantanethiol (134.4 mg) was added and stirred vigorously until the solution turned colorless. Then, a freshly made $NaBH_4$ solution (76 mg, dissolved in 5 mL cold Nanopure water) was added to the reaction mixture all at once. The solution immediately turned dark. After 10 min, the solution containing the crude product was evaporated to near dryness. The black product was washed with methanol for four times. The solid was then extracted with CH_2Cl_2. The species insoluble in CH_2Cl_2 were discarded. The extracted cluster solution (in CH_2Cl_2) was evaporated to dryness, then extracted for a second time. Finally, the cluster solution was evaporated to dryness, and 50 mg solid was obtained. The as-obtained clusters contained a mixture of different sizes which were converted into monodisperse clusters following a size-focusing step. For the size-focusing step, the clusters were mixed with excess adamantanethiol (252 mg) and co-dissolved in toluene (2 mL). The solution was heated to 90 ˚C and maintained at this temperature for more than 24 h. The final product was washed with methanol for four times and then extracted with CH_2Cl_2 (repeated three times). The finally extracted CH_2Cl_2 solution contained quite pure $Au_{38}S_2(SR)_{20}$ clusters. The asobtained clusters were crystallized by methanol vapor diffusion into a toluene solution of clusters.

The synthesis of Au_{40}(o-MBT)$_{24}$ cluster[119]

The Au_{40}(o-MBT)$_{24}$ was synthesized by a two-step size focusing method. In the first step, 0.25 mmol of $HAuCl_4$ was reduced by 1.27 mmol of 2-methylbenzenethiolate (o-MBT) to form Au(I)-o-MBT polymers in a toluene solution containing 0.29 mmol of TOAB. The Au(I)-oMBT polymers were further reduced to size-mixed Aux(o-MBT)y clusters by 2.5 mmol of $NaBH_4$ (dissolved in 5 mL of water). In the second step, the polydispersed Aux(o-MBT)y clusters were reacted with excess of o-MBT thiol at 90 °C for 48 h. Clusters were separated from the reaction mixture by precipitation with methanol and crystallized in the pentane/CH_2Cl_2 solvents

The synthesis of Au_{44}(2,4-DMBT)$_{26}$ cluster[120]

$HAuCl_4$•$4H_2O$ (100 mg) dissolved in 2 mL water was added to 15 mL of CH_2Cl_2 solution containing TOABr (154 mg). The mixture was vigorously stirred for ~ 30 min until the phase transfer was completed. The water layer was removed using a separatory funnel, and three equivalents of 2,4-Dimethylbenzenethiol(2,4-DMBTH) (0.7284 mmol) were added to the organic layer. After continuously stirring for ~ 3 h, 3 mL of aqueous solution containing 47 mg of $NaBH_4$ was quickly added to the cooled reaction mixture (0 °C) at once. The reduction was allowed to proceed overnight. A rotary evaporator was employed to remove the solvent under reduced pressure, and then a large amount of methanol was used to clean the product to remove excess TBBTH and TOAB. Next, 100 μL of 2,4-DMBTH was added to the precursor under 40 °C for subsequent etching. The crude products dissolved in 1 mL of CH2CL2 were pipetted onto four pieces of PTLC plate (10 cm × 20 cm), and the separation was conducted in a developing tank (solvent: CH2CL2/petroleum ether = 10/25, v/v) for ~ 30 min. A knife was used to cut the bands of Au_{44}(2,4-DMBT)$_{26}$ in the PTLC plate, which were extracted by pure CH_2Cl_2. Single crystals of Au_{44}(2,4-DMBT)$_{26}$ were formed by vapor diffusion of acetonitrile into the toluene solution of cluster over one month.

The synthesis of $Au_{44}(PhC\equiv C)_{28}$ cluster[50]

A freshly prepared solution of $NaBH_4$ (0.95 mg in 1 mL of ethanol) was added dropwise to 4 mL $CHCl_3$ suspension of 0.15 mmol $PhC\equiv CAu$ under vigorous stirring. The color changed from yellow to pale brown and finally to dark brown. The reaction continued for 16 h at room temperature in air in the dark. Then phenylacetylene (0.3 mL) and pyridine (0.3 mL) were added to the mixture and the reaction continued for

24 h under ambient conditions. The volume of the mixture was evaporated to 0.6 mL and excess (15 mL) n-hexane was added to give a dark solid. This crude solid was dissolved with mixed solvents containing 1.5 mL CH_2Cl_2 and 0.1 mL CH_3OH, and the resulting solution was subject to diffusion of pentane: hexane (1:1, v/v) to afford black crystals after two weeks (8.4 % yield).

The synthesis of $Au_{52}(TBBT)_{32}$ cluster[119]

In the first step, 0.125 mmol of $HAuCl_4$ was reacted with 0.625 mmol of 4-tert-butylbenzenethiolate(TBBT) in 10 mL THF, followed by reduction to size-mixed $Au_x(TBBT)_y$ clusters by 1.25 mmol of $NaBH_4$ (in 5 mL of water). In the second step, the $Au_x(TBBT)_y$ mixture was reacted with excess TBBT thiol at 80 °C for 24 h. Clusters were separated from the reaction mixture by precipitation with methanol and crystallized in the pentane/CH_2Cl_2 solvents.

The synthesis of $[Au_{60}Se_2(PPh_3)_{10}(SePh)_{15}]^+$ cluster[76]

$HAuCl_4 \cdot 3H_2O$ (0.1576 g) was dissolved in 5 mL nanopure water, and TOABr (0.2558 g) was dissolved in 10 mL toluene. These two solutions were combined in a 25 mL trineck round-bottom flask. After about 15 min, the phase transfer was completed, leaving a clear aqueous phase at the bottom of the flask; the aqueous was then removed. The toluene solution of Au^{III} was cooled to 0 °C in an ice bath over 30 min without stirring. Then, PPh_3 (0.315 g) was added into the toluene solution of Au^{III}. After 5 min, 5 mL ice-cold aqueous solution of $NaBH_4$ (0.08 g, 2.11 mmol) was rapidly added with vigorously stirring. This led to the formation of the $Au_n(PPh_3)_m$ clusters. After about 1 h, PhSeH (50 mL) was directly added to the toluene solution of the $Au_n(PPh_3)_m$ clusters without any treatment. Then, the reaction was allowed to proceed for 36 h. After that, the aqueous phase was removed. The mixture in the organic phase was rotavaporated, and then washed several times with ethanol to remove the redundant PhSeH, PPh_3, and by-products until the optical absorption spectrum shows five stepwise peaks at 353, 435, 510, 600 and 835 nm. Finally, the pure $Au_{60}Se_2(PPh_3)_{10}(SeR)_{15}$ were obtained.

The synthesis of $Au_{60}S_6(SCH_2Ph)_{36}$ cluster[121]

Ten milligrams of $Au_{38}(PET)_{24}$ was dissolved in 1 mL of toluene containing 0.5 mL of $PhCH_2SH$. Next, the reaction proceeded overnight at 100 °C under nitrogen atmosphere, and then was terminated by the addition of excess methanol. The crude product was washed with petroleum ether and methanol four times, dissolved in CH_2Cl_2, and then subjected to separation and purification by PTLC. Single crystals of the purified clusters were grown by the vapour diffusion of acetonitrile into a toluene solution of clusters at 5 °C, and black-coloured crystals formed after one week.

The synthesis of $Au_{92}(TBBT)_{44}$ cluster[122]

In the first step, $HAuCl_4 \cdot 3H_2O$ (0.11 mmol, 45 mg) and TBBT thiol (0.55 mmol, 90 µL) were mixed in 10 mL methanol, and stirred for 30 min to form yellowish precipitate of Au(I)-TBBT complexes which were collected and redispersed in 10 mL THF by sonication. The reaction mixture was stirred gently and cooled down to −4 °C. Then $NaBH_4$ (0.8 mmol, 30 mg dissolved in 1 mL cold H_2O) was injected to the reaction mixture all at once. The color of the solution changed to black within 5s, indicating the reduction of Au(I)-TBBT complexes into polydispersed $Au_x(TBBT)_y$ nanoparticles. After reacting for 18 h, the THF solvent was removed, and the $Au_x(TBBT)_y$ nanoparticles were separated by first precipitating with methanol, and then extracting with CH_2Cl_2. In the second step, ~25 mg of $Au_x(TBBT)_y$ nanoparticles were dissolved in 1 mL toluene and 100 µL TBBT thiol, and stirred at 60 °C for 24 h. Then, additional 100 µL of TBBT thiol was added and stirred at 80 °C for another 24 h. After that, the nanoparticles were collected by first precipitating with methanol and then extracting with CH_2Cl_2. The $Au_{92}(TBBT)_{44}$ nanoparticles were crystallized by vapor diffusion of CH_3CN into a toluene solution of the nanoparticles. Rhombic black crystals were obtained and characterized by X-ray crystallography.

The synthesis of Au_{102}(p-MBA)$_{44}$ cluster[12]

Solutions of 28 mM $HAuCl_4$ and of 95 mM *p*-MBA, 300 mM NaOH, were combined with methanol and water to give 3 mM $HAuCl_4$, 12 mM p-mercaptobenzoic acid (*p*-MBA), 47 % methanol. The mixture was allowed to equilibrate for 1 h, adjusted to 10 mM $NaBH_4$ (by addition of a 150 mM solution in water) and agitated on a Vortex mixer for 5 h. Product was precipitated with 10 % (v/v) of 2.5 M NaCl and 1 vol methanol, pelleted for 5 min at top speed in a microcentrifuge, resuspended in 70 % methanol, pelleted again, dried overnight at room temperature, and resuspended in water. A screen around a starting condition of 300 mM NaCl, 100 mM sodium acetate, pH 2.5, 46 % methanol was performed for each new cluster preparation. Thin black rods appeared after three days. Crystals were frozen within a day or two of appearance, since more extensive growth would lead to greater mosaicity.

The synthesis of $Au_{103}S_2$(SNap)$_{41}$ cluster[123]

The as-synthesized clusters were used as the starting material for ligand-exchange induced size/structure transformation to $Au_{103}S_2$(S-Nap)$_{41}$. Typically, 10 mg of pure $Au_{99}(SPh)_{42}$ was dissolved in a mixed solution of 1 mL of toluene and 1 mL of 4-tert-butyltoluene. Then, 240 mg of 2-thionaphthol was added to the solution. The solution was heated and kept at 80 °C for 48 h. Methanol was added to the reaction mixture to precipitate the product, followed by centrifugation, and the solid product was washed with methanol to remove excess thiol; this washing procedure was performed several times and finally pure $Au_{103}S_2$(S-Nap)$_{41}$ was extracted with CH_2Cl_2. The yield of the reaction was ~40 % (on gold atom basis). Single crystal growth of the product was performed with vapor diffusion of methanol into a 1,2,4-trichlorobenzene solution of the clusters (~3 mg/mL).

The synthesis of $Au_{108}S_{24}(PPh_3)_{16}$ cluster[73]

Solid H-SC$(SiMe_3)_3$ (0.29 g) was added to a solution of Ph_3PAuCl (0.50 g) in 30 mL THF. The yellow mixture was stirred for 10 min. $NaBH_4$ (0.08 g) was dissolved in water and slowly added to the yellow mixture. The mixture reacted fast and became warm and black immediately. After 30 min of stirring the mixture was left overnight. Et_2O (50 mL) was added to dissolve the black precipitate and to separate the organic and the aqueous phase. The phases were separated and the organic phase was dried under vacuum to give a brown precipitate. The brown precipitate was washed with pentane, toluene and Et_2O and is afterwards extracted with 30 mL of THF, where 90 mg are dissolved. The extract was stored at 40 °C. After 3 weeks beside a thin film also black, hexagonal crystals of $Au_{108}S_{24}(PPh_3)_{16}$ was formed.

The synthesis of Au_{130}(p-MBT)$_{50}$ cluster[124]

In the first step, 0.4 mmol of $HAuCl_4 \cdot 3H_2O$ (dissolved in 5 mL nanopure water) was mixed with 0.46 mmol of TOABr (dissolved in 10 mL toluene). The solution was vigorously stirred for 15 to 20 min to allow the transfer of gold salt into the toluene phase, followed by the removal of aqueous phase. Then, 2 mmol of *p*-MBT was added to the flask, and the solution was kept stirring for 30 min. 3 mmol of $NaBH_4$ (dissolved in 5 mL ice cold nanopure water) was rapidly added to the reaction flask. The reaction was stopped after 5 min. The aqueous phase was discarded. The organic phase was dried by rotary evaporation. The as-obtained, size mixed $Au_x(p\text{-MBT})_y$ were washed with methanol 3 times and then extracted with CH_2Cl_2. In the second step, the obtained $Au_x(p\text{-MBT})_y$ gold clusters were reacted with 0.6 mL *p*-MBT in 1 mL toluene at 80 °C in air atmosphere with gentlestirring. The reaction was monitored by MALDI-MS and UV-vis spectroscopy. Once the pure $Au_{130}(p\text{-MBT})_{50}$ was obtained (monitored by MALDI-MS), the reaction was stopped (typically, 20 to 30 h). Then the product was washed with methanol and extracted with CH_2Cl_2. Needle-like single crystals of Au_{130} $(p\text{-MBT})_{50}$ cluster were obtained by vapor diffusion of acetonitrile into toluene solution of clusters.

The synthesis of $Au_{133}(TBBT)_{52}$ cluster[41]

$HAuCl_4.3H_2O$ (0.3 g) and TOABr (0.42 g) were dissolved in ethyl acetate (30 mL) and stirred for 2 h at 500 rpm. Thereafter, two equivalent TBBT was added and stirred for another 4 h. To this reaction mixture $NaBH_4$ (0.29 g) was added rapidly, which turned the solution color to black with the evolution of gas bubbles. After about 24 h of stirring, the resultant product was dried using rotary evaporation to remove excess solvent. Then, to the crude product a few drops of distilled water was added and washed with methanol 3–4 times to remove excess thiol and other reaction byproducts. The crude mixture was dissolved in a minimum amount of toluene (400 μL) and 0.5 mL TBBT in a 10 mL round-bottom flask and subjected to thermochemical treatment or etching at 80 °C and stirred for about 6 days at 500 rpm. $Au_{133}(TBBT)_{52}$ was separated using a 24 inch size exclusion chromatography column packed with Biorad SX1 beads soaked in THF. 10–20 mg of the etched product was dissolved in minimum amount of stabilized THF (<400 μL) and loaded carefully on the flat bed of the column to ensure effective separation.

The synthesis of Au_{246}(p-MBT)$_{80}$ cluster[125]

The Au_{246}(*p*-MBT)$_{80}$ were synthesized by a two-step size focusing method. In the first step, 1 mmol of $HAuCl_4$ (dissolved in 5 mL of H_2O) was mixed with 1.16 mmol of TOABr (dissolved in 10 mL of toluene). After vigorously stirring for 5 min, the clear aqueous phase was removed. Then 4 mmol of *p*-MBT thiol was added into the toluene phase. After vigorously stirring for 30 min, 10 mmol of $NaBH_4$ (dissolved in 5 mL of H_2O) was rapidly added to the reaction solution all at once. The color of the solution immediately changed to black. After 10 min of reaction, the aqueous phase was removed, and the black toluene phase was dried by rotary evaporation. The precipitates were washed with methanol three times. The size-mixed Au_x(*p*-MBT)$_y$ were extracted from the precipitates with CH_2Cl_2 and dried. In the second step, the as-prepared Au_x(*p*-MBT)$_y$ were mixed with 1 mL of *p*-MBT thiol and 1 mL of toluene. The solution was heated at 80 °C and gently stirred. The reaction was allowed to proceed for approximately 10 h. After that, the product was washed with methanol to remove excess thiol, and extracted with CH_2Cl_2. The as-obtained Au_{246} (*p*-MBT)$_{80}$ was ~90 % pure and further purification was performed by solvent fractionation with toluene/methanol to remove the smaller nanoparticles, and finally molecularly pure Au_{246}(*p*-MBT)$_{80}$ was obtained. Single crystals of the cluster were obtained by vapor diffusion of acetonitrile into a toluene solution of the pure Au_{246}(*p*-MBT)$_{80}$ clusters.

The synthesis of Au_{279}(TBBT)$_{84}$ cluster[126]

Step 1: Crude Synthesis. 200 mg $HAuCl_4 \cdot 3H_2O$ and 280 mg TOABr were dissolved in ethyl acetate (20 mL) in a 100 mL roundbottom flask under vigorous stirring for 2 h. Two equivalent TBBT was added to the red-colored reaction mixture and stirred for 4 h. The nearly clear polymeric $Au^I_x(SR)_y$ mixture was reduced with 192 mg $NaBH_4$ dissolved in ice cold water (6 mL). Upon reduction, the reaction mixture turns black instantaneously, and the reaction was stopped after 24 h. Then the solvent was removed by rotary evaporation, and the black colored crude product was washed with methanol to remove excess thiol and other byproducts (4 times, 20 mL).

Step 2: Thermochemical Treatment (Etching). The crude was etched with 400 µL of TBBT and 500 µL of toluene in a 10 mL roundbottom flask at 85 °C for 4 – 6 d. The etching reaction was monitored daily to follow the reaction progress, The etched product was rotary evaporated to remove the solvent and washed with methanol to remove the excess thiols. The etched product was washed with methanol (4 times, 20 mL) to remove excess thiol and byproducts, followed by CH_2Cl_2/toluene extraction. These nanocrystals are very stable and can withstand 85 °C under ambient conditions and excess thiol for ~10 days

Step 3: Isolation of Molecularly Pure Au_{279} Nanocrystals and Crystallization. Pink-colored Au_{279}(TBBT)$_{84}$ plasmonic gold nanocrystal was isolated by using size exclusion chromatography (SEC). The Bio-Rad SX1 support beads were used as a stationary phase, and THF-BHT solvent was used for loading the sample and as a mobile phase to separate the product. Typically, 20 mg of etched product was loaded on a column with 1 in. diameter and ~20 in. long bed size. The eluted product was collected in fractions and screened using MALDI-TOF-MS under high laser fluence. It is very crucial to collect the data under high laser fluence and wide mass range (3 – 200 kDa) to reveal any higher mass polydisperse clusters present. SEC purified F-279 under high laser fluence. Pure fractions were washed with methanol (10 mL) to remove residual amounts of BHT present in the sample and analyzed using ESI-MS. Then, molecularly pure $Au_{279}(TBBT)_{84}$ nanocrystals were crystallized by vapor diffusion of pentane into CH_2Cl_2 solution of Au_{279} nanocrystals.

5.5 Critical Safety Considerations

In this article, most of the chemicals for the synthesis of gold clusters are nontoxic or low toxic in the condition of one can be strictly compliance with experimental safety regulations. However, some chemicals and experiment conditions should be paid special attention.

a. For all the synthetic procedures in the lab, safety glasses, lab coat, long pants and glove are required.
b. All the experiments should be conducted in fume hood.
c. Special attention should be paid when organic solvents (e. g. THF, DMF, CH_2Cl_2) ligands (e. g. phosphine, thiolate, alkynyl) are used. These organic solvents and ligands may cause serious discomfort and pain if inhalation or in contact with skin, or swallowed.
d. The $HAuCl_4$ is a strong corrosive acid that should be paid special attention and make sure that the use of a horn spoon instead of metallic spoon.
e. When alkynyl ligands is used to synthesize whether the gold clusters or any related precursor, due to the explosive nature of metallic alkynyls, great care should be taken and only small amounts should be used.

5.6 Conclusion and Future Perspective

In this article, synthetic strategies, characterization methodologies and instrumentation techniques for characterization of atomically-precise Au clusters have been summarized. “Size-focusing” and LEIST are two key methodologies that have been developed for attaining gold clusters with size control. These two methodologies have largely expanded the “universe” of Au clusters.

The characterization techniques in the context of geometrical structures reveal a strong molecular character of gold clusters. Important characterization techniques of these gold clusters, including mass spectrometry, UV-visible absorption spectrometry, X-ray single crystal diffractometer, electron diffraction and extended X-ray absorption fine structure, are presented. Identification and characterization of gold clusters have been achieved in terms of nuclearity (size), molecular formulae, and geometrical structures by the combination of these techniques.

Giant clusters with more than 100 metal atoms are particularly exciting, as they can exhibit size-dependent structural rules and provide important information about cluster stability. Such giant clusters will also be of critical importance for materials chemists to probe and understand the transition from the molecular to the metallic state. New breakthroughs are needed in achieving atomic precision for particles larger than 2 nm in diameter and also in crystallizing such particles for total structure determination by X-ray crystallography.

Cluster crystals as materials have not been examined. A fruitful area of gold cluster materials is yet to be explored. Spontaneous reactions involving metal and ligand exchange and the new examples of isomeric transformations between clusters suggest that many new examples of this science are possible. These explorations could lead to new rules of cluster chemistry analogous to molecular science. Regardless of the fact that many properties of gold clusters have been discovered, the exploration of their practical applications is still in its infancy. Owing to the unique properties, it can be anticipated that further research on gold clusters will stimulate broad scientific and technological interests in the near future.

Funding: This work was financial supported by the Program of Shanxi Province Hundred Talent Project, the National Natural Science Foundation of China (No. 21701168) and Liaoning Natural Science Foundation (No. 20170540897). and open project Foundation of State Key Laboratory of Physical Chemistry of Solid Surfaces, Xiamen University (No.201709).

Appendix

Table 1: A summary of typical synthetic protocols of ligand protected atomically-precise gold clusters determined by single crystal diffraction so far.

Core	Ligating mode	Chemical Composition	UV (characteristic peak)/nm	Other Characterization	Ref.
Au_4	P	$Au_4(\mu\text{-}I)_2(PPh_3)_4$	None	none	84
Au_5	P	$[Au_5(dppmH)_3(dppm)](NO_3)_2$	none	none	85
Au_6	P	$[Au_6(PPh_3)_6]NO_3$	319, 331, 453,476	none	16
Au_7	P	$[Au_7(PPh_3)_7]^+$	none	NMR, Mossbauer	109
Au_8	p	$[Au_8(PPh_3)_6I]PF_6$	none	NMR, Mossbauer	109
Au_8	C P	$[Au_8(C_2But)_6(PPh_2C_6H_4PPh_2)_2](PF_6)_2$	573	NMR, ESI-MS, PXRD, EXAFS	13
Au_9	P	$[Au_9(P(C_6H_4\text{-}p\text{-}Me)_3)_8][PF_6]_3$	none	none	110

(continued)

Table 1 (continued)

Core	Ligating mode	Chemical Composition	UV (characteristic peak)/nm	Other Characterization	Ref.
Au_{10}	P	$[Au_{10}Cl_3(PCy_2Ph)_6]NO_3$	none	none	20
Au_{11}	P	$Au_{11}(PPh_3)_7Cl_3$	318, 406	NMR	13–14
Au_{13}	P	$[Au_{13}(PMe_2Ph)_{10}Cl_2](PF_6)_3$	360,490	ESI-MS	11
Au_{13}	P	$[Au_{13}(Dppm)_6](BPh_4)_3$	450,800	ESI-MS,TGA	111
Au_{14}	P	$[Au_{14}(PPh_3)_8(NO_3)_4]$	none	NMR	22
Au_{18}	S	$[Au_{18}(SC_6H_{11})_{14}]$	520, 590	ESI-MS, IR,SEC, NMR	112
Au_{19}	C P	$[Au_{19}(PhC \equiv C)_9(Hdppa)_3](SbF_6)_2$	277, 388,548, 934	NMR, ESI-MS, IR	66
Au_{20}	S	$[Au_{20}(TBBT)_{16}]$	none	none	113
Au_{20}	P	$[Au_{20}(PPh_3)_4]Cl_4$	486, 360	ESI-MS, NMR	26
Au_{21}	S	$[Au_{21}(S\text{-}Adm)_{15}]$	none	ESI-TOF-MS	114
Au_{22}	C	$Au_{22}(C_{32}H_{36}P_2)_6$	456	ESI-MS, NMR	28
Au_{23}	S	$[Au_{23}(SC_6H_{11})_{16}]^-$	570	ESI-MS,TGA	115
Au_{23}	C P	$[Au_{23}(PhC \equiv C)_9(PPh_3)_6](SbF_6)_2$	273,380,525, 600	ESI-MS, XPS	67
Au_{24}	P S	$[Au_{24}(PPh_3)_{10}(PET)_5X_2]^+$	383,560	ESI-MS, CV	116
Au_{24}	Se	$[Au_{24}(SePh)_{20}]$	380, 530, 620	none	55
Au_{24}	S	$[Au_{24}(SAdm)_{16}]$	580, 690	ESI-MS	117
Au_{25}	S	$[Au_{25}(PET)_{18}]$	400, 450, 670	NMR	65
Au_{25}	P S	$[Au_{25}(PPh_3)_{10}(SC_nH_{2n+1})\text{-}_5Cl_2]^{2+}$	670	ESI-MS	61
Au_{25}	Se	$[Au_{25}(SePh)_{18}]$	430,620, 1050	NMR, MALDI-MS, CV	54
Au_{28}	P	$[Au_{28}(TBBT)_{20}]$	365,480, 580	CD, ESI-MS	41
Au_{30}	S	$[Au_{30}S(S\text{-}t\text{-}Bu)_{18}]$	630	CD, ESI-MS	75
Au_{36}	S	$[Au_{36}(TBBT)_{24}]$	375, 570	ESI-MS	40
Au_{36}	C	$[Au_{36}(PhC \equiv C)_{24}]$	640	ESI	51
Au_{36}	S	$Au_{36}(SCH_2Ph\text{-}^tBu)_8Cl_{20}$	365, 420, 502	XPS	118
Au_{38}	S	$[Au_{38}(PET)_{24}]$	1050, 750, 620, 560, 520, 490	none	119
Au_{38}	S	$[Au_{38}S_2(S\text{-}Adm)_{20}]$	650,750	none	120
Au_{40}	S	$[Au_{40}(o\text{-}MBT)_{24}]$	none	none	121
Au_{44}	S	$[Au_{44}(2,4\text{-}DMBT)_{26}]$	331, 389, 442, 543, 670	ESI-MS,TGA,XPS	122
Au_{44}	C	$[Au_{44}(PhC \equiv C)_{28}]$	558	ESI	51
Au_{52}	S	$[Au_{52}(TBBT)_{32}]$	none	none	121
Au_{60}	Se	$[Au_{60}Se_2(PPh_3)_{10}(SePh)_{15}]^+$	353, 435, 510, 600, 835	ESI, CV,TGA	77
Au_{60}	S	$[Au_{60}S_6(SCH_2Ph)_{36}]$	345,600	ESI	123
Au_{92}	S	$[Au_{92}(TBBT)_{44}]$	440, 660, 850	ESI	124
Au_{102}	S	$[Au_{102}(p\text{-}MBA)_{44}]$	none	none	12

(continued)

Table 1 (continued)

Core	Ligating mode	Chemical Composition	UV (characteristic peak)/nm	Other Characterization	Ref.
Au_{103}	S	$[Au_{103}S_2(SNap)_{41}]$	none	SAXS, TEM, ESI, NMR	125
Au_{108}	S	$[Au_{108}S_{24}(PPh_3)_{16}]$	none	EDX, DLS,NMR	74
Au_{130}	S	$[Au_{130}(p\text{-}MBT)_{50}]$	none	NMR,	126
Au_{133}	S	$[Au_{133}(TBBT)_{52}]$	none	TEM, ESI,NMR	42
Au_{246}	S	$[Au_{246}(p\text{-}MBT)_{80}]$	470	MALDI	127
Au_{279}	S	$[Au_{279}(TBBT)_{84}]$	510	MALDI	128

Table 2: Terms and Abbreviations.

Term	Abbreviations
Ligand exchange-induced size/structure transformation	LEIST
Cambridge Crystallographic Data Centre	CCDC
Electron diffraction	ED
Extended X-ray absorption fine structure	EXFAS
Scanning transmission electron microscopy	STEM
1,8-bis(diphenylphosphino)octane	dppo
1,3-propanediylbis(diphenylphosphine)	dppp
1,3-bis(diethylphosphino)propane	depp
1,5-bis(diphenylphosphino)pentane	dpppe
1,6-bis(diphenylphosphino)hexane	dpph
1,2-bis(diphenylphosphino)ethane	dppp
Self-assembled monolayers	SAMs
Tetraoctylammonium bromide	TOABr
Tetrahydrofuran	THF
Phenylethanethiolate	PET
4-tert-butylbenzenethiolate	TBBT
High performance liquid chromatography	HPLC
Polyacrylamide gel electrophoresis	PAGE
Phenylacetylene	PA
Highest occupied molecular orbital	HOMO
Lowest unoccupied molecular orbital	LUMO
1,1′-bis(diphenylphosphino)ferrocene	dppf
Electrospray ionization	ESI
Matrix-assisted laser desorption ionization	MALDI
Nuclear magnetic resonance	NMR
trans-2-[3-(4-tert-butylphenyl)-2-methyl-2-propenylidene]malononitrile	DCTB
Laser desorption ionization	LDI
Ion mobility–mass spectrometry	IM-MS
Energy collision-induced dissociation	CID
penta(ethylene glycol) thiolate	SPEG

(continued)

Table 2 (continued)

Term	Abbreviations
Time-dependent density functional theory	TD-DFT
Face-centred cubic	fcc
Single-crystal X-ray crystallography	SXRD
Aberration-corrected electron microscopy	AC-TEM
Diffusion-ordered NMR spectroscopy	DOSY
X-Ray photoelectron spectroscopy	XPS
X-ray absorption spectroscopy	XAS
X-ray absorption near-edge structure	XANES
Powder X-ray diffraction spectroscopy	PXRD
bis(dipheny1-phosphino) methane	dppmH
bis-(diphenylphosphino)methane	Dppm
Bis(diphenylphosphino)amine	Hdppa
Adamantanethiolate	S-Adm
2-Methylbenzenethiolate	o-MBT
2,4-Dimethylbenzenethiol	DMBT
p-Mercaptobenzoic acid	p-MBA
p-Methylbenzenethiolate	p-MBT

References

[1] Jin R, Zeng C, Zhou M, Chen Y. Atomically precise colloidal metal nanoclusters and nanoparticles: fundamentals and opportunities. Chem Rev. 2016;116(18):10346–413.

[2] Chakraborty I, Pradeep T. Atomically precise clusters of noble metals: emerging link between atoms and nanoparticles. Chem Rev. 2017;117(12):8208–71.

[3] Jin R. Atomically precise metal nanoclusters: stable sizes and optical properties. Nanoscale. 2015;7(5):1549–65.

[4] Fang J, Zhang B, Yao Q, Yang Y, Xie J, Yan N. Recent advances in the synthesis and catalytic applications of ligand-protected, atomically precise metal nanoclusters. Coord Chem Rev. 2016;322:1–29.

[5] Li G, Jin R. Atomically precise gold nanoclusters as new model catalysts. Acc Chem Res. 2013;46(8):1749–58.

[6] Pensa E, Cortes E, Corthey G, Carro P, Vericat C, Fonticelli MH, et al. The chemistry of the sulfur-gold interface: in search of a unified model. Acc Chem Res. 2012;45(8):1183–92.

[7] Yu Y, Luo Z, Chevrier DM, Leong DT, Zhang P, Jiang D-E, et al. Identification of a highly luminescent $Au_{22}(SG)_{18}$ nanocluster. J Am Chem Soc. 2014;136(4):1246–49.

[8] Liu P, Qin R, Fu G, Zheng N. Surface coordination chemistry of metal nanomaterials. J Am Chem Soc. 2017;139(6):2122–31.

[9] Li G, Abroshan H, Liu C, Zhuo S, Li Z, Xie Y, et al. Tailoring the electronic and catalytic properties of Au_{25} nanoclusters via ligand engineering. ACS Nano. 2016;10(8):7998–8005.

[10] Mingos DMP, Broda J. Gold clusters, colloids and nanoparticles I, vol. 161. Cham: Springer, 2014.

[11] Briant CE, Theobald BRC, White JW, Bell LK, Mingos DMP, Welch AJ. Synthesis and X-Ray structural characterization of the centered icosahedral gold cluster compound $Au_{13}(PMe_2Ph)_{10}Cl_2(PF_6)_3^-$ the realization of a theoretical prediction. Chem Commun. 1981;5:201–02.

[12] Jadzinsky PD, Calero G, Ackerson CJ, Bushnell DA, Kornberg RD. Structure of a thiol monolayer-protected gold nanoparticle at 1.1 Å resolution. Science. 2007;318(5849): 430–33.

[13] Koshevoy IO, Lin C-L, Karttunen AJ, Haukka M, Shih C-W, Chou P-T, et al. Octanuclear gold(I) alkynyl-diphosphine clusters showing thermochromic luminescence. Chem Commun. 2011;47(19):5533–35.

[14] McPartlin M, Mason R, Malatesta L. Novel cluster complexes of gold(0)–gold(I). J Chem Soc D: Chem Commun. 1969;7:334–334.

[15] Albano VG, Bellon PL, Manassero M, Sansoni M. Intermetallic pattern in metal-atom clusters-structural studies on $Au_{11}X_3(PR_3)_7$ species. Chem Commun. 1970;18:1210–11.

[16] Briant CE, Hall KP, Mingos DMP. Synthesis and structural characterisation of $[Au_6(PPh_3)_6]^{-}(NO_3)_2{\cdot}3CH_2Cl_2$; an edge-shared bitetrahedral gold cluster. J Organomet Chem. 1983;254(1): C18–C20.

[17] Briant CE, Hall KP, Mingos DMP, Wheeler AC. Synthesis and structural characterisation of hexakis (triphenyl phosphine) hexagold (2+) nitrate, $[Au_6(PPh_3)6][NO_3]_2$, and related clusters with edgesharing bitetrahedral geometries. J Chem Soc Dalton Trans. 1986;3:687–92.

[18] Hall KP, Theoblad BR, Gilmour DI, Mingos DMP, Welch AJ. Synthesis and structural characterization of $[Au_9\{P(p\text{-}C_6H_4OMe)_3\}_8](BF_4)_3$; a cluster with a centred crown of gold atoms. J Chem Soc Chem Commun. 1982;10:528–30.

[19] Wen F, Englert U, Gutrath B, Simon U. Crystal structure, electrochemical and optical properties of $Au_9(PPh_3)_8(NO_3)_3$. Eur J Inorg Chem. 2008;1:106–11.

[20] Briant CE, Hall KP, Wheeler AC, Mingos DMP. Structural characterization of $Au_{10}Cl_3(PCy_2Ph)_6(NO_3)$ (Cy = Cyclohexyl) and the development of a structural principle for high nuclearity gold clusters. J Chem Soc Chem Commun. 1984;4:248–50.

[21] Van Der Velden J, Vollenbroek F, Bour J, Beurskens P, Smits J, Bosnian W. Gold clusters containing bidentate phosphine ligands. Preparation and X-Ray structure investigation of $[Au_5(dppmH)_3(dppm)](NO_3)_2$ and $[Au_{13}(dppmH)_6](NO_3)_n$. Recueil Des Travaux Chimiques Des Pays-Bas. 1981;100(4):148–52.

[22] Gutrath BS, Oppel IM, Presly O, Beljakov I, Meded V, Wenzel W, et al. $Au_{14}(PPh_3)_8(NO_3)_4$: an example of a new class of $Au(NO_3)$-Ligated superatom complexes. Angewandte Chemie-Int Edition. 2013;52(12):3529–32.

[23] Teo BK, Shi XB, Zhang H. Pure gold cluster of 1-9-9-1-9-9-1 layered structure – A novel 39-Metal-Atom cluster $(Ph_3P)_{14}Au_{39}Cl_6Cl_2$ with an interstitial gold atom in a hexagonal antiprismatic cage. J Am Chem Soc. 1992;114(7):2743–45.

[24] Maoz R, Cohen SR, Sagiv J. Nanoelectrochemical patterning of monolayer surfaces. Toward Spatially Defined Self-Assembly Nanostructures, Advanced Materials. 1999;11 (1):55–61.

[25] Jian N, Stapelfeldt C, Hu K-J, Fröba M, Palmer RE. Hybrid atomic structure of the Schmid cluster $Au_{55}(PPh_3)_{12}Cl_6$ resolved by aberration-corrected STEM. Nanoscale. 2015;7(3):885–88.

[26] Chen J, Zhang Q-F, Williard PG, Wang L-S. Synthesis and structure determination of a new Au_{20} nanocluster protected by tripodal tetraphosphine ligands. Inorg Chem. 2014; 53(8):3932–34.

[27] Wan X-K, Yuan S-F, Lin Z-W, Wang Q-M. A chiral gold nanocluster Au_{20} protected by tetradentate phosphine ligands. Angewandte Chemie. 2014;126(11):2967–70.

[28] Chen J, Zhang Q-F, Bonaccorso TA, Williard PG, Wang L-S. Controlling gold nanoclusters by diphospine ligands. J Am Chem Soc. 2014;136(1):92–95.

[29] Pettibone JM, Hudgens JW. Synthetic approach for tunable, size-selective formation of monodisperse, diphosphine-protected gold nanoclusters. J Phys Chem Lett. 2010;1(17):2536–40.

[30] Hudgens JW, Pettibone JM, Senftle TP, Bratton RN. Reaction mechanism governing formation of 1,3-bis (diphenylphosphino)propane-protected gold nanoclusters. Inorg Chem. 2011;50 (20):10178–89.

[31] Pettibone JM, Hudgens JW. Gold cluster formation with phosphine ligands: etching as a size-selective synthetic pathway for small clusters?. ACS Nano. 2011;5(4):2989–3002.

[32] Bertino MF, Sun Z-M, Zhang R, Wang L-S. Facile syntheses of monodisperse ultrasmall Au clusters. J Phys Chem B. 2006;110(43):21416–18.

[33] Golightly JS, Gao L, Castleman AW, Bergeron DE, Hudgens JW, Magyar RJ, et al. Impact of swapping ethyl for phenyl groups on diphosphine-protected undecagold. J Phys Chem C. 2007;111(40):14625–27.

[34] Bain CD, Troughton EB, Tao YT, Evall J, Whitesides GM, Nuzzo RG. Formation of monolayer films by the spontaneous assembly of organic thiols from solution onto gold. J Am Chem Soc. 1989;111(1):321–35.

[35] Jin R. Quantum sized, thiolate-protected gold nanoclusters. Nanoscale. 2010;2(3):343–62.

[36] Brust M, Walker M, Bethell D, Schiffrin DJ, Whyman R. Synthesis of thiol-derivatized gold nanoparticles in a 2-Phase liquid-liquid system. J Chem Soc Chem Commun. 1994;7:801–02.

[37] Jin R, Qian H, Wu Z, Zhu Y, Zhu M, Mohanty A, et al. Size focusing: a methodology for synthesizing atomically precise gold nanoclusters. J Phys Chem Lett. 2010;1(19):2903–10.

[38] Wu Z, MacDonald MA, Chen J, Zhang P, Jin R. Kinetic control and thermodynamic selection in the synthesis of atomically precise gold nanoclusters. J Am Chem Soc. 2011;133 (25):9670–73.

[39] Zeng C, Qian H, Li T, Li G, Rosi NL, Yoon B, et al. Total structure and electronic properties of the gold nanocrystal $Au_{36}(SR)_{24}$. Angewandte Chemie-Int Ed. 2012;51(52):13114–18.

[40] Zeng C, Li T, Das A, Rosi NL, Jin R. Chiral structure of thiolate-protected 28-Gold-Atom nanocluster determined by X-ray crystallography. J Am Chem Soc. 2013;135(27):10011–13.

[41] Zeng C, Chen Y, Kirschbaum K, Appavoo K, Sfeir MY, Jin R. Structural patterns at all scales in a nonmetallic chiral $Au_{133}(SR)_{52}$ nanoparticle. Sci Adv. 2015;1(2):e1500045–e1500045.

[42] Negishi Y, Nobusada K, Tsukuda T. Glutathione-protected gold clusters revisited: bridging the gap between gold(I)-thiolate complexes and thiolate-protected gold nanocrystals. J Am Chem Soc. 2005;127(14):5261–70.

[43] Tsunoyama H, Negishi Y, Tsukuda T. Chromatographic isolation of “missing” Au_{55} clusters protected by alkanethiolates. J Am Chem Soc. 2006;128(18):6036–37.

[44] Qian H, Zhu Y, Jin R. Isolation of ubiquitous $Au_{40}(SR)_{24}$ clusters from the 8 kDa gold clusters. J Am Chem Soc. 2010;132(13):4583–85.

[45] Knoppe S, Boudon J, Dolamic I, Dass A, Buergi T. Size exclusion chromatography for semipreparative scale separation of $Au_{38}(SR)_{24}$ and $Au_{40}(SR)_{24}$ and larger clusters. Anal Chem. 2011;83 (13):5056–61.

[46] Qian H, Jin R. Synthesis and electrospray mass spectrometry determination of thiolate-protected $Au_{55}(SR)_{31}$ nanoclusters. Chem Commun. 2011;47(41):11462–64.

[47] Nimmala PR, Yoon B, Whetten RL, Landman U, Dass A. $Au_{67}(SR)_{35}$ nanomolecules: characteristic size-specific optical, electrochemical, structural properties and first-principles theoretical analysis. J Phys Chem. 2013;117(2):504–17.

[48] Maity P, Tsunoyama H, Yamauchi M, Xie S, Tsukuda T. Organogold clusters protected by phenylacetylene. J Am Chem Soc. 2011;133(50):20123–25.

[49] Maity P, Wakabayashi T, Ichikuni N, Tsunoyama H, Xie S, Yamauchi M, et al. Selective synthesis of organogold magic clusters $Au_{54}(C \equiv CPh)_{26}$. Chem Commun. 2012;48(49):6085–87.

[50] Wan X-K, Guan Z-J, Wang Q-M. Homoleptic Alkynyl-Protected gold nanoclusters: $au_{44}(PhC \equiv C)_{28}$ and $Au_{36}(PhC \equiv C)_{24}$. Angewandte Chemie-Int Ed. 2017;56(38):11494–97.

[51] Negishi Y, Kurashige W, Kamimura U. Isolation and structural characterization of an octane-selenolate-protected Au_{25} cluster. Langmuir. 2011;27(20):12289–92.

[52] Xu Q, Wang S, Liu Z, Xu G, Meng X, Zhu M. Synthesis of selenolate-protected $Au_{18}(SeC_6H_5)_{14}$ nanoclusters. Nanoscale. 2013;5(3):1176–82.

[53] Song Y, Zhong J, Yang S, Wang S, Cao T, Zhang J, et al. Crystal structure of $Au_{25}(SePh)_{18}$ nanoclusters and insights into their electronic, optical and catalytic properties. Nanoscale. 2014;6(22):13977–85.

[54] Song Y, Wang S, Zhang J, Kang X, Chen S, Li P, et al. Crystal structure of selenolate-protected $Au_{24}(SeR)_{20}$ nanocluster. J Am Chem Soc. 2014;136(8):2963–65.

[55] Takagi N, Ishimura K, Matsui M, Fukuda R, Matsui T, Nakajima T, et al. How can we understand au_8 cores and entangled ligands of selenolate- and thiolate-protected gold nanoclusters $Au_{24}(ER)_{20}$ and $Au_{20}(ER)_{16}$ (E = Se, S; R = Ph, Me)? A theoretical study. J Am Chem Soc. 2015; 137(26):8593–602.

[56] Kurashige W, Yamazoe S, Kanehira K, Tsukuda T, Negishi Y. Selenolate-Protected Au_{38} nanoclusters: isolation and structural characterization. J Phys Chem Lett. 2013;4(18):3181–85.

[57] Kurashige W, Yamaguchi M, Nobusada K, Negishi Y. Ligand-Induced stability of gold nanoclusters: thiolate versus Selenolate. J Phys Chem Lett. 2012;3(18):2649–52.

[58] Das A, Li T, Nobusada K, Zeng Q, Rosi NL, Jin R. Total structure and optical properties of a phosphine/thiolate-protected Au_{24} nanocluster. J Am Chem Soc. 2012;134(50):20286–89.

[59] Nunokawa K, Onaka S, Ito M, Horibe M, Yonezawa T, Nishihara H, et al. Synthesis, single crystal X-ray analysis, and TEM for a single-sized Au_{11} cluster stabilized by SR ligands: the interface between molecules and particles. J Organomet Chem. 2006;691(4):638–42.

[60] Shichibu Y, Negishi Y, Watanabe T, Chaki NK, Kawaguchi H, Tsukuda T. Biicosahedral gold clusters $Au_{25}(PPh_3)_{10}(SC_nH_{2n+1})_5Cl_2^{2+}$ (n=2-18): A stepping stone to cluster-assembled materials. J Phys Chem C. 2007;111(22):7845–47.

[61] Qian H, Eckenhoff WT, Bier ME, Pintauer T, Jin R. Crystal structures of Au_2 complex and Au_{25} nanocluster and mechanistic insight into the conversion of polydisperse nanoparticles into monodisperse Au_{25} nanoclusters. Inorg Chem. 2011;50(21):10735–39.

[62] Jin R, Liu C, Zhao S, Das A, Xing H, Gayathri C, et al. Tri-icosahedral gold nanocluster $Au_{37}(PPh_3)_{10}(SC_2H_4Ph)_{10}X_2^+$: linear assembly of icosahedral building blocks. ACS Nano. 2015; 9(8):8530–36.

[63] Teo BK, Zhang H. Synthesis and structure of a neutral trimetallic biicosahedral cluster, $(Ph_3P)_{10}Au_{11}Ag_{12}Pt_2Cl_7$. A comparative study of molecular and crystal structures of vertex-sharing biicosahedral mixed-metal nanoclusters. J Cluster Sci. 2001;12(1):349–83.

[64] Kang X, Song Y, Deng H, Zhang J, Liu B, Pan C, et al. Ligand-induced change of the crystal structure and enhanced stability of the Au_{11} nanocluster. RSC Adv. 2015;5(82):66879–85.

[65] Wan X-K, Tang Q, Yuan S-F, Jiang D-E, Wang Q-M. Au_{19} nanocluster featuring a V-shaped Alkynyl-Gold motif. J Am Chem Soc. 2015;137(2):652–55.

[66] Wan X-K, Yuan S-F, Tang Q Jiang D-E, Wang Q-M. Alkynyl-protected Au_{23} nanocluster: A 12-electron system. Angewandte Chemie-Int Ed. 2015;54(20):5977–80.

[67] Wan X-K, Xu WW, Yuan S-F, Gao Y, Zeng X-C, Wang Q-M. A near-infrared-emissive Alkynyl-protected Au_{24} nanocluster. Angewandte Chemie-Int Ed. 2015;54(33):9683–86.

[68] Canales F, Gimeno MC, Laguna A, Jones PG. Aurophilicity at sulfur centers. Synthesis and reactivity of the complex $S(Au_2dppf)$; Formation of polynuclear sulfur-centered complexes. Crystal structures of $S(Au_2dppf)$ center dot $2CHCl_3$, (mu-Au_2dppf){$S(Au_2dppf)$}$_2(OTf)_2$ center dot $8CHCl_3$, and $S(AuPPh_2Me)_2(Au_2dppf)(ClO_4)_2$ center dot $3CH_2Cl_2$. J Am Chem Soc. 1996; 118(20):4839–45.

[69] Canales F, Gimeno C, Laguna A, Villacampa MD. Aurophilicity at sulfur centers. Synthesis of the polyaurated species $S(AuPR_3)_n^{(n-2)+}$ (n=2–6). Inorganica Chim Acta. 1996;244(1):95–103.

[70] Yam VWW, Cheng ECC, Zhu NY. A novel polynuclear gold-sulfur cube with an unusually large Stokes shift. Angewandte Chemie-Int Ed. 2001;40(9):1763–65.

[71] Lee TK-M, Zhu N, Yam V-W-W. An unprecedented luminescent polynuclear gold(I) mu(3)-Sulfido cluster with a thiacrown-like architecture. J Am Chem Soc. 2010;132(50):17646–48.

[72] Hau FK-W, Lee TK-M, Cheng E-C-C, Au VK-M, Yam V-W-W. Luminescence color switching of supramolecular assemblies of discrete molecular decanuclear gold(I) sulfido complexes. Proc Natl Acad Sci U S A. 2014;111(45):15900–05.

[73] Kenzler S, Schrenk C, Schnepf A. $Au_{108}S_{24}(PPh_3)_{16}$: a highly symmetric nanoscale gold cluster confirms the general concept of metalloid clusters. Angewandte Chemie-Int Ed. 2017;56(1): 393–96.

[74] Crasto D, Malola S, Brosofsky G, Dass A, Hakkinen H. Single crystal XRD structure and theoretical analysis of the chiral $Au_{30}S(S\text{-}t\text{-}Bu)_{18}$ cluster. J Am Chem Soc. 2014;136(13):5000–05.

[75] Kenzler S, Schrenk C, Frojd AR, Hakkinen H, Clayborne AZ, Schnepf A. Au70S20(PPh3)12: an intermediate sized metalloid gold cluster stabilized by the Au4S4 ring motif and Au-PPh3 groups. Chem Commun. 2018;54:248–51.

[76] Song Y, Fu F, Zhang J, Chai J, Kang X, Li P, et al. The magic Au_{60} nanocluster: a new cluster-assembled material with five Au_{13} building blocks. Angewandte Chemie-Int Ed. 2015; 54(29):8430–34.

[77] Dass A, Holt K, Parker JF, Feldberg SW, Murray RW. Mass spectrometrically detected statistical aspects of ligand populations in mixed monolayer $Au_{25}L_{18}$ nanoparticles. J Phys Chem C. 2008;112(51):20276–83.

[78] Dass A, Stevenson A, Dubay GR, Tracy JB, Murray RW. Nanoparticle MALDI-TOF mass spectrometry without fragmentation: $au_{25}(SCH_2CH_2Ph)_{18}$ and mixed monolayer $Au_{25}(SCH_2CH_2Ph)_{18\text{-}x}(L)_x$. J Am Chem Soc. 2008;130(18):5940–46.

[79] Tracy JB, Crowe MC, Parker JF, Hampe O, Fields-Zinna CA, Dass A, et al. Electrospray ionization mass spectrometry of uniform and mixed monolayer nanoparticles: $au_{25}(S(CH_2)_2Ph)_{18}$ and $Au_{25}(S(CH_2)_2Ph)_{18\text{-}x}(SR)_x$. J Am Chem Soc. 2007;129(51):16209–15.

[80] Negishi Y, Chaki NK, Shichibu Y, Whetten RL, Tsukuda T. Origin of magic stability of thiolated gold clusters: A case study on $Au_{25}(SC_6H_{13})_{18}$. J Am Chem Soc. 2007;129(37):11322–23.

[81] Harkness KM, Cliffel DE, McLean JA. Characterization of thiolate-protected gold nanoparticles by mass spectrometry. Analyst. 2010;135(5):868–74.

[82] Fields-Zinna CA, Sampson JS, Crowe MC, Tracy JB, Parker JF, deNey AM, et al. Tandem mass spectrometry of thiolate-protected Au nanoparticles $Na_xAu_{25}(SC_2H_4Ph)_{18\text{-}y}(S(C_2H_4O)_5CH_3)_y$. J Am Chem Soc. 2009;131(38):13844–51.

[83] Chaki NK, Negishi Y, Tsunoyama H, Shichibu Y, Tsukuda T. Ubiquitous 8 and 29 kDa gold: alkanethiolate cluster compounds: mass-spectrometric determination of molecular formulas and structural implications. J Am Chem Soc. 2008;130(27):8608–09.

[84] Zhu M, Lanni E, Garg N, Bier ME, Jin R. Kinetically controlled, high-yield synthesis of Au_{25} clusters. J Am Chem Soc. 2008;130(4):1138–39.

[85] Tracy JB, Kalyuzhny G, Crowe MC, Balasubramanian R, Choi J-P, Murray RW. Poly(ethyleneglycol) ligands for high-resolution nanoparticle mass spectrometry. J Am Chem Soc. 2007; 129(21):6706–07.

[86] Zhu M, Aikens CM, Hollander FJ, Schatz GC, Jin R. Correlating the crystal structure of a thiol-protected Au_{25} cluster and optical properties. J Am Chem Soc. 2008;130(18):5883–85.

[87] Devadas MS, Bairu S, Qian H, Sinn E, Jin R, Ramakrishna G. Temperature-dependent optical absorption properties of monolayer-protected Au_{25} and Au_{38} clusters. J Phys Chem Lett. 2011; 2(21):2752–58.

[88] Li ZY, Young NP, Di Vece M, Palomba S, Palmer RE, Bleloch AL, et al. Three-dimensional atomic-scale structure of size-selected gold nanoclusters. Nature. 2008;451(7174):46–U2.

[89] Salorinne K, Lahtinen T, Koivisto J, Kalenius E, Nissinen M, Pettersson M, et al. Nondestructive size determination of thiol-stabilized gold nanoclusters in solution by diffusion ordered NMR spectroscopy. Anal Chem. 2013;85(7):3489–92.

[90] Terrill RH, Postlethwaite TA, Chen C-H, Poon C-D, Terzis A, Chen A, et al. Monolayers in three dimensions: NMR, SAXS, thermal, and electron hopping studies of alkanethiol stabilized gold clusters. J Am Chem Soc. 1995;117(50):12537–48.

[91] Parker JF, Choi J-P, Wang W, Murray RW. Electron self-exchange dynamics of the nanoparticle couple $Au_{25}(SC_2Ph)_{18}{}^{0/1-}$ by nuclear magnetic resonance line-broadening. J Phys Chem C. 2008;112(36):13976–81.

[92] Qian H, Zhu M, Gayathri C, Gil RR, Jin R. Chirality in gold nanoclusters probed by NMR spectroscopy. ACS Nano. 2011;5(11):8935–42.

[93] Goulet PJG, Lennox RB. New insights into Brust-Schiffrin metal nanoparticle synthesis. J Am Chem Soc. 2010;132(28):9582–84.

[94] Li Y, Zaluzhna O, Xu B, Gao Y, Modest JM, Tong YJ. Mechanistic insights into the Brust-Shiffrin two-phase synthesis of organo-chalcogenate-protected metal nanoparticles. J Am Chem Soc. 2011;133(7):2092–95.

[95] Wu Z, Jin R. Stability of the two Au– S binding modes in $Au_{25}(SG)_{18}$ nanoclusters probed by NMR and optical spectroscopy. ACS Nano. 2009;3(7):2036–42.

[96] Wu Z, Gayathri C, Gil RR, Jin R. Probing the structure and charge state of glutathione-capped $Au_{25}(SG)_{18}$ clusters by NMR and mass spectrometry. J Am Chem Soc. 2009; 131(18):6535–42.

[97] Venzo A, Antonello S, Gascon JA, Guryanov I, Leapman RD, Perera NV, et al. Effect of the charge state (z =-1, 0, +1) on the nuclear magnetic resonance of monodisperse $Au_{25}(S(CH_2)_2Ph_{18})^z$ clusters. Anal Chem. 2011;83(16):6355–62.

[98] Clayden NJ, Dobson CM, Hall KP, Mingos DMP, Smith DJ. Studies of gold cluster compounds using high-resolution ^{31}P solid-state nuclear magnetic resonance spectroscopy. J Chem Soc Dalton Trans. 1985;9:1811–14.

[99] Tanaka A, Takeda Y, Imamura M, Sato S. Dynamic final-state effect on the Au_{4f} core-level photoemission of dodecanethiolate-passivated Au nanoparticles on graphite substrates. Phys Rev B. 2003;68(19):195415.

[100] Yao T, Sun Z, Li Y, Pan Z, Wei H, Xie Y, et al. Insights into initial kinetic nucleation of gold nanocrystals. J Am Chem Soc. 2010;132(22):7696–701.

[101] Yamazoe S, Takano S, Kurashige W, Yokoyama T, Nitta K, Negishi Y, et al. Hierarchy of bond stiffnesses within icosahedral-based gold clusters protected by thiolates. Nat Commun. 2016;7:10414.

[102] Zhang P. X-ray spectroscopy of gold-thiolate nanoclusters. J Phys Chem C. 2014;118(44): 25291–99.

[103] Li Y, Cheng H, Yao T, Sun Z, Yan W,Jiang Y, et al. Hexane-driven icosahedral to cuboctahedral structure transformation of gold nanoclusters. J Am Chem Soc. 2012; 134(43):17997–8003.

[104] Jiang Y, Huang Y, Cheng H, Liu Q, Xie Z, Yao T, et al. Solvent influence on the role of thiols in growth of thiols-capped Au nanocrystals. J Phys Chem C. 2014;118(1):714–19.

[105] Wu Z, Chen J, Jin R. One-pot synthesis of $Au_{25}(SG)_{18}$, 2- and 4-nm gold nanoparticles and comparison of their size-dependent properties. Adv Funct Mater. 2011;21(1):177–83.

[106] Demartin F, Manassero M, Naldini L, Ruggeri R, Sansoni M. Synthesis and X-Ray characterization of an iodine-bridged tetranuclear gold cluster, Di-Mu-Iodo-Tetrakis(Triphenylphosphine)-Tetrahedro-Tetragold. J Chem Soc Chem Commun. 1981;5:222–23.

[107] Vandervelden JWA, Bour JJ, Vollenbroek FA, Beurskens PT, Smits JMM. Synthesis of a new pentanuclear gold cluster by metal evaporation. Preparation and X-ray structure determination

of [tris{bis(diphenylphosphino) methane}][bis(diphenylphosphino)methanido]pentagold dinitrate. J Chem Soc Chem Commun. 1979;24:1162–63.

[108] Vandervelden JWA, Beurskens PT, Bour JJ, Bosman WP, Noordik JH, Kolenbrander M, et al. Intermediates in the formation of gold clusters – Preparation and X-Ray-analysis of $Au_7(PPh_3)_7^+$ and synthesis and characterization of $Au_8(PPh_3)_6IPf_6$. Inorg Chem. 1984;23(2): 146–51.

[109] Bellon PL, Cariati F, Manassero M, Naldini L, Sansoni M. Novel gold clusters – Preparation, properties, and X-Ray structure determination of salts of Octakis(Triarylphosphine) enneagold, $Au_9L_8X_3$. Chem Commun. 1971;22:1423–24.

[110] Jin S, Du W, Wan S, Kang X, Chen M, Hu D, et al. Thiol-induced synthesis of phosphine-protected gold nanoclusters with atomic precision and controlling the structure by ligand/metal engineering. Inorg Chem. 2017;56(18):11151–59.

[111] Chen S, Wang S, Zhong J, Song Y, Zhang J, Sheng H, et al. The structure and optical properties of the $Au_{18}(SR)_{14}$ nanocluster. Angewandte Chemie-Int Ed. 2015;54(10):3145–49.

[112] Zeng C, Liu C, Chen Y, Rosi NL, Jin R. Gold-Thiolate ring as a protecting motif in the $Au_{20}(SR)_{16}$ nanocluster and implications. J Am Chem Soc. 2014;136(34):11922–25.

[113] Chen S, Xiong L, Wang S, Ma Z, Jin S, Sheng H, et al. Total structure determination of $Au_{21}(S\text{-}Adm)_{15}$ and geometrical/electronic structure evolution of thiolated gold nanoclusters. J Am Chem Soc. 2016;138(34):10754–57.

[114] Das A, Li T, Nobusada K, Zeng C, Rosi NL, Jin R. Nonsuperatomic $Au_{23}(SC_6H_{11})_{16}^-$ nanocluster featuring bipyramidal Au_{15} kernel and trimeric $Au_3(SR)_4$ motif. J Am Chem Soc. 2013;135(49):18264–67.

[115] Crasto D, Barcaro G, Stener M, Sementa L, Fortunelli A, Dass A. $Au_{24}(SAdm)_{16}$ nanomolecules: X-ray crystal structure, theoretical analysis, adaptability of adamantane ligands to form $Au_{23}(SAdm)_{16}$ and $Au_{25}(SAdm)_{16}$, and its relation to $Au_{25}(SR)_{18}$. J Am Chem Soc. 2014;136(42):14933–40.

[116] Yang S, Chai J, Song Y, Kang X, Sheng H, Chong H, et al. A new crystal structure of Au_{36} with a Au_{14} kernel cocapped by Thiolate and Chloride. J Am Chem Soc. 2015;137(32):10033–35.

[117] Qian H, Eckenhoff WT, Zhu Y, Pintauer T, Jin R. Total structure determination of thiolate-protected Au_{38} nanoparticles. J Am Chem Soc. 2010;132(24):8280–81.

[118] Liu C, Li T, Li G, Nobusada K, Zeng C, Pang G, et al. Observation of body-centered cubic gold nanocluster. Angewandte Chemie-Int Ed. 2015;54(34):9826–29.

[119] Zeng C, Chen Y, Liu C, Nobusada K, Rosi NL, Jin R. Gold tetrahedra coil up: kekule-like and double helical superstructures. Sci Adv. 2015;1(9):e1500425.

[120] Liao L, Zhuang S, Yao C, Yan N, Chen J, Wang C, et al. Structure of chiral $Au_{44}(2,4\text{-}DMBT)_{26}$ nanocluster with an 18-Electron shell closure. J Am Chem Soc. 2016;138(33):10425–28.

[121] Gan Z, Chen J, Wang J, Wang C, Li M-B, Yao C, et al. The fourth crystallographic closest packing unveiled in the gold nanocluster crystal. Nat Commun. 2017;8:14739–44.

[122] Zeng C, Liu C, Chen Y, Rosi NL, Jin R. Atomic structure of self-assembled monolayer of thiolates on a tetragonal Au_{92} nanocrystal. J Am Chem Soc. 2016;138(28):8710–13.

[123] Higaki T, Liu C, Zhou M, Luo T-Y, Rosi NL, Jin R. Tailoring the structure of 58-Electron gold nanoclusters: $au_{103}S_2(S\text{-}Nap)_{41}$ and its implications. J Am Chem Soc. 2017;139(29): 9994–10001.

[124] Chen Y, Zeng C, Liu C, Kirschbaum K, Gayathri C, Gil RR, et al. Crystal structure of barrel-shaped chiral $Au_{130}(p\text{-}MBT)_{50}$ nanocluster. J Am Chem Soc. 2015;137(32):10076–79.

[125] Zeng C, Chen Y, Kirschbaum K, Lambright KJ, Jin R. Emergence of hierarchical structural complexities in nanoparticles and their assembly. Science. 2016;354(6319):1580–84.

[126] Sakthivel NA, Theivendran S, Ganeshraj V, Oliver AG, Dass A. Crystal structure of faradaurate-279: $au_{279}(SPh\text{-}tBu)_{84}$ plasmonic nanocrystal molecules. J Am Chem Soc. 2017;139(43): 15450–59.

Bionotes

Professor Jiangwei Zhang received his BSc from Beijing University of Chemical Technology (2011) and PhD from Tsinghua University in 2016. He joined State Key Laboratory of Catalysis, Dalian Institute of Chemical Physics, Chinese Academy of Sciences (CAS) as an assisstant professor in 2016. His research interests is synthesis of cluster-based organic-inorganic hybrids materials.

Zhimin Li received her BSc in chemistry from Lanzhou University in 2014. She is currently a PhD candidate under the supervision of professor Gao Li from State Key Laboratory of Catalysis, Dalian Institute of Chemical Physics, CAS. Her research interests is synthesis of oxide-supported Au/Pt cluster catalysts and their catalytic applications.

Kai Zheng received his BSc in applied chemistry from China University Geosciences, Wuhan in 2011. He is currently a PhD candidate under the supervision of Prof. Gao Li from State Key Laboratory of Catalysis, Dalian Institute of Chemical Physics, CAS. His research focused on the synthesis of ligand-protected Au clusters and their applications.

Professor Gao Li received his BSc (2004) from Hunan Normal University, and PhD (2016) from Shanghai Jiaotong University. After his postdoctoral research in Carnegie Mellon University (United States, 2011-2014), he joined State Key Laboratory of Catalysis, Dalian Institute of Chemical Physics, CAS as a professor in 2014. His current research interests focused on the preparation and application of metal clusters.

Index

https://doi.org/10.1515/9783110345100-006